ResearchOnline@JCU

JAMES COOK UNIVERSITY AUSTRALIA

This file is part of the following work:

Vithana, Vidushi Prabhashwari (2025) ***Rare earth metal corrosion inhibitors: synthesis, structure, and corrosion inhibiting properties.*** **PhD Thesis, James Cook University.**

Access to this file is available from:

https://doi.org/10.25903/zqax%2Dkc60

Copyright © 2025 Vidushi Prabhashwari Vithana

The author has certified to JCU that they have made a reasonable effort to gain permission and acknowledge the owners of any third party copyright material included in this document. If you believe that this is not the case, please email researchonline@jcu.edu.au

Rare Earth Metal Corrosion Inhibitors: Synthesis, structure, and corrosion inhibiting properties

A thesis submitted for the degree of

Doctor of Philosophy

by

Vidushi Prabhashwari Vithana

B.Sc. (Hons) in Chemistry

College of Science and Engineering

James Cook University

January 2025



When you're nervous about stepping outside of your comfort zone, remind yourself:
"it feels scary because it's unfamiliar, not because I'm in capable."

-@MichellCClark-

Declaration

I hereby declare that this Ph.D. thesis is my own original work and has not been submitted, in whole or in part, for any other degree or diploma at any university or institution of higher education. All information derived from the published and unpublished work of others has been properly acknowledged in the text, and a complete list of references is provided.

Vidushi Prabhashwai Vithana

College of Science and Engineering

James Cook University

Acknowledgements

Completing this Ph.D. has been a significant journey, and I am deeply grateful to all those who have supported me along the way. First and foremost, I would like to express my sincere gratitude to my advisor, Prof. Peter Junk, for your continuous guidance, encouragement, and immense knowledge. Your unwavering support and belief in my capabilities have been crucial in the completion of this work. It was truly an honour to be part of the Junk group, sharing in the good times and memorable moments. From the very first day I contacted you, you have provided me with countless opportunities, not only in research but also in making the best life possible while being far away from home. Prof. Junk and Vicki will always hold a special place in my heart as my "Aussie parents".

I would like to express my deepest gratitude to Prof. Glen Deacon. Your guidance, insights, and constructive feedback have been invaluable throughout my Ph.D. journey. Whether it was reviewing my papers, providing suggestions, or giving feedback on presentations, you were always there to support me. You've played a significant role in helping me become a better scientific writer, and for that, I am forever grateful. I would also like to extend my appreciation to Dr. Murray Davis, my secondary supervisor. Thank you for always being there for me and involving me in demonstrations.

I am forever grateful to Dr. Zhifang Guo for all the support you've given me throughout my Ph.D. You have been an incredible friend, a big sister, and a mentor over the past three and half years. Thank you for your guidance, from giving me my first laboratory training to introducing me to air-sensitive techniques, assisting with reactions, and guiding me through crystallography. These experiences have greatly enriched my research, and I am deeply appreciative of all you've done. A heartfelt thanks to my fellow Junk group members, both past and present—especially Halim, Angus, Ramees, Ameen, and Naveena, transfer students Titouan and Thibaud, as well as my office mates Kalpani and Alex. I truly appreciate all your support and the wonderful memories we have shared. A special mention to my good friend Kalpani for your support and companionship.

My thanks also extend to the past and present physical science staff, including Associate Professor George Vamvounis for teaching me how to use the TGA instrument and for having me in demonstrations, Dr. Mark Robertson for your assistance with NMR spectroscopy, and Dr. Mark Barnes for his help with lab demonstrations.

I am grateful to Dr. Winnie Lee, Shiyoh Nobile, and Dr. Dana Roberts for their support during demonstration sessions. I have truly enjoyed your company in the teaching labs and

during our dinner nights. I would also like to thank Dr. Brendon Jones for his assistance in running X-ray powder diffractometer and to Dr. Joan Zapiter for her help with the NMR spectroscopy.

I sincere thanks go to Dr. Anthony E. Somers from Deakin University for conducting the electrochemical measurements to evaluate corrosion inhibitor performance. My gratitude also goes to Dr. David Turner for organizing Australian Synchrotron time for us during our visits to Melbourne.

To all my wonderful friends in Townsville, you've truly become my family here. I'm specially greatful to Piyumi akka, Niro ayya, Eranga, Viraj, Aloka, Yashith, Yashika and Sahan for your incredible support throughout our friendship and my studies—whether it was sharing in my joy, giving advice, or standing by me during challenging times. A special mention goes to Chathrika akka and Shakila ayya, my first friends in Townsville, for welcoming me warmly and being great friends from the beginning.

My deepest gratitude goes to my family (amma, thaththa, akka, and malli), whose unwavering support and unconditional love have been my source of strength throughout this journey. To my in-laws, aunties (nanda and sudu amma) and my girls Siya, Sandi and Chira, your constant encouragement has meant the world to me.

Last but not least, my husband and best friend, Thim, you are my rock. Thank you for standing by my side throughout this journey. I am beyond grateful for your patience, support, understanding, and love. You have been there to lift me up when I was down and to celebrate my successes, always encouraging me every step of the way.

Thank you all.

Statement of the Contribution of Others

This thesis included the following contribution from others:

Funding

Tuition fee offset, stipend and research costs: Australian Research Council Discovery Project grant (DP200100568).

Travel grants for conferences and the purchase of necessary research materials: Competitive research training (CRT) grants and Eric Booth Memorial Grants in Chemistry from the College of Science and Engineering, James Cook University.

Intellectual support

Thesis supervision: Professor Peter C. Junk and Dr. Murray Davis

Editorial Support: Professor Peter C. Junk, Professor Glen B. Deacon and Dr Zhifang Guo.

X-ray diffraction data collection, solving and refining of crystal structures: Dr. Zhifang Guo

Electrochemical studies: Dr. Anthony E. Somers

Output Related to the Thesis

Peer Reviewed publications

1. **V. P. Vithana**, Z. Guo, G. B. Deacon, A. E. Somers and P. C. Junk, Synthesis, Structure, and Corrosion Inhibiting Properties of REIII 3-Thiophenecarboxylate Complexes. *New J. Chem*. 2022, **46**, 19104–19111. (DOI: https://doi.org/10.1039/D2NJ03556A)

    - Featured on the front cover of the issue.

2. **V. P. Vithana**, Z. Guo, G. B. Deacon, A. E. Somers and P. C. Junk, RE(III) 3-Furoate Complexes: Synthesis, Structure, and Corrosion Inhibiting Properties. *Molecules* 2022, **27**, 8836. (DOI: https://doi.org/10.3390/molecules27248836)

3. **V. P. Vithana**, Z. Guo, G. B. Deacon, and P. C. Junk, Synthesis, structures, and corrosion inhibition of various alkali metal carboxylate complexes. *Molecules* 2023, **28**, 5515. (DOI: https://doi.org/10.3390/molecules28145515)

    - Highlighted the paper on the journal webpage.
    - Recognized as the most notable inorganic chemistry article for the period of June-August 2023

4. **V. P. Vithana**, Z. Guo, G. B. Deacon, and P. C. Junk, Rare Earth 2-Methyl-3-furoate Complexes: Effect of Steric Hindrance on Corrosion Inhibitor Properties. *Eur. J. Inorg. Chem.* 2024, e202300722. (DOI: https://doi.org/10.1002/ejic.202300722)

    - Featured on the front cover of the issue.

5. **V. P. Vithana**, Z. Guo, G. B. Deacon, and P. C. Junk, Contrasting Reactions of Carbodiimides With Divalent Lanthanoid Species. *Chem. Eur. J.* e202500759. (DOI: https://doi.org/10.1002/chem.202500759)

    - Featured on the inside cover of the issue.

Conference Presentations

1. **V. P. Vithana (2022).** Synthesis, Structure, and Corrosion Inhibiting Properties of REIII 3-Thiophenecarboxylate Complexes, Oral presentation at OZOM13: 13th Australasian Organometallics Meeting, Cairns (Australia), July 11-14/2022.
2. **V. P. Vithana (2023)**. RE(III) 3-furoate and 3-thiophene carboxylate complexes: Synthesis, structure, and corrosion inhibiting properties, Poster presentation at ICFE-11: 11th International Conference on f Elements, Strasbourg (France), August 22-26/2023.
3. **V. P. Vithana (2023).** Rare Earth Metal (REM) Carboxylate Complexes: Synthesis, structure, and corrosion inhibiting properties", Oral presentation at OZOM14: 14th Australasian Organometallics Meeting, Canberra (Australia), December 4-7/2023.
    - Awarded a best talk prize from Chemical Communication
4. **V. P. Vithana (2024).** Contrasting reactions of carbodiimides with divalent Organolanthanoids, Oral presentation at IC'24: RACI Inorganic Chemistry Conference, Sydney (Australia), December 8-12/2024.

Abstract

This thesis focuses on the synthesis, structural characterisation, and evaluation of rare earth (RE) carboxylate complexes as corrosion inhibitors for mild steel. Chapters 2–4 present the development of new RE complexes with organic carboxylic acid inhibitors and their corrosion mitigation effectiveness. Chapter 5 compares the corrosion inhibition properties of alkali metal salts of carboxylic acid moieties with their RE counterparts. Chapter 6 investigates the reactivity of highly reactive lanthanoid complexes with unsaturated carbodiimide substrates (RN=C=NR') and the synthesis and structural characterisation of cationic organolanthanoid(II) complexes.

Chapter 1 of the thesis provides an overview of the chemistry of rare earth metals, including their availability, properties, and applications. Furthermore, it discusses the corrosion process and explores the use of rare earth metal carboxylates as corrosion inhibitors.

Chapter 2 details the synthesis of two series of RE 3-thiophenecarboxylate (3tpc) complexes *via* metathesis reactions between RE chlorides/nitrates and Na(3tpc). X-ray crystallography, TGA, elemental analysis, IR spectroscopy, and powder XRD were used for structural characterisation. Light rare earth metals form nonacoordinate 1D polymeric complexes $[Ln(3tpc)_3(H_2O)_3]_n$ (RE = La, Ce, Pr, Nd, Sm, Gd) while the heavier elements including yttrium form dimeric structures $[Ln_2(3tpc)_6(H_2O)_4]\cdot H_2O$ (RE = Dy, Ho, Y, Er, Lu) with eight coordinated metal centers. The corrosion inhibition behaviour of the compounds has been examined using immersion studies and electrochemical measurements on AS1020 mild steel surfaces by a 0.01 M NaCl medium. Corrosion inhibition of mild steel was tested through immersion studies in a 0.01 M NaCl medium, revealing that $[Y_2(3tpc)_6(H_2O)_4]\cdot H_2O$ had the highest inhibition efficiency of 68%. Potentiodynamic polarization (PP) measurements showed these compounds act as anodic inhibitors.

Chapter 3 discusses the synthesis of RE 3-furoate (3fur) complexes, which form two types of structures: Type 1 monometallic complexes with 2D polymeric networks $[RE(3fur)_3(H_2O)_2]_n$ (RE = La, Ce, Pr, Nd, Gd, Dy, Ho, Y), and type 2 bimetallic complexes with 3D polymeric systems $[NaRE(3fur)_4]_n$ (RE = Ho, Y, Er, Yb, Lu). The stoichiometric mole ratio used (RE: Na(3fur) = 1:3 or 1:4) in the metathesis reaction determines whether type 1 or type 2 is formed with Ho and Y. Weight loss measurements indicate that $[Y(3fur)_3(H_2O)_2]_n$ offers 90% corrosion resistance after 168 hours of immersion, with similar results observed in PP measurements.

Chapter 4 describes the synthesis and characterisation of six RE 2-methyl-3-furoate (2m3fur) complexes, which form linear polymers. X-ray diffraction revealed two distinct structural groups: $\{[RE_2(2m3fur)_6(EtOH)]\cdot H_2O\}_n$ (RE=La, Ce, Pr) and $[RE_3(2m3fur)_9]_n$ (RE=Y, Er, Yb). The corrosion inhibition efficiency of $[Y_3(2m3fur)_9]_n$ was 59%, lower than that of yttrium 3-furoate, suggesting that the steric effect of the methyl group reduces the efficacy of corrosion inhibition.

In Chapter 5, fourteen complexes of the alkali metals Li-Cs with 3-thiophenecarboxylate (3tpc), 2-methyl-3-furoate (2m3fur), 3-furoate (3fur), 4-hydroxycinnamate (4hocin), and 4-hydroxybenzoate (4hob) ions were prepared *via* neutralisation reactions between the alkali metal base and the parent carboxylic acids. X-ray crystallography, XPD, IR, and TGA were used for structural analysis. All were obtained as coordination polymers (except for dinuclear $[Li_2(2m3fur)_2(H_2O)_3]$) with a wide variety of carboxylate-binding modes. Under conditions that normally gave coordinated carboxylate ions, the ligation of hydrogen dicarboxylate ions was observed in $[Cs\{H(3tpc)_2\}]_n$ and $Rb\{H(4hocin)_2\}]_n.nH_2O$. The alkali-metal carboxylates showed corrosion inhibitor properties inferior to those of the corresponding rare-earth carboxylates.

Chapter 6 includes the synthesis of three new lanthanoid complexes featuring 2,6-di-*tert*-butyl-4-ethylphenolate to further explore their reactivity profiles. This chapter mainly discusses the contrasting reactions of unsaturated carbodiimide substrates (RN=C=NR') with Ln(II) lanthanoid species. Notably, the reactions of the divalent 2,6-di-*tert*-butyl-4-ethylphenolatosamarium complex, $[Sm(OAr^{Et})_2(thf)_3]$ with N,N'-diisopropylcarbodiimide (*i*PrNCN*i*Pr) resulted in the formation of the oxalamidinatosamarium(III) complex $[(OAr^{Et})_2Sm(\mu\text{-}C_2N_4iPr_4)Sm(OAr^{Et})_2]\cdot 2PhMe$. In contrast, the use of the bulkier N,N'-dicyclohexylcarbodiimide (CyNCNCy) led to the formation of a formamidinatosamarium(III) complex $[Sm(OAr^{Et})_2(CyNC(H)NCy)(thf)_2]\cdot 2thf$. Reactions of rare earth metals (RE = Yb, Eu) with one molar equivalent of bis(phenylethynyl)mercury and two molar equivalent of N,N'-dicyclohexylcarbodiimide yielded lanthanoid *C*-phenylethynylamidinate complexes. Lastly, the first example of a cationic europium phenoxide complex, $[Eu_2(OMes)_3(thf)_6]^+[BPh_4]^-\cdot 1.5thf$, was synthesized *via* a selective protolytic cleavage by treating $[Eu_3(OMes)_6(thf)_6]$ with $[Et_3NH][BPh_4]$.

Overall, this thesis highlights the development of novel rare earth carboxylate complexes as corrosion inhibitors, showcasing their unique structural features and inhibition

properties. Complexes such as $[Y(3fur)_3(H_2O)_2]_n$ exhibited high efficacy in corrosion mitigation. Data suggest that furoate moieties are more effective than thiophene groups, but the addition of a methyl group to the furan ring reduces efficiency. The synthesis of 14 new alkali metal carboxylate complexes fills a gap in structural studies of these compounds. The final chapter explores the reactivity of highly reactive lanthanoid complexes with organic substrates under inert conditions, advancing the understanding of Ln(II) coordination chemistry particularly carbodiimide activation and the formation of redox-active cationic species.

Abbreviations

Ar	Aryl
nBu	*n*-Butyl
*t*Bu	*tert*-butyl
$(BPh_4)^-$	tetraphenylborate anion
bpy	2,2'-bipyridine
Cp	Cyclopentadienyl ($C_5H_5^-$)
Cy	Cyclohexyl
Dipp	Diisopropylphenyl
EA	Elemental analysis
EDTA	Ethylenediaminetetraacetic acid
EtOH	ethanol
Et	Ethyl
Et_2O	Diethyl ether
$[Et_3NH][BPh_4]$	Triethylamine Tetraphenylborate
equiv	equivalent(s)
3furH	3-furoic acid
h	Hour
4hocinH	4-hydroxycinnamic acid
HOdpp	2,6-diphenylphenol
HOmes	2,4,6-trimethylphenol
$HOAr^H$	2,6-di-*tert*-butylphenol
$HOAr^{Me}$	2,6-di-*tert*-butyl-4-methylphenol
$HOAr^{OMe}$	2,6-di-*tert*-butyl-4-methoxyphenol
$HOAr^{Et}$	2,6-di-*tert*-butyl-4-ethylphenol
$HOAr^{tBu}$	2,4,6-tri-*tert*-butylphenol
$HOAr^{iPr}$	2,6-diisopropylphenol
4hobH	4-hydroxybenzoic acid
IR	Infrared
*i*Pr	Isopropyl
IUPAC	International Union of Pure and Applied Chemistry
LCMS	Liquid chromatography-mass spectrometry
Ln	Lanthanoid (La-Lu)

M	metal
Me	Methyl
mp	Melting point
min	Minute
2m3furH	2-methyl-3-furoic acid
NMR	Nuclear magnetic resonance
Ph	Phenyl
PhMe	Toluene
PP	Potentiodynamic Polarisation
ppm	Parts per million
r.t.	room temperature
RE	Rare Earth (Y, Sc, La-Lu)
REE	Rare earth element
RTP	Redox transmetallation/protolysis
solv	Solvent
3tpcH	3-thiophene carboxylic acid
thf	Tetrahydrofuran
UV	Ultraviolet

Table of Contents

Declaration i

Acknowledgements ii

Statement of the Contribution of Others iv

Output Related to the Thesis v

Abstract vii

Abbreviations x

Table of Contents xii

Chapter 1: Introduction to Rare Earth Metal Corrosion Inhibitors 1

1.1 The Corrosion Process 1

1.2 Chemistry of Rare Earth Metals 2

1.2.1 RE Element Abundancy and Availability 2

1.2.2 Properties of RE Elements 3

1.2.3 Uses and Applications of RE Elements 5

1.2.4 Rare Earth carboxylate complexes 5

1.3 Rare Earth Metals as Corrosion Inhibitors 6

1.3.1. Use of RE Metals as Corrosion Inhibitors for Aluminum Alloys 6

1.3.2 Use of RE Metals as Corrosion Inhibitors for Zinc and Galvanized Steel 8

1.3.3 Use of RE Metals as Corrosion Inhibitors for Mild Steel 10

1.4 Organic Compounds Containing Heteroatoms as Corrosion Inhibitors 12

1.5 Rare Earth Metal Carboxylates as Corrosion Inhibitors 16

1.6 General Approach and Current Study 24

1.7 References 26

Chapter 2: Synthesis, Structural Characterisation and Corrosion Inhibiting Properties of Rare Earth 3-thiophenecarboxylate Complexes 32

2.1 Introduction 32

2.1.1 Thiophene and its Derivatives 32

2.1.2 Organic Compounds Containing Sulfur Atoms as Corrosion Inhibitors……. *33*

2.1.3 Current Study *35*

2.2 Results and Discussion 36

2.2.1 Synthesis and Characterisation *36*

2.2.2 X-ray Crystal Structures *41*

2.2.2.1 1D Polymeric Chains of $[RE(3tpc)_3(H_2O)_3]_n$ Complexes (RE = La, Ce, Pr, Nd, Sm, Gd) 41

2.2.2.2 Dimeric Structures of $[RE_2(3tpc)_6(H_2O)_4]\cdot H_2O$ Complexes (RE = Dy, Ho, Y, Er, Lu) 44

2.2.3 Corrosion Inhibition *46*

2.2.3.1 Immersion Tests 46

2.2.3.2 Potentiodynamic Polarisation (PP) 48

2.3 Conclusions 50

2.4 Experimental 50

2.4.1 Synthesis of 3-thiophenecarboxylate (3tpc)- RE Aqua Complexes *50*

2.4.2 Corrosion Testing *53*

2.5 X-ray Crystal Data 53

2.6 References 55

Chapter 3: RE(III) 3-furoate Complexes: Synthesis, Structure, and Corrosion Inhibiting Properties 59

3.1 Introduction 59

3.1.1 Furan and its Derivatives *59*

3.1.2 Organic Compounds Containing Oxygen Atoms as Corrosion Inhibitors *60*

3.1.3 Current Study *62*

3.2 Results and Discussion 62

3.2.1 Synthesis and characterisation *62*

3.2.2 X-ray crystal structures *68*

3.2.2.1 Monometallic 2D polymeric chains of $[RE(3fur)_3(H_2O)_2]_n$ complexes (RE = La (3.1), Ce (3.2), Pr (3.3), Nd (3.4), Gd (3.5), Dy (3.6), Ho (3.7), Y (3.8))..... 69

3.2.2.2 Bimetallic 3D polymeric chains of $[NaRE(3fur)_4]_n$ complexes (RE = Ho (3.9), Y (3.10), Er (3.11), Yb (3.12), Lu (3.13))..... 71

3.2.3 Corrosion Inhibition..... *75*

3.2.3.1 Immersion Tests..... 75

3.2.3.2 Potentiodynamic polarisation..... 78

3.3 Conclusions..... 79

3.4 Experimental..... 80

3.4.1 Synthesis of 3-furoate (3fur)- RE aqua complexes..... *80*

3.4.2 Corrosion Testing..... *83*

3.5 X-ray crystal data..... 83

3.6 References..... 86

Chapter 4: Rare Earth 2-methyl-3-furoate Complexes: Effect of Steric Hindrance on Corrosion Inhibitor Properties..... 89

4.1 Introduction..... 89

4.1.1 Impact of Structural Variations in Carboxylate Frameworks on Corrosion Mitigation Activity..... *89*

4.1.2 Current Study..... *92*

4.2 Results and Discussion..... 93

4.2.1 Synthesis and Characterisation..... *93*

4.2.2 X-ray Crystal Structures..... *97*

4.2.1.1 1D Polymeric Chains of $\{[RE_2(2m3fur)_6(EtOH)]\cdot H_2O\}_n$ Complexes (RE = La, Ce, Pr)..... 98

4.2.2.2 1D Polymeric Chains of $[RE_3(2m3fur)_9]_n$ Complexes (RE = Y, Er, Yb)..... 101

4.2.3 Corrosion Inhibition..... *105*

4.2.3.1 Immersion Tests..... 105

4.3 Conclusions 107
4.4 Experimental 107
4.4.1 Synthesis of 2-methyl-3-furoate (2m3fur) RE complexes 107
4.4.2 Corrosion Testing 109
4.5 X-ray Crystal Data 109
4.6 References 111
Chapter 5: Synthesis, Structures, and Corrosion Inhibition of Various Alkali Metal Carboxylate Complexes 113
5.1 Introduction 113
5.1.1 Alkali Metal Salts of Carboxylic Acids as Corrosion Inhibitors 113
5.1.2 Current Study 114
5.2 Results and Discussion 115
5.2.1 Synthesis and characterisation 115
5.2.2 X-ray crystal structures 125
5.2.2.1. M(3tpc) Complexes (M = Li (5.1), K (5.2), Rb (5.3), Cs (5.4)) 127
5.2.2.2. M(2m3fur) Complexes (M = Li (5.5), K (5.6)) 134
5.2.2.3. 2D polymeric chain of the $[Li(3fur)]_n$ (5.7) complex 138
5.2.2.4. M(4hocin) Complexes (M = K (5.8), Rb (5.9), Cs (5.10)) 140
5.2.2.5. M(4hob) Complexes (M = Li (5.11), K (5.12), Rb (5.13), Cs (5.14)) 148
5.2.3 Corrosion Inhibition 156
5.2.3.1. Immersion Tests 156
5.3 Conclusions 158
5.4 Experimental 159
5.4.1 Synthesis of alkali metal carboxylate Complexes 159
5.4.2 Corrosion Testing 163
5.5 X-ray Crystal Data 163
5.6 References 166

Chapter 6 : Interaction of highly reactive lanthanoid complexes with organic substrates 168

6.1 Introduction 168

6.1.1 Lanthanoid aryloxide complexes in organometallic chemistry 168

6.1.1.1 Synthetic pathways to rare earth aryloxide complexes 171

6.1.2 Classical divalent lanthanoid complexes in organometallic chemistry ..172

6.1.3 Reactions of organolanthanoid complexes with unsaturated carbodiimide substrates 173

6.1.3.1 The insertion of carbodiimides into an existing metal-carbon/ metal-nitrogen bonds for the formation of Ln metal amidinate and guanidinate complexes 174

6.1.3.2 Reductive coupling of carbodiimides with low-valent metal complexes 176

6.1.4 Cationic lanthanoid tetraphenylborate complexes 178

6.1.5 Current study 181

6.2 Results and Discussion 182

6.2.1 Synthesis of divalent rare earth aryloxide complexes 182

6.2.2 Contrasting reactions of carbodiimides with divalent lanthanoid species 188

6.2.2.1 Reactions of Carbodiimides with Samarium(II) bis(2,6-di-*tert*-butyl-4-ethylphenolate) 188

6.2.2.2 The one pot reaction of divalent Ln metal with N,N′-dicyclohexylcarbodiimide (CyNCNCy) using $Hg(PhCC)_2$. 193

6.2.3 Synthesis and characterisation of cationic lanthanoid phenoxide complexes 199

6.3 Conclusion 202

6.4 Experimental 203

6.4.1 General Considerations 203

6.4.2 Syntheses 204

6.5 X-ray Crystal Data 208
6.6 References 211
Chapter 7: Concluding Chapter 218
7.1 Overview 218
7.2 Summary of Findings 218
7.3 Recommendations for Future Research 218
7.4 Contribution 222
7.5 References 223
Appendix One 224
Appendix Two 227

Chapter 1: Introduction to Rare Earth Metal Corrosion Inhibitors.

1.1 The Corrosion Process

Corrosion degradation by chemical and/or electrochemical reactions [1,2] is a widespread and extremely costly issue for engineering materials in diverse industries. Over 3% of the world's Gross Domestic Production equating to US $2.5 trillion is spent annually to replace and reduce the damage caused by corrosion.[3,4] A major part of this cost includes the maintenance and replacement of water recirculating pipelines, bridges, and water tanks associated with cooling systems.[2,5] Without a proper control method to mitigate corrosion, such assets would have a significantly limited lifetime.[6] The latest reports by NACE international's IMPACT researchers have revealed that the application of currently available corrosion control practices could save between US $375 and US $875 billion annually. Thus 15-35% of the global cost of corrosion could be saved.[4]

Mild steel is extensively used as an engineering material in diverse industries due to its relatively low cost, high machinability, and widespread availability.[7] A range of factors such as pressure, temperature, and aggressive acidic environmental conditions[2] can lead to premature failure in mild steel structures. Corrosion of mild steel in solution is induced by an electrochemical process, that happens between the metallic material and the surrounding medium.

The corrosion reaction is composed of two half-cell reactions. The oxidation reaction or the metal dissolution reaction takes place on the anodic site of the surface (Equation 1 and/or 2), while the reduction of oxygen or protons occurs at the cathodic site (Equation 3 and/or 4).[8–10] Figure 1.1 illustrates the mode of action of the corrosion process.

Anodic Reactions:

$$Fe \longrightarrow Fe^{2+} + 2e^{-} \qquad \text{(Eq.1)}$$

$$Fe^{2+} \longrightarrow Fe^{3+} + e^{-} \qquad \text{(Eq.2)}$$

Cathodic Reactions:

$$O_2 + 2H_2O + 4e^{-} \longrightarrow 4OH^{-} \qquad \text{(Eq.3)}$$

$$2H^{+} + 2e^{-} \longrightarrow H_2 \qquad \text{(Eq.4)}$$

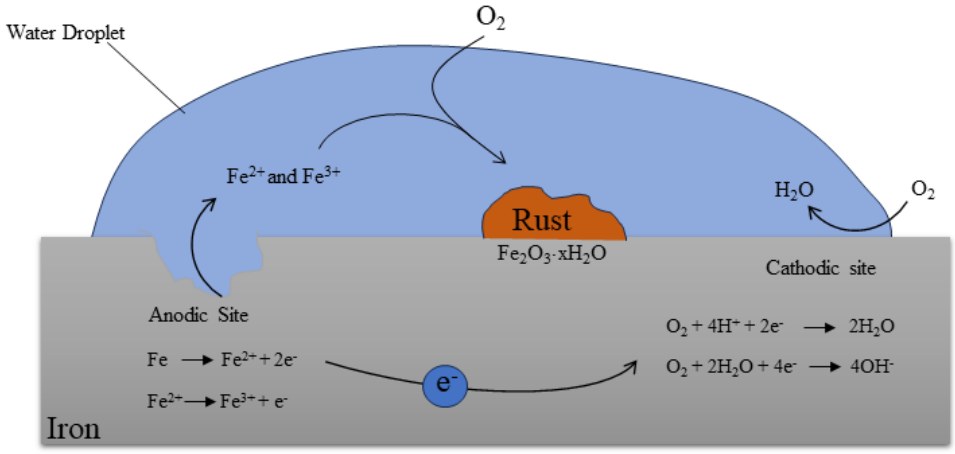


Figure 1.1: Schematic diagram of corrosion process in an aqueous medium.

In the corrosion process, the product from anodic reaction is coupled with the cathodic reaction, depositing solid corrosion products on the metal surfaces. In the case of iron and mild steel (high iron content), reaction of the ferrous ions with OH^- ions lead to the formation of iron hydroxide $Fe(OH)_2$, which subsequently undergoes further oxidation to form various forms of iron oxide, mainly Fe_2O_3 (hematite) and also $FeO(OH)$ (goethite).

$$Fe^{2+} + 2OH^- \longrightarrow Fe(OH)_2 \qquad \text{(Eq.5)}$$

$$4Fe(OH)_2 + O_2 + 2H_2O \longrightarrow 4Fe(OH)_3 \qquad \text{(Eq.6)}$$

$$2Fe(OH)_3 \longrightarrow Fe_2O_3 \text{ (red rust)} + 3H_2O \qquad \text{(Eq.7)}$$

$$Fe(OH)_3 \longrightarrow FeO(OH) + H_2O \qquad \text{(Eq. 8)}$$

1.2 Chemistry of Rare Earth Metals

The Rare Earth (RE) elements are a set of 17 elements with similar properties. These include 15 lanthanoid elements in the La-Lu group and two of the Group 3 metals, scandium, and yttrium in the periodic table as defined by the International Union of Pure and Applied Chemistry (IUPAC).[8,11] Scandium and yttrium are categorized as rare earth elements (REEs) due to their tendency to be found in the same ore deposits as the lanthanoids, and they also display similar chemical properties.[4] The name "Rare earth" was derived from the Latin term 'terra rarae'.[3] Despite implying rarity, these elements are not particularly scarce. However, for a significant duration they were believed to be rare.[5]

1.2.1 RE Element Abundancy and Availability

The most common rare earth, cerium, ranks as the 25th most abundant element, existing in quantities comparable to copper and surpassing the abundance of more widely known metals like cobalt, tin, and lead. Even the rarest natural occurring rare earth mineral, thulium, is as prevalent as bismuth and more abundant than mercury, arsenic, cadmium, or selenium. However, promethium, the rarest of the rare earth elements, exists only in trace quantities in natural minerals due to the lack of stable or long-lived isotopes.[12,13]

When considering the overall abundance of lanthanoids in the Earth's crust, the Oddo-Harkins rule is observed within rare earth metals. This rule suggests that elements with even atomic numbers are more abundant than their odd-numbered neighbours. Additionally, lighter lanthanoids tend to be more abundant than their heavier counterparts.[14]

Despite their high relative abundance, the pronounced similarities among rare earth elements in their trivalent oxidation state have made the separation of these minerals challenging and consequently relatively expensive.[14–16] Hence, the industrial utilization of rare earths was economically unfeasible until separation techniques were developed and optimized in the late 1950s and early 1960s. Ion-exchange chromatography marked the initial method that enabled rapid high-purity separation of the lanthanoids.[13,16]

The principal rare earth ores include monazite (Ln, Th)PO_4, xenotime (Y, Ln)PO_4, and bastnasite $LnFCO_3$. Monazite and bastnasite dominate among the light lanthanoids, whereas xenotime prevails among the heavier lanthanoids and contains significantly more yttrium. Additionally, ion-absorption ores found in southern China are crucial sources of these elements.[13,14,16,17]

1.2.2 Properties of RE Elements

Rare earth metals are highly electropositive[13,16], hence they are readily oxidized by air and their compounds predominantly possess ionic characteristics.[16] In general, the electrode potential of $Ln^{3+} + 3e \rightarrow Ln^0$ ($E° \approx$ ca. -2.3 V) is comparable to the reduction of group II magnesium (-2.34 V) and more negative than the reduction of group III Al^{3+} (-1.67 V).[13,16]

Besides their comparable electro positivity to Mg, rare earth metals exhibit similar chemical behaviours to the heavy group 2 metals,[13,14] and their reactivity[14] surpasses that of transition metals.

The most stable and commonly observed oxidation state for all rare earth elements is the trivalent state. However, divalent, and tetravalent oxidation states are also observed. For

more than 90 years, only Sm, Eu, and to a lesser extent Yb were known to form Ln^{2+}, while Ce and, less commonly, Pr and Tb could form Ln^{4+} ions. However, it is now known that all rare earths, except Pm, form compounds in the divalent state.[18–20]

Rare earth complexes exhibit a wide range of coordination numbers, typically ranging from six to twelve. This is due to their relatively large ionic radii and high oxidation states.[14]

As the atomic number increases from La to Lu in the series, there is a gradual decrease in the atomic/ionic radii of lanthanoids. This phenomenon, known as the lanthanoid contraction, occurs due to the inadequate shielding of the growing effective nuclear charge by 4f electrons.[14,16]

The overall decrease in ionic radii by 0.17 Å from La^{3+} to Lu^{3+}[13] demonstrates a notable effect, particularly evident with Ho^{3+} and Er^{3+}, as their ionic radius becomes similar to that of Y^{3+}.[16] This effect leads to a decrease in coordination number and an increase in the stability of lanthanoid complexes with the same ligand systems, thereby influencing the structural outcome of these complexes.[1]

Table 1.1: Selected properties of rare earth metals and ions.

Atomic No	**Name/Symbol**	**Electronic configuration**		**M^{3+} Radius (Å)[a]**	**Common Oxidation States**
		Atom	**RE^{3+}**		
21	Scandium (Sc)	$3d^1\ 4s^2$	[Ar]	0.87	3
39	Yttrium (Y)	$4d^1\ 5s^2$	[Kr]	1.01	3
57	Lanthanum (La)	$5d^1\ 6s^2$	[Xe]	1.16	3
58	Cerium (Ce)	$4f^1\ 5d^1\ 6s^2$	$4f^1$	1.14	3, 4
59	Praseodymium (Pr)	$4f^3\ 6s^2$	$4f^2$	1.13	3
60	Neodymium (Nd)	$4f^4\ 6s^2$	$4f^3$	1.11	3
61	Promethium (Pm)	$4f^5\ 6s^2$	$4f^4$	1.09	3
62	Samarium (Sm)	$4f^6\ 6s^2$	$4f^5$	1.08	2, 3
63	Europium (Eu)	$4f^7\ 6s^2$	$4f^6$	1.07	2, 3
64	Gadolinium (Gd)	$4f^7\ 5d^1\ 6s^2$	$4f^7$	1.05	3
65	Terbium (Tb)	$4f^9\ 6s^2$	$4f^8$	1.04	3
66	Dysprosium (Dy)	$4f^{10}\ 6s^2$	$4f^9$	1.03	3
67	Holmium (Ho)	$4f^{11}\ 6s^2$	$4f^{10}$	1.02	3
68	Erbium (Er)	$4f^{12}\ 6s^2$	$4f^{11}$	1.00	3
69	Thulium (Tm)	$4f^{13}\ 6s^2$	$4f^{12}$	0.99	3
70	Ytterbium (Yb)	$4f^{14}\ 6s^2$	$4f^{13}$	0.98	2, 3
71	Lutetium (Lu)	$4f^{14}\ 5d^1\ 6s^2$	$4f^{14}$	0.98	3

† *Adapted with permission from "Chapter: 1 The chemistry of rare earth metals, compounds, and corrosion inhibitors; Book: Rare Earth-Based Corrosion Inhibitors" by T. Behrsing, G.B. Deacon, P.C. Junk, 2014, Elsevier Books, page number 3. Copyright (2015) by Elsevier.*

[a]Ionic radii for eight coordinate RE^{3+} atoms.[21]

1.2.3 Uses and Applications of RE Elements

RE elements are utilized in a wide array of applications,[11] with their largest market by weight being in glass polishing and ceramics.[22]

One of the common applications of RE elements include their use in therapeutic and diagnostic fields, such as serving as MRI agents in modern medicine due to their unique properties, like radiation emission or magnetism.[12,16,22]

RE elements have also been utilized in agriculture as fertilizers to enhance the production and quality of crops.[12,23] Other applications include, but are not limited to, the utilization of rare earth minerals in manufacturing fluorescent lighting, LED screens, lasers, and rechargeable batteries.[12,16]

The RE elements market also encompasses the use of permanent magnets, particularly the high-strength and cost-effective neodymium-iron-boron magnets. These magnets find applications ranging from microphones to electric motors in hybrid vehicles.[12,14,16,22]

Lanthanum-rich mixed rare earth compounds have also shown themselves to be potent chemical catalysts for fluid catalytic cracking in petroleum refining.[22]

Several lanthanoid ions, such as Eu^{3+} and Tb^{3+}, exhibit luminescent properties utilized in various applications, including temperature sensors and in bioimaging.[16,22,24]

New applications of RE metals include the use of superconducting substances containing lanthanum or yttrium, as well as their uses in hydrogen-based refrigeration and energy storage.[22]

1.2.4 Rare Earth carboxylate complexes

Rare earth carboxylates constitute the largest class of rare earth-based coordination polymers,[16] showcasing diverse structural types and coordination modes.[25–28] Due to the highly oxophilic nature of RE elements, the formation of rare earth carboxylate complexes is favourable. Rare earth carboxylate complexes normally exhibit a variety of structural motifs, often favouring dimeric and linear polymeric structures. These complexes are known for their high coordination numbers, achieved through the favourable large size and high charge of lanthanoid ions, the multiplicity of carboxylate binding modes and the lack of directionality in lanthanoid-carboxylate binding.[25] Typically, chelating and bridging carboxylate modes

dominate, often accompanied by varying levels of hydration or solvation to complete the coordination sphere. Several common binding modes are shown in Figure 1.2.

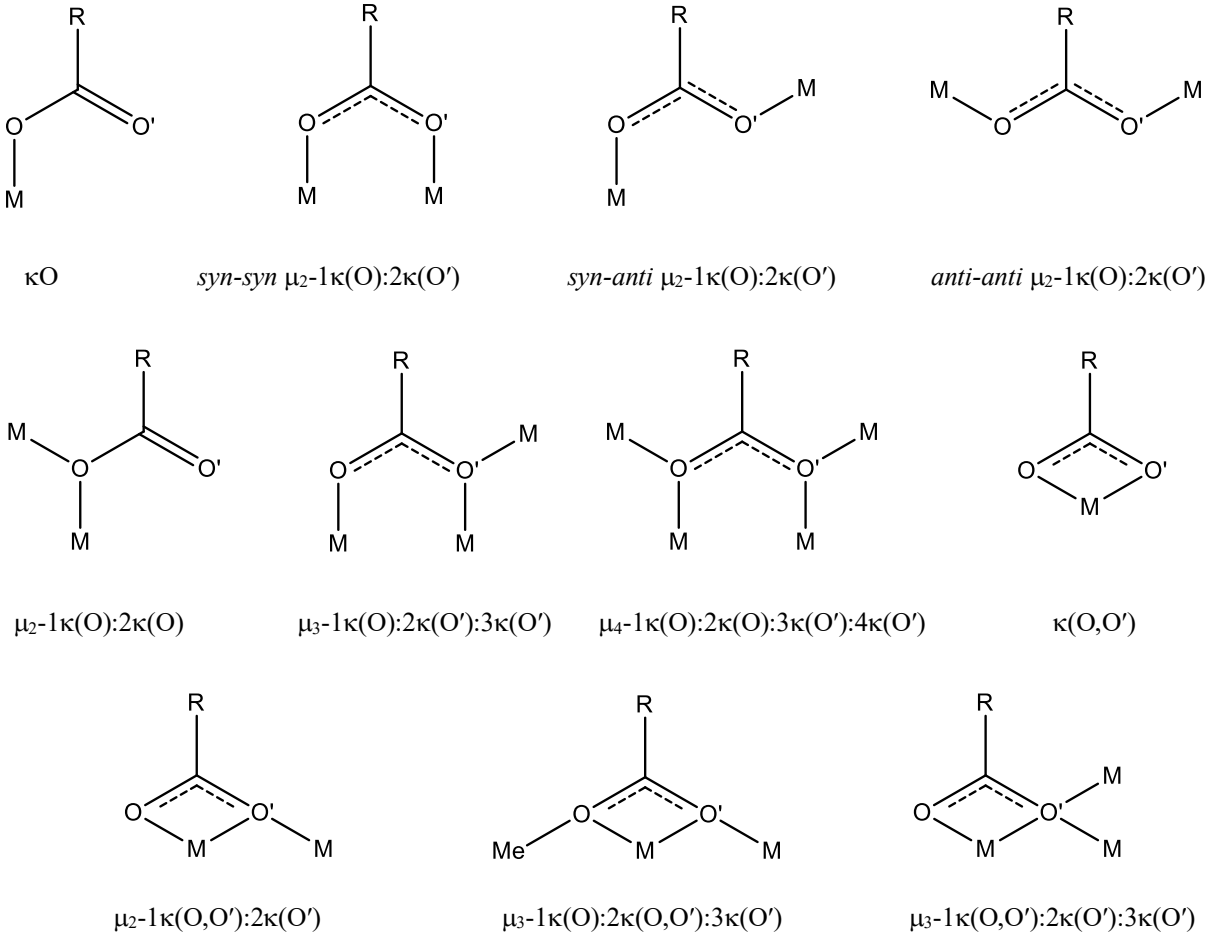


Figure 1.2: Common metal carboxylate coordination modes.

1.3 Rare Earth Metals as Corrosion Inhibitors

To protect metals and alloys from corrosion, a range of approaches are used. Among these, one of the most promising and cost-efficient methods involves using corrosion inhibitors.[29–31] For over a century, chromate compounds have been extensively utilized as corrosion inhibitors for a wide array of metals and alloys.[29,31–34] However, the high toxicity and carcinogenic properties associated with hexavalent chromium have led to a significant reduction in their usage.[31,35] Rare earth (RE) salts have emerged as promising alternatives to chromates due to their effectiveness, relatively low cost, and are environmentally friendly properties.[9,11,31,36]

1.3.1. Use of RE Metals as Corrosion Inhibitors for Aluminum Alloys

In 1984, Hinton's group started research studies at Aeronautical Research Lab (ARL), Australia, focusing on exploring the potential of RE metal salts as corrosion inhibitors. Their work throughout the late 1980s concentrated on the use of these salts as effective corrosion inhibitors for aluminum alloys.[9,36]

In 1985, Hinton et al. demonstrated the impact of three RE metal chlorides, namely $CeCl_3$, $LaCl_3$ and YCl_3 on the corrosion rate of AA7075 Al alloy in 0.1 M sodium chloride solutions. The results highlighted that these rare earth chlorides could decrease the corrosion rate by approximately tenfold, even at concentrations as low as 100 ppm. [9,37]

Another test has been conducted using atomic absorption spectroscopy (AAS) to examine the effectiveness of rare earth metal salts in retarding the further development of corrosion. Hinton points out that the corrosion rate appears to decrease significantly by adding the three rare earth chlorides mentioned above to the 0.1 M NaCl test solutions at the specific time indicated by the arrow (Figure 1.3). According to the weight loss data, the addition of $LaCl_3$, and $CeCl_3$ reduced the corrosion rate by a factor of 10, while that of YCl_3 was only a factor of 5.[9,37]

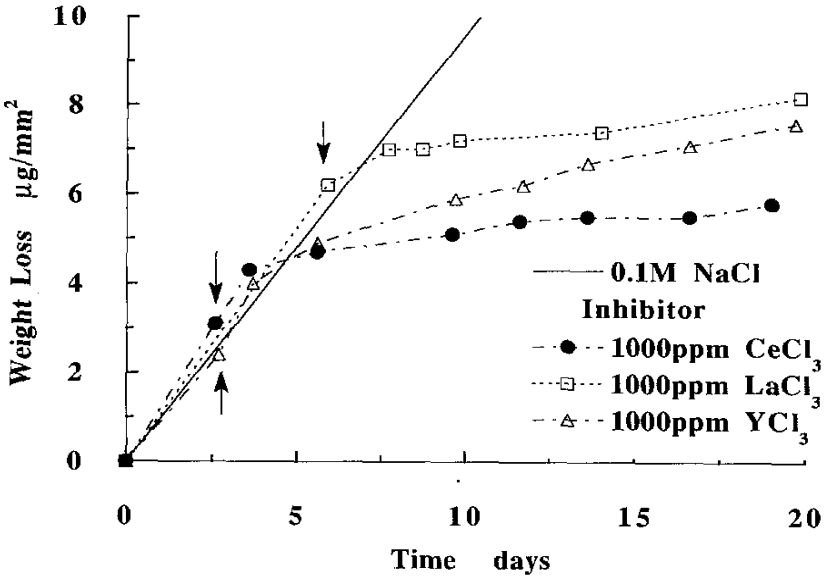


Figure 1.3: Weight loss of Al alloy 7075 in 0.1 M NaCl, as a function of time, before and after the addition (arrow) of three rare earth chlorides.

† *Reprinted with permission from "Handbook on the Physics and Chemistry of Rare Earths" by B.R.W. Hinton, 1995, Elsevier Books, 21(1), page number 40. Copyright (2024) by Elsevier.*

Two separate studies conducted by the same author in 1985[37] and 1992[36] demonstrated the anticorrosion activity of several Ce salts for 7075 type Al alloy immersed in NaCl. The

inhibition performance suggested that the anion of the Ce salt also influences the inhibitor's performance. Among the tested compounds, cerium perchlorate and acetate showed a significant level of inhibition. In a similar study in 1987, Baldwin and coworkers employed several cerium salt-based inhibitors for the protection of Al alloy 2014. Through total immersion tests, they demonstrated that $Ce_2(SO_4)_3$ and $CeCl_3$ were capable of inhibiting corrosion by more than 95%, in a 0.6 M NaCl solution.[9] All these studies collectively establish that the presence of rare-earth metals delays the susceptibility to corrosion attack on Al alloy in the short term.

Table 1.2 : The effect of various Ce salts on the corrosion rate of Al alloy 7075 and 2014 in 0.1 M NaCl solution. [9,36]

Cerium Salt	**Corrosion Rate ($\mu gm^{-2}s^{-1}$)**	
	7075: 0.1M NaCl. [Ce salt] =1000 ppm	**2014: 0.6M NaCl. [Ce salt] = 2mM**
None	7.6-9.6	9.09
Chloride	0.41-0.58	0.22
Nitrate	-	1.70
Sulfate	0.45-0.48	0.11
Perchlorate	0.16	1.37
Oxalate	-	1.82
Acetate	0.06	-

† *Adapted with permission from "Handbook on the Physics and Chemistry of Rare Earths" by B.R.W. Hinton, 1995, Elsevier Books, 21(1), page number 38. Copyright (1998) by Elsevier.*

1.3.2 Use of RE Metals as Corrosion Inhibitors for Zinc and Galvanized Steel

The use of $CeCl_3$ to minimize the corrosion effect on zinc and galvanized steel was reported by Hinton and Wilson during the second half of the 1980s.[38] The results obtained from the weight loss studies indicated that corrosion rates were significantly reduced by the addition of 100 ppm or more concentrated $CeCl_3$ in 0.1 M NaCl. As shown in Figure 1.4, immersion in the solution containing 1000ppm reduced the corrosion rate of Zn by a factor of 10, while the corrosion rate of galvanized steel was reduced by approximately half compared to the rate in the control solution (0.1 M sodium chloride).

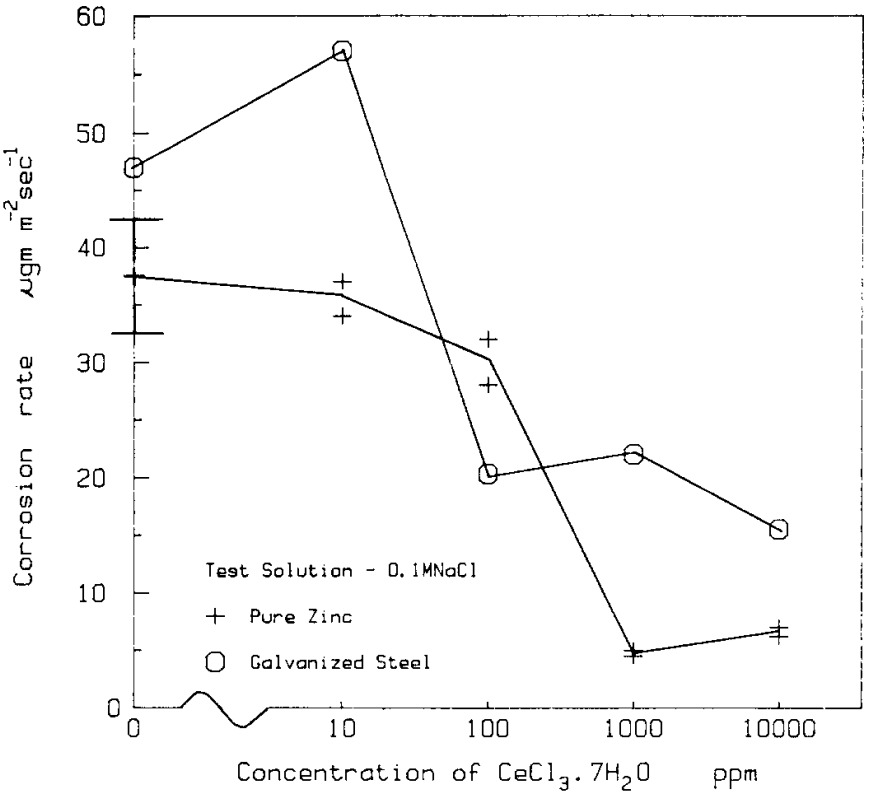


Figure 1.4: Corrosion rate variation of Zn and galvanized steel in 0.1 M NaCl at different $CeCl_3$ concentrations.

† *Reprinted with permission from "The corrosion inhibition of zinc with cerous chloride" by B.R.W. Hinton, L. Wilson, 1989, Corrosion Science, 29(8), page number 969. Copyright (1989) by Elsevier.*

The authors also conducted an immersion test with zinc and zinc-coated steel in tap water, demonstrating that the inhibitory performance improves with the increase of $CeCl_3$ concentration up to 1000 ppm. However, at a concentration of 10000 ppm, the corrosion rate increased considerably, which may be attributed to the high chloride ion concentration in the solution (Figure 1.5).[38]

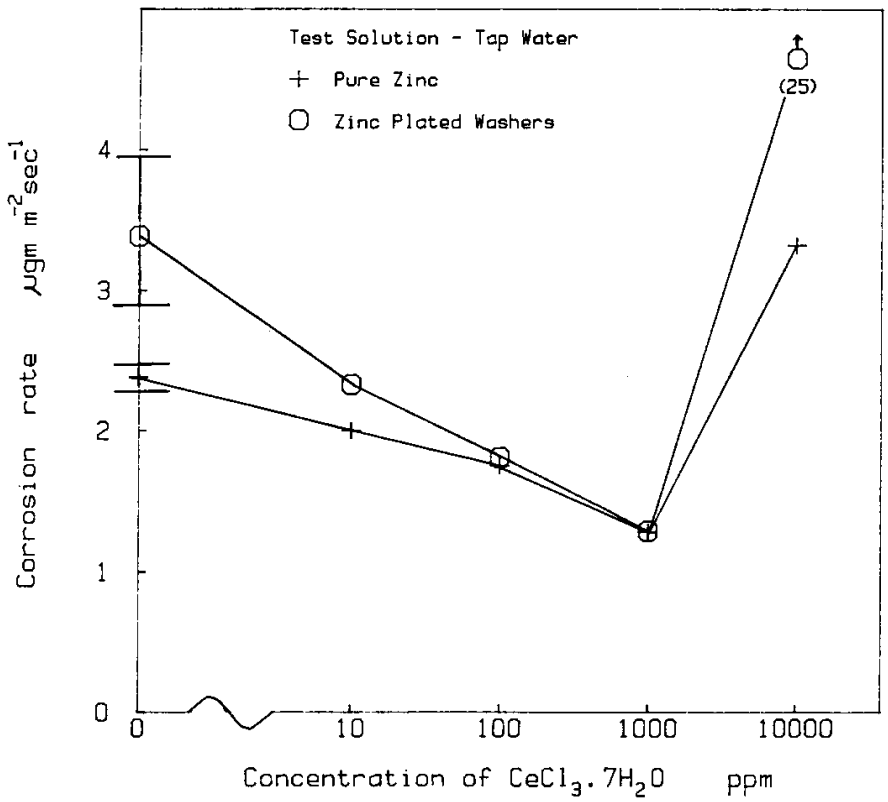


Figure 1.5: Corrosion rate variation of Zn and galvanized steel in tap water at different $CeCl_3$ concentrations.

† *Reprinted with permission from "The corrosion inhibition of zinc with cerous chloride" by B.R.W. Hinton, L. Wilson, 1989, Corrosion Science, 29(8), page number 978. Copyright (1989) by Elsevier.*

1.3.3 Use of RE Metals as Corrosion Inhibitors for Mild Steel

The use of RE metal salts to inhibit corrosion of mild steel was first demonstrated by Goldie and McCarroll in a patent.[9,39] They found that the corrosion inhibition efficiency of steel in aerated 3.5% NaCl solutions, produced by 0.001 M $La(NO_3)_3$ and $Ce(NO_3)_3$ was 82% and 91%, correspondingly.

Hinton's work, based on weight loss data, also highlighted the effectiveness of $CeCl_3$ in inhibiting corrosion of AS 1020 in aerated quiescent tap water at two pH levels. This study indicated that at pH 5.5, only 50 ppm concentration is required to decrease corrosion rate substantially and increasing Ce concentrations above that had a very small effect on the corrosion reduction rate. However, at the pH value of 6.5, more than 200 ppm concentrations of $CeCl_3$ were needed to have an efficient inhibition activity. The above observation was suggested to occur as a result of precipitation of Ce^{3+} ions from the solution at a lower concentration under pH 6.5-7 [9] (Figure 1.6).

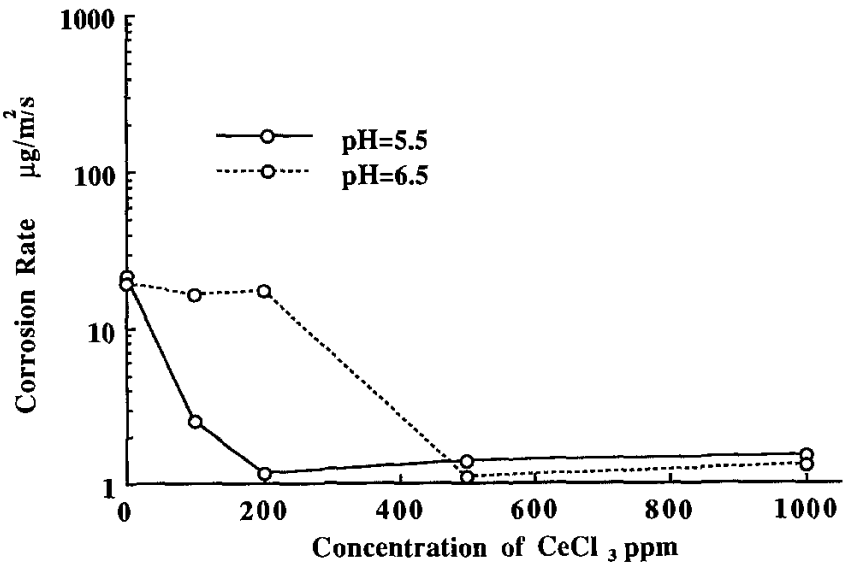


Figure 1.6: Corrosion rate variation of mild steel with the $CeCl_3$ concentration in tap water at pH 5.5 and 6.5.

† *Reprinted with permission from "Handbook on the Physics and Chemistry of Rare Earths" by B.R.W. Hinton, 1995, Elsevier Books, 21(1), page number 46. Copyright (1998) by Elsevier.*

Hinton and coworkers have also examined the ability of rare earth salts as corrosion inhibitors of mild steel under various states of aeration conditions as given in Figure 1.7. The analysis results indicated that $CeCl_3$ was most effective in continuously aerated quiescent soft tap water with an inhibition efficiency of 99.2%.[9]

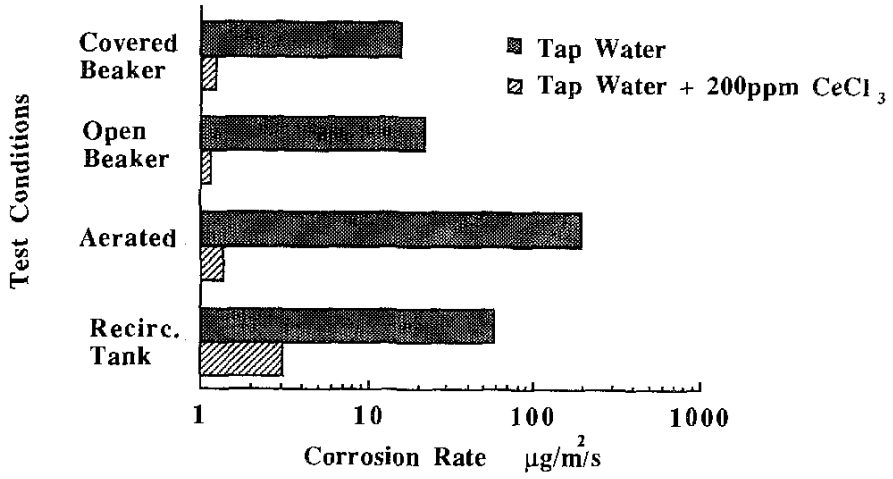


Figure 1.7: The variation of corrosion rate of mild steel with respect to the type of aeration in untreated tap water and tap water with $CeCl_3$.

† *Reprinted with permission from "Handbook on the Physics and Chemistry of Rare Earths" by B.R.W. Hinton, 1995, Elsevier Books, 21(1), page number 47. Copyright (1998) by Elsevier.*

The potential of $CeCl_3$ as an inhibitor of corrosion of mild steel in hard water and hard water with elevated chloride levels have also been reported. Furthermore, $CeCl_3$ has been shown as an excellent corrosion inhibitor in recirculating water systems over a long period up to several months, and it was observed that the corrosion rate changed very little over this time.[9]

It has been proposed in the previously published literature that $CeCl_3$ exhibits a cathodic inhibition mechanism by slowing down the cathodic oxygen reduction reaction.[9,37] However, Issacs and Davenport's experiment contradicts this claim and suggests that rare earth salts may not behave as cathodic inhibitors all the time. During their study using the vibrating probe technique, it was found that Ce^{3+} ions were behaving as an anodic inhibitor for steel, as there was the disappearance in large anodic current density along with an increase in open-circuit potential value.[9]

In a patent, Kreh et al. demonstrated a method of inhibiting corrosion of a metal by a water-soluble organic rare earth metal chelate at pH 6. Even though several different rare-earth metal chelate systems were investigated, neither a mechanism nor detailed experimental information was reported.[40]

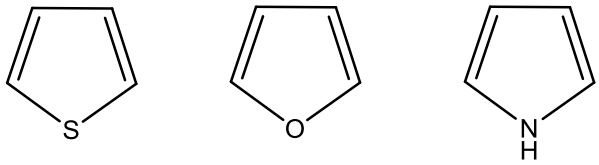
1.4 Organic Compounds Containing Heteroatoms as Corrosion Inhibitors

Corrosion protection *via* organic corrosion inhibitors is associated with the formation of protective layers on metals.[41] The incorporation of organic inhibitors into coatings can offer a promising approach to impart self-healing properties when the coating is partially damaged.[42] Adsorption is determined by various factors including the chemical structure of organic inhibitors, their surface charge, pH and/or electrode potential and the distribution of charge in the molecule. Organic compounds are widely utilized as corrosion inhibitors in industry because they are effective across a broad temperature range, exhibit good solubility, are compatible with protected materials, and possess relatively low toxicity.[10,43]

Previous studies demonstrated that among the organic systems, compounds containing heteroatoms with high electron density, such as sulfur, nitrogen, and oxygen, are considered to have a higher inhibiting performance due to their strong affinity to metallic surfaces.[43–47] Heterocyclic compounds having polar functional groups such as carboxylate, hydroxyl groups, and conjugated π-electrons of double and triple bonds have been reported as effective corrosion inhibitors.[48–50] The extent of the absorption of these inhibitors depends on several factors like the magnitude of the charge present and the nature of the metal, nature of substituents, inhibitor molecule's electronic structure, the environmental conditions, etc.[6] Inhibition efficiency of

these heteroatoms are reported to be the reverse order of electronegativity: P > S > N > O.[10] Organic compounds of this type tend to adsorb on the metal surface through the delocalized pi electrons and lone pair electrons of heteroatoms, binding with the empty d orbitals on the metal surface atoms to form a stable coordination bond.[51,52]

Thiophene, furan, and pyrrole belong to the family of five-membered heterocycles, containing four carbon atoms and one atom of sulfur, oxygen, or nitrogen, respectively. All these molecules have six π-electron aromaticity. However, the aromatic character of thiophene is much closer to benzene than the other two compounds. Further, the electronegativity of both carbon and sulfur are closer in value, while nitrogen and oxygen have higher electronegativity.[53]

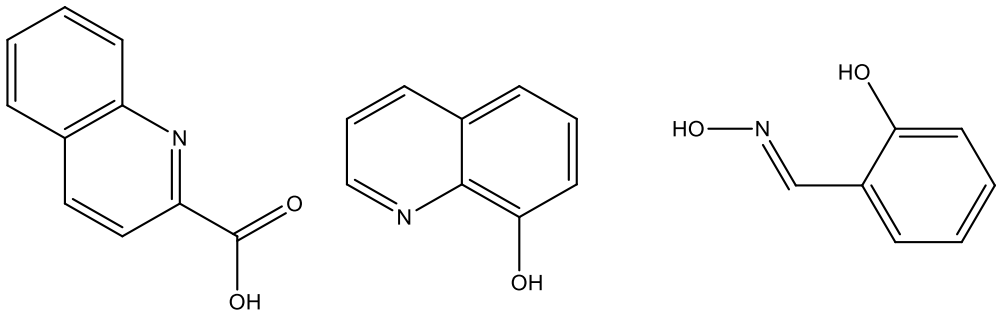


(a) Thiophene (b) Furan (c) Pyrrole

Figure 1.8: Chemical Structures of five-membered aromatic heterocyclic compounds; (a) Thiophene, (b) Furan and (c) Pyrrole.

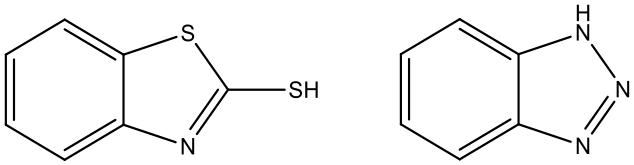
N-heterocycles, such as imidazole, quinoline, and pyridine compounds, typically exhibit easier degradation, leading to reduced environmental pollution. Additionally, they have the capability to form a protective film, serving as a barrier against corrosive agents, and often demonstrate robust corrosion inhibition properties.[54]

Lamaka et al. conducted research on the inhibitory impact of various organic compounds on the corrosion of AA2024 in a neutral Cl^- solution. The findings indicated that quinaldic acid (1), salicylaldoxime (2), and 8-hydroxyquinoline (3) offer corrosion protection for AA2024 by creating a thin adsorptive organic layer of insoluble complexes on the alloy's surface. This layer effectively suppresses the dissolution of aluminium, magnesium as well as copper from the corrosion-active intermetallic zones.[55]



(1) (2) (3)

The corrosion inhibitory effect of numerous triazole and thiazole derivatives has been studied in past years for both copper and its alloys, as well as aluminium-based alloys[55–58]. In one such study conducted by Zheludkevich et al., involving the 2024 aluminium alloy in a neutral chloride solution, 2-mercaptobenzothiazole (4) and benzotriazole (5) have demonstrated effective results, providing long-term corrosion protection while decreasing the rates of both the anodic and cathodic reactions.[42]



(4) (5)

Surfactants, a type of organic inhibitor, consist of amphiphilic molecules, each comprising a hydrophobic tail and a hydrophilic head which can be easily synthesised at a low cost and exhibits high effectiveness and efficiency in inhibiting corrosion. Presence of a positively charged nitrogen atom and an amphiphilic structure in quaternary ammonium salts have led for their utilization as highly effective corrosion inhibitors. The emergence of a new generation of quaternary ammonium salts known as Gemini surfactants where two standard surfactant monomers are linked by a spacer group, represents a fascinating class of surfactants recently employed as corrosion inhibitors. This is due to their more efficient surface properties, characterised by low values of both critical micelle concentration and surface energy.[10,59]

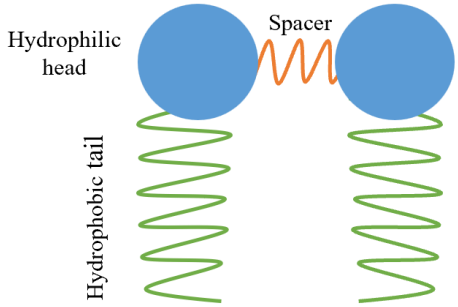
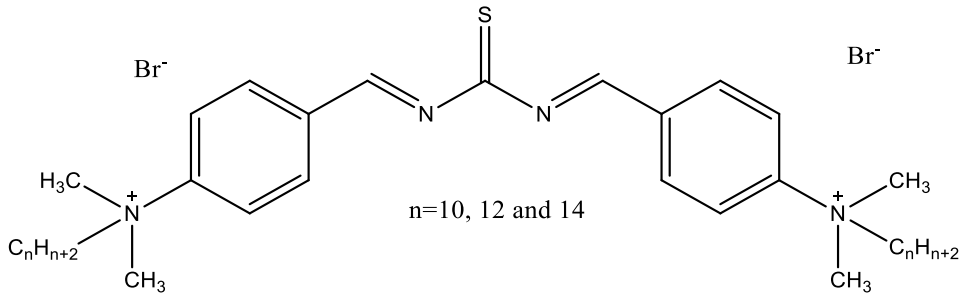


Figure 1.9: Shape of the Gemini surfactant molecule.

Hegazy reported on the synthesis of three Schiff base-based cationic Gemini surfactants (6) with different chain lengths by increasing the number of methylene groups and used them as corrosion inhibitors for carbon steel in a 1M HCl solution.



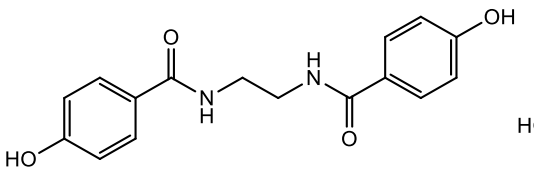
(6)

Their inhibiting properties increase with the lengthening of the methylene groups, in the following order:

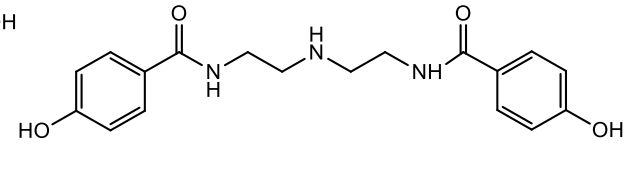
bis(p-(N,N,N-tetradecyldimethylammonium bromide)benzylidene thiourea (14-S-14) > bis(p-(N,N,N-dodecyldimethylammonium bromide)benzylidene thiourea (12-S-12) > bis(p-(N,N,N-decyldimethylammonium bromide)benzylidene thiourea (10-S-10).

Polarization measurements revealed that the cationic Gemini surfactants act as mixed-type inhibitors, effectively blocking the active sites on the metal surface and inhibiting the corrosion of carbon steel.[60]

The investigation into the corrosion inhibition effect of two novel benzamide derivatives N,N-bis (p-hydroxybenzoyl) ethylenediamine (7) and N,N-bis (p-hydroxybenzoyl) diethylenetriamine (8) has revealed that they act as mixed-type inhibitors. Moreover, the corrosion inhibition efficiency of both compounds exceeded 95%.[61]

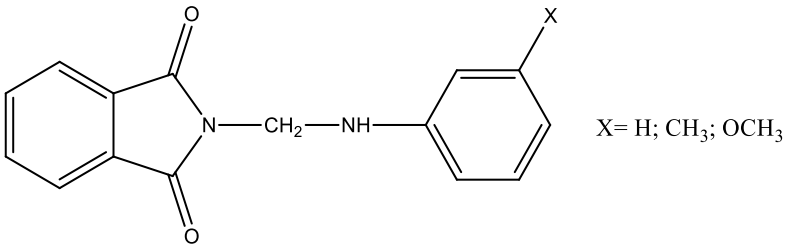


(7)



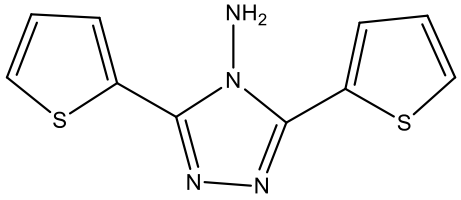
(8)

Fouda et al. explored the corrosion inhibition potential of certain phthalimide derivatives (9) on copper in acidic environments using weight loss and polarization methods. Findings demonstrated that these organic compounds exhibit notable inhibitory properties, although higher temperatures were found to adversely affect their inhibition efficiency. Moreover, it was observed that incorporating nucleophilic groups (–CH_3 or –OCH_3) at the *meta* position (at position X) of the phenylamino group enhances the protective efficiency. This enhancement is attributed to the increased electron density of the surface-active centre of the molecule (–N–), resulting in stronger adsorption.[62]



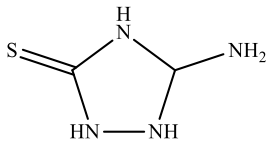
(9)

Bentiss and co-workers conducted research on the corrosion inhibitor 3, 5-bis (2-thienyl)-4-amino-l,2,4-triazole (10) on mild steel in acidic environments. Electrochemical impedance spectroscopy revealed an anodic type of inhibition action. The most effective inhibition was observed in 1M HCl compared to the 0.5M H_2SO_4 medium. Over time, inhibition efficiency increases due to the formation of a protective layer through the adsorption of the inhibitor on the metal surface, further suppressing the metal dissolution reaction.[63]

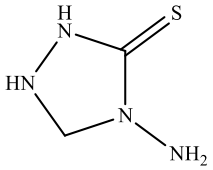


(10)

Osman et al. investigated the impact of 2-amino-5-thio-1,3,4-triazolidine (11) and 4-amino-3-thio-1,2,4-triazolidine (12) on the corrosion inhibition of steel in acidic medium with the concentration of 3M H_2SO_4. Their findings indicated that both compounds act as mixed inhibitors. Compound (11) exhibited greater efficiency compared to compound (12) by a factor of 1.3, attributed to the presence of an additional sulfur atom in compound, which enhances electron density on the molecular structure.[64,65]



(11)

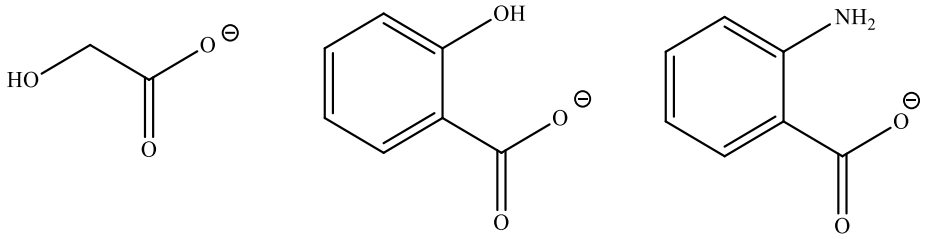


(12)

1.5 Rare Earth Metal Carboxylates as Corrosion Inhibitors

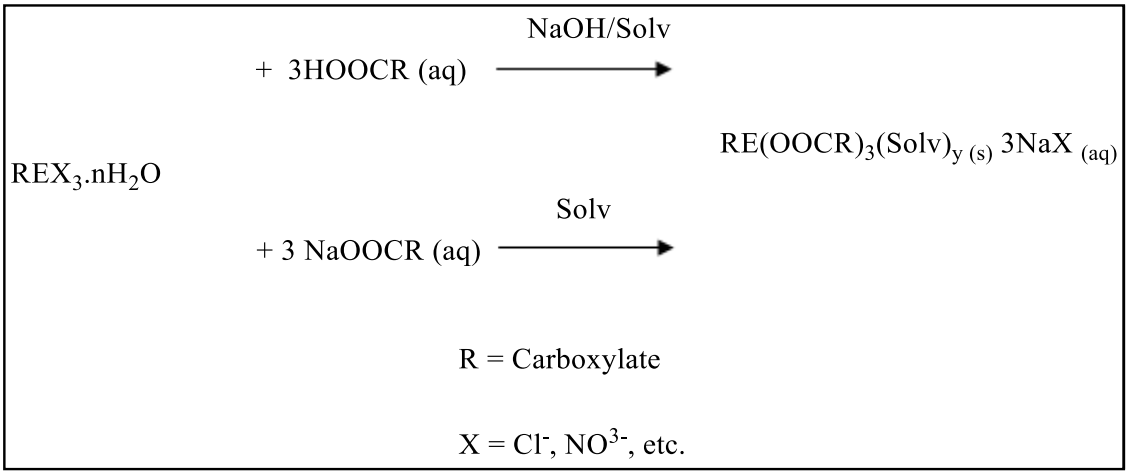
Forsyth et al. hypothesized that combining RE metal ions with an organic ligand, for instance, carboxylates would form new complexes with improved inhibitory effects. They proposed that these lanthanoid carboxylate complexes suppress both cathodic and anodic reactions synergistically by combining the inhibitory properties of the individual components. Their initial study on cerium (III) with three simple carboxylate derivatives (glycolate (13),

salicylate (14), and anthranilate (15)) led to complexes with promising corrosion inhibition properties on mild steel. Among them, cerium salicylate was the best performer, and the presence of both COO^- and OH groups on the aromatic organic inhibitor appears to have a beneficial effect on corrosion resistance. Corrosion tests and electrochemical measurements suggested that these compounds act as mixed inhibitors at the beginning and dominate by cathodic inhibition after 24 hours.[6] Further work reported a successful synthesis of heterometallic Ce-Fe salicylate bimetallic complexes to model the protective film forms on metal surfaces.[66]



(13) (14) (15)

Since then, over the past two decades, several compounds have been synthesised *via* metathesis reaction as shown in Scheme 1.1. These compounds are mainly prepared either by combining rare earth metal salts with carboxylic acids deprotonated with aqueous NaOH or treating with the preformed sodium salt of the ligand in a 1:3 mole ratio.[8,67]



Scheme 1.1: Metathesis reactions for rare earth carboxylate compounds.[8,67]

Blin et al. have evaluated a series of lanthanoid cinnamate compounds and assessed their surface protection properties on mild steel using weight loss tests and linear polarization resistance measurements. Lanthanum and cerium *para*-substituted derivatives have shown excellent inhibition performance for mild steel in NaCl solutions.[33,35] Thus the inhibition performance of cinnamate anions appeared to be improved with the introduction of O-CH_3,

NO_2 and OH substituents to the *para* position of the benzene ring. These studies are consistent with the previous work of Forsyth et al., where they have shown mixed inhibition and synergistic effect of organic and RE metal components.[6,68] Following on from that Deacon and coworkers have reported the synthesis and structural properties of anhydrous trivalent lanthanoid cinnamates.[68]

Amongst all the RE metal tertiary cinnamate based compounds tested so far $RE(4hocin)_3$ (4hocin = 4-hydroxycinnamate) demonstrated to have the highest inhibition efficiency with reduced corrosion rate similar to sodium chromate at one-fourth the concentration.[33,35,68,69]

Blin et al. conducted further studies using electrochemical methods to investigate the corrosion mitigation mechanism of $La(4hocin)_3$ on steel. The results of the experiment demonstrated that $La(4hocin)_3$ has an effect on both cathodic and anodic reactions. However, the predominant inhibition response was observed to change with the concentration of the inhibitor. A strong anodic response was exhibited at 800 ppm concentration, where the inhibitor displayed the highest level of protection against corrosion, and the inhibition effect improved with time.[69]

More recently, Catubig et al. have shown that $La(4hocin)_3$ acts as corrosion inhibiting pigment in polyurethane-coated mild steel. The results of filiform scribe tests suggested that $La(4hocin)_3$ stifled the initiation and propagation of both delamination and filiform corrosion of mild steel. In this application, the RE complex acted as a mixed inhibitor at neutral conditions, while anodic inhibition was observed at the filament tip under oxygen-depleted acidic conditions. Figure 1.10 illustrates the corrosion process of the coated metal in the presence and the absence of the inhibitor.[70]

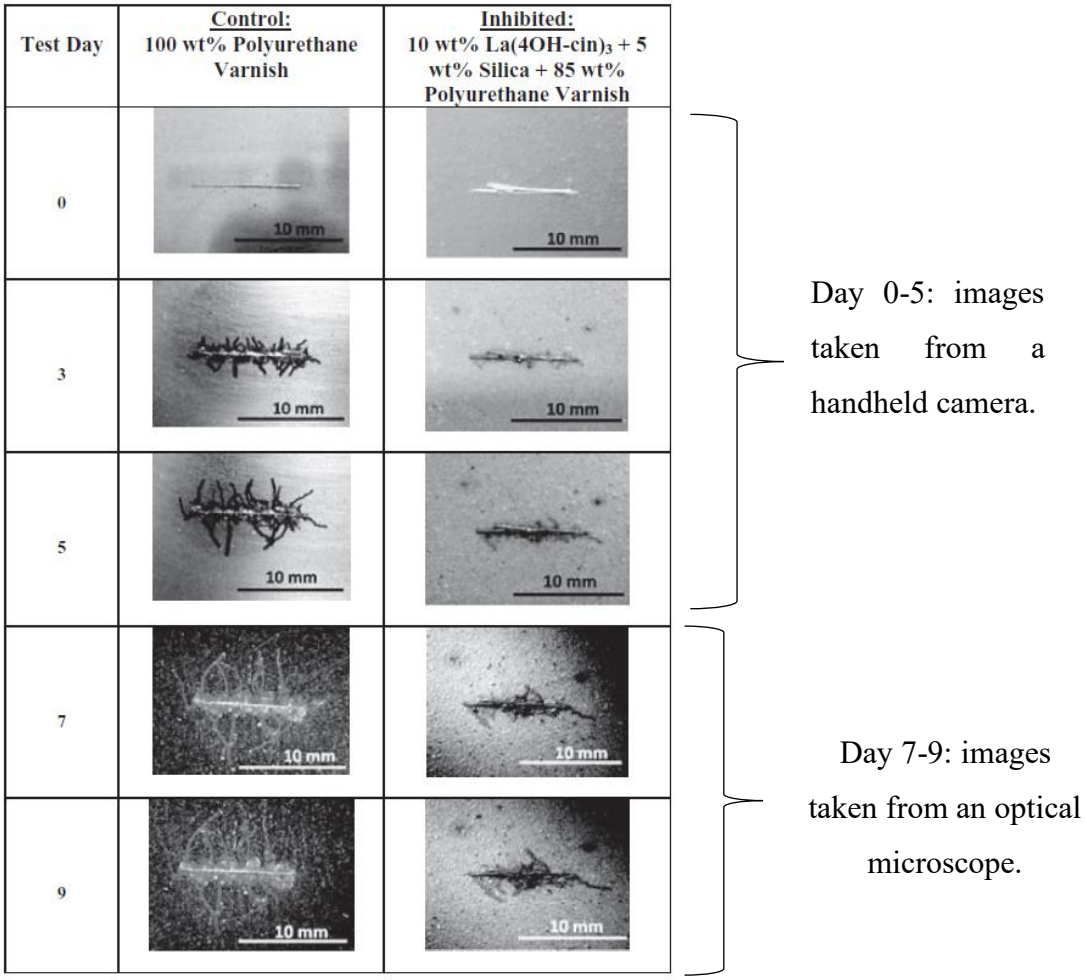


Figure 1.10: The growth of filament formation over 9 days in inhibited and control samples.

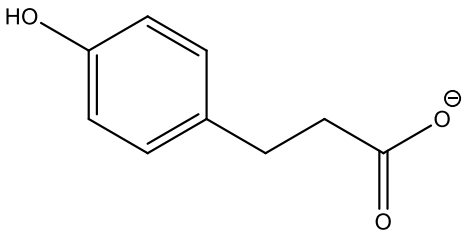
† *Reprinted with permission from "Effects of Corrosion Inhibiting Pigment Lanthanum 4-Hydroxy Cinnamate on the Filiform Corrosion of Coated Steel" by R. Catubig, M. Seter, W. Neil, M. Forsyth, B. Hinton, 2011, Journal of the Electrochemical Society, 158(11), page number C354. Copyright (2024) by IOP Publishing, Ltd.*

Seter et al. reported a detailed investigation on the speciation phenomenon of $La(4hocin)_3$ with its anti-corrosion performance as a function of pH and concentrations in 0.01 M salt solution for AS1020 steel. According to this study, an outstanding inhibition was performed by this compound under alkaline conditions and at relatively high concentrations. The study also showed that speciation in solution of $La(4hocin)_3$ is crucial for strong anodic protection observed at neutral and slightly basic pH. In contrast, at pH 2.5, lower mixed inhibition was observed due to the dissolution of lanthanum 4-hydroxycinnamate into separate entities as $LaCl_4^-$ and cinnamates. It was noted here that under acidic pH values and at lower concentrations, the nature of inhibition was predominantly cathodic due to the presence of excess $LaCl_4^-$ ions.[71]

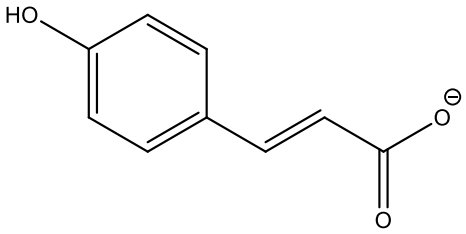
Results of another study confirmed the remarkable corrosion inhibition efficacy of $La(4hocin)_3$, while $Pr(4hocin)_3$ also showed comparable performance. The performance of $La(3hocin)_3$ (3hocin = 3-hydroxycinnamate) was only slightly less effective. On the other hand, $Ce(4hocin)_3$ and $La(2hocin)_3$ (2hocin = 2-hydroxycinnamate) demonstrated poorer inhibition efficiencies. The work here hypothesized that the difference in inhibition performance was influenced by the nature of the rare earth metal centre as well as the structural variation of the hydroxycinnamate ligand. It was noted a difference in the fragmentation pattern of the mass spectrum of $Ce(4hocin)_3$, indicating a difference in the speciation behaviour of the inhibitor, compared to the analogous praseodymium and lanthanum counterparts. This behaviour was consistent with the poor corrosion protection performance of $Ce(4hocin)_3$. As mentioned by the authors, one of the reasons for having such a difference, is related to its significantly higher solubility. It was also hypothesized that the existence of two oxidation states for cerium, as Ce^{3+} and Ce^{4+} might also be related to the difference in the electrospray mass spectrum, hence the inhibition properties. The orientation of the hydroxyl substituent also influences the bonding and protective film formation. In $La(2hocin)_3$, the hydroxyl group is positioned in the *ortho* position. This specific geometry alters the steric effect and prevents further interactions with the neighbouring molecules.[72]

Nam et al. reported the corrosion inhibition properties of cerium, lanthanum and praseodymium 4-hydroxycinnamates in CO_2 containing NaCl solutions. Even in this experiment $Ce(4hocin)_3$ showed the lowest inhibition action. The increasing order of the inhibition efficiency of the studied compounds was in the order of $Ce(4hocin)_3 < La(4hocin)_3 < Pr(4hocin)_3$.[73] Electrochemical and surface analysis data of another study also suggested $Pr(4hocin)_3$ as a novel effective steel corrosion inhibitor in naturally aerated and CO_2 containing salt solutions.[74]

The corrosion inhibition performance of lanthanum 3-(4'-hydroxyphenyl) propanoate (16) was studied and compared with the corresponding 4-hydroxycinnamate compound (17). The negative test results of the former established the importance of inclusion of the -CH=CH- unit for excellent anti-corrosion activity. It was also suggested that lanthanum 3-(4'-hydroxyphenyl)- propionate gave poor protection due to the lower stability of the complex in the test solution.[67]

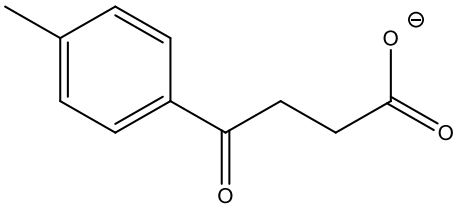


(16)



(17)

Further studies on the use of other RE carboxylate compounds as effective corrosion inhibitors has been reported in the literature. Other researchers synthesised a series of novel RE 3-(4' methylbenzoyl)propanoate (mbp) (18) compounds.[75] The structure of this ligand is different from 4-hydroxycinnamate as mbp has a carbonyl functionality in addition to the carboxylate group. It has been reported to involve hydrogen bonds between that carbonyl group oxygen and the hydroxyl groups on the steel surface, providing a greater level of inhibition.[76,77]



(18)

Further, the parent acid produced by Ciba specialty chemicals (known as Irgacor 419) is commercially used as a corrosion inhibitor when incorporated with 4-ethylmorpholine in a 2:1 ratio, as Irgacor 1405 in paint formulations.[75] According to the previously reported investigations on $[RE(mbp)_3(H_2O)]$ complexes with various RE metals, $Y(mbp)_3$ exhibited the best inhibition activity and behaved as a mixed inhibitor.[5,78] The inhibitor effectiveness was thought to be dependent on the type of RE metal present, and the order was reported as $Y(mbp)_3 > Nd(mbp)_3 > Ce(mbp)_3 > La(mbp)_3$.[5]

The difference in the behaviour in the performance of the RE mbp compounds was suggested to be associated with the ionic radius of the RE metal cation. Among the studied compounds, the RE ion with the smallest ionic radius, Y^{3+}, forms the most stable complex, thus its mbp complex provides the highest level of protection. Based on the polarization data, a synergistic effect was seen with $Y(mbp)_3$, as the reduction in corrosion current density was more effective compared to the combined effect of separate mbp and RE ions.[5] Moreover, 24 h immersion experiments showed that the inhibition performance of $Y(mbp)_3$ was also higher

than the well-known inhibitor La(4hocin)$_3$ at 0.25 mM concentration.[78] According to the surface analysis data and spectroscopy, Forsyth et al. have suggested a mechanism through which the RE mbp complex inhibits the corrosion. A very thin bimetallic Fe-carboxylate-RE complex is proposed to be formed on the metal surface upon the immersion of coupons in the inhibitor solution. In addition to that, a mixture of RE and iron oxide/hydroxide species will also be precipitated on the steel surface. Although RE(mbp)$_3$(H_2O) complexes show promising anticorrosion properties, the RE complexes of mbp failed to show any C=O-RE bonding interactions.[5,78]

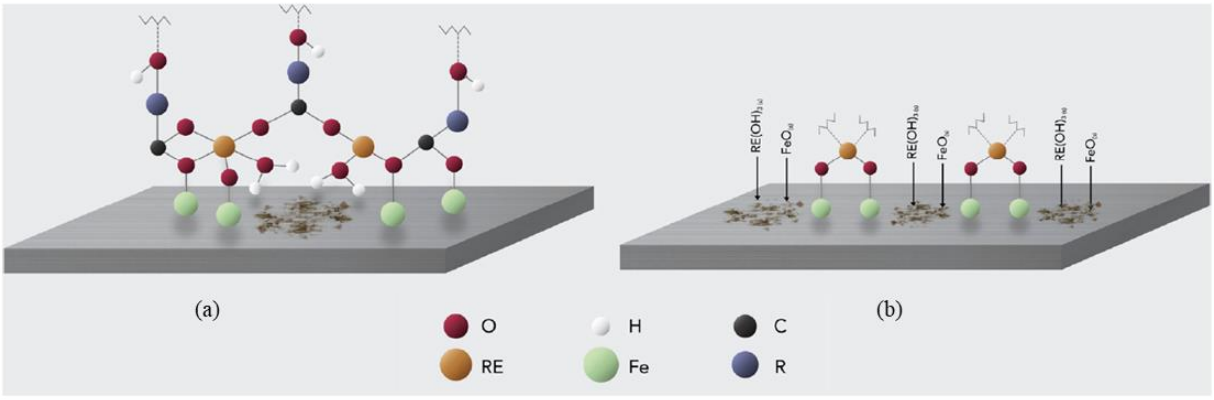
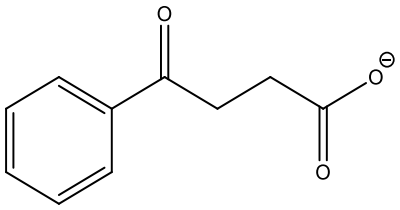


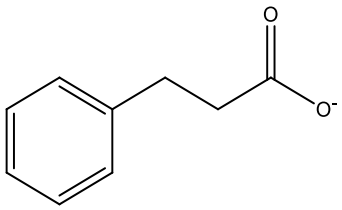
Figure 1.11: (a)The proposed mechanism of coordination of the complex to the iron on the surface and (b) the components present on the metal surface.

† *Reprinted with permission from "New, environmentally friendly, rare earth carboxylate corrosion inhibitors for mild steel" by A. E. Somers, B. R. W. Hinton, C. de Bruin-Dickason, G. B. Deacon, P. C. Junk, M. Forsyth, 2018, Corrosion Science, 139, page number 436. Copyright (2018) by Elsevier*

The low solubility of the excellent yttrium complex restricted the further investigation of the importance of carbonyl functionality in corrosion inhibition. Thus, to provide a basic understanding of the significance of the carbonyl group on inhibition activity, a study was conducted with a corresponding benzoyl derivative with improved solubility. In this study, rare earth complexes of 3-benzoylpropanoate (19) were compared with the analogous 3-phenylpropionate (20) compounds without the carbonyl group.[25]

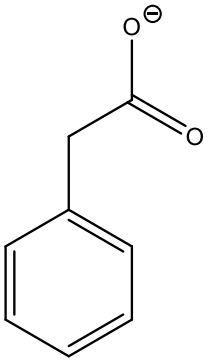


(19)



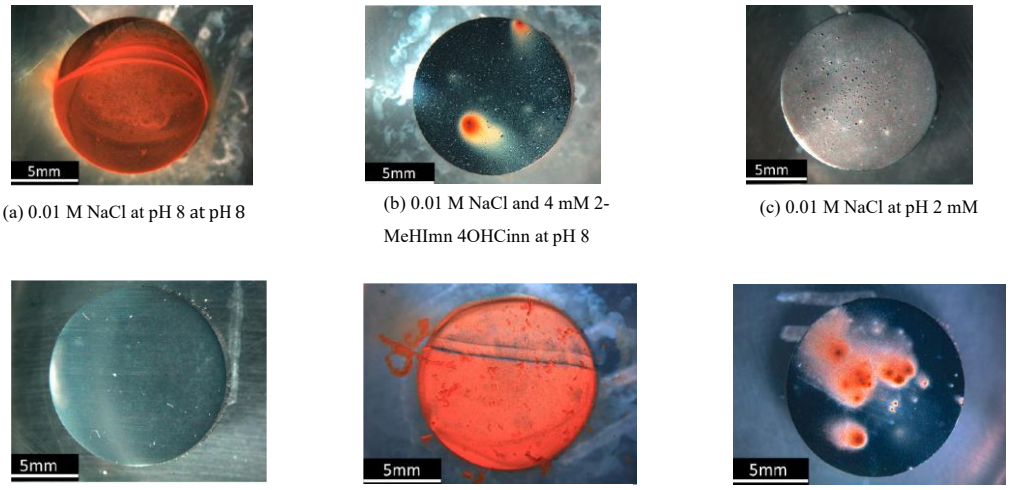
(20)

In recent years a range of phenylacetato (21) rare earth complexes were prepared in the presence of aqua and 2,2'-bipyridine (bpy) co-ligands.[3] Previous studies reported that the presence of bpy helps the formation of structurally well-defined dimers,[79,80] so it enabled to compare structures and the inhibitory effect of aqua and bpy species. According to the corrosion test results, out of all the tested compounds, $[Nd(PhAc)_3(H_2O)]_n$ (PhAc = phenylacetato) showed the highest inhibitory performance against mild steel with 55% percentage inhibition. However, the overall poor anti-corrosion performance of tested species in the above study suggested the importance of having additional non-coordinating donor groups for an effective inhibitory activity.[3]



(21)

In 2015, another study was carried out to develop a new compound that could inhibit microbiologically influenced corrosion. In this work, the RE cation was replaced by protic imidazolinium to make a totally organic complex with carboxylate anions.[29,81] 2-methylimidazolinium 4-hydroxycinnamate (2-Me-HImn 4hocin) has been shown to produce a high level of inhibition activity on mild steel in neutral chloride solutions across a wide range of pH conditions, particularly at pH 2 and 8.[29]



(a) 0.01 M NaCl at pH 8 at pH 8

(b) 0.01 M NaCl and 4 mM 2-MeHImn 4OHCinn at pH 8

(c) 0.01 M NaCl at pH 2 mM

(d) 0.01 M NaCl and 4 mM 2-MeHImn 4OHCinn at pH 2

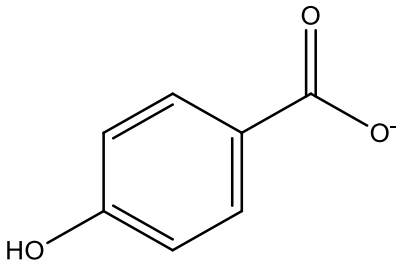
(e) 0.01 M NaCl neutral pH

(f) 0.01 M NaCl and 4 mM 2-MeHImn 4OHCinn neutral pH

Figure 1.12: Optical images of the mild steel coupons after 24 h immersion in 0.01 M NaCl solutions with and without 2-MeHImn 4OHCinn inhibitor at different pH values.

† *Adapted with permission from "Synergistic Corrosion Inhibition of Mild Steel in Aqueous Chloride Solutions by an Imidazolinium Carboxylate Salt" by A. L. Chong, J. I. Mardel, D. R. MacFarlane, M. Forsyth, A. E. Somers, 2016, ACS Sustainable Chemistry & Engineering, 4(3), page number 1749. Copyright (2016) by American Chemical Society*.

In 2023, Moon et al. synthesised a series of rare earth(III) 4-hydroxybenzoate (4hob) complexes using aqua and 2,2'-bipyridine (bpy) as co-ligands. Among the synthesised compounds, the Ce, La, and Y aqua complexes exhibited promising corrosion inhibition properties. Replacing water with bpy further enhanced their inhibition performance. All tested complexes were reported to surpass the established Ce(III) salicylate in effectiveness.[82]



(22)

1.6 General Approach and Current Study

Rare-earth compounds have emerged as promising and environmentally acceptable replacements for toxic chromates. It has been shown that a combination of rare earth metals with organic corrosion inhibitors is capable of providing effective mixed corrosion inhibition with synergism. Previous studies have found that cerium salicylate,[8] lanthanum 4-

hydroxycinnamate[35] yttrium 3-(4'-methylbenzoyl)propionates[78] and 4-hydroxybenzoate[82] are excellent inhibitors for mild steel in sodium chloride solutions.

The focus of the first section of our current study is on the development of new rare earth complexes, utilizing 3-thiophenecarboxylates (3tpc), 3-furoate (3-fur) and 2-methyl-3-furoate(2m3fur), in seeking improved rare earth carboxylate inhibitors on mild steel. The outstanding inhibitor properties of thiophene and furan derivatives makes the preparation and testing of their lanthanoid complexes of considerable interest. To examine the effect of steric inhibition on carboxylate coordination and capacity for corrosion inhibition, a 2-methyl group is introduced into the into the 3-furoate ion, compared with the inhibitory effect of unsubstituted lanthanoid 3-furoate complexes. RE(III) carboxylate complexes [$RE(O_2CR)_3$] are prepared through simple metathesis reactions of rare earth metal salts with stoichiometric amounts of the respective carboxylate derivatives.

Understanding the structural properties and corrosion inhibitor behaviour of alkali salts of organic carboxylic acid moieties have remained poorly explored. Thus, the preparation and testing of alkali salts of well-known corrosion inhibitors (4-hydroxycinnamate(4ohcin) and 4-hydroxybenzoate (4ohb)) as well as new alkali salt complexes (3tpc, 3fur and 2m3fur) will also be approached.

The synthesis and characterisation of these complexes, as well as the assessment of their corrosion mitigation performance, are detailed in Chapters 2 through 5. Weight loss data obtained from immersion studies were evaluated according to American Standard Test Methods (ASTM).[83] Potentiodynamic Polarization (PP) scans were employed as the electrochemical technique to identify the most effective inhibitors. AS1020 grade mild steel was used as the standard material for evaluating the performance of the rare earth carboxylate inhibitors.

Chapter 6, which focuses on the interaction of highly reactive lanthanoid complexes with organic substrates, differs from the previous chapters because all reactions were conducted under inert conditions. This chapter delves into the reactivity of these lanthanoid complexes, enhancing our understanding of Ln(II) coordination chemistry, particularly regarding the insertion and reductive coupling reactions of carbodiimides and the development of redox-active cationic species. Additionally, it includes a review of rare earth aryloxides and the reactivity of organolanthanoid compounds, topics not covered in the general introduction, which primarily discusses rare earth corrosion inhibitors. This is because the design of novel replacement corrosion inhibitors constitutes the bulk of the research presented in this thesis.

1.7 References

1 S. J. Garcia, J. M. C. Mol, J. H. W. de Wit, T. H. Muster, A. E. Hughes, T. Miller, T. Markley, J. Mardel and H. Terryn, Advances in the Selection and Use of Rare-Earth-Based Inhibitors for Self-Healing Organic Coatings, in *Self-Healing Properties of New Surface Treatments*, eds. Fedrizzi L., Fürbeth W. and Montemor F., Maney Publishing, United Kingdom, EFC., 2011, vol. 58, pp. 148–183.

2 N. Hossain, M. Asaduzzaman Chowdhury and M. Kchaou, *J. Adhes. Sci. Technol.*, 2021, **35**, 673–690.

3 E. Mottram, S. Hamilton, J. S. Moon, J. Wang, G. Bousrez, A. E. Somers, G. B. Deacon and P. C. Junk, *J. Coord. Chem.*, 2020, **73**, 2677–2697.

4 E. Bowman, N. Thompson, D. Gl, O. Moghissi, M. Gould and J. Payer, *NACE International*, 2016.

5 A. E. Somers, B. R. W. Hinton, C. de Bruin-Dickason, G. B. Deacon, P. C. Junk and M. Forsyth, *Corros. Sci.*, 2018, **139**, 430–437.

6 M. Forsyth, K. Wilson, T. Behrsing, C. Forsyth, G. B. Deacon and A. Phanasgoankar, *Corrosion*, 2002, **58**, 953–960.

7 Odio O.B., Chinwuko C.E., Chukwuneke L.J. and Sinebe E.J., *Int. J. Sci. Technol. Res.*, 2014, **3**, 306–310.

8 M. Forsyth, M. Seter, B. Hinton, G. Deacon and P. Junk, *Aust. J. Chem.*, 2011, **64**, 812–819.

9 B. Hinton, Corrosion Prevention and Control, in *Handbook on the Physics and Chemistry of Rare Earths*, eds. Gschneidner K. A. and Eyring L., Elsevier Science B.V., Amsterdam, 1995, vol. 21, pp. 29–92.

10 B. Brycki, I. Kowalczyk, A. Szulc, O. Kaczerewska and M. Pakiet, Organic Corrosion Inhibitors, in *Corrosion Inhibitors, Principles and Recent Applications*, ed. Mohmood Aliofkhazraei, IntechOpen, London, 2018, vol. 3, p. 33.

11 T. Behrsing, V. L. Blair, F. Jaroschik, G. B. Deacon and P. C. Junk, *Molecules*, 2024, **29**, 688.

12 V. Balaram, *Geoscience Frontiers*, 2019, **10**, 1285–1303.

13 F. Cotton, G. Wilkinson, C. Murillo and M. Bochmann, *Advanced Inorganic Chemistry*, John Wiley & Sons, New York, 6th edn., 1999.

14 S. Cotton, *Lanthanide and Actinide Chemistry*, John Wiley & Sons, Chichester, 2006.

15 A. E. Hughes, J. M. C. Mol and I. S. Cole, The cost and availability of rare earth-based corrosion inhibitors in *Rare Earth-Based Corrosion Inhibitors*, eds. Forsyth M. and Hinton B., Woodhead Publishing, Cambridge, 2014, pp. 291–305.

16 T. Behrsing, G. B. Deacon and P. C. Junk, The chemistry of rare earth metals, compounds, and corrosion inhibitors in *Rare Earth-Based Corrosion Inhibitors*, eds. Forsyth M. and Hinton B., Woodhead Publishing, Cambridge, 2014, pp. 1–37.

17 S. Cotton, *Two centuries of the rare earths* in Chimie nouvelle N° 133, 2020, pp1-12.

18 M. R. Macdonald, J. E. Bates, J. W. Ziller, F. Furche and W. J. Evans, *J. Am. Chem. Soc.*, 2013, **135**, 9857–9868.

19 W. J. Evans, *Inorg. Chem.*, 2007, **46**, 3435–3449.

20 M. N. Bochkarev, *Coord. Chem. Rev.*, 2004, **248**, 835–851.

21 R. D. Shannon, *Acta Crystallogr. A*, 1976, **32**, 751–767.

22 S. B. Castor and J. B. Hedrick, Rare Earth Elements in *Industrial minerals and rocks*, eds. J. E. Kogel, J. M. Barker, N. C. Trivedi and S. T. Krukowski, Society for Mining, Metallurgy, and Exploration, Inc., 7th edn., 2006, vol. 7, pp. 769–792.

23 H. El-Ramady, *VDM Verlag Dr. Müller*, 2010, 1–85.

24 P. W. Atkins, *Inorganic Chemistry*, Oxford University Press, Oxford, 5th edn., 2010.

25 N. C. Thomas, O. A. Beaumont, G. B. Deacon, C. Gaertner, C. M. Forsyth, A. E. Somers and P. C. Junk, *Aust. J. Chem.*, 2020, **73**, 1250–1259.

26 A. Ouchi, Y. Suzuki, Y. Ohki and Y. Koizumi, *Coord. Chem. Rev.*, 1988, **92**, 29–43.

27 C.-H. Huang, *Rare earth coordination chemistry: Fundamentals and Applications*, John Wiley & Sons, Peking University, China, 2010.

28 R. Janicki, A. Mondry and P. Starynowicz, *Coord. Chem. Rev.*, 2017, **340**, 98–133.

29 A. L. Chong, J. I. Mardel, D. R. MacFarlane, M. Forsyth and A. E. Somers, *ACS Sustain. Chem. Eng.*, 2016, **4**, 1746–1755.

30 M. Ghorbani, J. Soto Puelles, M. Forsyth, R. A. Catubig, L. Ackland, L. Machuca, H. Terryn and A. E. Somers, *J. Phys. Chem. Lett.*, 2020, **11**, 9886–9892.

31 J. Sinko, *Prog. Org. Coat.*, 2001, **42**, 267–282.

32 Y. Peng, A. E. Hughes, G. B. Deacon, P. C. Junk, B. R. W. Hinton, M. Forsyth, J. I. Mardel and A. E. Somers, *Corros. Sci.*, 2018, **145**, 199–211.

33 F. Blin, S. G. Leary, K. Wilson, G. B. Deacon, P. C. Junk and M. Forsyth, *J. Appl. Electrochem.*, 2004, **34**, 591–599.

34 M. Forsyth, T. Markley, D. Ho, G. B. Deacon, P. Junk, B. Hinton and A. Hughes, *Corrosion*, 2008, **64**, 191–197.

35 F. Blin, S. G. Leary, G. B. Deacon, P. C. Junk and M. Forsyth, *Corros. Sci.*, 2006, **48**, 404–419.

36 B. R. W. Hinton, *J. Alloys Compd.*, 1992, **180**, 15–25.

37 B. Hinton, N. Ryan, D. Arnott, P. Trathen, L. Wilson and B. Williams, *Corrosion Australasia*, 1985, **10**, 12.

38 B. R. W. Hinton and L. Wilson, *Corros Sci*, 1989, **29**, 967–985.

39 B. P. F. Goldie, J. J. McCarroll, Australian Patent AU-32947/84, 1984.

40 R. P. Kreh, J. Richardson, V. R. Kuhn, R. M. Spotnitz, C. G. Carter, V. Jovancicevic, European Patent 0538970A2, 1992.

41 T. Markley, F. Blin, M. Forsyth and B. Hinton, Multifunctional Rare Earth Organic Corrosion Inhibitors in *Rare Earth-Based Corrosion Inhibitors*, eds. M. Forsyth and B. Hinton, Woodhead Publishing, Cambridge, 2014, pp. 117–142.

42 M. Zheludkevich, K. Yasakau, S. K. Poznyak and M. Ferreira, *Corros. Sci.*, 2005, **47**, 3368–3383.

43 Y. Meng, W. Ning, B. Xu, W. Yang, K. Zhang, Y. Chen, L. Li, X. Liu, J. Zheng and Y. Zhang, *RSC Adv.*, 2017, **7**, 43014–43029.

44 R. Solmaz, E. Altunba and G. Karda, *Mater. Chem. Phys.*, 2011, **125**, 796–801.

45 M. Elayyachy, A. el Idrissi and B. Hammouti, *Corros. Sci.*, 2006, **48**, 2470–2479.

46 A. M. Al-Sabagh, N. M. Nasser, A. A. Farag, M. A. Migahed, A. M. F. Eissa and T. Mahmoud, *Egypt. J. Pet.*, 2013, **22**, 101–116.

47 S. M. Abd El Haleem, S. Abd El Wanees, E. E. Abd El Aal and A. Farouk, *Corros. Sci.*, 2013, **68**, 1–13.

48 D. A. Winkler, M. Breedon, A. E. Hughes, F. R. Burden, A. S. Barnard, T. G. Harvey and I. Cole, *Green Chem.*, 2014, **16**, 3349–3357.

49 D. Daoud, T. Douadi, H. Hamani, S. Chafaa and M. Al-Noaimi, *Corros. Sci.*, 2015, **94**, 21–37.

50 C. Verma, E. E. Ebenso and M. A. Quraishi, Ionic Liquids as Green Corrosion Inhibitors for Industrial Metals and Alloys in *Green Chem.*, IntechOpen, 2018, pp. 103-132.

51 A. Galal, N. F. Atta and M. H. S. Al-Hassan, *Mater. Chem. Phys.*, 2005, **89**, 38–48.

52 K. F. Khaled, *J. Electrochem. Soc.*, 2010, **157**, C116-C124.

53 S. Gronowitz, Thiophene and Its Derivatives, Part One in *The Chemistry of Heterocyclic Compounds*, eds. A. Weissberger. and E. C. Taylor, John Wiley & Sons, New York, 2009, vol 44.

54 J. Wang, L. An, J. Wang, J. Gu, J. Sun and X. Wang, *Adv. Colloid Interface Sci.*, 2023, 321.

55 S. V. Lamaka, M. L. Zheludkevich, K. A. Yasakau, M. F. Montemor and M. G. S. Ferreira, *Electrochim. Acta.*, 2007, **52**, 7231–7247.

56 A. N. Khramov, N. N. Voevodin, V. N. Balbyshev and M. S. Donley, *Thin Solid Films*, 2004, **447–448**, 549–557.

57 J. B. Matos, E. D'elia, O. E. Barcia, O. R. Mattos, N. Pébère and B. Tribollet, *Electrochim. Acta*, 2001, **46**, 1377–1383.

58 L. Tommesani, G. Brunoro, A. Frignani, C. Monticelli and M. Dal Collet, *Corros. Sci.*, 1997, **39**, 1221–1237.

59 F. E. T. Heakal and A. E. Elkholy, *J. Mol. Liq.*, 2017, **230**, 395–407.

60 M. A. Hegazy, *Corros. Sci.*, 2009, **51**, 2610–2618.

61 M. A. Abbas, E. I. Arafa, E. S. Gad, M. A. Bedair, O. E. El-Azabawy and H. I. Al-Shafey, *Inorg. Chem. Commun.*, 2022, **143**, 109758.

62 A. S. Fouda, A. A. El-Aal and A. B. Kandil, *Desalination*, 2006, **201**, 216–223.

63 F. Bentiss, M. Lagrenee, M. Traisnel and J. C. Hornez, *Corros. Sci.*, 1999, **41**, 789–803.

64 M. M. Osman and E. Khamis Al-Hanash, *Corrosion Prevention and Control*, 1994, **41**, 60.

65 M. M. Osman, E. Khamis, A. F. Hefny and A. Michael, *Anti-Corrosion Methods and Materials*, 1994, **41**, 3–7.

66 G. B. Deacon, C. M. Forsyth, T. Behrsing, K. Konstas and M. Forsyth, *Chem. Commun.*, 2002, **2**, 2820–2821.

67 G. B. Deacon, P. C. Junk, W. W. Lee, M. Forsyth and J. Wang, *New J. Chem.*, 2015, **39**, 7688–7695.

68 G. B. Deacon, C. M. Forsyth, P. C. Junk, M. Hilder, S. G. Leary, C. Bromant, I. Pantenburg, G. Meyer, B. W. Skelton and A. H. White, *Z. Anorg. Allg. Chem.*, 2008, **634**, 91–97.

69 F. Blin, P. Koutsoukos, P. Klepetsianis and M. Forsyth, *Electrochim. Acta*, 2007, **52**, 6212–6220.

70 R. Catubig, M. Seter, W. Neil, M. Forsyth and B. Hinton, *J. Electrochem. Soc.*, 2011, **158**, C353.

71 M. Seter, B. Hinton and M. Forsyth, *J. Electrochem. Soc.*, 2012, **159**, C181–C189.

72 M. Seter, G. M. A. Girard, W. W. Lee, G. Deacon, P. Junk, B. Hinton and M. Forsyth, *AIMS Mater. Sci.*, 2015, **2**, 1–15.

73 N. D. Nam, M. Mathesh, B. Hinton, M. J. Y. Tan and M. Forsyth, *J. Electrochem. Soc.*, 2014, **161**, C527–C534.

74 N. D. Nam, A. Somers, M. Mathesh, M. Seter, B. Hinton, M. Forsyth and M. Y. J. Tan, *Corros. Sci.*, 2014, **80**, 128–138.

75 C. N. de Bruin-Dickason, G. B. Deacon, C. M. Forsyth, S. Hanf, O. B. Heilmann, B. R. W. Hinton, P. C. Junk, A. E. Somers, Y. Q. Tan and D. R. Turner, *Aust. J. Chem.*, 2017, **70**, 478–484.

76 M. Frey, S. G. Harris, J. M. Holmes, D. A. Nation, S. Parsons, P. A. Tasker, S. J. Teat and R. E. P. Winpenny, *Angew. Chem. Int. Ed.*, 1998, **37**, 3245–3248.

77 M. Frey, S. G. Harris, J. M. Holmes, D. A. Nation, S. Parsons, P. A. Tasker and R. E. P. Winpenny, *Chem. Eur. J.*, 2000, **6**, 1407–1415.

78 Y. Peng, A. E. Hughes, G. B. Deacon, P. C. Junk, B. R. W. Hinton, M. Forsyth, J. I. Mardel and A. E. Somers, *Corros. Sci.*, 2018, **145**, 199–211.

79 M. Zhang, R. Hu, F. Liang and Z. Zhou, *J. Coord. Chem.*, 2006, **59**, 177–186.

80 L. Tian, I. Ren, J. J. Zhang, S. J. Sun, H. M. Ye, J. H. Bai and R. F. Wang, *J. Chem. Eng. Data*, 2009, **54**, 69–74.

81 A. L. Chong, M. Forsyth and D. R. Macfarlane, *Electrochim. Acta*, 2015, **159**, 219–226.

82 J. Moon, Z. Guo, O. A. Beaumont, S. Hamilton, G. Bousrez, E. Mottram, J. Wang, A. E. Somers, G. B. Deacon and P. C. Junk, *New J. Chem.*, 2023, **47**, 16843–16854.

83 *American-Standard-Test-Methods in ASTM G31-72*, Philadelphia, USA, 2004.

Chapter 2: Synthesis, Structural Characterisation and Corrosion Inhibiting Properties of Rare Earth 3-thiophenecarboxylate Complexes.

2.1 Introduction

2.1.1 Thiophene and its Derivatives

Thiophene, with the formula C_4H_4S, is a five-membered heterocyclic compound and the simplest representative of stable aromatic structures containing sulfur. It exits as a stable, colourless liquid that closely resembles benzene in odor and boiling point. Initially discovered by Viktor Meyer in 1882 as an impurity in commercial benzene, it was identified as the first representative of a new ring system and named thiophene. Thiophenes occur naturally in coal tar and petroleum.[1] Additionally, over the past few years, certain thiophene derivatives have also been isolated from plants in the family Compositae.[2]

The sulfur atom in the structure of thiophene acts as an electron-donating heteroatom, contributing two electrons to the aromatic sextet. This characteristic makes thiophene an electron-rich heterocycle.[3,4] This electron-donating behaviour of sulfur is reflected in the lower dipole moment of thiophene when compared to its saturated analogue, tetrahydrothiophene (O.52 D vs. 1.90 D),[5] emphasizing the role of the lone pair on sulfur in enhancing its aromaticity.[6] One significant characteristic of thiophene is its capacity to serve as a ligand in coordination complexes. The sulfur atom within thiophene has the ability to coordinate with metal ions, making it valuable in catalysis and in the synthesis of metal-containing compounds.[7]

Thiophenes have seen widespread use over the last three decades across various areas, including the production of pharmaceuticals, agrochemicals, dyes, polymers, and veterinary drugs.[7,8] Thiophene-containing compounds are recognized for their diverse biological activities, including antioxidant activity,[9] anti-inflammatory effects, and inhibition of HIV Protease.[10] Moreover, they play a significant role in the development of thienopyridine-class antiplatelet agents for treating cardiovascular diseases.[7,11] Additionally, besides their biological activity, thiophene derivatives also demonstrate antiradiation activity.[12] The interest in thiophene oligomers stems from their broad spectrum of photobiological effects.[3,13] Thiophene, along with its oligomers and substituted derivatives, can undergo chemical or electrochemical polymerization processes.[13] For example, the polymer polythiophene is known for its outstanding

electrical conductivity, and employed in manufacturing electronic devices like solar cells and transistors.[7,14] Furthermore, thiophene derivatives frequently serve as semiconducting, light-harvesting, or electroluminescent materials.[15,16] Thiophene is extensively researched and utilized in the production of commercial agricultural fungicides, such as penthiopyrad and isofetamid, owing to its broad and effective antifungal properties.[17] Furthermore, in the dye industry, thiophene serves as a foundational component for the synthesis of various dyes, including azo dyes.[18]

2.1.2 Organic Compounds Containing Sulfur Atoms as Corrosion Inhibitors

Corrosion protection by organic corrosion inhibitors is related to the development of protective layers on metals.[19] Among organic systems, compounds containing hetero atoms are considered to have a higher inhibiting performance due to their strong affinity for metallic surfaces.[20–22] A group of CSIRO researchers developed a rapid screening test to investigate the inhibitive capacity of a series of structurally related compounds on aluminium alloys, and showed that -*para* and -*ortho* thiol substituted carboxylates could strongly inhibit corrosion on AA2024 and AA7075 alloys.[23]

A study was carried out by Szklarska-Smialowska and Kaminski in 1973 to investigate the effect of nucleophilic and electrophilic substituents on the thiophene ring on corrosion inhibition ability of mild steel in 1N H_2SO_4 solution. The results of the study showed that irrespective of the nature of the substituent, the replacement of a hydrogen atom on the thiophene ring would increase the inhibition performance. When considering nucleophilic substituents, with the increase in electron density in the thiophene ring, protective ability improved. However, contradictory results were observed for thiophene derivatives with electrophilic substituents. Even though the electron-withdrawing groups reduce the electron density of the aromatic ring, inhibition efficiency increased. Hence, it was explained as follows: by introducing polar electrophilic substituents (for example, 2-COOH, 2-$COCH_3$, 2-CHO, 2-$COOCH_3$), the dipole moment of the molecule increases, and it leads to stronger adsorption on the metal surface.[24]

Similar work was done by Fouda et al. [25] in 1986 and studied the inhibitive characteristics of some thiophene derivatives towards the corrosion of iron in 2N HNO_3. The results also indicated that the substitution of the *ortho* hydrogen atom on the thiophene ring with an electrophilic group increased the inhibition performance, and the

order of the inhibition efficiency of the functional groups was -CHO > -$COCH_3$ > -COOH > -H. This behaviour correlated with the dipole moment of the molecule. However, according to another explanation, in strongly acidic solutions (pH around 0), thiophene exists in equilibrium with its cationic form as shown in Figure 10. Thus, the introduction of an electron-withdrawing group on the ring would increase the positive charge of the protonated form. As a result of that, coulombic interaction will be improved, and adsorption ability will also be increased.

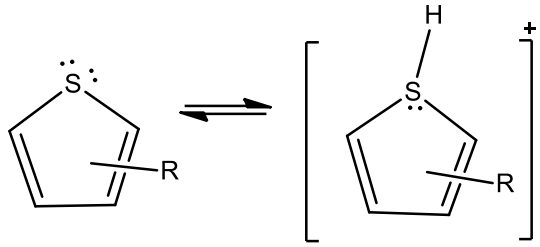
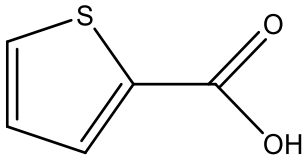
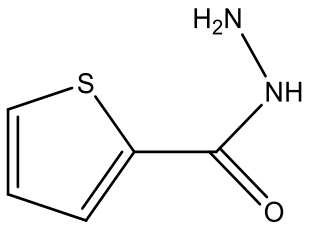


Figure 2.1: Equilibrium between thiophene and its cationic form.[25]

The inhibitive effect of thiophene derivatives on carbon metal steel corrosion in 1M HCl was also reported by Fouda and coworkers. It was shown that the corrosion inhibition potential was in the order of 2-thiophenecarboxylic acid hydrazide > 2-thiophenecarboxylic acid. The obtained results suggested that the presence of a higher number of adsorption centres attribute to stronger adsorption on the surface of the metal, hence greater inhibition efficiency.[26]

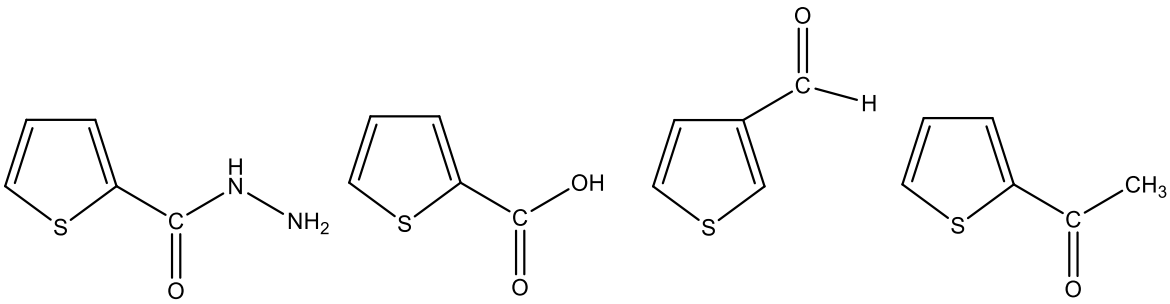


2-thiophene carboxylic acid and



2-thiophene carboxylic acid hydrazide

Similar findings were obtained by other authors while investigating the inhibition efficiency of four thiophene derivatives on stainless steel in an acidic medium containing chloride ions. The corrosion inhibition followed the order of 2-thiophene carboxylic acid hydrazide (TCH) > 2-thiophene carboxylic acid (TCA) ≈ 3-thiophene carboxaldehyde (TCAL) > 2-acetylthiophene (ACT).



(a) TCH (b) TCA (c) TCAL (d) ACT

The results of this study demonstrated that the following factors influence corrosion inhibition efficiency.[27]

i. the nature of the molecular structure
ii. the number of substituents present, and
iii. the electronic density of the sulfur atom

2.1.3 Current Study

In seeking improved rare earth carboxylate inhibitors, the focus of our current study is on the development of novel RE complexes incorporating 3-thiophenecarboxylic acid inhibitors. Given the promising inhibitor properties of thiophene derivatives, we have undertaken a study on lanthanoid complexation by 3-thiophene carboxylate.

Herein we now report the preparation and structural characterisation of a range of rare-earth (RE) 3-thiophenecarboxylate (3tpc) complexes (RE = La, Ce, Pr, Nd, Sm, Gd, Dy, Ho, Y, Er, Lu). All eleven 3-thiophenecarboxylate complexes were characterised by IR, elemental analysis, TGA measurements and powder XRD. Where single crystals suitable for X-ray crystallography are obtained, and they were analysed crystallographically.

The aim is to examine how the lanthanoid contraction impacts the crystal structures of these compounds and to investigate the various structural motifs displayed by these complexes across the lanthanoid series.

Additionally, all of these compounds underwent screening for their effectiveness in mitigating corrosion of mild steel. Immersion tests and potentiodynamic polarization

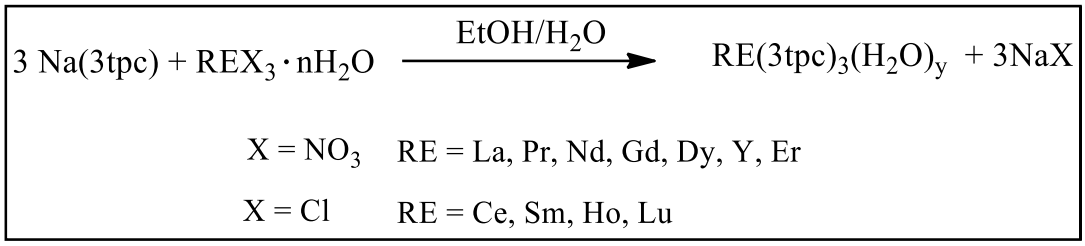
were utilized to evaluate the anti-corrosion properties of each compound compared to a control.

All the work in this chapter resulted in a publication in the journal *New Journal of Chemistry* (see reprint in Appendix Two).

2.2 Results and Discussion

2.2.1 Synthesis and Characterisation

The complexes $[RE(3tpc)_3(H_2O)_3]_n$ (RE = La, Ce, Pr, Nd, Sm, Gd) and $[RE_2(3tpc)_6(H_2O)_4]\cdot H_2O$ (RE = Dy, Ho, Y, Er, Lu) were synthesised in good yields by salt elimination metathesis reactions between sodium 3-thiophenecarboxylate and a suitable RE salt (mole ratio 3:1) as shown in Scheme 2.1. All reactions immediately gave a precipitate of the relevant rare earth complex. The pH of the reaction media was maintained within the range of 5-7.



Scheme 2.1: The synthesis of RE 3-thiophenecarboxylate complexes.

In all cases, bulk products were separated as precipitates. Single crystals of the complexes suitable for X-ray crystallography were obtained by slow evaporation of the mother liquor after filtration of the reaction mixture to isolate the precipitate. The compositions of the complexes were derived from X-ray crystallography together with elemental analysis and thermogravimetric analysis (TGA). The characterisation of the bulk samples was carried out after drying to constant weight over silica gel. Only the Lu complex **2.11** lost water from the single crystal composition under the drying conditions and both coordinated and lattice water was lost. In the microanalysis data four complexes had low % C, a frequent problem with rare earth metal-organic compounds,[28–34] but additional % RE analyses and TGA data leave little doubt as to the bulk composition.

The X-ray powder diffraction patterns of the bulk samples $[RE(3tpc)_3(H_2O)_3]_n$ (RE = La**(2.1)**, Ce**(2.2)**, Pr**(2.3)**, Nd**(2.4)**, Sm**(2.5)**, Gd**(2.6)**) are identical to each other and agree with the simulated pattern of $[Pr(3tpc)_3(H_2O)_3]_n$ derived from the single-crystal data (Figure 2.2). Powder XRD analyses of $[RE_2(3tpc)_6(H_2O)_4]\cdot H_2O$ (RE = Dy**(2.7)**,

Ho**(2.8)**, Y**(2.9)**, Er**(2.10)**, Lu**(2.11)**) show similar powder diffractograms and they are almost identical to the generated powder diffractogram for $[Er_2(3tpc)_6(H_2O)_4]\cdot H_2O$ (Figure 2.3). In the case of **2.11**, this similarity obtains despite dehydration. These data indicate there are two isostructural groupings for the series of RE elements.

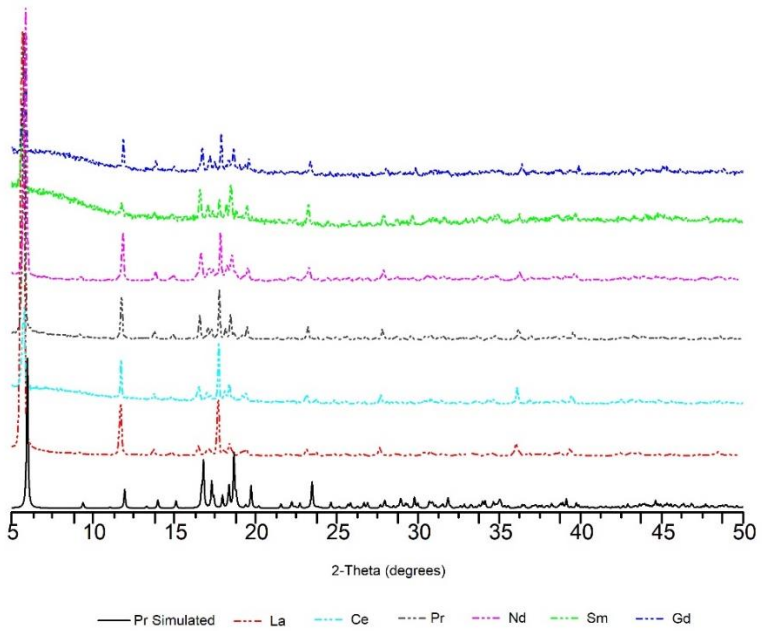


Figure 2.2: PXRD diffractograms of the $[RE(3tpc)_3(H_2O)_3]_n$ **(2.1-2.6)** series at room temperature.

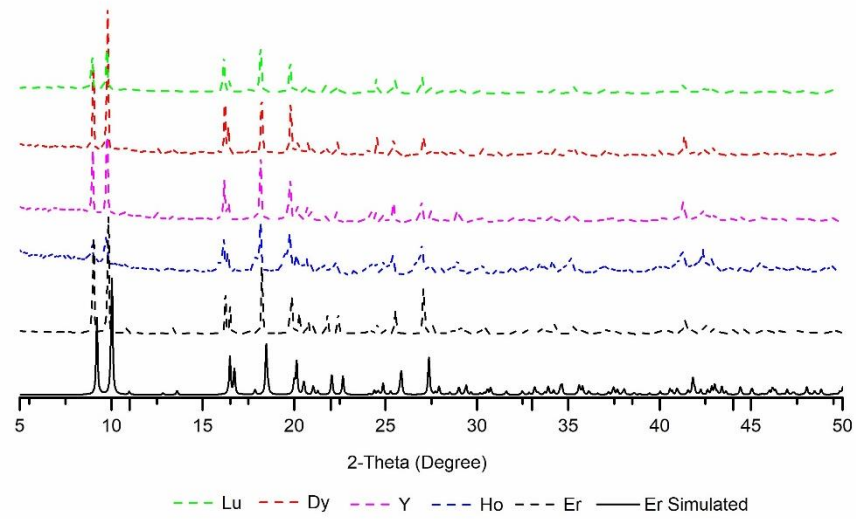


Figure 2.3: PXRD diffractograms of the $[RE_2(3tpc)_6(H_2O)_4]\cdot H_2O$ **(2.7-2.11)** series at room temperature.

The IR spectra within each isostructural series $[RE(3tpc)_3(H_2O)_3]_n$ (RE = La, Ce, Pr, Nd, Sm, Gd) (Figure 2.4) and $[RE_2(3tpc)_6(H_2O)_4]\cdot H_2O$ (RE = Dy, Ho, Y, Er, Lu) (Figure 2.5) are the same, apart from the absence of water absorption for **2.11**. Thus,

important spectral data are listed for only one compound from each group (RE = Pr **(2.3)**; RE = Er **(2.10)**). The data of the complexes in series $[RE(3tpc)_3(H_2O)_3]_n$ is only slightly different from that of series $[RE_2(3tpc)_6(H_2O)_4]\cdot H_2O$. This observation suggests comparable binding modes in the compounds with each series.

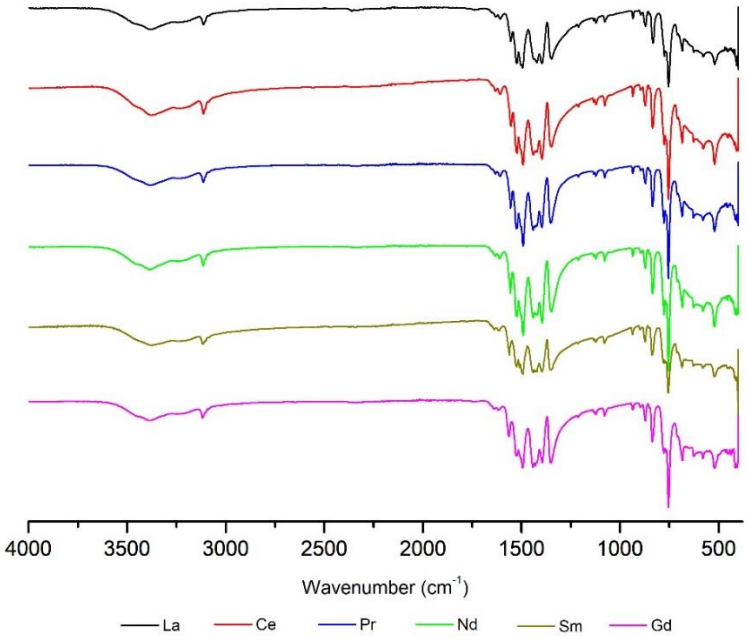


Figure 2.4: IR spectra of the $[RE(3tpc)_3(H_2O)_3]_n$ **(2.1-2.6)** series.

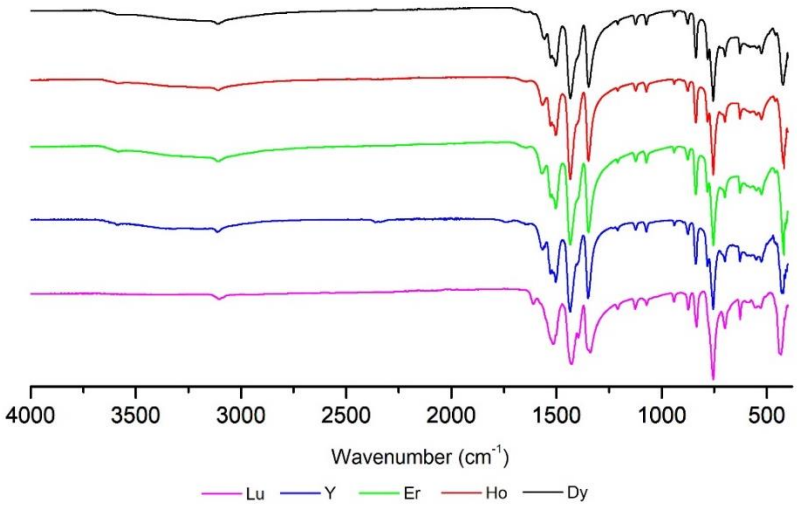


Figure 2.5: IR spectra of the $[RE_2(3tpc)_6(H_2O)_4]\cdot H_2O$ **(2.7-2.11)** series.

The broad bands at 3200-3550 cm^{-1} are characteristic of the coordinated and lattice water molecules. All the compounds exhibit the strong absorption bands characteristic of asymmetric and symmetric stretching vibrations of the carboxylate groups of the ligand 3tpc at 1530 - 1395cm^{-1}. The relatively small splitting between the

asymmetric and symmetric modes are consistent with the bridging and chelating carboxylates exhibited in the structures (below).[35]

Table 2.1: Selected infrared bands (cm^{-1}) of the RE 3-thiophenecarboxylate complexes.

Complex	**$\nu(OH)_{water}$**	**$\nu_{as}(CO_2)$**	**$\nu_s(CO_2)$**	**$\Delta\nu$†**	**$\delta(CO_2)$**
$[Pr(3tpc)_3(H_2O)_3]_n$	3381	1525,1493	1395	98	685
$[Er_2(3tpc)_6(H_2O)_4]\cdot H_2O$	3326	1528,1504	1394	110	699

The TGA of bulk samples of $[RE(3tpc)_3(H_2O)_3]_n$ (**RE** = La, Ce, Pr, Nd, Sm, Gd) and $[RE_2(3tpc)_6(H_2O)_4]\cdot H_2O$ (**RE** = Dy, Ho, Y, Er) (discussed above) showed loss of water around 100 °C (Figure 2.6 and 2.7) consistent with the single-crystal compositions, while the TGA data obtained from the bulk sample of $[Lu_2(3tpc)_6(H_2O)_4]\cdot H_2O$ **(2.11)** showed significantly different behaviour as the compound had lost all the lattice and coordinated water from the structure derived from the single crystal composition prior to the measurement, and is also evident from elemental analyses.

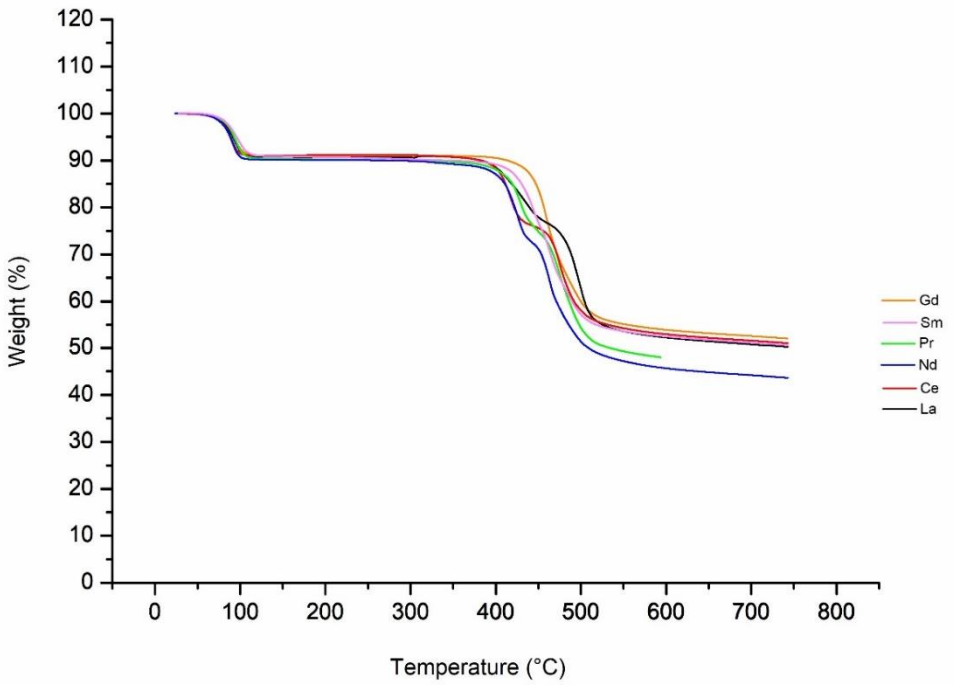


Figure 2.6: TGA thermograms of the $[RE(3tpc)_3(H_2O)_3]_n$ **(2.1-2.6)** series.

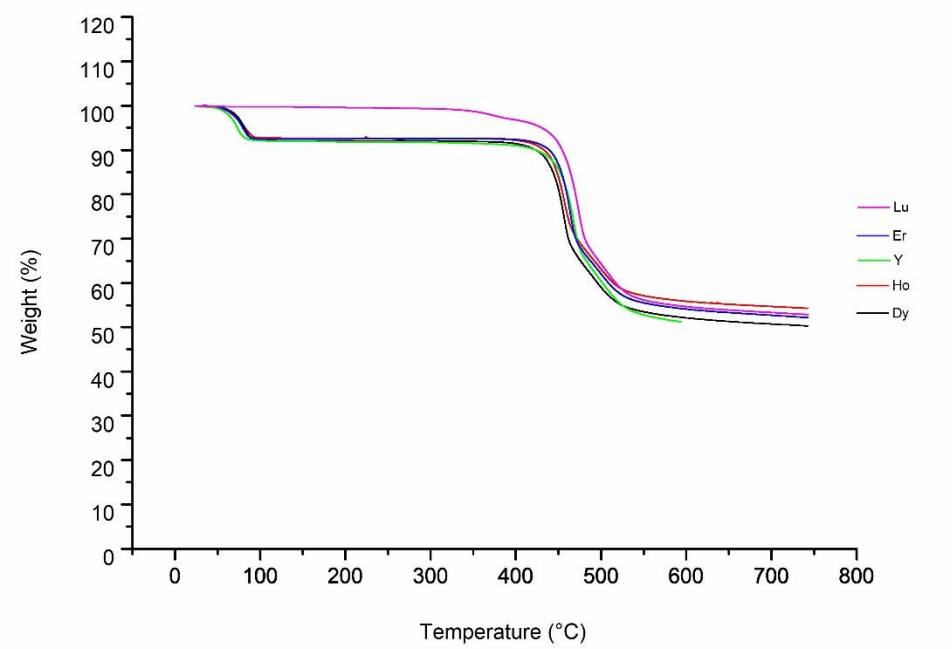


Figure 2.7: TGA thermograms of the $[RE_2(3tpc)_6(H_2O)_4]\cdot H_2O$ **(2.7-2.11)** series.

Further defined loss is observed for all the compounds at *ca*. 400-500 °C, plausibly from the decomposition of the anhydrous complexes into $RE_2(CO_3)_3$ and the diheteroaryl ketone. Such thermal behaviour of metal carboxylates is known.[36,37] This interpretation is supported by the infrared spectra (Figure 2.8) of the residues after thermolysis of $[Nd(3tpc)_3(H_2O)_3]_n$ and $[Er_2(3tpc)_6(H_2O)_4]\cdot H_2O$ to 500 °C as they corresponded closely to that reported for $[Dy_2(CO_3)_3].4H_2O$.[38] There is evidence of an intermediate formation in the TGA data of **2.1–2.4**, but not **2.5, 2.6.** The weight loss corresponds approximately to formation of $RE_2(3tpc)_4(CO_3)$ (see Experimental). The instability of this intermediate for **2.5** and **2.6** perhaps relates to greater stability of the final carbonate species relative to the intermediate as the ionic radius of RE^{3+} decreases.

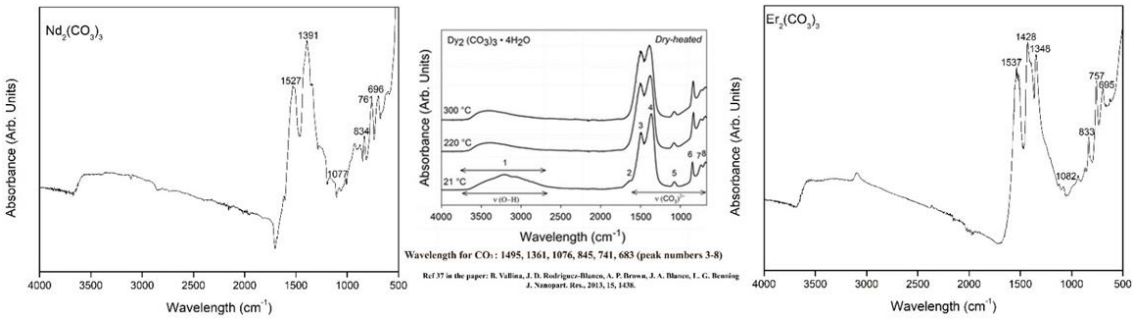
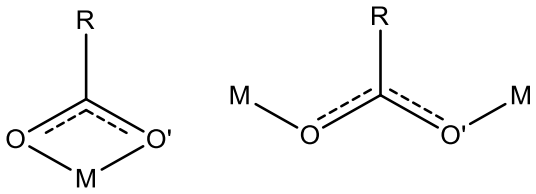


Figure 2.8: IR spectra of $Nd_2(CO_3)_3$ (left) from thermal decomposition of **2.4**, reported $Dy_2(CO_3)_3\cdot 4H_2O$ (middle) and $Er_2(CO_3)_3$ (right) from thermal decomposition of **2.10**.

2.2.2 X-ray Crystal Structures

Crystal structures of $[RE(3tpc)_3(H_2O)_3]_n$ (RE = La, Ce, Pr, Nd, Sm, Gd) and $[RE_2(3tpc)_6(H_2O)_4]\cdot H_2O$ (RE = Dy, Ho, Y, Er, Lu) were determined. The structures exhibit two types of carboxylate ligand binding modes : chelating κ(O, O′) and bridging μ_2-1κ(O):2κ(O′).



κ(O, O′) *anti-anti* μ_2-1κ(O):2κ(O′)

2.2.2.1 1D Polymeric Chains of $[RE(3tpc)_3(H_2O)_3]_n$ Complexes (RE = La, Ce, Pr, Nd, Sm, Gd)

The isostructural series of complexes $[RE(3tpc)_3(H_2O)_3]_n$ (RE = La **(2.1)**, Ce **(2.2)**, Pr **(2.3)**, Nd **(2.4)**, Sm **(2.5)**, Gd **(2.6)**) form a 1D polymeric chain with nine coordinated rare-earth ions and crystallize in the monoclinic space group $P2_1/c$. The representative structure of $[Pr(3tpc)_3(H_2O)_3]_n$ is discussed here, and part of the polymeric structure is shown in Figure 2.9.

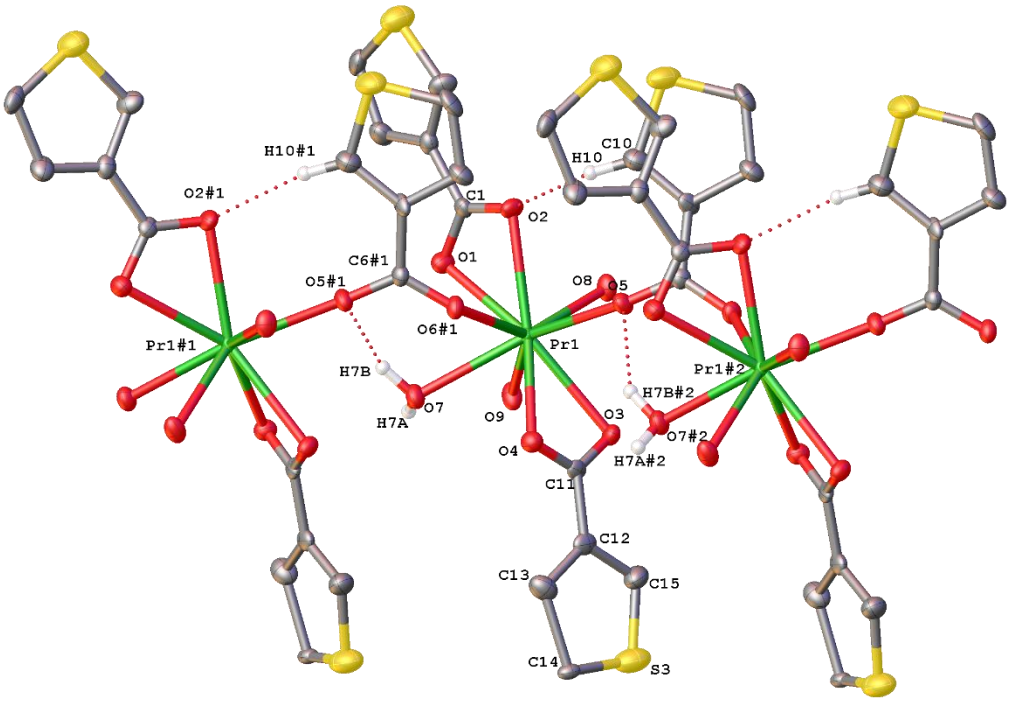


Figure 2.9: Molecular diagram of $[Pr(3tpc)_3(H_2O)_3]_n$ **(2.3)** generated from single-crystal XRD data. (representative of RE = La **(2.1)**, Ce **(2.2)**, Nd **(2.4)**, Sm **(2.5)**, Gd **(2.6)**). Thermal ellipsoids are drawn at the 50% probability level. The hydrogen atoms except for those forming hydrogen bonds have been omitted for clarity. Selected bond lengths (Å) and angles (°) (Data for **2.1-2.6** in Table 2.2). **2.3** Pr1-O1 2.570(5), Pr1-O2 2.531(5), Pr1-O3 2.577(5), Pr1-O4 2.523(5), Pr1-O5 2.468(5), Pr1-O6#1 2.489(5), Pr1-O7 2.538(5), Pr1-O8 2.485(5), Pr1-O9 2.495(5), Pr1#1-Pr1-Pr1#2 118.274(13), O8-Pr1-O9 71.056(16), O9-Pr1-O7 67.955(14)°, O7-Pr1-O8 135.002(16), C1...Pr1...C11 172.918(3), Symmetry Code: $^{\#1}$ +X, ½-Y, ½+Z; $^{\#2}$ +X, ½-Y, -½+Z.

The coordination environment of the asymmetric unit comprises two different carboxylate ligand binding modes and water molecules resulting in distorted tricapped trigonal prismatic geometry about the metal centre (Figure 2.10). There are four chelating oxygen atoms from two κ (O,O′) carboxylates (binding through O1,2 and O3,4), one bridging oxygen atom from each of two *anti-anti* μ_2-1κ(O):2κ(O′) carboxylates (binding through O5, O6#1) and three ligated water oxygen atoms (O7, O8, O9).

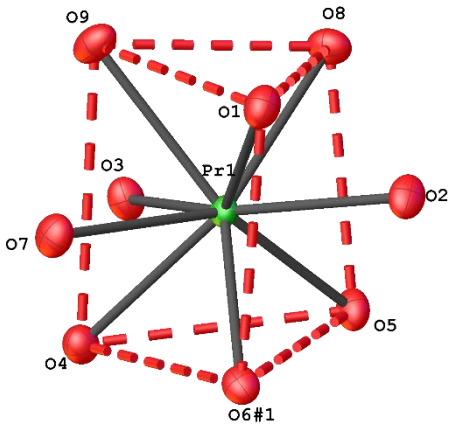


Figure 2.10: Orientation of bonding oxygen atoms surrounding the Pr1 metal centre, illustrating its overall geometry. For clarity, non-metal atoms, except those directly adjacent to the metal centre, are omitted. The red dashed lines (----) represent the triangular prism formed by the oxygen atoms with O2, O3 and O7 as the capping atoms of the trigonal prism. Symmetry equivalents: $^{\#1}$ +X, ½-Y, ½+Z.

The structure forms a 1D polymeric chain through a bridging carboxylate ligand O5#1-C6#1-O6#1 between the 9 coordinated Pr1 and Pr1#1 atoms. The distance between each adjacent Pr metal centre is 6.2763(9) Å, with Pr1#1-Pr1-Pr1#2 at an angle of 118 .274(13)°. The average Pr-O bond length observed for complex **2.3** is 2.520(2) Å, with

the shortest bond Pr1-O5 (2.468(5) Å) and the longest bond Pr1-O3 (2.577(5) Å). The former involves a bridging oxygen rather than any of the terminal oxygens. The two chelating rings are quite symmetrical. The ligated water oxygen atoms have angles with Pr1 at of 71.056(16)° (O8-Pr1-O9), 67.955(14)° (O9-Pr1-O7), and 135.002(16)° (O7-Pr1-O8) respectively. The two chelating carboxylate ligands have a *trans* disposition C1…Pr1…C11 172.918(3)°.

The effect of the ionic radii on the variation in the RE-O bond length can be examined (Table 2.2). A decrease in the average RE-O bond distance across the RE series from La to Gd [RE = La 2.557(1) Å, Ce 2.540(1)Å, Pr 2.520(2) Å, Nd 2.501(1) Å, Sm 2.473(2) Å, Gd 2.452(1) Å] is consistent with lanthanoid contraction.[39]

Table 2.2: Selected bond lengths and distances (Å) for the isostructural $[RE(3tpc)_3(H_2O)_3]_n$ series.

	La1 (2.1)	**Ce1 (2.2)**	**Pr1 (2.3)**	**Nd1 (2.4)**	**Sm1 (2.5)**	**Gd1 (2.6)**
RE1#1 =RE1#2	6.3117(9)	6.2961(3)	6.2763(9)	6.2360(9)	6.2060(9)	6.1655(9)
O1	2.610(3)	2.598(3)	2.570(5)	2.529(4)	2.525(5)	2.478(4)
O2	2.583(3)	2.552(3)	2.531(5)	2.553(3)	2.464(5)	2.494(3)
O3	2.568(3)	2.602(3)	2.577(5)	2.555(4)	2.518(4)	2.451(3)
O4	2.620(3)	2.550(3)	2.523(5)	2.502(3)	2.499(5)	2.514(3)
O5	2.501(3)	2.484(3)	2.468(5)	2.464(3)	2.430(4)	2.413(3)
O6#1	2.510(3)	2.504(3)	2.489(5)	2.456(3)	2.441(4)	2.421(3)
O7	2.577(3)	2.518(3)	2.538(5)	2.461(3)	2.434(5)	2.410(3)
O8	2.524(3)	2.499(3)	2.485(5)	2.469(3)	2.452(4)	2.418(3)
O9	2.518(3)	2.557(3)	2.495(5)	2.523(3)	2.493(4)	2.471(3)

There is hydrogen bonding from one of the bridging oxygen atoms O5 and one water oxygen atom O7#1 attached to the adjacent metal centre. Moreover, an H bond forms between O2-H10-C10 resulting in an unusual 7-membered ring (Figure 2.9 and Table 2.3).

Table 2.3: Hydrogen bonds for $[Pr(3tpc)_3(H_2O)_3]_n$ (**2.3**) [d/Å and </°].

D-H…A	**d(D-H)**	**d(H…A)**	**d(D…A)**	**<(DHA)**
O7#2-H7B#2…O5	0.8699	2.2476	2.9587	138.882
C10-H10…O2	0.9502	2.1510	3.0093	149.599

2.2.2.2 Dimeric Structures of $[RE_2(3tpc)_6(H_2O)_4]\cdot H_2O$ Complexes (RE = Dy, Ho, Y, Er, Lu)

The molecular structure of $[Er_2(3tpc)_6(H_2O)_4]\cdot H_2O$ can be found in Figure 2.11 and is a representative of the isomorphous series of dimeric complexes $[RE_2(3tpc)_6(H_2O)_4]\cdot H_2O$ (RE = Dy **(2.7)**, Ho **(2.8)**, Y **(2.9)**, Lu **(2.11)**) that crystallizes in monoclinic $P2_1/c$ space group with eight coordinate lanthanoid ions exhibiting distorted square antiprismatic geometry (Figure 2.12).

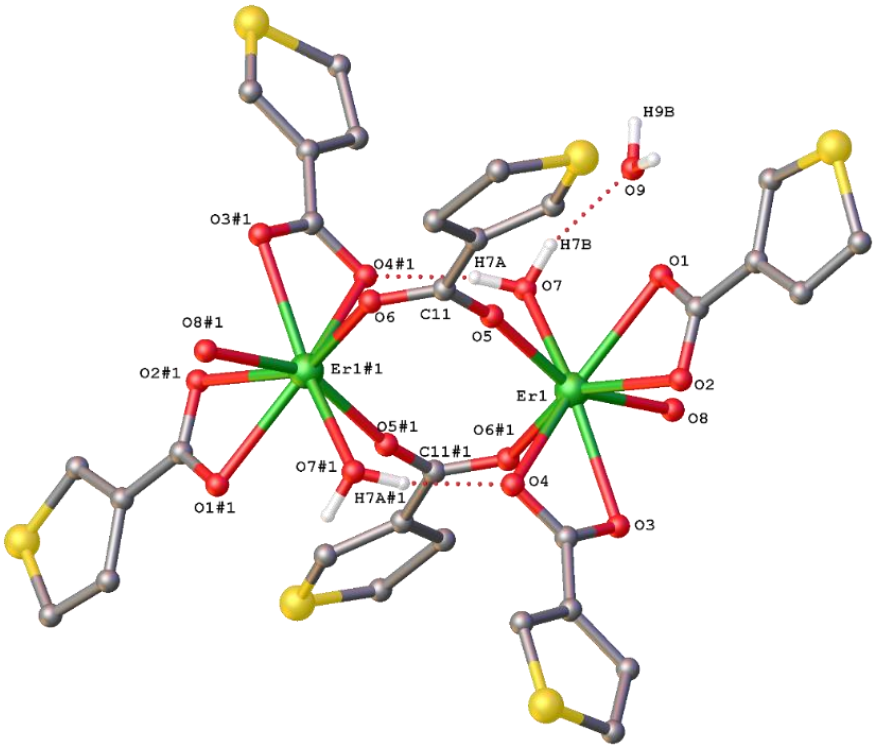


Figure 2.11: Molecular diagram of $[Er_2(3tpc)_6(H_2O)_4]\cdot H_2O$ **(2.10)** generated from single-crystal XRD data. (representative of Dy **(2.7)**, Ho **(2.8)**, Y **(2.9)**, Lu **(2.11)**). Thermal ellipsoids are drawn at the 50% probability level. The hydrogen atoms except for those having hydrogen bonds have been omitted for clarity. Selected bond lengths (Å) (Data for **2.7-2.11** in Table 2.4). **2.10** Er1-O1 2.426(2), Er1-O2 2.398(2), Er1-O3 2.433(2), Er1-O4 2.394(2), Er1-O5 2.229(2), Er1-O6#1 2.283(2), Er1-O7 2.385(2), Er1-O8 2.330(2) O8-Er1-H7A 85.124(6), C1…Er1…C6 104.735(3), O5-Er1-O6#1 114.374(4). Symmetry Code: $^{\#1}$ 2-X,1-Y,1-Z.

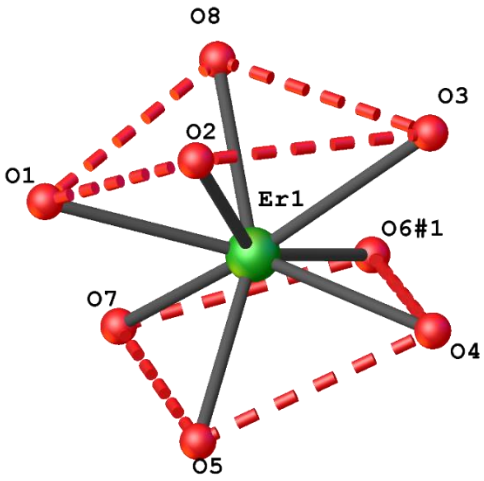


Figure 2.12**:** The overall geometry surrounding the Er1 metal centre. Non-metal atoms, except those directly adjacent to the metal centre, are omitted for clarity. The red dashed lines (----) represent the distorted square planes forming the distorted square antiprism. Symmetry equivalents: $^{\#1}$ 2-X, 1-Y, 1-Z.

The bond lengths of the isostructural series are given in Table 2.4. Only one half of the dimer, containing Er1 is unique while Er1#1 is symmetry generated. The carboxylate ligands are coordinated through two different carboxylate binding modes. The complex **2.10** contains four κ(O,O′) carboxylates binding through the oxygen atoms O1,2 and O3,4 at Er1 and O1#1,2#1 and O3#1,4#1 at Er1#1. The chelating carboxylate ligands show quite symmetric chelation. Two *anti-anti* μ_2-1κ(O):2κ(O′) carboxylate ligands bridge the two metal centres through O5,O6 and O5#1,O6#1. Finally, four coordinated water molecules are bound through O7,O8 at Er1 and O7#1,O8#1 at Er1#1. The Er-O bond length in complex **2.10** ranges from 2.229(2) Å to 2.433(2) Å with an average of 2.36 Å. Similarly, to the nine coordinated $[RE(3tpc)_3(H_2O)_3]_n$, the shortest RE-O distance is observed for the bridging oxygen. The coordinated water oxygen atoms form a O8-Er1-O7 angle of 85.12(7)° while the two chelating carboxylate ligands form a C1…Er1…C6 angle of 104.735(3)°. This contrasts their *trans* disposition in **2.3**. The bridging oxygen atoms form an angle of 114.374(4)° between themselves through O5-Er1-O6#1.

In accord with the lanthanoid contraction, a decrease in the average RE-O bond lengths across the series from Dy to Lu (RE = Dy 2.378(1) Å, Ho 2.373(2) Å, Y 2.367(4) Å, Er 2.360(1) Å, Lu 2.328(1) Å) is observed.[39]

Table 2.4: Selected bond lengths and distances (Å) for the isostructural $[RE_2(3tpc)_6(H_2O)_4]\cdot H_2O$ series.

	Dy1 (2.7)	**Ho1 (2.8)**	**Y1 (2.9)**	**Er1 (2.10)**	**Lu1 (2.11)**
RE1#1=RE1#2	4.3346(5)	4.4325(6)	4.4708(10)	4.4809(4)	4.5153(2)
O1	2.446(2)	2.435(4)	2.405(19)	2.426(2)	2.367(2)
O2	2.423(2)	2.410(4)	2.435(2)	2.398(2)	2.409(2)
O3	2.459(2)	2.455(4)	2.437(2)	2.433(2)	2.368(2)
O4	2.400(2)	2.401(4)	2.402(19)	2.394(2)	2.396(2)
O5	2.285(3)	2.249(4)	2.235(2)	2.229(2)	2.187(2)
O6#1	2.325(2)	2.294(5)	2.290(2)	2.283(2)	2.240(3)
O7	2.325(2)	2.395(4)	2.392(2)	2.385(2)	2.299(2)
O8	2.361(2)	2.342(4)	2.341(18)	2.330(2)	2.355(2)

There is hydrogen bonding involving two of the κ (O,O′) carboxylate oxygen atoms O4, 4#1, two of the ligated water oxygen atoms O7#1,O7 and the lattice water oxygen atom O9 in the dimeric structure (Table 2.5).

Table 2.5: Hydrogen bonds for $[Er_2(3tpc)_6(H_2O)_4]\cdot H_2O$ (**2.10**) [d/Å and </°].

D-H…A	**d(D-H)**	**d(H…A)**	**d(D…A)**	**<(DHA)**
O7-H7B …O9	0.8628(2)	1.9557(6)	2.7291(6)	148.551(2)
O7-H7A …O4#1	0.8615(2)	1.8623(2)	2.7107(3)	167.887(16)

2.2.3 Corrosion Inhibition

2.2.3.1 Immersion Tests

Table 2.6 provides a summary of the results obtained from weight loss measurements for steel coupons over seven days in 0.01M NaCl solutions in the presence of $RE(3tpc)_3$. At the end of the test period, visual inspections (Figure 2.13) of all the

coupons indicated dullness and signs of pitting. However, when considering the general uniformity, the coupons placed in inhibitor solutions were significantly less affected compared to the control coupons.

Table 2.6: Corrosion rates ($\mu gm^{-2}s^{-1}$) and percentage inhibition (η) for mild steel coupons immersed in specific solutions for seven days.

Solution	**Concentration**		**Solubilities (ppm)[a]**		**Avg Weight Loss (mg)**	**Corrosion Rate ($\mu gm^{-2}s^{-1}$)**	**Percentage Inhibition (η)**
	ppm	**M**	**In H_2O**	**In NaCl (0.01M)**			
Control - NaCl	580	10			16.50	30.5	0
2.1	500	0.871	900	580	10.40	19.36	37
2.2	500	0.869	900	590	9.95	18.8	38
2.3	500	0.867	900	590	8.99	16.28	47
2.4	500	0.863	950	590	9.75	18.91	38
2.5	500	0.853	850	550	7.55	14.87	51
2.6	500	0.844	790	520	6.00	11.87	61
2.7	500	0.425	920	520	6.77	12.62	59
2.8	500	0.423	870	530	6.00	12.01	61
2.9	500	0.485	600	500	5.30	9.65	68
2.10	500	0.421	700	540	6.25	11.58	62
2.11	500	0.449	900	550	7.30	14.13	54

[a] Solubilities of the compounds in 0.01 M NaCl solution were lower than that in distilled water. Therefore, the immersion tests were done with the compounds at 500 ppm concentration.

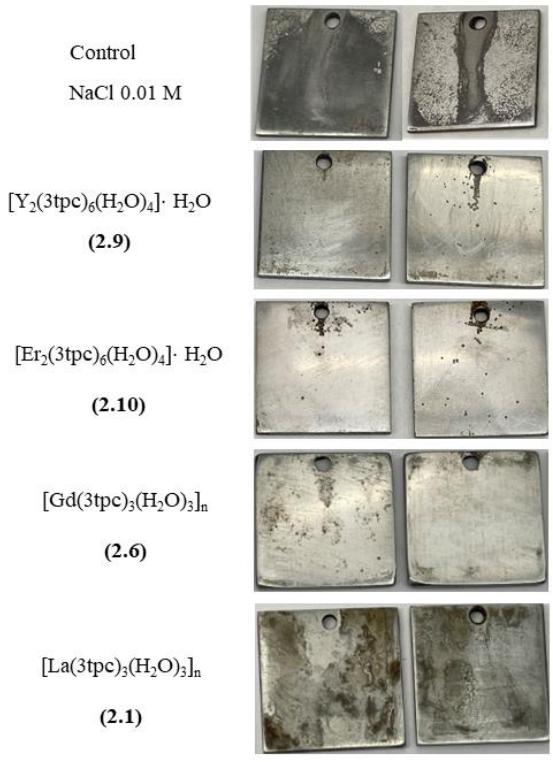


Figure 2.13: Visual comparisons pictures of few sample coupons after 7 days immersion in inhibitor solutions in NaCl 0.01M. (left – Trial 1; right – Trial 2).

The weight loss of the coupons during the immersion test period is considered the primary measure of corrosion. Thus, the corrosion rates of the inhibitor solutions were calculated by using the equation described in Eq 2.1:

$$\text{Corrosion rate (R)} = \frac{KW}{ATD} \qquad (2.1)$$

K = A constant; W = Weight loss (g); A = Coupon area (cm^2); T = Time of exposure (168 h); D = Density of the test metal

Then using these data, the percentage corrosion inhibition (η) of each compound was calculated (Eq 2.2):

$$\eta = \frac{R(Control) - R(inhibitor)}{(R(Control))} \times 100 \qquad (2.2)$$

Consistent with visual inspections, weight loss measurements also indicated that $[La(3tpc)_3(H_2O)_3]_n$ **(2.1)** has the lowest inhibition efficiency with an η = 36.5% and $[Y_2(3tpc)_6(H_2O)_4]\cdot H_2O$ **(2.9)** resulted in the best performance with nearly 68% of effectiveness at the concentration used in the experiment (500 ppm). The inhibitive properties of the compounds correlate to some extent with the decreasing atomic radius of rare earth metals, but Gd and Y are positive outliers and Nd and Lu negative ones. The light rare earth (La-Nd) complexes were less effective than the heavier derivatives with Pr the best performer of the former group. In this context, it is interesting that the anti-corrosion performance of cerium diphenyl phosphate is enhanced by Pr.[40] The overall trend is dissimilar to behaviour of salicylate[41] and 4-hydroxycinnamate[42] complexes where Ce and La complexes respectively perform best. With heavier lanthanoids there is improved protection from Sm to Gd and then near similar behavior from Gd-Er with a decline to Lu. However, Y with a similar ionic radius to Er performs best, reminiscent of the superiority of the yttrium complex in the 3-(4'-methylbenzoyl)propanoate series.[43] This reinforces increasing evidence that the influence of the rare earth is ligand dependent. The low solubility of the complexes has deterred pursuing attempts at higher concentrations.

2.2.3.2 Potentiodynamic Polarisation (PP)

Based on the Gd, Y and Er complexes performing best in the weight loss studies, we only investigated these three compounds in the potentiodynamic polarisation studies. The results of these experiments are shown in Table 2.7. $[Gd_2(3tpc)_6(H_2O)_4]\cdot H_2O$ **(2.6)** and $[Y_2(3tpc)_6(H_2O)_4]\cdot H_2O$ **(2.9)** showed the lowest i_{corr}, at 0.953 and 0.981 $\mu A/cm^2$ respectively. With the compounds present in the solution there is a shift in E_{corr} to more positive values as compared to the control, indicative of anodic inhibition dominating the reduction in i_{corr}. Representative PP scans in Figure 2.14 show the marked reduction in the anodic arm when the compounds are present, with some reduction in the cathodic kinetics. Such a response is typical of these types of compounds.[44] However, the performance of the yttrium compound was somewhat inferior to that of yttrium 3-(4'-methylbenzoyl)propanoate.[45]

Table 2.7: Summary of corrosion parameters obtained from potentiodynamic polarisation tests in control and inhibited solutions after 24 h immersion.

Solution	**i_{corr} ($\mu A/cm^2$)**	**Std. Dev.**	**E_{corr} (mV)**	**Std. Dev.**	**Percentage Inhibition (%)**
Control - NaCl	2.875	0.108	-638	4	-
$[Gd(3tpc)_3(H_2O)_3]_n$	0.953	0.135	-515	5	70
$[Y_2(3tpc)_6(H_2O)_4]. H_2O$	0.981	0.121	-530	9	68
$[Er_2(3tpc)_6(H_2O)_4]. H_2O$	1.414	0.263	-578	6	38

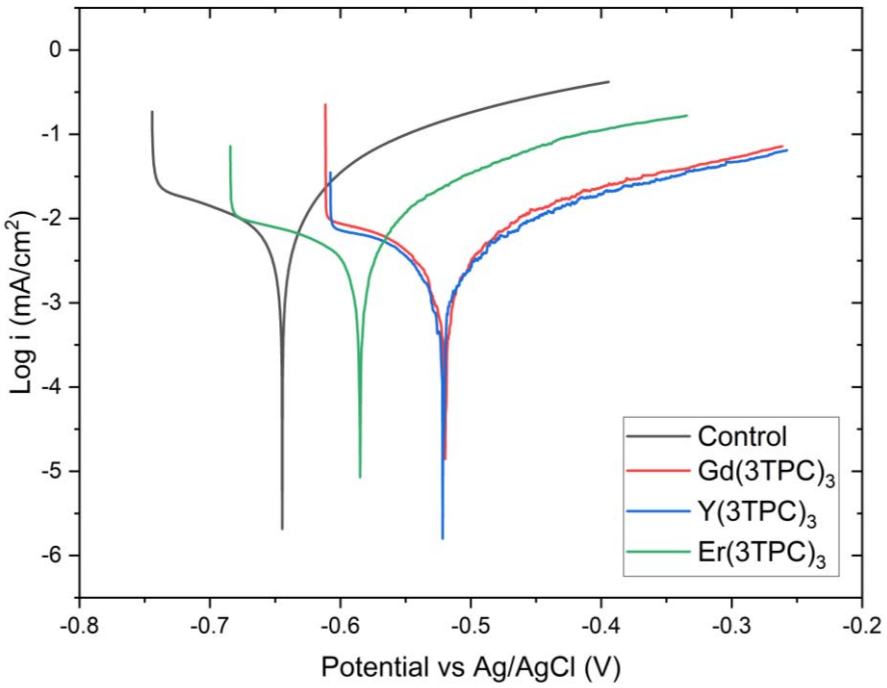


Figure 2.14: Representative potentiodynamic polarisation scans after 24 hours for 0.01 M NaCl control, and solutions with 0.01 M NaCl and 500ppm of $[Gd(3tpc)_3(H_2O)_3]_n$ **(2.6)**, $[Y_2(3tpc)_6(H_2O)_4]\cdot H_2O$ **(2.9)** or $[Er_2(3tpc)_6(H_2O)_4]$. H_2O **(2.10)**.

2.3 Conclusions

A series of RE 3-thiophenecarboxylate complexes have been successfully synthesised and characterised. All the compounds crystallized in one of the two structural groups based on single-crystal X-ray crystallography and powder diffraction with similar IR spectra and TGA behaviour within each class. Type 1 structures, $[RE(3tpc)_3(H_2O)_3]_n$ (**RE** = La, Ce, Pr, Nd, Sm, Gd), are one dimensional polymers in which the coordination number of the RE atom is nine. By contrast, Type 2 compounds form dimeric structures, $[RE_2(3tpc)_6(H_2O)_4]\cdot H_2O$ (**RE** = Dy, Ho, Y, Er, Lu), with a lanthanoid coordination number of eight. The lanthanoid contraction is reflected in a reduction of RE-O bond lengths as well as the decrease in coordination number.

Weight loss measurements indicate that $[Y_2(3tpc)_6(H_2O)_4]\cdot H_2O$ **(2.9)** has the best corrosion inhibition performance for mild steel in aqueous NaCl solution, while $[La(3tpc)_3(H_2O)_3]_n$ **(2.1)** is the least effective. Potentiodynamic polarisation confirmed the superior performance of $[Y_2(3tpc)_6(H_2O)_4]\cdot H_2O$ **(2.9)** but also gave a similar result for $[Gd_2(3tpc)_6(H_2O)_4]\cdot H_2O$ **(2.6)**. The compounds act predominantly as anodic inhibitors. A comparison of Y complex data suggests introduction of a thiophene moiety into a carboxylate is not quite as effective as a 3-(4'-methylbenzoyl) group.[45]

2.4 Experimental

For materials and general Considerations, see Appendix One.

2.4.1 Synthesis of 3-thiophenecarboxylate (3tpc)- RE Aqua Complexes

General Synthetic Method: 3-thiophenecarboxylic acid (0.449 g, 3.5 mmol) was dissolved in 95% ethanol (15ml) and treated with an equimolar amount of NaOH in distilled water (10 ml). The solution was stirred for 1 h and the pH was adjusted to 7-8 using standard pH paper. Three molar equivalent of the sodium 3-thiophenecarboxylate was slowly added to one equivalent of the lanthanoid salt solution and stirred for 2 hours while maintaining the pH at 5. The resultant precipitate was collected and washed with distilled water followed by ethanol and air-dried for 2-3 days. The mother liquor was

allowed to slowly evaporate at room temperature and XRD-suitable single crystals were separated from it.

$[La(3tpc)_3(H_2O)_3]_n$ (2.1)

White powder. Yield: 0.58 g (86%). m.p. >300 ℃. Elemental analysis for $C_{15}H_{15}LaO_9S_3$ (MW: 574.37 $gmol^{-1}$): Calculated (%) C 31.37, H 2.63, La 24.18; Found (%) C 31.56, H 2.50, La 23.39. IR (cm^{-1}): 3376m, 3113m, 1607w, 1556m, 1524s, 1494s, 1441s, 1397s, 1351s, 1123w, 1078w, 935w, 871w, 835m, 776s, 755s, 626m, 685m, 578s, 520s, 411s. TGA weight loss (50-110 ℃): 9.09% (Calc. for loss of $3\times H_2O$ = 9.40%); weight loss (340-460 ℃): 15.4% (Calc. for formation of $La_2(CO_3)(O_2CR)_4$ = 16.9%); weight loss (340-540 ℃): 38.0% (Calc. for formation of $La_2(CO_3)_3$ = 39.8%).

$[Ce(3tpc)_3(H_2O)_3]_n$ (2.2)

White powder. Yield: 0.49 g (73%). m.p. >300 ℃. Elemental analysis for $C_{15}H_{15}CeO_9S_3$ (MW: 575.58 $gmol^{-1}$): Calculated (%) C 31.30, H 2.63, Ce 24.34. Found (%) C 31.46, H 2.48, Ce 24.26. IR (cm^{-1}): 3380m, 3113m, 1608w, 1554m, 1522s, 1492s, 1440s, 1396s, 1348s, 1123w, 1077w, 935w, 871w, 835m, 776s, 754s, 626m, 685s, 578s, 521s, 408s; TGA weight loss (50-110 ℃): 9.02% (Calc. for loss of $3\times H_2O$ = 9.38%); weight loss (330-450 ℃): 15.7% (Calc. for formation of $Ce_2(CO_3)(O_2CR)_4$ =16.9%); weight loss (330-560 ℃): 37.5% (Calc. for formation of $Ce_2(CO_3)_3$ = 39.9%).

$[Pr(3tpc)_3(H_2O)_3]_n$ (2.3)

Pale green powder. Yield: 0.51 g (76%). m.p. >300 ℃. Elemental analysis for $C_{15}H_{15}O_9PrS_3$ (MW: 576.38 $gmol^{-1}$): Calculated (%) C 31.26, H 2.62, Pr 24.45; Found (%) C 31.42, H 2.54, Pr 24.11. IR (cm^{-1}): 3381m, 3112m, 1609w, 1556m, 1525s, 1493s, 1441s, 1395s, 1351s, 1123w, 1078w, 935w, 871w, 836m, 777s, 754s, 685s, 627m, 579s, 520s, 411s. TGA weight loss (50-110 ℃): 9.43% (Calc. for loss of $3\times H_2O$ = 9.37%); weight loss (340-450 ℃): 16.4% (Calc. for formation of $Pr_2(CO_3)(O_2CR)_4$ = 16.9%); weight loss (340-560 ℃): 39.2% (Calc. for formation of $Pr_2(CO_3)_3$ = 40.1%).

$[Nd(3tpc)_3(H_2O)_3]_n$ (2.4)

Purple powder. Yield: 0.51 g (76%). m.p. >300 ℃. Elemental analysis for $C_{15}H_{15}NdO_9S_3$ (MW: 579.71 $gmol^{-1}$): Calculated (%) C 31.08, H 2.61, Nd 24.88; Found (%) C 31.28, H 2.49, Nd 24.62. IR (cm^{-1}): 3379m, 3114m, 1611w, 1557m, 1522s, 1492s, 1441s, 1395s, 1351m, 1123w, 1078w, 871w, 836m, 777s, 754s, 626m, 685s, 579s, 521s,

408s. TGA weight loss (50-110 ℃): 9.74% (Calc. for loss of 3×H_2O = 9.31%); weight loss (340-450 ℃): 17.2% (Calc. for formation of $Nd_2(CO_3)(O_2CR)_4$ = 16.8%); weight loss (340-560 ℃): 41.6% (Calc. for formation of $Nd_2(CO_3)_3$ = 40.4%).

$[Sm(3tpc)_3(H_2O)_3]_n$ (2.5)

White powder. Yield: 0.37 (54%). m.p. >300 ℃. Elemental analysis for $C_{15}H_{15}O_9S_3Sm$ (MW: 585.83 $gmol^{-1}$): Calculated (%) C 30.75, H 2.58, Sm 25.67; Found (%) C 29.49, H 2.23, Sm 25.95. IR (cm^{-1}): 3373m, 3116m, 1612w, 1559m, 1522s, 1491s, 1438s, 1395s, 1351s, 1123w, 1078w, 935w, 872w, 836m, 754s, 627m, 684s, 579s, 519s, 414s. TGA weight loss (55-120 ℃): 9.07% (Calc. for loss of 3×H_2O = 9.17%); weight loss (370-540 ℃): 37.0% (Calc. for formation of $Sm_2(CO_3)_3$ = 40.8%).

$[Gd(3tpc)_3(H_2O)_3]_n$ (2.6)

White powder. Yield: 0.44 g (63%). m.p. >300 ℃. Elemental analysis for $C_{15}H_{15}GdO_9S_3$ (MW: 592.72 $gmol^{-1}$): Calculated C 30.40, H 2.55, Gd 26.53; Found (%) C 29.22, H 2.16, Gd 26.96. IR (cm^{-1}): 3382m, 3118m, 1566m, 1529s, 1495s, 1431s, 1396m, 1354s, 1124w, 1079w, 873m, 838m, 784m, 755s, 685s, 627m, 580m, 522s, 414s. TGA weight loss (55-115 ℃): 9.0% (Calc. for loss of 3×H_2O = 9.11%); weight loss (370-550 ℃): 38.5% (Calc. for formation of $Gd_2(CO_3)_3$ = 41.7%).

$[Dy_2(3tpc)_6(H_2O)_4]\cdot H_2O$ (2.7)

White powder. Yield: 0.47 g (69%). m.p. >300 ℃. Elemental analysis for $C_{30}H_{28}Dy_2O_{17}S_6$ (MW: 1177.92 $gmol^{-1}$): Calculated (%) C 30.59, H 2.40, Dy 27.59; Found (%) C 29.37, H 2.12, Dy 27.19. IR (cm^{-1}): 3254 w, 3109w, 1557m, 1527s, 1503s, 1434s, 1346s, 1209w, 1123w, 1073w, 940w, 875w, 837s, 780s, 755s, 699m, 628m, 526m, 423s. TGA weight loss (40-95 ℃): 7.76 % (Calc. for loss of 5×H_2O = 7.64%); weight loss (380-570 ℃): 38.5% (Calc. for formation of $Dy_2(CO_3)_3$ = 42.9%).

$[Ho_2(3tpc)_6(H_2O)_4]\cdot H_2O$ (2.8)

Yellow powder. Yield: 0.58 g (85%). m.p. >300 ℃. Elemental analysis for $C_{30}H_{28}Ho_2O_{17}S_6$ (MW: 1182.78 $gmol^{-1}$): Calculated (%) C 30.46, H 2.39, Ho 27.89; Found (%) C 29.97, H 2.25, Ho 28.84. IR (cm^{-1}): 3292w, 3111w, 1566m, 1528s, 1503s, 1428s, 1348s, 1123w, 1073w, 940w, 875w, 837m, 781m, 754s, 699m, 627m, 526m, 420s. TGA weight loss (40-95 ℃): 7.19 % (Calc. for loss of 5×H_2O = 7.61%); weight loss (395-570 ℃): 36.1% (Calc. for formation of $Ho_2(CO_3)_3$ = 43.1%).

$[Y_2(3tpc)_6(H_2O)_4]\cdot H_2O$ (2.9)

White powder. Yield: 0.41 g (69%). m.p. >300 °C. Elemental analysis for $C_{30}H_{28}O_{17}S_6Y_2$ (MW: 1030.73 $gmol^{-1}$): Calculated (%) C 34.96, H 2.74, Y 17.25; Found (%) C 33.38, H 2.53, Y 17.55. IR (cm^{-1}): 3341w, 3106w, 1567m, 1529s, 1504s, 1434s, 1402s, 1349s, 1209w, 1123w, 1073w, 940w, 875 w, 838m, 782m, 754s, 698s, 627m, 550m, 525m, 422s. TGA weight loss (40-95 °C): 8.29% (Calc. for loss of $5\times H_2O$ = 8.73%); weight loss (400-570 °C): 38.4% (Calc. for formation of $Y_2(CO_3)_3$ = 34.7%).

$[Er_2(3tpc)_6(H_2O)_4]\cdot H_2O$ (2.10)

Pink powder. Yield: 0.50 g (72%). m.p. >300 °C. Elemental analysis for $C_{30}H_{28}Er_2O_{17}S_6$ (MW: 1187.44 $gmol^{-1}$): Calculated (%) C 30.34, H 2.38, Er 28.17; Found (%) C 30.32, H 2.36, Er 28.5. IR (cm^{-1}): 3326w, 3106w, 1568m, 1528s, 1504s, 1435s, 1394s, 1348s, 1123w, 1073w, 941w, 875w, 837m, 782m, 754s, 699m, 627m, 525m, 423s. TGA weight loss (40-95 °C): 7.36% (Calc. for loss of $5\times H_2O$ = 7.58%); weight loss (380-600 °C): 43.7% (Calc. for formation of $Er_2(CO_3)_3$ = 43.3%).

$[Lu_2(3tpc)_6(H_2O)_4]\cdot H_2O$ (2.11)

White powder. Yield: 0.59 g (84%). m.p. >300 °C. Elemental analysis for $C_{30}H_{28}Lu_2O_{17}S_6$ (MW: 1202.86 $gmol^{-1}$): Calculated (%) C 30.16, H 1.69, Lu 29.29; $C_{30}H_{18}Lu_2O_{12}S_6$ (MW: 1112.78 $gmol^{-1}$, loss of 5 H_2O): Calculated (%) C 32.35, H 1.62, Lu 31.45; Found (%) C 32.04, H 1.56, Lu 32.07. IR (cm^{-1}): 3103w, 1610w, 1515s, 1428s, 1396s, 1339s, 1208w, 1125w, 1071w, 941w, 873w, 834m, 754s, 699m, 626m, 529w, 430s. TGA weight loss (340-600 °C): 43.8% (Calc. for formation of $Lu_2(CO_3)_3$ = 44.1%).

2.4.2 Corrosion Testing

For the corrosion testing procedures used for weight loss experiments and potentiodynamic polarisation (PP) experiments, see Appendix One.

2.5 X-ray Crystal Data

For details on X-ray crystallography, see Appendix One.

Crystal data and refinement details are shown in Table 2.8 and 2.9.

Table 2.8: Crystal data and structural refinement for compounds $[RE(3tpc)(H_2O)_3]_n$ (RE = La, Ce, Pr, Nd, Sm, Gd).

Compound	**2.1**	**2.2**	**2.3**	**2.4**	**2.5**	**2.6**
Formula	$C_{15}H_{15}LaO_9S_3$	$C_{15}H_{15}CeO_9S_3$	$C_{15}H_{15}O_9PrS_3$	$C_{15}H_{15}NdO_9S_3$	$C_{15}H_{15}O_9S_3Sm$	$C_{15}H_{15}GdO_9S_3$
M_r	574.36	575.57	576.36	579.69	585.80	592.70
Space	$P2_1/c$	$P2_1/c$	$P2_1/c$	$P2_1/c$	$P2_1/c$	$P2_1/c$
a (Å)	15.070(3)	15.0999(6)	15.059(3)	15.020(3)	15.042(3)	14.960(3)
b (Å)	12.120(2)	12.1722(4)	12.157(2)	12.070(2)	12.055(2)	12.000(2)
c (Å)	10.840(2)	10.8103(3)	10.775(2)	10.720(2)	10.666(2)	10.600(2)
α (°)	90	90	90	90	90	90
β (°)	100.41(3)	100.769(3)	100.81(3)	100.78(3)	101.00(3)	101.07(3)
γ (°)	90	90	90	90	90	90
V (Å^3)	1947.3(7)	1951.93(12)	1937.5(7)	1909.1(7)	1898.6(7)	1867.5(7)
Z	4	4	4	4	4	4
ρ_{calc}, gcm^{-3}	1.959	1.959	1.976	2.017	2.049	2.108
μ, mm^{-1}	2.562	2.699	22.751	3.095	3.470	3.935
N_τ	41288	11030	3776	3344	3819	39196
N (R_{int})	3420	4592(0.0457	3776	3344	3819	3298(0.0491
R_1(I >	0.0345	0.0408	0.0522	0.0342	0.0615	0.0312
wR_2 (all	0.0968	0.0851	0.1412	0.1060	0.1791	0.0896
GOF	1.099	1.034	1.050	1.080	1.047	1.037

Table 2.9: Crystal data and structural refinement for compounds $RE_2(3tpc)_3(H_2O)_4]\cdot H_2O$ **(**RE = Dy, Ho, Y, Er, Lu).

Compoun	**2.7**	**2.8**	**2.9**	**2.10**	**2.11**
Formula	$C_{30}H_{28}Dy_2O_{17}S_6$	$C_{30}H_{28}Ho_2O_{17}S_6$	$C_{30}H_{28}O_{17}S_6Y_2$	$C_{30}H_{28}Er_2O_{17}S_6$	$C_{30}H_{28}Lu_2O_{17}S_6$
M_r	1177.88	1182.74	1030.70	1187.40	1202.82
Space	$P2_1/c$	$P2_1/c$	$P2_1/c$	$P2_1/c$	$P2_1/n$
a (Å)	9.9091(7)	9.9388(6)	9.920(2)	9.9187(7)	9.8729(3)
b (Å)	19.1194(7)	19.2401(11)	19.170(4)	19.1800(7)	19.2032(5)
c (Å)	11.0210(7)	11.0949(8)	11.080(2)	11.0843(7)	11.0534(4)
α (°)	90	90	90	90	90
β (°)	115.932(8)	116.176(8)	116.41(3)	116.458(8)	116.308(4)
γ (°)	90	90	90	90	90
V (Å^3)	1877.8(2)	1904.0(2)	1887.1(8)	1887.8(2)	1878.57(12)
Z	2	2	2	2	2
ρ_{calc}, gcm^{-}	2.083	2.063	1.814	2.089	2.126
μ, mm^{-1}	4.357	4.528	3.466	4.821	5.633
N_τ	12382	8447	30379	36686	26278
N (R_{int})	3996(0.0339)	4364(0.0345)	3313(0.0407)	4315(0.0846)	5615(0.0460)
R_1(I >	0.0256	0.0484	0.0357	0.0235	0.0303
wR_2 (all	0.0581	0.0905	0.0978	0.0546	0.0620
GOF	1.051	1.136	1.073	1.036	1.051

2.6 References

1 J. A. Joule and K. Mills, *Heterocyclic Chemistry*, John Wiley & Sons Ltd, The Atrium, Southern Gate, Chichester, West Sussex, PO19 8SQ, United Kingdom, 5th edn., 2010.

2 R. Rossi, A. Carpita, M. Ciofalo and V. Lippolis, *Tetrahedron*, 1991, **47**, 8443–8460.

3 M. Temprado, M. V. Roux, P. Jiménez, J. Z. Dávalos and R. Notario, *J. Phys. Chem. A*, 2002, **106**, 11173–11180.

4 M. V. Roux, M. Temprado, P. Jiménez, J. Z. Dávalos, C. Foces-Foces, M. V. García and M. I. Redondo, *Thermochim. Acta*, 2003, **404**, 235–244.

5 T. J. Barton, R. W. Roth and J. G. Verkade, *J. Am. Chem. Soc.*, 1972, **94**, 8854–8857.

6 M. Szajda and J. N. Lam, Thiophenes and their Benzo Derivatives: Structure in *Comprehensive Heterocyclic Chemistry II*, eds. A. R. Katritzky, C. W. Rees and E. F. V Scriven, Pergamon, Oxford, 1996, pp. 437–490.

7 F. Carey, *Org. Chem. Curr. Res.*, 2023, **12**.

8 J. W. Pratt, Thiophene in *Ullmann's Encyclopedia of Industrial Chemistry*, John Wiley & Sons, Ltd, Weinheim, 2000.

9 I. C. F. R. Ferreira, M. J. R. P. Queiroz, M. Vilas-Boas, L. M. Estevinho, A. Begouin and G. Kirsch, *Bioorg. Med. Chem. Lett.*, 2006, **16**, 1384–1387.

10 L. Brault, E. Migianu, A. Néguesque, E. Battaglia, D. Bagrel and G. Kirsch, *Eur. J. Med. Chem.*, 2005, **40**, 757–763.

11 Y.-J. Wu, Heterocycles and Medicine: A Survey of the Heterocyclic Drugs Approved by the U.S. FDA from 2000 to Present in *Progress in Heterocyclic Chemistry, eds.* G. W. Gribble and J. A. Joule, Elsevier, Amsterdam, 2012, vol. 24, pp. 1–53.

12 A. Y. Hassan, M. M. Ghorab and O. M. Nassar, *Phosphorus, Sulfur, Silicon Relat. Elem.*, 1998, **134–135**, 77–86.

13 P. Novák, K. Müller, K. S. V Santhanam and O. Haas, *Chem. Rev.*, 1997, **97**, 207–282.

14 M. T. Ramesan and K. Suhailath, Role of nanoparticles on polymer composites in *Micro and Nano Fibrillar Composites (MFCs and NFCs) from Polymer Blends*, eds. R. K.

Mishra, S. Thomas and N. Kalarikkal, Woodhead Publishing, Cambridge, 2017, pp. 301–326.

15 J. Podlesný and F. Bureš, *Organics*, 2022, **3**, 446–469.

16 I. F. Perepichka and D. F. Perepichka, Eds., *Handbook of Thiophene-Based Materials: Applications in Organic Electronics and Photonics*, John Wiley & Sons, Ltd, Chichester, 2009.

17 H. Wu, X. Lu, J. Xu, X. Zhang, Z. Li, X. Yang and Y. Ling, *Molecules*, 2022, **27**, 8700

18 M. M. Abdou, *Am. J. Chem.*, 2013, **2013**, 126–135.

19 T. Markley, F. Blin, M. Forsyth and B. Hinton, Multifunctional rare earth organic corrosion inhibitors in *Rare Earth-Based Corrosion Inhibitors*, eds. M. Forsyth and B. Hinton, Woodhead Publishing Limited, Cambridge, 2014, pp. 117–142.

20 D. A. Winkler, M. Breedon, A. E. Hughes, F. R. Burden, A. S. Barnard, T. G. Harvey and I. Cole, *Green Chem.*, 2014, **16**, 3349–3357.

21 D. Daoud, T. Douadi, H. Hamani, S. Chafaa and M. Al-Noaimi, *Corros. Sci.*, 2015, **94**, 21–37.

22 C. Verma, E. E. Ebenso and M. A. Quraishi, Ionic Liquids as Green Corrosion Inhibitors for Industrial Metals and Alloys in *Green Chem.*, eds. Hosam El-din M. Saleh and Koller M., IntechOpen, London, 2018, pp. 103–132.

23 T. G. Harvey, S. G. Hardin, A. E. Hughes, T. H. Muster, P. A. White, T. A. Markley, P. A. Corrigan, J. Mardel, S. J. Garcia, J. M. C. Mol and A. M. Glenn, *Corros. Sci.*, 2011, **53**, 2184–2190.

24 Z. Szklarska-Smialowska and M. Kaminski, *Corros. Sci.,* 1973, **13**, 1-10.

25 A. S. Fouda, *Monatsheite fiir Chemic*, 1986, **117**, 159-165.

26 A. S. Fouda, A. A. Ibrahim and W. T. El-Behairy, *Der. Pharma. Chemica.*, 2014, **6,** 144-157.

27 A. Galal, N. F. Atta and M. H. S. Al-Hassan, *Mater. Chem. Phys.*, 2005, **89**, 38–48.

28 M. Salehisaki, N. E. Rad, G. B. Deacon, J. Wang, Z. Guo and P. C. Junk, *Inorganica Chim. Acta*, 2022, **539**, 120997.

29 G. J. Moxey, A. J. Blake, W. Lewis and D. L. Kays, *Eur. J. Inorg. Chem.*, 2015, **2015**, 5892–5902.

30 R. P. Kelly, T. D. M. Bell, R. P. Cox, D. P. Daniels, G. B. Deacon, F. Jaroschik, P. C. Junk, X. F. le Goff, G. Lemercier, A. Martinez, J. Wang and D. Werner, *Organometallics*, 2015, **34**, 5624–5636.

31 H. Sitzmann, T. Dezember, O. Schmitt, F. Weber, G. Wolmershäuser and M. Ruck, *Z. Anorg. Allg. Chem.*, 2000, **626**, 2241–2244.

32 L. H. J. Lajunen and G. R. Choppin, *Rev. Anal. Chem.*, 1989, **9**, 91–130.

33 D. P. Daniels, G. B. Deacon, D. Harakat, F. Jaroschik and P. C. Junk, *Dalton Trans.,* 2012, **41**, 267–277.

34 L. Hirneise, C. Maichle-Mössmer and R. Anwander, *Inorg. Chem.*, 2021, **60**, 18211–18224.

35 G. B. Deacon and R. J. Phillips, *Coord. Chem. Rev.*, 1980, **33**, 227–250.

36 G. B. Deacon, S. J. Faulks and G. N. Pain, *Adv. Organomet. Chem.*, 1986, **25**, 237–276.

37 G. B. Deacon, *Organomet. Chem. Rev., Sect. A*, 1970, **5**, 355.

38 B. Vallina, J. D. Rodriguez-Blanco, A. P. Brown, J. A. Blanco and L. G. Benning, *J. Nanopart. Res.,* 2013, **15**, 1438.

39 R. D. Shannon, *Acta Crystallogr. A*, 1976, **32**, 751–767.

40 T. A. Markley, A. E. Hughes, T. C. Ang, G. B. Deacon, P. Junk and M. Forsyth, *Electrochem. Solid-State Lett.,* 2007, **10**, C72-C75.

41 M. Forsyth, M. Seter, B. Hinton, G. Deacon and P. Junk, *Aust. J. Chem.,* 2011, **64**, 812–819.

42 F. Blin, S. G. Leary, G. B. Deacon, P. C. Junk and M. Forsyth, *Corros. Sci.,* 2006, **48**, 404–419

43 Y. Peng, A. E. Hughes,G. B. Deacon, P. C. Junk, B. R. W. Hinton, M. Forsyth, J. I. Mardel and A. E. Somers, *Corros. Sci.,* 2018, **145**, 199–211.

44 F. Blin, S. G. Leary, K. Wilson, G. B. Deacon, P. C. Junk and M. Forsyth, *J. Appl. Electrochem.,* 2004, **34**, 591–599.

45 A. E. Somers, B. R. W. Hinton, C. de Bruin-Dickason, G. B. Deacon, P. C. Junk and M. Forsyth, *Corros. Sci.*, 2018, **139**, 430–437.

46 CrysAlisPRO v.39. Agilent Technologies Ltd., Yarnton, Oxfordshire, England.

Chapter 3: RE(III) 3-furoate Complexes: Synthesis, Structure, and Corrosion Inhibiting Properties.

3.1 Introduction

3.1.1 Furan and its Derivatives

Furan with the molecular formula C_4H_4O and a low molecular weight of 68 $gmol^{-1}$ is a widely recognized member of a group of unsaturated heteroaromatic compounds consisting of five-membered rings. This group includes other notable compounds such as pyrrole and thiophene (See Chapter 2).[1]

It is a colourless, relatively stable chemical, with a boiling point of 31°C. It has a pleasant odour (NTP 1993) and exhibits slight solubility in water. Furan is widely used as a precursor to the commonly used solvent tetrahydrofuran (thf) due to its accessibility and commercial significance.[2,3]

Even though thiophene is one of the most prevalent components in organic conjugated materials, its oxygen congener furan, and furan derivatives have not gained equivalent attention. Nonetheless, furan possesses chemical properties such as reduced size, diminished aromaticity, and enhanced electron richness, making it highly desirable for incorporation into conjugated systems.[4]

For over a century, the synthesis of furans has garnered significant interest due to the crucial role of these heterocycles in both natural and synthetic substances, as well as the need for more selective and versatile synthesis methods.[5–8] Furan derivatives, which can be synthesised from saccharidic renewable resources, offer a unique advantage because of their widespread availability — biomass exists virtually worldwide, ensuring continuous replenishment.[1] Specifically, there is a growing demand for the development of routes facilitating the straightforward synthesis of substituted furans under mild conditions using readily available starting materials, marking an important objective in this field.[6]

The exploration of the structural characteristics of furan and its derivatives has received significant interest because of their use in various applications.[9] Various furan derivatives have demonstrated useful properties as agrochemical bioregulators. For instance, 2-furoic acid has been shown to enhance hypoxic stress resistance in wheat, thus boosting crop yield and quality.[10]

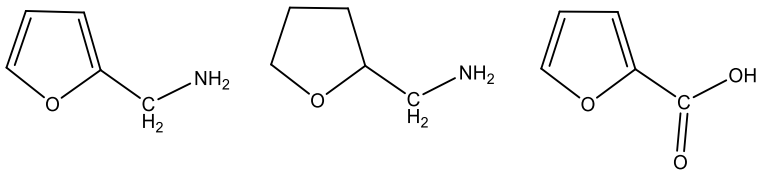
Furan and its derivatives occur naturally in many foods and beverages at trace levels, contributing to their flavour profiles.[2] Additionally, several furan derivatives have found utility in the food and feed industry, primarily serving as taste enhancers. Furfural, for instance, is a significant component of the furans essential for the formation of key coffee aroma constituents.[10]

In the area of wood and paper product manufacturing, the addition of furan-containing compounds offers the potential for several remarkable property enhancements. When considering the essential oil/cosmetic industry, a range of highly conjugated furans have been synthesised and utilized as UV absorbers in sunscreens. Maleic anhydride has found widespread application in the textile and fibres industry.[10] Some molecules incorporating furan rings have demonstrated important properties as dyes and photosensitizers[11]. Furthermore, several furan derivatives serve as additives in the fuel and oil industry.[12] Tetrahydrofuran, for example, has been found to enhance ignition in ethanol-based diesel fuels. [10]

When looking at carboxylic acid derivatives of the parent compound furan, 2- and 3-furancarboxylic acids exhibit distinct applications, such as in cosmetic or pharmaceutical formulations for topical use due to their anti-inflammatory, anti-irritant, and antimicrobial effects.[9] These furancarboxylic acids have shown potential as hypolipidemic agents.[13] Moreover, 2-furancarboxylic acid also exhibits antitumor properties.[14]

3.1.2 Organic Compounds Containing Oxygen Atoms as Corrosion Inhibitors

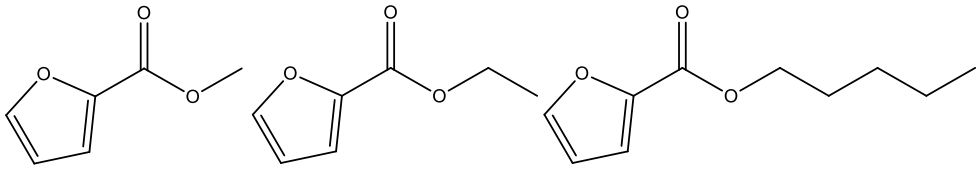
Organic systems containing hetero atoms are considered to have an advanced inhibiting ability due to the strong interactions between N, O and S atoms and the metallic surfaces.[15–18] Although there are many studies of heterocyclic compounds as corrosion inhibitors for mild steel, only a limited amount of literature is reported on furan and its derivatives for such applications. Vaidyanathan and Hackerman [19] investigated the structural effect of some furan derivatives on corrosion inhibition and the effect on the dissolution of iron. The inhibition efficiency of the tested compounds follows the order 2-furoic acid> furfurylamine > tetrahydrofurfurylamine. The inhibition ability of the furoic acid was explained on the basis of the electron-donating ability of heterocyclic ring oxygen as well as the carboxylic oxygen.



Furfuryl amine Tetrahydrofurfuryl amine 2-Furoic acid

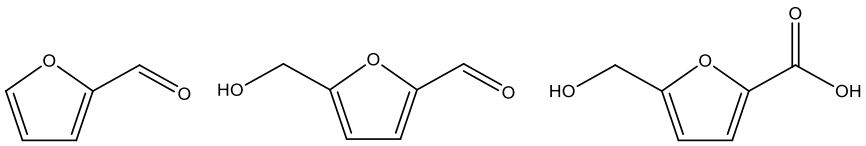
Another study has reported the effectiveness of a few furan derivatives on carbon steel corrosion in 1M HCl solution using gravimetric, and electrochemical measurements. The tested compounds (furfuryl alcohol, 2-methylfuran, and furfurylamine) demonstrated a good capacity to inhibit corrosion even at very low concentrations, and furfuryl alcohol showed the maximum inhibition efficacy. The results obtained in this study suggested that the inhibition efficiency is based on the molecular structure and electron-donating ability of the heteroatoms.[20]

Khaled tested three furan derivatives (methyl 2-furoate, ethyl 2-furoate, and amyl 2-furoate) on mild steel in 1M HCl to evaluate the anti-corrosive properties with respect to the changes in substituent and polarity of the compound. It was suggested that the protection of mild steel occurs through donating or sharing electrons with the metal surface, forming a stable covalent coordination bond (chemisorption). [21]



Methyl 2-furoate Ethyl 2-furoate Amyl 2-furoate

Recently, a theoretical study was carried out to evaluate the inhibitory efficiency of three furan derivatives, namely furan-2-carbaldehyde, 5-(hydroxymethyl)furfural, and 5-(hydroxymethyl)furoic acid on Cu, Fe, Al, and Sn surfaces.



Furan-2-carbaldehyde 5-(hydroxymethyl)furfural 5-(hydroxymethyl)furoic acid

The results of the above computational experiments suggested that among the tested compounds, 5-(hydroxymethyl)furoic acid, which consists of both carboxylic and hydroxyl functional groups, could be a potential candidate to use as a corrosion inhibitor, especially on the iron surface in an acidic environment. Furthermore, compared to the other two derivatives,

5-(hydroxymethyl)furoic acid has smaller electronegativity. Thus, it has a greater tendency to donate electrons and adsorb on metal surfaces.[22,23]

3.1.3 Current Study

In this chapter, we discuss the synthesis and characterisation of RE 3-furoate complexes (3furH = 3-furoic acid, Chart 3.1) and the corrosion inhibitory properties for AS 1020 mild steel in 0.01 M NaCl corrosive media, to examine whether the oxygen donor atom might prove more efficacious than sulfur (Chapter 2). The synthesised compounds were characterised using several techniques including single-crystal X-ray crystallography. Moreover, the corrosion inhibition properties of the synthesised compounds were determined by weight loss experiments combined with potentiodynamic polarization measurements.

All the work in this chapter resulted in a publication in the journal *Molecules* (see reprint in Appendix Two).

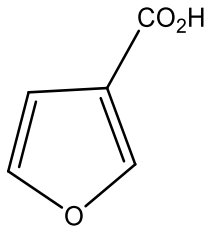
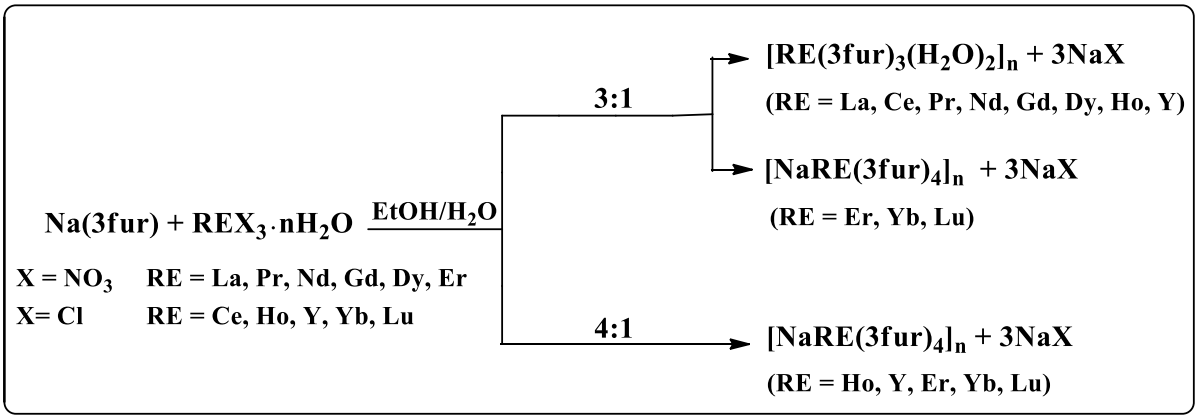


Chart 3.1: Structure of 3-furoic acid (3furH).

3.2 Results and Discussion

3.2.1 Synthesis and characterisation

When the syntheses were carried out with a ligand: RE stoichiometry of 3:1, eight homometallic complexes $[RE(3fur)_3(H_2O)_2]_n$ (RE = La **(3.1)**, Ce **(3.2)**, Pr **(3.3)**, Nd **(3.4)**, Gd **(3.5)**, Dy **(3.6)**, Ho **(3.7)**, Y **(3.8)**), as well as Na-RE bimetallic complexes $[NaRE(3fur)_4]_n$ (RE = Er **(3.11)**, Yb **(3.12)**, Lu **(3.13)**), were obtained. Upon treating the ligand and RE salts in a 4:1 mole ratio, heterobimetallic complexes $[NaHo(3fur)_4]_n$ (**3.9**) and $[NaY(3fur)_4]_n$ (**3.10**) were obtained in addition to the complexes **3.11**, **3.12** and **3.13**, but La to Dy still gave $[RE(3fur)_3(H_2O)_2]_n$. Thus, the ratio used in the metathesis reaction appeared to affect the identity of the final complex for holmium and yttrium (Scheme 3.1).



Scheme 3.1: Synthesis of RE 3-furoate complexes. The ratios shown in the Scheme refer to the Na(3fur): REX_3 ratios of reactants.

In all cases, single crystals of the compounds were obtained by slow evaporation of the mother liquor after filtration to isolate the precipitate formed. The bulk samples of complexes $[RE(3fur)_3(H_2O)_2]_n$ (**3.1-3.8**) (Figure 3.1) and $[NaRE(3fur)_4]_n$ (**3.9-3.13**) (Figure 3.2) gave X-ray powder diffraction patterns that are identical in each respective group and are in agreement with the patterns generated from the single-crystal data.

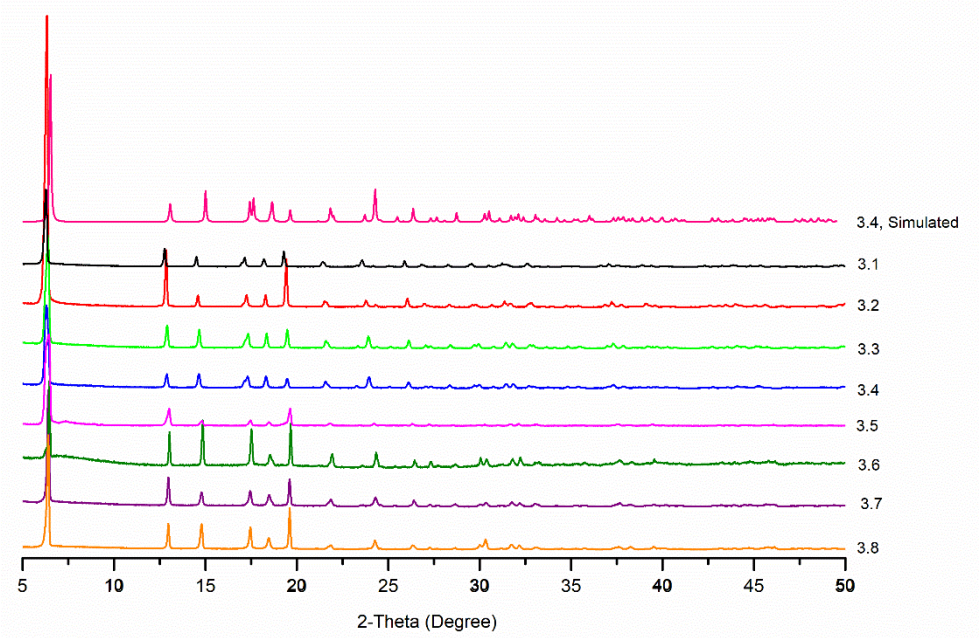


Figure 3.1: PXRD diffractograms of the $[RE(3fur)_3(H_2O)_2]n$ **(3.1-3.8)** series compared to the simulated pattern of $[Nd(3fur)_3(H_2O)_2]_n$ (**3.4**).

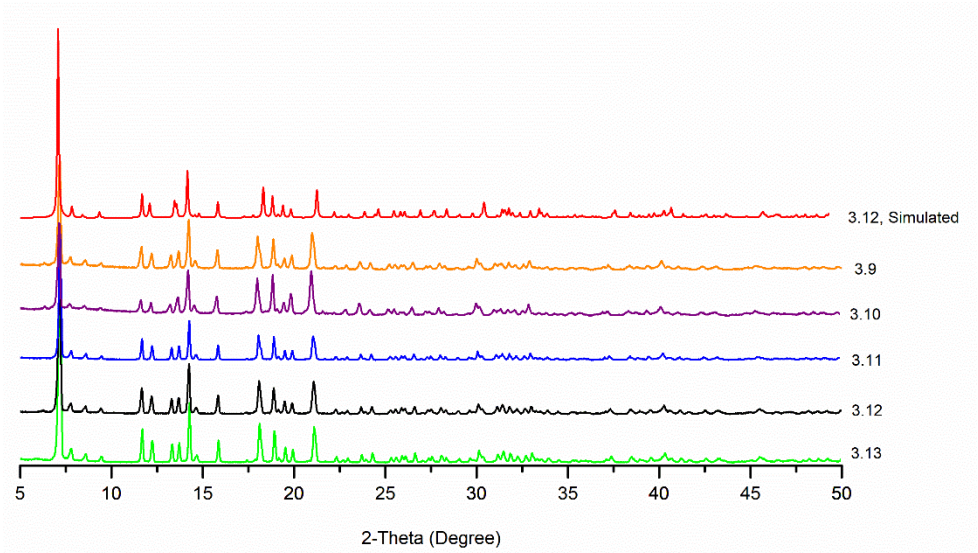


Figure 3.2: PXRD diffractograms of the $[NaRE(3fur)_4]_n$ **(3.9-3.13)** series compared to the simulated pattern of $[NaYb(3fur)_4]_n$ (**3.12)**.

Satisfactory elemental analyses were obtained for all the compounds, with the exception of compound **3.12,** with a low % C value. This is a frequent issue recognized for rare earth and alkaline earth complexes within previous literature.[24–30] However, X-ray crystallographic data together with additional % RE analyses and TGA data offer further evidence to confirm the final chemical compositions of the complexes.

The IR spectra of $[RE(3fur)_3(H_2O)_2]_n$ (**3.1-3.8**) (Figure 3.3) and $[NaRE(3fur)_4]_n$ (**3.9-3.13**) complexes (Figure 3.4) show strong similarities in major bands within each isostructural series. Thus, the significant IR bands for only one compound from each series (**3.4** and **3.12)** are listed in Table 3.1. (Other data are compiled in the Experimental Section). For the $[RE(3fur)_3(H_2O)_2]_n$ compounds broad O-H stretching bands in the range of 3200-3550 cm^{-1} are comparable and attributed to the presence of coordinated water molecules. IR spectra of all the RE complexes show strong asymmetric and symmetric carboxylate stretching bands at 1530-1350 cm^{-1}. Relatively small $\Delta\nu(CO_2^-)$ values are indicative of the presence of chelating and /or bridging carboxylate ligands.[31]

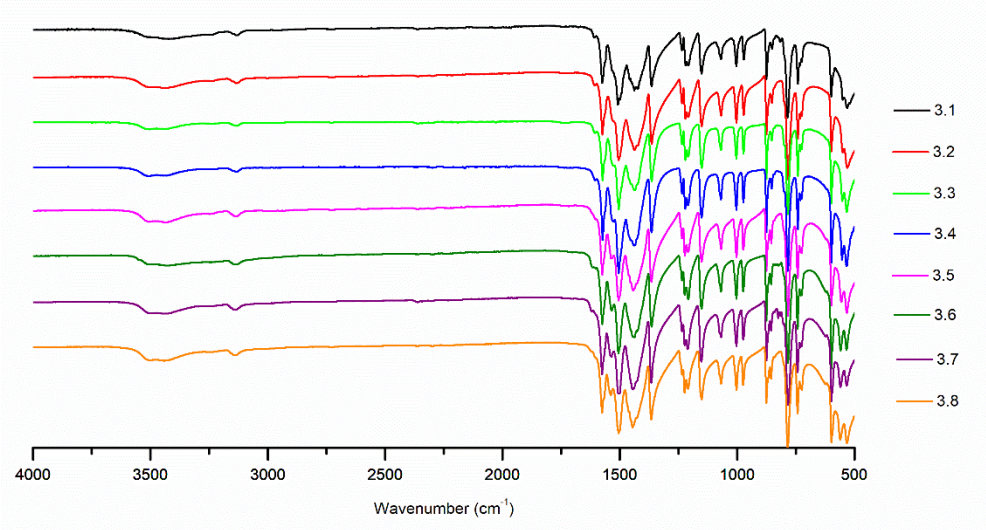


Figure 3.3: IR spectra of the $[RE(3fur)_3(H_2O)_2]_n$ **(3.1-3.8)** series.

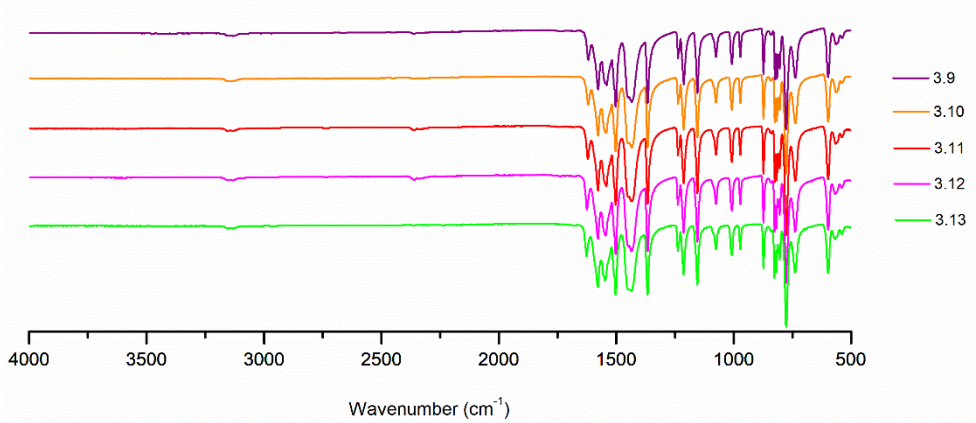


Figure 3.4: IR spectra of the $[NaRE(3fur)_4]_n$ **(3.9-3.13)** series.

Table 3.1: Selected infrared bands (cm-1) of the REIII 3-furoate complexes.

Compound	**$\nu(OH)_{water}$**	**$\nu_{as}(CO_2^-)$**	**$\nu_s(CO_2^-)$**	**$\Delta\nu = (\nu_{as}-\nu_s)avg$**	**$\delta(CO_2)$**
$[Nd(3fur)_3(H_2O)_2]_n$ (3.4)	3431	1505	1365	140	598
$[NaYb(3fur)_4]_n$ (3.12)	-	1502	1366	136	598

A TGA study was conducted to establish the thermal behaviour of the complexes as well as the intermediates and products formed during the thermolysis. TGA curves of the bulk samples of compounds **3.1-3.8** (Figure 3.5) showed a steep initial weight loss (*ca*. 75-130 °C), which corresponds to the loss of two molecules of water and the results are in agreement with the composition determined crystallographically as $[RE(3fur)_3(H_2O)_2]_n$. In line with the single-crystal compositions of the compounds **3.9-3.13**, their thermograms (Figure 3.6) do not indicate any weight loss owing to the loss of coordinated or lattice solvent molecules. Further weight

loss is observed for all the compounds at *ca*. 370-500 °C. However, the TGA plot of **3.1** exhibits significantly different behaviour as the product formation starts and finishes at lower temperature than for the rest of the compounds in the isostructural series.

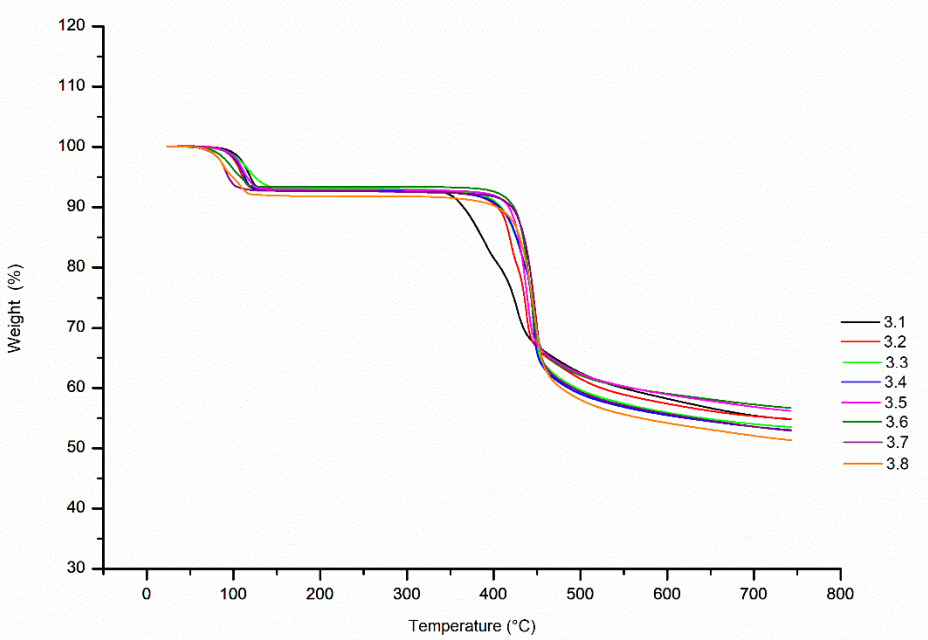


Figure 3.5: TGA thermograms of the $[RE(3fur)_3(H_2O)_2]_n$ **(3.1-3.8)** series.

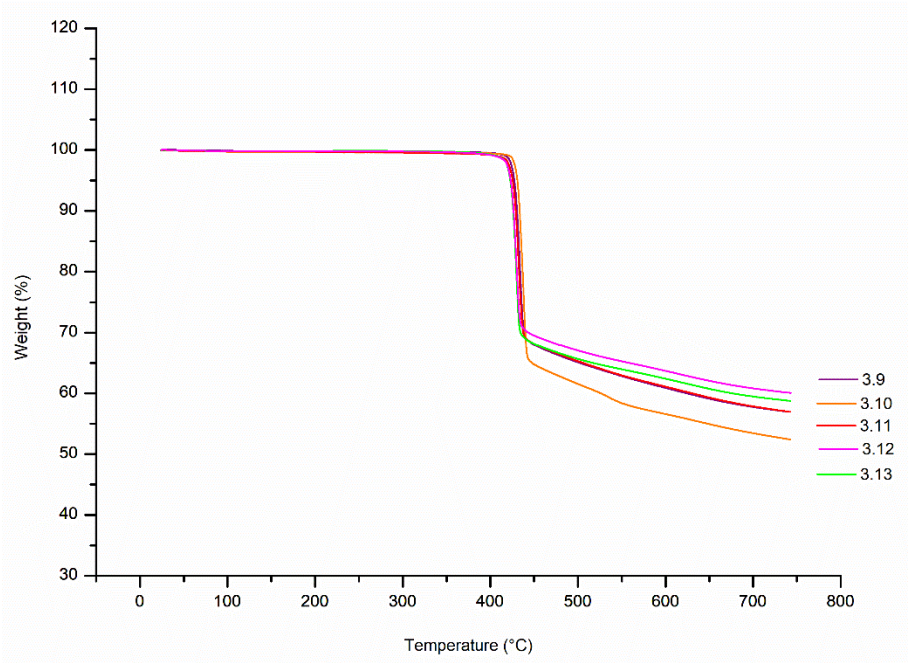


Figure 3.6: TGA thermograms of the $[NaRE(3fur)_4]_n$ **(3.9-3.13)** series.

The decomposition of the anhydrous complexes yielded the respective products $RE_2(CO_3)_3$ in the $[RE(3fur)_3(H_2O)_2]_n$ series and $Na_3RE(CO_3)_3$ in the $[NaRE(3fur)_4]_n$ series. The IR spectra of the residues of compounds **3.2** and **3.12** after thermolysis to 500 °C support this

interpretation[32,33] since they correspond well with the previously reported spectrum of $[Dy_2(CO_3)_3].4H_2O$ (Figure 3.7).[34] However, for the residues of $[RE(3fur)_3(H_2O)_2]_n$ compounds, there is not sufficient weight loss for $RE_2(CO_3)_3$ alone. Residual 3-furoate ligand could not be detected in the residue by IR spectra, so there must be an amorphous or IR silent coproduct such as $RE(OH)_3$, RE_2O_3, or REC_2. Metal carboxylates have a number of possible decomposition paths including the formation of carbonates and oxides.[35,36]

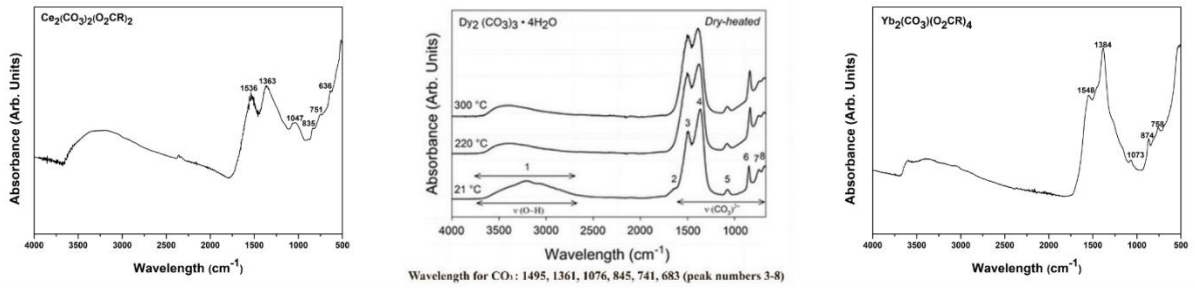


Figure 3.7: IR spectra of $Ce_2(CO_3)_2$ (left) from thermal decomposition of **3.2**, reported $Dy_2(CO_3)_3{\cdot}4H_2O$ (middle)[34] and $Na_3Yb(CO_3)_3$ (right) from thermal decomposition of **3.12**.

Liquid chromatography-mass spectrometry (LCMS) studies have been used to investigate the composition of complexes **3.6**, **3.9** and **3.13** in solution. In the mass spectrum of monometallic complex **3.6** the molecular ion peak $[Dy(3fur)_2(H_2O)_2]^+$ can be detected at m/z 419.1 with the correct isotope patterns. Other than that, the related ion such as $[Dy(3fur)(OH)EtOH]^+$, can be also observed. The bimetallic complexes **3.9** and **3.12** were also examined by LCMS. In the positive mode of complex **3.6,** $[Ho_2(3fur)_4(HCO_3)(H_2O)]^+$ and $[Na_2Ho(3fur)_3(3furH)(HCO_3)(H_2O)]^+$ were detected at m/z 853.5 and 735.2 respectively, with low intensity. Finally, compound **3.13** in LCMS led to a highly intense peak as $[Na_2(CO_3)Lu(3fur)_4(H_2O)_2]^-$ in the negative mode at m/z 761 (Figure 3.8). Interestingly, mass spectrometry results suggest that the bimetallic complexes remain considerably intact in solution. Furthermore, the observations of LCMS experiments have revealed that all the tested complexes retain some form of rare earth carboxylate fragments in solution.

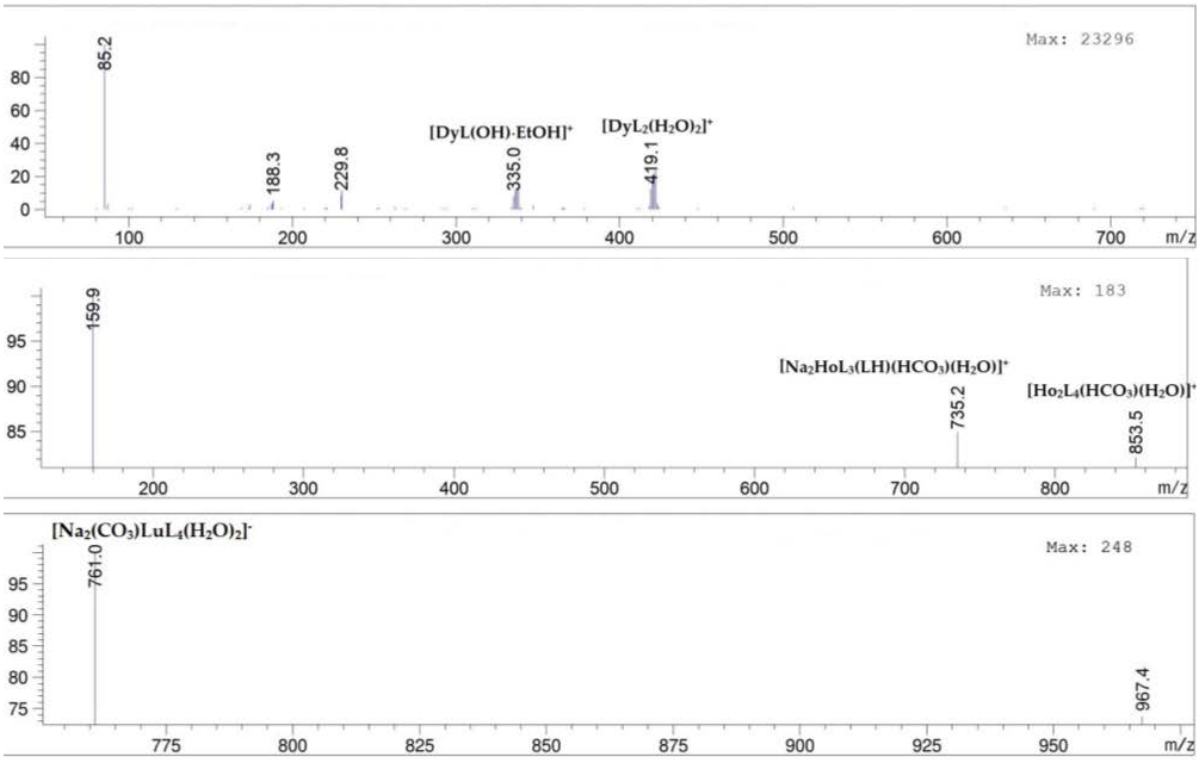
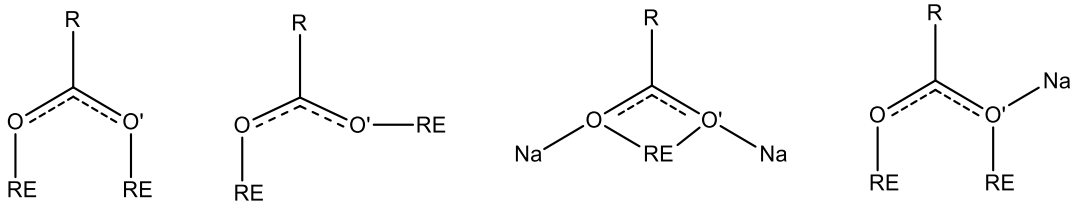


Figure 3.8: Mass spectra of the complexes **3.6**, **3.9** and **3.13**.

3.2.2 X-ray crystal structures

There are three distinct carboxylate ligand binding modes, namely bridging μ-1κ(O):2κ(O′), chelating double bridging μ_3-1κ(O):2κ(O,O′):3κ(O′) and double bridging μ_3-1κ(O):2κ(O′):3κ(O′) observed in the structures (Figure 3.9).



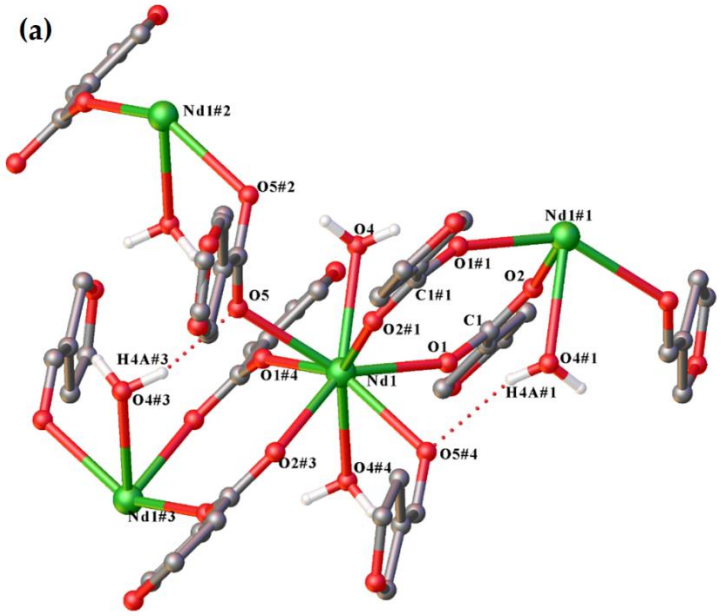
(i) μ-1κ(O):2κ(O′) (ii) μ-1κ(O):2κ(O′) (iii) μ_3-1κ(O):2κ(O,O′):3κ(O′) (iv) μ_3-1κ(O):2κ(O′):3κ(O′)

3.1-3.8 **3.1-3.8** **3.9-3.13** **3.9-3.13**

Figure 3.9: Different coordination modes observed for carboxylate ligand (3-furoate) in rare earth complexes. (i): *syn-syn* (ii): *syn-anti.*

3.2.2.1 Monometallic 2D polymeric chains of $[RE(3fur)_3(H_2O)_2]_n$ complexes (RE = La (3.1), Ce (3.2), Pr (3.3), Nd (3.4), Gd (3.5), Dy (3.6), Ho (3.7), Y (3.8))

This isomorphous series of complexes crystallizes in the monoclinic *C*2/*c* space group and the compounds have 2D polymeric structures. A representative structure of $[Nd(3fur)_3(H_2O)_2]_n$ **(3.4)** is shown in Figure 3.10. Experimentally found H bonds of the compound $[Nd(3fur)_3(H_2O)_2]_n$ are shown in Figure 3.10 (a) and H bond lengths are listed in Table 3.2. The eight-coordinate rare earth metal atoms have distorted square antiprismatic geometry (Figure 3.11). The coordination environment comprises of six bridging μ-1κ(O):2κ(O′) carboxylate ligands binding through O(1, 1#4, 2#1, 2#3, 5, 5#4) and two ligated aqua molecules O(4, 4#4). The backbone of the 1D polymeric chain is constructed through eight-membered rings (Nd1-O2#1-C1#1-O1#1-Nd1#1-O2-C1-O1) formed by *syn-syn* bridging bidentate carboxylates between adjacent Nd1 and Nd1#1 metal centres. The 1D polymeric chain of Nd atoms is nonlinear with Nd1#1-Nd1-Nd1#3 at an angle of 167.339(5)° and the distance between the adjacent Nd^{3+} metal centres in the chain is 5.1246(18) Å. The two ligated water oxygen atoms form a O4-Nd1-O4#4 *cisoid* angle of 127.16(6)°. Two of the bridging carboxylate oxygen atoms (O5 and O5#4) are involved in hydrogen bonding to water oxygen atoms (O4#3 and O4#1) attached to the adjacent metal centres. The 1D polymeric chain propagates into a 2D network by *syn-anti* bridging bidentate ligands (O5, 5#2) between Nd1 and Nd1#2 metal atoms.



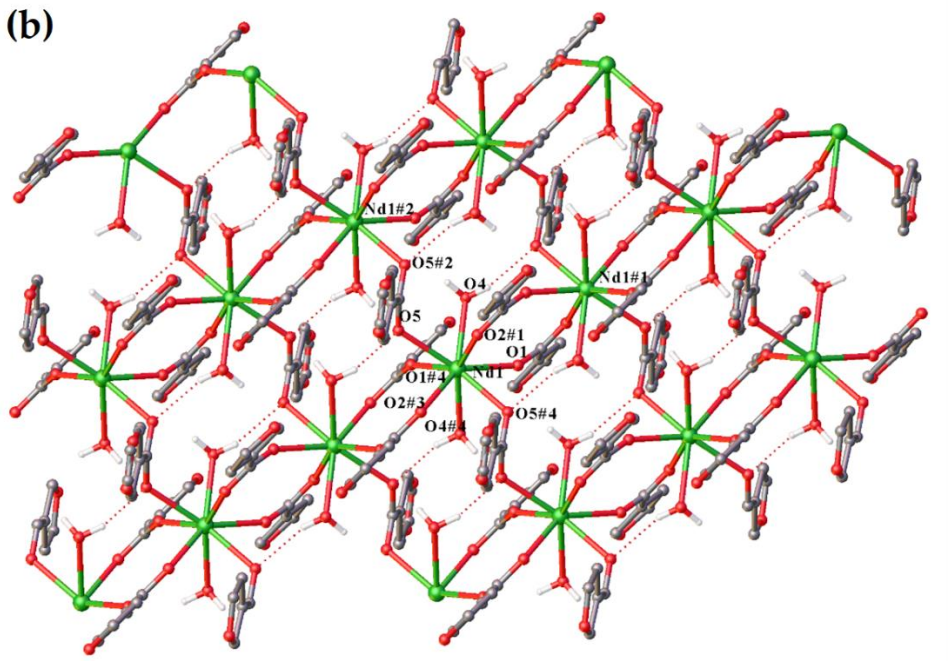


Figure 3.10: **(a)** The immediate coordination environment around Nd metal atoms in $[Nd(3fur)_3(H_2O)_2]_n$ **(3.4)**; (**b**) 2D polymeric chain of **3.4** generated from single-crystal XRD data. (representative of RE = La **(3.1)**, Ce **(3.2)**, Pr **(3.3)**, Gd **(3.5)**, Dy **(3.6)**, Ho **(3.7)**, Y **(3.8)**). Thermal ellipsoids are drawn at the 50% probability level. Selected bond lengths (Å) and angles (°) (Data for **3.1-3.8** in Tables 3.3 and 3.4) **3.4** Nd1-O1#4 2.3487(15), Nd1-O1 2.3487(15), Nd1-O2#1 2.3991(13), Nd1-O2#3 2.3991(13), Nd1-O5#4 2.4848(14), Nd1-O5 2.4848(14), Nd1-O4#4 2.5830(14), Nd1-O4 2.5830(14), Nd1…Nd1#1 5.1246(18), Nd1#1-Nd1-Nd1#3 167.339(5), O4-Nd-O4#4 127.16(6), Symmetry Codes: $^{\#1}$1/2-X,3/2-Y,-Z; $^{\#2}$ 1-X,+Y,3/2-Z; $^{\#3}$1/2+X,3/2-Y,1/2+Z:,$^{\#4}$1-X,+Y,1/2-Z.

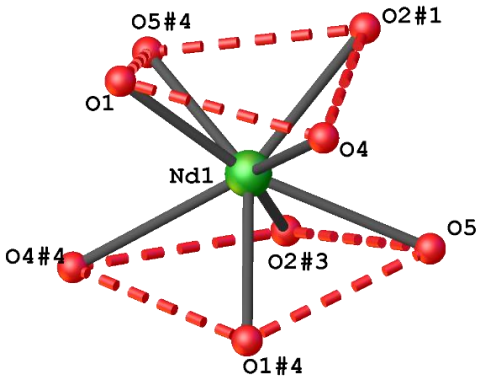


Figure 3.11**:** The overall geometry featuring the orientation of oxygen atoms around the Nd1 metal centre. Non-metal atoms, except those directly adjacent to the metal centre, are omitted

for clarity. The red dashed lines (----) represent the square planes forming the distorted square antiprism. Symmetry equivalents: #1 1/2-X,3/2-Y,-Z; #3 1/2+X,3/2-Y,1/2+Z; #4 1-X,+Y,1/2-Z.

Table 3.2: Hydrogen bonds for $[Nd(3fur)_3(H_2O)_2]_n$ (**3.4**) [d/Å and </°].

D-H…A	d(D-H)	d(H…A)	d(D…A)	<(DHA)
O4#1-H4A#1…O5#4	0.8534(14)	2.1716(15)	2.954(2)	152.32(10)
O4#3-H4A#3…O5	0.8534(14)	2.1716(15)	2.954(2)	152.32(10)

The lanthanoid contraction[37] is observed across the period from La to Y with a decrease in the average RE-O bond distance (Table 3.3) [RE = La 2.512 Å, Ce 2.487 Å, Pr 2.470 Å, Nd 2.454 Å, Gd 2.404 Å, Dy 2.379 Å, Ho 2.365 Å, Y 2.365 Å].

Table 3.3: Selected bond lengths and RE…RE distances (Å) for the isostructural $[RE(3fur)_3(H_2O)_2]_n$ series.

	La1 **(3.1)**	Ce1 **(3.2)**	Pr1 **(3.3)**	Nd1 **(3.4)**	Gd1 **(3.5)**	Dy1 **(3.6)**	Ho1 **(3.7)**	Y1 **(3.8)**
RE1 =RE1#1	5.1559(18)	5.1374(18)	5.1306(18)	5.1246(18)	5.0823(18)	5.0582(18)	5.0451(18)	5.0528(18)
O1#4	2.410(2)	2.385(2)	2.3624(18)	2.3487(15)	2.2968(19)	2.267(2)	2.252(4)	2.2535(14)
O1	2.410(2)	2.385(2)	2.3624(18)	2.3487(15)	2.2968(19)	2.267(2)	2.252(4)	2.2535(14)
O2#1	2.459(2)	2.4306(19)	2.4139(16)	2.3991(13)	2.3443(17)	2.308(2)	2.294(4)	2.2969(12)
O2#3	2.459(2)	2.4306(19)	2.4139(16)	2.3991(13)	2.3443(17)	2.308(2)	2.294(4)	2.2969(12)
O5#4	2.538(2)	2.513(2)	2.5010(17)	2.4848(14)	2.4464(18)	2.436(2)	2.422(4)	2.4196(14)
O5	2.538(2)	2.513(2)	2.5009(17)	2.4848(14)	2.4464(18)	2.436(2)	2.422(4)	2.4197(14)
O4#4	2.640(2)	2.621 (19)	2.6026(17)	2.5830(14)	2.5276(18)	2.506(2)	2.494(4)	2.4908(13)
O4	2.640(2))	2.621 (19)	2.6026(17)	2.5830(14)	2.5276(18)	2.506(2)	2.494(4)	2.4908(13)

Table 3.4: Selected bond angles (°) for the isostructural $[RE(3fur)_3(H_2O)_2]_n$ series.

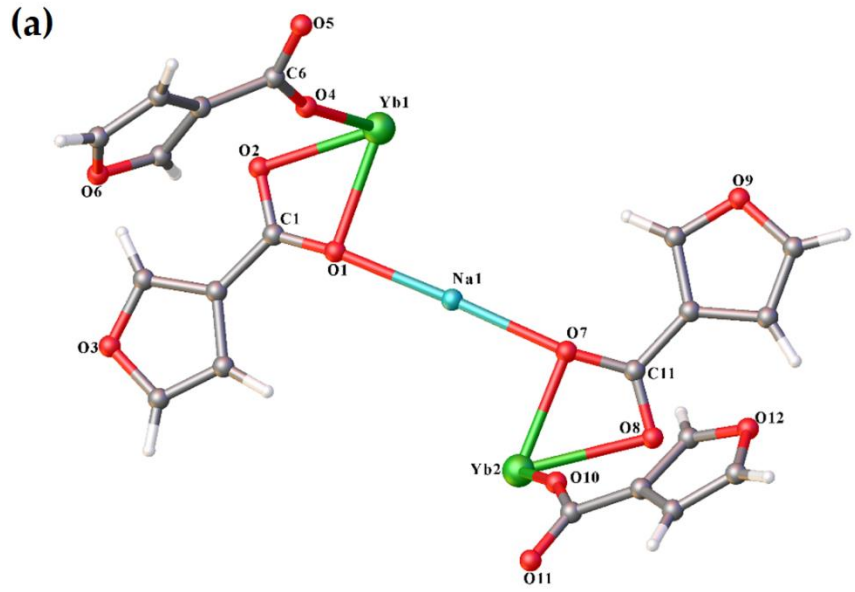
	(3.1)	**(3.2)**	**(3.3)**	**(3.4)**	**(3.5)**	**(3.6)**	**(3.7)**	**(3.8)**
O4-Nd-O4#4	126.59(10)	126.72(9)	126.91(7)	127.16(6)	127.28(9)	127.46(10)	127.36(18)	127.62(6)
Nd1#1-Nd1-Nd1#3	167.764(13)	167.565(13)	167.485(13)	167.339(5)	166.961(13)	166.873(13)	166.706(13)	166.725(13)

3.2.2.2 Bimetallic 3D polymeric chains of $[NaRE(3fur)_4]_n$ complexes (RE = Ho (3.9), Y (3.10), Er (3.11), Yb (3.12), Lu (3.13))

Single crystals of X-ray crystallography quality were obtained for all five Ho, Y, Er, Yb and Lu analogues. The isostructural series of complexes form a 3D polymeric network and crystallize in the tetragonal *P*-4*n*2 space group. A representative structure $[NaYb(3fur)_4]_n$ can be found in Figure 3.12. The Yb1 and Yb2 atoms are bridged by the O1-Na1-O7 moiety present in the asymmetric unit of the crystal structure (Figure 3.12(a)). The Yb1 metal centre is bonded by chelating carboxylate oxygen atoms O1,2 and O1#1,2#1 of two μ_3-1κ(O):2κ(O,O′):3κ(O′)

ligands. There are also four carboxylate ligands bridging through oxygen atoms O4, 4#1, 5#2, 5#3 of μ_3-1κ(O):2κ(O′):3κ(O′). The ligand binding modes contained within the coordination sphere of the Yb2 metal atom are similar to those of the above-mentioned Yb1 metal atom, but Yb-O bond distances are different in each case (Table 3.5). Six coordinated Na1 is ligated through O1, 2#1, 7, 8#4 of four μ_3-1κ(O):2κ(O,O′):3κ(O′) coordinated modes and the other two sites are occupied by oxygen atoms O5#2 and O11#6 of two μ_3-1κ(O):2κ(O′):3κ(O′) carboxylate ligands. Yb1 and Na1, and Yb2 and Na1 are bridged by oxygen atoms O1, 2#1, O5#2 and O 7, 8#4, 11#6 respectively (Figure 3.12(b)).

Yb1 and Yb1#3 metals are connected by four μ_3-1κ(O):2κ(O′):3κ(O′) ligands binding through O4-C6-O5, O5#2-C6#2-O4#2, O4#1-C6#1-O5#1 and O5#3-C6#3-O4#3 with all having the same O-C-O bond angle of 123.6(4)°, and Yb1…Yb1#3 distance of 4.0237(9) Å. In a similar manner, Yb2 is connected with Yb2#5 by four carboxylates with all of them having an O-C-O bond angle of 123.4(4)°. Yb2 atoms are linked through these bridging oxygens to form dimeric units with a Yb2…Yb2 separation of 4.0006(4) Å and these dimers propagate to form 1D channels. However, the successive Yb2 chains are perpendicular to each other, thus constructing two types of chains. As mentioned above, symmetric bridging between adjacent $Yb1^{(III)}$ atoms leads to the formation of dimeric Yb1 channels that crosslink the neighbouring Yb2 channels running along the perpendicular direction, into a two-dimensional grid. Finally, sodium metal atoms connect all dimers into a 3D coordination polymer, namely $[NaYb(3fur)_4]_{n.}$ (Figure 3.12(c)).



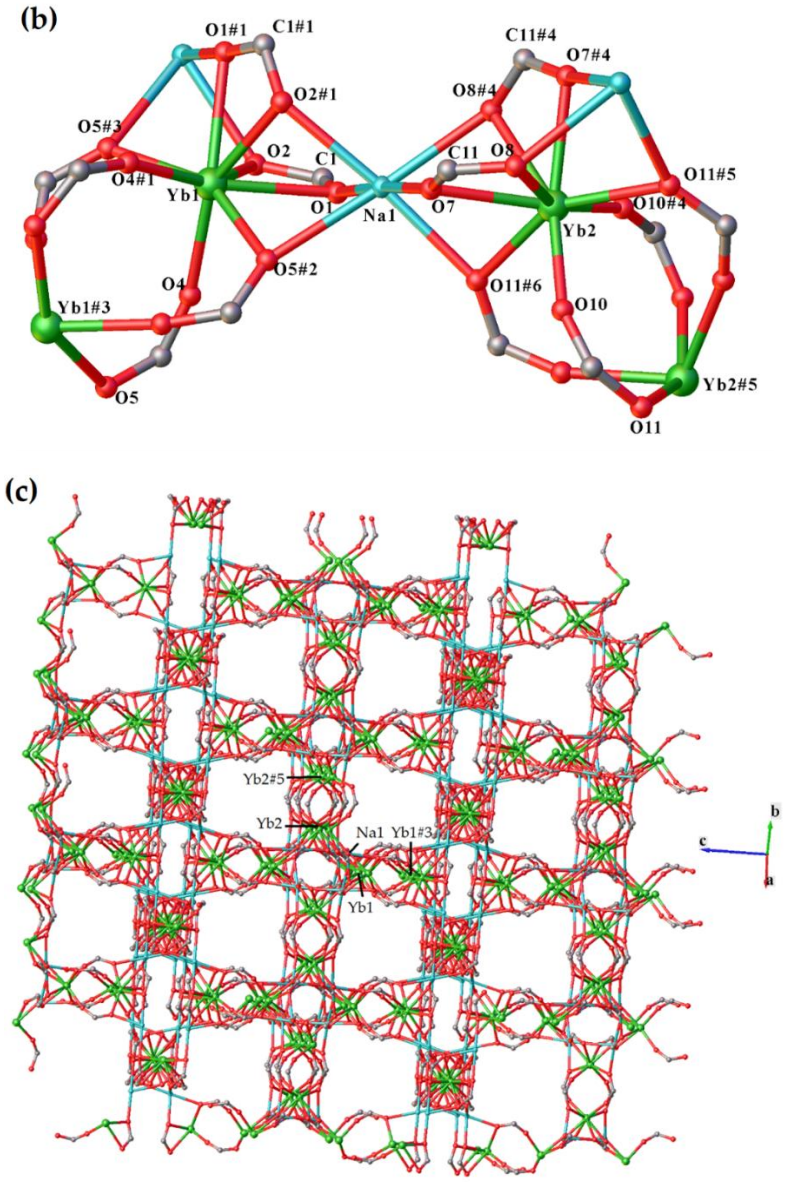


Figure 3.12**(a)** Asymmetric unit of $[NaYb(3fur)_4]_n$ (**3.12**) generated from single-crystal XRD data. (representative of RE = Ho **(3.9)**, Y **(3.10)**, Er **(3.11)**, Lu **(3.13)**) **(b)** The immediate coordination environment around Yb1, Yb2 and Na1 metals atoms in **3.12** (furan rings are omitted for clarity). Thermal ellipsoids are drawn at the 50% probability level. Selected bond lengths (Å) and angles (°) (Data for **3.9-3.13** in Tables 3.5 and Table 3.6).**3.12** Yb1-O1 2.360(3), Yb1-O2 2.432(3), Yb1-O4 2.208(3), Yb1-O5#2 2.321(3), Yb2-O7 2.317(3), Yb2-O8 2.495(3), Yb2-O10 2.180(3), Yb2-O11#6 2.349(3), Na1-O1 2.317(3), Na1-O2#1 2.338(4), Na1-O5#2 2.428(4), Na1-O7 2.323(4), Na1-O8#4 2.369(4), Na1-O11#6 2.367(4), C1-Yb1-C1#1 85.81(19), C11-Yb2-C11#4 82.54(18), Yb1-Na1-Yb2 175.26(7); **(c)** The 3D framework

of **3.12**; Symmetry codes: [#1]1-X,1-Y,+Z; [#2]+Y,1-X,1-Z; [#3]1-Y,+X,1-Z; [#4]3/2-Y,3/2-X,3/2-Z; [#5]-1/2+Y,1/2+X,3/2-Z; [#6]1-X,2-Y,+Z.

All RE^{3+} ions are eight coordinated with two chelating ligands and four bridging ligands in distorted square antiprismatic geometry, Na1 is six-coordinate with six bridging ligands, and the donor atoms have an octahedral arrangement (Figure 3.12).

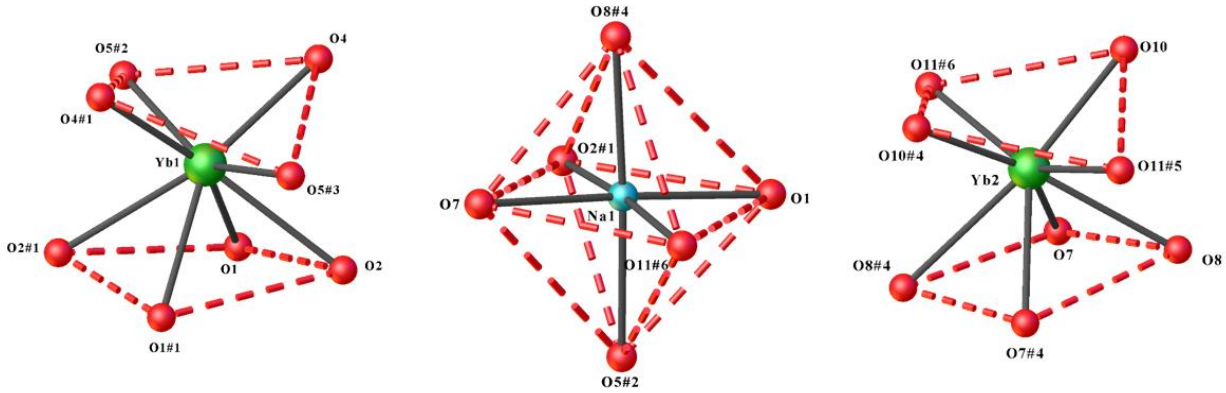


Figure 3.13: The distinct geometries around Yb1, Na1, Yb2 of **3.12,** highlighting the orientation of the bonding oxygen atoms around each metal centres. Non-metal atoms, except those directly surrounding the metal centres, are omitted for clarity. Symmetry equivalents used: [#1]1-X,1-Y,+Z; [#2]+Y,1-X,1-Z; [#3]1-Y,+X,1-Z; [#4]3/2-Y,3/2-X,3/2-Z; [#5]-1/2+Y,1/2+X,3/2-Z; [#6]1-X,2-Y,+Z. The red dashed lines (----) represent the distorted planes formed by the oxygen atoms.

The RE-O and Na-O bond lengths are listed in Table 3.5. The average Yb1-O, Yb2-O and Na1-O bond lengths are 2.330 Å, 2.335 Å and 2.358 Å, correspondingly. The longest RE-O bond length observed in the structure is between Yb2-O8 and Yb2-O8#4 at 2.495(3) Å with Yb2-O10 and Yb2-O10#4 having the shortest RE-O bond distance of 2.180(3) Å. The longest Yb-O bonds are from the oxygen atoms O8 and O8#4 (both chelating and bridging), while the shortest bond lengths are from bridging oxygen atoms O10 and O10#4. The chelating μ_3-1κ(O):2κ(O,O′):3κ(O′) carboxylate ligands form *cisoid* angles of 85.81(19)° (C1-Yb1-C1#1) and 82.54(18)° (C11-Yb2-C11#4). The metal-metal distance between Yb1….Na1 and Yb2…Na1 are 3.3826(18) and 3.3720(18) respectively with Yb1-Na1-Yb2 at an angle of 175.26(7)°. The effect of the lanthanoid contraction[37] is reflected across the series with the reduction of average RE-O bond distances in 1D chains (Table 3.5).

Table 3.5: Selected bond lengths and Na…RE distances (Å) for the isostructural $[NaRE(3fur)_4]_n$ **(3.9-3.13)** series.

	Ho1 (**3.9**)	Y1 (**3.10**)	Er1 (**3.11**)	Yb1 (**3.12**)	Lu1 (**3.13**)
Na1	3.403(2)	3.4031(15)	3.401(3)	3.3841(16)	3.381(2)
O1	2.392(4)	2.384(3)	2.372(5)	2.360(3)	2.351(4)
O1#1	2.392(4)	2.384(3)	2.372(5)	2.360(3)	2.351(4)
O2	2.453(4)	2.457(3)	2.449(6)	2.432(3)	2.428(4)
O2#1	2.453(4)	2.457(3)	2.449(6)	2.432(3)	2.428(4)
O4	2.238(4)	2.239(3)	2.221(5)	2.208(3)	2.196(4)
O4#1	2.238(4)	2.238(3)	2.222(5)	2.208(3)	2.196(4)
O5#2	2.357(3)	2.356(2)	2.340(5)	2.321(3)	2.313(4)
O5#3	2.357(3)	2.356(2)	2.340(5)	2.321(3)	2.313(4)
	Ho2 **(3.9)**	Y2 **(3.10)**	Er2 **(3.11)**	Yb2 **(3.12)**	Lu2 **(3.13)**
Na1	3.398(2)	3.4005(15)	3.392(3)	3.3705(16)	3.374(2)
O7	2.356(3)	2.355(2)	2.340(5)	2.317(3)	2.312(4)
O7#4	2.355(3)	2.355(2)	2.340(5)	2.317(3)	2.311(4)
O8	2.510(4)	2.507(3)	2.509(6)	2.495(3)	2.492(4)
O8#4	2.510(4)	2.507(3)	2.509(6)	2.495(3)	2.492(4)
O10	2.212(4)	2.213(3)	2.207(5)	2.180(3)	2.170(4)
O10#4	2.212(4)	2.213(3)	2.207(5)	2.180(3)	2.170(4)
O11#5	2.391(4)	2.390(3)	2.367(5)	2.349(3)	2.341(4)
O11#6	2.391(4)	2.390(3)	2.367(5)	2.349(3)	2.341(4)
	Na1 **(3.9)**	Na1 **(3.10)**	Na1 **(3.11)**	Na1 **(3.12)**	Na1 **(3.13)**
O1	2.323(4)	2.320(3)	2.327(6)	2.317(3)	2.310(5)
O2#1	2.347(4)	2.348(3)	2.347(6)	2.338(4)	2.334(5)
O5#2	2.418(4)	2.420(3)	2.429(6)	2.428(4)	2.430(5)
O7	2.344(5)	2.340(3)	2.344(7)	2.332(4)	2.333(5)
O8#4	2.388(4)	2.387(3)	2.389(6)	2.369(4)	2.374(5)
O11#6	2.367(4)	2.373(3)	2.368(6)	2.367(4)	2.368(5)

Table 3.6: Selected bond angles (°) for the isostructural $[NaRE(3fur)_4]_n$ **(3.9-3.13)** series.

	3.9	**3.10**	**3.11**	**3.12**	**3.13**
C1-Yb1-C1#1	85.3(2)	85.18(15)	85.2(3)	85.81(9)	85.7(2)
C11-Yb2-C11#4	82.3(2)	82.48(15)	82.7(3)	82.54(18)	83.1(2)
Yb1-Na1-Yb2	174.29(7)	174.32(5)	174.54910)	175.26(7)	175.50(8)

3.2.3 Corrosion Inhibition

3.2.3.1 Immersion Tests

Immersion studies were conducted over seven days in 0.01 M NaCl control solution and in the presence of inhibition systems to access the longer-term performance of these

inhibitors for mild steel. The testing was conducted for the compounds at 800 ppm as the solubility limit for $[Y(3fur)_3(H_2O)_2]_n$ in 0.01 M sodium chloride solution is close to 800 ppm. However, $[Ce(3fur)_3(H_2O)_2]_n$ and $[Pr(3fur)_3(H_2O)_2]_n$ compounds had maximum solubilities as high as 3000 ppm.

Table 3.7 presents a summary of the weight loss measurements after 168 h of immersion in specific inhibitor solutions. The corrosion rate (R) of each inhibitor compound was evaluated and then percentage corrosion inhibition (η) was calculated using Eq 2.1 and 2.2 described in Chapter 2.

Table 3.7: Observed weight loss, corrosion rates ($\mu gm^{-2}s^{-1}$) and percentage inhibition (η) for mild steel coupons immersed in specific solutions at 800 ppm concentrations in 0.01 M NaCl for seven days.

Solution	**Concentration**		**Solubility in 0.01 M NaCl (ppm)**	**Avg Weight Loss (mg)**	**Corrosion Rate ($\mu gm^{-2}s^{-1}$)**	**Inhibition, η (%)**
	ppm	**mM**				
Control – NaCl	580	10	-	19.6	39.09	-
$[La(3fur)_3(H_2O)_2]_n$ **3.1**	800	1.57	2000	2.6	5.14	87
$[Ce(3fur)_3(H_2O)_2]_n$ **3.2**	800	1.57	3000	3.7	8.30	79
$[Pr(3fur)_3(H_2O)_2]_n$ **3.3**	800	1.57	3000	6.1	10.58	73
$[Nd(3fur)_3(H_2O)_2]_n$ **3.4**	800	1.56	2500	5.1	10.17	74
$[Gd(3fur)_3(H_2O)_2]_n$ **3.5**	800	1.57	1000	6.2	11.23	71
$[Dy(3fur)_3(H_2O)_2]_n$ **3.6**	800	1.52	830	3.0	6.38	84
$[Ho(3fur)_3(H_2O)_2]_n$ **3.7**	800	1.50	920	2.9	5.86	85
$[Y(3fur)_3(H_2O)_2]_n$ **3.8**	800	1.75	800	1.9	3.9	90
$[NaHo(3fur)_4]_n$ **3.9**	800	1.27	1800	6.0	12.00	70
$[NaY(3fur)_4]_n$ **3.10**	800	1.44	1900	4.9	9.87	75
$[NaEr(3fur)_4]_n$ **3.11**	800	1.26	1800	5.1	10.17	74
$[NaYb(3fur)_4]_n$ **3.12**	800	1.25	1700	2.4	4.7	88
$[NaLu(3fur)_4]_n$ **3.13**	800	1.25	1500	7.7	13.36	66
[Na(3fur)]	800	-	>7000	16.51	27.62	29

The corrosion rates of the samples placed in the inhibitor solutions were found to be significantly lower than that of control coupons. As shown in Table 3.7, $[Y(3fur)_3(H_2O)_2]_n$ **(3.8)** has the highest inhibitor efficiency of 90%. Furthermore, the visual inspection of the surface immersed in $[Y(3fur)_3(H_2O)_2]_n$ containing solutions also suggests a minimum corrosive attack on the steel surface with relatively less surface roughness (Figure 3.14).

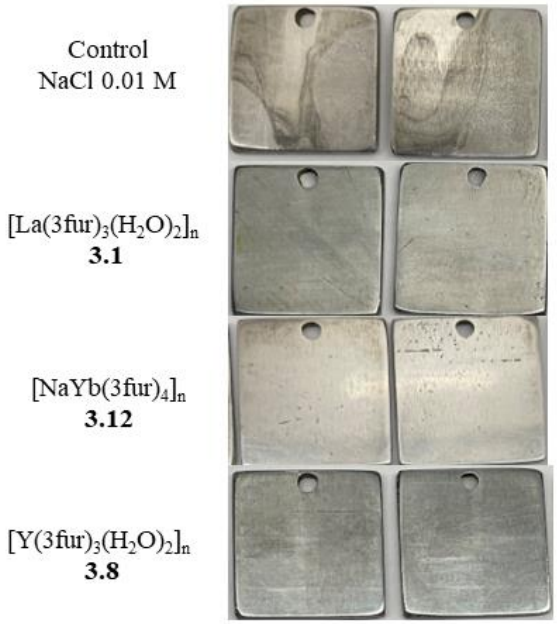


Figure 3.14: Mild steel coupons immersed in control and the three best inhibited solutions for 168 h (left – Trial 1; right – Trial 2).

As a group, $[RE(3fur)_3(H_2O)_2]_n$ complexes showed better inhibition performance than the bimetallic $[NaRE(3fur)_4]_n$ species. This was evident from the better level of protection achieved by monometallic Y^{III} and Ho^{III} inhibited solutions compared to the Na-Y and Na-Ho bimetallic compounds. This may be a consequence of the presence of coordinated sodium in the compounds in the latter instance. The influence of sodium on inhibition efficiency can be seen by comparing the immersion test results of sodium 3-furoate (Na(3fur)) with the rare earth carboxylate complexes in Table 3.7. It has also been shown in previous literature that the corrosion rates of sodium carboxylates on steel are generally higher than that of rare earth analogues.[38] However, the **3.12** complex is a positive outlier since it gave the second-best performance with an η of 88%.

When considering lighter rare earths (La-Nd) the efficiency decreased from La-Nd. The level of protection by the heavy rare earths correlates with the decreasing atomic radius of the rare earth metals since the inhibitive effect increased from Gd-Y among the $[RE(3fur)_3(H_2O)_2]_n$ class. A similar trend was observed to some extent with $[NaRE(3fur)_4]_n$ complexes with

improved protection from Ho to Yb, but Lu is a negative outlier. The low solubility of most of the complexes has hampered attempts at concentration studies. The performance was better than of the analogous rare earth 3-thiophenecarboxylates,[39] discussed in Chapter 2 suggesting that an oxygen substituent may be more beneficial than sulfur, but the 3fur complexes were tested at somewhat higher concentration owing to greater solubility.

3.2.3.2 Potentiodynamic polarisation

The results of the potentiodynamic polarisation (PP) experiments are shown in Table 3.8. $[Y(3fur)_3(H_2O)_2]_n$ **3.8** showed the lowest i_{corr}, at 0.56 μA/cm^2, and **3.8**>**3.12**>**3.1** in effectiveness. After 24 h immersion, with the compounds present in the solution there is a shift in corrosion potential (E_{corr}) values towards more positive direction compared to the control solution, indicative of anodic inhibition dominating the reduction in i_{corr}.

Table 3.8: Summary of corrosion parameters obtained from potentiodynamic polarisation tests in control and inhibited solutions after 24 h immersion.

Solution	i_{corr} (μA/cm^2)	Std. Dev.	E_{corr} (mV)	Std. Dev.	Percentage Inhibition (%)
Control - NaCl	2.88	0.11	-638	4	
$[La(3fur)_3(H_2O)_2]_n$ **3.1**	1.09	0.09	-473	5	62
$[Y(3fur)_3(H_2O)_2]_n$ **3.8**	0.56	0.08	-445	4	80
$[NaYb(3fur)_4]_n$ **3.12**	0.89	0.07	-468	29	69

Representative PP scans in Figure 3.15 shows the marked reduction in the anodic branch with the addition of inhibitors, and some reduction in the cathodic kinetics. According to the previous literature,[38] this is a typical behaviour of these types of compounds. However, the efficacy of $[Y(3fur)_3(H_2O)_2]_n$ was somewhat inferior to that of yttrium 3-(4'-methylbenzoyl)propanoate,[40] which though is limited by low solubility. For this reason, yttrium 3-furoate may potentially be more useful.

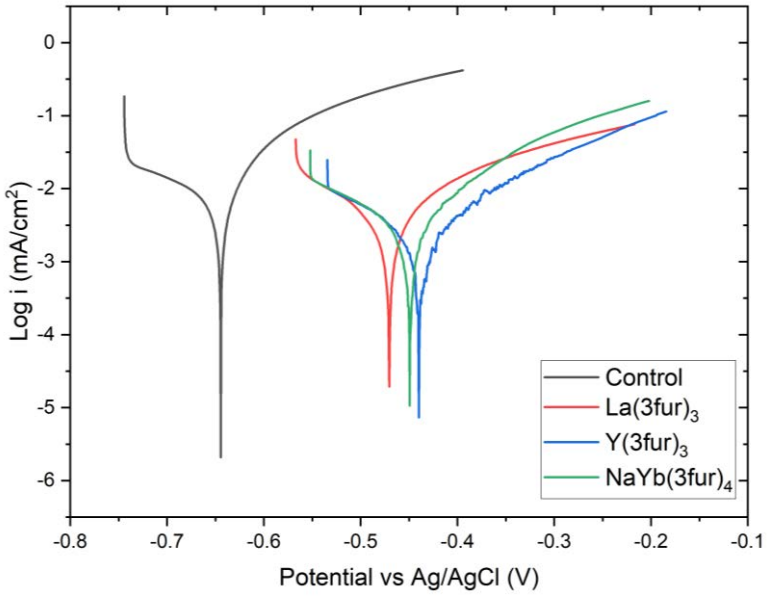


Figure 3.15: Representative potentiodynamic polarisation scans after 24 hours for 0.01 M NaCl control, and solutions with 0.01 M NaCl and 800ppm of $[Y(3fur)_3(H_2O)_2]_n$ **(3.8)**, $[La(3fur)_3(H_2O)_2]_n$ **(3.1)** and $[NaYb(3fur)_4]_n$ **(3.12)**.

3.3 Conclusions

A series of novel rare earth 3-furoate complexes were synthesised and characterised. The 13 structures identified in this study could be separated into two groups based on their molecular composition as below.

- **Type 1**- Monometallic 2D polymeric network of $[RE(3fur)_3(H_2O)_2]_n$
  (RE = La, Ce, Pr, Nd, Gd, Dy, Ho, Y)
- **Type 2** - Bimetallic 3D polymeric network of $[NaRE(3fur)_4]_n$
  (RE = Ho, Y, Er, Yb, Lu)

The ability to obtain two different structural motifs from $HoCl_3$ and YCl_3 at 1:3 and 1:4 (rare earth:ligand) mole ratios indicates that the stoichiometry used in the metathesis reaction affects the final complex formation. The lanthanoid contraction was evident with a reduction of the average RE-O bond distance across each series.

The immersion studies showed that at 800 ppm inhibitor concentrations for mild steel in 0.01 M NaCl solutions, $[Y(3fur)_3(H_2O)_2]_n$ **(3.8)** was the best performing inhibitor with $[NaYb(3fur)_4]_n$ **(3.12)** and $[La(3fur)_3(H_2O)_2]_n$ **(3.1)** exhibiting comparable inhibition performance. Potentiodynamic polarisation confirmed the superior performance of $[Y(3fur)_3(H_2O)_2]_n$ **(3.8)**. The compounds act predominantly as anodic inhibitors. A comparison

of Y complex data suggests that the introduction of a furoate moiety into a carboxylate is more effective than the thiophene group but not as effective as a 3-(4'-methylbenzoyl) group.[39,40]

3.4 Experimental

For materials and general considerations, see Appendix One.

3.4.1 Synthesis of 3-furoate (3fur)- RE aqua complexes

General Synthetic Method: 3-furoic acid (0.392 g, 3.5 mmol) was dissolved in 95% ethanol (15ml) and deprotonated with an equimolar amount of aqueous sodium hydroxide. The solution was stirred for 1 h and the pH was adjusted to 7-8. Treatment of the sodium 3-furoate with a hydrated rare earth chloride or nitrate (mole ratio 3:1) in water at pH 5 gave rare earth 3-furoate **3.1**-**3.8** and **3.11**-**3.13**. Under similar reaction conditions, the metathesis reaction of the preformed ligand and the corresponding rare earth salt with 4:1 stoichiometry resulted in the Na-RE bimetallic 3-furoate **3.9**-**3.13** complexes**.** The resultant precipitates were filtered off and air-dried for 2-3 days. Crystals were obtained upon slow evaporation of the mother liquor at room temperature.

$[La(3fur)_3(H_2O)_2]_n$ (3.1)

White powder. Yield: 0.38 g (65%). m.p. 245 °C (dec.). Elemental analysis for $C_{15}H_{13}LaO_{11}$ (MW: 508.16 $gmol^{-1}$): Calculated (%) C 35.45, H 2.58, La 27.33; Found (%) C 35.57, H 2.42, La 27.50. IR (cm^{-1}): 3421 w, 3132 w, 1575 s, 1507 s, 1437 s, 1364 s, 1235 m, 1219 m, 1209 m, 1151 m, 1068 m, 1003 m, 971 m, 875 s, 851 w, 784 s, 741 s, 731 m, 598 s, 550 s, 531 s, 435 s. TGA weight loss (76-131 °C): 7.0% (Calc. for loss of $2\times H_2O$ = 7.1%); weight loss (328-420 °C): 31.0% (Calc. for the formation of $La_2(CO_3)_3$ = 47.9%).

$[Ce(3fur)_3(H_2O)_2]_n$ (3.2)

White powder. Yield: 0.45 g (76%). m.p. 260 °C (dec.). Elemental analysis for $C_{15}H_{13}CeO_{11}$ (MW: 509.37 $gmol^{-1}$): Calculated (%) C 35.37, H 2.57, Ce 27.51; Found (%) C 35.52, H 2.40, Ce 27.64. IR (cm^{-1}):3439 w, 3134 w, 1574 s, 1505 s, 1437 s, 1364 s, 1235 m, 1220 m, 1209 m, 1151 m, 1068 m, 1003 m, 972 m, 874 s, 851 w, 783 s, 741 s, 731 m, 598 s, 550 s, 531 s, 434 s. TGA weight loss (71-120 °C): 6.9% (Calc. for loss of $2\times H_2O$ = 7.1%); weight loss (364-475 °C): 31.9% (Calc. for the formation of $Ce_2(CO_3)_3$ = 47.8%).

$[Pr(3fur)_3(H_2O)_2]_n$ (3.3)

Pale green powder. Yield: 0.48 g (80%). m.p. 240 °C (dec.). Elemental analysis for $C_{15}H_{13}O_{11}Pr$ (MW: 510.16 $gmol^{-1}$): Calculated (%) C 35.31, H 2.57, Pr 27.62; Found (%) C 35.39, H 2.39, Pr 27.42. IR (cm^{-1}): 3442 w, 3133 w, 1573 s, 1525 w, 1504 s, 1434 s, 1364 s, 1234 m, 1220 m, 1209 m, 1150 m, 1069 m, 1003 m, 972 m, 875 s, 852 w, 786 s, 741 s, 730 m, 598 s, 552 s, 533 s, 438 s. TGA weight loss (70-154 °C): 6.9% (Calc. for loss of $2\times H_2O$ = 7.1%); weight loss (368-492 °C): 31.7% (Calc. for the formation of $Pr_2(CO_3)_3$ = 47.7%).

$[Nd(3fur)_3(H_2O)_2]_n$ (3.4)

Purple powder. Yield: 0.42 g (70%), m.p. 260 °C (dec.). Elemental analysis for $C_{15}H_{13}NdO_{11}$ (MW: 513.49 $gmol^{-1}$): Calculated (%) C 35.08, H 2.55, Nd 28.09; Found (%) C 35.35, H 2.33, Nd 27.94. IR (cm^{-1}): 3431 w, 3134 w, 1573 s, 1527 w, 1505 s, 1439 s, 1364 s, 1234 m, 1221 m, 1209 m, 1151 m, 1069 m, 1003 m, 973 m, 875 s, 852 w, 783 s, 741 s, 730 m, 598 s, 553 s, 534 s, 439 s. TGA weight loss (76-123 °C): 6.9% (Calc. for loss of $2\times H_2O$ = 7.0%); weight loss (365-495 °C): 32.4% (Calc. for the formation of $Nd_2(CO_3)_3$ = 47.4%).

$[Gd(3fur)_3(H_2O)_2]_n$ (3.5)

White powder. Yield: 0.37 g (60%). m.p. 260 °C (dec.). Elemental analysis for $C_{15}H_{13}GdO_{11}$ (MW: 526.50 $gmol^{-1}$): Calculated C 34.22, H 2.49, Gd 29.87; Found (%) C 33.91, H 2.39, Gd 29.62. IR (cm^{-1}): 3440 w, 3134 w, 1574 s, 1537 w, 1505 s, 1443 s, 1365 s, 1234 m, 1222 m, 1209 m, 1151 m, 1068 m, 1002 m, 973 m, 875 s, 854 w, 784 s, 742 s, 730 m, 598 s, 556 s, 533 s, 438 s TGA weight loss (75-130°C): 6.9% (Calc. for loss of $2\times H_2O$ = 6.8 %); weight loss (374-490 °C): 30.2% (Calc. for the formation of $Gd_2(CO_3)_3$ = 46.2%).

$[Dy(3fur)_3(H_2O)_2]_n$ (3.6)

White powder. Yield: 0.49 g (79%). m.p. 260 °C (dec.). Elemental analysis for $C_{15}H_{13}DyO_{11}$ (MW: 531.75 $gmol^{-1}$): Calculated (%) C 33.88, H 2.46, Dy 30.56; Found (%) C 33.52; H 2.34; Dy 30.70. IR (cm^{-1}): 3420 w, 3135 w, 1574 s, 1534 m, 1505 s, 1437 s, 1364 s, 1234 m, 1223 m,1207 m, 1151 s, 1068 m, 1003 m, 974 m, 875 s, 855 w, 783 s, 742 s, 730 m, 598 s, 559 s, 534 s, 442 s. LCMS: (m/z): Calc. for $[Dy(3fur)(OH).EtOH]^+$ 338.0, $[Dy(3fur)_2(H_2O)_2]^+$ 422.0; found 337.1, 422.1. TGA weight loss (60-124 °C): 6.7% (Calc. for loss of $2\times H_2O$ = 6.8%); weight loss (390-482 °C): 30.1% (Calc. for the formation of $Dy_2(CO_3)_3$ = 45.7%).

$[Ho(3fur)_3(H_2O)_2]_n$ (3.7)

Yellow powder. Yield: 0.38 g (61%). m.p. 260 °C (dec.). Elemental analysis for $C_{15}H_{13}HoO_{11}$ (MW: 534.18 $gmol^{-1}$): Calculated (%) C 33.73, H 2.45, Ho 30.87; Found (%) C 33.75, H 2.35, Ho 30.84. IR (cm^{-1}): 3441 w, 3135 w, 1575 s, 1535 m, 1501 s, 1444 s, 1365 s, 1234 m, 1223 m, 1210 m, 1152 s, 1068 m, 1003 m, 973 m, 874 s, 855 m, 782 s, 742 s, 730 m, 598 s, 560 s, 533 s, 442 s. TGA weight loss (63-110 °C): 6.9% (Calc. for loss of $2\times H_2O$ = 6.7%); weight loss (380-491 °C): 31.5% (Calc. for the formation of $Ho_2(CO_3)_3$ = 45.5%).

$[Y(3fur)_3(H_2O)_2]_n$ (3.8)

White powder. Yield: 0.36 g (67%). m.p. 230 °C (dec.). Elemental analysis for $C_{15}H_{13}O_{11}Y$ (MW: 458.16 $gmol^{-1}$): Calculated (%) C 39.32, H 2.86, Y 19.40; Found (%) C 39.64, H 2.62, Y 19.80. IR (cm^{-1}): 3441 w, 3136 w, 1575 s, 1538 m, 1505 s, 1445 s, 1366 s, 1234 m, 1223 m, 1209 m, 1151 s, 1068 m, 1002 m, 974 m, 875 s, 855 m, 784 s, 742 s, 724 m, 598 s, 561 s, 531 s, 441 s. TGA weight loss (55-135 °C): 7.9% (Calc. for loss of $2\times H_2O$ = 7.9%); weight loss (372-498 °C): 35.1% (Calc. for the formation of $Y_2(CO_3)_3$ = 53.1%).

$[HoNa(3fur)_4]_n$ (3.9)

Yellow powder. Yield: 0.31 g (56%). m.p. 200 °C (dec.). Elemental analysis for $C_{20}H_{12}HoNaO_{12}$ (MW: 632.22 $gmol^{-1}$): Calculated (%) C 38.00, H 1.91, Ho 26.09. Found (%) C 37.52, H 1.90, Ho 26.11. IR (cm^{-1}): 3131 w, 2363 w, 1619 m, 1577 s, 1541 s, 1502 s, 1434 s, 1366 s, 1237 m, 1212 s, 1154 s, 1075 m, 1007 m, 971 m, 872 s, 840 w, 824 s, 815 s, 804 s, 776 s, 737 s, 598 s, 564 w, 539 w, 457 s. LCMS: (m/z): Calc. for $Na_2Ho(3fur)_3(3furH)(HCO_3)(H_2O)]^+$ 735.0, $[Ho_2(3fur)_4(HCO_3)(H_2O)]^+$ 853.0; found 735.2, 853.5. TGA weight loss (403-454 °C): 33.1% (Calc. for the formation of $Na_3Ho(CO_3)_3$ = 34.6%).

$[NaY(3fur)_4]_n$ (3.10)

White powder. Yield: 0.25 g (51%). m.p. 240 °C (dec.). Elemental analysis for $C_{20}H_{12}NaO_{12}Y$ (MW: 556.20 $gmol^{-1}$): Calculated (%) C 43.19, H 2.17, Y 15.98; Found (%) C 42.54, H 1.87, Y 15.81. IR (cm^{-1}): 3131w, 2361w, 1619m, 1577s, 1543s, 1503s, 1434s, 1366s, 1237m, 1212s, 1154s, 1075m, 1007m, 971m, 872s, 841w, 824s, 816s, 804s, 776s, 737s, 598s, 563w, 539w, 461s. TGA weight loss (410-457 °C): 37.1% (Calc. for the formation of $Na_3Y(CO_3)_3$ = 39.2%).

$[NaEr(3fur)_4]_n$ (3.11)

Pink powder. Yield: 0.33 g (59%). m.p. 240 °C (dec.). Elemental analysis for $C_{20}H_{12}ErNaO_{12}$ (MW: 634.55 $gmol^{-1}$): Calculated (%) C 37.86, H 1.91, Er 26.36; Found (%) C 37.78, H 1.83, Er 26.54. IR (cm^{-1}): 3136 w, 2361 w, 1621 m, 1577 s, 1542 s, 1502 s, 1433 s, 1366 s, 1237 m, 1213 s, 1154 s, 1075 m, 1007 m, 971 m, 873 s, 840 w, 824 s, 816 s, 804 s, 776 s, 737 s, 598 s, 566 w, 539 w, 457 s; TGA weight loss (400-453 °C): 32.2% (Calc. for the formation of $Na_3Er(CO_3)_3$ = 34.4%).

$[NaYb(3fur)_4]_n$ (3.12)

White powder. Yield: 0.34 g (60%). m.p. 240 °C (dec.). Elemental analysis for $C_{20}H_{12}YbNaO_{12}$ (MW: 640.33 $gmol^{-1}$): Calculated (%) C 37.51, H 1.89, Yb 27.02; Found (%) C 36.35, H 1.82, Yb 27.03. IR (cm^{-1}): 3132 w, 2360 w, 1624 m, 1578 s, 1545 s, 1502 s, 1434 s, 1366 s, 1237 m, 1213 s, 1154 s, 1075 m, 1007 m, 971 m, 873 s, 840 w, 825 s, 818 s, 804 s, 776 s, 738 s, 598 s, 567 w, 540 w, 457 s. TGA weight loss (400-452°C): 31.3% (Calc. for the formation of $Na_3Yb(CO_3)_3$ = 34.1%).

$[NaLu(3fur)_4]_n$ (3.13)

White powder. Yield: 0.29 g (51%). m.p. 250 °C (dec.). Elemental analysis calculated for $C_{20}H_{12}LuNaO_{12}$ (MW: 642.26 $gmol^{-1}$) Calculated (%) C 37.40, H 1.88, Lu 27.24; Found (%) C 36.75, H 1.82, Lu 27.31. IR (cm^{-1}):): 3132 w, 2360w, 1626 m, 1578 s, 1547 s, 1503 s, 1435 s, 1366 s, 1238 m, 1213 s, 1154 s, 1075 m, 1007 m, 971 m, 873 s, 840 w, 826 s, 818 s, 804 s, 776 s, 738 s, 598 s, 568 w, 540 w, 459 s. LCMS: (m/z): Calc. for $[Na_2(CO_3)Lu(3fur)_4(H_2O)_2]^-$ 761.0; found 761.0. TGA weight loss (397-450 °C): 32.2% (Calc. for the formation of $Na_3Lu(CO_3)_3$ = 33.9%).

3.4.2 Corrosion Testing

For the corrosion testing procedures used for weight loss experiments and potentiodynamic polarisation (PP) experiments, see Appendix One.

3.5 X-ray crystal data

For details on x-ray crystallography, see Appendix One.

Crystal data and refinement details are given in Table 3.9 and 3.10.

Table 3.9: Crystal data and structural refinement for $[RE(3fur)_3(H_2O)_2]_n$ (RE = La, Ce, Pr, Nd, Gd, Dy, Ho) complexes.

Compound	**3.1**	**3.2**	**3.3**	**3.4**	**3.5**	**3.6**	**3.7**	**3.8**
Formula	$C_{15}H_{13}LaO_{11}$	$C_{15}H_{13}CeO_{11}$	$C_{15}H_{13}O_{11}Pr$	$C_{15}H_{13}NdO_{11}$	$C_{15}H_{13}GdO_{11}$	$C_{15}H_{13}DyO_{11}$	$C_{15}H_{13}HoO_{11}$	$C_{15}H_{13}O_{11}Y$
M_r	508.16	509.37	510.16	513.49	526.50	531.75	534.18	458.16
Space	C2/c	C2/c	C2/c	C2/c	C2/c	C2/c	C2/c	C2/c
a (Å)	11.500(2)	11.513(2)	11.533(2)	11.547(2)	11.493(2)	11.461(2)	11.434(2)	11.446(2)
b (Å)	27.339(6)	27.247(5)	27.173(5)	27.114(5)	26.991(5)	26.918(5)	26.886(5)	26.889(5)
c (Å)	6.0950(12)	6.0820(12)	6.0720(12)	6.0560(12)	6.0220(12)	6.0140(12)	5.9990(12)	6.0030(12)
α (°)	90	90	90	90	90	90	90	90
β (°)	117.29(3)	117.75(3)	118.04(3)	118.27(3)	118.65(3)	118.85(3)	118.89(3)	118.84(3)
γ (°)	90	90	90	90	90	90	90	90
V (Å^3)	1703.0(7)	1688.4(7)	1679.5(7)	1669.9(7)	1639.4(7)	1625.2(7)	1614.8(7)	1618.4(7)
Z	4	4	4	4	4	4	4	4
ρ_{calc}, g cm^{-3}	1.982	2.044	2.018	2.042	2.133	2.173	2.197	1.880
μ, mm^{-1}	2.569	2.757	2.962	3.171	4.108	4.661	4.964	3.667
N_τ	9803	27366	9244	18672	18366	8857	8562	18244
N (R_{int})	1473(0.0389)	1507(0.0634)	1449(0.0360)	1462(0.0251)	1386(0.0267)	1396(0.0382)	1407(0.0753)	1417(0.0501)
$R_1(I > 2\sigma(I))$	0.0230	0.0240	0.0179	0.0136	0.0156	0.0207	0.0379	0.0201
wR_2 (all data)	0.0612	0.0616	0.0468	0.0323	0.0410	0.0524	0.0991	0.0544
GOF	1.048	1.087	1.097	1.158	1.095	1.073	1.035	1.077

Table 3.10: Crystal data and structural refinement for $[NaRE(3fur)_4]_n$ (RE = Ho, Y, Er, Yb, Lu) complexes.

Compound	**3.9**	**3.10**	**3.11**	**3.12**	**3.13**
Formula	$C_{20}H_{12}HoNaO_{12}$	$C_{20}H_{12}NaO_{12}Y$	$C_{20}H_{12}ErNaO_{12}$	$C_{20}H_{12}NaO_{12}Yb$	$C_{20}H_{12}LuNaO_{12}$
M_r	632.22	556.20	634.55	640.33	642.26
Space group	P-4n2	P-4n2	P-4n2	P-4n2	P-4n2
a (Å)	14.257(2)	14.240(2)	14.2457(2)	14.184(2)	14.177(2)
b (Å)	14.257(2)	14.240(2)	14.2457(2)	14.184(2)	14.177(2)
c (Å)	21.587(4)	21.691(4)	21.5746(5)	21.501(4)	21.541(4)
α (°)	90	90	90	90	90
β (°)	90	90	90	90	90
γ (°)	90	90	90	90	90
V (Å^3)	4387.8(15)	4398.4(15)	4378.35(16)	4326.0(15)	4329.5(15)
Z	8	8	8	8	8
ρ_{calc}, g cm^{-3}	1.914	1.680	1.925	1.966	1.971
μ, mm^{-1}	3.691	2.736	3.918	4.409	4.646
N_τ	50797	53087	28175	49021	50096
N (R_{int})	4167(0.0478)	4496(0.0565)	6598(0.0738)	3815(0.0390)	4128(0.0521)
$R_1(I > 2\sigma(I))$	0.0201	0.0296	0.0377	0.0129	0.0202
wR_2 (all data)	0.0549	0.0817	0.0934	0.0358	0.0522
GOF	1.068	1.043	1.047	1.095	1.090

3.6 References

1 A. Gandini and M. N. Belgacem, *Prog. Polym. Sci.*, 1997, **22**, 1203–1379.

2 J. Vranova and Z. Ciesarova, *Czech. J. Food Sci.*, 2009, **27**, 1–10.

3 J. A. Joule and K. Mills, Furans: Reactions and Synthesis in *Heterocyclic Chemistry*, John Wiley & Sons Ltd, The Atrium, Southern Gate, Chichester, West Sussex, PO19 8SQ, United Kingdom, 5th edn., 2010.

4 H. Cao and P. A. Rupar, *Chem. Eur. J.*, 2017, **23**, 14670–14675.

5 T. L. Gilchrist, *J. Chem. Soc., Perkin Trans. 1*, 1999, 2849–2866.

6 R. C. D. Brown, *Angew. Chem., Int. Ed.*, 2005, **44**, 850–852.

7 X. L. Hou, H. Y. Cheung, T. Y. Hon, P. Lo Kwan, T. H. Lo, S. Y. Tong and H. N. C. Wong, *Tetrahedron*, 1998, **54**, 1955–2020.

8 D. M. X. Donnelly and M. J. Meegan, Furans and their Benzo Derivatives (iii) Synthesis and Applications in *Comprehensive Heterocyclic Chemistry*, eds. A. R. Katritzky and C. W. Rees, Pergamon, Oxford, 1984, pp. 657–712.

9 M. V. Roux, M. Temprado, P. Jiménez, Pérez-Parajón and R. Notario, *J. Phys. Chem. A.*, 2003, **107**, 11460–11467.

10 B. A. Keay and P. W. Dibble, Furans and their Benzo Derivatives: Application in *Comprehensive Heterocyclic Chemistry II*, eds. A. R. Katritzky, C. W. Rees and E. F. V Scriven, Pergamon, Oxford, 1996, pp. 395–436.

11 J. Liotier, V. M. Mwalukuku, S. Fauvel, A. J. Riquelme, J. A. Anta, P. Maldivi and R. Demadrille, *Solar RRL*, 2022, **6**, 2100929.

12 F. B. Ahmad, M. A. Kalam, Z. Zhang and H. H. Masjuki, *Energy Conv.Manag.: X*, 2022, **14**, 100222.

13 I. H. Hall, W. L. Williams, R. K. A. Jr. and M. Knowles, *Pharm. Res.*, 1985, **2**, 233–238.

14 Z. Sajadi, M. M. Abrishami, Paricher-Mohseni, J. M. Chapman and I. H. Hall, *J. Pharm. Sci.*, 1984, **73**, 266–267.

15 D. A. Winkler, M. Breedon, A. E. Hughes, F. R. Burden, A. S. Barnard, T. G. Harvey and I. Cole, *Green Chem.*, 2014, **16**, 3349–3357.

16 D. Daoud, T. Douadi, H. Hamani, S. Chafaa and M. Al-Noaimi, *Corros. Sci.*, 2015, **94**, 21–37.

17 C. Verma, E. E. Ebenso and M. A. Quraishi, Ionic Liquids as Green Corrosion Inhibitors for Industrial Metals and Alloys in *Green Chem.*, eds. Hosam El-din M. Saleh and Koller M., IntechOpen, London, 2018, pp. 103–132.

18 T. H. Pham, W.-H. Lee, G.-H. Son, T. T. Tran and J.-G. Kim, *Materials*, 2022, **15**, 6631.

19 H. Vaidyanathan and N. Hackerman, *Corros. Sci.*, 1917, **11**, 737-750.

20 E. Machnikova, K. H. Whitmire and N. Hackerman, *Electrochim. Acta*, 2008, **53**, 6024–6032.

21 K. F. Khaled, *J. Electrochem. Soc.*, 2010, **157**, C116–C124.

22 H. Bourzi, R. Oukhrib, B. el Ibrahimi, H. A. Oualid, Y. Abdellaoui, B. Balkard, S. el Issami, M. Hilali, L. Bazzi and C. Len, *Sustainability,* 2020, **12**, 3304

23 M. Forsyth, K. Wilson, T. Behrsing, C. Forsyth, G. B. Deacon and A. Phanasgoankar, *Corrosion*, 2002, **58**, 953–960.

24 L. H. J. Lajunen and G. R. Choppin, *Rev. Anal. Chem.*, 1989, **9**, 91–130.

25 H. Sitzmann, T. Dezember, O. Schmitt, F. Weber, G. Wolmershäuser and M. Ruck, *Z. Anorg Allg. Chem.*, 2000, **626**, 2241–2244.

26 D. P. Daniels, G. B. Deacon, D. Harakat, F. Jaroschik and P. C. Junk, *Dalton Trans.*, 2012, **41**, 267–277.

27 G. J. Moxey, A. J. Blake, W. Lewis and D. L. Kays, *Eur. J. Inorg. Chem.*, 2015, **2015**, 5892–5902.

28 R. P. Kelly, T. D. M. Bell, R. P. Cox, D. P. Daniels, G. B. Deacon, F. Jaroschik, P. C. Junk, X. F. Le Goff, G. Lemercier, A. Martinez, J. Wang and D. Werner, *Organometallics*, 2015, **34**, 5624–5636.

29 L. Hirneise, C. Maichle-Mössmer and R. Anwander, *Inorg Chem*, 2021, **60**, 18211–18224.

30 M. Salehisaki, N. E. Rad, G. B. Deacon, J. Wang, Z. Guo and P. C. Junk, *Inorg. Chim. Acta.*, 2022, **539**, 120997.

31 G. B. Deacon and R. J. Phillips, *Coord. Chem. Rev.*, 1980, **33**, 227–250.

32 A. S. R. Chesman., D. R. Turner, B. Moubaraki, K. S. Murray, G. B. Deacon and S. R. Batten, *Chem. Eur. J.*, 2009, **15**, 5203–5207.

33 A. S. R. Chesman, D. R. Turner, B. Moubaraki, K. S. Murray, G. B. Deacon and S. R. Batten, *Dalton Trans.*, 2012, **41**, 10903–10909.

34 B. Vallina, J. D. Rodriguez-Blanco, A. P. Brown, J. A. Blanco and L. G. Benning, *J. Nanopart. Res.,* 2013, **15**, 1-13.

35 G. B. Deacon, *Organomet. Chem. Rev., Sect. A*, 1970, **5**, 355.

36 G. B. Deacon, S. J. Faulks and G. N. Pain, *Adv. Organomet. Chem.*, 1986, **25**, 237–276.

37 R. D. Shannon, *Acta Crystallogr. A*, 1976, **32**, 751–767.

38 F. Blin, S. G. Leary, K. Wilson, G. B. Deacon, P. C. Junk and M. Forsyth, *J. Appl. Electrochem.*, 2004, **34**, 591–599.

39 V. P. Vithana, Z. Guo, G. B. Deacon, A. E. Somers and P. C. Junk, *New J. Chem.*, 2022, **46**, 19104–19111.

40 A. E. Somers, B. R. W. Hinton, C. de Bruin-Dickason, G. B. Deacon, P. C. Junk and M. Forsyth, *Corros. Sci.*, 2018, **139**, 430–437.

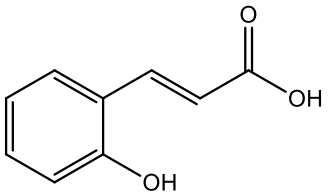
Chapter 4: Rare Earth 2-methyl-3-furoate Complexes: Effect of Steric Hindrance on Corrosion Inhibitor Properties.

4.1 Introduction

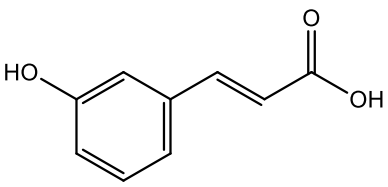
4.1.1 Impact of Structural Variations in Carboxylate Frameworks on Corrosion Mitigation Activity

The development of corrosion inhibitors based on carboxylate frameworks has demonstrated that subtle changes in structure can result in significant alterations in their ability to protect mild steel surfaces. The incorporation of O–CH_3, NO_2, CH_3, COOH or OH substituent groups into the organic component has resulted some of the best inhibition performance documented thus far.[1,2] Previous research has indicated that the inhibition efficacy of RE 4-hydroxy cinnamate compounds has been notably enhanced in comparison to their unsubstituted counterparts, attributed to the presence of the functional group at the *para* position.[2–4]

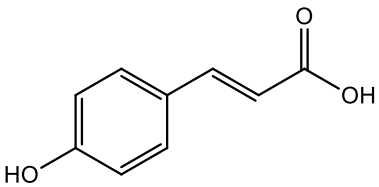
Following the initial findings on the corrosion-inhibiting properties of compounds closely related to La(4hocin)$_3$ on mild steel, Seter et al.[5] later in 2015 reported on the influence of the orientation of the hydroxy substituent on the hydroxycinnamate anion, which resulted in significant changes in corrosion inhibition activity. The subsequent introduction of *ortho* and *meta* substitutions on the 2- and 3-hydroxycinnamate resulted in changes in steric effects. These property alterations then affected the bonding of the carboxylate to the rare earth and the steel surface, as well as the formation of protective films.



2-hydroxycinnamic acid



3-hydroxycinnamic acid



4-hydroxycinnamic acid

The *para*-substituted hydroxyl group from the 4-hydroxycinnamate ligand can form intermolecular interactions through hydrogen bonding with nearby inhibitor molecules, effectively increasing the thickness of the protective film. In the case of La(3hocin)$_3$, film formation could be very similar, as the hydroxyl group is capable of promoting further interactions. However, for the La(2hocin)$_3$ inhibitor, the *ortho*-substitution causes the hydroxyl groups to be shielded by the phenyl ring, sterically

hindering further interactions and therefore eliminating the possibility of forming a multilayer surface film. Consequently, this leads to diminished inhibition efficiencies compared to one of the top-performing compounds, La(4hocin)$_3$, while lanthanum 3-hydroxycinnamate offers an inhibition level between the two.

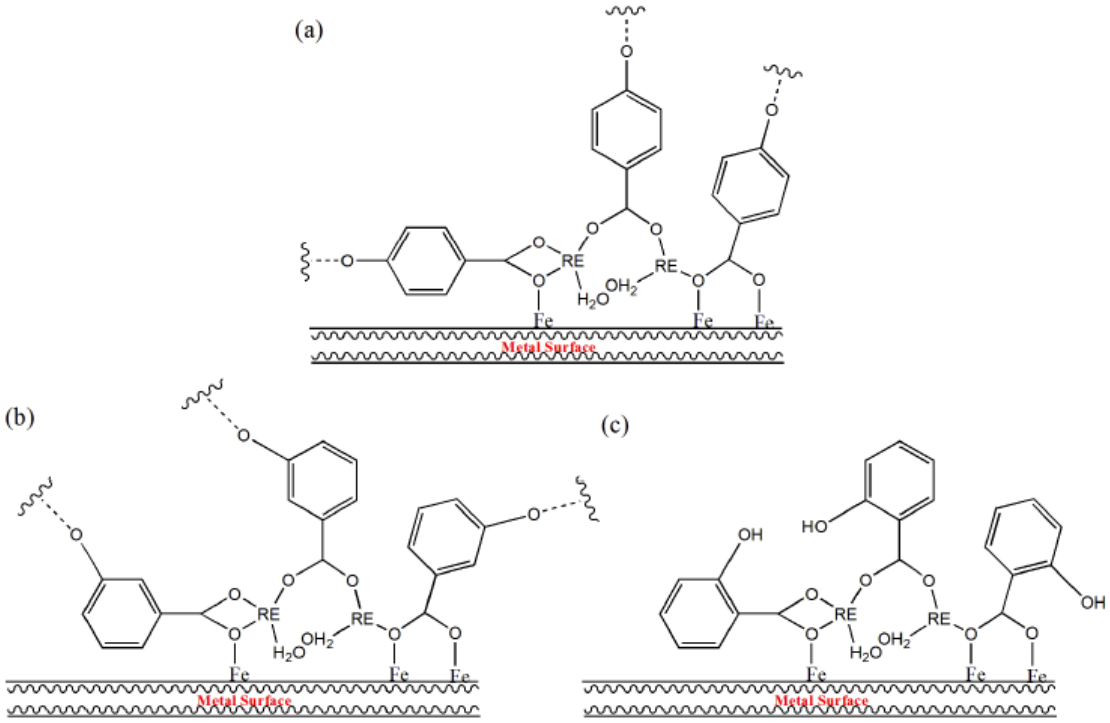
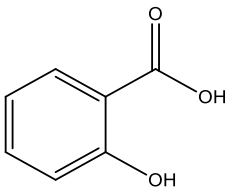


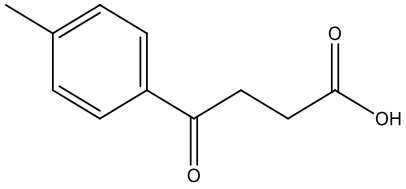
Figure 4.1: A schematic proposed mechanism of action for protecting a steel substrate through the use of the inhibitor (a) RE(4hocin)$_3$ where RE = La, Ce and Pr, (b) La(3hocin)$_3$ and (c) La(2hocin)$_3$.[5]

For higher-level corrosion inhibition, the organic anion should form a stable bond with the underlying metal surface. The presence of a secondary functional group also plays an important role in determining whether high corrosion inhibition could be achieved. In one of the initial studies conducted by Forsyth et al.[1] a comparison was made between salicylate-based inhibitors and glycolate and anthranilate compounds. It was demonstrated that cerium salicylate outperformed the others, suggesting that the presence of both COO- and OH- groups on the aromatic organic inhibitor has a beneficial effect on corrosion resistance.



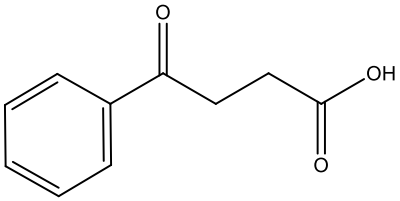
Salicylic acid

Another such example is found in one of the well-established corrosion inhibitors used commercially for water-borne polymer coatings on iron, produced by Ciba Specialty Chemicals: 3-(4-methylbenzoyl)propanoic acid (mbpH).

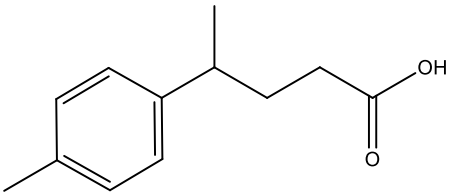


3-(4-Methylbenzoyl)propanoic acid

Testing of this compound and other related derivatives (1) and (2) has demonstrated that the presence of a carbonyl group, along with a methyl substituent on the *para* position significantly enhances their effectiveness as corrosion inhibitors in protective coatings. Hydrogen bonding interactions between the carbonyl group and hydroxyl groups on the surface have been reported to form a significantly more stable complex.[6–8]

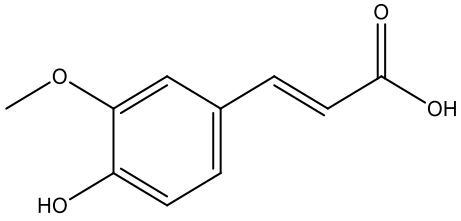


(1)



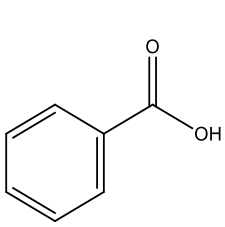
(2)

The significant influence of even minor structural variation of the carboxylate frameworks on corrosion mitigation activity is further evident in the greater effectiveness of lanthanoid 4-hydroxy-3-methoxycinnamic acid (ferulic acid) with a methoxy group substitution, in comparison to analogous 4-hydroxycinnamate compounds.[9]

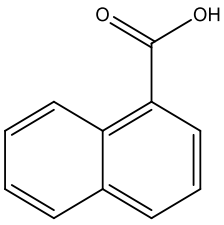


Ferulic acid

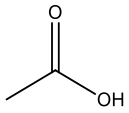
In this study, another three carboxylate ligands namely benzoic acid (BenzH), 1-naphthoic acid (1-NaphH), and acetic acid (AcH) were also examined to evaluate how the absence of crucial structural subunits affects inhibition activity. All three ligands exhibited poor inhibition efficiencies.[9]



Benzoic acid

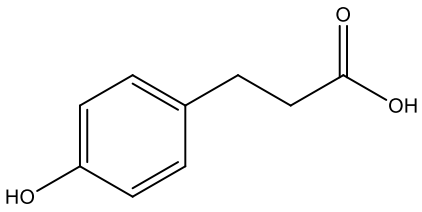


1-Naphthoic acid



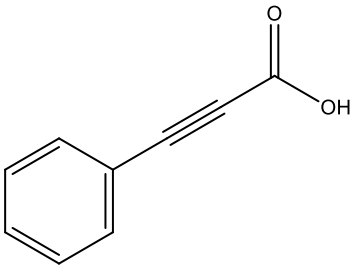
Acetic acid

The incorporation of additional unsaturation or donor capacity seems to be beneficial. Deacon et al.[10] (2015) highlighted the significance of the –CH=CH– functionality between the carboxylic group and the aromatic moiety by demonstrating the markedly negative anti-corrosion behaviour observed with the saturated analogue of 4-hydroxycinnamates, 3-(4-hydroxylphenyl)propionate (4hpp).

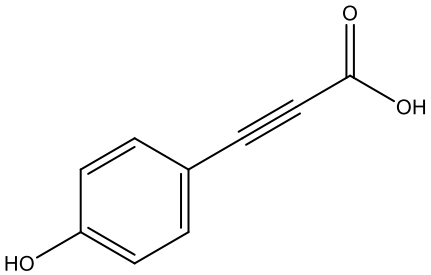


3-(4-hydroxylphenyl)propionic acid

In a separate study conducted in 2020, the alkyne analogues of cinnamate and 4-hydroxy cinnamates, namely 3-phenylpropiolate (PP) and 3-(4-hydroxyphenyl)propiolate (HOpp), were investigated. However, the results indicated inferior corrosion protection at the same lanthanoid concentrations.[9]



3-Phenylpropiolic acid



3-(4-Hydroxyphenyl)propiolic acid

4.1.2 Current Study

Over the past two decades, the combination of the properties of rare earth ions and aromatic carboxylates has given rise to the development of highly effective dual-function rare earth carboxylate corrosion inhibitors. The analysis of emerging trends in the inhibiting action of various carboxylate anions alone suggests that factors such as additional unsaturation, aromaticity, functional groups, the presence of donor heteroatoms, molecule size, donor capacity, and electron charge density play a significant role in achieving higher levels of inhibition.[8,11–15] Such observations support an inhibition model whereby a carboxylatolanthanoid species binds to a hydroxidoiron(III) group on a corroding surface through a donor group-hydroxide interaction.[11,12,16]

To examine this concept further, we have utilised our recent discovery of the high inhibitor activity of lanthanoid 3-furoate complexes.[15] Accordingly, we have introduced a 2-methyl group into the 3-furoate ion and examined the effect of its steric inhibition on carboxylate coordination and capacity for corrosion inhibition. Six lanthanoid complexes of 2-methyl-3-furoate have been prepared, their structures examined by X-ray crystallography, X-ray powder diffraction, and thermogravimetric analysis, and corrosion testing outcomes based on weight loss measurements determined.

All the work in this chapter resulted in a publication in the journal *European Journal of Inorganic Chemistry* (see reprint in Appendix Two).

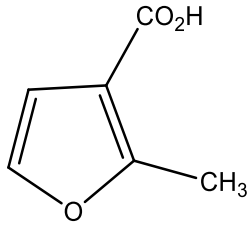
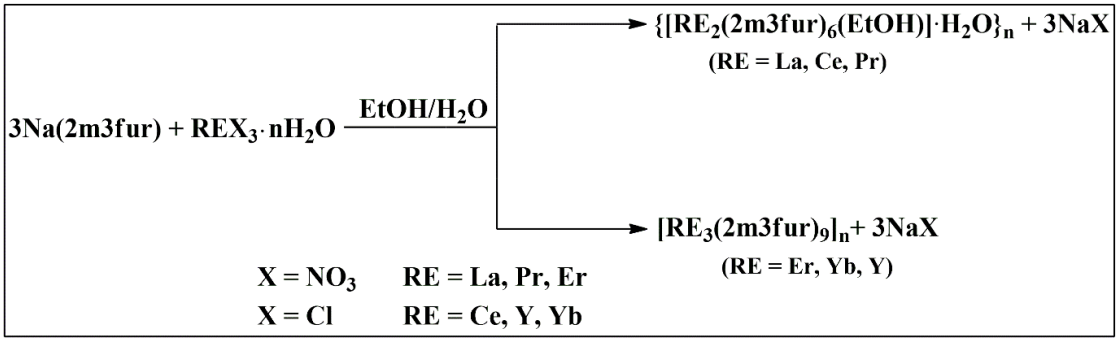


Chart 4.1. Structure of 2-methyl-3-furoic acid (2m3furH).

4.2 Results and Discussion

4.2.1 Synthesis and Characterisation

The complexes $\{[RE_2(2m3fur)_6(EtOH)]\cdot H_2O\}_n$ (RE = La **(4.1)**, Ce **(4.2)**, Pr **(4.3)**) and $[RE_3(2m3fur)_9]_n$ (RE = Y **(4.4)**, Er **(4.5)**, Yb **(4.6)**) were prepared in moderate to good isolated yields by using metathesis reactions between sodium 2-methyl-3-furoate and the corresponding RE salts (at a mole ratio of 3:1) as shown in Scheme 4.1.



Scheme 4.1: The synthesis of RE 2-methyl-3-furoate complexes.

The compositions of all these complexes were determined through a combination of X-ray crystallography, elemental analysis and TGA. Growing crystals for X-ray diffraction proved to be particularly challenging when using the 2-methyl-3-furoate ligand. However, in this study, we successfully obtained single crystals suitable for X-ray crystallography for **4.3, 4.4, 4.5** and **4.6**. In each instance, the bulk products were isolated as powders.

All attempts to obtain crystals of **4.1** were unsuccessful. Nevertheless, X-ray powder diffractograms suggest it is isomorphous with **4.3** (Figure 4.2). Data for **4.2** were incomplete, resulting in the acquisition of only the unit cell. However, the unit cell parameters and the powder diffractogram of this complex indicate that it is isomorphous with **4.3**.

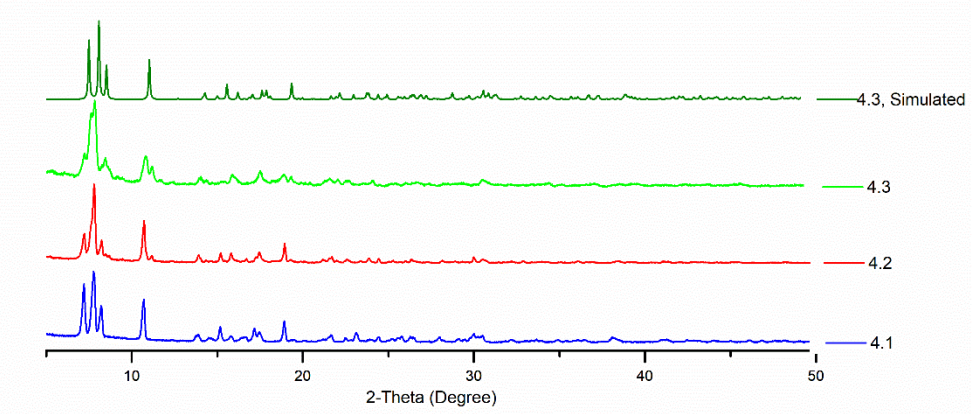


Figure 4.2: PXRD diffractograms of the $[RE_2(2m3fur)_6(EtOH)]\cdot H_2O$ (RE = La, Ce, Pr) series compared to the simulated pattern of $[Pr_2(2m3fur)_6(EtOH)]\cdot H_2O$ **(4.3)**.

TGA analyses of compound **4.1** and **4.2** yielded results consistent with the crystal composition of $\{[RE_2(2m3fur)_6(EtOH)]\cdot H_2O\}_n$, indicating the simultaneous loss of one water molecule and one ethanol molecule in a single step. The presence of a broad band in the range 3200-3550 cm^{-1} in the IR spectra of **4.1** and **4.2** is consistent with the

presence of water and ethanol (O–H stretching) in the compounds. The elemental analysis data indicate that complexes **4.1** and **4.2** experienced ethanol loss from their single crystal compositions under the microanalysis drying conditions. As for compound **4.3**, elemental analysis, TGA and IR indicate that, during the drying process, both coordinated ethanol and lattice water were removed from the crystals (Figure 4.3 and 4.4).

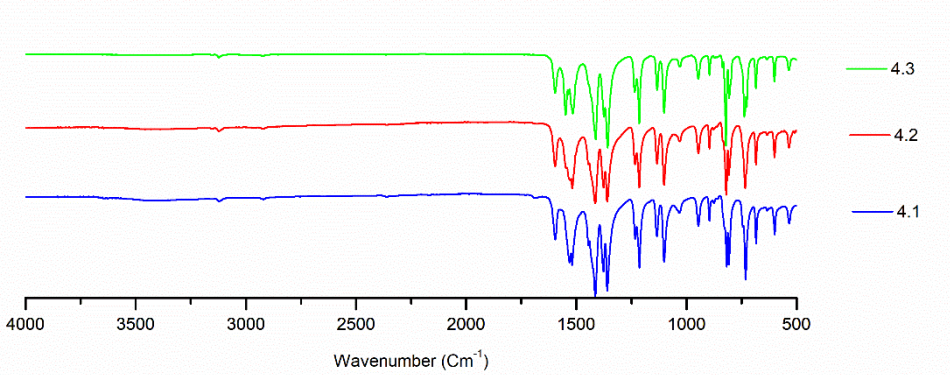


Figure 4.3: IR spectra of the $[RE_2(2m3fur)_6(EtOH)]\cdot H_2O$ (RE = La, Ce, Pr) series.

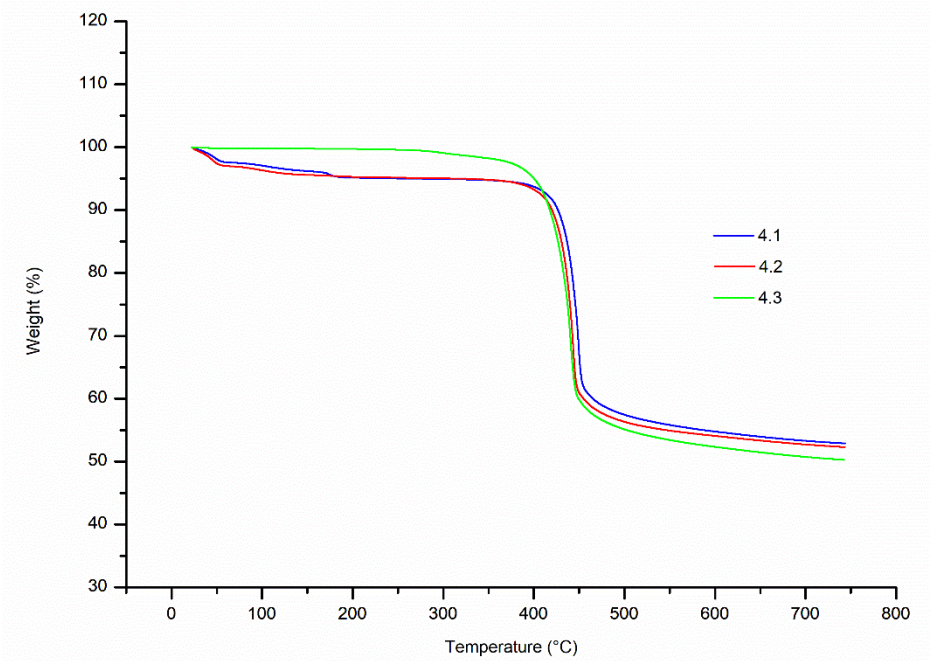


Figure 4.4: TGA thermograms of the $[RE_2(2m3fur)_6(EtOH)]\cdot H_2O$ (RE = La, Ce, Pr) series.

For compounds **4.4**, **4.5**, and **4.6**, the powder XRD analyses closely resembled the patterns generated from the single-crystal data (Figure 4.5).

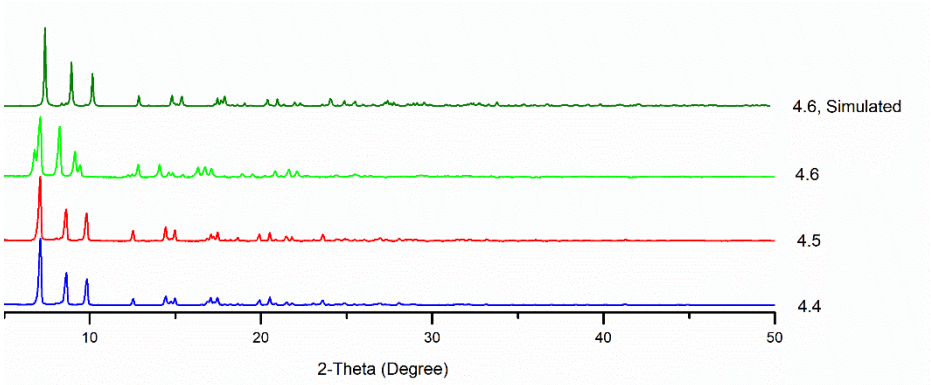


Figure 4.5: PXRD diffractograms of the $[RE_3(2m3fur)_9]_n$ (RE = Y, Er, Yb) series compared to the simulated pattern of $[Yb_3(2m3fur)_9]_n$ **(4.6).**

Consistent with the single-crystal compositions of compounds **4.4** and **4.5**, their thermograms and IR spectra do not exhibit any weight reduction attributable to the removal of coordinated or lattice solvent molecules (Figure 4.6 and Figure 4.7). Conversely, **4.6** displayed hygroscopic properties, evident from the thermal analysis. Thus, TGA data for **4.6** revealed additional water content, with the loss of four water molecules occurring in a single step below 150 °C (Figure 4.7). Nevertheless, the IR spectrum, recorded after drying to a constant weight, did not exhibit a broad band in the range 3200-3550 cm^{-1} (Figure 4.6), and the elemental analyses of **4.4-4.6** were consistent with anhydrous compounds.

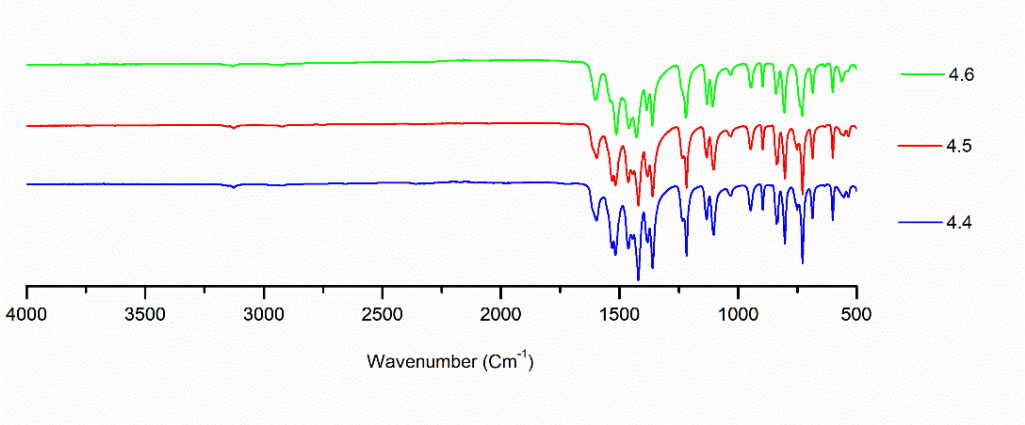


Figure 4.6: IR spectra of the $[RE_3(2m3fur)_9]_n$ (RE = Y, Er, Yb) series.

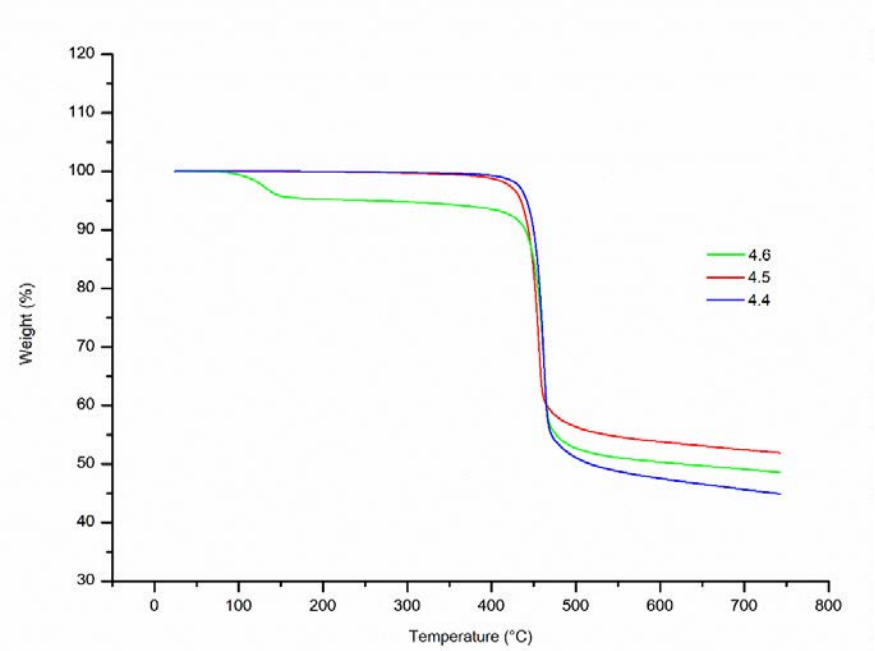


Figure 4.7: TGA thermograms of the $[RE_3(2m3fur)_9]_n$ (RE = Y, Er, Yb) series.

The infrared spectra of all complexes exhibited distinctive peaks within the range of 1560-1360 cm^{-1} corresponding to carboxylate COO^- stretching bands. The IR spectra of the compounds exhibit strong similarities in major bands within each isostructural series. Therefore, we have listed the significant IR bands for only one compound from each series, specifically **4.2** and **4.5**, in Table 4.1.

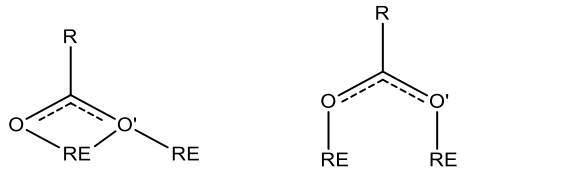
Table 4.1: Selected infrared bands (cm^{-1}) of the RE^{III} 2-methyl-3-furoate complexes.

Compound	$\nu(OH)_{water}$	$\nu_{as}(CO_2^-)$	$\nu_s(CO_2^-)$	$\Delta\nu = (\nu_{as}-\nu_s)avg$	$\delta(CO_2)$
$\{[Ce_2(2m3fur)_6(EtOH)]\cdot H_2O\}_n$ **(4.2)**	3458	1518	1377,1360	149.5	684
$[Er_3(2m3fur)_9]_n$ **(4.5)**	-	1531,1517	1381,1360	153.5	686

4.2.2 X-ray Crystal Structures

There are only two distinct carboxylate ligand binding modes in the structures, namely bridging tridentate μ-1κ(O,O′):2κ(O′) and *syn-syn* bridging bidentate μ-1κ(O):2κ(O′) (Figure 4.8). In comparison, analogous 3fur complexes display four unique binding modes: *syn-syn* μ-1κ(O):2κ(O′), *syn-anti* μ-1κ(O):2κ(O′), μ_3-1κ(O):2κ(O,O′):3κ(O′) and μ_3-1κ(O):2κ(O′):3κ(O′).[15]

Due to poor quality of crystals of **4.5** (R_{int} 19.96%), compound **4.5** is presented for connectivity purposes only. However, **4.5** is isomorphous with **4.4** and **4.6**.



(i) μ-1κ(O,O′):2κ(O′) (ii) *syn-syn* μ-1κ(O):2κ(O′)

Figure 4.8: Coordination forms of 2-methyl-3-furoate ions in the rare earth complexes presented here.

4.2.1.1 1D Polymeric Chains of $\{[RE_2(2m3fur)_6(EtOH)]\cdot H_2O\}_n$ Complexes (RE = La, Ce, Pr)

The molecular structure of $\{[Pr_2(2m3fur)_6(EtOH)]\cdot H_2O\}_n$ **(4.3)** is depicted in Figure 4.9 and serves as a representative of the isomorphous series of 1D polymeric complexes, $\{[RE_2(2m3fur)_6(EtOH)]\cdot H_2O\}_n$ (RE = La **(4.1)**, Ce **(4.2)** and Pr **(4.3)**). The structure of $\{[Pr_2(2m3fur)_6(EtOH)]\cdot H_2O\}_n$ is binuclear, crystallizing in the monoclinic $P2_1/c$ space group, containing two distinct Pr^{+3} metal centres within the asymmetric unit. There is only one carboxylate binding mode, resulting in a distorted bicapped square antiprism (SAP)-type deca coordination for Pr1 and a distorted tricapped trigonal prism-type nine coordination for Pr2 as shown in Figure 4.10.

The coordination sphere around the Pr1 metal centre comprises eight chelating oxygen atoms from four μ-1κ(O,O′):2κ(O′) carboxylates (O4,5), (O7,8), (O13#1,14#1), (O16#1,17#1) and two bridging oxygen atoms from μ-1κ(O):2κ(O,O′) carboxylates (O1, O10). The Pr2 metal centre is nine coordinate, featuring four chelating oxygen atoms from two μ-1κ(O,O′):2κ(O′) carboxylates (O10,11), (O1#2,2#2), four bridging oxygen atoms from μ-1κ(O):2κ(O,O′) carboxylates (O5, O7, O13, O16), and one oxygen atom (O19) from the ligated ethanol.

The two metal centres are connected by three ligands (through O5, O7, O10), forming a 1D polymeric chain and this chain propagates in an alternating sequence of Pr2#1…Pr1…Pr2…Pr1#2. The metal-metal distance between Pr1….Pr2 and Pr2…Pr1#2 are 3.8477(8) Å and 3.8433(8) Å respectively, with Pr2#1-Pr1-Pr2 and Pr1-

Pr2-Pr1#2 angles of 177.360(9)°. The angles formed at the bridging oxygen atoms are 95.78(8)° (Pr1-O5-Pr2), 99.73(9)° (Pr1-O7-Pr2) and 95.70(3)° (Pr1-O10-Pr2) (Figure 4.8).

Additionally, the lattice water oxygen atom (O20) forms a hydrogen bond with the oxygen atom (O19) of the ligated ethanol molecule within the asymmetric unit. The experimentally observed hydrogen bonding interactions are listed in Table 4.2. Selected bond lengths and bond angles of **4.3** are provided in Table 4.3 and 4.4.

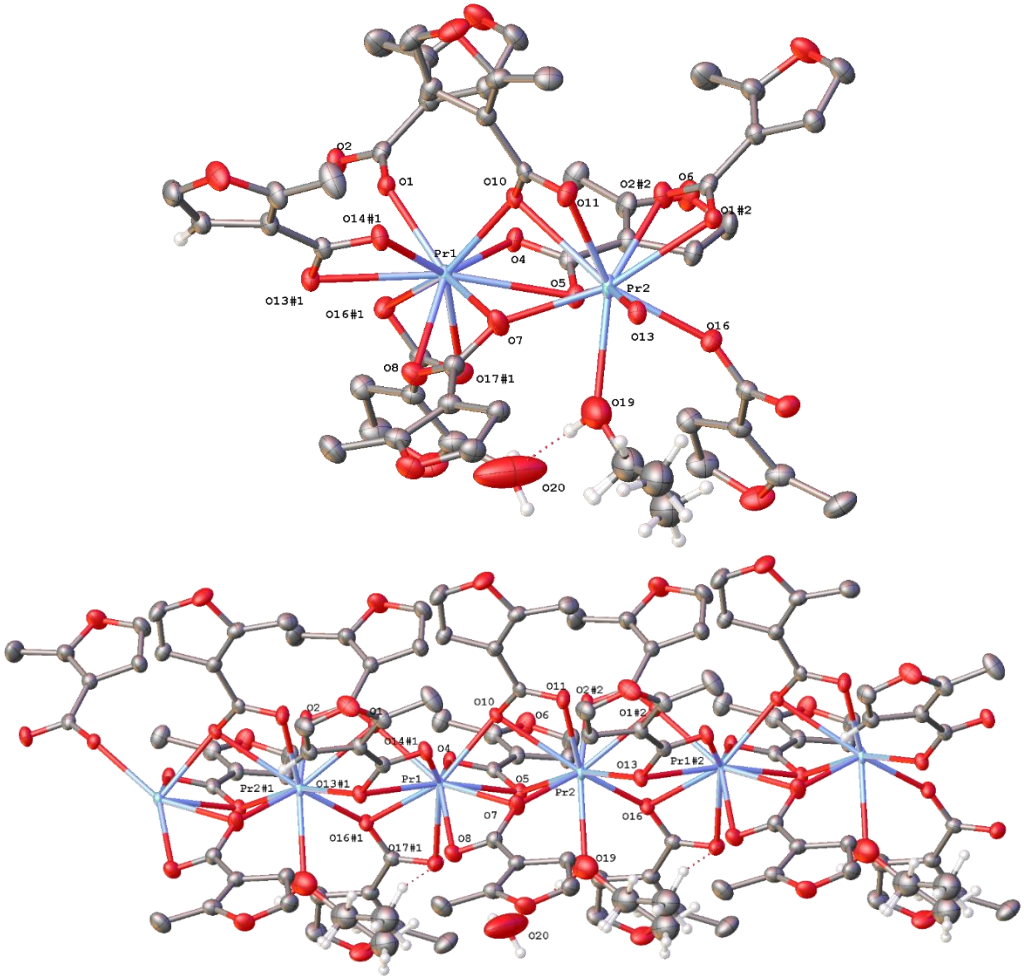


Figure 4.9: **(a)** The immediate coordination environment around Pr metal atoms in $\{[Pr_2(2m3fur)_6(EtOH)]\cdot H_2O\}_n$ **(4.3)**; (**b**) 1D polymeric chain of **4.3** generated from single-crystal XRD data. (representative of **4.1, 4.2**).Carbon atoms are shown in grey. Thermal ellipsoids are drawn at the 50% probability level. Selected bond lengths (Å) and angles (°) **4.3** Pr1-O1 2.401(2), Pr1-O4 2.456(3), Pr1-O5 2.779(3), Pr1-O7 2.603(3), Pr1-O8 2.529(3), Pr1-O10 2.411(2), Pr1-O13#1 2.830(3), Pr1-O14#1 2.464(3), Pr1-O16#1 2.604(2), Pr1-O17#1 2.558(3), Pr2-O5 2.396(3), Pr2-O7 2.428(3), Pr2-O10 2.768(2), Pr2-O11 2.434(3), Pr2-O13 2.391(3), Pr2-O16 2.436(3), Pr2-O19 2.619(4), Pr2-O1#2

2.716(2), Pr2-O2#2 2.451(3), Pr1….Pr2 3.8477(8), Pr2…Pr1#2 3.8433(8), Pr2#1-Pr1-Pr2 177.360(9), Pr1-Pr2-Pr1#2 177.360(9), Pr1-O5-Pr2 95.78(8), Pr1-O7-Pr2 99.73(9), Pr1-O10-Pr2 95.70(3), Symmetry Codes: $^{\#1}$1+X,+Y,+Z; $^{\#2}$ -1+X,+Y,+Z.

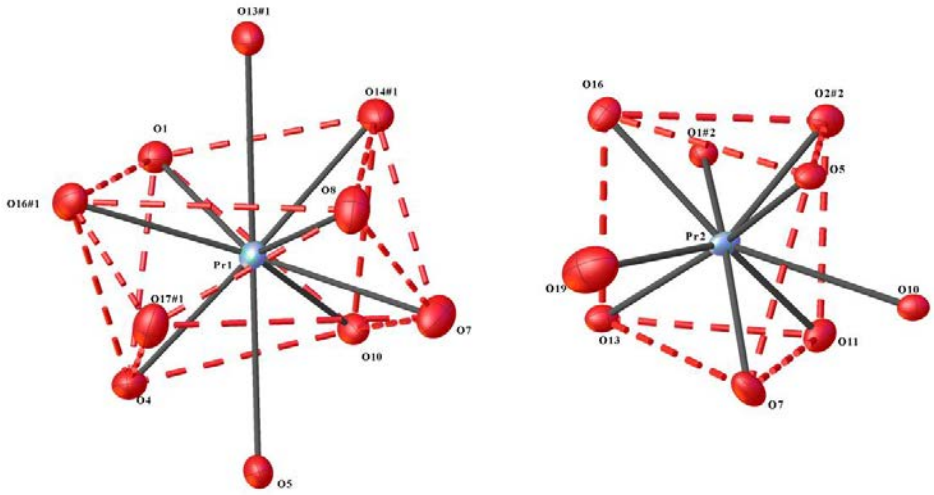


Figure 4.10: Orientation of the bonding oxygen atoms around Pr1 and Pr2 metal centres of **4.3** showing their overall geometries**.** Except for those directly surrounding the metal centres, other non-metal atoms are omitted for clarity. Symmetry equivalents used: $^{\#1}$1+X,+Y,+Z; $^{\#2}$ -1+X,+Y,+Z. The red dashed lines (----) represent the distorted planes formed by the oxygen atoms.

Table 4.2: Hydrogen bonds for $[Pr_2(2m3fur)_6(EtOH)]\cdot H_2O$ **4.3** [d/Å and </°].

D-H…A	**d(D-H)**	**d(H…A)**	**d(D…A)**	**<(DHA)**
O19-H19…O20	0.858(9)	1.880(13)	2.736(8)	176(6)

Table 4.3: Selected bond lengths and Pr…Pr distances (Å) for $[Pr_2(2m3fur)_6(EtOH)]\cdot H_2O$ **4.3**.

	Pr1		**Pr2**
Pr2	3.8477(8)	Pr1#2	3.8433(8)
O1	2.401(2)	O5	2.396(3)
O4	2.456(3)	O7	2.428(3)
O5	2.779(3)	O10	2.768(2)
O7	2.603(3)	O11	2.434(3)
O8	2.529(3)	O13	2.391(3)
O10	2.411(2)	O16	2.436(3)
O13#1	2.830(3)	O19	2.619(4)
O14#1	2.464(3)	O1#2	2.716(2)

O16#1	2.604(2)	O2#2	2.451(3)
O17#1	2.558(3)		

Table 4.4: Selected bond angles (°) for $[Pr_2(2m3fur)_6(EtOH)]\cdot H_2O$ **4.3**.

Pr2#1-Pr1-Pr2	177.360(9)
Pr1-O5-Pr2	95.78(8)
Pr1-O7-Pr2	99.73(9)
Pr1-O10-Pr2	95.70(3)

At first sight, the higher coordination numbers (10, 9) in **4.1-4.3** than in RE 3-furoate (3fur) complexes discussed in Chapter 3, $[RE(3fur)_3(H_2O)_2]_n$ (RE = La-Ho, Y), which are eight coordinate, is counter intuitive given the greater bulk of 2m3fur. However, the higher coordination numbers are associated with longer RE-O bonds relieving strain about the metal centre (Table 4.5). The simpler carboxylate coordination in **4.1-4.3** than in the 3fur analogues may be attributable to reduced access to one of the carboxylate oxygens owing the bulk of the Me group. Any electronic effect of the methyl group is outweighed by the steric effect as shown by the considerable simplification of the carboxylate coordination compared with that in lanthanoid 3-furoates.

Table 4.5: Average RE-O bond length comparison of Pr 3-furoate and Pr 2-methyl-3-furoate complexes.

	<RE1-O>	**<RE2-O>**
$[Pr(3fur)_3(H_2O)_2]_n$[15]	2.43	
$\{[Pr_2(2m3fur)_6(EtOH)]\cdot H_2O\}_n$	2.56	2.53

4.2.2.2 1D Polymeric Chains of $[RE_3(2m3fur)_9]_n$ Complexes (RE = Y, Er, Yb)

The asymmetric unit of the isostructural series of complexes $[RE_3(2m3fur)_9]_n$ (RE = Y **(4.4)**, Er **(4.5)** and Yb **(4.6)**) comprises three unique RE metal centres, forming a 1D polymeric chain. They crystallize in the $P2_1/c$ space group. A representative structure, $[Yb_3(2m3fur)_9]_n$ is shown in Figure 4.11.

Yb1 and Yb3 are both eight-coordinate and Yb2 is seven coordinate. The arrangement around the Yb1 metal centre is distorted square antiprismatic, whereas a distorted dodecahedral arrangement can be seen around Yb3 (Figure 4.12). Each Yb ion

is coordinated by chelating oxygen atoms from two μ-1κ(O,O′):2κ(O′) carboxylates. Specifically, Yb1 is bound by (O15,16) and (O22#2,23#2), whereas Yb3 is coordinated by (O20,21) and (O11#1,12#1). In the case of Yb1, three additional coordination sites are occupied by carboxylate oxygen atoms (O4, O5, O14) originating from μ-1κ(O):2κ(O′) bridging ligands. Conversely, Yb3 possesses only two such bridging oxygen atoms (O3#1,25) surrounding it. The final coordination oxygen atom (O12) of Yb1 is derived from a μ-1κ(O):2κ(O,O′) bridge, while two of these bridging oxygen atoms (O18,22) complete the coordination sphere around Yb3.

The stereochemistry of the seven coordinated Yb2 is pentagonal bipyramidal (Figure 4.12), and it is coordinated by two oxygen atoms (O17,18) from a μ-1κ(O,O′):2κ(O′) chelating carboxylate, two oxygen atoms (O16, O20) from μ-1κ(O):2κ(O,O′) bridging carboxylate ligands, and three bridging oxygen atoms (O7, O19, O24) from μ-1κ(O):2κ(O′) carboxylate groups.

The one-dimensional polymeric chain of **4.6** exhibits a slight wave, with angles of 157.006(12)°, 160.657(10)°, and 148.256(15)° between Yb1-Yb2-Yb3, Yb2-Yb3-Yb1#1 and Yb#2-Yb1-Yb2, respectively.

Table 4.6 presents the list of Yb-O bond lengths observed in the crystal structure. The overall average Yb-O bond distance is 2.32 Å, with Yb3-O12#1 being the longest and Yb2-O7 the shortest. The average bond lengths around each Yb metal centre are as follows: Yb1 (2.335(1) Å), Yb2 (2.292(1) Å), Yb3 (2.338(1) Å). There is an increase of approximately 0.04 Å in the average Yb-O bond length at Yb1 and Yb3 metal centres compared to the Yb2 metal centre, a result which correlates with the increasing coordination number of Yb^{3+}.

The separation between each pair of Yb metal centres is as follows: Yb1…Yb2 (4.1275(9) Å), Yb2…Yb3 (3.8100(9) Å) and Yb3…Yb1#1 (3.7230(8) Å). Yb1…Yb2 is bridged by three oxygen atoms from one μ-1κ(O):2κ(O,O′) bridge and two μ-1κ(O):2κ(O′) bridges, while Yb2…Yb3 and Yb3…Yb1#1 are each bridged by oxygen atoms from two μ-1κ(O):2κ(O,O′) bridges and one μ-1κ(O):2κ(O′) bridge. The impact of the lanthanoid contraction [17] is evident in the decreased RE-O bond distances within the 1D chains of Y^{3+}, Er^{3+} and Yb^{3+} complexes (Table 4.6).

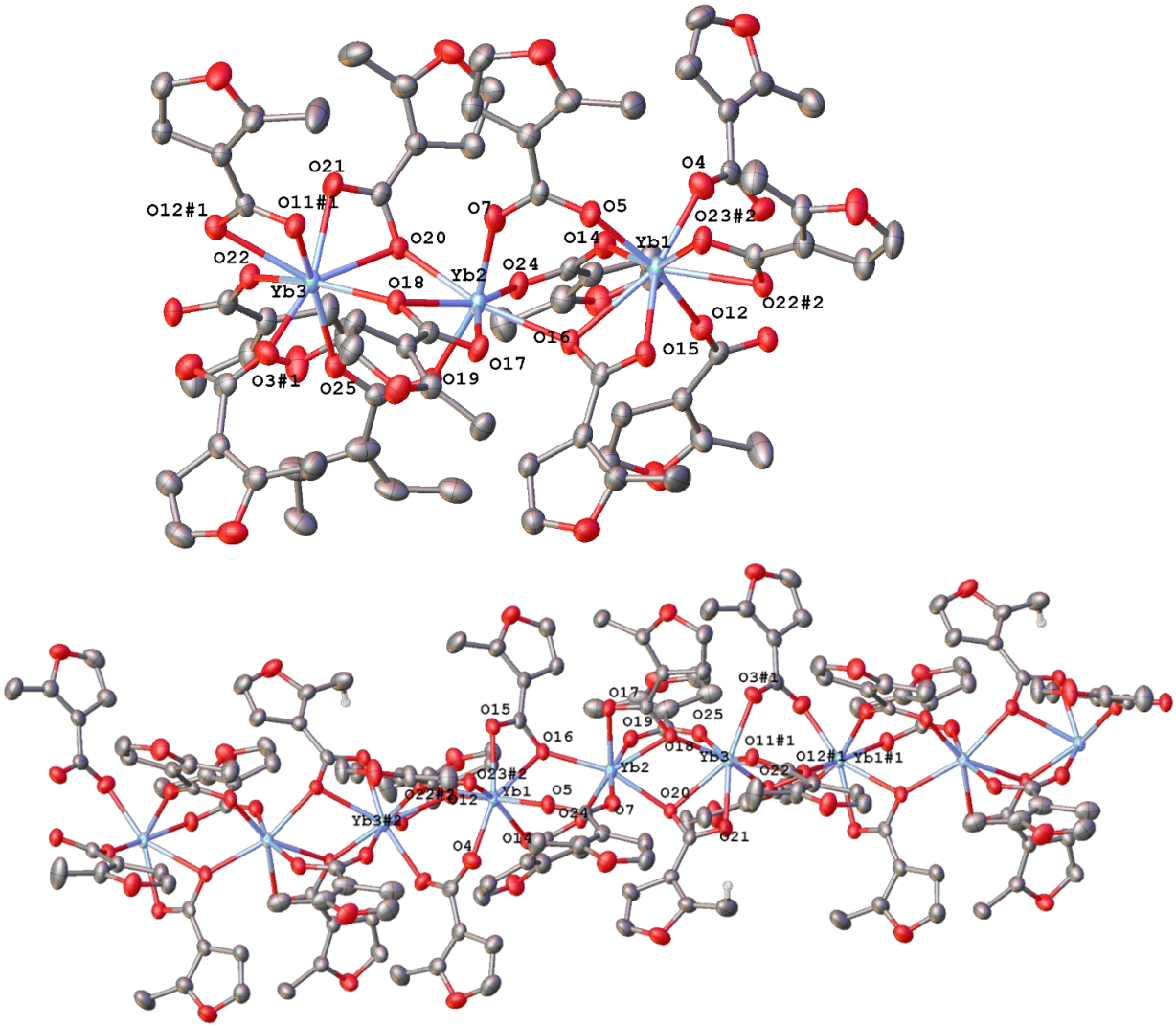


Figure 4.11: **(a)** The immediate coordination environment around Yb metal atoms in $RE_3(2m3fur)_9]_n$ **(4.6);** (**b**) 1D polymeric chain of **4.6** generated from single-crystal XRD data. (representative of **4.4, 4.5**). Carbon atoms are shown in grey. Thermal ellipsoids are drawn at the 50% probability level. Selected bond lengths (Å) and angles (°) (Data for all three compounds are in Tables 4.6 and Table 4.7).**4.6** Yb1-O4 2.228(3), Yb1-O5 2.210(3), Yb1-O12 2.270(3), Yb1-O14 2.230(3), Yb1-O15 2.314(3), Yb1-O16 2.553(3), Yb1-O22#2 2.519(3), Yb1-O23#2 2.359(3), Yb2-O7 2.192(3), Yb2-O16 2.287(3), Yb2-O17 2.328(3), Yb2-O18 2.474(3), Yb2-O19 2.213(3), Yb2-O20 2.318(3), Yb2-O24 2.231(3), Yb3-O18 2.246(3), Yb3-O20 2.516(3) Yb3-O21 2.312(3), Yb3-O22 2.234(3), Yb3-O25 2.252(3), Yb3-O3#1 2.250(3) Yb3-O3#1 2.250(3), Yb3-O11#1 2.307(3), Yb3-O12#1 2.583(3), Yb1…Yb2 4.1275(9), Yb2…Yb3 3.8100(9), Yb3…Yb1#1 3.7230(8). Yb1-Yb2-Yb3 157.006(12), Yb2-Yb3-Yb1#1 160.657(10), Yb#2-Yb1-Yb2 148.256(15) Symmetry Codes: $^{\#1}$1-X,1/2+Y,1/2-Z; $^{\#2}$1-X,-1/2+Y,1/2-Z.

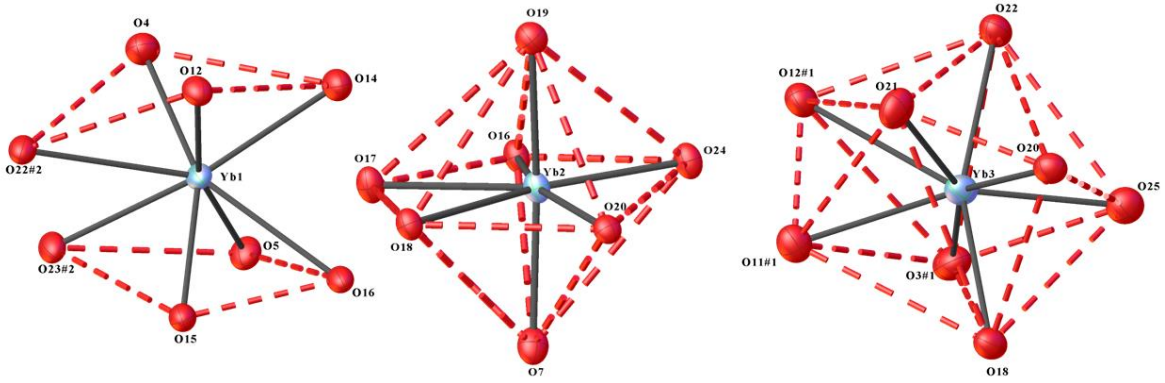


Figure 4.12: Distorted square antiprismatic, pentagonal bipyramidal, and distorted dodecahedral geometries around the Yb1, Yb2, and Yb3 metal centres of **4.6**, respectively, For clarity, only the atoms directly surrounding the metal centres are shown, while other non-metal atoms are omitted. Symmetry equivalents used: $^{\#1}$1-X,1/2+Y,1/2-Z; $^{\#2}$1-X,-1/2+Y,1/2-Z.. The red dashed lines (----) represent the planes formed by the oxygen atoms.

Table 4.6: Selected bond lengths and RE…RE distances (Å) for the isostructural $[RE_3(2m3fur)_9]_n$ complexes (**RE** = Y, Er, Yb) complexes (**4.5** for connectivity only).

	Y1 **(4.4)**	Er1 **(4.5)**	Yb1 **(4.6)**		Y2 **(4.4)**	Er2 **(4.5)**	Yb2 **(4.6)**		Y3 **(4.4)**	Er3 **(4.5)**	Yb3 **(4.6)**
RE2	4.1375(10)	4.10	4.1275(9)	RE3	3.8413(10)	3.82	3.8100(9)	RE1#1	3.731(1)	3.72	3.7230(8)
O4	2.243(4)	2.23	2.228(3)	O7	2.217(4)	2.26	2.192(3)	O18	2.273(4)	2.25	2.246(3)
O5	2.243(4)	2.24	2.210(3)	O16	2.319(4)	2.29	2.287(3)	O20	2.532(4)	2.52	2.516(3)
O12	2.308(4)	2.29	2.270(3)	O17	2.363(4)	2.34	2.328(3)	O21	2.357(4)	2.36	2.312(3)
O14	2.253(14)	2.23	2.230(3)	O18	2.491(4)	2.49	2.474(3)	O22	2.260(4)	2.26	2.234(3)
O15	2.358(4)	2.34	2.314(3)	O19	2.254(4)	2.24	2.213(3)	O25	2.277(4)	2.28	2.252(3)
O16	2.561(4)	2.56	2.553(3)	O20	2.335(4)	2.32	2.318(3)	O3#1	2.286(4)	2.27	2.250(3)
O22#2	2.535(4)	2.53	2.519(3)	O24	2.258(4)	2.23	2.231(3)	O11#1	2.349(4)	2.35	2.307(3)
O23#2	2.390(4)	2.37	2.359(3)					O12#1	2.556(4)	2.56	2.583(3)

Table 4.7: Selected bond angles (°) for the isostructural $[RE_3(2m3fur)_9]_n$ complexes (**4.5** for connectivity only).

	4.4	**4.5**	**4.6**
RE1-RE2-RE3	156.93(2)	157	157.006(12)
RE2-RE3-RE1#1	159.95(2)	160	160.657(10)
RE#2-RE1-RE2	148.98(2)	149	148.256(15)

As two of the Y atoms of **4.4** have the same coordination number as in $[Y(3fur)_3(H_2O)_2]_n$ in Chapter 3, it is possible to compare <Y-O> values (Table 4.8), and

they suggest a slight lengthening in **4.4,** consistent with a steric effect by the methyl group. The steric effect of the methyl group prevails over its electronic effect, as evidenced by the significant simplification of the carboxylate coordination compared to that in lanthanoid 3-furoates, and by Y-O bond lengthening in **4.4**.

Table 4.8: Average RE-O bond length comparison of Y 3-furoate and Y 2-methyl-3-furoate complexes.

	<RE1-O>	**<RE2-O>**	**<RE3-O>**
$[Y(3fur)_3(H_2O)_2]_n$[15] **3.8**	2.32		
$[Y_3(2m3fur)_9]_n$ **4.4**	2.36	2.32	2.36

4.2.3 Corrosion Inhibition

4.2.3.1 Immersion Tests

Immersion studies were conducted over a seven-day period, both in a 0.01 M NaCl control solution and with the presence of inhibition systems at room temperature (25 °C), to evaluate the long-term performance of these inhibitors on mild steel.

Table 4.9 presents a summary of the weight loss measurements for mild steel coupons after 168 h of immersion in specific inhibitor solutions. The weight loss of the coupons during the immersion test period serves as a primary measure of corrosion. The testing was conducted for the compounds at 800 ppm, as the solubility limit for $[Er_3(2m3fur)_9]_n$ **4.5** in 0.01 M sodium chloride solution is 800 ppm.

The corrosion rate (R) for each inhibitor compound was calculated, and subsequently, the percentage corrosion inhibition (%) was determined using Equations **2.1** and **2.2** described in Chapter 2.

Table 4.9: Observed weight loss, corrosion rates ($\mu g/m^2s$) and percentage inhibition (η) for mild steel coupons immersed in specific solutions at 800 ppm concentrations in 0.01 M NaCl for seven days.

Solution	**Concentration**		**Solubility in 0.01 M NaCl (ppm)**	**Avg Weight Loss (mg)**	**Corrosion Rate ($\mu g/m^2s$)**	**Inhibition, η (%)**
	ppm	**mM**				
Control - NaCl	580	10	-	19.6	39.1	-
$\{[Ce_2(2m3fur)_6(EtOH)]\cdot H_2O\}_n$ **4.2**	800	0.731	1800	12.6	24.0	39
$\{[Pr_2(2m3fur)_6(EtOH)]\cdot H_2O\}_n$ **4.3**	800	0.730	1500	8.8	20.9	46

$[Y_3(2m3fur)_9]_n$ **4.4**	800	0.574	850	8.5	16.2	59
$[Er_3(2m3fur)_9]_n$ **4.5**	800	0.491	800	11.3	21.6	45
$[Yb_3(2m3fur)_9]_n$ **4.6**	800	0.486	830	9.7	18.5	53
$[Ce(3fur)_3(H_2O)_2]_n$ [15] **(Chapter 3)**	800	1.57	3000	3.7	8.3	79
$[Y(3fur)_3(H_2O)_2]_n$ [15] **(Chapter 3)**	800	1.75	800	1.9	3.9	90

Consistent with visual inspections (Figure 4.13), weight loss measurements also indicated that $[Y_3(2m3fur)_9]_n$ **4.4** exhibited the highest inhibition efficiency at 59% among the tested compounds, while $\{[Ce_2(2m3fur)_6(EtOH)]\cdot H_2O\}_n$ **4.2** showed the lowest performance with an inhibition efficiency of approximately 39%.

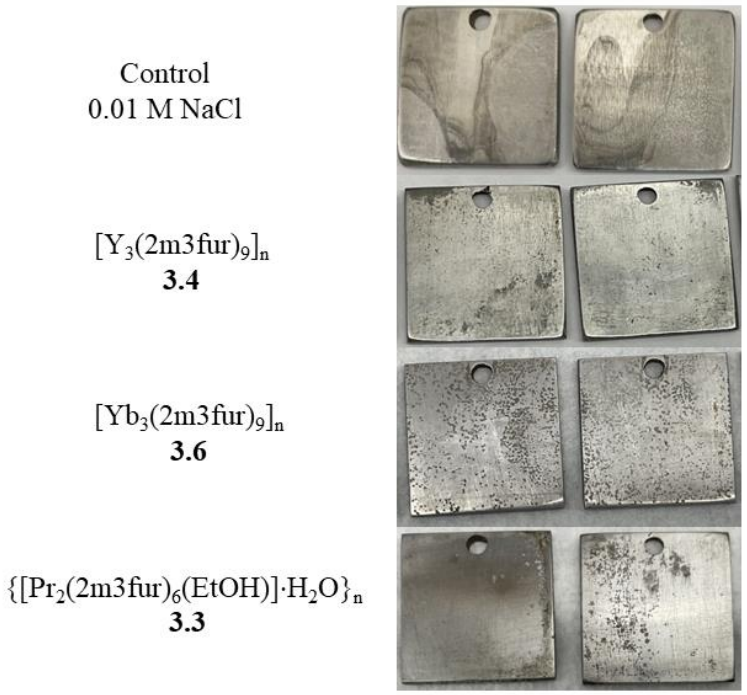


Figure 4.13: Mild steel coupons immersed in control and the three best inhibited solutions for 168 h (Left – Trial 1; right – Trial 2.)

The limited solubility of most of the complexes hindered attempts to conduct studies at higher concentration. The performance of the RE 2-methyl-3-furoate complexes was not as effective as the analogous rare earth 3-furoate complexes (see Table 4.9 for a comparison of Ce and Y complexes),[15] suggesting that the methyl substituent on the furoate ring may cause steric hindrance of inhibitor function. Because of the less effective inhibitor performance, electrochemical assessments of inhibition were not pursued.

4.3 Conclusions

Two series of RE 2-methyl-3-furoate complexes, $\{[RE_2(2m3fur)_6(EtOH)]\cdot H_2O\}_n$ (RE = La **(4.1)**, Ce **(4.2)**, Pr **(4.3)**) and $[RE_3(2m3fur)_9]_n$ (RE = Y **(4.4)**, Er **(4.5)**, Yb **(4.6)**) have been successfully synthesized. These compounds crystallized in one of the two distinct structural groups, as determined through single-crystal X-ray crystallography. The synthesis process yielded moderate to good, isolated yields of crystalline materials, and these complexes were comprehensively characterised by various techniques, including IR spectroscopy, powder XRD, TGA, and microanalyses.

The light rare earth metals form one-dimensional polymeric structures, $\{[RE_2(2m3fur)_6(EtOH)]\cdot H_2O\}_n$ complexes (**RE** = La, Ce, Pr) with one ten and one nine coordinate RE atom. Conversely, the heavier rare earth metals have one-dimensional polymeric chains in the $[RE_3(2m3fur)_9]_n$ complexes (RE = Y, Er, Yb), with three unique RE metal centres, two eight coordinate and one seven coordinate.

In immersion studies conducted with mild steel in 0.01 M NaCl solutions at inhibitor concentrations of 800 ppm, $[Y_3(2m3fur)_9]_n$ **(4.6)** emerged as the most effective inhibitor among the compounds tested, demonstrating a 59% inhibition rate. Nevertheless, the most efficient inhibitor in this study proved to be less effective than the RE 3-thiophenecarboxylate[14] and 3-furoate[15] complexes studied previously in Chapter 2 and 3, respectively. It is plausible that the steric effect of the methyl substituent impedes binding of the inhibitor to OH groups on the corroded steel surface, thereby reducing inhibitor protection.

4.4 Experimental

For materials and general considerations, see Appendix One.

4.4.1 Synthesis of 2-methyl-3-furoate (2m3fur) RE complexes

General Synthetic Method: 2-Methyl-3-furoic acid (0.504 g, 4 mmol) was dissolved in 95% ethanol (15ml) and subjected to deprotonation by an equimolar quantity of aqueous sodium hydroxide. The solution mixture was stirred for one hour, after which the pH was adjusted to fall within the range 7-8. Subsequently, three molar equivalents of sodium 2-methyl-3-furoate were treated with one molar equivalent of the hydrated rare earth salt solution at a pH level of 5 to form rare earth 2-methyl-3-furoate complexes. The resulting solid precipitates were isolated by filtration and allowed to air-dry for 2-3

days. Finally, crystals were obtained through slow evaporation of the mother liquor at room temperature.

{[La_2(2m3fur)$_6$(EtOH)]·H_2O}$_n$ (4.1)

White powder. Yield: 0.76 g (52%). m.p. 230 °C (dec.). Elemental analysis for $C_{38}H_{38}La_2O_{20}$ (MW: 1092.51 gmol^{-1}): Calculated (%) C 41.78, H 3.51, La 25.40; $C_{36}H_{32}La_2O_{19}$ (MW: 1046.44 gmol^{-1}, loss of 1 EtOH): Calculated (%) C 41.32, H 3.08, La 26.55; Found (%) C 41.39, H 2.62, La 26.65. IR (cm^{-1}): 3430w, 3123w, 2920w, 1682w, 1595m, 1530s, 1519s, 1445m, 1414s, 1376s, 1359s, 1232m, 1213s, 1134m, 1101s, 1033w, 946m, 896m, 875w, 817s, 807s, 731s, 684m, 634w, 599m, 534m, 462s. TGA weight loss (30-200°C): 4.9% (Calc. for loss of 1×H_2O and 1× EtOH = 5.8%).

{[Ce_2(2m3fur)$_6$(EtOH)]·H_2O}$_n$ (4.2)

White powder. Yield: 0.76 g (52%). m.p. 230°C (dec.). Elemental analysis for $C_{38}H_{38}Ce_2O_{20}$ (MW: 1094.93 gmol^{-1}): Calculated (%) C 41.68, H 3.50, Ce 25.60: $C_{36}H_{32}Ce_2O_{19}$ (MW: 1048.86 gmol^{-1}, loss of 1 EtOH): Calculated (%) C 41.22, H 3.08, Ce 26.72; Found (%) C 41.55, H 2.54, Ce 27.26. IR (cm^{-1}): 3458w, 3122w, 2922w, 1596m, 1527s, 1518s, 1444m, 1414s, 1376s, 1359s, 1232m, 1214s, 1133m, 1102s, 1031w, 946m, 895m, 876w, 819s, 807s, 733s, 684m, 634w, 600m, 534m, 466s, 457s. TGA weight loss (30-175 °C): 4.8% (Calc. for loss of 1×H_2O and 1× EtOH = 5.8%); Monoclinic $P2_1/n$, unit Cell: a = 7.6700(15), b = 22.470(4), c = 23.620(5), β = 98.85(3), which is similar to **4.3.**

{[Pr_2(2m3fur)$_6$(EtOH)]·H_2O}$_n$ (4.3)

Pale green powder. Yield: 0.64 g (48%). m.p. 230 °C (dec.). Elemental analysis for $C_{38}H_{38}O_{20}Pr_2$ (MW: 1096.51 gmol^{-1}): Calculated (%) C 41.62, H 3.49, Pr 25.70; $C_{36}H_{30}O_{18}Pr_2$ (MW: 1032.43 gmol^{-1}, loss of 1 EtOH and 1 H_2O): Calculated (%) C 41.88, H 2.93, La 27.30; Found (%) C 41.70, H 2.50, Pr 27.95. IR (cm^{-1}): 3122w, 2923w, 1596m, 1548s, 1534m, 1515s, 1412s, 1375s, 1358s, 1235m, 1214s, 1133m, 1102s, 1030w, 946m, 895m, 876w, 836w, 821s, 806s, 737s, 726s, 685m, 634w, 600m, 535m, 466s, 458s.

$[Y_3(2m3fur)_9]_n$ (4.4)

White powder. Yield: 0.45 g (73%). m.p. 270 °C (dec.). Elemental analysis for $C_{54}H_{45}O_{27}Y_3$ (MW: 1392.63 $gmol^{-1}$): Calculated (%) C 46.57, H 3.26, Y 19.20; Found (%) C 46.64, H 2.92, Y 19.60. IR (cm^{-1}): 3127w, 2922w, 1596m, 1532s, 1517s, 1462s, 1445m, 1420s, 1381m, 1360s, 1233m, 1217s, 1132m, 1103m, 1030w, 946m, 895m, 837m, 802s, 750m, 728s, 685m, 600m, 553w, 534w, 473s.

$[Er_3(2m3fur)_9]_n$ (4.5)

Pink powder. Yield: 0.51 g (70%). m.p. 270 °C (dec.). Elemental analysis for $C_{54}H_{45}O_{27}Er_3$ (MW: 1627.69 $gmol^{-1}$): Calculated C 39.85, H 2.79, Er 30.80; Found (%) C 39.80, H 2.58, Er 31.32. IR (cm^{-1}): 3127w, 1596m, 1531s, 1517s, 1463m, 1444s, 1420s, 1381m, 1360s, 1233m, 1217s, 1131m, 1103s, 1030w, 947m, 895m, 837m, 802s, 751w, 728s, 688m, 600m, 553m, 534w, 472s.

$[Yb_3(2m3fur)_9]_n$ (4.6)

White powder. Yield: 0.40 g (55%). m.p. 270 °C (dec.). Elemental analysis for $C_{54}H_{45}O_{27}Yb_3$ (MW: 1645.04 $gmol^{-1}$): Calculated (%) C 39.43, H 2.76,Yb 31.60; Found (%) C 39.55, H 2.50, Yb 31.70. IR (cm^{-1}): 3129w, 2923w, 1599m, 1538m, 1513s, 1460s, 1428s, 1385m, 1361s, 1220s, 1130m, 1107m, 1030w, 945m, 896m, 840m, 805s, 729s, 684m, 634w, 600m, 562m, 536w, 469s. TGA weight loss (90-175 °C): 4.4% (Calc. for loss of $4\times H_2O$ (Assuming absorb water = 4.2%)).

4.4.2 Corrosion Testing

For the corrosion testing procedures used for weight loss experiments, see Appendix One.

4.5 X-ray Crystal Data

For details on x-ray crystallography, see Appendix One.

Crystal data and refinement details are given in Table 4.10.

Table 4.10: Crystal data and structural refinement for rare earth 2-methyl-3-furoate complexes.

	4.3	**4.4**	**4.5**	**4.6**
Formula	$C_{38}H_{38}O_{20}Pr_2$	$C_{54}H_{45}O_{27}Y_3$	$C_{54}H_{45}Er_3O_{27}$	$C_{54}H_{45}O_{27}Yb_3$
M_r	1096.50	1392.63	1627.68	1645.02
Space group	$P2_1/n$	$P2_1/c$	$P2_1/c$	$P2_1/c$
a (Å)	7.6890(15)	12.333(3)	12.353(3)	12.313(3)
b (Å)	21.872(4)	22.716(5)	22.618(5)	22.592(5)
c (Å)	23.833(5)	20.408(4)	20.432(4)	20.386(4)
α (°)	90	90	90	90
β (°)	98.35(3)	103.19(3)	103.36(3)	103.67(3)
γ (°)	90	90	90	90
V (Å^3)	3965.6(14)	5567(2)	5554(2)	5510(2)
Z	4	4	4	4
ρ_{calc}, g cm^{-3}	1.837	1.662	1.946	1.983
μ, mm^{-1}	2.513	3.192	4.582	5.141
N_τ	91584	64968	64519	63365
N (R_{int})	6954(0.0221)	9654(0.0959)	9600(0.1996)	9507(0.0428)
$R_1(I > 2\sigma(I))$	0.0315	0.0526	0.0612	0.0258
wR_2 (all data)	0.0754	0.1341	0.1566	0.0669
GOF	1.111	1.048	0.998	1.044

4.6 References

1 M. Forsyth, K. Wilson, T. Behrsing, C. Forsyth, G. B. Deacon and A. Phanasgoankar, *Corrosion*, 2002, **58**, 953–960.

2 F. Blin, S. G. Leary, G. B. Deacon, P. C. Junk and M. Forsyth, *Corros. Sci.*, 2006, **48**, 404–419.

3 F. Blin, S. G. Leary, K. Wilson, G. B. Deacon, P. C. Junk and M. Forsyth, *J. Appl. Electrochem.*, 2004, **34**, 591–599.

4 W. W. Lee, *Ph.D. thesis,* Monash University, 2010.

5 M. Seter, G. M. A. Girard, W. W. Lee, G. Deacon, P. Junk, B. Hinton and M. Forsyth, *AIMS Mater. Sci.*, 2015, **2**, 1–15.

6 M. Frey, S. G. Harris, J. M. Holmes, D. A. Nation, S. Parsons, P. A. Tasker and R. E. P. Winpenny, *Chem. Eur. J.*, 2000, **6**, 1407–1415.

7 M. Frey, S. G. Harris, J. M. Holmes, D. A. Nation, S. Parsons, P. A. Tasker, S. J. Teat and R. E. P. Winpenny, *Angew. Chem. Int. Ed.,* 1998, **37**, 3245–3248.

8 Y. Peng, A. E. Hughes, G. B. Deacon, P. C. Junk, B. R. W. Hinton, M. Forsyth, J. I. Mardel and A. E. Somers, *Corros. Sci.*, 2018, **145**, 199–211.

9 A. V. Zabula, S. Dey, J. R. Robinson, T. Cheisson, R. F. Higgins, G. Bhargava, R. C. Nahas, D. Cinoman, M. Kerins, E. C. Houze and E. J. Schelter, *Corros. Sci.*, 2020, **165**, 108377

10 G. B. Deacon, P. C. Junk, W. W. Lee, M. Forsyth and J. Wang, *New J. Chem.*, 2015, **39**, 7688–7695.

11 M. Forsyth, M. Seter, B. Hinton, G. Deacon and P. Junk, *Aust. J. Chem.*, 2011, **64**, 812–819.

12 A. E. Somers, G. B. Deacon, B. R. W. Hinton, D. R. Macfarlane, P. C. Junk, M. Y. J. Tan and M. Forsyth, *J. Indian Inst. Sci.*, 2016, **96**, 285–292.

13 A. E. Somers, B. R. W. Hinton, C. de Bruin-Dickason, G. B. Deacon, P. C. Junk and M. Forsyth, *Corros. Sci.*, 2018, **139**, 430–437.

14 V. P. Vithana, Z. Guo, G. B. Deacon, A. E. Somers and P. C. Junk, *New J. Chem.*, 2022, **46**, 19104–19111.

15 V. P. Vithana, Z. Guo, G. B. Deacon, A. E. Somers and P. C. Junk, *Molecules*, 2022, **27**, 8836.

16 A. E. Somers, Y. Peng, A. L. Chong, M. Forsyth, D. R. MacFarlane, G. B. Deacon, A. E. Hughes, B. R. W. Hinton, J. I. Mardel and P. C. Junk, *Corros. Eng., Sci. Technol.*, 2020, **55**, 311–321.

17 R. D. Shannon, *Acta Crystallogr. A*, 1976, **32**, 751–767.

Chapter 5: Synthesis, Structures, and Corrosion Inhibition of Various Alkali Metal Carboxylate Complexes.

5.1 Introduction

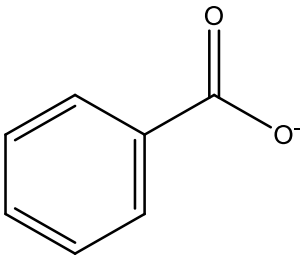
5.1.1 Alkali Metal Salts of Carboxylic Acids as Corrosion Inhibitors

The alkali metals are highly prevalent in the Earth's crust and, two out of the eight most common elements found in the crust belong to the Group 1 elements. The importance of alkali metals specifically Na^+ and K^+ ions, in biology, cannot be overstated.[1] Approximately one-third of all proteins rely on the presence of metal ions for their structural stability and proper functioning.[2] The extensive utilization of alkali metal compounds in diverse technical applications emphasizes their immense importance in both chemistry and biology. These applications range from the utilization of lithium compounds in batteries, organic synthesis, and pharmaceuticals, to the use of sodium in silicate-based glasses, and the use of potassium ions to enhance the scratch resistance of glass surfaces.[1]

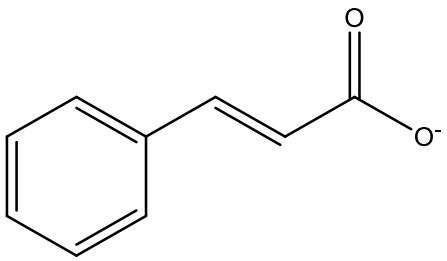
Since the use of alkali metal salts of carboxylic acids have been claimed to prevent corrosion in water treatment facilities,[3] the sodium salts are usually tested for comparison with the rare earth carboxylates, and inevitably perform much worse.[3–7] Moreover, preliminary immersion studies done by Wormwell and Mercer[8] have demonstrated that lithium and potassium benzoates also exhibit inhibitory properties against mild steel corrosion. However, relatively high doses of alkali metal carboxylates are needed to achieve a good inhibitory effect, where they often act as anodic inhibitors.[9,10] Mercer et al. [3,11] examined a series of benzoate compounds as corrosion inhibitors and concluded that the introduction of various substituents (-CH_3, -NO_2, NH_2, -OH, CH=CH) improves the inhibition performance of benzoates.

Further, Mercer demonstrated a prominent improvement in the inhibition activity of mild steel with cinnamates by the presence of a carbon-carbon double bond between the benzene ring and the carboxylate group.[3] In addition, the corrosion inhibition properties of alkali metal cinnamate, nitrocinnamate, and acetate complexes were investigated in neutral and slightly alkaline oxidizing environments with low chloride concentrations, demonstrating favourable inhibition efficiency. However, it has been

reported that the corrosion rates, determined through the weight loss data, were generally higher for sodium salts in comparison to their rare earth-substituted analogues.[5]



Benzoate



Cinnamate

In a separate study, the inhibitory effect of sodium glutarate on the corrosion of carbon steel in a neutral 0.02M NaCl solution was examined. The findings from electrochemical measurements indicated a weak inhibitory action at low concentrations, while a notable enhancement in efficiency was observed at higher concentrations.[12]

For cooling water systems, specifically for aluminium-based components in vehicles, alkali metal-based inhibitors have been reported to be used. Such inhibitors include alkali metal salts of borates, silicates, benzoates, nitrates, nitrites, and molybdates.[13,14]

In the study reported by Chan Rosado and M. A. Pech-Canul, the inhibition activity of the disodium salt of the aliphatic acid glutaric for steel in 0.02 M NaCl was investigated. The results of this experiment revealed poor inhibition at lower concentrations of 1 mM and 5 mM, while better inhibiting action was achieved with the increase in concentration (32 mM or greater).[12]

5.1.2 Current Study

Whilst we have regularly compared the performance of sodium salts with their rare earth counterparts, we have not examined Li, K, Rb, Cs analogues. When we examined the CCDC structural data base, there were no structures of the alkali metal derivatives of the carboxylic acids (1)-(4) (Chart 5.1) used in preparing the rare earth inhibitors surveyed in this study.[15] In the case of 4-hydroxybenzoic acid (4hobH, (5) Chart 5.1), only the structure of the sodium salt has been determined from X-ray powder data,[16] whilst structures of potassium and rubidium hydrogen di-4-hydroxybenzoates [M[H(4hob)$_2$]] (M = K, Rb)[17,18] are known, but not the M(4hob) derivatives. There was also a lack of vertical (Li-Cs) studies of structures of rare-earth carboxylates.[1,2] In view

of this lack of detailed structural studies, in this chapter we have investigated the synthesis and structures of a series of alkali metal carboxylate complexes. Furthermore, considering that alkali metal salts of the carboxylate ions are used as precursor in RE carboxylate-based inhibitors, we have also investigated the corrosion inhibitor properties of these compound to compare their performances with their respective RE counterparts.

All the work in this chapter resulted in a publication in the journal *Molecules* (see reprint in Appendix Two).

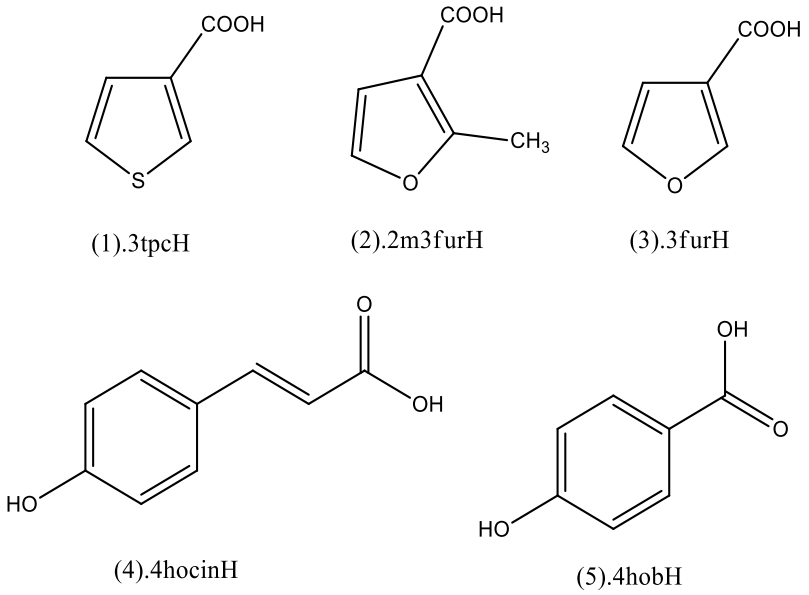
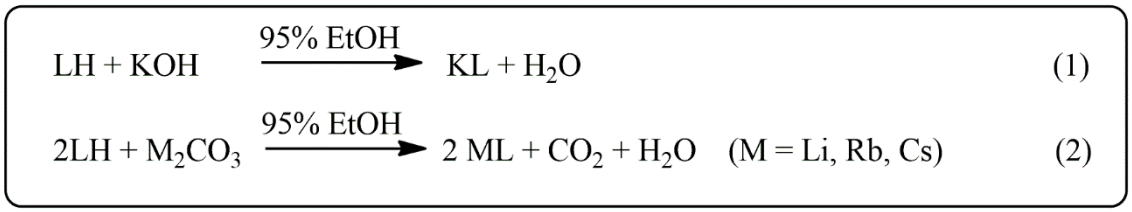


Chart 5.1: Structures of **(1)** 3- thiophenecarboxylic acid (3tpcH), **(2)** 2-methyl-3-furoic acid (2m3furH), **(3)** 3-furoic acid (3furH), **(4)** 4-hydroxycinnamic acid (4hocinH), and **(5)** 4-hydroxybenzoic acid (4hobH).

5.2 Results and Discussion

5.2.1 Synthesis and characterisation

By varying the preparative conditions, the synthesis of alkali metal (Li–Cs) complexes of 3-thiophenecarboxylate (3tpc) (M = Li **(5.1)**, K **(5.2)**, Rb **(5.3)**, Cs **(5.4)**), 2-methyl-3-furoate (2m3fur)) (M = Li **(5.5)**, K **(5.6)**, 3-furoate (3fur)) (M = Li **(5.7)**), 4-hydroxycinnamate (4hocin) (M = K **(5.8)**, Rb **(5.9)**, Cs **(5.10)**), and 4-hydroxybenzoate (4hob)) (M = Li **(5.11)**, K **(5.12)**, Rb **(5.13)**, Cs **(5.14)**) complexes were carried out by neutralisation reactions in aqueous solution (Scheme 5.1).



Scheme 5.1: The synthesis of alkali metal carboxylate complexes.

Only the complexes that were characterised by single crystal XRD are reported in this chapter. When complexed with sodium, none of the five ligands formed crystalline products suitable for X-ray crystallography. The bulk samples of sodium complexes were characterised by powder XRD, IR and TGA, and the results suggest that they have dissimilar structural profiles compared to the other alkali metal carboxylate complexes in the same group. Therefore, further characterisations were not carried out. In the case of **5.4** and **5.9**, acid salts [M{H(L)$_2$}] (M = Rb, Cs) were obtained, despite intentionally maintaining a 1:1 M: LH reaction stoichiometry (M = alkali metal; L = Ligand) to prevent incorporation of the carboxylic acid into the product (see Introduction for previous similar issues). Among the structures, **5.4**, **5.6**, and **5.11** exhibited slight hygroscopicity. This was evident from the thermal analysis of **5.4** and **5.6**, as well as the microanalysis of **5.11**, which showed values consistent with water absorption.

The compositions of the [M(3tpc)]$_n$ (M = Li, K, Rb, and Cs) complexes were determined through X-ray crystallography, elemental analysis, and thermogravimetric analysis (TGA). Elemental analysis agreed with the single crystal composition for all four compounds. The TGA results of **5.1**, **5.2,** and **5.3** (Figure 5.1) were consistent with the compositions from single-crystal data. However, the TGA of **5.4** showed a loss of 0.5 water molecules in a single step below 150 °C. This is presumably due to the hygroscopic nature of these compounds.

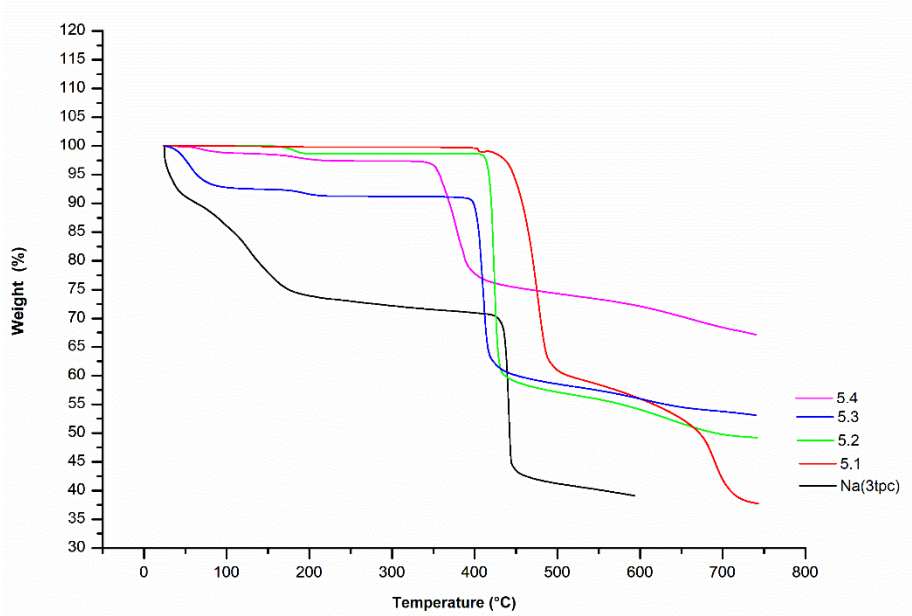


Figure 5.1: TGA thermograms of the $[M(3tpc)]_n$ series (M =Na, Li **(5.1)**, K **(5.2)**, Rb **(5.3)**, Cs **(5.4)**).

Nonetheless, powder XRD analyses of all four compounds showed close similarities to the patterns generated from the single-crystal data (Figure 5.2).

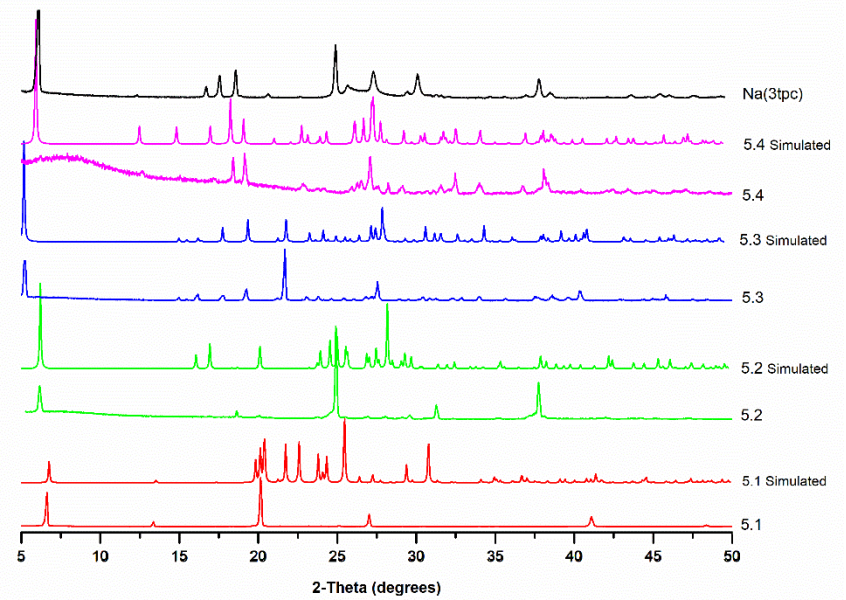


Figure 5.2: PXRD diffractograms of the $[M(3tpc)]_n$ series(M = Na, Li **(5.1)**, K **(5.2)**, Rb **(5.3)**, Cs **(5.4)**) at room temperature compared to their simulated patterns.

In the $[M(2m3fur)]_n$ (M = Li, K) series, the TGA and elemental analysis of compound **5.5** aligns with the composition determined crystallographically as $[Li_2(2m3fur)_2(H_2O)]$. Although the elemental analyses of compound **5.6** matches the composition of $[K_2(2m3fur)_2(H_2O)]_n$ of the crystal structure, the TGA of the bulk

precipitate indicated the presence of water of crystallisation (Figure 5.3). The weight loss below 200 °C, indicated the evolution of nearly two water molecules. This suggests that the compound may be hygroscopic after undergoing drying to a constant weight over silica gel.

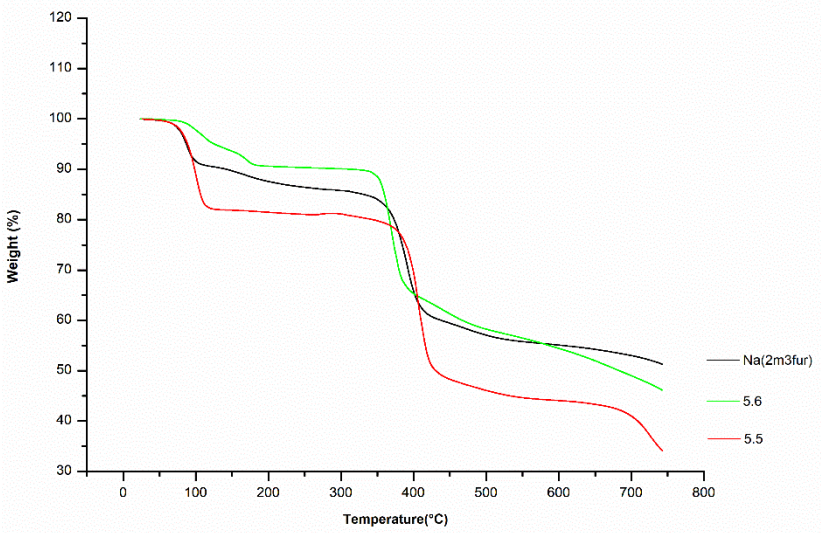


Figure 5.3: TGA thermograms of the $[M(2m3fur)]_n$ series (M = Na, Li **(5.5)**, K **(5.6)**).

Nonetheless, the powder XRD analyses revealed similar d-spacings to those generated from single crystal data for both **5.5** and **5.6** (Figure 5.4).

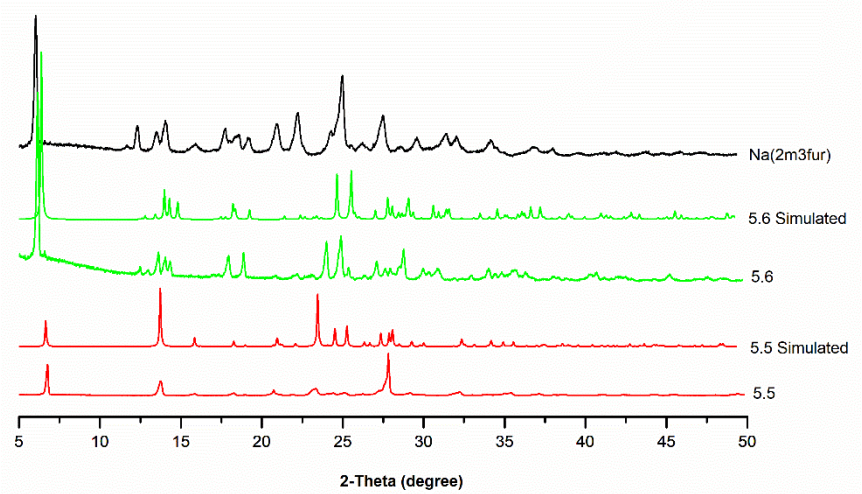


Figure 5.4: PXRD diffractograms of the $[M(2m3fur)]_n$ series (M = Na, Li**(5.5)**, K **(5.6)**) at room temperature compared to their simulated patterns.

The elemental analysis of lithium-3-furoate (**5.7**) aligns with the calculated percentage composition for $[Li(3fur)]_n$ **(5.7)**, and the thermogravimetric analysis (Figure 5.5) and the IR analysis (Figure 5.6) of the sample confirm the absence of any water.

Additionally, the powder diffractogram obtained from the bulk precipitate matches the calculated diffractogram based on single crystal data (Figure 5.7).

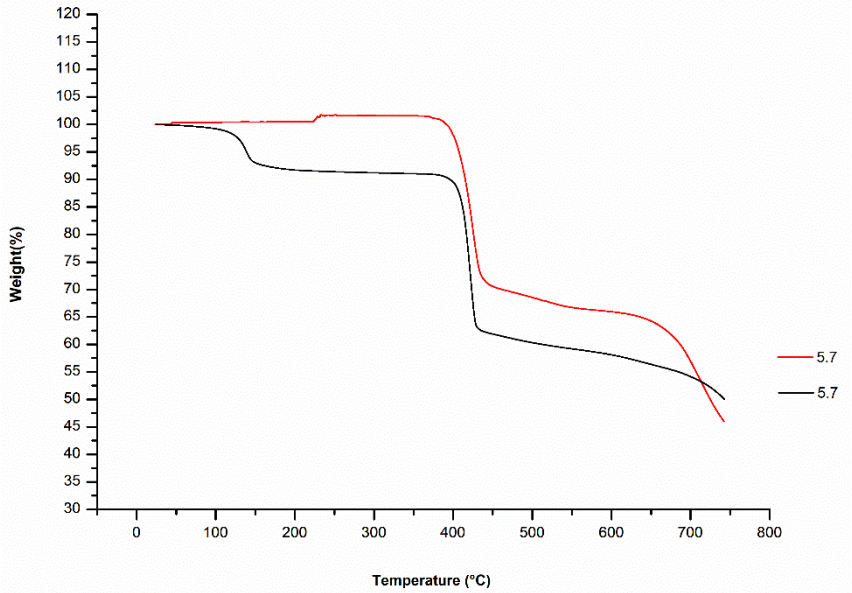


Figure 5.5: TGA thermograms of [Na(3fur)] and $[Li(3fur)]_n$ **(5.7)**.

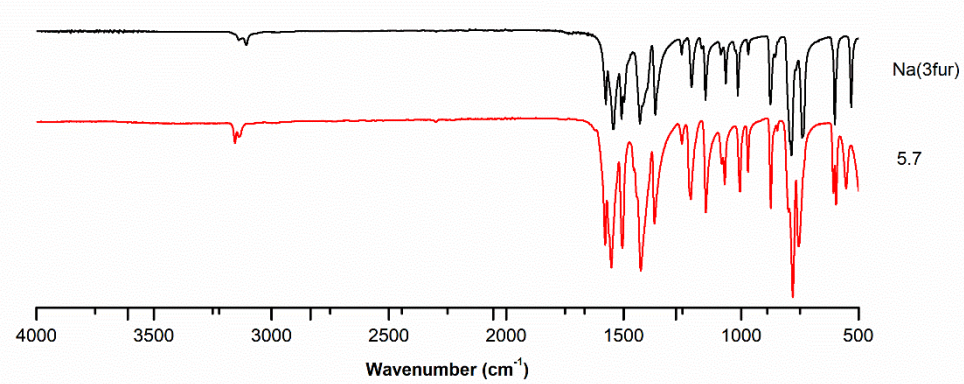


Figure 5.6: IR spectra of [Na(3fur)] and $[Li(3fur)]_n$ **(5.7)**.

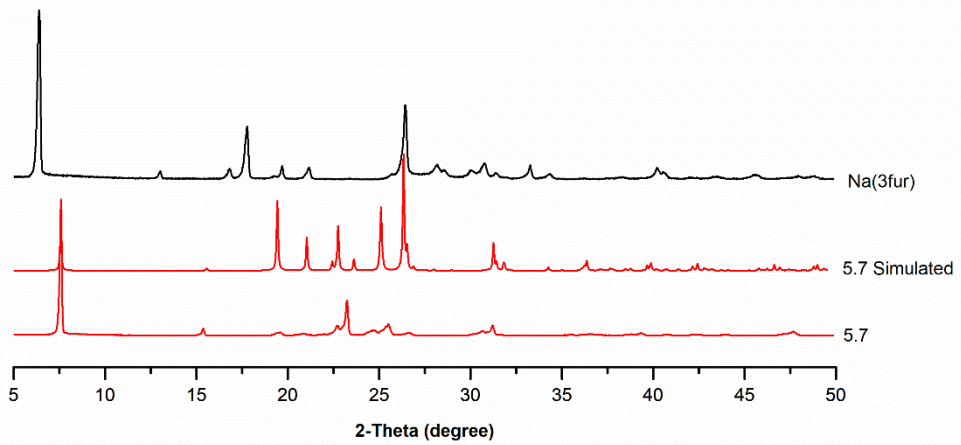


Figure 5.7: PXRD diffractograms of [Na(3fur)] and $[Li(3fur)]_n$ **(5.7)** at room temperature compared to the simulated pattern of **5.7**.

All three compounds in the M(4hocin) series (M = K, Rb, and Cs) have different compositions. The TGA of compound **5.8** yielded results consistent with its crystal composition, revealing the loss of three water molecules in a single step below 100 °C (Figure 5.8), but the elemental analysis of **5.8** indicated a loss of 1.5 ligated water molecules due to the drying of the samples over silica gel. Nonetheless, the powder diffractogram of the bulk sample matches the one generated from the crystal data (Figure 5.9).

In the case of compound **5.9**, the structure was determined as $[Rb\{H(4hocin)_2\}]_n.nH_2O$, but the analysis of the bulk product through microanalysis and TGA suggests that 0.75 4hocinH had been lost from the crystal composition. Unlike in **5.8**, the experimental powder diffractogram of the bulk sample **5.9** exhibited a noticeable difference when compared to the diffractogram generated from the crystal data attributed to loss of 4hocinH. Upon drying the crystals of compound **5.9** over silica gel, they seemed to lose their crystalline form and appear more amorphous.

By comparison, the caesium analogue prepared under similar conditions, was determined by crystallography to be $[Cs(4hocin)(H_2O)]_n$, which was consistent with the elemental analysis and TGA results. The powder XRD analysis of the bulk sample of **5.10** closely resembles the powder diffractogram generated from crystal data, but a few minor discrepancies could be observed (Figure 5.9).

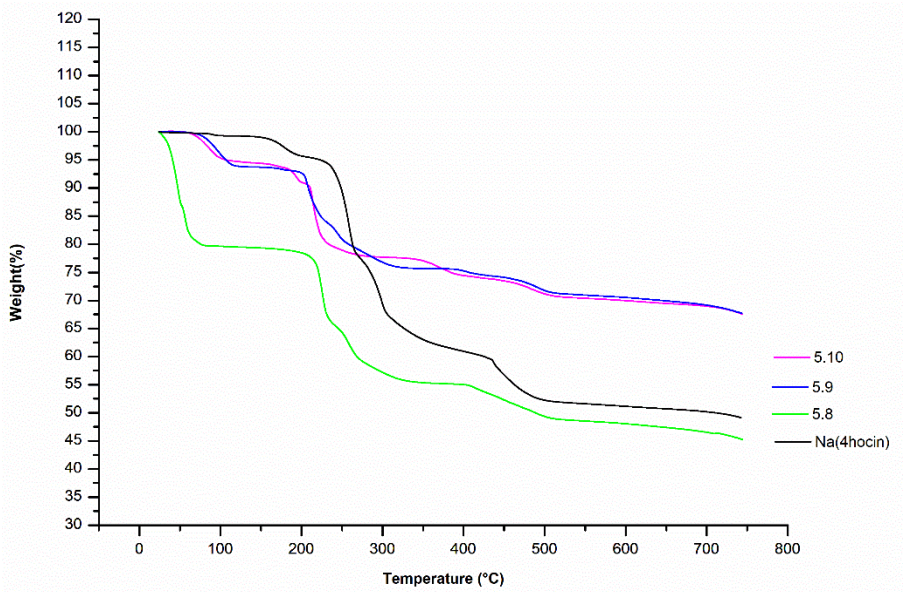


Figure 5.8: TGA thermograms of the $[M(4hocin)]_n$ series (M = Na, K **(5.8)**, Rb **(5.9)**, Cs **(5.10)**).

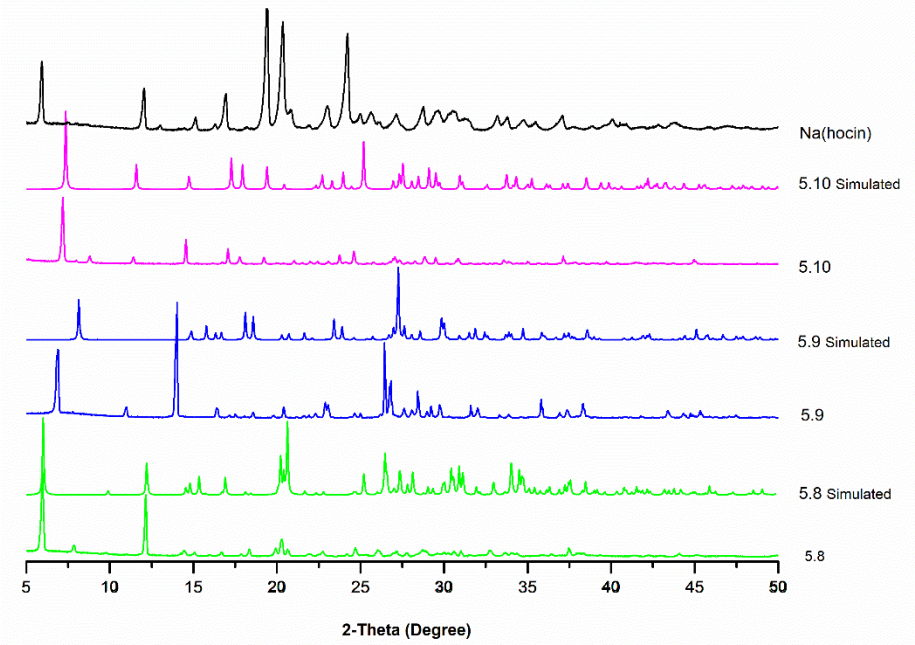


Figure 5.9: PXRD diffractograms of the $[M(4hocin)]_n$ series (M = Na, K **(5.8)**, Rb **(5.9)**, Cs **(5.10)**) at room temperature compared to their simulated patterns.

The TGA thermal data of **5.11** (Figure 5.10) indicated that it is an anhydrous compound, which aligns with the X-ray composition of $[Li(4hob)]_n$. However, the elemental analysis of the complex indicated the presence of some water suggesting it is slightly hygroscopic. The powder diffractogram closely resembles the generated powder diffractogram obtained from the crystal data (Figure 5.11), indicating that the structural integrity is maintained.

The TGA analysis of **5.12** revealed the loss of three water molecules in two steps, occurring below 75 °C and below 150 °C. However, the elemental analyses of the bulk sample yielded a molecular composition of $[K(4hob)(H_2O)]_n$ as opposed to the composition derived from the crystal data namely $[K(4hob)(H_2O)_3]_n$, indicating efflorescence. Additionally, the experimentally obtained powder diffractogram differs from the powder diffractogram generated based on its crystal data, consistent with the water loss (Figure 5.11).

The two complexes, **5.13** and **5.14**, have the general formulae $[M(4hob)(H_2O)]_n$ (M = Rb or Cs) by elemental analyses (C, H). The TGA results for **5.13** are in support but the bulk $[Cs(4hob)(H_2O)]_n$ (**5.14**) lost a small fraction of coordinated water during drying prior to TGA. The powder diffractograms of both compounds exhibited some similarities and displayed peaks that matched the generated diffractograms based on their crystal data.

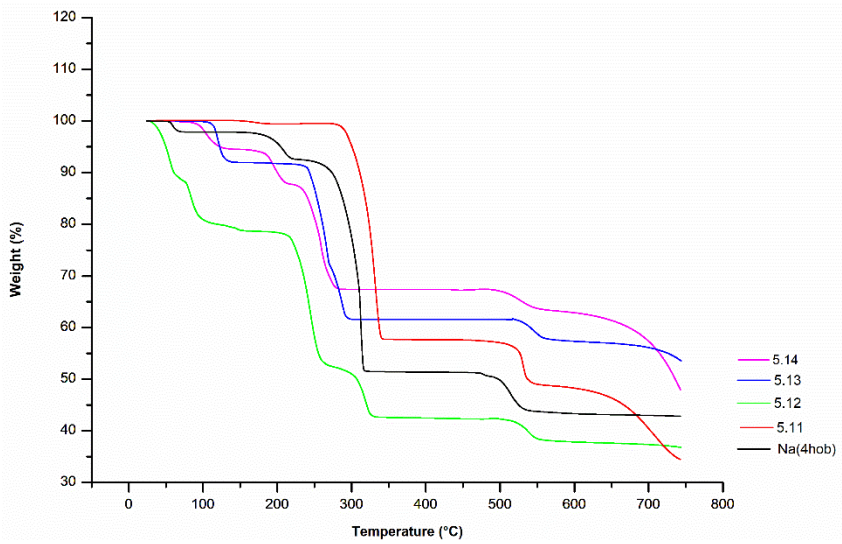


Figure 5.10: TGA thermograms of the $[M(4hob)]_n$ series (M = Na, Li **(5.11)**, K **(5.12)**, Rb **(5.13)**, Cs **(5.14)**).

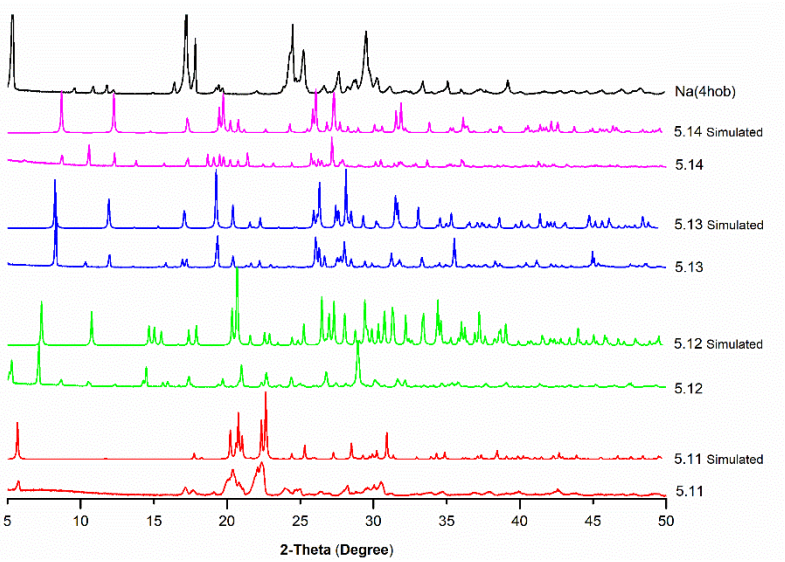


Figure 5.11: PXRD diffractograms of the $[M(4hob)]_n$ series (M = Na, Li **(5.11)**, K **(5.12)**, Rb **(5.13)**, Cs **(5.14)**) at room temperature compared to their simulated patterns.

Table 5.1 presents a summary of the significant absorption bands observed in the IR spectra of all 14 compounds.

Table 5.1: Selected IR bands alkali metal 3tpc, 2m3fur, 3fur, 4hocin and 4hob complexes.

Compounds	**Significant Bands (cm^{-1})**				
	ν(OH)	**ν(C=C) propenyl**	**$\nu_{as}(CO_2^-)$**	**$\nu_s(CO_2^-)$**	**$\Delta\nu^a$**
$[Li_2(3tpc)_2]_n$ **(5.1)**	-	-	1566,1514	1414,1399	133.5
$[K_2(3tpc)_2]_n$ **(5.2)**	-	-	1558,1516	1412,1401	130.5
$[Rb(3tpc)(H_2O)]_n$ **(5.3)**	3348	-	1563,1512	1405	132.5
$[Cs\{H(3tpc)_2\}]_n$ **(5.4)**	-	-	1560,1510	1398,1384	144
$[Li_2(2m3fur)_2(H_2O)_3]$ **(5.5)**	3301,3373	-	1544,1521	1428	104.5
$[K_2(2m3fur)_2(H_2O)]_n$ **(5.6)**	3354	-	1532,1517	1418	106.5
$[Li(3fur)]_n$ **(5.7)**	-	-	1552	1428	124
$[K(4hocin)(H_2O)]_n$ **(5.8)**	3114,3444	1636	1531,1511	1371	150
$[Rb\{H(4hocin)_2\}]_n \cdot nH_2O$ **(5.9)**	3241	1634	1537,1514	1381	144.5
$[Cs(4hocin)(H_2O)]_n$ **(5.10)**	3200	1633	1537,1514	1378	147.5
$[Li(4hob)]_n$ **(5.11)**	3351	-	1556	1399	157
$[K(4hob)(H_2O)_3]_n$ **(5.12)**	3437	-	1533	1361	172
$[Rb(4hob)(H_2O)]_n$ **(5.13)**	3317	-	1529,1509	1381	138
$[Cs(4hob)(H_2O)]_n$ **(5.14)**	3202	-	1529,1509	1376	143

[a] $\Delta\nu = \nu_{as}(CO_2) - \nu_s(CO_2)$

Having absorption bands in the region of 1617-1682 cm^{-1} in **5.4** confirms the presence of an $[H(3tpc)_2]$ ligand with the C(O)OHO(O)C group (Figure 5.12).

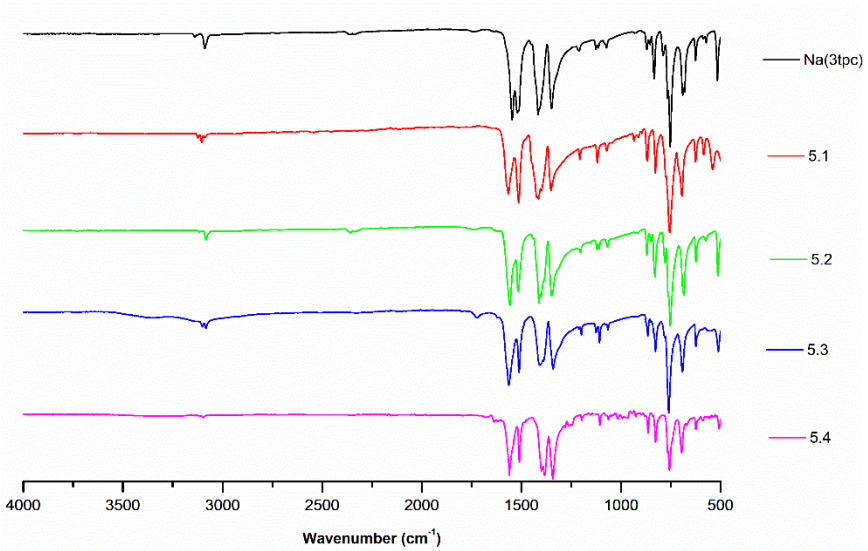


Figure 5.12: IR spectra of the $[M(3tpc)]_n$ series (M = Na, Li**(5.1)**, K **(5.2)**, Rb **(5.3)**, Cs **(5.4)**).

The IR spectra for all three compounds in the [M(4hocin)] series have a band of moderate intensity in the range 1633-1636 cm^{-1}, which corresponds to the stretching of the propenyl C=C double bond. The consistent υ(C=C) frequencies indicate that the propenyl group is not engaged in coordination.[19] The carbonyl absorption band of $[H(4hocin)_2]$ in the range 1617-1682 cm^{-1} is not clear in the spectrum of compound **5.9** (Figure 5.13).

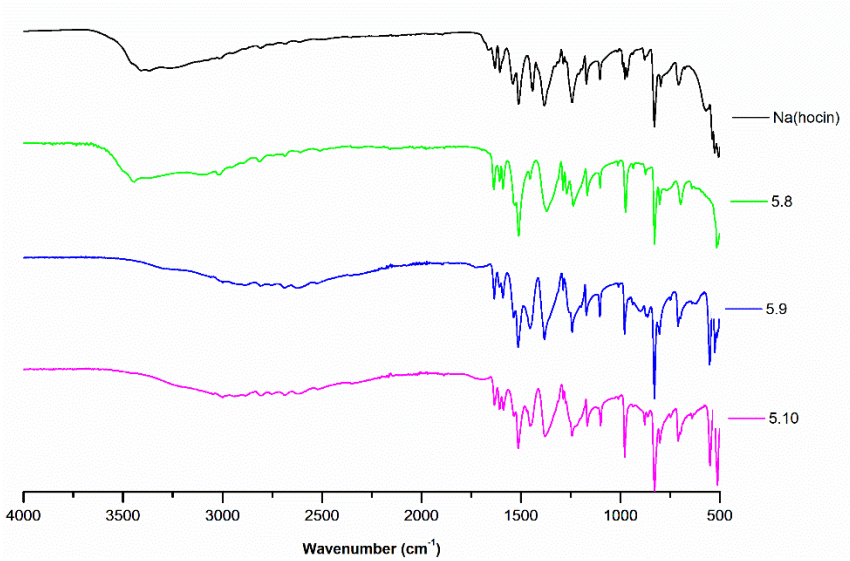


Figure 5.13: IR spectra of the $[M(4hocin)]_n$ series (M = Na, K **(5.8)**, Rb **(5.9)**, Cs **(5.10)**).

The IR spectra of all complexes displayed peaks corresponding to carboxylate COO^- stretching bands in the range of 1560-1360 cm^{-1} (Figure 5.6,5.12-5.15). These peaks included both asymmetric stretching bands (1509 to 1556 cm^{-1}) and symmetric

stretching bands (1361-1399 cm^{-1}). Additionally, the presence of a broad band in the range of 3200-3550 cm^{-1} indicates the presence of water molecules and hydrogen-bonded alcohol O–H stretching (3400-3200 cm^{-1}) in the compounds.

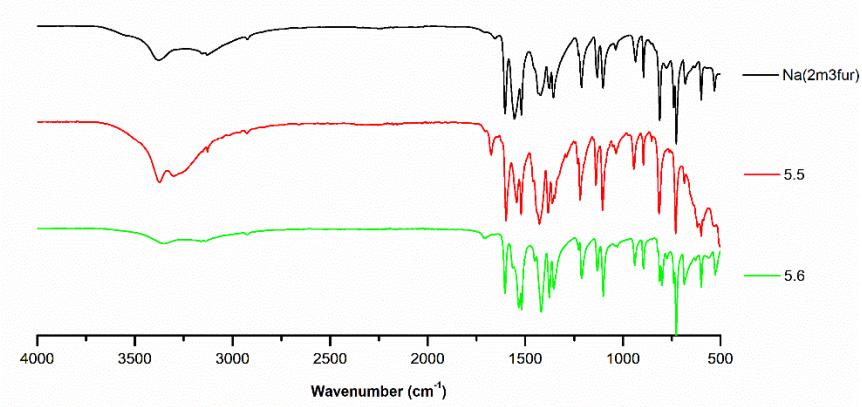


Figure 5.14: IR spectra of the $M(2m3fur)]_n$ series (M = Na, Li**(5.5)**, K **(5.6)**)

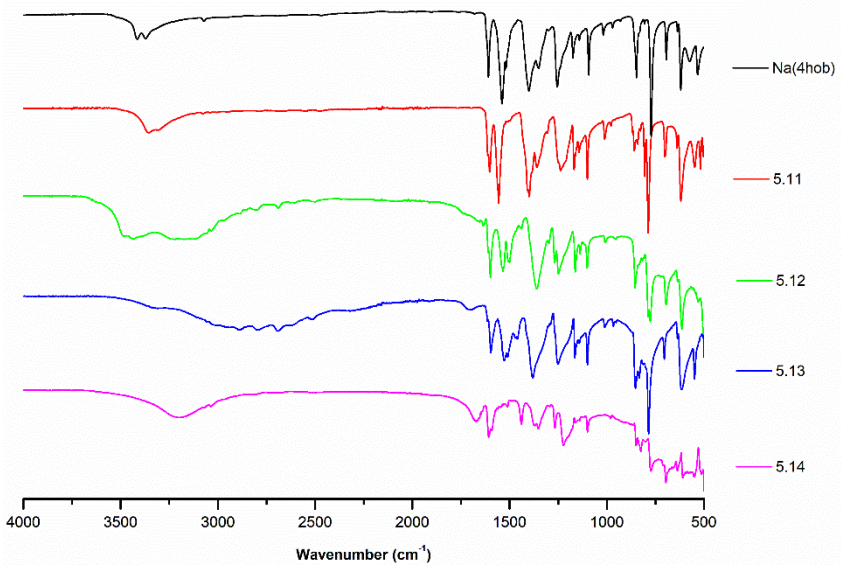


Figure 5.15: IR spectra of the $[M(4hob)]_n$ series (M = Na, Li **(5.11)**, K **(5.12)**, Rb **(5.13)**, Cs **(5.14)**).

5.2.2 X-ray crystal structures

The carboxylate binding modes observed in the complexes are shown in Figure 5.16 and a summary of the features of the structures is given in Table 5.2. The increase in the average metal-oxygen bond distances, as well as the increase in the coordination number, can be observed as the ionic radii increase from Li to Cs[20] within each series. However, **5.8** stands out as an outlier in this trend (Table 5.2).

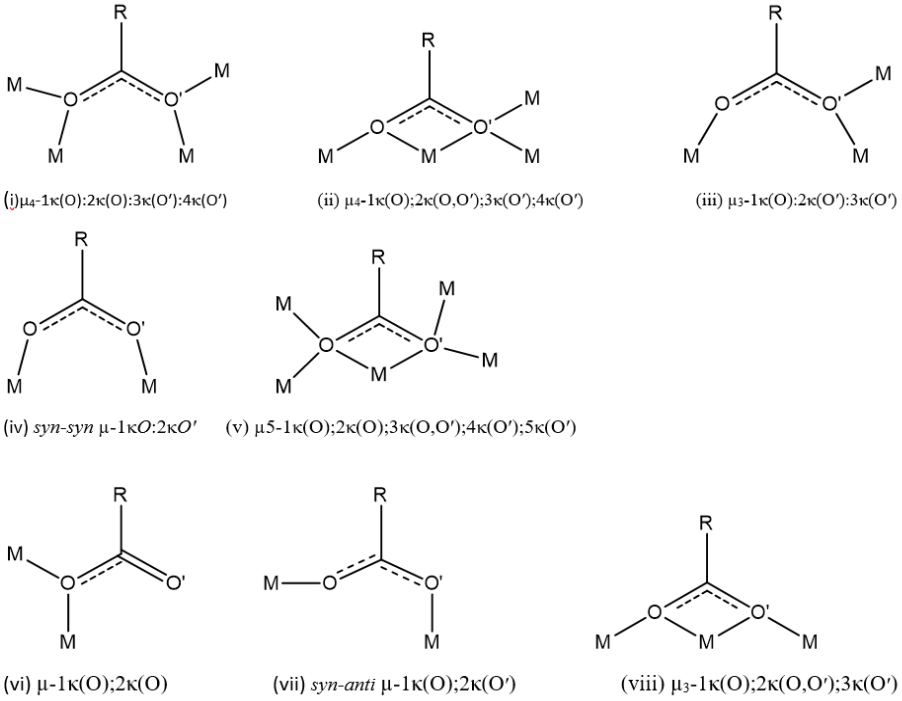


Figure 5.16: Different coordination modes observed for 3tpc, 2m3fur, 3fur, 4hocin and 4hob ions.

Table 5.2: Crystallization conditions, geometry, coordination number, carboxylate ligation and average M-O bond distance for alkali metal 3tpc, 2m3fur, 3fur, 4hocin and 4hob complexes.

Compound	M atom	Geometry	Coordination number	Ligation	Avg M-O (Å)
5.1	Li1	Tetrahedral	4	4× (i)	1.963(4)
	Li2	Tetrahedral	4	4× (i)	1.963(4)
5.2	K1	Irregular polyhedron	5	1×(ii)[a]; 3×(ii)[b]	2.791(3)
	K2	Irregular polyhedron	5	1×(ii)[a]; 3×(ii)[b]	2.767(3)
5.3	Rb1	Distorted capped trigonal prismatic	7	3×(iii); 4×μ_4-H_2O	2.995(1)
5.4	Cs1	Cubic	8	8× (i)	3.152(1)
5.5	Li1	Tetrahedral	4	2× (iv); 1×H_2O; 2×μ_2-H_2O	1.957(2)
5.6	K1	Distorted pseudo pentagonal bipyramidal	8	1×(ii)[a];3×(v)[b];1×(ii)[b]; 2×μ_3-H_2O	2.841(4)
	K2	Distorted pseudo	6	1×(v)[a];2×(ii)[b];1×(v)[b]; 1×μ_3-H_2O	2.750(5)

		square pyramidal			
5.7	Li1	Tetrahedral	4	4× (i)	1.978(2)
5.8	K1	Distorted tricapped trigonal prismatic	9	2× (vi); 3×μ_3-H_2O; 2×μ_2-H_2O; 2×μ_2-H_2O;	2.977(1)
5.9	Rb1	Irregular polyhedron	6	4× (vii); 2× phenolic O	2.932(1)
5.10	Cs1	Irregular polyhedron	8	1×(viii)[a]; 2×(viii)[b]; 2×μ_2-H_2O; 2× phenolic O	3.349(2)
5.11	Li1	Tetrahedral	4	4× (i)	1.953(4)
5.12	K1	Square antiprismatic	8	2× (vi); 1×H_2O; 3×μ_3-H_2O; 2×μ_2-H_2O	2.912(4)
5.13	Rb1	Square antiprismatic	8	4× (i); 2×μ_2-H_2O; 2× phenolic O	3.049(5)
5.14	Cs1	Square antiprismatic	8	4× (i); 2×μ_2-H_2O; 2× phenolic O	3.217(1)

[a]Chelating, [b] Unidentate

5.2.2.1. M(3tpc) Complexes (M = Li (5.1), K (5.2), Rb (5.3), Cs (5.4))

$[Li_2(3tpc)_2]_n$ **(5.1)** crystallizes in the *Pna*2_1 space group as a two-dimensional network. There are two tetracoordinated metal atoms, each Li1 and Li2, with a tetrahedral geometry. Each lithium atom is coordinated to four μ_4-1κ(O):2κ(O):3κ(O′):4κ(O′) carboxylate oxygen atoms, namely Li1- O1, 3, 2#2, 4#4 and Li2- O2, 3#3, 1#4, 4#4. Li1 and Li2 are linked together in alternating six-member rings, forming a 1D chain produced by the bridging of five μ_4-1κ(O):2κ(O):3κ(O′):4κ(O′) carboxylate oxygen atoms (O1, O2, O4#4, O3, O4). The Li1…Li2 separation is 3.146(11) Å, and Li1#4…Li2 separation is 3.116(10) Å. The five oxygen atoms in the six membered rings have distinct coordination angles: Li1–O1–C1 (139.3(4)°), Li2–O2–C1 (115.9(3)°) Li1–O4#4–Li2 (105.6(4)°), Li1-O3-C6 (138.7(4)°) and Li2#1-O4-C6 (115.6(3)°) (Figure 5.17).

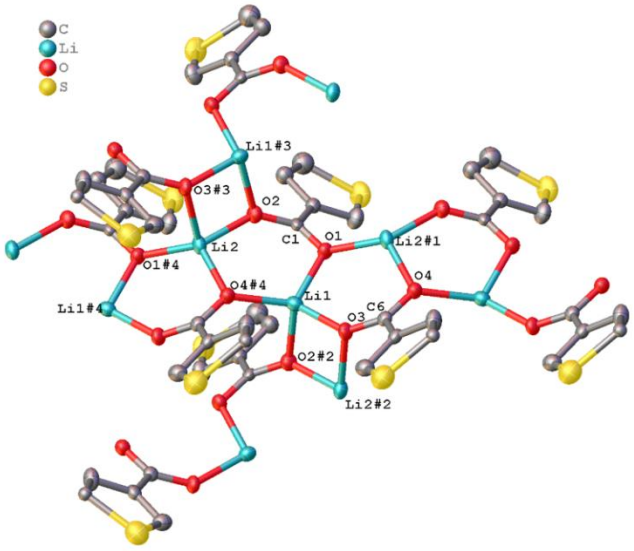


Figure 5.17: The asymmetric unit of $[Li_2(3tpc)_2]_n$ **(5.1)** (generated from single-crystal XRD data) expanded to show the Li coordination spheres. Thermal ellipsoids are drawn at the 50% probability level. Symmetry codes: $^{\#1}$ +X,1+Y,+Z; $^{\#2}$ 1/2+X,1/2-Y,+Z; $^{\#3}$ -1/2+X,1/2-Y,+Z; $^{\#4}$ +X,-1+Y, +Z.

The Li2#1-Li1-Li2-Li1#4 chain of the complex crosslinks with neighbouring chains through bridging 3tpc ligands, forming a 2D network. Li2 is connected to the Li1#3 metal atom of the neighbouring chain through oxygen atoms (O2 and O3#3), while Li1 is bound to Li2#2 through bridging oxygen atoms (O3 and O2#2). In both cases, there is a separation of 2.712(9) Å, forming four membered rings that are perpendicular to each other (Figure 5.18). The longest metal-oxygen bond in the structure is between Li2-O3#3, while the shortest bond is between Li1-O3.

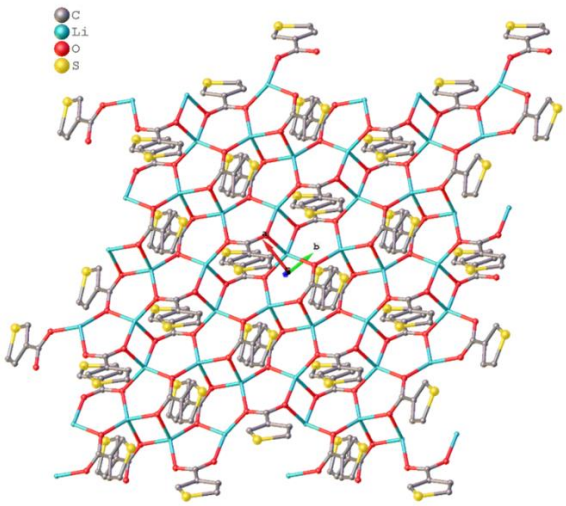


Figure 5.18: Projection along the *c*-axis showing the crystal packing of **5.1** into a 2D network.

The complex $[K_2(3tpc)_2]_n$ **(5.2)** crystallizes in the orthorhombic $Pca2_1$ space group as a 2D polymer. The asymmetric unit is composed of two potassium atoms, K1 and K2, both of which are five-coordinated. The geometry around the five coordinated K is distorted from any regular polyhedron due to the arrangements of three bridging ligands and one chelating ligand atom around the metal atoms. K1 and K2 are separated by a distance of 4.208(2) Å and are linked by two μ4-1κ(O);2κ(O,O′);3κ(O′);4κ(O′) ligands (O1,2 and O3,4) (Figure 5.19).

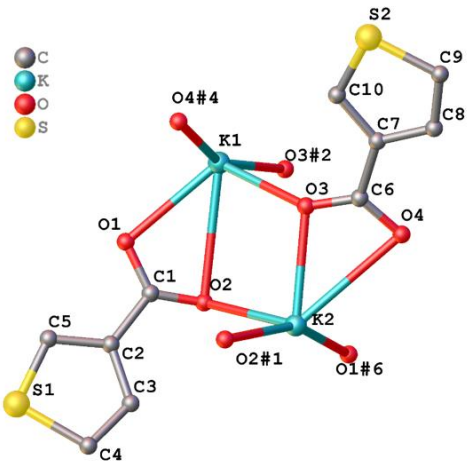


Figure 5.19: The asymmetric unit of $[K_2(3tpc)_2]_n$ **(5.2)** (generated from single-crystal XRD data) expanded to show the K coordination. Thermal ellipsoids are drawn at the 50% probability level. Symmetry codes: $^{\#1}$+X,-1+Y,+Z; $^{\#2}$+X,1+Y,+Z; $^{\#4}$1/2+X,-Y,+Z; $^{\#6}$-1/2+X,1-Y,+Z.

The former pair are chelated to K1 and bridge to K2, K2#2, and K2#3, while the latter pair are chelated to K2 and bridge to K1, K1#1, and K1#5 through carboxylate oxygen bonds (Figure 5.20). The dinuclear units are connected into a 1D chain by the *chelating, bridging* ligands between K2 and K1#6 (through O1#6) as well as between K1 and K2#4 (through O4#4), separated by distances of 4.058 (2) Å and 4.108 (2) Å, respectively. The 1D polymeric chain extends into a 2D network by the coordination of the bridging ligand (through O3 and O2#1) to the metal atoms in neighbouring chains with an inter-chain distance (K1…K1#1 and K2…K2#1) of 3.9751 (1) Å. The longest metal-oxygen bond is 3.155(7) Å between K1 and O2, involving a chelating oxygen atom. The shortest metal-oxygen bond is 2.635(6) Å between K2-O1#6, arising from a bridging oxygen atom.

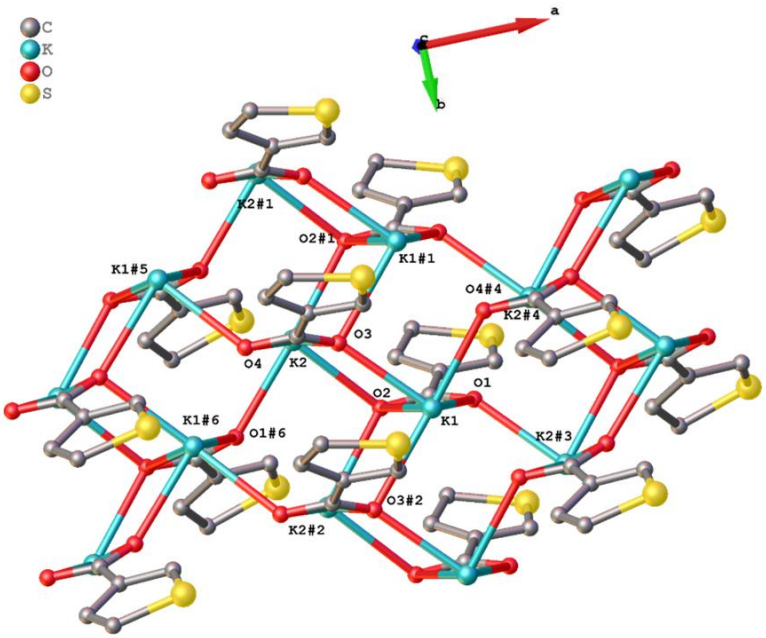


Figure 5.20: *c*-axis projection of the crystal packing of **5.2**. Symmetry codes: $^{\#1}$+X,-1+Y, +Z; $^{\#2}$+X,1+Y, +Z; $^{\#3}$1/2+X,1-Y,+Z; $^{\#4}$1/2+X,-Y,+Z; $^{\#5}$-1/2+X,-Y,+Z; $^{\#6}$-1/2+X,1-Y,+Z.

The complex $[Rb(3tpc)(H_2O)]_n$ **(5.3)** consists of mononuclear units linked to form a polymer (see below) and crystallizes in the monoclinic $P2_1/c$ space group. The seven-coordinate rubidium metal centres have distorted capped trigonal prismatic geometry. Three of the seven coordinating oxygen atoms are provided by carboxylate ligands, while the remaining four oxygen atoms are from water. In the structure (Figure 5.21), only one carboxylate binding mode is observed, with three μ_3-1κ(O):2κ(O′):3κ(O′) carboxylates coordinating through the oxygen atoms O1, O1#2, and O2#6. The four oxygen atoms in the ligated water molecules are O3, O3#4, O3#7, and O3#8, with each water oxygen bound to four rubidium atoms. Specifically, O3 binds to Rb1, Rb1#1, Rb1#2 and Rb1#7. μ_4-aqua ligands are rare but known.[21–24] Compound **5.3** forms a one-dimensional (1D) polymer *via* bridged Rb1#7…Rb1…Rb1#1 chains. The separation between the Rb metal centres is Rb1…Rb1#1 (5.1213(12) Å), and Rb1#7…Rb1 (4.8220(13) Å), respectively, with Rb1#7…Rb1…Rb1#1 at an angle of 51.910(19)°.

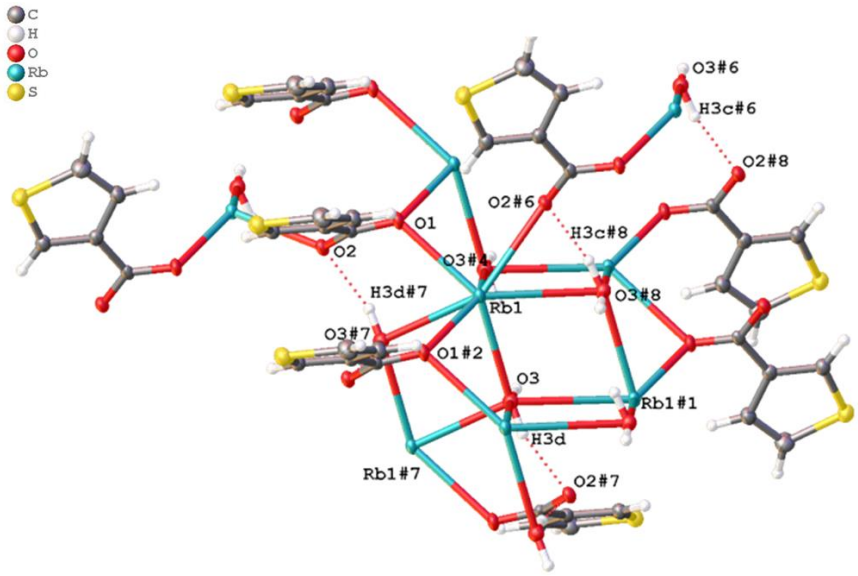


Figure 5.21: The immediate coordination environment around Rb metal atom in $[Rb(3tpc)(H_2O)]_n$ **(5.3)** generated from single-crystal XRD data. Carbon atoms are shown in grey. Thermal ellipsoids are drawn at the 50% probability level. Symmetry codes: $^{\#1}$1-X,1/2+Y,3/2-Z; $^{\#2}$+X,1+Y,+Z; $^{\#4}$+X,-1+Y,+Z; $^{\#6}$+X,1/2-Y,1/2+Z; $^{\#7}$1-X,2-Y,1-Z; $^{\#8}$1-X,-1/2+Y,3/2-Z.

The longest Rb–O bond is from a water oxygen, Rb1–O3#8 (3.278(3) Å), and the shortest bond is for a bridging Rb1–O1 (2.828(2) Å). The coordinated water oxygens O3 and O3#4 appear to connect the wave-like 1D polymers into a two-dimensional (2D) chain (Figure 5.22). All four-water oxygen atoms found in the Rb coordination environment are involved in hydrogen bonding to carboxylate-O (Figure 5.21, Table 5.3), forming an extensive network of hydrogen bonding and further linking the 2D network together**.**

Table 5.3: Hydrogen bonding Parameters [d/Å and </°] for compounds $[Rb(3tpc)(H_2O)]$ **(5.3)**.

D-H…A	**d(D-H)**	**d(H…A)**	**d(D…A)**	**<(DHA)**
O3#7-H3d#7…O2	0.8701(17)	2.026(17)	2.861(3)	160.46(5)
O3-H3d…O2#7	0.8701(17)	2.026(17)	2.861(3)	160.46(5)

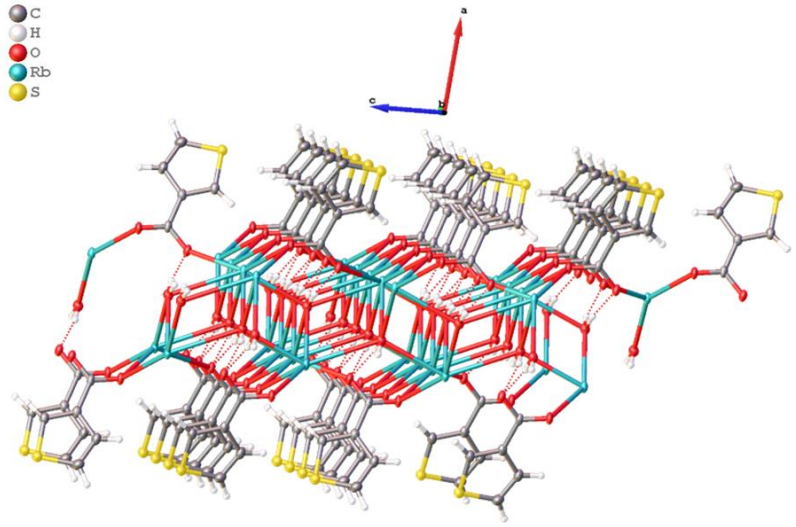


Figure 5.22: Projection along the *b*-axis of **5.3** showing the 2D network.

The polymeric complex $[Cs\{H(3tpc)_2\}]_n$ **(5.4)** crystallises in the space group *C*2/*c*. Although the reaction stoichiometry was intentionally maintained at 1:1 Cs:3tpcH to avoid the incorporation of excess unreacted proligand in the structure, only partial deprotonation of the carboxylic acid group occurred. As a result, a hydrogen atom is symmetrically shared between two carboxylate groups, making a $(HL_2)^-$ ligand. The Cs atom is eight-coordinate with cubic geometry. In the asymmetric unit, the ligand bridges Cs1 and Cs1#2 *via* O1, and the only binding mode observed for the structure is μ_4-1κ(O):2κ(O):3κ(O′):4κ(O′). Even though the crystal structure of **5.4** does not indicate the presence of either coordinated or lattice water molecules, TGA of the bulk sample revealed the presence of 0.5 water molecules.

The observed partial deprotonation results in both the Cs^+ cation and the O–H hydrogen atom being located on crystallographic inversion centres. In the asymmetric unit, both entities carry an effective charge of 0.5+, effectively counterbalancing the negative charge of the $3tpc^-$ anion. The oxygen atoms of the carboxylate groups from the two ligands are involved in forming symmetrical bonds with the hydrogen atom located on the inversion centre (Figure 5.23). This results in O–H bond lengths of 1.232(4) Å which are longer than those of a typical O–H covalent bond (0.97 Å)[25] but shorter compared to the lengths observed in O..H hydrogen bond interactions. The symmetrical hydrogen bond that is observed is commonly accompanied by a significantly short O...O distance (2.460 Å here). The coordinated O from the $3tpc^-$ anion bridges the 1D polymers, forming a two-dimensional (2D) chain (Figure 5.24).

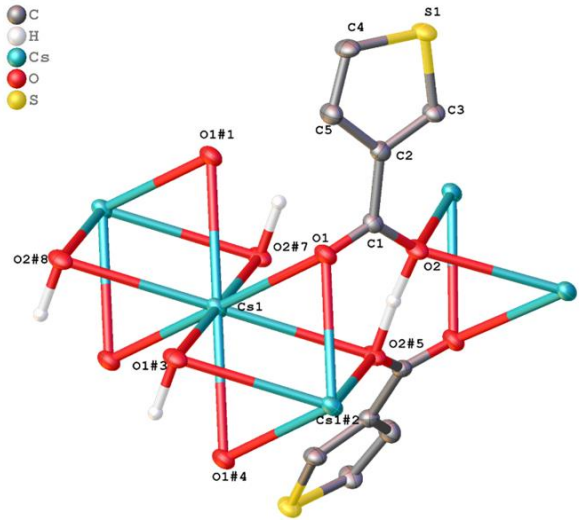


Figure 5.23: The asymmetric unit of $[Cs\{H(3tpc)_2\}]_n$ **(5.4)** (generated from single-crystal XRD data) expanded to illustrate the Cs coordination, highlighting the presence of a centrosymmetric hydrogen atom located between the two carboxylate groups. Thermal ellipsoids are drawn at the 50% probability level. Symmetry codes: $^{\#1}$+X,1+Y,+Z; $^{\#2}$+X,-1+Y,+Z; $^{\#3}$1-X,2-Y,1-Z; $^{\#4}$1-X,1-Y,1-Z; $^{\#5}$1-X,+Y,1/2-Z; $^{\#7}$1-X,1+Y,1/2-Z; $^{\#8}$+X,2-Y,1/2+Z.

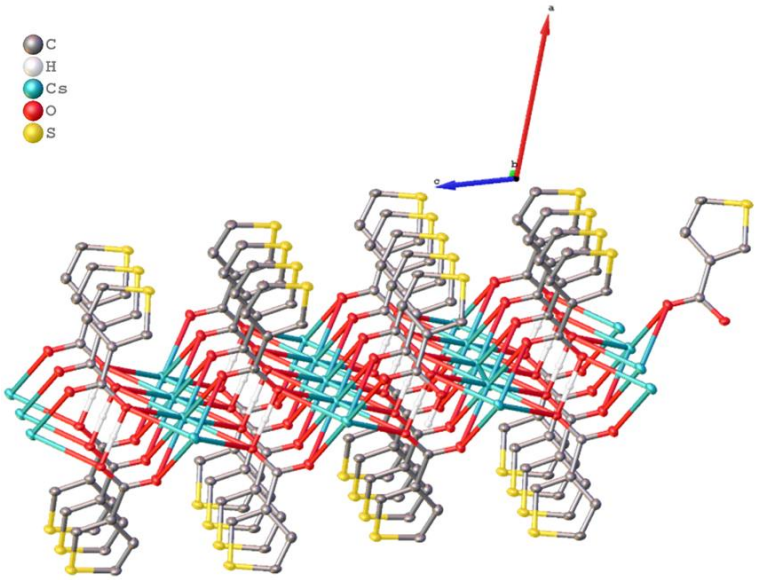


Figure 5.24: The crystal packing of **5.4** is shown in a *b*-axis projection. The hydrogen atoms except for those forming symmetrical hydrogen bonds have been omitted for clarity.

Despite multiple attempts to refine the hydrogen atom as disordered, appearing on either side of the inversion centre, it consistently reverted back to the inversion centre. Determining the precise location of a hydrogen atom solely based on X-ray diffraction

data presents a challenge. Nonetheless, by examining the distance between oxygen atoms and analyzing the hydrogen atom behaviour during refinement, we have confidence in its location. Therefore, we can conclude that only partial deprotonation of 3tpcH occurs in **5.4**. Table 5.4 and 5.5 provide detailed information regarding bond distances and angles.

Table 5.4: Selected bond lengths and M…M distances (Å) for $[M(3tpc)]_n$ series (M = Li **(5.1)**, K **(5.2)**, Rb **(5.3)**, Cs **(5.4)**).

5.1		**5.2**		**5.3**		**5.4**	
Li1- O1	1.958(8)	K1-O1	2.730(6)	Rb1-O1	2.828(2)	Cs1-O1	3.025(4)
Li1-O3	1.924(8)	K1-O2	3.155(7)	Rb1-O3	3.000(2)	Cs1-O1#3	3.025(4)
Li1-O4#1	1.982(8)	K1-O3	2.662(6)	Rb1-O1#2	2.846(2)	Cs1-O1#1	3.128(4)
Li1-O2#2	1.989(8)	K1-O4#4	2.662(6)	Rb1-O2#6	2.920(2)	Cs1-O1#4	3.128(3)
Li2-O2	1.934(8)	K1-O3#2	2.744(6)	Rb1-O3#8	3.278(3)	Cs1-O2#5	3.304(3)
Li2-O4#4	1.966(8)	K2-O2	2.688(6)	Rb1-O3#4	3.043(2)	Cs1-O2#8	3.304(3)
Li2-O3#3	2.004(8)	K2-O3	2.673(6)	Rb1-O3#7	3.049(3)	Cs1-O2#7	3.151(3)
Li2-O1#4	1.947(8)	K2-O4	3.117(6)	Rb1…Rb1#1	5.1213(12)	Cs1-O2#6	3.151(3)
Li1…Li2	3.146(11)	K2-O2#1	2.722(5)	Rb1#7…Rb1	4.8220(13)	Cs1…Cs1#2	3.962(8)
Li1…Li2#1	3.116(10)	K2-O1#6	2.635(6)				
Li2…Li1#4	3.116(10)	K1…K2	4.208(2)				
Li1…Li2#2	2.712(9)	K1…K2#4	4.108(2)				
Li2…Li1#3	2.712(9)	K2…K1#6	4.058(2)				
		K1…K1#1	3.9751(1)				
		K2…K2#1	3.9751(1)				

Table 5.5: Selected bond angles (°) for $[M(3tpc)]_n$ series (M = Li **(5.1)**, K **(5.2)**, Rb **(5.3)**.

5.1		**5.2**		**5.3**	
Li1-O1-C1	139.3(4)	K1#6…K2…K1	85.85(3)	Rb1#7…Rb1…Rb1#1	51.910(19)
Li2-O2-C1	115.9(3)	K2…K1…K2#4	85.15(2)	O2#8-Rb1-O3#4	71.00(6)
Li1-O4#4-Li2	105.6(4)			O3#8-Rb1-O3	71.52(6)
Li1-O3-C6	138.7(4)°			O3#8-Rb1-O3#4	71.00(6)
Li2#1-O4-C6	115.6(3)°			O3#8-Rb1-O3#7	133.11(8)
				O3-Rb1-O3#7	74.28(7)
				O3-Rb1-O3#4	80.89(6)
				O3#7-Rb1-O3#4	74.74(7)

5.2.2.2. M(2m3fur) Complexes (M = Li (5.5), K (5.6))

The dinuclear unit of $[Li_2(2m3fur)_2(H_2O)_3]$ **(5.5)** consists of two, tetra coordinated lithium metal centres, and crystallizes in the orthorhombic *Pbcn* space group. The stereochemistry around each metal is tetrahedral. (Figure 5.25).

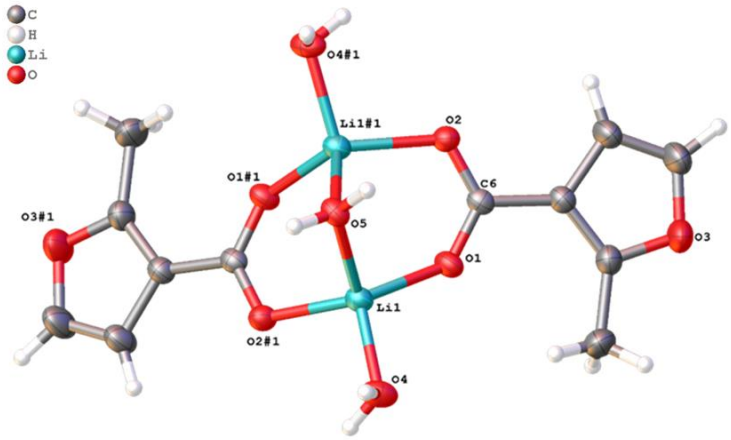


Figure 5.25: Molecular diagram of the dinuclear $[Li_2(2m3fur)_2(H_2O)_3]$ (**5.5**), generated from single-crystal XRD data. Thermal ellipsoids are drawn at the 50% probability level. Symmetry code: $^{\#1}$1-X,+Y,1/2-Z.

The complex **5.5** contains two *syn-syn* μ-1κ*O*:2κ*O′* carboxylate ligands (O(1,2) and symmetry-related O(1#1,2#1) and three coordinated water molecules (O4,O4#1,O5). The Li1…Li1#1 separation measured is 2.758(8) Å. The shortest Li-O bond is formed by the ligated water molecules O4 and its symmetry equivalent O4#1 (1.893(3) Å), while the longest bond is Li1-O5 (2.034(3) Å) of the bridging water molecule. The bridging oxygen atoms of the carboxylate ligands form an angle of 123.49(14)° at O1-Li1-O2#1 (and the symmetry equivalent O1#1-Li1-O2). The O5 oxygen atom from a coordinated water molecule bridges the two metal atoms of the dinuclear complex, forming a Li1-O5-Li1#1 angle of 85.41(15)°. The angle between the bound water molecules and the metal is *cisoid* for O4-Li-O5 and its symmetry equivalent, O4#1-Li1#1-O5 (116.51(13)°).

The two-dimensional polymer $[K_2(2m3fur)_2(H_2O)]_n$ **(5.6)** crystallizes in the monoclinic $P2_1/c$ space group. Despite the crystal structure being monohydrate, thermal analysis of the bulk precipitate indicated the presence of an extra water molecule. The asymmetric unit of the compound contains two distinct potassium metal centres. K1 is eight-coordinated; but it can be considered as pseudo seven coordinated if the carboxylate takes one coordinated site, resulting in a distorted pseudo-pentagonal bipyramidal stereochemistry. Thus, O4 and a chelating carboxylate are in axial positions, with an O4-K1-C7#5 angle of 168.53 (4)°, while O1, O1#5, O2#4, O7#2 and O7#6 are in equatorial positions. The six-coordinated K2 can be regarded as distorted pseudo-square pyramidal if the carboxylate is considered to occupy one coordination position. In this case, four

basal oxygen atoms (O2#3,4#1,5,7) form a square plane, while the carboxylate is in the axial position.

The carboxylate ligand binds in two unique modes, μ_5-1κ(O);2κ(O);3κ(O,O′);4κ(O′);5κ(O′) and μ_4-1κ(O);2κ(O);3κ(O,O′);4κ(O′). Eight coordinated K1 is ligated by two chelating oxygen atoms (O4#5,5#5) of a μ_4-1κ(O);2κ(O);3κ(O,O′);4κ(O′) linked carboxylate, bridging oxygen atoms (O1, O1#5, O2#4) of three μ_5-1κ(O);2κ(O);3κ(O,O′);4κ(O′);5κ(O′), one bridging oxygen atom (O4) of a μ_4-1κ(O);2κ(O);3κ(O,O′);4κ(O′) and two ligated water oxygen atoms (O7#2,7#6). K2 is surrounded by a μ_5-1κ(O);2κ(O);3κ(O,O′);4κ(O′);5κ(O′) chelate (O1#1,2#1), two bridging oxygen atoms from a μ_4-1κ(O);2κ(O);3κ(O,O′);4κ(O′) (O5,O4#1) ligand, one bridging oxygen atom from μ_5-1κ(O);2κ(O);3κ(O,O′);4κ(O′);5κ(O′) (O2#3) bridges and one ligated water oxygen atom (O7) resulting in a 6-coordinate metal atom (Figure 5.26).

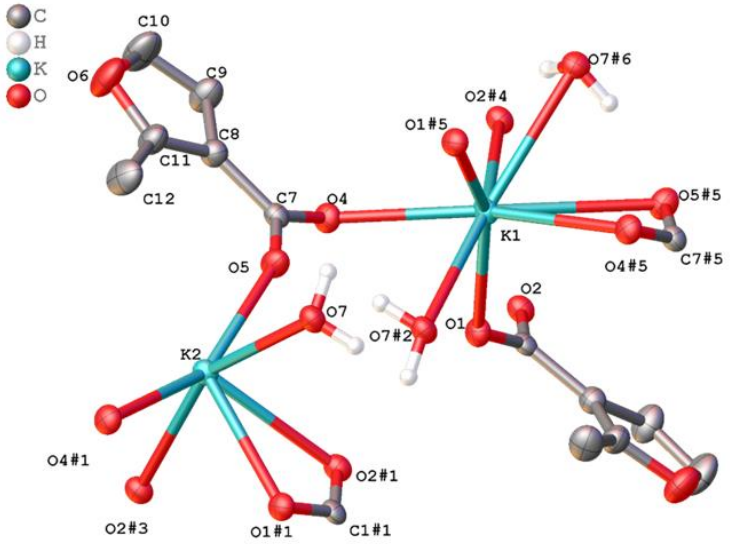


Figure 5.26: The expanded asymmetric unit of $[K_2(2m3fur)_2(H_2O)]_n$ **(5.6)** (generated from single-crystal XRD data) expanded to show the K1 and K2 coordination sphere. Thermal ellipsoids are drawn at the 50% probability level. Symmetry codes: #1 +X,3/2-Y,-1/2+Z; #2 1-X,1-Y,1-Z; #3 1-X,1/2+Y,3/2-Z; #4 1-X,1-Y,2-Z; #5 1-X,-1/2+Y,3/2-Z; #6 +X,1/2-Y,1/2+Z.

The repeating asymmetric units in the one-dimensional polymeric chain are oriented in opposite directions with a slight wave. The propagation of the complex into a 1D polymer occurs through bridged K2…K1…K2#7…K1#7…K2#8 chains, and four-membered rings of K1–O4–K2#7–O2#4 are formed between the adjacent asymmetric units in the 1D polymeric chain. Adjacent metal centres in the **5.6** compounds have

K2…K1 separations of 6.1085(12) Å and K1…K2#7 of 3.6743(8) Å. The average K–O bond lengths observed in **5.6** are as follows: K1 with a bond length of 2.841 Å, and K2 with a bond length of 2.750 Å. The longer bond length observed for K1 can be attributed to its higher coordination number. The K–O bond distances vary within the structure, ranging from the shortest bond involving bridging K2-O5 (2.6548(12) Å) to the longest bond involving chelating K1-O5#5 (3.0462(13) Å). The latter bond length is consistent with K1 being the eight coordinated metal centre in **5.6**.

The adjacent polymeric chains are oriented in opposite directions, and they further extend to form a 2D network through the bridging of the water-oxygen atoms, as well as the carboxylate oxygen, from within the chain to the neighbouring chain (Figure 5.27).

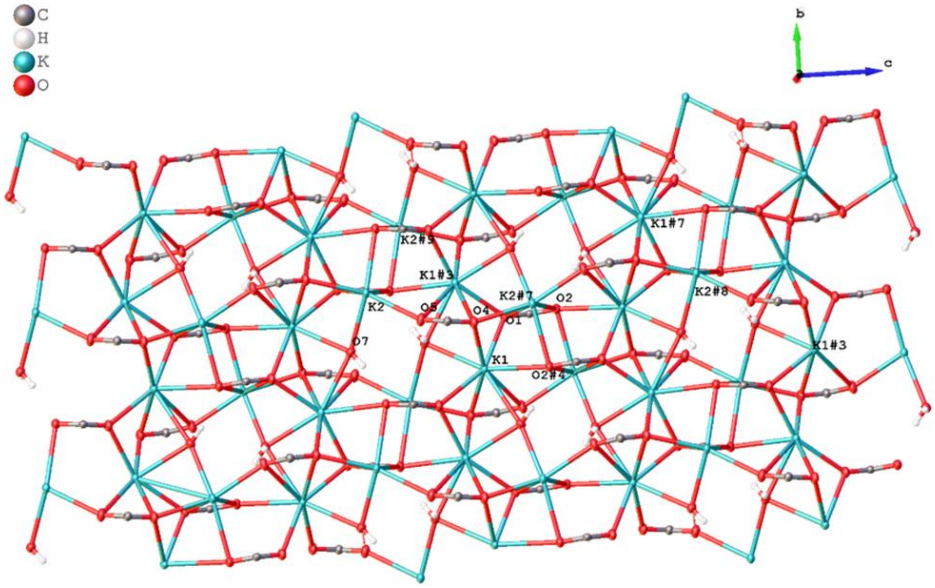


Figure 5.27: A *a*-axis projection of the crystal packing of **5.6.** (2-methyl-3-furan rings have been omitted for clarity). Symmetry codes: $^{\#3}$ 1-X,1/2+Y,3/2-Z; $^{\#4}$ 1-X,1-Y,2-Z; $^{\#7}$ +X, 3/2-Y, 1/2+Z; $^{\#8}$ +X, +Y, 1+Z; $^{\#9}$ 1-X, 2-Y, 1-Z.

Tables 5.6 and 5.7 respectively show the bond distances and bond angles of the individual metal centres to their surrounding oxygen atoms in the $[M(2m3fur)]_n$ series (M = Li, K).

Table 5.6: Selected bond lengths and M…M distances (Å) for $[M(2m3fur)]_n$ series (M = Li **(5.5)**, K **(5.6)**).

5.5	**5.6**	**5.6 (cont.)**

Atoms	Bond Lengths	Atoms	Bond Lengths	Atoms	Bond Lengths
Li1- O1	1.910(3)	K1-O1	2.7019(12)	K2-O7	2.6942(12)
Li1-O4	1.893(3)	K1-O4	2.7397(12)	K2-O5	2.6548(12)
Li1-O5	2.034(3)	K1-O7#2	2.8308(12)	K2-O1#1	2.8213(13)
Li1-O2#1	1.992(3)	K1-O1#5	2.7025(12)	K2-O2#1	2.8517(14)
Li1…Li1#1	2.758(5)	K1-O4#5	2.8618(12)	K2-O4#1	2.6833(12)
		K1-O5#5	3.0462(13)	K2-O2#3	2.7962(12)
		K1-O7#6	2.8843(12)	K1…K2	6.1085(12)
		K1-O2#4	2.9599(13)	K1…K2#7	3.6743(8)

Table 5.7: Selected bond angles (°) for $[M(2m3fur)]_n$ series (M = Li **(5.5)**, K **(5.6)**).

5.5		**5.6**	
O1-Li1-O2#1	123.49(14)	O4#5-C7#5-O5#5	124.09(14)
O1#1-Li1#1-O2	123.49(14)	O1#1-C1#1-O2#1	124.46(14)
Li1-O5-Li1#1	85.41(15)	O7#2-K1-O7#6	148.20(3)
O4-Li-O5	116.51(13)	O4-C7-O5	124.09(14)
O4#1-Li1#1-O5	116.51(13)	O4-K1-C7#5	168.53(4)
O1-C6-O2	123.14(12)	O7-K2-O2#3	152.91(4)
		O5-K2-O4#1	153.67(4)

5.2.2.3. 2D polymeric chain of the $[Li(3fur)]_n$ (5.7) complex

The complex $[Li(3fur)]_n$ **(5.7)** forms a 2D polymeric sheet with tetracoordinated lithium ions and crystallizes in the monoclinic space group $P2_1/c$ with a tetrahedral stereochemistry. Four μ_4 -1κ(O);2κ(O);3κ(O′);4κ(O′) oxygen atoms (O1, O1#3, O2#4, O2#5) complete the coordination sphere around the metal centre (Figure 5.28.).

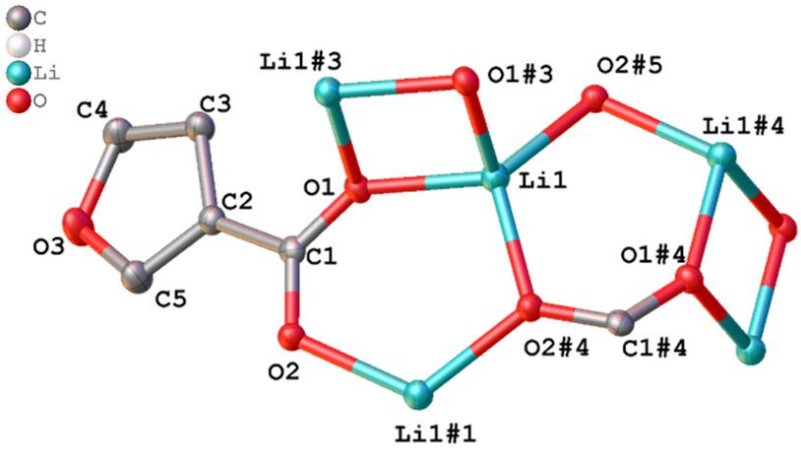


Figure 5.28: The asymmetric unit of $[Li(3fur)]_n$ **(5.7)** (generated from single-crystal XRD data) expanded to show the Li coordination sphere. Thermal ellipsoids are drawn at the

50% probability level. Symmetry codes: #1 1-X,1/2+Y,3/2-Z; #2 +X,1+Y,+Z; #3 1-X,-Y,1-Z; #4 1-X,-1/2+Y,3/2-Z; #5 +X,-1+Y,+Z.

The Li–O bond lengths range from 1.935(3) Å (Li1-O1) to 2.025(3) Å (Li1-O1#3) (Table 5.8) with an average bond length of 1.978 Å. The two unique, alternating six-membered rings formed by the five-bridging oxygen atoms, O1, O2, O2#4, O1#4, and O2#5, form the backbone of the 1D polymeric chain, where Li1#1…Li1…Li1#4 forms an angle of 114.93 (16)° with Li1-Li#1 and Li1-Li1#4 separations of 3.155(3) Å. The successive 1D chains are oriented in opposite directions, thus constructing two types of chains. The carboxylate oxygen atoms, O1, O1#3 of the carboxylate μ_4-1κ(O);2κ(O);3κ(O′);4κ(O′) ligand bridge lithium metals of neighbouring chains, leading to the formation of a two-dimensional (2D) network with a Li1-Li#3 distance of 2.758(5) Å (Figure 5.29).

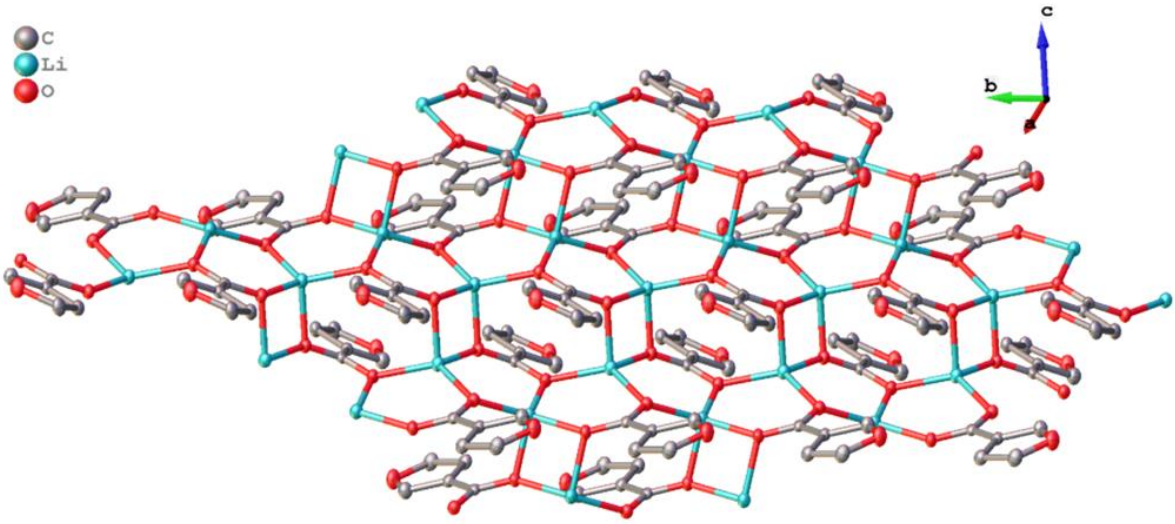


Figure 5.29: Crystal packing of **5.7** into a **2D** network (Aromatic H atoms are omitted for the clarity).

Table 5.8: Selected bond lengths and Li…Li distances (Å) for $[Li(3fur)]_n$ (**5.7**).

Li1- O1	1.935(3)
Li1-O1#3	2.025(3)
Li1-O2#5	1.996(3)
Li1-O2#4	1.954(3)
Li1…Li1#1	3.155(3)
Li1…Li1#4	3.155(3)
Li1…Li1#3	2.758(5)

Table 5.9: Selected bond angles (°) for $[Li(3fur)]_n$ (**5.7**).

Li1#1…Li1…Li1#4	114.93(16)
C1-O1-Li1	141.84(12)
C1-O2-Li1#1	116.97(12)
Li1-O2#4-Li1#1	106.05(9)
Li1-O2#5-Li1#4	106.05(9)
Li1#4-O1#4-C1#4	141.84(12)

5.2.2.4. M(4hocin) Complexes (M = K (5.8), Rb (5.9), Cs (5.10))

The 2D polymeric complex $[K(4hocin)(H_2O)_3]_n$ **(5.8)** crystallises in the space group $P2_1/c$ with a distorted tricapped trigonal prismatic geometry. The nine coordinate potassium atoms are each attached to two μ-1κ(O);2κ(O) carboxylates and seven oxygen atoms from aqua ligands. The water oxygen atom O4 is bound to three potassium atoms (K1, K1#2, K1#3), while O5 and O6 are each bound to two potassium atoms, namely K1 and K1#3 and K1 and K1#1, respectively. The chain propagation exhibits a twist, with an angle of 126.48(2)° between K1#1…K1…K1#2, and the distance between K1…K1#1 is 3.9478 (7) Å. Four ligated aqua molecules link neighbouring polymeric chains that run in opposite directions, forming a 2D network through O4, O4#3, O5 and O5#3 (Figure 5.30). μ_3-H_2O coordination is known. For recent examples see references 26-28.[26–28]

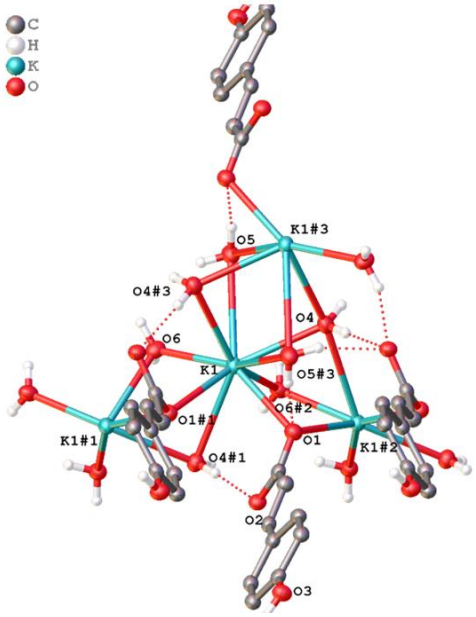
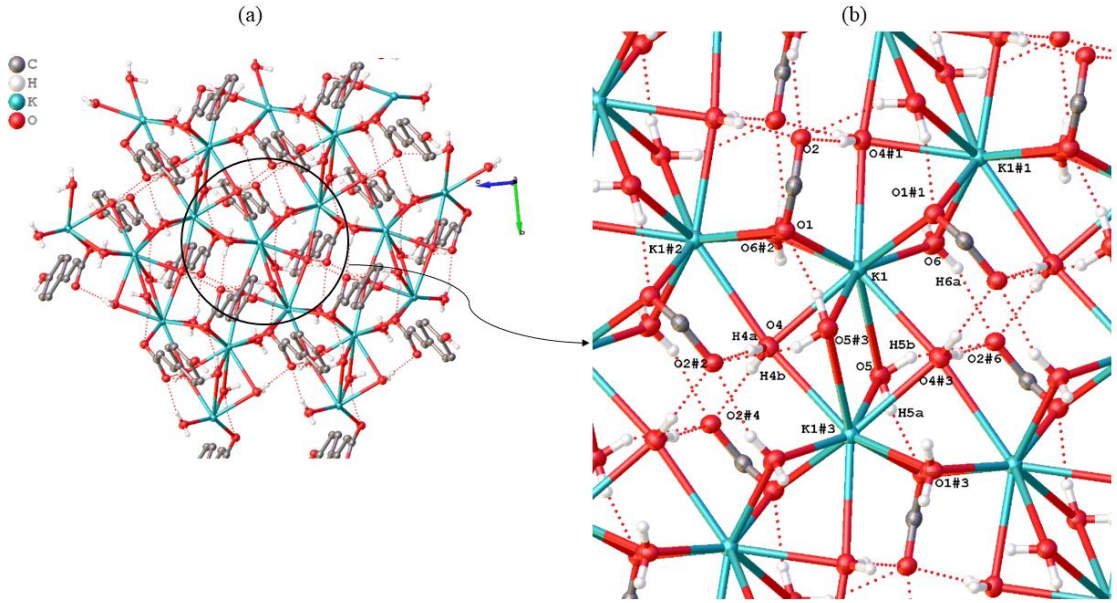


Figure 5.30: The immediate coordination environment of potassium in $[K(4hocin)(H_2O)_3]_n$ **(5.8)**, generated from single-crystal XRD data. Carbon atoms are shown in grey. Thermal ellipsoids are drawn at the 50% probability level. Hydrogen

atoms except for those forming H bonds are omitted for clarity. Symmetry codes: [#1] +X,3/2-Y,1/2+Z; [#2] +X,3/2-Y,-1/2+Z; [#3] -X,2-Y,-Z.

As summarized in Table 5.13 the longest metal-oxygen bond occurs between K1 and O5 (3.3762(14) Å), while the shortest bond is between K1 and O6 (2.7326(15) Å), both originating from ligated water molecules. The ligated water molecules form an extensive network of hydrogen bonding (Figure 5.31 and Table 5.10), along with the carboxylate oxygen atoms of the ligands, which further interconnect the adjacent 1D chains into a 2D intermolecular framework.



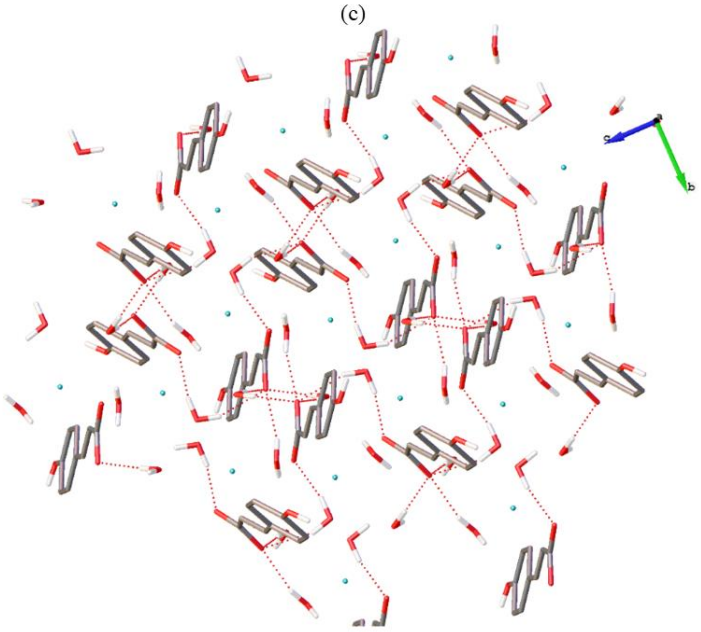


Figure 5.31: **(a).** A projection along the *a*-axis of **5.8. (b).** H bonding interactions in $[K(4hocin)(H_2O)]_3]_n$ **(c).** The hydrogen-bonded network formed by the 4hocin and water molecules (K–O coordination bonds are omitted for clarity). Symmetry codes: $^{\#1}$ +X,3/2-Y,1/2+Z; $^{\#2}$ +X,3/2-Y,-1/2+Z; $^{\#3}$ -X,2-Y,-Z; $^{\#4}$ -X,-1/2+Y,1/2-Z; $^{\#5}$ -X,-1/2+Y,-1/2-Z; $^{\#6}$ -X, 1/2+Y,1/2-Z.

Table 5.10: Hydrogen bonding parameters [d/Å and </°] for the compound $[K(4hocin)(H_2O)]_3]_n$ **(5.8)**

D-H…A	**d(D-H)**	**d(H…A)**	**d(D…A)**	**<(DHA)**
O5-H5a…O1#3	0.8503(12)	1.908(13)	2.730(18)	162.41(9)
O3-H3d…O2#7	0.8701(17)	2.065(12)	2.861(3)	160.46(5)
O5-H5b…O2#6	0.8499(13)	2.065(12)	2.8636(18)	156.38(9)
O6-H6a…O2#6	0.8500(13)	2.0067(12)	2.7491(18)	145.41(9)
O4-H4b…O2#4	0.856(16)	2.002(17)	2.8539(18)	174(2)
O4-H4a…O2#2	0.853(17)	1.981(17)	2.8331(18)	176(3)

The three-dimensional polymeric complex $[Rb\{H(4hocin)_2\}]_n \cdot nH_2O$ **(5.9)** crystallizes in the space group *C*2/*c*. Similar to compound **5.4**, **5.9** exhibits only partial deprotonation of the ligand despite utilizing equal amounts of metal salt and ligand. The hydrogen atom exhibits centrosymmetric sharing between the carboxylate groups, making a $[HL_2]^-$ ligand, which is reinforced by the positioning of both the Rb^+ cation and the O...H...O hydrogen atom on crystallographic inversion centres. A noticeably short

O…O distance (2.469(2) Å) and the behaviour of the hydrogen atom observed during refinement further support this centrosymmetric arrangement and confirm the location of this hydrogen atom.

The asymmetric unit of **5.9** consists of a single type of Rb atom and is expanded to depict the complete Rb coordination sphere in Figure 5.32. The arrangement of the 6-coordinated Rb metal centre is distorted from any regular polyhedron. Contrary to **5.4**, in the asymmetric unit of **5.9**, the ligand is connected to Rb1 by the carboxylate oxygen atom (O1), which also binds to an H atom on the inversion centre. Within the structure, the water molecule functions as a focus for crystallization through hydrogen bonding, and it does not form coordination bonds with the rubidium centre. The coordination sphere of **5.9** consists of four bridging μ-1κ(O):2κ(O′) carboxylate-O atoms (O1, 1#5, 2#3, 2#4) and two phenolic-O atoms (O3#1 and O3#2) of the ligand.

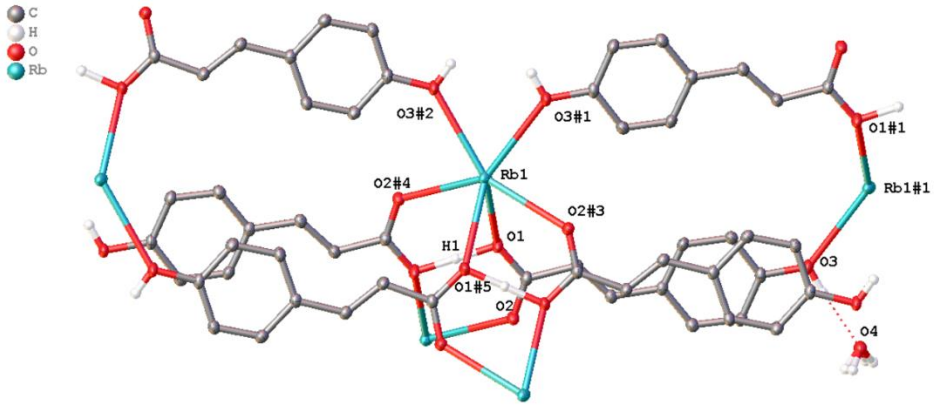


Figure 5.32: The expanded asymmetric unit of **5.9** (generated from single-crystal XRD data) reveals the coordination of Rb atoms. Carbon atoms are shown in grey. Thermal ellipsoids are drawn at the 50% probability level. H atoms of the ligand except for phenolic hydroxyl group are omitted for the clarity; H of $H(4hocin)_2^-$ is H1. Symmetry Codes: $^{\#1}$3/2-X,3/2-Y,1-Z; $^{\#2}$-1/2+X,3/2-Y,-1/2+Z; $^{\#3}$+X,1-Y,1/2+Z; $^{\#4}$1-X,1-Y,-Z; $^{\#5}$1-X,+Y,1/2-Z.

These Rb-O bond lengths vary from a shorter distance of 2.8868(12) Å for Rb1-O1 and the symmetry equivalent Rb1-O1#5, involving the bridging μ-1κ(O):2κ(O′) oxygen atoms (O1 and O1#5) to a longer distance of 2.9685(13) Å between Rb1-O2#3 and Rb1-O2#4 involving the bridging μ-1κ(O):2κ(O′) oxygen atoms (O2#3 and O2#4) (Table 5.13). The metal atoms within the 1D chains are linked together by phenolic-hydroxy groups of the 4-hydroxybenzoate ligands. The adjacent chains in the 2D network are further connected by the bridging carboxylate oxygen atoms. The hydrogen bonding

involving the phenolic-hydroxy groups and the carboxylate oxygen atoms of the ligand with the lattice water of crystallization holds the neighbouring chains of polymers together, forming an extended three-dimensional packing arrangement of the polymeric chains (Figure 5.33. and Table 5.11).

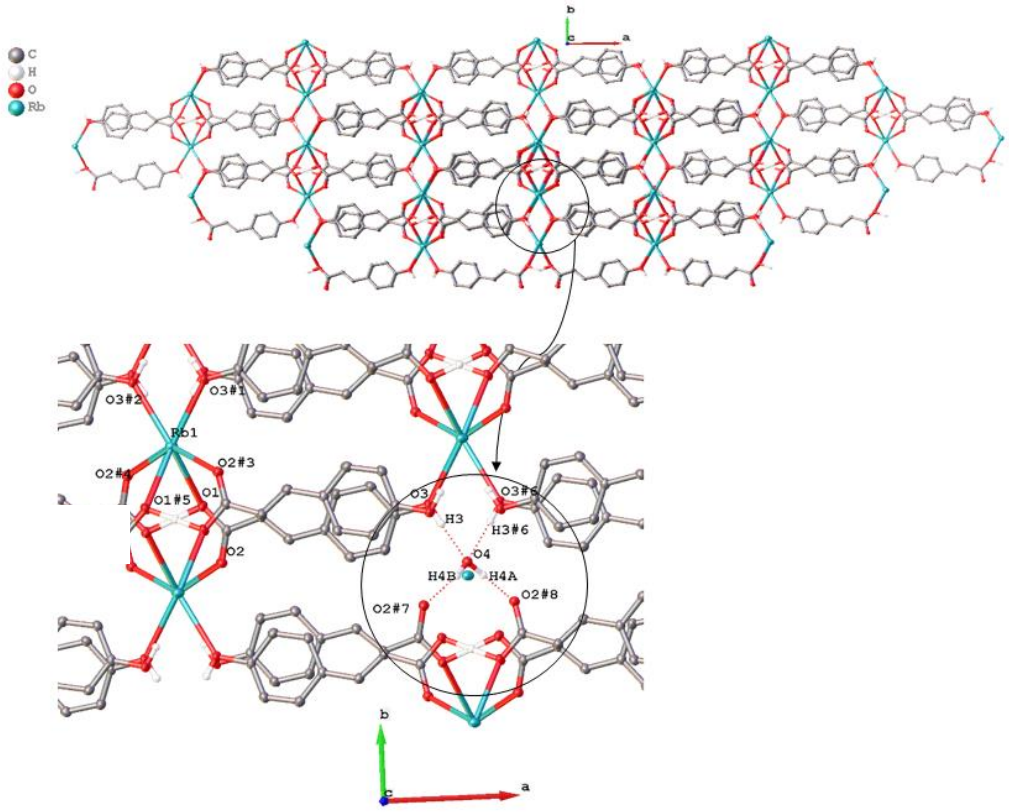


Figure 5.33: **(a).** A *c*-axis projection of the crystal packing of **5.9. (b).** An alternative view of crystal packing by omitting the Rb-O coordination to show the hydrogen-bonds forming an extended 3D packing arrangement. Symmetry Codes: $^{\#1}$ 3/2-X,3/2-Y,1-Z; $^{\#2}$ -1/2+X,3/2-Y,-1/2+Z; $^{\#3}$ +X,1-Y,1/2+Z; $^{\#4}$ 1-X,1-Y,-Z; $^{\#5}$ 1-X,+Y,1/2-Z; $^{\#6}$ 2-X,+Y,3/2-Z; $^{\#7}$ 3/2-X,1/2-Y,1-Z; $^{\#8}$ 1/2+X,1/2-Y,1/2+Z.

Table 5.11: Hydrogen bonding parameters [d/Å and </°] for the compound $[Rb\{H(4hocin)_2\}]_n.nH_2O$ **(5.9).**

D-H…A	d(D-H)	d(H…A)	d(D…A)	<(DHA)
O3-H3…O4	0.8400(12)	1.9027(14)	2.7319(18)	168.95(8)
O3#6-H3#6…O4	0.8400(12)	1.9027(14)	2.7319(18)	168.95(8)
O4-H4B…O2#7	0.850(1)	1.8812(10)	2.7139(15)	166.05(3)
O4-H4A…O2#8	0.8506(10)	1.8718(11)	2.7139(15)	170.22(4)

The X-ray crystal structure of $[Cs(4hocin)(H_2O)]_n$ **(5.10)** reveals a monoclinic crystal system with a $P2_1$ space group. The eight coordinated caesium atoms have two

bridging oxygen atoms (O1, O2#2) and two chelating oxygen atoms (O1#1, 2#1) from three μ_3-1κ(O);2κ(O,O′);3κ(O′) ligands, two water molecules (O4, O4#3), and two phenolic oxygen atoms of the ligand (O3#4, O3#5). Four oxygen atoms are close to the plane with the Cs centre, while the other four oxygen atoms sit on one side of the plane. This arrangement creates an irregular eight-coordinated polyhedron (Figure 5.34).

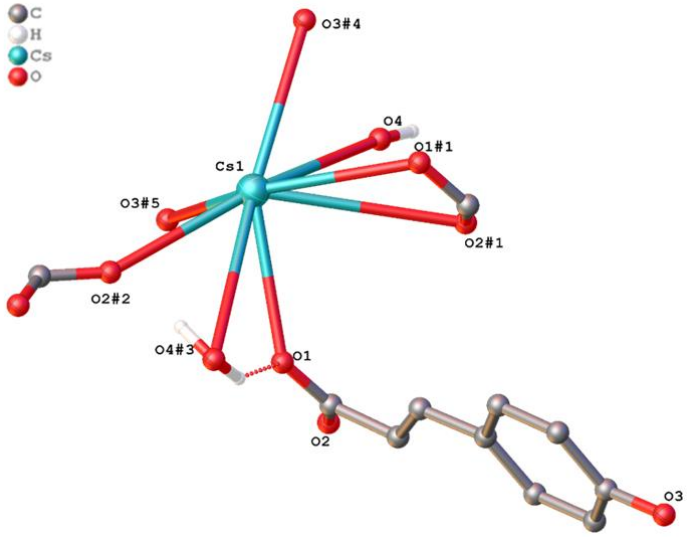


Figure 5.34: The asymmetric unit of $[Cs(4hocin)(H_2O)]_n$ **(5.10)** (generated from single-crystal XRD data) expanded to show the complete Cs coordination sphere. Carbon atoms are shown in grey. Thermal ellipsoids are drawn at the 50% probability level. Symmetry codes: $^{\#1}$1+X,+Y,+Z; $^{\#2}$-X,1/2+Y,2-Z; $^{\#3}$1-X,1/2+Y,2-Z; $^{\#4}$+X,+Y,1+Z; $^{\#5}$-1+X,+Y,-1+Z.

The Cs-O bond lengths for the bridging carboxylates are consistently shorter than their chelating counterparts (Table 5.13). The angle between the bridging water oxygen atoms O4 and O4#3, which originates from the adjacent caesium atom, has an O4-Cs1-O4#3 angle of 138.84(10)°. The carboxylate-O1,2 as well as the phenolic oxygen atom O3#5, link the metal centres into a 1D chain with a Cs1…Cs1#6 distance of 4.3870(9) Å and Cs1#1...Cs1…Cs1#6 angle of 180°. A phenolic oxygen atom, O3, bridges the adjacent metal centre in neighbouring chains, forming a 2D layer network in the *ac*-plane (Figure 20(a)). A projection along the *a*-axis (Figure 5.35(b)) illustrates the interconnection of these 2D networks by a bridging polydentate ligand (*via* O1, 2), a coordinated aqua molecule (O4), as well as hydrogen bonding interactions (Table 5.12) into an overall 3D structure.

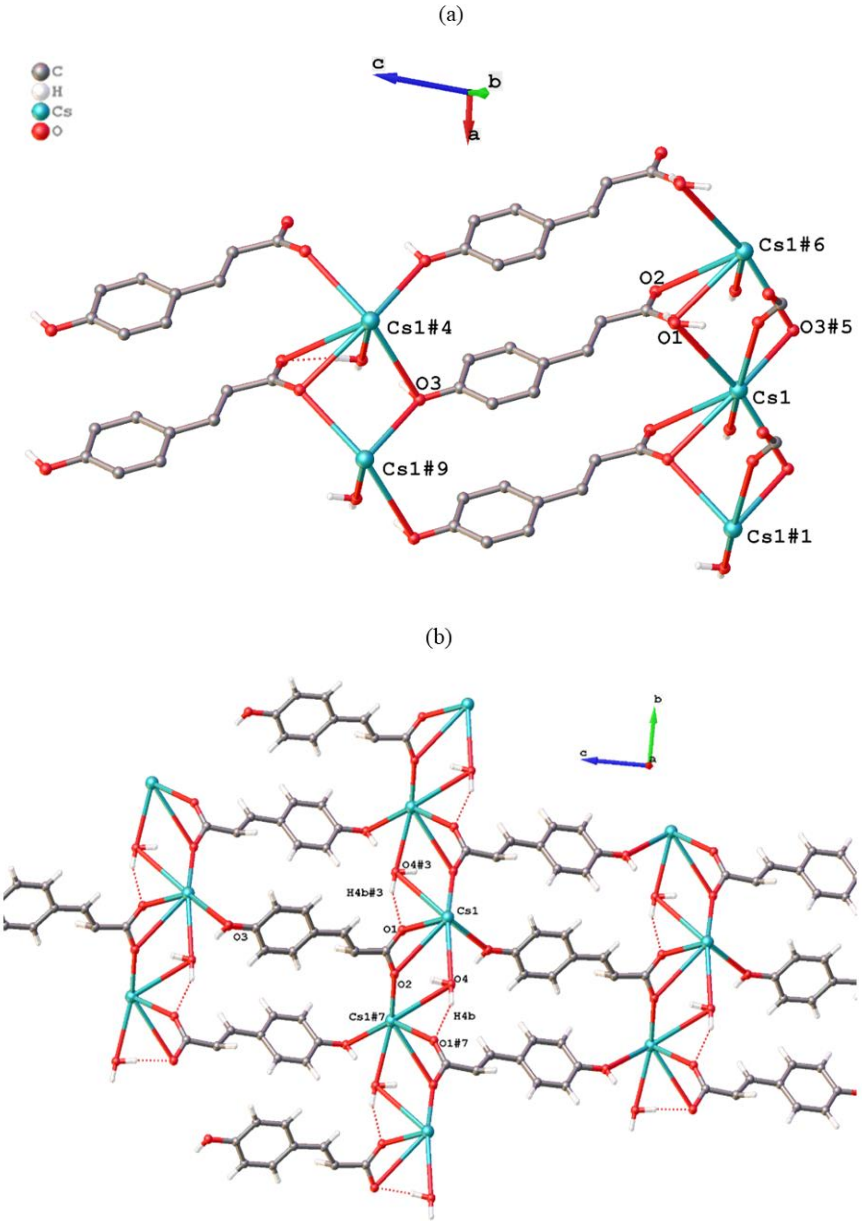


Figure 5.35: **(a).** A projection along *ac*- plane shows the formation of a 2D layer network of **5.10** (H atoms except for those forming H-bonds are omitted for clarity) **(b).** A projection along the *a*-axis of showing interaction that links the 2D networks together. Symmetry codes: $^{\#1}$1+X,+Y,+Z; $^{\#2}$-X,1/2+Y,2-Z; $^{\#3}$1-X,1/2+Y,2-Z; $^{\#4}$+X,+Y,1+Z; $^{\#5}$-1+X,+Y,-1+Z; $^{\#6}$-1+X,+Y,+Z; $^{\#7}$1-X,-1/2+Y,2-Z; $^{\#9}$1+X,+Y,1+Z.

Table 5.12: Hydrogen bonding parameters [d/Å and </°] for the compound $[Cs(4hocin)(H_2O)]_n$ **(5.10)**.

D-H…A	**d(D-H)**	**d(H…A)**	**d(D…A)**	**<(DHA)**
O4-H4b…O1#7	0.870(5)	1.923(5)	2.703(7)	148.5(4)
O4#3-H4b#3…O1	0.870(5)	1.923(5)	2.703(7)	148.5(4)

Table 5.13: Selected bond lengths and M…M distances (Å) for $[M(4hocin)]_n$ series (M = K **(5.8)**, Rb **(5.9)**, Cs **(5.10)**).

5.8		**5.9**		**5.10**	
K1-O1	2.7658(14)	Rb1-O1	2.8868(12)	Cs1-O1#1	3.138(5)
K1-O1#1	2.9157(16)	Rb1-O1#5	2.8868(12)	Cs1-O1	3.020(5)
K1-O4	2.8052(13)	Rb1-O2#3	2.9685(13)	Cs1-O2#1	3.788(6)
K1-O4#1	3.1099(14)	Rb1-O2#4	2.9685(13)	Cs1-O2#2	3.059(6)
K1-O4#3	2.9297 (13)	Rb1-O3#1	2.9396(12)	Cs1-O3#4	3.386(5)
K1-O5	3.3762(14)	Rb1-O3#2	2.9396(12)	Cs1-O3#5	3.3069(5)
K1-O5#3	3.3087(15)			Cs1-O4	3.310(5)
K1-O6	2.7326(15)			Cs1-O4#3	3.788(5)
K1-O6#1	2.8497(16)			Cs1…Cs1#6	4.3870(9)
K1…K1#1	3.9478(7)				
K1…K1#3	4.0171(9)				
O4-K1-O4#1	132.96(4)				
O4-K1-O4#3	91.10(4)				
O4#1-K1-O4#3	135.77(17)				

Table 5.14: Selected bond angles (°) for $[M(4hocin)]_n$ series (M = K **(5.8)**, Rb **(5.9)**, Cs **(5.10)**).

5.8		**5.9**		**5.10**	
K1#1…K1…K1#2	126.48(2)	O3#1-Rb1-O3#2	67.40(5)	O4-Cs1-O4#3	138.84(10)
O4-K1-O5	70.01(4)	O3-Rb1#1-O1#1	67.40(5)	O1-Cs1-O2#2	72.29(12)
O4-Ki-O5#3	61.19(4)			O3#4-Cs1-O3#5	85.48(12)
O4-K1-O6#2	73.35(4)			Cs1-O3#5-Cs1#6	85.48(12)
O4-K1-O4#1	132.96(4)			Cs1#1...Cs1…Cs1#6	180
O4-K1-O6	132.70(4)				
O4-K1-O4#3	91.10(4)				
O5-K1-O4#3	59.26(4)				
O5-K1-O6	66.60(4)				
O5-K1-O4#1	130.89(4)				
O5-K1-O6#2	84.10(4)				
O5-K1-O5#3	106.13(3)				
O6-K1-O4#3	82.61(4)				
O6-K1-O4#1	70.29(4)				
O6-K1-O6#2	84.27(4)				
O6-C1-O5#3	150.03(4)				
O4#3-C1-O4#1	135.768(17)				
O4#3-C1-O5#3	69.66(4)				
O4#3-C1-O6#2	143.32(4)				
O4#1-C1-O5#3	122.97(4)				
O4#1-K1-O6#2	69.13(4)				
O5#3-K1-O6#2	124.90(4)				

5.2.2.5. M(4hob) Complexes (M = Li (5.11), K (5.12), Rb (5.13), Cs (5.14))

The complex $[Li(4hob)]_n$ **(5.11)** crystallizes in the monoclinic $P2_1/c$ space group and exhibits similar ligand binding modes and coordination environments as the **5.7** structure (Table 5.2). Analogous to the **5.7** structure, the structure of **5.11** also forms a 1D polymeric chain through the two alternate six-membered rings involving the bridging oxygen atoms O1, O2, O2#4, O1#4, and O2#5 (Figure 5.36.).

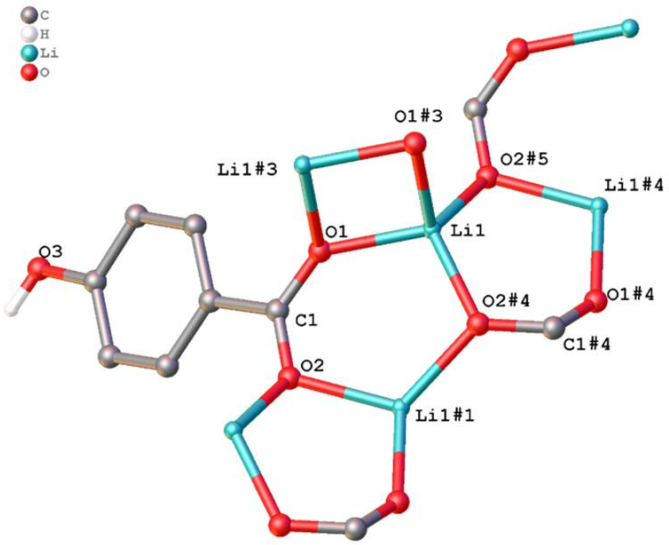


Figure 5.36: The asymmetric unit of $[Li(4hob)]_n$ **(5.11)** (generated from single-crystal XRD data) expanded to show the Li coordination sphere. Thermal ellipsoids are drawn at the 50% probability level. Symmetry codes: $^{\#1}$1-X,1/2+Y,1/2-Z; $^{\#2}$ +X,1+Y,+Z; $^{\#3}$1-X,-Y,1-Z; $^{\#4}$1-X,-1/2+Y,1/2-Z; $^{\#5}$+X,-1+Y,+Z.

In comparison, the compound **5.11** forms an angle of 109.6(4)° between Li1#1…Li1…Li1#4, with Li1…Li1#1 and Li1…Li1#4 separations of 3.086(8) Å. The shortest and longest Li-O bonds are attributed to Li1-O1 (1.921(7) Å) and Li-O1#3 (1.969(8) Å), respectively (Table 5.17). A 2D layer is formed in a similar manner to the **5.7** compound through the bridging oxygen atoms (O1, O1#3) of the μ_4-1κ(O);2κ(O);3κ(O′);4κ(O′) ligand, linking Li…Li1#3 at a distance of 2.700(14) Å (Figure 5.37). Although the crystallographic determination indicating the compound as anhydrous, elemental analysis data of the complex indicated the presence of a quarter of a water molecule.

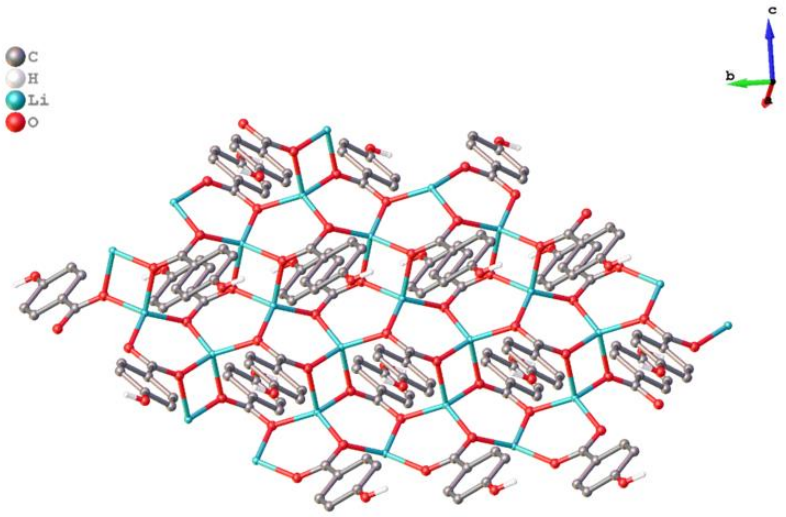


Figure 5.37: Extended diagram of $[Li(4hob)]_n$ **(5.11)** (Aromatic H atoms are omitted for clarity).

The $[K(4hob)(H_2O)_3]_n$ **(5.12)** complex forms a 2D polymeric sheet with eight coordinate potassium ions and crystallizes in the monoclinic $P2_1/c$ space group with a square antiprismatic array. A partial representation of the polymeric structure is shown in Figure 5.38. In the asymmetric unit, there is one μ_2-1κ(O):2κ(O) carboxylate bond (binding through O2) along with three ligated water molecules (O4, O5, and O6). The metal atom achieves a total coordination of eight by interacting with another μ_2-1κ(O):2κ(O) oxygen atom (O2#1) and three additional ligated water oxygen atoms (O4#2, O5#3, O5#4) from adjacent metal atoms. The structure forms a non-linear 1D polymeric chain through bridging oxygen O2, connecting K1 and K1#2 and O2#1 between K1 and K1#1 atoms (both at 3.9243(7) Å) with K1#1…K1…K1#2 at an angle of 128.53(2)°.

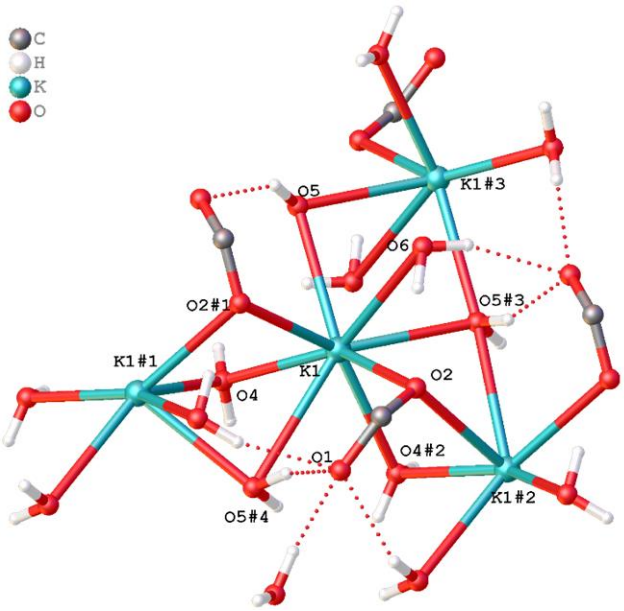


Figure 5.38: The asymmetric unit of $[K(4hob)(H_2O)_3]_n$ **(5.12)** (generated from single-crystal XRD data) expanded to show the K coordination. Carbon atoms are shown in grey. Thermal ellipsoids are drawn at the 50% probability level. Symmetry codes: #1 +X,3/2-Y,-1/2+Z; #2 +X,3/2-Y,1/2+Z; #3 2-X,2-Y,1-Z; #4 2-X,-1/2+Y,1/2-Z.

The average K-O bond length observed in complex **5.12** is 2.912(4) Å, with the shortest bond being K1-O4 (2.734(13) Å) and the longest bond being K1-O5#4 (3.172(5) Å) (Table 5.17). Both the longest and shortest bonds involve ligated aqua ligands rather than any of the bridging carboxylate oxygens. The adjacent polymeric chains connected to form a 2D network through the bridging of the water-oxygen atoms (O5, O5#3). There is a significant presence of hydrogen bonding in the system, involving the carboxylate oxygen atoms and the OH groups of all six coordinated water molecules. Figure 5.39 illustrates the hydrogen bonding pattern observed, while Table 5.15 provides the corresponding hydrogen bonding parameters. These hydrogen bonds play a crucial role in holding the neighbouring chains of polymers tightly together, further connecting the extended two-dimensional packing. It is noteworthy that none of the phenolic-hydroxy groups participate in these hydrogen-bonding interactions.

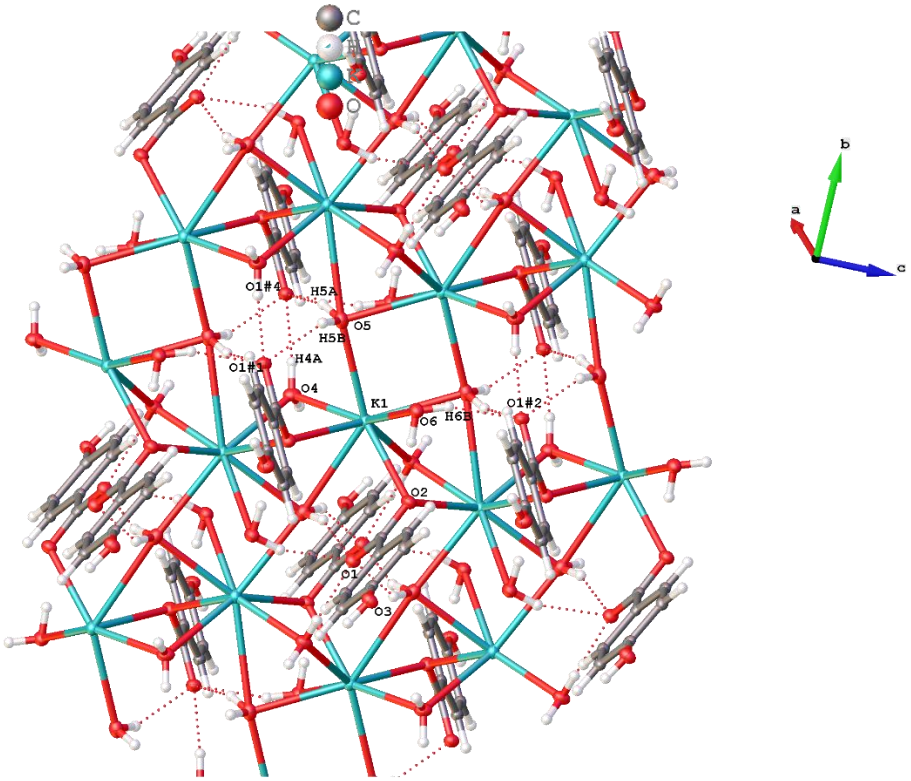


Figure 5.39: The packing diagram of the 1D polymeric chains of **5.12** linked by O…H...O hydrogen bonds into a 2D network (The 1D polymeric chain is propagating along the *c*-axis). Symmetry codes: [#1] +X,3/2-Y,-1/2+Z; [#2] +X,3/2-Y,1/2+Z; [#3] 2-X,2-Y,1-Z; [#4] 2-X,-1/2+Y,1/2-Z.

Table 5.15: Hydrogen bonding parameters [d/Å and </°] for compounds $[K(4hob)(H_2O)_3]_n$ **(5.12).**

D-H…A	**d(D-H)**	**d(H…A)**	**d(D…A)**	**<(DHA)**
O4-H4a…O1#4	0.8754(11)	1.9342(11)	2.7503(16)	154.50(8)
O5-H5a…O1#4	0.8705(11)	1.9513(11)	2.7756(16)	157.51(7)
O5-H5b…O1#1	0.8706(11)	2.1136(11)	2.8718(17)	145.21(7)
O6-H6b…O1#2	0.8697(11)	2.099(11)	2.8776(16)	161.42(7)

$[Rb(4hob)(H_2O)]_n$ **(5.13)** crystallizes in the monoclinic $P2_1/c$ space group with a square antiprismatic donor atom arrangement around Rb. Figure 5.40 illustrates the structure of the extended asymmetric unit of **5.13**.

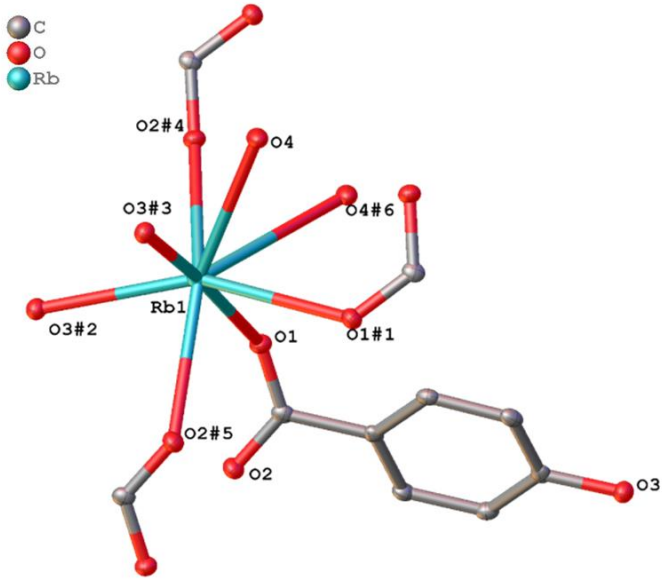


Figure 5.40: The asymmetric unit of $[Rb(4hob)(H_2O)]_n$ **(5.13)** (generated from single-crystal XRD data) showing the total coordination sphere. Carbon atoms are shown in grey. Thermal ellipsoids are drawn at the 50% probability level. Hydrogen atoms are omitted for clarity. Symmetry codes: $^{\#1}$+X,1/2-Y,-1/2+Z; $^{\#2}$-1+X,+Y,+Z; $^{\#3}$-1+X,1/2-Y,-1/2+Z; $^{\#4}$-X,-1/2+Y,3/2-Z; $^{\#5}$-X,1-Y,1-Z; $^{\#6}$-X,-Y,1-Z.

Within the polymeric structure, there are eight coordinate rubidium atoms bonded by four bridging carboxylate oxygen atoms (O1, O1#1, O2#4, O2#5). Additionally, two phenolic oxygen atoms O(3#2, 3#3) from the μ_4-1κ(O);2κ(O);3κ(O′);4κ(O′) 4hob ligand and two coordinated water oxygen atoms O4 and O4#6 contribute to the coordination. The metal centre achieves a total coordination of eight by incorporating another ligated water oxygen atom (O4#6) bridging from the adjacent metal centre. The binding of the phenolic oxygen atom to the metal centre is also observed in the **5.10** structure. Each 4-hydroxybenzoate ligand in the chain forms bonds with four Rb atoms, following the same coordination pattern. For **5.13**, the average Rb-O bond distance is 3.0486 Å. Among the Rb-O bonds, the bridging Rb1-O1 bond is the shortest (2.844(14) Å) (Table 5.17). On the other hand, one of the ligated water molecules exhibits the longest Rb-O bond distance of 3.570 (16) Å (Rb1-O4#6). The two ligated water oxygen atoms form an O4-Rb1-O4#6 angle of 82.89(4)°.

The metal atoms in the 1D chain (Rb1#1…Rb1…Rb1#7) are linked together through carboxylate-O1, and the phenolic oxygen atom O3#2 with a Rb1…Rb1#1 distance of 4.0584(8) Å at an angle of 162.109(5)°. A phenolic oxygen atom, O3, bridges to a Rb metal in a neighbouring chain, forming a 2D network in the *ac*-plane (Figure

5.41a). When projected along the *a*-axis (Figure 5.41b), it becomes apparent how these 2D networks are linked together by alternative four-membered rings (through coordinated aqua molecules (O4 and O4#4)) and eight-membered rings (through two bridging ligands), resulting in an overall 3D structure.

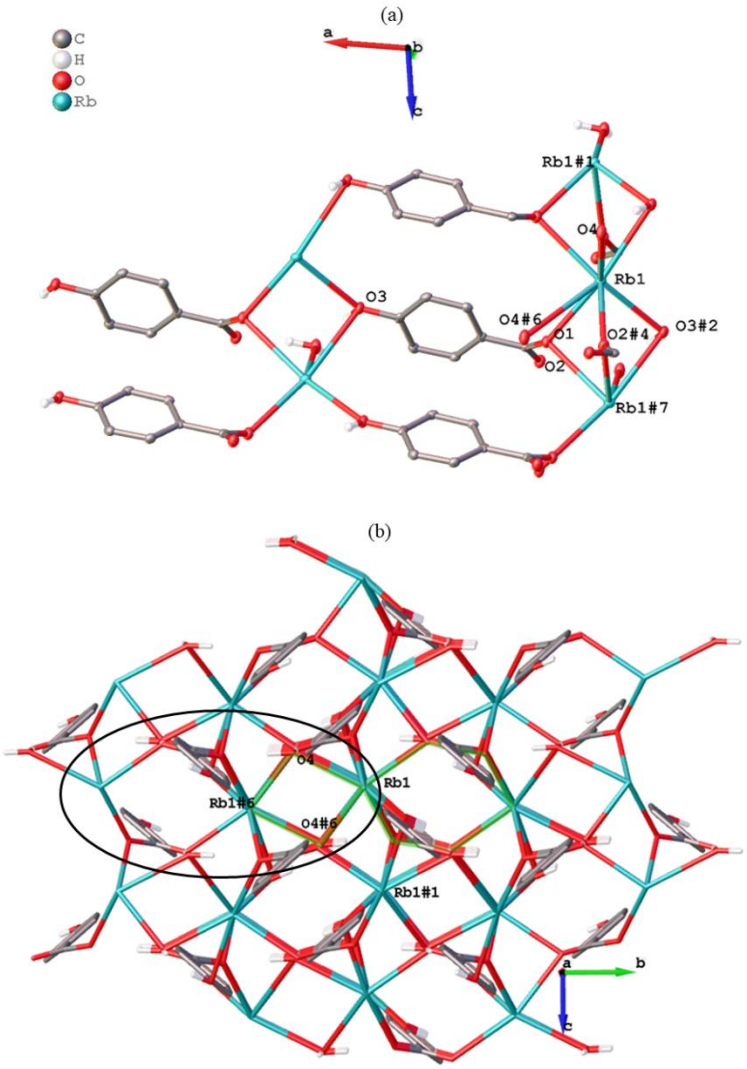


Figure 5.41: (a). A projection along the ac-plane shows the formation of a 2D layer network of **5.13** (b). A projection along the a-axis of **5.13** showing alternative four and eight membered rings(circled) that links the 2D networks together. Symmetry codes: #1+X,1/2-Y,-1/2+Z; #2-1+X,+Y,+Z; #3-1+X,1/2-Y,-1/2+Z; #4-X,-1/2+Y,3/2-Z; #5-X,1-Y,1-Z; #6-X,-Y,1-Z; #7 +X, 1/2-Y, 1/2+Z.

$[Cs(4hob)(H_2O)]_n$ **(5.14)** crystallizes in the monoclinic $P2_1/c$ space group and exhibits square antiprismatic eight coordination. Although the crystal structures of **5.13** and **5.14** have different unit cells due to the inequivalent β-angles and a slight variation in the *c*-axis, the ligand binding modes within the asymmetric units remain the same.

Furthermore, the eight coordinated metal atoms in both cases have similar coordination environments (Table 5.2). The 1D polymeric chain of Cs atoms is nonlinear with Cs1#1-Cs1-Cs1#7 at an angle of 168.391(8)°. The separation of the metal atoms in the 1D chains is longer in **5.14** (4.3322(9) Å), compared to 4.0584 (8) Å in **5.13** (Table 5.17). In contrast to **5.13**, the average Cs-O bond distance in **5.14** is slightly longer (3.2165 Å). The disparity in the metal-metal distance and the average metal-oxygen bond distances between **5.13** and **5.14** aligns with the increase in the ionic radii of eight-coordinate monovalent caesium compared to rubidium [20]. Similar to **5.13**, the bridging Cs1-O1 bond in **5.14** is the shortest (3.012(3) Å), while the coordinated water oxygen O4#6 exhibits the longest Cs-O bond distance of 3.761(3) Å (Cs1-O4#6). The two ligated water oxygen atoms form an O4-Cs1-O4#6 angle of 81.89(4)°.

Additionally, the interactions that join the 1D networks and contribute to the overall 3D structure are similar in both **5.13** and **5.14**. However, the **5.14** structure exhibits a network of H-bonding (Table 5.16) that holds the 3D network together (Figure 5.42).

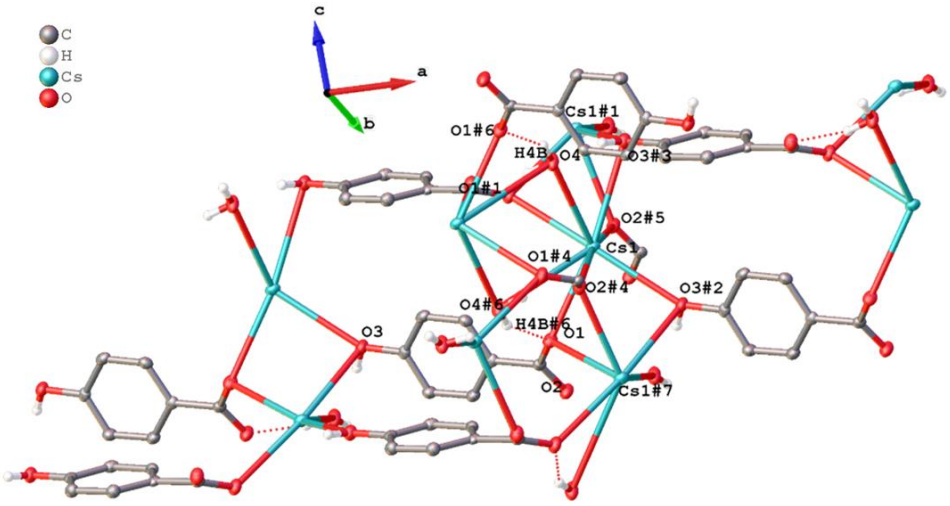


Figure 5.42: Molecular diagram of $[Cs(4hob)(H_2O)]_n$ **(5.14)**, generated from single-crystal XRD data, indicating the immediate coordination environment around Cs1. Carbon atoms are shown in grey. Thermal ellipsoids are drawn at the 50% probability level. Hydrogen atoms, except for those involved in forming H bonds, are omitted for clarity. The 1D polymeric chain propagates along the *c*-axis, while a 2D framework forms in the ac-plan. The 2D polymeric chains are linked by alternative four- and eight-membered rings, resulting in the formation of a 3D network along the *b*-axis.) Symmetry

codes: [#1] +X,1/2-Y,1/2+Z; [#2] 1+X,+Y,+Z; [#3] 1+X,1/2-Y,1/2+Z; [#4]2-X,-1/2+Y,1/2-Z; [#5] 2-X,1-Y,1-Z,; [#6] 2-X,-Y,1-Z; [#7] +X,1/2-Y,-1/2+Z.

Table 5.16: Hydrogen bonding parameters [d/Å and </°] for compounds $[Cs(4hob)(H_2O)]_n$ **(5.14).**

D-H…A	**d(D-H)**	**d(H…A)**	**d(D…A)**	**<(DHA)**
O4-H4B…O1#6	0.850(3)	1.956(3)	2.742(4)	153.2(2)
O4#6-H4B#6…O1	0.850(3)	1.956(3)	2.742(4)	153.2(2)

Table 5.17: Selected bond lengths and M…M distances (Å) for $[M(4hob)]_n$ series (M = Li **(5.11)**, K **(5.12)**, Rb **(5.13)**, Cs **(5.14)**).

5.11		**5.12**		**5.13**		**5.14**	
Li1- O1	1.921(7)	K1-O2	2.869.(13)	Rb1-O1	2.844 (14)	Cs1-O1	3.012(3)
Li1-O1#3	1.969(8)	K1-O2#1	2.917(15)	Rb1-O1#1	2.997(14)	Cs1-O1#1	3.166(3)
Li1-O2#5	1.958(8)	K1-O4	2.734(13)	Rb1-O4	3.028(13)	Cs1-O4	3.217(3)
Li1-O2#4	1.962(7)	K1-O5	2.939 (12)	Rb1-O4#6	3.570 (16)	Cs1-O4#6	3.761(3)
Li1…Li1#2	3.086(8)	K1-O6	3.021(13)	Rb1-O2#4	2.947 (12)	Cs1-O2#4	3.079(3)
Li1…Li1#4	3.086(8)	K1-O4#2	2.848(8)	Rb1-O2#5	2.936 (12)	Cs1-O2#5	3.136(3)
Li1…Li1#3	2.700(14)	K1-O5#3	2.799(5)	Rb1-O3#2	2.946 (13)	Cs1-O3#2	3.108(3)
		K1-O5#4	3.172(5)	Rb1-O3#3	3.120(15)	Cs1-O3#3	3.253(3)
		K1…K1#1	3.9243(7)	Rb1…Rb1#1	4.0584(8)	Cs1…Cs1#1	4.3322(9)
		K1…K1#2	3.9243(7)				

Table 5.18: Selected bond angles (°) for $[M(4hob)]_n$ series (M = Li **(5.11)**, K **(5.12)**, Rb **(5.13)**, Cs **(5.14)**).

5.11		**5.12**	
Li1#1…Li1…Li1#4	109.6(4)	K1#1…K1…K1#2	128.53(2)
Li1-O1-C1	136.4(3)	O4–K1–O5	79.41(3)
Li1#1-O2-C1	116.3(3)	O4–K1–O6	150.87(3)
Li1-O2#4-Li1#1	103.9(2)	O5–K1–O6	73.92(3)
Li1-O2#5-Li1#4	103.9(2)	O4–K1–O4#2	83.47(7)
Li1#4-O1#4-C1#4	136.4(3)	O4–K1–O5#3	126.55(17)
		O4–K1–O5#4	65.96(5)
		O5–K1–O5#3	88.46(12)
		O5–K1–O5#4	135.06(11)
		O5–K1–O4#2	135.79(6)
		O6–K1–O4#2	124.17(15)
		O6–K1–O5#3	64.79(2)
		O6–K1–O5#4	128.46(8)
		O4#2–K1–O5#3	69.92(19)
		O4#2–K1–O5#4	69.35913)
		O5#4–K1–O5#3	134.98(5)
		K1-O2-K1#2	85.41(4)

		O2-K1-O6	55.27(3)
		O2-K1-O4	144.96(4)
		O2-K1-O4	127.89(9)

5.13		**5.14**	
Rb1#1…Rb1…Rb1#7	162.109(5)	Cs1#1…Cs1…Cs1#7	168.391(8)
O3#2-Rb1-O3#3	100.26(4)	O3#2-Cs1-O3#3	105.97(9)
O4-Rb1-O4#6	82.89(4)	O4-Cs1-O4#6	81.89(4)
Rb1-O3#2-Rb1#7	83.93(3)	Cs1-O3#2-Cs1#7	85.82(7)

5.2.3 Corrosion Inhibition

5.2.3.1. Immersion Tests

The immersion tests were conducted as an initial screening, lasting for seven days in a 0.01M NaCl control solution. After the completion of the test, digital photographs were taken of the sample coupons (Table 5.19). Since the primary objective of the current study was to observe and compare the effectiveness of alkali metal complexes of various carboxylate derivatives with rare earth metal carboxylate corrosion inhibitors, detailed immersion analysis was not pursued for all the compounds. The corrosion rates (R) of the inhibitor solutions and the percentage corrosion inhibition (η) were determined by applying Equation **2.1** and **2.2**, outlined in Chapter 2.

Table 5.19: Mild steel coupons immersed in control and selected inhibitor solutions for 168 h.

	Before cleaning the corrosion product	After Cleaning the corrosion product (left – Trial 1; right – Trial 2)
Control 0.01 M NaCl		
$[Li_2(3tpc)_2]_n$ **(5.1)**		
$[K_2(3tpc)_2]_n$ **(5.2)**		

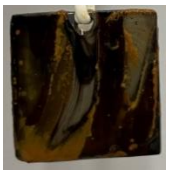
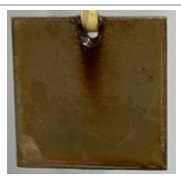
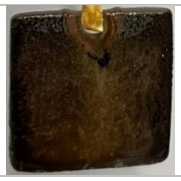
$[Rb(3tpc)(H_2O)]_n$ **(5.3)**		
$[K_2(2m3fur)_2(H_2O)]_n$ **(5.6)**		
$[Li(3fur)]_n$ **(5.7)**		
$[K(4hocin)(H_2O)]_3]_n$ **(5.8)**		
$[K(4HoB)(H_2O)_3]_n$ **(5.12)**		

Table 5.20 provides a summary of the weight loss measurements obtained after 168 hours of immersing the samples in specific inhibitor solutions. Upon examination of the results, it was found that the mild steel coupons immersed in 800 ppm $[K(4hocin)(H_2O)]_3]_n$ **(5.8)** exhibited the highest corrosion inhibition rates, reaching 80%. On the other hand, $[K_2(2m3fur)_2(H_2O)]_n$ **(5.6)** displayed the lowest inhibition efficiency, with only 9% corrosion inhibition. The remaining tested compounds demonstrated inhibition efficiencies ranging from 25% to 31%.

Table 5.20: Observed weight loss, corrosion rates ($\mu gm^{-2}s^{-1}$) and percentage inhibition (η) for mild steel coupons immersed in specific solutions at 800 ppm concentrations in 0.01 M NaCl for seven days.

Solution	**Concentration**		**Corrosion rate ($\mu gm^{-2}s^{-1}$)**	**% Inhibition (η)**
	ppm	**mM**		
Control-NaCl	580	10	39.1	-
$[Li_2(3tpc)_2]_n$ **(5.1)**	800	2.98	27.1	31
$[K_2(3tpc)_2]_n$ **(5.2)**	800	2.41	28.8	26
$[Rb(3tpc)(H_2O)]_n$ **(5.3)**	800	3.47	27.4	30
$[K_2(2m3fur)_2(H_2O)]_n$ **(5.6)**	800	2.31	35.7	9
$[Li(3fur)]_n$ **(5.7)**	800	6.78	29.2	25

$[K(4hocin)(H_2O)]_3]_n$ **(5.8)**	800	3.12	7.5	80
$[K(4hob)(H_2O)_3]_n$ **(5.12)**	800	3.47	29.7	24

Previous studies involving 4-hydroxycinnamate as the ligand have indicated that the corrosion rates calculated from the weight loss data were generally higher for sodium salts compared to their rare earth metal-substituted analogues.[5] In Chapter 2, 3 and 4 with RE 3-thiophenecarboxylate,[29] 3-furoate,[4] and 2-methyl-3-furoate[30] we have demonstrated the inhibition properties of rare earth metal analogues. By comparing both sets of results (Table 5.20 and 5.21), it is evident that the corrosion rates of alkali metal carboxylate on steel are generally much higher than those of rare earth analogues, indicating the value of rare earth carboxylates in inhibition.

Table 5.21: Anticorrosion data for some corresponding rare earth carboxylates.

Ligand	**Solutions**	**Concentration**		**Corrosion Rate ($\mu gm^{-2}s^{-1}$)**	**% Inhibition (η)**	**Chapter/ Ref**
		ppm	**mM**			
3tpc	$[La(3tpc)_3(H_2O)_3]_n$	500	0.871	19.4	36	Chapter 2/[29]
3tpc	$[Ce(3tpc)_3(H_2O)_3]_n$	500	0.869	18.8	38	Chapter 2/[29]
3tpc	$[Y_2(3tpc)_6(H_2O)_4].H_2O$	500	0.485	9.65	68	Chapter 2/[29]
3fur	$[La(3fur)_3(H_2O)_2]_n$	800	1.57	5.14	87	Chapter 3/[4]
3fur	$[Ce(3fur)_3(H_2O)_2]_n$	800	1.57	8.3	79	Chapter 3/[4]
3fur	$[Y(3fur)_3(H_2O)_2]_n$	800	1.75	3.9	90	Chapter 3/[4]
2m3fur	$\{[Ce_2(2m3fur)_6(EtOH)]\cdot H_2O\}_n$	800	0.731	24.0	39	Chapter 4/[30]
2m3fur	$[Y_3(2m3fur)_9]_n$	800	0.574	16.2	59	Chapter 4/[30]
4ohcin	$La(4hocin)_3$	500	0.7	3.2	91	[5]
4ohcin	$Ce(4hocin)_3$	200	0.28	5.7	84	[5]

5.3 Conclusions

Fourteen new complexes of the alkali metals with, 3-thiophenecarboxylate (3tpc), 2-methyl-3-furoate (2m3fur), 3-furoate (3fur), 4-hydroxycinnamate (4hocin), and 4-hydroxybenzoate (4hob), have been synthesised. The synthesis gave moderate yields of crystalline materials, and the complexes were characterised by IR spectroscopy, powder XRD, TGA, and microanalyses. Furthermore, X-ray crystallographic examination of single crystals of all compounds revealed unique structures for each of them. In the series of compounds, only the $[Li_2(2m3fur)_2(H_2O)_3]$ **(5.5)** complex crystallized as a coordination dinuclear complex with four-coordinate lithium atoms. In contrast, all other complexes were found to be polymeric, with varying coordination numbers and

stereochemistry. Compounds **5.4** and **5.9** incorporate $[HL_2]^-$ ligands rather than simple carboxylate groups and exhibit centrosymmetric O...H...O interactions between the carboxylate ions.

To investigate the potential application of the complexes as corrosion inhibitors, weight loss measurements were conducted, but were less effective than their rare earth counterparts.

5.4 Experimental

For materials and general considerations, see Appendix One.

5.4.1 Synthesis of alkali metal carboxylate Complexes

General Synthetic Method: Each ligand acid (LH; L = 3tpc (0.384 g, 3 mmol), 2m3fur (0.284 g, 2.25 mmol), 3fur (0.252 g, 2.25 mmol), 4hocin (0.410 g, 2.5 mmol), and 4hob (0.345 g, 2.5 mmol)) was dissolved in 15 ml of 95% ethanol and neutralized with an equimolar amount of aqueous potassium hydroxide, as shown in Scheme 5.1: Eq 1, to produce KL compounds. Sodium complexes were also synthesized using the same procedure, employing NaOH instead. For the synthesis of lithium, rubidium, and caesium carboxylate complexes, ligand acid solutions in ethanol (LH) were neutralized with a half-molar amount of aqueous Li_2CO_3, Rb_2CO_3, and Cs_2CO_3, respectively (Scheme 5.1: Eq 2). The resulting solutions were stirred at room temperature for 2 hours, transferred to separate vials, and left to stand for several days at room temperature, resulting in precipitates. These precipitates were dried over silica gel. Crystals were obtained by subsequent recrystallization of the bulk products of **5.1**, **5.2**, **5.3**, **5.5**, **5.6** from 95% ethanol and **5.4**, **5.7**, **5.8, 5.9, 5.10, 5.11**, **5.12**, **5.13** and **5.14** from water/ethanol (95/5 %v/v).

$[Li_2(3tpc)_2]_n$ (5.1)

White powder. Yield: 0.20 g (50%). m.p. >300 °C. Elemental analysis for $C_{10}H_6Li_2O_4S_2$ (MW: 268.15 $gmol^{-1}$): Calculated (%) C 44.79, H 2.26; Found (%) C 44.08, H 2.20. IR (cm^{-1}): 3123w, 3105w, 3083w, 1566s, 1514s, 1414s, 1399s, 1352s, 1206m, 119m, 1071m, 935w, 913w, 896w, 869m, 827m, 756s, 694s, 626m, 585m, 540m, 430s.

$[K_2(3tpc)_2]_n$ (5.2)

White powder. Yield: 0.25 g (50%). m.p. >300 ℃. Elemental analysis for $C_{10}H_6K_2O_4S_2$ (MW: 332.47 $gmol^{-1}$): Calculated (%) C 36.12, H 1.82; Found (%) C 36.26, H 1.77. IR (cm^{-1}):3115w, 3083w, 2358w, 2340w, 1738w, 1614w, 1558s, 1516s, 1412s, 1401s, 1348s, 1204m, 1121m, 1109m, 1067m, 916w, 870m, 849w, 830m, 779m, 753s, 683s, 624m, 574w, 514m, 457w, 442w.

$[Rb(3tpc)(H_2O)]_n$ (5.3)

White powder. Yield: 0.62 g (90%). m.p. >300 ℃. Elemental analysis for $C_5H_5O_3RbS$ (MW: 230.62 $gmol^{-1}$): Calculated (%) C 26.04, H 2.19; Found (%) C 26.54, H 1.98. IR (cm^{-1}): 3348w, 3100w, 3083w, 1723w, 1563s, 1512s, 1405s, 1341s, 1210m, 1199m, 1125m, 1108m, 1065m, 866m, 827m, 760s, 692s, 624m, 553m, 511m, 458w. TGA weight loss (26-110 ℃): 7.4% (Calc. for loss of 1×H_2O = 7.8%).

$[Cs\{H(3tpc)_2\}]_n$ (5.4)

White powder. Yield: 0.23 g (20%). m.p. >300 ℃. Elemental analysis for $C_{10}H_7CsO_4S_2$ (MW: 388.20 $gmol^{-1}$): Calculated (%) C 30.94, H 1.82; Found (%) C 30.80, H 1.73. IR (cm^{-1}): 3097w, 1682w, 1636w, 1617w, 1560s, 1510s, 1398s, 1384s, 1342s, 1280w, 1261w, 1197w, 1152w, 1106m, 1063w, 1015w, 994w, 973w, 945w, 926w, 864m, 826m, 765s, 757s, 696s, 670w, 624m, 591w, 557w, 537w, 508m, 439w. TGA weight loss (40-220 ℃): 2.5%; (Calc. for loss of 0.5×H_2O (assuming absorb water = 2.3%)).

$[Li_2(2m3fur)_2(H_2O)_3]$ (5.5)

White powder. Yield: 0.18 g (51%). m.p. 250 ℃ (dec.). Elemental analysis for $C_{12}H_{16}Li_2O_9$ (MW: 318.13 $gmol^{-1}$): Calculated (%) C 45.30, H 5.07; Found (%) C 44.56, H 4.68. IR (cm^{-1}): 3373m, 3301m, 3128w, 2926w, 1675w, 1598s, 1544m, 1521s, 1458m, 1428s, 1383s, 1361m, 1349m, 1289w, 1248w, 1231w, 1219m, 1138m, 1104s, 1052w, 1035w, 944m, 895m, 852w, 815s, 761w, 729s, 685m, 618s, 599s, 588s, 530s, 500s, 462s. TGA weight loss (50-120 ℃): 17.68% (Calc. for loss of 3×H_2O = 16.97%).

$[K_2(2m3fur)_2(H_2O)]_n$ (5.6)

White powder. Yield: 0.19 g (50%). m.p. 280 ℃ (dec.). Elemental analysis for $C_{12}H_{12}K_2O_7$ (MW: 346.42 $gmol^{-1}$): Calculated (%) C 41.61, H 3.49; Found (%) C 41.53, H 3.29. IR (cm^{-1}): 3373m, 3301m, 3128w, 2926w, 1675w, 1598s, 1544s, 1521s, 1458m,

1428s, 1383s, 1361s, 1349s, 1289w, 1231w, 1219s, 1138m, 1104s, 1052w, 1035w, 944m, 895m, 815s, 761w, 729s, 685m, 618s, 599s, 588s, 530s, 500s, 462s; TGA weight loss (35-180℃): 9.4% (Calc. for loss of 2×H_2O (assuming absorb water = 9.9%)).

$[Li(3fur)]_n$ (5.7)

White powder. Yield: 0.21 g (80%). m.p. 280 ℃ (dec.). Elemental analysis for $C_5H_3LiO_3$ (MW: 118.01 $gmol^{-1}$): Calculated (%) C 50.88, H 2.56;. Found (%) C 50.78, H 2.50. IR (cm^{-1}): 3154w, 3132w, 2298w, 1563s, 1552s, 1505s, 1428s, 1368m, 1251w, 1213m, 1149m, 1069m, 1004m, 970mw, 873m, 780s, 752s, 606m, 595m, 553m, 468s.

$[K(4hocin)(H_2O)_3]_n$ (5.8)

White powder. Yield: 0.44 g (69%). m.p. 200 ℃ (dec.). Elemental analysis for $C_9H_{13}KO_6$ (MW: 256.29 $gmol^{-1}$): Calculated (%) C 42.18, H 5.11; $C_9H_{10}KO_{4.5}$ (MW: 229.27 gmol-1,loss of 1.5 H_2O): Calculated (%)C 47.15, H 4.40; Found (%) C 46.51, H 4.27. IR (cm^{-1}): 3444m, 3023w, 2815w, 1636m, 1607w, 1590m, 1531w, 1511s, 1454w, 1371s, 1289m, 1270m, 1237s, 1167m, 1102m, 1013w, 973s, 936w, 874w, 829s, 802m, 697m, 641w, 516s, 465s, 452s, 460m. TGA weight loss (25-90 ℃): 20.3% (Calc. for loss of 3×H_2O = 21.1%).

$[Rb\{H(4hocin)_2\}]_n \cdot nH_2O$ (5.9)

White powder. Yield: 0.63 g (59%). m.p. 200 ℃ (dec.). Elemental analysis for $C_{18}H_{17}O_7Rb$ (MW: 430.79 $gmol^{-1}$): Calculated (%) C 50.19, H 3.98; $C_{11.25}H_{11}O_{4.75.13}$ (MW: 307.67 $gmol^{-1}$, loss of 0.75 4hocin): Calculated (%) C 43.92, H 3.60; Found (%) C 44.19, H 3.67. IR (cm^{-1}): 3287w, 2624m, 1634m, 1608w, 1591m, 1537w, 1514s, 1454s, 1381s, 1288w, 1243s, 1198w, 1171m, 1103m, 1010w, 979s, 939m, 900m, 864m, 828s, 804s, 748w, 710m, 628w, 551s, 525s, 515s, 458m. TGA weight loss (50-115 ℃): 6.0% (Calc. for loss of 1×H_2O from $\{[Rb(4hocin)(4hocinH)_{0.25}]\cdot(H_2O)\}_n$ = 5.9%).

$[Cs(4hocin)(H_2O)]_n$ (5.10)

White powder. Yield: 0.68 g (86%). m.p. 200 ℃ (dec.). Elemental analysis for $C_9H_9CsO_4$ (MW: 314.07 $gmol^{-1}$): Calculated (%) C 34.53, H 2.58; Found (%) C 34.41, H 2.90. IR (cm^{-1}): 3212m, 2999m, 2808m, 2687m, 1887w, 1633m, 1607m, 1588m, 1535w, 1514s, 1453s, 1379s, 1287w, 1243s, 1167m, 1099m, 1010w, 978s, 938w, 878m,

861w, 827s, 802m, 748w, 710m, 661w, 641w, 549s, 511s, 459m. TGA weight loss (50-120 ℃): 5.4% (Calc. for loss of 1×H_2O = 5.7%).

$[Li(4hob)]_n$ (5.11)

White powder. Yield: 0.26 g (72%). m.p. 270 ℃ (dec.). Elemental analysis for $C_7H_5LiO_3$ (MW: 144.05 $gmol^{-1}$): Calculated (%) C 58.37, H 3.50; $C_7H_{5.5}LiO_{3.25}$ (MW: 148.56 $gmol^{-1}$, absorbed 0.25 H_2O): Calculated (%)C 56.59, H 3.73; Found (%) C 56.37, H 3.36. IR (cm^{-1}): 3357m, 1602s, 1556, 1399s, 1360m, 1238s, 1168s, 1143m, 1100s, 1011m, 978w, 858m, 841w, 805m, 787s, 701m, 638w, 619s, 548m, 518m, 503w, 450s, 425s.

$[K(4hob)(H_2O)_3]_n$ (5.12)

White colour powder Yield: 0.48 g (83%). m.p. 260 ℃ (dec.). Elemental analysis for $C_7H_{11}KO_6$ (MW: 230.26 $gmol^{-1}$): Calculated (%) C 36.51, H 4.81; $C_7H_7KO_4$ (MW: 194.23 $gmol^{-1}$,loss of 2 H_2O): Calculated (%) C 43.29, H 3.63; Found (%) C 43.84, H 3.38. IR (cm^{-1}): 3437s, 3175s, 2689w, 1635w, 1599s, 1533s, 1501m, 1438w, 1361s, 1297w, 1268m, 1248s, 1163s, 1138m, 1100s, 1008w, 953w, 854s, 787s, 776s, 695s, 614s, 530m, 470s, 432s. TGA weight loss (27-150 ℃): 21.2% (Calc. for loss of 3×H_2O = 23.4%).

$[Rb(4hob)(H_2O)]_n$ (5.13)

White powder. Yield: 0.33 g (56%). m.p. 270 ℃ (dec.). Elemental analysis for $C_7H_7O_4Rb$ (MW: 240.60 $gmol^{-1}$): Calculated (%) C 34.94, H 2.93; Found (%) C 34.92, H 2.77. IR (cm^{-1}): 3300w, 3018m, 2890m, 2798m, 2694m, 1914w, 1694w, 1597s, 1530s, 1510s, 1462m, 1380s, 1252s, 1165s, 1142m, 1100s,1011w, 967w, 849s, 834s, 816w 784s, 704s, 614s, 549s, 496s. TGA weight loss (100-140 ℃): 7.5% (Calc. for loss of 1×H_2O = 7.5%).

$[Cs(4hob)(H_2O)]_n$ (5.14)

White powder. Yield: 0.66 g (92%). m.p. 270 ℃ (dec.). Elemental analysis for $C_7H_7CsO_4$ (MW: 288.04 $gmol^{-1}$): Calculated (%) C 29.19, H 2.45; Found (%) C 29.39, H 2.41. IR (cm^{-1}): 3194m, 3036w, 2809w, 2675w, 2522w, 2114w, 1660s, 1607s, 1591s, 1512w, 1440m, 1377m, 1355m, 1316w, 1267m, 1227s, 1162s, 1099s, 925m, 849s, 768s,

697s, 666m, 638m, 612s, 546m, 522w, 498s ; TGA weight loss (75-130 ℃): 5.3% (Calc. for loss of 1×H_2O = 6.2%).

5.4.2 Corrosion Testing

For the corrosion testing procedures used for weight loss experiments, see Appendix One.

5.5 X-ray Crystal Data

For details on x-ray crystallography, see Appendix One. Detailed information regarding the crystal data and refinement can be found in Table 5.22.

Table 5.22: Crystal data and structural refinement for alkali metal carboxylate complexes.

	5.1	**5.2**	**5.3**	**5.4**	**5.5**
Formula	$C_{10}H_6Li_2O_4S_2$	$C_{10}H_6K_2O_4S_2$	$C_5H_5O_3RbS$	$C_{10}H_7CsO_4S_2$	$C_{12}H_{16}Li_2O_9$
M_r	268.15	332.47	230.62	388.19	318.13
Space group	*Pna*2$_1$	*Pca*2$_1$	*P*2$_1$/*c*	*C*2/*c*	*Pbcn*
a (Å)	8.2726(2)	11.2493(2)	16.150(3)	28.169(6)	7.2566(15)
b (Å)	5.2114(1)	3.97510(10)	3.9200(8)	3.9620(8)	8.3455(17)
c (Å)	26.1699(6)	28.4846(5)	11.610(2)	11.582(2)	25.301(5)
α (°)	90	90	90	90	90
β (°)	90	90	95.06(3)	106.22(3)	90
γ (°)	90	90	90	90	90
V (Å^3)	1128.23(4)	1273.75(5)	732.1(3)	1241.2(5)	1532.3(5)
Z	4	4	4	4	4
ρ_{calc}, g cm^{-3}	1.579	1.734	2.092	2.077	1.379
μ, mm^{-1}	4.279	9.691	6.988	3.317	1.002
N_τ	7684	13706	15745	6572	4655
N (R_{int})	1675 (0.0397)	1995(0.0819)	1295(0.0584)	1062(0.0993)	1499(0.0335)
$R_1(I > 2\sigma(I))$	0.0334	0.0552	0.0299	0.0427	0.0383
wR_2 (all data)	0.0858	0.1419	0.0829	0.1014	0.1022
GOF	1.112	1.059	1.095	1.094	1.056

	5.6	**5.7**	**5.8**	**5.9**	**5.10**
Formula	$C_{12}H_{12}K_2O_7$	$C_5H_3LiO_3$	$C_9H_{13}KO_6$	$C_{18}H_{17}O_7Rb$	$C_9H_9CsO_4$
M_r	346.42	118.01	256.29	430.79	314.07
Space group	$P2_1/c$	$P2_1/c$	$P2_1/c$	$C2/c$	$P21$
a (Å)	13.830(3)	11.110(2)	14.430(3)	21.901(4)	4.3870(9)
b (Å)	7.4700(15)	5.3200(11)	11.130(2)	10.628(2)	9.882(2)
c (Å)	14.050(3)	8.2900(17)	7.0500(14)	7.3180(15)	12.131(2)
α (°)	90	90	90	90	90
β (°)	91.50(3)	90.43(3)	98.04(3)	97.94(3)	98.13(3)
γ (°)	90	90	90	90	90
V (Å^3)	1451.0(5)	489.97(17)	1121.1(4)	1687.0(6)	520.62(19)
Z	4	4	4	4	2
ρ_{calc}, g cm^{-3}	1.586	1.600	1.518	1.696	2.003
μ, mm^{-1}	0.682	0.130	0.484	2.975	3.542
N_τ	22578	7697	24948	9183	5565
N (R_{int})	2553(0.0640)	862(0.0534)	1979(0.0649)	1437(0.0292)	1750(0.0694)
$R_1(I > 2\sigma(I))$	0.0287	0.0407	0.0351	0.0223	0.0328
wR_2 (all data)	0.0921	0.0989	0.0963	0.0580	0.0720
GOF	1.144	1.113	1.092	1.190	1.147

	5.11	**5.12**	**5.13**	**5.14**
Formula	$C_7H_5LiO_3$	$C_7H_{11}KO_6$	$C_7H_7O_4Rb$	$C_7H_7CsO_4$
M_r	144.05	230.26	240.60	288.04
Space group	$P2_1/c$	$P2_1/c$	$P2_1/c$	$P2_1/c$
a (å)	14.904(3)	12.343(3)	10.107(2)	10.120(2)
b (å)	5.0420(10)	11.252(2)	10.007(2)	10.100(2)
c (å)	8.4750(17)	7.0700(14)	8.0180(16)	8.6200(17)
α (°)	90	90	90	90
β (°)	99.38(3)	102.18(3)	98.55(3)	102.88(3)
γ (°)	90	90	90	90
V (å^3)	628.3(2)	989.8(4)	801.9(3)	858.(9)
Z	4	4	4	4
ρ_{calc}, g cm^{-3}	1.523	1.593	1.993	2.227
μ, mm^{-1}	0.117	0.555	6.143	4.282
N_τ	1062	10907	8922	18355
N (R_{int})	1062(twinned)	1679(0.0269)	1377(0.0237)	1471(0.0501)
$R_1(I > 2\sigma(I))$	0.0334	0.0253	0.0148	0.0189
wR_2 (all data)	0.0950	0.0704	0.0412	0.0498
GOF	1.056	1.093	1.116	1.123

5.6 References

1 R. F. Koby and T. P. Hanusa, Lithium, Sodium, Potassium, Rubidium, and Cesiumin in *Comprehensive Coordination Chemistry III*, eds. E. C. Constable, G. Parkin and Q. J. Lawrence, Elsevier, Oxford, 2021, vol. 3, pp. 2–48, ch. 3.02.

2 T. P. Hanusa, Group 1s and 2s in *Comprehensive Coordination Chemistry II*, eds. J. A. McCleverty and T. B. Meyer, Elsevier: Oxford, 2004, vol. 3, pp. 1–92, ch. 3.1.

3 M. Forsyth, K. Wilson, T. Behrsing, C. Forsyth, G. B. Deacon and A. Phanasgoankar, *Corrosion*, 2002, **58**, 953–960.

4 V. P. Vithana, Z. Guo, G. B. Deacon, A. E. Somers and P. C. Junk, *Molecules*, 2022, **27**, 8836.

5 F. Blin, S. G. Leary, K. Wilson, G. B. Deacon, P. C. Junk and M. Forsyth, *J. Appl. Electrochem.*, 2004, **34**, 591–599.

6 A. E. Somers, B. R. W. Hinton, C. de Bruin-Dickason, G. B. Deacon, P. C. Junk and M. Forsyth, *Corros. Sci.*, 2018, **139**, 430–437.

7 M. Forsyth, M. Seter, B. Hinton, G. Deacon and P. Junk, *Aust. J. Chem.*, 2011, **64**, 812–819.

8 F. Wormwell and A. D. Mercer, *J. Appl. Chem.*, 1952, **2**, 150–160.

9 F. Blin, S. G. Leary, G. B. Deacon, P. C. Junk and M. Forsyth, *Corros. Sci.*, 2006, **48**, 404–419.

10 M. Forsyth, K. Wilson, T. Behrsing and G. B. Deacon, *Corros. Sci.*, 2002, **44**, 2651–2656.

11 A. D. Mercer, in *Proceedings of the 5th European Symposium on Corrosion Inhibitors*, University of Ferrara, Ferrara, Italy, 1980, pp. 563–581.

12 G. Chan-Rosado and M. A. Pech-Canul, *Int. J. Corros.*, 2016, **2016**, 8013706.

13 J. L. Maes, S. S. Lievens US Patent US 6,398,984 B1, 2002.

14 V. S. Saji, *Recent Patents Corros. Sci*, 2010, **2**, 6–12.

15 ConQuest 2.0.4. Version 5.41; ConQuest: Cambridge, UK, 2023.

16 R. E. Dinnebier, R. Dreele, P. W. Stephens, S. Jelonek and J. Sieler, *J. Appl. Cryst*, 1999, **32**, 761–769.

17 J. M. Skinner and J. C. Speakman, *J. Chem. Soc.*, 1951, 185–191.

18 L. Manojlovi, *Acta Cryst*, 1968, **24**, 326.

19 D. L. Pavia, G. M. Lampman and G. S. Kriz, *Introduction to Spectroscopy*, Thompson Learning, Inc., 3rd edn., 2001.

20 R. D. Shannon, *Acta Crystallogr. A*, 1976, **32**, 751–767.

21 F. R. Dai, Y. Qiao and Z. Wang, *Inorg. Chem. Front.*, 2016, **3**, 243–249.

22 A. Mustapha, J. Reglinski and A. R. Kennedy, *Inorg. Chem. Commun.*, 2010, **13**, 464–467.

23 G. B. Deacon, C. M. Forsyth, E. Harika, P. C. Junk, J. W. Ziller and W. J. Evans, *J. Mater. Chem.*, 2004, **14**, 3144–3149.

24 F. R. Dai and Z. Wang, *J. Am. Chem. Soc.*, 2012, **134**, 8002–8005.

25 J. Demaison, M. Herman and J. Lievin, *Int. Rev. Phys. Chem.*, 2007, **26**, 391–420.

26 J. Wu and J. Q. Liu, *Synth. React. Inorg. Met.-Org. Nano-Met. Chem.,* 2010, **40**, 237–240.

27 F. Yuan, Y. Zhou, L. Li and H. Qian, *Synth. React. Inorg. Met.-Org. Nano-Met. Chem.,* 2016, **46**, 913–916.

28 M. Mehring, C. Nolde and M. Schürmann, *Appl. Organomet. Chem.,* 2004, **18**, 487–488.

29 V. P. Vithana, Z. Guo, G. B. Deacon, A. E. Somers and P. C. Junk, *New J. Chem.*, 2022, **46**, 19104–19111.

30 V. P. Vithana, Z. Guo, G. B. Deacon and P. C. Junk, *Eur. J. Inorg. Chem.*, 2024, **27**, e202300722.

Chapter 6: Interaction of highly reactive lanthanoid complexes with organic substrates.

6.1 Introduction

6.1.1 Lanthanoid aryloxide complexes in organometallic chemistry

The functional group of phenol is defined as a hydroxyl group bonded to a carbon atom in a benzene ring. This organic compound, also known as carbolic acid, is widely distributed in nature in coal tar.[1] Phenol chemistry has attracted attention for over two centuries due to its versatility and importance in industrial applications as a starting material for numerous intermediates and final products.[2]

The phenoxide salt formed with aqueous alkali hydroxide is notably more stable than the alkoxide ion, owing to resonance delocalization of the negative charge.[1]

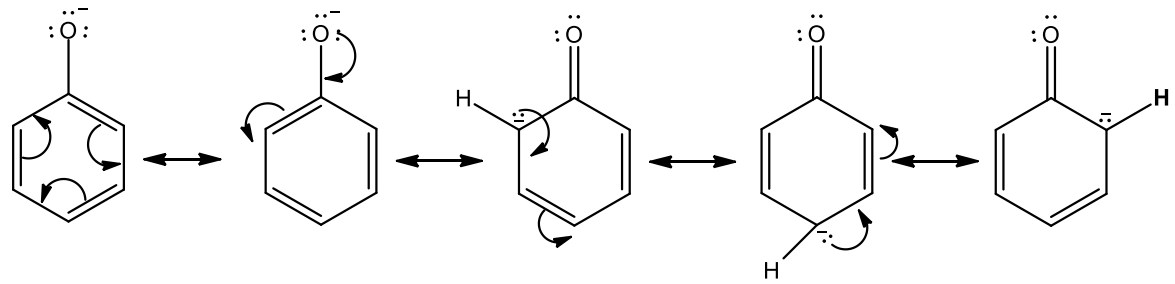


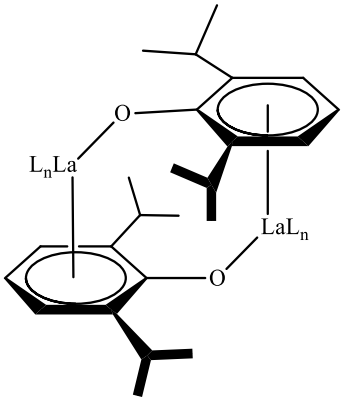
Chart 6.1: Resonance stabilisation of the phenoxide ion

Phenoxides are commonly employed as ligands due to their capacity to coordinate with metal centres, particularly hard acids. The substituents on the aromatic ring can be easily modified, leading to changes in reactivity, steric constraints, and overall metal coordination chemistry.[3,4]

In lanthanoid compounds, *ortho*-substituted phenoxides are commonly utilized due to the close proximity of the donor atom at the *ortho* position, which significantly influences the steric "cone" around each metal centre.[4]

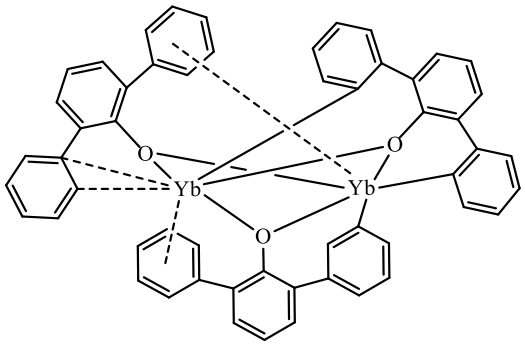
2,6-Di-iso-propylphenol (HOdip) is one of the most widely used aryloxide-type ligands in Ln(OR)x (x = 2, 3) chemistry. The moderately bulky 2,6-di-iso-propylphenolate ligand facilitates the formation of homoleptic rare earth complexes with fascinating structures. Rather unusual π-arene-bridged dimers were obtained with lanthanoid (Ln) bis(trimethylsilyl)amides *via* the alcoholysis route in refluxing toluene, resulting in $[Ln_2(\mu\text{-}\eta^6\text{-Odip})_2(Odip)_4)]$ (Ln= Nd, Sm).[5]

$$2Ln[N(SiMe_3)_2]_3 + 6HOdip \xrightarrow[\text{reflux}]{\text{toluene}} Ln_2(Odip)_6 + 6HN(SiMe_3)_2$$

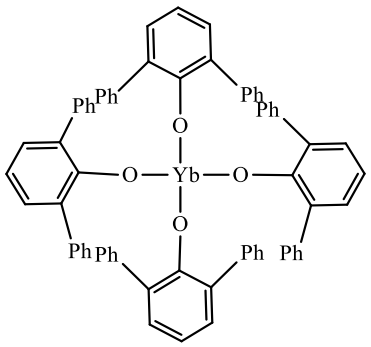


Divalent or trivalent rare earth complexes with bulky 2,6-diphenylphenols (HOdpp) have been extensively studied and have resulted in low-coordinate (<6) complexes. These homoleptic complexes are notable for their ability to form extensive intramolecular π-Ph...Ln interactions in $[Ln(Odpp)_3]$ and $[Ln_2(Odpp)_4]$ complexes, as well as for their highly irregular oxygen coordination.[6–9]

The formation of ionic mixed-valent rare earth aryloxide complexes is quite rare. Direct reactions of HOdpp with Yb at elevated temperatures in the presence of mercury resulted in the formation of a novel mixed-valent Yb(II/III) complex, $[Yb_3(Odpp)_7]$, containing both a cationic $[Yb_2(Odpp)_3]^+$ and an anionic $[Yb(Odpp)_4]^-$ species.[9]



$[Yb_2(Odpp)_3]^+$



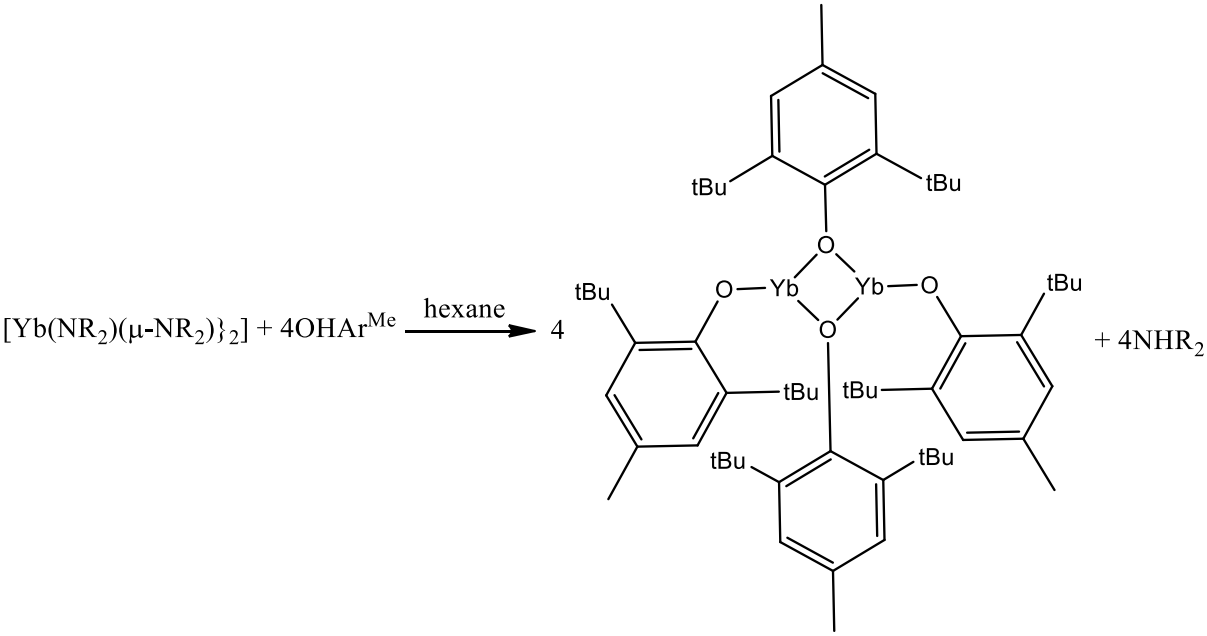
$[Yb(Odpp)_4]^-$

Similarly, in 2009, it was reported that treating Eu metal with HOdpp and LiOdpp under similar conditions led to the formation of a Eu(II/III) complex, $[Eu_2(Odpp)_3][Eu(Odpp)_4]\cdot 4PhMe$.[7]

The very bulky 2,6-di-*tert*-butyl-4-R-phenolate (OAr^R) ligands (where R = H, Me, *t*Bu) are one of the most extensively investigated aryloxide ligands in both divalent and trivalent

rare earth chemistry. [10–14] Notably, 2,6-di-*tert*-butyl-4-methylphenolate was the first aryloxide ligand introduced in divalent rare earth chemistry, dating back in 1989.[15] The high popularity of these aryloxide ligands can be attributed to their hydrocarbon solubility, steric protection, and ease of crystallization.[16,17] The use of these ligands allows for the formation of low-coordinate (3-5) species, including homoleptic tris- and bis-aryloxides,[12,13,16,18,19] as well as various 4- and 5-coordinate homometallic Lewis base adducts $[Ln(OAr)_x(solv)_n]$ (x = 2, 3; n = 1-3).[4,20] These species can be synthesized using a variety of common methods such as protolytic exchange, one-pot redox transmetallation/protolysis reactions (RTP), and metathesis reactions.

Irrespective of the size of the Ln cation, the donor solvents, or the nature of the molecule's charge, monometallic complexes have been successfully isolated using the 2,6-di-*tert*-butyl-phenoxide ligand and its derivatives.[4] An exceptional example in this class, prepared by a protolytic ligand exchange reaction, is the homoleptic, base-free dinuclear complex $[Yb(\mu\text{-}OAr^{Me})(OAr^{Me})]_2$.[13,18]



In contrast to the less bulky 2,6-di-iso-propylphenolate (Odip) and 2,6-diphenylphenolate (Odpp) ligands, the characterised 2,6-di-*tert*-butyl-4-R-phenolate derivatives did not report to exhibit any π-arene-bridged inter- or intramolecular interactions, likely due to the increased steric hindrance caused by the *tert*-butyl substituents.[4]

Overall, varying substitution patterns in particularly bulky phenolate ligands, such as 2,6-disubstituted ligands, have facilitated the stabilization and isolation of low-coordinated complexes.[3,4,10,16,19,21] Lanthanoid aryloxide complexes have shown potential in several

applications, including bioimaging, catalysis and material sciences. Bulky Ln(II) 2,6-di-*tert*-butyl-4-methylphenoxides have been employed as one electron reducing agents.[22] Moderately bulky aryloxides have gained attention as precursors in sol-gel applications, metal organic chemical vapour deposition (MOCVD),[23] and nanoparticle synthesis,[4] as well as for their ability to form oligomeric complexes with unusual trinuclear species.[10,24,25]

6.1.1.1 Synthetic pathways to rare earth aryloxide complexes

Several common synthetic approaches are there for the synthesis of highly reactive rare earth aryloxide complexes, however in this thesis only salt metathesis and redox transmetallation/protolysis (RTP) have been employed, and thus they are briefly discussed in detail below.

In preparation of rare earth organometallic complexes, the salt elimination or metathesis method is widely used and highly effective technique. This approach typically involves reacting an alkali metal salt of a ligand with a rare earth halide to synthesize both homoleptic and heteroleptic complexes.[26,27]

$$LnX_n + nML \longrightarrow [LnL_n] + nMX$$

Ln = Lanthanoid metal
X = Halide
M = Alkali metal
L =Anionic Ligand
n = 2/3

While salt elimination reactions are beneficial, they have several limitations.[27] The low solubility of LnX_n unsolvated compounds frequently leads to reduced yields and the formation of undesirable byproducts.[28,29] Additionally, the incomplete elimination of the alkali metal salt product can lead to the formation of heterometallic complexes.[28] Furthermore, the alkali metal halides may dissolve to some extent in certain organic solvents, which can adversely affect the effectiveness of salt elimination methods, making purification processes highly difficult.[26]

The redox transmetallation/protolysis reaction (RTP) combines two independent synthetic methods: redox transmetallation and protolysis. This versatile one-pot reaction procedure involves reacting excess free lanthanoid metals with an organometallic oxidant (such as diorganomercury(II) reagents like diphenyl mercury ($HgPh_2$), bs(pentafluorophenyl)mercury ($Hg(C_6F_5)_2$) and bis(phenylethynyl)mercury ($Hg(PhCC)_2$)) and a proligand (LH) such as a phenol, in a donor solvent (e.g., tetrahydrofuran (thf) or 1,2-

dimethoxyethane (DME)). This process typically produces highly reactive lanthanoid organic/organometallic complexes in high yields.[3]

$$Ln + (n/2)\ HgR_2 + n\ LH \longrightarrow Ln(L)n + (n/2)\ Hg + nRH$$

Ln = Lanthanoid Ligand
R = Ph, C_6F_5, PhCC
LH = Protic Ligand
n = 2/3

Some of these reactions, particularly when using less reactive diphenyl mercury or non-donor solvents like toluene, require the activation of free metals by adding a drop of mercury, applying ultrasonication, or heating.[3,30]

This method offers several advantages over metathesis reactions, including the use of only one air- and moisture-sensitive starting material and a relatively simple workup process.[31] After filtering to remove excess lanthanoid and the mercury byproduct, the mercury can also be recycled.[3] However, drawbacks of this method include environmental concerns and the toxicity of mercury reagents. Nonetheless, the use of diarylmercurials is considerably less hazardous than volatile dialkylmercurials like $HgMe_2$.[3,30,31]

Over the past two decades, the Junk/Deacon group has successfully synthesized and isolated a wide range of highly reactive lanthanoid aryloxides through RTP reactions, using $Hg(C_6F_5)_2$ as the primary oxidant.[3] They have also investigated the potential of pentafluorophenyl(pyridine)silver [$Ag(C_6F_5)py$] and tris(pentafluorophenyl)bismuth [$Bi(C_6F_5)_3$] as alternatives to diarylmercury (HgR_2) complexes in RTP reactions for synthesizing highly reactive RE aryloxides. This study indicates that the divalent complexes $[Eu(OAr^R)_2(thf)_3]\cdot thf$ (R =OMe, Me) can be isolated from RTP reactions with $Ag(C_6F_5)py$ and $Bi(C_6F_5)_3$, yielding similar results to those from RTP reactions with $Hg(C_6F_5)_2$.[32]

6.1.2 Classical divalent lanthanoid complexes in organometallic chemistry

Electron transfer has enabled numerous key reduction reactions in organic chemistry,[33] and in recent years, lanthanoids have increasingly contributed to this field. Historically, europium (Eu(II)) was one of the earliest lanthanoids used in aqueous redox chemistry as a one-electron reducing agent, demonstrating the potential of divalent lanthanoid salts as powerful reductants.[34–36] As discussed earlier in Chapter 1 lanthanoids are highly electropositive, with the +3-oxidation state being the most stable, especially in aqueous

environments. However, the divalent state was traditionally only accessible to europium, ytterbium, and samarium, which are referred to as the "classical" divalent lanthanoids.

Among these classical ions, samarium(II) and ytterbium(II) exhibit stronger reducing properties than europium(II), as evidenced by their standard reduction potentials: Eu^{2+}/Eu^{3+} = -0.43 V, Yb^{2+}/Yb^{3+} = -1.15 V, and Sm^{2+}/Sm^{3+} = -1.55 V.[37] The higher reduction potential of Sm(II) and Yb(II) sparked interest in their potential as powerful reducing agents in organometallic chemistry.

Synthesis of samarium diiodide (SmI_2) in 1979, by P. Girard and colleagues[37] gained widespread use due to its high reactivity, promoting numerous organic reactions and becoming a valuable reagent for the synthesis of organic derivatives. Samarium(II) based reductants, including the commercially available SmI_2, provide excellent chemo-, regio-, and diastereoselectivity, driving significant advancements in the field of reductive chemistry involving divalent lanthanoids.[38]

An intriguing aspect of researching the reactivity of divalent organolanthanoid complexes lies in the unpredictability and often unique nature of their reaction outcomes. This is primarily from their high reactivity, which frequently leads to a lack of selectivity. Understanding their reactivity towards unsaturated chemical bonds is crucial, as it holds significant potential for advancing the field.

6.1.3 Reactions of organolanthanoid complexes with unsaturated carbodiimide substrates

Carbodiimides are crucial substrates in studies of metal-based reactivity studies, leading to the formation of diverse range of coordination compounds with modified organic fragments.[39–41] These compounds (RN=C=NR') are a prominent example within the heterocumulenes class, characterised by their unsaturated structure based on the allene framework. Since the discovery of catalysts that facilitate the conversion of isocyanates to carbodiimides, with the removal of CO_2, the industrial scale production of carbodiimides has commenced, leading to their widespread use in various manufacturing processes.[42] Carbodiimides serve as excellent building blocks for the synthesis of a wide range of complex organic compounds and considered one of the most important classes of nitrogen reagents due to their diverse chemical properties.[41,43,44]

These compounds typically feature three reactive sites: a nitrogen atom, an electrophilic carbon centre, and unsaturated cumulene N=C=N bonds.[43,45] Their role as attractive precursors

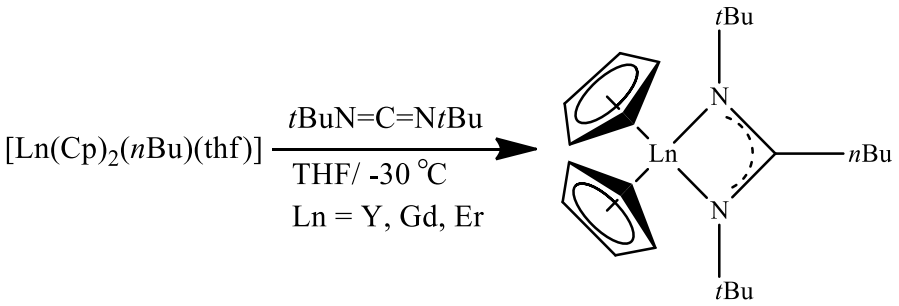
for N-heterocyclic ring synthesis through cycloaddition reactions is well-established.[42,43] As of 2020, more than 60 types of N-heterocycles have been synthesized using carbodiimides as the starting nitrogen source. Additionally, they are crucial in bioconjugation reactions, as well as in the synthesis and crosslinking of polyurethanes.[43] Reports also highlight their function as condensing agents in the synthesis of peptides and nucleotides.[42,46,47]

6.1.3.1 The insertion of carbodiimides into an existing metal-carbon/ metal-nitrogen bonds for the formation of Ln metal amidinate and guanidinate complexes

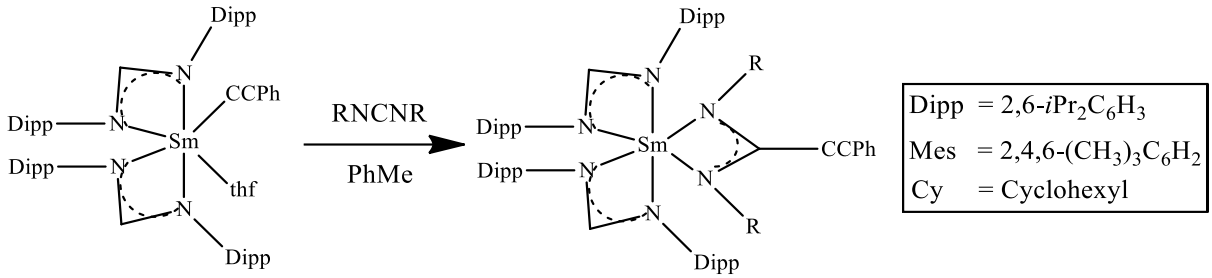
Both amidinate and guanidinate ligands are isoelectronic chelating agents that are attractive due to their electronic and steric properties, which can be manipulated by varying the substituents on the carbon and nitrogen atoms.

The insertion of carbodiimides into metal-carbon sigma bonds can lead to the formation of amidinato complexes. Amidinate anions, represented by the general formula $[RC(NR')_2]^-$, are nitrogen-based counterparts of carboxylate anions and have been extensively used as ligands in a variety of main group and transition metal complexes. They have also been utilized in lanthanoid metal coordination chemistry, offering a straightforward route to organolanthanoid amidinates.[48]

For example, the reaction of $[Ln(Cp)_2(n\text{Bu})(thf)]$ (Ln = Y, Gd, Er) with N,N'-di-*tert*-butylcarbodiimide yields the complexes $Ln(Cp)_2[t\text{BuNC}(n\text{Bu})Nt\text{Bu}]$ *via* the single-insertion of the carbodiimide into the Ln–C sigma bond.[49]



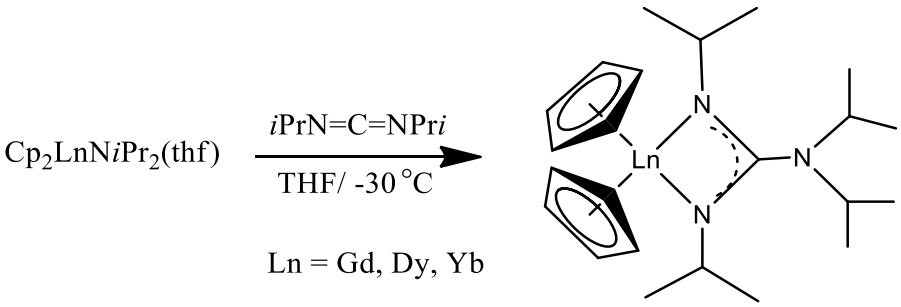
Cole et al. [50] reported the insertion of carbodiimides (RNCNR; R = Cy, Mes, Dipp) into a Sm-C bond of the trivalent $[Sm(L)_2(C{\equiv}CPh)(thf)]$ (L = N,N′-bis(2,6-diisopropylphenyl)formamidinate) in toluene, which resulted in the formation of the respective propiolamidinate complexes $[Sm(L)_2RNC(C{\equiv}CPh)NR]$ (R= Cy or Mes). However, the corresponding reaction with DippNCNDipp did not occur.



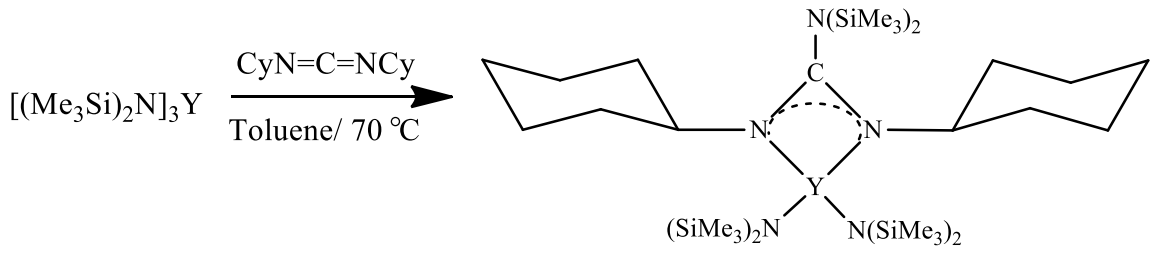
R = Mes, Cy; R≠Dipp

Guanidinate ligands, closely related to amidinate anions, differ primarily in the presence of a tertiary amino group at the central carbon atom of the NCN unit, as indicated by the general formula $[R_2NC(NR')_2]$.

The coordination chemistry of guanidinates began in 1970 with Lappert and coworkers' discovery of the first guanidinate transition metal complexes.[51] Insertion reactions of carbodiimides into Ln-N bonds have been used to synthesize guanidinate lanthanoid complexes, resulting in low-valent lanthanoid species.[52] The complex $Ln(Cp)_2[i\text{PrNC}(N i\text{Pr}_2)N i\text{Pr}]$ (Ln = Gd, Dy, Yb) have been prepared by insertion of N,N′-di-isopropyl-carbodiimide into Ln-N bonds of organolanthanoid amides $Cp_2LnN i\text{Pr}_2(thf)$ under mild reaction conditions. The reaction rate is reported to vary significantly depending on the solvent used.[53]

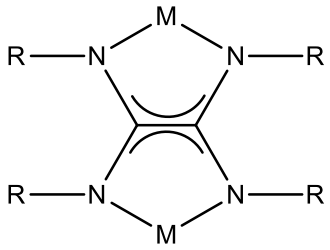


The reaction of N,N'-dicyclohexylcarbodiimide and $Y[N(SiMe_3)_2]_3$ in toluene at 70 °C proceeds *via* insertion of carbodiimide into one of the Y-N bonds, affording the monoguanidinate diamide derivative $Y[N(SiMe_3)_2]_2\{CyNC(N(Me_3Si)_2)NCy]$.[54]

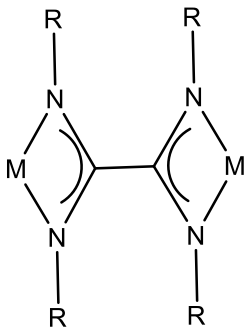


6.1.3.2 Reductive coupling of carbodiimides with low-valent metal complexes

The reductive coupling of carbodiimides with low-valent metal complexes has provided an exciting and straightforward reaction method, leading to novel metallocycles. Oxalamidino metal complexes typically exhibit molecular structures of diamide or diamidinate, based on how the bridging ligand coordinates to the metal centres.[40,55]

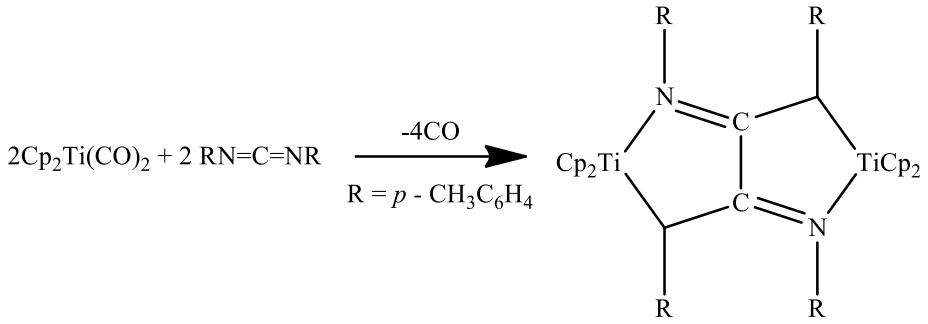


Diamide

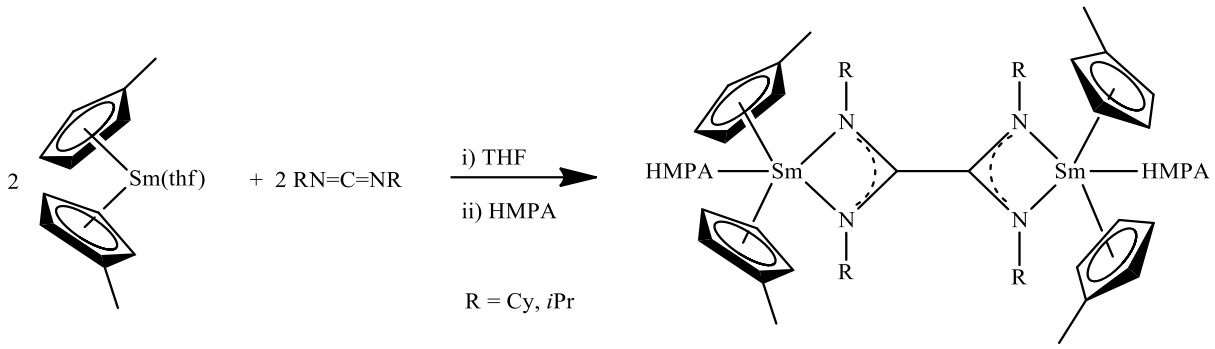


Diamidinate

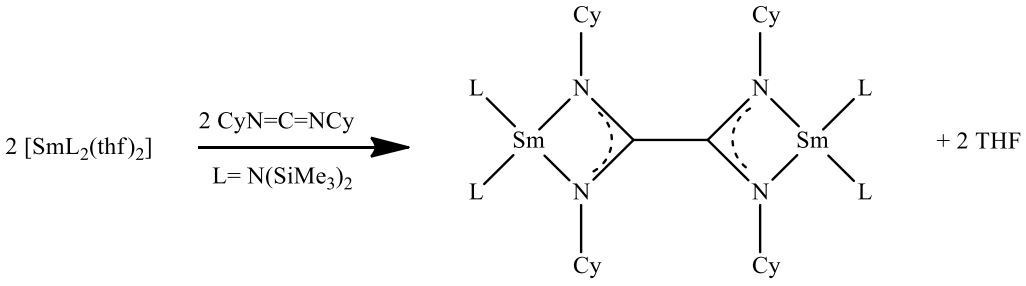
The first example of reductive coupling of carbodiimide was reported in 1979 with the low-valent transition metal complex dicarbonylbis(cyclopentadienyl)titanium(II) ($[C_5H_5]_2Ti(CO)_2$). The resulting complex is an example of a diamide-type structure.[56]



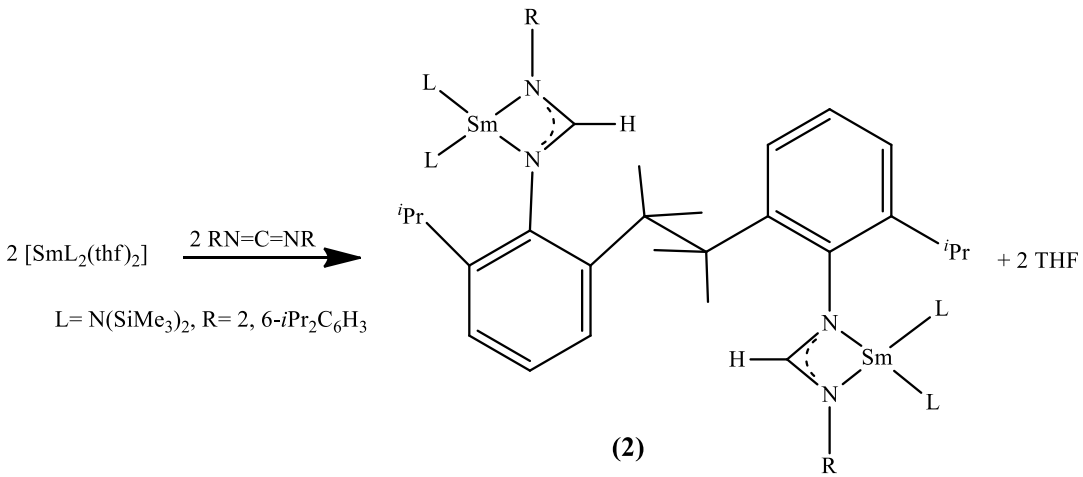
Potent reducing agents, organosamarium(II) complexes are known to react with various unsaturated substrates, resulting in bimetallic complexes through reductive coupling reactions.[22,57,58] The first samarium oxalamidino complex was reported in 2004, synthesized *via* reductive coupling of an isoelectronic carbodiimide using $[(MeC_5H_4)_2Sm(thf)]$ as the reducing agent, which facilitated C-C coupling. The structurally characterised oxalamidino metal complex was found to exhibit a diamidinate type molecular structure.[55]



The reduction reactions of a non-metallocene lanthanoid complex with bulky carbodiimides, leading to a lanthanoid (III) metallocyclic (LnNCN) framework, were reported in 2007. This study examines how the size of the R group in the carbodiimide substrate RNCNR (where R = *i*Pr, Cy, Dipp) influences the formation of different products. Using N,N′-dicyclohexylcarbodiimide resulted in the expected Sm(III) oxalamidinate complex **(1)** with [Sm{N(SiMe$_3$)$_2$}$_2$(thf)$_2$]. However, when using the bulkier N,N′-bis(2,6-diisopropylphenyl)carbodiimide, an unusual binuclear Sm(III) diformamidinate complex **(2)** was formed. This complex featured linked formamidinate resulting from hydrogen transfer and coupling of two isopropyl methine C atoms, rather than coupling at the diimide carbon atoms. This study demonstrated that the formation of the anticipated Ln(III) oxalamidinate with carbodiimides is not always exclusive.[40]

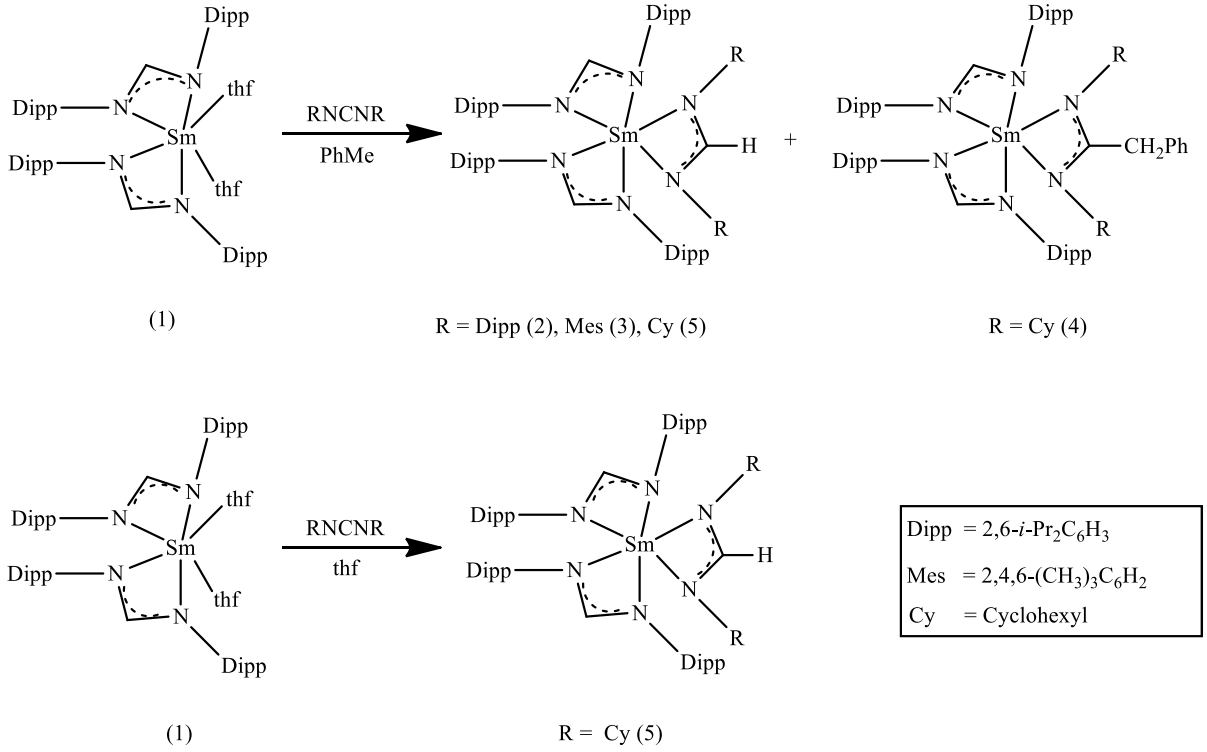


(1)



(2)

The one-electron transfer from the divalent complex [Sm(L)$_2$(thf)$_2$] (L = N,N′-bis(2,6-diisopropylphenyl)formamidinate (DippForm)) **(1)** to carbodiimides (RNCNR; R = Cy, Mes, Dipp) provides a convenient pathway to highly sterically crowded Sm(III) complexes. This study demonstrates that the chelating formamidinate ligand with bulky Dipp substituent seems to prevent the formation of diamidinate or diamide-coupled products. Additionally, the size of the R substituent on the carbodiimide greatly affects the reaction outcome. The reduction of DippNCNDipp in toluene by [Sm(L)$_2$(thf)$_2$] resulted in the formation of the homoleptic tris(formamidinato)samarium(III) complex [Sm(L)$_3$] **(2)**, whereas the reaction of MesNCNMes carbodiimide led to the formation of the heteroleptic complex [Sm(L)$_2$(MesNC(H)NMes)] **(3)**. In a similar reaction, CyNCNCy in toluene produced a mixture of the unexpected benzylamidinate complex [Sm(L)$_2$(CyNC(CH$_2$Ph)NCy)] **(4)** and the heteroleptic tris(formamidinato) complex [Sm(L)$_2$(CyNC(H)NCy)] **(5)**. However, when the reaction was carried out in thf, only the tris(formamidinato) complex (**5)** was isolated.[50]



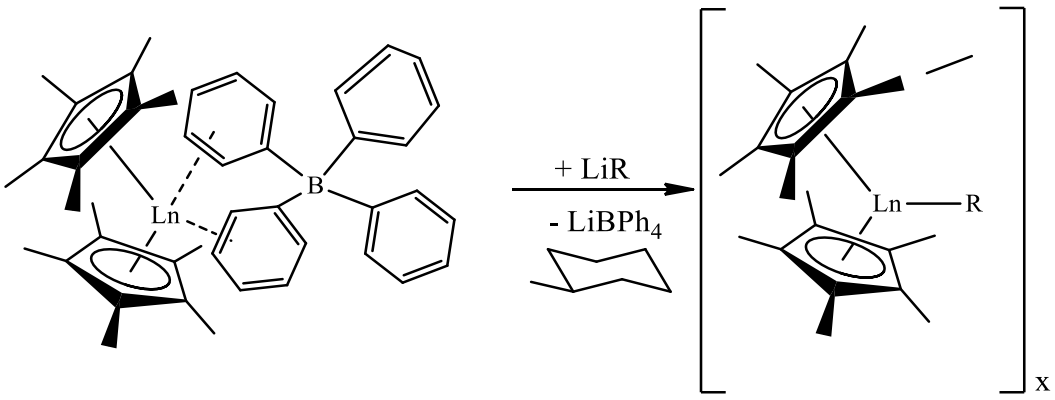
6.1.4 Cationic lanthanoid tetraphenylborate complexes

Cationic metal complexes have attracted significant attention because the formal positive charge on the central metal increases its electrophilicity, thereby enhancing their activity and selectivity in various olefin polymerizations and Lewis acid-catalyzed reactions.

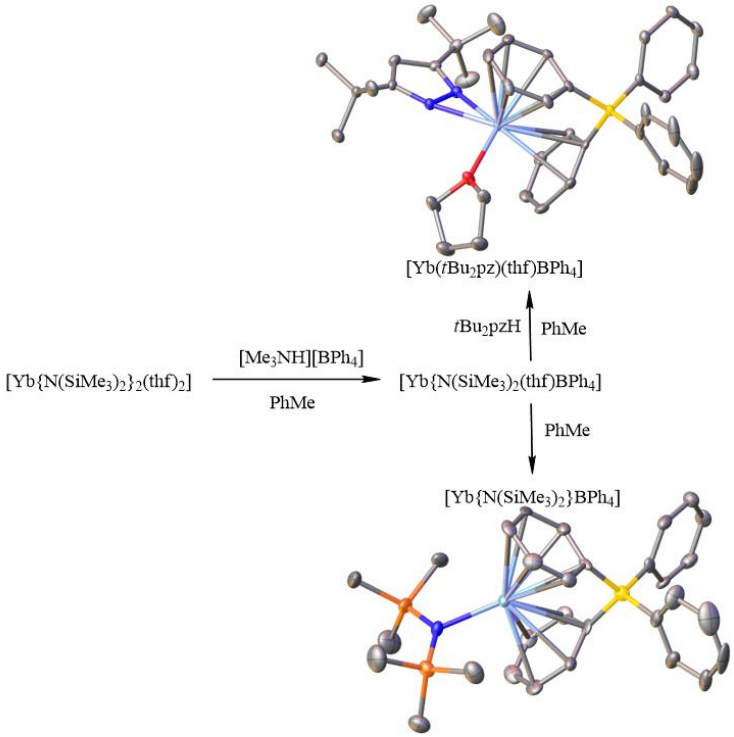
Recent developments have highlighted the synthesis of cationic organolanthanoid complexes as a particularly intriguing area in lanthanoid chemistry, with the potential for unusual reactivity attributed to their enhanced Lewis acid character.[59–62]

The readily available tetraphenylborate anion (BPh_4^-) has long been a valuable counter anion in f-element chemistry. In lanthanoid tetraphenylborates, BPh_4^- is reported to function either in its classical role as a non-coordinating anion[59,63–65] or chelating the metal through π-bonding interactions of the phenyl rings of BPh_4^- anion. The coordination modes vary widely, ranging from η^1- to η^6- chelating interactions.[62,66–68]

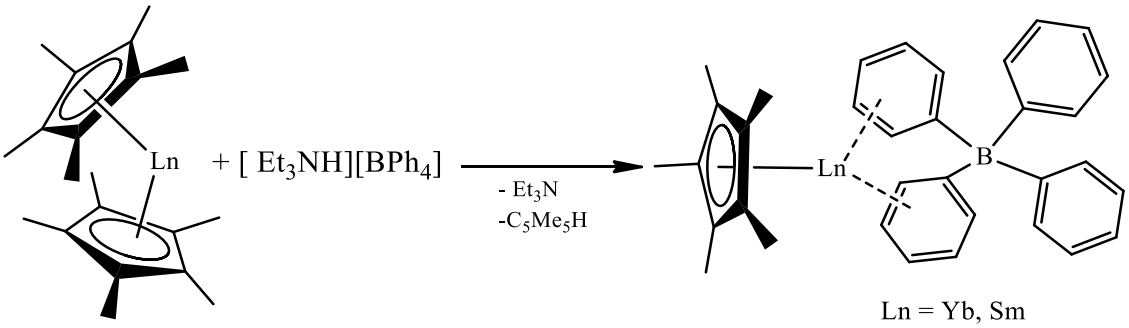
Cationic complexes of lanthanoid metals are well-known, with nearly all involving the metals in their most stable and commonly encountered +3 oxidation state.[62,68–70] In metallocene chemistry, trivalent tetraphenylborate metallocene cations, such as $(C_5Me_5)_2Ln(\eta\text{-}Ph)_2BPh_2$, have demonstrated their value as precursors for various f-element studies. For example, they provide an efficient pathway to unsolvated, sterically unsaturated alkyl lanthanoid metallocenes $[(C_5Me_5)_2LnR]_x$, which exhibit notable C-H activation behaviour.[71]



Cationic complexes of divalent lanthanoids are of particular interest due to their redox reactivity.[59] Deacon et al.[66] reported the first observation of two phenyl groups in the BPh_4^- ligand coordinating as η^6- ligands to a lanthanoid. This is illustrated by η^6:η^6-Yb–Ph_2BPh_2, representing a new class of lanthanoid ansa-metallocenes.[66]

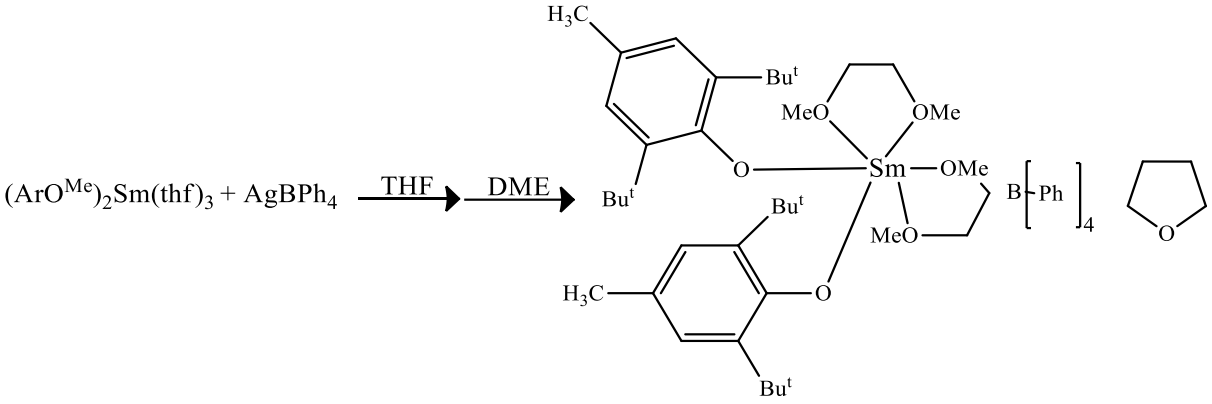


Unsolvated $(C_5Me_5)Ln(\eta^6{:}\eta^1\text{-}Ph)_2BPh_2$ complexes of the redox-active divalent metals, ytterbium(II) and samarium(II) were synthesized by Evans et al.[72] through the reaction of precursors $(C_5Me_5)_2Yb$ and $(C_5Me_5)_2Sm$ with $[Et_3NH][BPh_4]$. Preliminary reactivity studies indicate that these complexes function as valuable precursors in lanthanoid chemistry, similar to their trivalent counterparts as mentioned earlier.



The study of cationic lanthanoid phenoxide and alkoxide complexes has remained relatively underexplored. The first cationic *tert*-butoxide complexes, $[Y_3(\mu_3{-}Cl)(\mu_3{-}OR)_4(\mu{-}OR)_3(OR)_3(thf)_3]^+[BPh_4]^-$, $[Y_2(\mu{-}Cl)(\mu{-}OR)_2(OR)_2(thf)_4]^+[BPh_4]^-$, and $[Y(OR)(Cl)(thf)_5]^+[BPh_4]^-$ (R=*t*Bu) were synthesized in 1990 as representatives of a new class of yttrium alkoxides *via* metathesis reactions between yttrium alkoxide chloride $[Y_3(OR)_7Cl_2(thf)_2]$ (R = *t*Bu) and $AgBPh_4$ or $NaBPh_4$.[73]

The first example of a cationic samarium aryloxide complex, $[(ArO^{Me})_2Sm(DME)_2][BPh_4]\cdot thf$, was synthesized *via* the one-electron oxidation of $(ArO^{Me})_2Sm(thf)_3$ with $AgBPh_4$. Its ability to catalyse the ring-opening polymerization of ε-caprolactone (ε-CL) was reported to significantly exceed that of the corresponding trivalent complex, $(ArO^{Me})_3Sm(thf)_2$. This implies that the formal positive charge on the central metal enhances its electrophilicity, which benefits homogeneous catalysis.[74]



6.1.5 Current study

This chapter is divided into three key sections. First, novel rare earth aryloxide complexes are synthesized using the previously unexplored 2,6-di-*tert*-butyl-4-ethylphenolate ligand to investigate the coordination chemistry of these new ligands and also to facilitate reactivity studies. Secondly, contrasting reactions of unsaturated carbodiimide substrates (RN=C=NR') with Ln^{II} aryloxides have been explored, offering a promising route to novel amidinatolanthanoid complexes. In addition, the reactivity of a carbodiimide with organolanthanoid alkynyl complexes generated by redox transmetallation has been explored to examine insertion into Ln–C sigma bonds. Lastly, this chapter presents the synthesis and characterisation of the first redox-active cationic divalent europium phenoxide complex with a discrete tetraphenylborate (BPh_4) counterion, along with efforts to synthesize other organolanthanoid(II) tetraphenylborate complexes.

Overall, the goal is to investigate how different steric and electronic effects of ligands impact complex formation and to explore their unique reactivity profiles.

Some of the work in this chapter resulted in a publication in the journal *Chemistry—A European Journal* (see reprint in Appendix Two).

6.2 Results and Discussion

6.2.1 Synthesis of divalent rare earth aryloxide complexes

The redox transmetallation/ligand exchange reaction of bis(pentafluorophenyl)mercury ($Hg(C_6F_5)_2$), 2,6-di-*tert*-butyl-4-ethyl-phenol ($HOAr^{Et}$), and an excess of ytterbium in diethyl ether (Et_2O) yielded the red-coloured divalent ytterbium(II) complex $[Yb(OArEt)_2(Et_2O)_2]$ **(6.1)** in moderate yields. In a similar reaction with excess europium in thf, the green-coloured europium complex $[Eu(OAr^{Et})_2(thf)_3]\cdot thf$ **(6.2)** was produced, also in moderate yields.

The metathesis reaction between $[K(OAr^{Et})(thf)_x]$ and $[Sm(I)_2(thf)_2]$ in toluene resulted in the divalent, red-coloured complex $[Sm(OAr^{Et})_2(thf)_3]\cdot PhMe$ **(6.3)**, in average yield.

$$Yb + Hg(C_6F_5)_2 + 2HOAr^{Et} \xrightarrow{Et_2O} [Yb(OAr^{Et})_2(Et_2O)_2] \quad \textbf{(6.1)}$$

$$Eu + Hg(C_6F_5)_2 + 2HOAr^{Et} \xrightarrow{THF} [Eu(OAr^{Et})_2(thf)_3]\cdot thf \quad \textbf{(6.2)}$$

$$2[K(OAr^{Et})(thf)_x] + [SmI_2(thf)_2] \xrightarrow{PhMe} [Sm(OAr^{Et})_2(thf)_3]\cdot PhMe + 2KI \quad \textbf{(6.3)}$$

Scheme 6.1: Preparation of rare earth bis(aryloxides) **6.1** and **6.2** by RTP and **6. 3** by metathesis reactions.

Studies have shown that the stronger reducing power of Sm(II) often causes its oxidation by unreacted $Hg(C_6F_5)_2$, leading to a very low yield of the desired Sm(II) product and a high yield of the Sm(III) oxidation product.[75] Even when using weaker oxidants like diphenylmercury with 2,4,6-trimethylphenol (HOmes) in reactions with Eu, Sm, and Yb to obtain Ln(II) compounds, only europium was reported to produce the divalent trinuclear complex $[Eu_3(Omes)_3(thf)_6]$.[10] Therefore, to avoid the formation of Sm(III) oxidation products, a metathesis reaction was employed instead of the RTP reaction.

Satisfactory elemental analyses were obtained for complexes **6.1** and **6.2**. When bulk **6.3** was first isolated, the samarium analysis agreed with the composition determined from single crystals. However, microanalysis following overseas transfer to London indicated a significant loss of solvent, coordinated thf, and toluene.

The IR spectra of all three samples displayed the expected features of the OAr^{Et} ligand, with no OH absorptions, confirming phenol deprotonation and ruling out accidental hydrolysis. Compounds **6.2** and **6.3** exhibited medium-strong bands at 1040–1030 cm^{-1} and 880–860 cm^{-1}, which are attributed to the ring stretching modes of coordinated thf and is correlated with previous reports of thf solvated rare earth aryloxide complexes.[76]

The ^{1}H NMR spectra of the ytterbium and samarium compounds in C_6D_6 confirmed the proposed formulations, displaying a complex series of resonances for the OAr^{Et} ligands. Both compounds showed two environments for the aryloxide *tert*-butyl protons at different ratios, with lower field resonances integrating to a total of 36H. The overlapping resonances of coordinated thf and aryloxide make it impossible to integrate the thf signals in **6.3**. The paramagnetic nature of Eu(II)/(III) caused broad NMR signals , making them uninterpretable, thus, no further investigation was pursued. However, elemental analyses and crystallographic studies provided definitive confirmation of the complexes' identity.

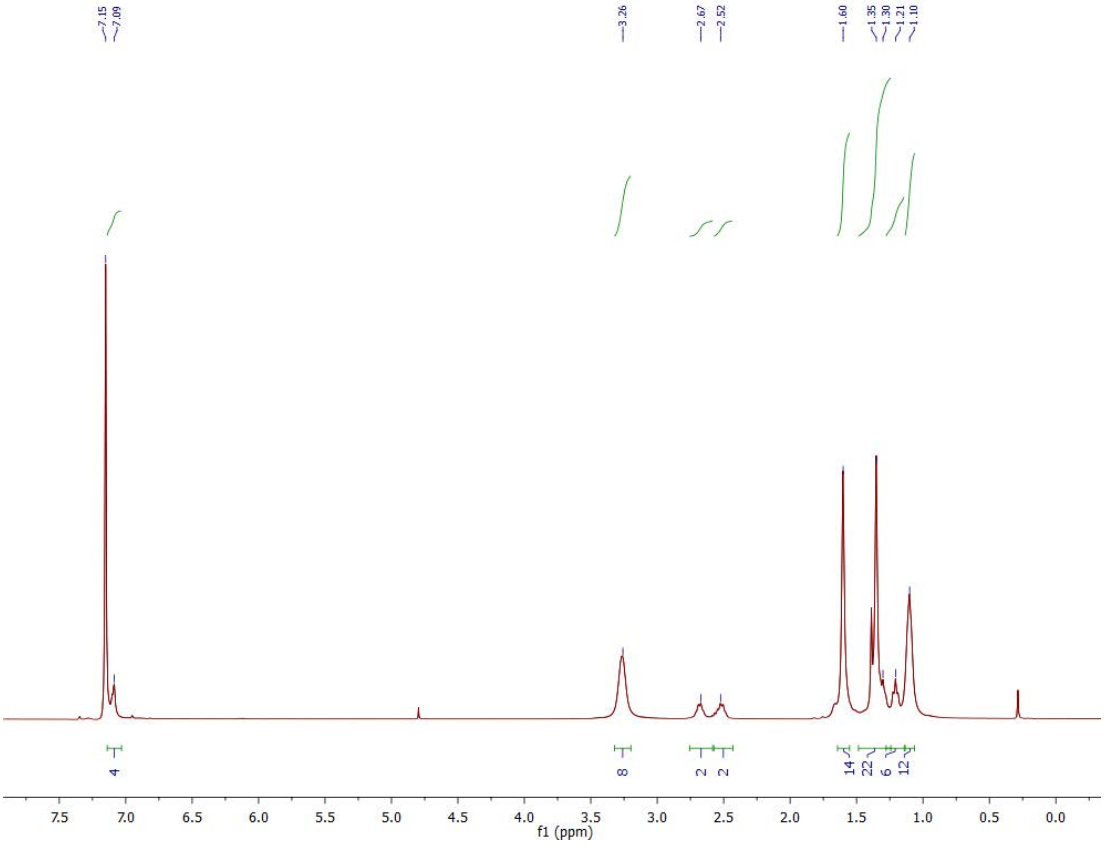


Figure 6.1: ^{1}H NMR spectrum of $[Yb(OAr^{Et})_2(Et_2O)_2]$ (**6.1**) in C_6D_6.

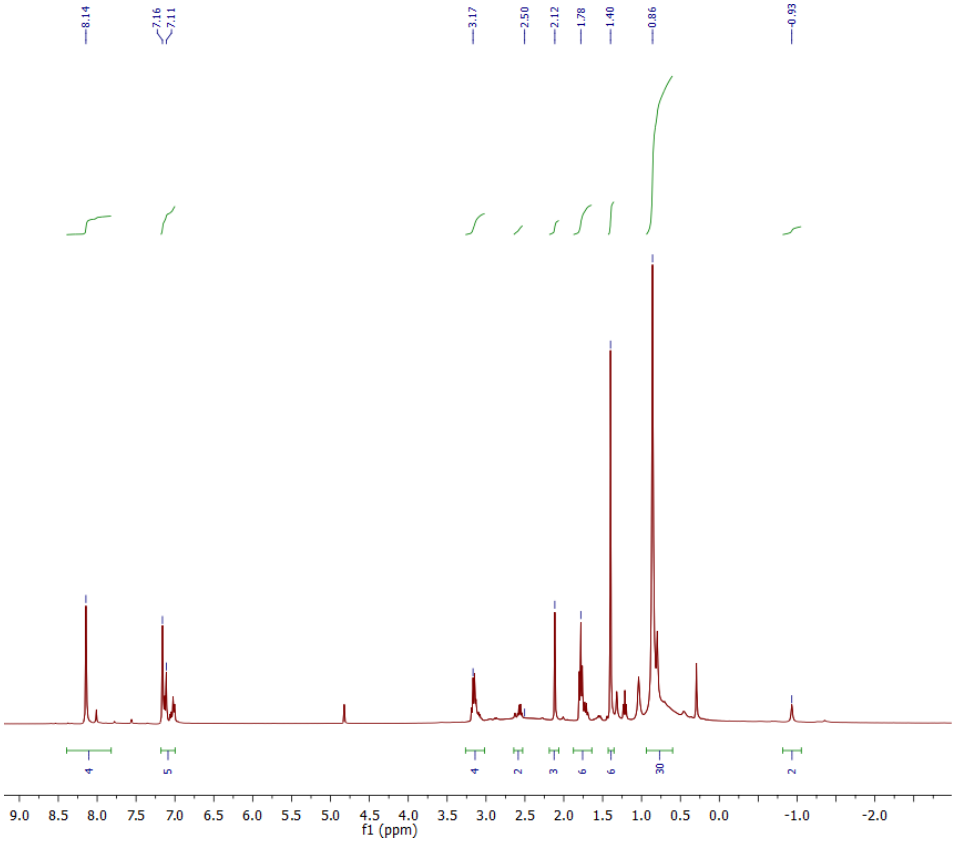


Figure 6.2: ^{1}H NMR spectrum of [Sm(OAr^{Et})$_2$(thf)$_3$]·PhMe (**6.3**) in C_6D_6.

Complex **6.1** crystallises in the monoclinic *C*2/*c* space group, with half of the molecule present in the asymmetric unit. The coordination geometry around the Yb centre consists of four oxygen atoms: two from the OAr^{Et} ligands (O1 and O1#1) and two from the Et$_2$O molecules (O2 and O2#1). The [Yb(OAr^{Et})$_2$(Et$_2$O)$_2$] complex indicates a monomeric, highly distorted tetrahedral arrangement, as evidenced by the significant variation in interligand angles (Table 6.1) from a regular tetrahedral geometry. The irregularity arises from the much larger ArO-Yb-OAr angles (110.49(12)°) compared to the (Et$_2$O)O-Yb-O(Et$_2$O) angles (91.25(13)°). The average Yb-OAr distances are approximately 0.25 Å shorter than the Yb-O(Et$_2$O) distances consist with the ligand charges. The lattice contains a single molecule of C_6D_6, as the crystals were grown from a C_6D_6 solution prepared in an NMR tube.

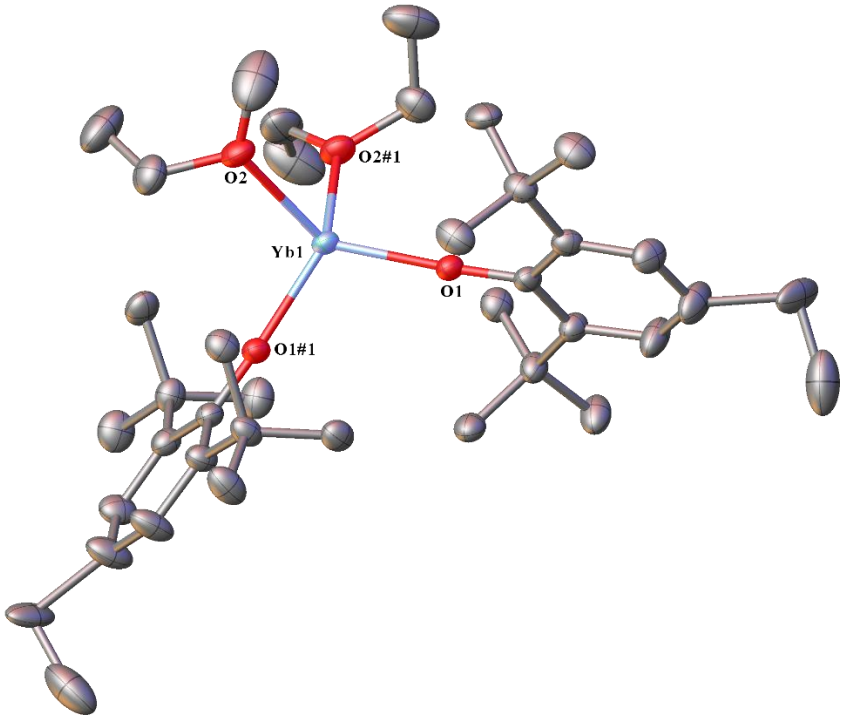


Figure 6.3: Molecular diagram of [Yb(OAr^{Et})$_2$(Et$_2$O)$_2$] **(6.1)** generated from single-crystal XRD data. Carbon atoms are shown in grey. Thermal ellipsoids are drawn at the 50% probability level. Hydrogen atoms and lattice C_6D_6 are omitted for clarity. Symmetry Code: $^{\#1}$ 1-X,+Y,1/2-Z.

Table 6.1: Selected bond angles and distances (Å) for compound **6.1**

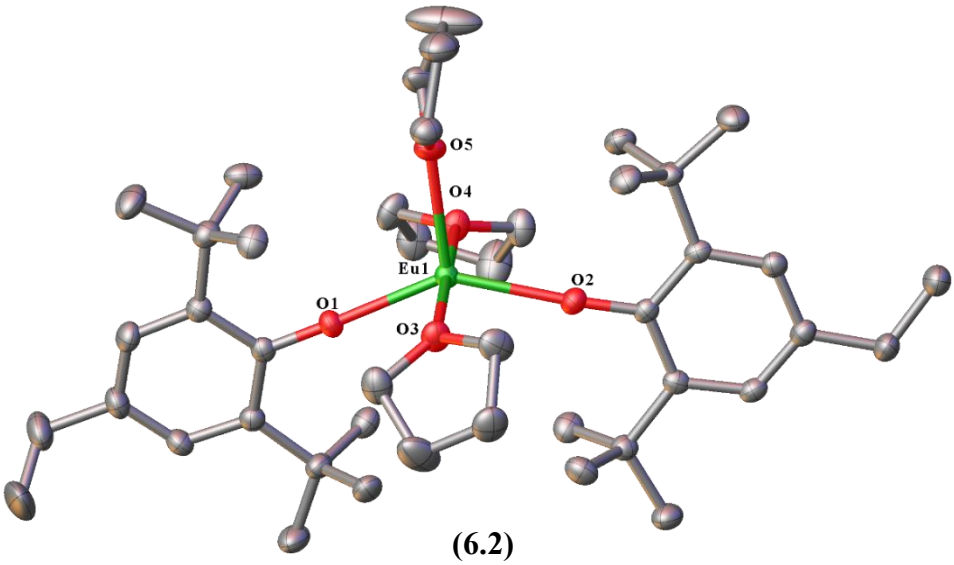
Angles (degrees)	O1(OAr)-Yb1-O1#1(OAr)	110.49(12)
	O2(Et$_2$O)-Yb1-O2#1 (Et$_2$O)	91.25(13)
	O2#1 (Et$_2$O)-Yb1-O1(OAr)	99.53(9)
	O2 (Et$_2$O)-Yb1-O1(OAr)	129.18(9)
	O2#1(Et$_2$O)-Yb1-O1#1(OAr)	129.18(9)
	O2 (Et$_2$O)-Yb1-O1#1(OAr)	99.53(9)
	Yb1-O1-C1	176.9(2)
Distances (Å)	Yb1-O1	2.140(2)
	Yb1-O2	2.396(3)

The divalent complex [Eu(OAr^{Et})$_2$(thf)$_3$]·thf **(6.2)** crystallizes in the monoclinic $P2_1/c$ space group as a monomer (Figure 6.4). The coordination sphere is five-coordinate, comprising two *transoid* aryloxide ligands (ArO-Ln-ArO angle: 143.97(6)°) (O1 and O2) and three thf ligands (O3, O4, O5). The Reedijk parameter[77] is 0.52 indicating stereochemistry essentially midway between square pyramidal and trigonal bipyramidal, but just favouring the latter. This is evidenced by the nearly linear O(thf)–Ln–O(thf) bond angle (175.07(6)°) along the axial

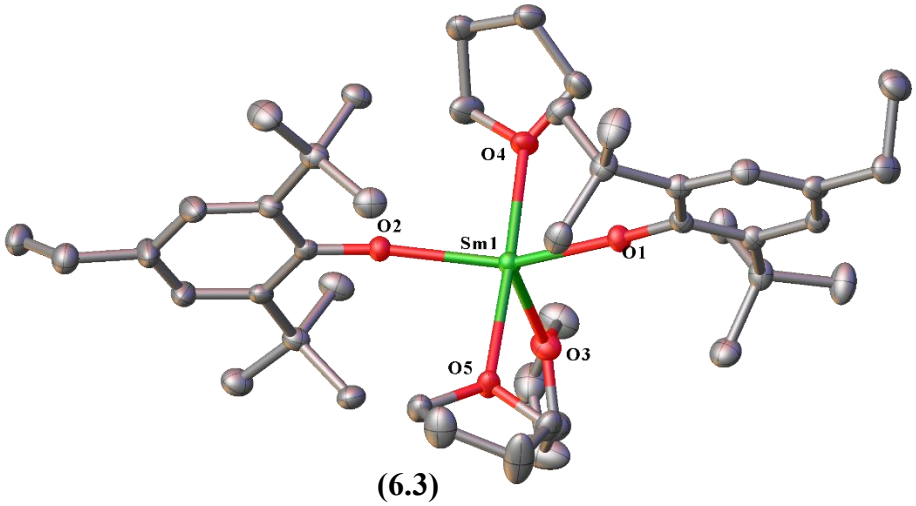
plane, with an average deviation of 15.98° from the ideal trigonal bipyramidal angle of 120° in the equatorial plane.

$[Sm(OAr^{Et})_2(thf)_3]\cdot PhMe$ **(6.3)** also crystallizes as a monomer in the monoclinic $P2_1/c$ space group (Figure 6.4). Its five-coordinate geometry closely resembles that of the Eu analogue, with a Reedijk parameter[77] ($\tau = 0.54$) slightly more towards trigonal bipyramidal geometry. In this distorted trigonal bipyramidal configuration, the axial plane features a nearly linear O(thf)–Sm–O(thf) bond angle of 177.76(5)°, while the equatorial plane is formed by the oxygen atoms of the two *transoid* aryloxide ligands and one thf oxygen. The samarium derivative **6.3** exhibits slightly longer average Ln–O bond distances (2.4688 Å) compared to the europium complex **6.2** (2.4544 Å), reflecting the larger ionic radius of Sm^{2+} in comparison to Eu^{2+}.

The five coordinate (low coordination number)complexes of **6.2** and **6.3** are analogous to several closely related derivatives, such as $[Ln(OAr^{Me})_2(thf)_3]$ (Ln = Sm, Eu, Yb; OAr^{Me} = 2,6-di-*tert*-butyl-4-methylphenolate) complexes,[78-81] and $[Ln(OAr^{OMe})_2(thf)_3]\cdot thf$ (Ln = Sm, Yb; (OAr^{OMe} = 2,6-di-*tert*-butyl-4-methoxyphenolat)[75] demonstrating that the ethyl substitution in the phenoxide ligand has little structural impact when thf co-ligands are present. Moreover, compound **6.3** is isomorphous with $[Sm(OAr^{OMe})_2(thf)_3].thf$[75] despite the different 4-substitutent (though similar chain length) and solvent of crystallization. The Sm-O bond lengths are comparable with those of the isomorph.[75]



(6.2)



(6.3)

Figure 6.4: Molecular diagrams of **6.2** and **6.3** generated from single-crystal XRD data. Carbon atoms are shown in grey.Thermal ellipsoids are drawn at the 50% probability level. Hydrogen atoms and lattice solvents are omitted for clarity.

Table 6.2: Selected bond angles and distances (Å) for compounds **6.2** and **6.3**.

Complex	$[Eu(OAr^{Et})_2(thf)_3]\cdot thf$ **(6.2)**		$[Sm(OAr^{Et})_2(thf)_3]\cdot PhMe$ **(6.3)**	
Angles (degrees)	O1-Eu1-O2	143.97(6)	O1-Sm1-O2	145.56(6)
	O3-Eu1-O4	175.07(6)	O4-Sm1-O5	177.76(5)
	O3-Eu1-O5	90.61(6)	O3-Sm1-O5	87.80(5)
	O4-Eu1-O5	94.13(6)	O3-Sm1-O4	92.90(5)
	O1-Eu1-O3	88.62(6)	O1-Sm1-O5	91.35(5)
	O1-Eu1-O4	88.58(6)	O1-Sm1-O4	90.50(5)
	O1-Eu1-O5	108.86(6)	O1-Sm1-O3	106.03(5)
	O2-Eu1-O3	89.54(6)	O2-Sm1-O5	87.57(5)
	O2-Eu1-O4	90.35(6)	O2-Sm1-O4	90.19(5)
	O2-Eu1-O5	107.14(6)	O2-Sm1-O3	108.33(5)
Distances (Å)	Eu1-O1	2.3077(16)	Sm1-O1	2.3202(15)
	Eu1-O2	2.3235(17)	Sm1-O2	2.3351(15)
	Eu1-O3	2.5446(18)	Sm1-O3	2.5434(18)
	Eu1-O4	2.5723(18)	Sm1-O4	2.5618(16)
	Eu1-O5	2.5237(18)	Sm1-O5	2.5833(16)

As discussed in the introduction, The RTP reactions have been extensively used in the synthesis of trivalent and divalent lanthanoid aryloxide complexes. The primary goal of this section was to prepare rare earth (RE) aryloxide complexes that have not been reported before, to be utilized as precursors in Sections 6.2.2 and 6.2.3. After achieving promising results with the synthesis of the samarium aryloxide complex $[Sm(OAr^{Et})_2(thf)_3]\cdot PhMe$ **6.3** *via* the metathesis route, two additional reactions were attempted. These involved $[K(Omes)(thf)_x]$ with $[Sm(I)_2(thf)_2]$, and $[K(Omes)(thf)_x]$ with $[Yb(I)_2(thf)_2]$ (Omes = 2,4,6-trimethylphenolate), aiming to yield the

respective divalent rare earth aryloxide complexes. However, no crystals could be isolated from these reactions, so they were not studied further.

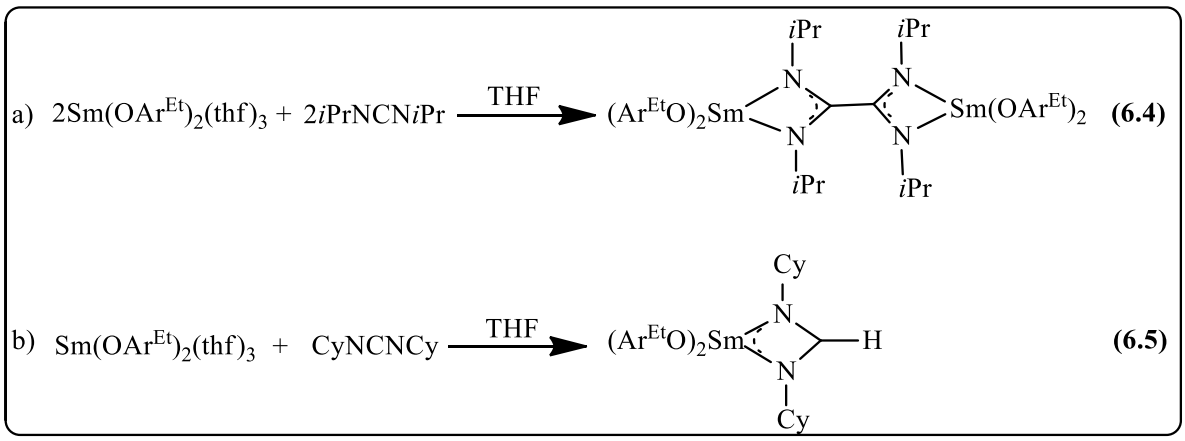
6.2.2 Contrasting reactions of carbodiimides with divalent lanthanoid species.

6.2.2.1 Reactions of Carbodiimides with Samarium(II) bis(2,6-di-*tert*-butyl-4-ethylphenolate).

The reaction of a deep red solution of $[Sm(OAr^{Et})_2(thf)_3]\cdot thf$ **(6.3)** with an equivalent amount of N,N'-diisopropylcarbodiimide (*i*PrC=N=C*i*Pr) (DIC) in thf at room temperature caused a colour change to light yellow, indicating oxidation to Sm(III). Crystals were isolated in moderate yield upon standing at -25 ˚C for several days. The resulting oxalamidinatosamarium(III) complex $[(OAr^{Et})_2Sm(\mu\text{-}C_2N_4iPr_4)Sm(OAr^{Et})_2]\cdot 2PhMe$ **(6.4)** was confirmed *via* X-ray crystallography, showing a diamidinate configuration where each Sm atom binds to one side of the tetraisopropyloxalamidinate (Scheme 6.2(a)).

Substituting the diisopropylcarbodiimide by the bulkier N,N'-dicyclohexylcarbodiimide (CyC=N=CCy) (DCC) caused a similar colour change, also indicating oxidation to Sm(III). However, the isolated product from this reaction was the formamidinatosamarium(III) complex $[Sm(OAr^{Et})_2(CyNC(H)NCy)(thf)_2]\cdot 2thf$ **(6.5)** (Scheme 6.2(b)), which was crystallized in low yield.

Furthermore, no evidence was found of competitive insertion of the carbodiimide into the Sm–O bond, (unlike guanidinate and amidinate formation involving Ln–N and Ln–C insertion), probably owing to the oxophilicity of lanthanoids.



Scheme 6.2: Reduction of carbodiimides by samarium(II) bis(2,6-di-*tert*-butyl-4-ethylphenolate): (a) oxalamidinatosamarium (III) complex **(6.4)**; and (b) formamidinatosamarium (III) complex **(6.5)** formation.

Fresh samples of both compounds **6.4** and **6.5** gave satisfactory %Sm values, whilst microanalyses after transport to the UK showed loss of 1 toluene of crystallization and two thf of crystallization from then crystal composition of **6.4** and **6.5** respectively. The solvent loss was also detected by ^{1}H NMR spectroscopy (see Experimental). **6.5** also gave a low %C, a common issue with rare-earth metal-organic compounds.[82–88]

The ^{1}H NMR spectrum of **6.4** is shifted away from the typical diamagnetic region, attributed to the paramagnetic Sm^{III} ion. The spectrum of **6.4** is complex, with the *tert*-butyl resonances appearing as three sharp singlets at -0.79, -0.64, and -0.42 ppm, integrating overall to 72 hydrogens. The isopropyl CH_3 protons, along with the CH_3 resonances from the ethyl substituent on the OAr^{Et} group, are spread over a wide chemical shift range of 0.30 to 2.04 ppm. Only one lattice toluene molecule is observed in the ^{1}H NMR spectrum.

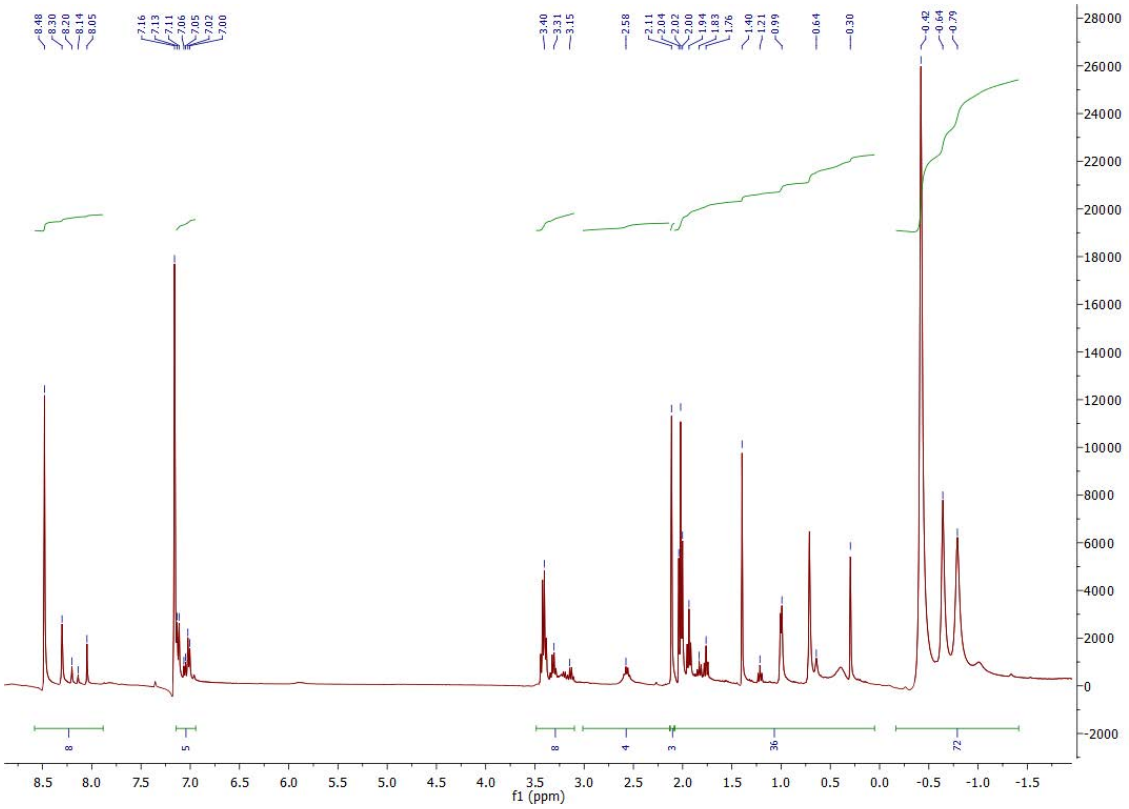


Figure 6.5: ^{1}H NMR spectrum of $[(OAr^{Et})_2Sm(\mu\text{-}C_2N_4iPr_4)Sm(OAr^{Et})_2]\cdot 2PhMe$ **(6.4)** in C_6D_6.

In the ^{1}H NMR spectrum of complex **6.5**, signal broadening occurs due to the paramagnetic Sm^{III} ion, complicating assignment and integration, especially in the upfield region. A pronounced downfield shift for the formamidinate backbone NC*H*N appears as a singlet at δ=7.98 ppm. The singlet at δ = 8.15 ppm is assigned to the aromatic CH protons of the phenyl ring. Coordinated thf CH_2 signals are expected in the broad upfield region, but no lattice thf was detected in the proton NMR spectrum.

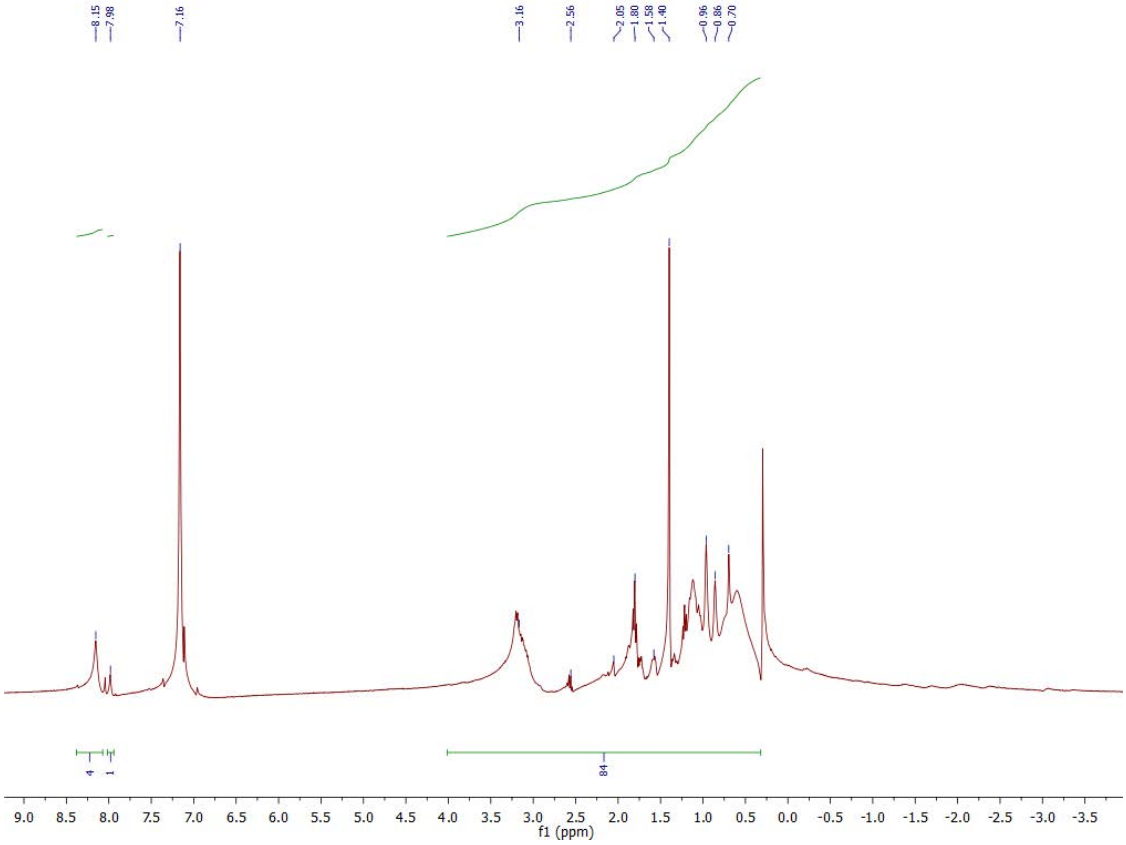


Figure 6.6: ^{1}H NMR spectrum of $[Sm(OAr^{Et})_2(CyNC(H)NCy)(thf)_2]\cdot 2thf$ **(6.5)** in C_6D_6.

Complex **6.4** crystallizes in the triclinic space group *P*-1, and the molecular structure adopts a diamidinate configuration rather than a diamide (Figure 6.7). Each Sm atom is bound to one side of the tetraisopropyloxalamidinate ($(iPr)_2N_2C\text{-}CN_2(iPr)_2^{2-}$) ligand, which functions as a bridging tetradentate ligand by chelating both Sm atoms (Sm1 and Sm2) through four nitrogen atoms (N1, N2, N3, N4). Two OAr^{Et} ligands coordinate to each metal centre, giving the Sm atoms a coordination number of four (binding through O1,O2 at Sm1 and O3,O4 at Sm2). Each metal atom assumes a pseudo-trigonal-planar geometry if the oxalamidinate ligands are treated point donors (through C4 and C50). The phenolate groups are positioned above and below the plane formed by the Sm, two nitrogen atoms, and one of the central carbon atoms of the oxalamidinate ligand, oriented to minimize interactions with the isopropyl groups.

The two planes formed by the atoms Sm1, N1, N2, C4 and Sm2, N3, N4, C50 are nearly perpendicular, with dihedral angle of 91.0(5)° between them while the trigonal planes are also approximately orthogonal (dihedral angle 85.3(3)°). This staggered arrangement minimizes interactions between the neighbouring isopropyl groups. The central C–C bond length is characteristic of a single bond, while the C–N bond lengths in the C_2N_4 unit fall between typical single and double bond lengths (Table 6.4), indicating an electronically delocalized CN_2 units within the diamidinate moiety.

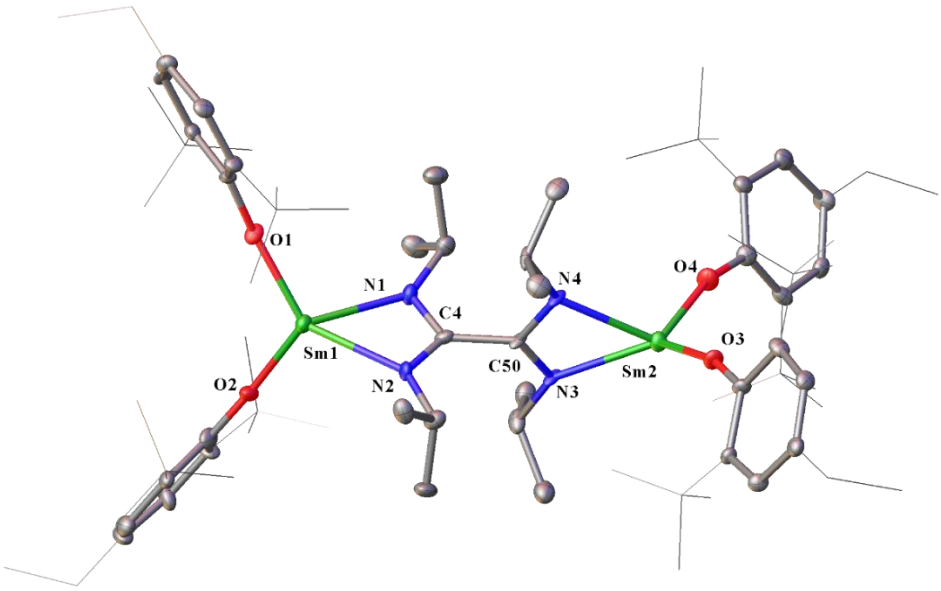


Figure 6.7: Molecular diagram of complex **6.4** generated from single-crystal XRD data. Carbon atoms are shown in grey. Thermal ellipsoids are drawn at the 30% probability level. Hydrogen atoms and the two lattice toluene molecules are omitted for clarity. *Tert*-butyl and ethyl groups are drawn as wireframe for clarity.

Table 6.3: Selected bond angles and distances (Å) for compound **6.4**

Angles (degrees)	O1-Sm1-O2	114.4(3)	Distances (Å)	C4-C50	1.488(17)
	N1-Sm1-N2	56.6(4)		N1-C4	1.370(15)
	N1-C4-N2	113.7(12)		N2-C4	1.337(16)
	O1-Sm1-N1	105.8(4)		N4-C50	1.378(15)
	O2-Sm1-N2	111.1(4)		N3-C50	1.288(15)
	O1-Sm1-N2	133.9(4)		Sm1-N1	2.364(11)
	O2-Sm1-N1	118.7(4)		Sm1-N2	2.416(10)
	O3-Sm1-O4	113.8(4)		Sm2-N4	2.36(1)
	N3-Sm2-N4	56.1(3)		Sm2-N3	2.382(10)
	N3-C4-N4	113.3(12)		Sm1-O1	2.090(8)
	O3-Sm2-N3	132.8(4)		Sm1-O2	2.063(9)
	O3-Sm2-N4	103.3(4)		Sm2-O3	2.140(9)

	O4-Sm2-N4	114.2(4)		Sm2-O4	2.115(9)
	O4-Sm2-N3	113.4(4)			

The complex $[Sm(OAr^{Et})_2(CyNC(H)NCy)(thf)_2]\cdot 2thf$ **(6.5)** crystallizes in the monoclinic $P2_1/c$ space group, with the asymmetric unit comprising half of the molecule. The samarium atom is six-coordinate, bonded to two OAr^{Et} ligands (through O1 and O1#1), two thf molecules (through O2 and O2#1), and two nitrogen atoms (through N1 and N1#1) from the chelating formamidinate fragment. The geometry around the samarium centre is near pseudo square pyramidal, considering the κ(N,N′) formamidinate ligand as a single-point donor from the central carbon atom of the 1,3-diazaallyl unit (Figure 6.8).

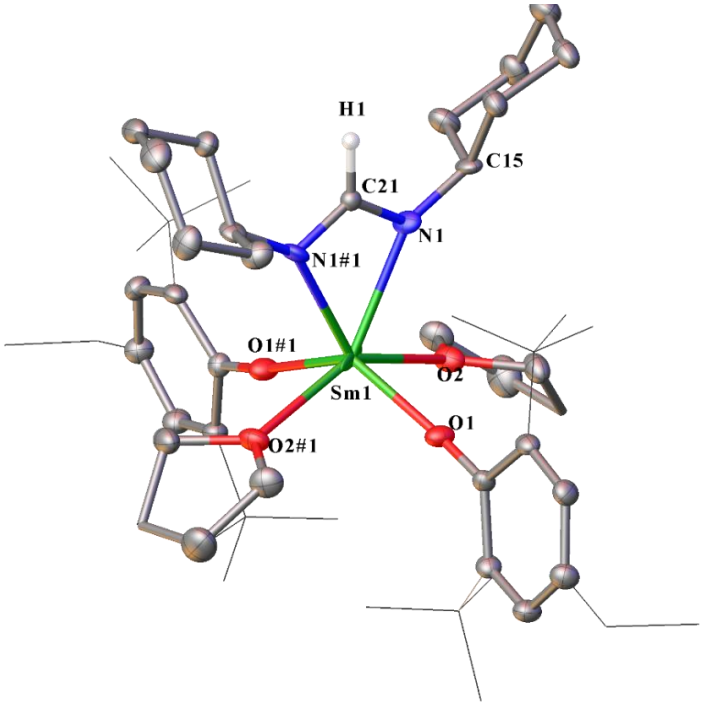


Figure 6.8: Molecular diagram of complex **6.5** generated from single-crystal XRD data. Carbon atoms are shown in grey. Thermal ellipsoids are drawn at the 50% probability level. Hydrogen atoms (except for the hydrogen in the formamidinate fragment), as well as with two lattice thf molecules are omitted for clarity. *Tert*-butyl and ethyl groups were drawn as wireframe for clarity.

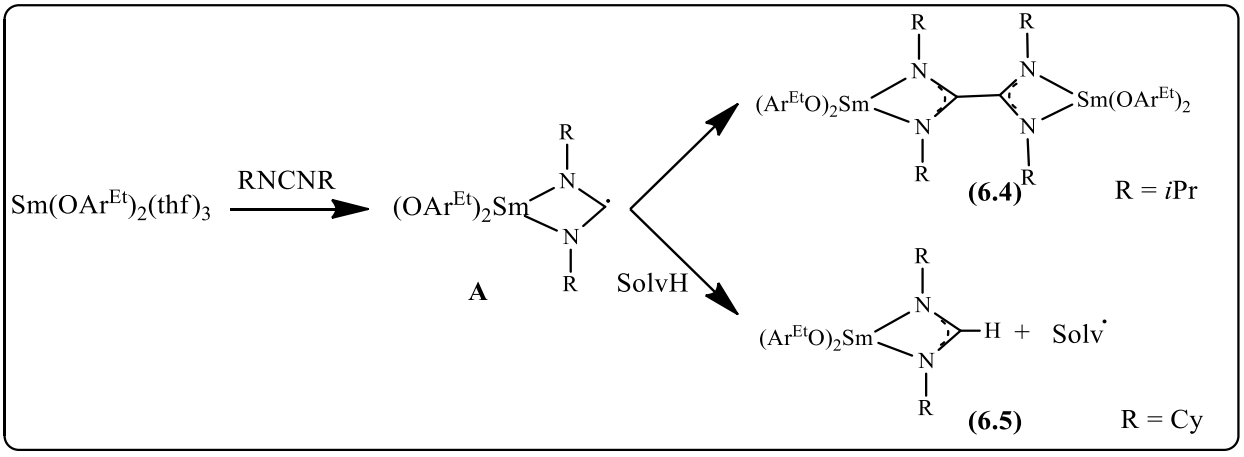
Similar to **6.4** the C–N distances within the formamidinate group are shorter than typical C–N single bonds, and the Sm–O(thf) bond lengths are longer than Sm–O(OAr), consistent with the ligand charges.

Table 6.4: Selected bond angles and distances (Å) for compound **6.5**

Angles (degrees)	O1-Sm1-O1#1	137.68	Distances (Å)	Sm1-N1	2.45
	O2-Sm1-O2#1	145.18		Sm1-O1	2.22

	N1-C21-N1#1	118.71		Sm1-O2	2.49
	N1-Sm1-N1#1	55.54		Sm1-C21	1.32
	C21-N1-Sm1	92.88		C21-H1	1.06
	C21-N1-C15	120.73		N1-C15	1.45
	N1-C21-H1	120.65		C21-N1	1.32

The differing outcomes with **6.4** and **6.5** can be rationalised by one electron transfer to the carbodiimide, forming a radical anion (species A in Scheme 6.3), which, for the less bulky carbodiimide, dimerises to form the oxalamidinate ligand. In contrast, the bulkier radical undergoes hydrogen abstraction from the solvent or reagents before dimerization can occur. H-abstraction from thf in lanthanoid chemistry has precedent, e.g.[89,90] This outcome is simpler than when H-abstraction occurs from the methine moiety of the diisopropyl group, which leads to coupling through the methine carbons.[40]



Scheme 6.3: Suggested reaction pathways for the formation of oxalamidinate **(6.4)** and formamidinate **(6.5)** complexes through the reduction of carbodiimides by $[Sm(OAr^{Et})_2(thf)_3]\cdot thf$

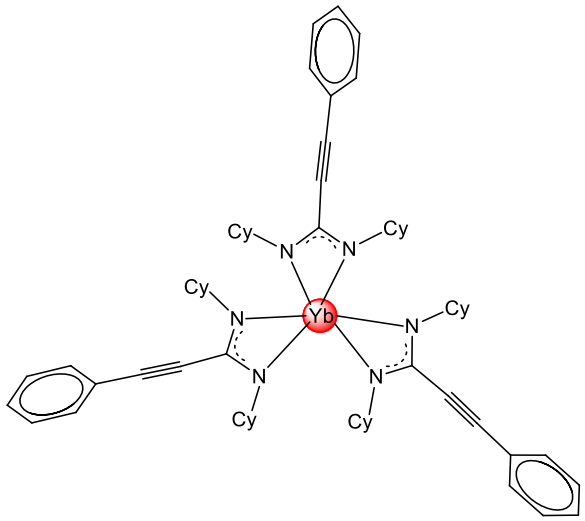
Several attempts were made using various divalent and trivalent rare earth aryloxides with bulky carbodiimides, each featuring different R groups. Unfortunately, none of these reactions produced crystals suitable for X-ray crystallography, so further analysis was not conducted.

6.2.2.2 The one pot reactions of Ln metals with $Hg(PhCC)_2$ and N,N′-dicyclohexylcarbodiimide (CyNCNCy).

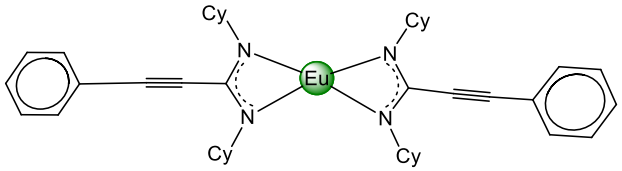
The reaction between an excess of rare earth metal, one molar equivalent of bis(phenylethynyl)mercury ($Hg(PhCC)_2$), and two molar equivalents of N,N′-dicyclohexylcarbodiimide (CyNCNCy) in tetrahydrofuran (thf) at room temperature gave amidinate complexes resulting from insertion of carbodiimide molecules into the Ln-C sigma

bonds of the Ln-CCPh species. The observed reactions are formulated in Scheme 6.4. The characterisation of each product was performed using elemental analysis, single-crystal X-ray crystallography, IR and NMR spectroscopy, and melting point determination.

$$2Yb + 3Hg(PhC{\equiv}C)_2 + 6\ CyN{=}C{=}NCy \xrightarrow[\text{r.t. 3 days}]{\text{THF}} 2[Yb\{CyNC(CCPh)NCy\}_3]{\cdot}2thf \quad \textbf{6.6}$$



$$Eu + Hg(PhC{\equiv}C)_2 + 2\ CyN{=}C{=}NCy \xrightarrow[\text{r.t. 3 days}]{\text{THF}} [Eu\{CyNC(CCPh)NCy\}_2(thf)_2] \quad \textbf{6.7}$$



Scheme 6.4: Synthesis of $[Yb^{III}\{CyNC(C{\equiv}CPh)NCy\}_3]{\cdot}2thf$ **(6.6)** and $[Eu\{CyNC(C{\equiv}CPh)NCy\}_2(thf)_2]$ **(6.7)**.

The reaction with Yb proceeds with the formation of yellow crystals of the homoleptic tris(amidinato) complex $[Yb^{III}\{CyNC(C{\equiv}CPh)NCy\}_3]{\cdot}2thf$ (**6.6**). As the redox transmetallation between Yb metal and $Hg(CCPh)_2$ yields a divalent polymer $[Yb(CCPh)_2]_n$,[91] the oxidation state outcome is unexpected, and a divalent complex analogous to **6.7** was anticipated. The formation of **6.6** is explicable if the expected $\{Yb[CyNC(C{\equiv}CPh]NCy)_2\}$ is strongly reducing as it can then be oxidised by $Hg(CCPh)_2$ to give a trivalent alkynyl $[Yb^{III}\{CyNC(C{\equiv}CPh)NCy\}_3]{\cdot}2thf$ into which a further carbodiimide can be inserted to give **6.6**.

$$2[Yb\{CyNC(C{\equiv}CPh)NCy\}_2] + Hg(CCPh)_2 \longrightarrow 2\,[Yb\{CyNC(C{\equiv}CPh)NCy\}_2CCPh] + Hg \quad (1)$$

$$[Yb\{CyNC(C{\equiv}CPh)NCy\}_2CCPh] + CyN{=}C{=}NCy \longrightarrow [Yb\{CyNC(C{\equiv}CPh)NCy\}_3] \quad (2)$$

There is precedent for reaction (1) in that the divalent Sm complex $[Sm(DippForm)_2(thf)_2]$, (DippFormH = N,N'-bis(2,6-diisopropylphenyl)formamidine), reacts with bis(phenylethynyl)mercury to give $[Sm(DippForm)_2CCPh(thf)]$ with deposition of mercury metal.[90]

Elemental analyses of complex **6.6** and **6.7** were consistent with the single crystal compositions. The ^{1}H NMR spectrum of **6.6** exhibited broadening and shifting of signals due to the paramagnetism of Yb^{III}, making assignment and integration challenging, particularly in the upfield region. The cyclohexyl protons appeared alongside an additional 2.5 equivalents of THF from the solution, spanning a range of 3.94 to 1.50 ppm. The crystals were highly moisture sensitive and had to be quickly removed from the solution to ensure stability for NMR analysis. As a result, they retained 20 hydrogen atoms from residual free THF. The aromatic CH protons of the phenyl group were observed as two distinct resonances, one at 13.79 ppm, while the rest appeared over a range of 7.43 to 6.73 ppm, along with protons from C_6D_6 solvent. A meaningful NMR spectrum could not be obtained for **6.7** because of paramagnetism. The most noteworthy feature of the IR spectra of **6.6** and **6.7** are bands attributable to C≡C stretching at 2210-2120 cm^{-1}.[92] Bands observed around 1500–1650 cm^{-1} are assigned to delocalized C..N stretching vibrations.[93] IR spectrum of **6.7** also displayed two distinct bands at 1043 and 886 cm^{-1}, corresponding to coordinated thf.[94]

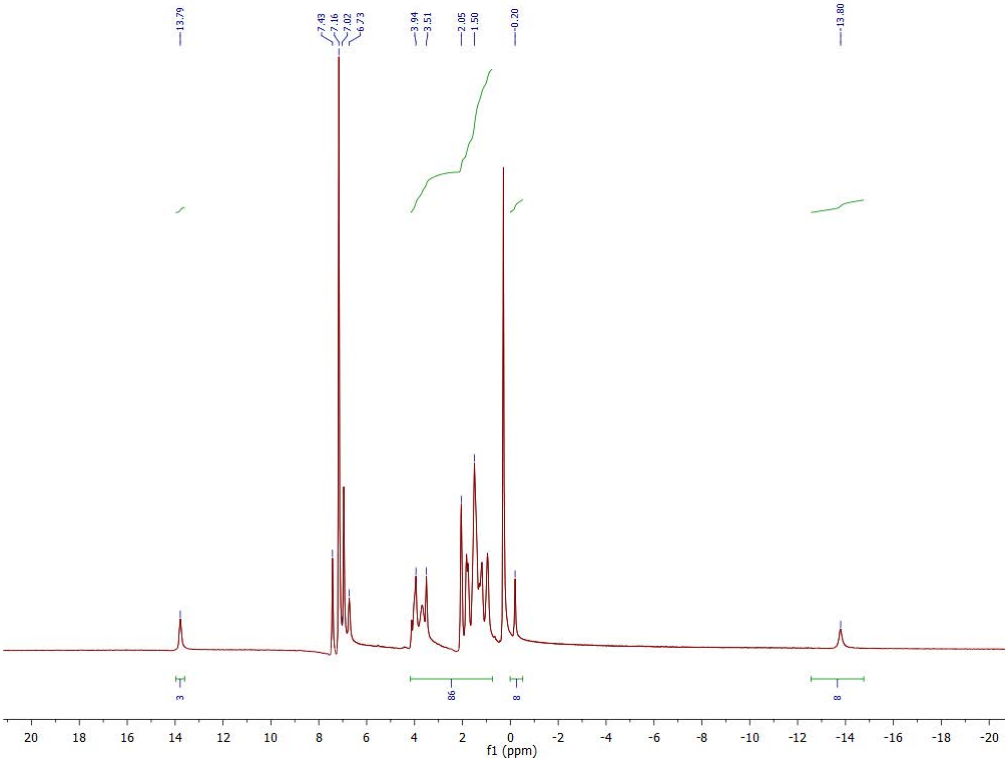


Figure 6.9: ^{1}H NMR spectrum of $[Yb^{III}\{CyNC(C{\equiv}CPh)NCy\}_3]\cdot 2thf$ **(6.6)** in C_6D_6.

Several attempts were made to extend the study of Yb and Eu with N,N'-diisopropylcarbodiimide to establish a direct comparison with the Sm system. Unfortunately, none of these reactions produced crystals suitable for X-ray crystallography after trying many methods and solvents, so further studies were not conducted. Likewise, the reaction of Sm metal with $Hg(CCPh)_2$ and either carbodiiomide did not have a satisfactory outcome.

The atom-to-atom connectivity in single crystals of compound (**6.6**) was determined through X-ray structure analysis. The six coordinated complex crystallizes in the triclinic *P-1* space group, adopting a pseudo-trigonal planar geometry if the phenylethynyl-substituted amidinate ligands are considered as point donors positioned at the central carbon atoms. The complex has six nitrogen atoms from three κ (N,N′) amidinate CyNC(C≡CPh)NCy ligands, binding through N1,2, N3,4 and N5,6, which are arranged in a three-vane propeller configuration. The C≡CPh groups, bound to the carbon atom of the CyNCNCy backbone, are linear with the Ph group positioned furthest from the metal centre (Figure 6.10).

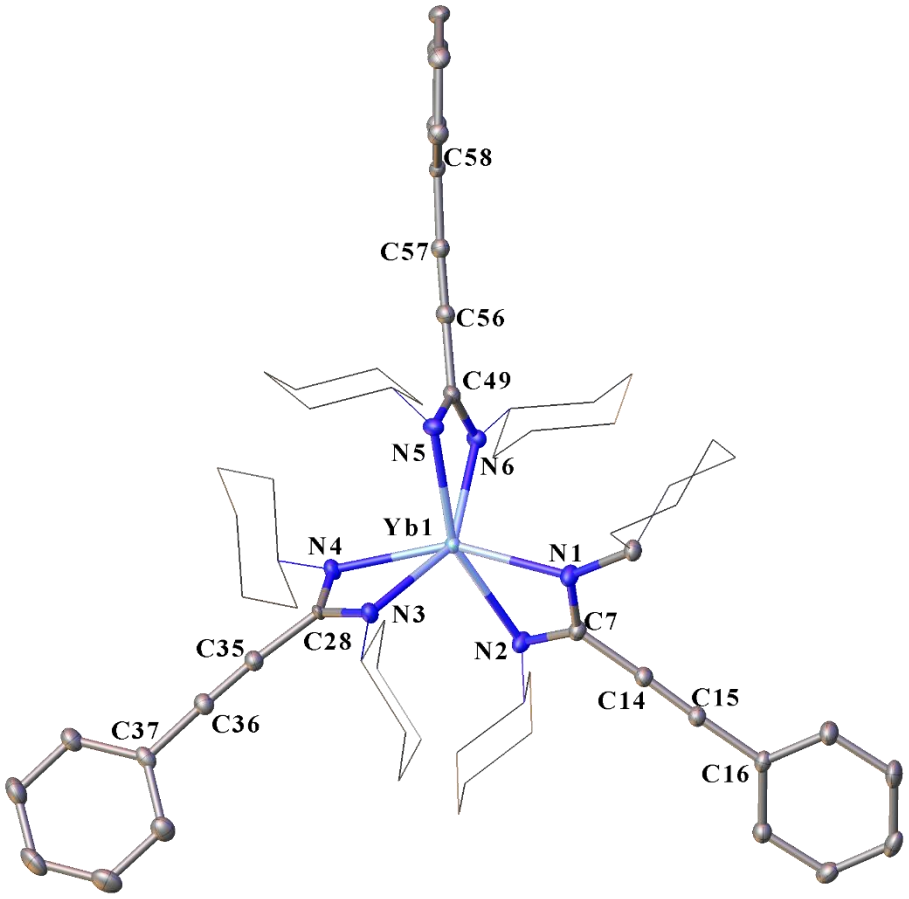


Figure 6.10: Molecular diagram of complex **6.6** generated from single-crystal XRD data. Thermal ellipsoids are drawn at the 30% probability level. Hydrogen atoms along with two lattice thf molecules are omitted for clarity. Cyclohexyl rings were drawn as wireframe for clarity.

The C-N bond lengths in the amidinate groups are nearly equivalent and significantly shorter than typical C–N single bonds,[95] suggesting that the π-electrons of the C=N double bonds are delocalized across the N–C–N unit. The Yb–N distances of Cy-substituted nitrogen atoms, as listed in Table 6.6, fall between the typical Yb-N single bond lengths and donor N:→ Yb bond lengths, which range from 2.19-2.69 Å.[53,96–98] In particular, they are similar to but marginally shorter than those (2.328(4)-2.354(5)Å)[90] of six coordinate [Yb(EtForm)$_3$].2thf (EtForm = N,N'-bis(2,6-diethylphenyl)formamidinate, suggesting comparable steric demands between the present amidinate ligand and the bulky fomamidinate EtForm. The C≡C bond lengths are close to those (1.204(2) and 1.206(2) Å) of diphenylacetylene.[99] L–Yb–L angles, as defined by the C–Yb–C angle (where C refers to the NCN carbon atom), are listed in Table 6.5.

Table 6.5: Selected bond distances (Å) and angles for compound **6.6**.

Angles (degrees)	C28-Yb1-C49	116.91(5)	Distances (Å)	Yb1-N1	2.3179(15)
	C7-Yb1-C49	124.44(5)		Yb1-N2	2.3366(15)
	C7-Yb1-C28	118.64(5)		Yb1-N3	2.3358(16)
	N1-Yb1-N2	58.28(5)		Yb1-N4	2.3236(15)
	N3-Yb1-N4	58.27(6)		Yb1-N5	2.3183(15)
	N5-Yb1-N6	58.42(5)		Yb1-N6	2.3224(15)
	C7-C14-C1	178.2(2)		N1-C7	1.334(2)
	C14-C15-C16	177.9(2)		N2-C7	1.328(2)
	C28-C35-C36	174.3(2)		N6-C49	1.332(2)
	C35-C36-C37	177.5 (2)		N5-C49	1.332(2)
	C49-C56-C57	173.3(2)		N3-C28	1.317(2)
	C56-C57-C58	176.3(2)		N4-C28	1.350(2)
				C14-C15	1.193(3)
				C35-C36	1.196(3)
				C56-C57	1.194(3)

Complex **6.7** crystallizes in the monoclinic system, space group $P2_1/c$. The molecular structure is depicted in Figure 6.11, with selected bond lengths and angles provided in Table 6.6. In the monomeric complex, the Eu atom is six-coordinate, with four N atoms from a chelating amidinates fragments (binding through N1,2 and N3,4) coordinating in a κ-N,N'-fashion and two *trans*-thf donor molecules (O1 and O2; O1-Eu-O2 174.7(2)°). The coordination geometry is pseudo-square planar, when regarding the κ-N,N′-amidinate CyNC(C≡CPh)NCy ligands occupying a single coordination site at the central carbon atoms (C7 and C28) of the NCN fragments.

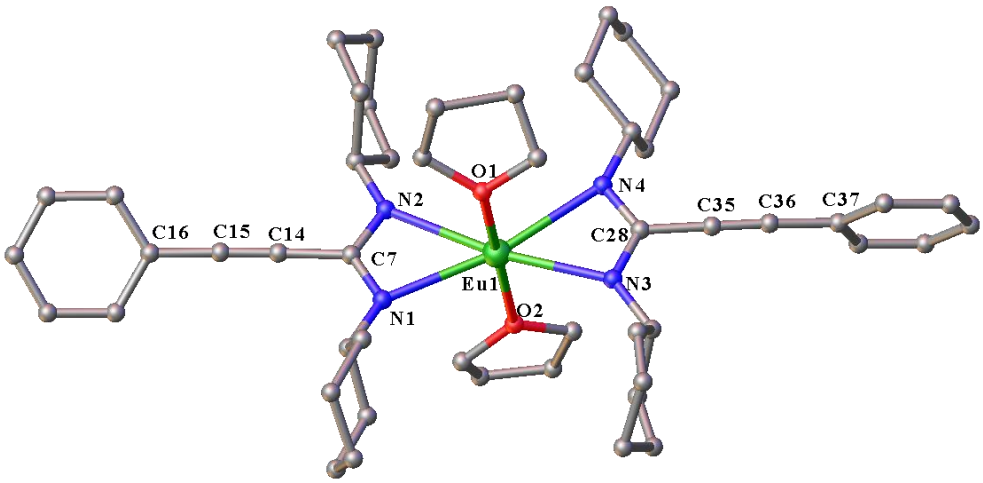


Figure 6.11: Molecular diagram of complex **6.7** generated from single-crystal XRD data. Thermal ellipsoids are drawn at the 10% probability level. Hydrogen atoms are omitted for clarity.

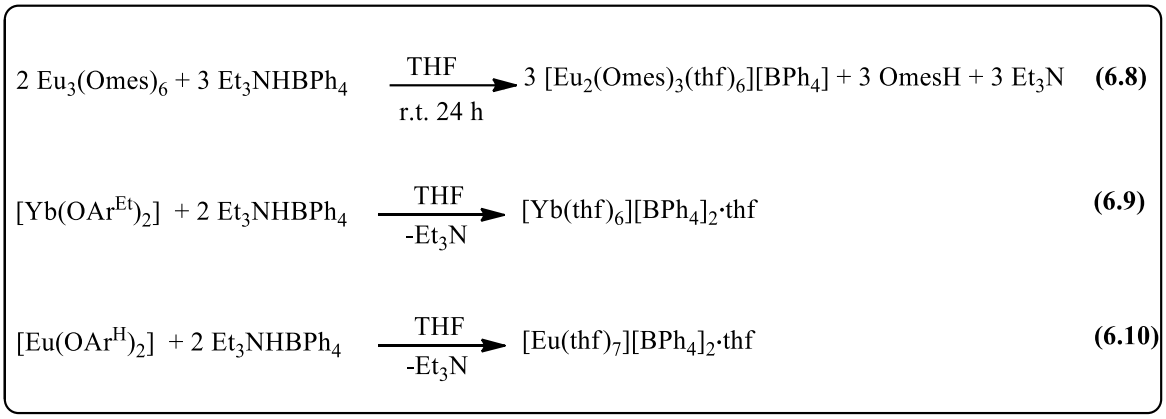
Similar to compound **6.6** the bond distances of the C–N bonds suggest they are intermediate in length between a single and a double bond, indicating electronic delocalization throughout the two NCN units of the amidinate fragment. The europium–nitrogen bond lengths in complex **6.7** are longer than those in complex **6.6** by 0.25 Å, which is less than the 0.30 Å expected from the ionic radius difference between six coordinate Eu^{2+} and six coordinate Yb^{3+}.[100] This implies greater crowding in **6.6** than expected for the reduction in size. As for **6.6**, the C≡C bond lengths are near those of diphenylacetylene.[99]

Table 6.6: Selected bond distances (Å) and angles for compound **6.7**.

Angles (degrees)	C7-Eu1-C28	169.9(2)	Distances (Å)	Eu1-O1	2.535(5)
	O21-Eu1-O2	174.7(2)		Eu1-O2	2.538(5)
	C7-Eu1-O2	92.87(17)		Eu1-N1	2.546(5)
	C7-Eu1-O1	88.63(17)		Eu1-N2	2.611(6)
	C28-Eu1-O1	91.73(16)		Eu1-N3	2.520(6)
	C28-Eu1-O2	87.68(16)		Eu1-N4	2.616(5)
	N3-Eu1-N4	52.80(19)		N1-C7	1.312(9)
	N3-C28-N4	119.5(6)		N2-C7	1.328(8)
	N1-Eu1-N2	52.25(18)		N3-C28	1.331(8)
	N1-C7-N2	118.7(6)		N4-C28	1.315(8)
	N1-Eu1-N3	137.6(2)		C14-C15	1.188(8)
	N1-Eu1-N4	169.2(2)		C35-C36	1.189(8)
	N2-Eu1-N3	170.18(18)			
	N2-Eu1-N4	117.42(19)			
	C7-C14-C15	176.8(7)			
	C14-C15-C16	178.6(7)			
	C28-C35-C36	177.1(7)			
	C35-C36-C37	175.9(7)			

6.2.3 Synthesis and characterisation of cationic lanthanoid phenoxide complexes

The complex $[Eu_3(Omes)_6(thf)_6]$[10] was treated with $[Et_3NH][BPh_4]$[101] in thf, and the mixture was stirred overnight. Yellow crystals of $[Eu_2(Omes)_3(thf)_6]^+[BPh_4]^-\cdot 1.5thf$, suitable for X-ray crystallographic analysis, were obtained after storing the concentrated solution at -25°C for several weeks. This compound consists of a well-separated cation, $[Eu_2(Omes)_3(thf)_6]^+$, and an anion, $[BPh_4]^-$, with 1.5 thf molecules per unit cell (Scheme 6.6).



Scheme 6.5: Synthesis of complexes **6.8-6.10**.

Compound **6.8** was characterised using IR spectroscopy, elemental analysis, melting point determination, and X-ray crystallography. Due to the paramagnetic nature of Eu^{2+} complexes, ^{1}H NMR spectroscopy was not applicable for confirming the identity of the product. IR spectra of compound exhibits (C=C_{Ar}) absorptions around 1570-1600 cm^{-1} and three δ(C–H_{Ar}) bands between 700–800 cm^{-1}, consistent with the presence of free B–Ph groups.

The dimeric complex **6.8** crystallizes in the triclinic space group *P*-1, with each Eu ion being six-coordinate. The coordination environment comprises of three bridging Omes ligands (O1, O2 and O3) and three oxygen atoms of thf molecules (O4-O6 for Eu1 and O7-O9 for Eu2) (Figure 6.12). The stereochemistry of **6.8** is distorted trigonal prismatic.

The structure features a similar unusual Eu(μ-OAr)$_3$Eu framework, as seen in the reported binuclear structures [Eu_2(Odpp)$_4$][102] and [Eu_2(OC_6H_3-2,6-Me_2)$_4$(dme)$_3$],[103] where in both cases, the two europium centres are bridged by three oxygens from OAr groups, with one europium centre also having a terminal OAr ligand.

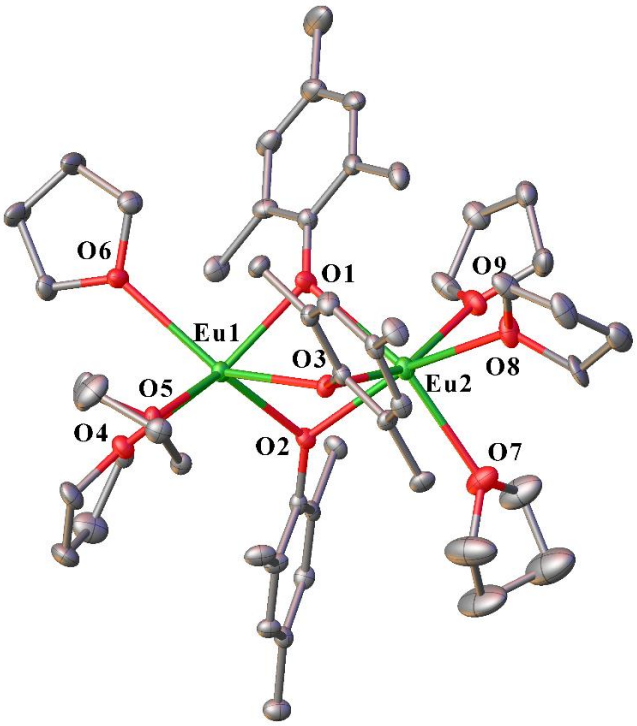


Figure 6.12: Molecular diagram of the cation in complex $[Eu_2(Omes)_3(thf)_6][BPh_4]\cdot 1.5thf$ **(6.8)** generated from single-crystal XRD data. Carbon atoms are shown in grey. Thermal ellipsoids are drawn at the 10% probability level. The lattice thf molecules and hydrogen atoms have been omitted for clarity.

The average Eu-O (Omes) bond length is 2.461 Å, shorter than the Eu-O (thf) bond length (2.591 Å), which are consistent with the ligand charges. These bond lengths closely resemble those in $[Eu_3(Omes)_6(thf)_6]$,[10] where 2.494 Å for Eu-O (Omes) and 2.644 Å for Eu-O (thf). Additionally, the O_{br}–Eu–O_{br} bond angles are smaller than the O_{ter}–Eu–O_{ter} angles observed for the terminal thf ligands. The $[BPh_4]$ anion displays typical bond distances.

Table 6.7: Selected bond distances (Å) and angles for compound **6.8**.

Angles (degrees)	O1-Eu1-O2	74.8(2)	Distances (Å)	Eu1-O1	2.449(7)
	O1-Eu1-O3	75.5(2)		Eu1-O2	2.473(6)
	O2-Eu1-O3	76.79(19)		Eu1-O3	2.457(6)
	O1-Eu2-O2	74.8(2)		Eu1-O4	2.610(7)
	O1-Eu2-O2	74.992)		Eu1-O5	2.606(7)
	O2-Eu2-O3	77.1(2)		Eu1-O6	2.606(7)
	O4-Eu1-O5	80.6(2)		Eu2-O1	2.474(7)
	O4-Eu1-O6	80.7(2)		Eu2-O2	2.449(6)
	O5-Eu1-O6	83.0(2)		Eu2-O3	2.466(6)
	O7-Eu2-O8	84.0(3)		Eu2-O7	2.587(8)
	O7-Eu2-O9	89.1(3)		Eu2-O8	2.586(7)
	O8-Eu2-O9	84.9(3)		Eu2-O9	2.557(8)

	Eu1-O1-Eu2	89.8(2)			
	Eu1-O2-Eu2	89.84(19)			
	Eu1-O3-Eu2	89.82(19)			

Several attempts were made to synthesize the analogous cationic complexes using [Yb(OAr^{Et})$_2$(Et_2O)$_2$] and [Eu(OAr^{H})$_2$(thf)$_3$] with the same [Et_3NH][BPh_4] as in the previous reaction. However, the results were disappointing, yielding only the corresponding ytterbium and europium bis(tetraphenylborates) as isolated products (Scheme 6.6). These fully solvated Ln(II) dications, free of any coordinating anions: [Yb(thf)$_6$(BPh_4)$_2$]·thf[59] and [Eu(thf)$_7$(BPh_4)$_2$]·thf][104] were confirmed by single-crystal X-ray crystallography, and the unit cell parameters were consistent with the reported structures.[59,104]

6.3 Conclusion

In this chapter, three novel divalent lanthanoid complexes (**6.1**, **6.2** and **6.3**) featuring the 2,6-di-*tert*-butyl-4-ethylphenolate ligand were synthesized using RTP and metathesis reactions to facilitate reactivity studies.

Our initial goal was to explore the reactivity of various carbodiimides with novel and previously reported divalent and trivalent lanthanoid aryloxides of differing steric bulk, aiming to insert the carbodiimide into the Ln–O backbone to create new ligands—an insertion type not previously reported. However, none of these complexes yielded the anticipated Ln–O insertion products. Interestingly, the divalent samarium bis(phenoxide) complex [Sm(OAr^{Et})$_2$(thf)$_3$]·PhMe **(6.3)** exhibits differing reductive reactivity with carbodiimides, depending on steric factors, and not insertion into the Sm–O bonds. With the less bulky N,N'-bis(diisopropylcarbodiimide), one electron reduction and coupling yields a bimetallic oxalamidinatosamarium(III) complex **(6.4)**, whereas the bulkier N,N'-dicyclohexylcarbodiimide gives the mononuclear formamidinatosamarium(III) complex **(6.5)**. On the other hand, insertion reactions dominate on reaction of bis(phenylethynyl)lanthanoid(II) species, Ln(CCPh)$_2$ (Ln = Eu, Yb), generated *in situ* from Ln metal and Hg(CCPh)$_2$, with N,N'-dicyclohexylcarbodiimide. Whilst Eu(CCPh)$_2$, gives a divalent *C*-phenylethynylamidinate, [Eu{CyNC(C≡CPh)NCy}$_2$(thf)$_2$] **(6.7)**, the ytterbium analogue yields trivalent [Yb^{III}\{CyNC(C≡CPh)NCy\}$_3$]·2thf. **(6.6)**. Since the redox transmetallation between Yb metal and Hg(CCPh)$_2$ is known to yield divalent Yb(CCPh)$_2$, an additional oxidation and insertion step must be involved in the current reaction. Thus, carbodiimide reactions with lanthanoid species provide a wide variety of outcomes.

Lastly, despite the challenges in isolating organolanthanoid(II) tetraphenylborates in donor solvents, primarily due to the ease of forming solvated dications, the first redox-active cationic divalent europium phenoxide complex **(6.8)** was successfully synthesized.

6.4 Experimental

6.4.1 General Considerations

The compounds prepared in this work are extremely sensitive to air and moisture, and all manipulations were performed under a nitrogen atmosphere using vacuum-nitrogen line techniques, and a glove box with purified nitrogen, ensuring rigorous exclusion of air and water. $[Eu(OAr^{H})_2(thf)_3]$[76] $[Eu_3(Omes)_6(thf)_6]$[10] and $[Et_3NH][BPh_4]$[101] were prepared by the procedure described in literature methods. Lanthanoid metals were obtained from Molycorp, or Eutectix and large chunks were filed in the glove box prior to use. Solvents (thf, C_6D_6, toluene) were dried by distillation over sodium or sodium benzophenone ketyl and then stored under nitrogen over 4 Å molecular sieves. Diethyl ether and hexane were purified by an SPS and stored over 4 Å molecular sieves before use.

The following reagents were commercially available and used without further purification: 2,6-di-*tert*-butyl-4-ethylphenol ($HOAr^{Et}$), 2,6-di-*tert*-butylphenol ($HOAr^{H}$), 2,4,6-trimethylphenol (HOmes), 2,6-diphenylphenol (HOdpp), 1,2-diiodoethane, diphenyl mercury ($HgPh_2$), N,N'-dicyclohexylcarbodiimide (DCC) and N,N'-diisopropylcarbodiimide (DIC). Bis(pentafluorophenyl)mercury ($Hg(C_6F_5)_2$),[29] bis(phenylethynyl)mercury ($Hg(PhCC)_2$),[105] and $SmI_2(thf)_2$[37] were prepared using literature methods. Infrared spectra (4000–400 cm^{-1}) were obtained as Nujol mulls between NaCl plates with a Nicolet™ iS™ FTIR spectrometer. ^1H NMR spectra were recorded on a Bruker 400 MHz instrument, with chemical shifts referenced against residual solvent peaks. Microanalyses were conducted by the Elemental Analysis Service, London Metropolitan University, with all samples sealed in tubes under nitrogen before transport. Metal analyses were performed by using EDTA titrations with Xylenol Orange as the indicator, following acid digestion and buffering with hexamethylenetatramine. Melting points were measured in sealed glass capillaries under nitrogen and are uncalibrated.

6.4.2 Syntheses

[Yb(OAr^{Et})$_2$(Et$_2$O)$_2$] (6.1)

A mixture of ytterbium metal powder (0.346g, 2 mmol), Hg(C_6F_5)$_2$ (0.534g, 1mmol) and 2,6-di-*tert*-butyl-4-ethylphenol (HOAr^{Et}) (0.469 g, 2 mmol) were stirred for 3 days in diethylether (15 ml) at room temperature. After allowing the suspension to settle, the precipitated mercury and unreacted Yb metal were filtered from the reaction mixture. The resulting solution was then concentrated in vacuo (to approximately 10 mL) and cooled to -25 ºC, yielding red coloured crystals after several days. Yield: 0.44 g (56%). m.p. 120 °C (dec.). Elemental analysis for $C_{40}H_{70}O_4Yb$ (MW: 788.02 gmol^{-1}): Calculated (%) C 60.97, H 8.95, Yb 21.96; Found (%) C 59.66, H 8.31, Yb 22.50. IR (Nujol, cm^{-1}): 1716m, 1654w, 1647w, 1602w, 1559s, 1529s, 1511m, 1385s, 1352s, 1324s, 1259s, 1213s, 1148, 1121s, 1090s, 1037s, 996m, 954w, 911m, 875s, 832s, 799s, 778s, 717w. ^{1}H NMR (400 MHz, C_6D_6, 25 °C, ppm): δ = 7.09 (s, 4H, $H_{3,5}$(OAr^{Et})), 3.26 (s, 8H, α-H(Et$_2$O)), 2.67 (m, 2H, CH_2(OAr^{Et})), 2.52 (m, 2H, CH_2(OAr^{Et})), 1.60 (s, 14 H, C(CH_3)$_3$(OAr^{Et})), 1.35(s, 22 H, C(CH_3)$_3$(OAr^{Et})), 1.21 (s, 6H, CH_3(OAr^{Et})), 1.10 (s, 12H, β-H(Et$_2$O)).

[Eu(OAr^{Et})$_2$(thf)$_3$]·thf (6.2)

A mixture of europium metal powder (0.304 g, 2 mmol), Hg(C_6F_5)$_2$ (0.534 g, 1 mmol) and 2,6-di-*tert*-butyl-4-ethylphenol (HOAr^{Et}) (0.469 g, 2 mmol) were stirred for 5 days in tetrahydrofuran (15 mL) at room temperature. After allowing the suspension to settle, the precipitated mercury and unreacted Eu metal were filtered from the reaction mixture. Then the resulting solution was concentrated in vacuo (to approximately 10 mL) and cooled to -25 ºC yielding green coloured crystals after several days. Yield:0.55 g (60%). m.p. 130-134 °C. Elemental analysis for $C_{48}H_{82}EuO_6$ (MW: 907.09 gmol^{-1}): Calculated (%) C 63.55, H 9.11, Eu 16.75; Found (%) C 62.55, H 9.08, Eu 16.46. IR (Nujol, cm^{-1}): 1756m, 1653w, 1647w, 1602m, 1560w, 1502w, 1457s, 1417s, 1379s, 1344m, 1323s, 1259s, 1213w, 1198w, 1179w, 1120w, 1068m, 1030s, 920m, 873s, 817s, 789s, 707m, 668m.

[Sm(OAr^{Et})$_2$(thf)$_3$]·PhMe (6.3)

A solution of 2,6-di-*tert*-butyl-4-ethylphenol (HOAr^{Et}) (2.3438g, 10.0 mmol) and excess potassium (0.44 g, 11.0 mmol) was distilled in thf (30 mL) under a N_2 atmosphere. After 4 hours, this solution was directly filtered and added dropwise to a deep blue solution of [Sm(I)$_2$(thf)$_2$] (2.74 g, 5.0 mmol), in tetrahydrofuran (20 mL). The resulting deep red solution

was stirred overnight. The solution was then concentrated *in vacuo,* dissolved in toluene (30 mL) and stirred for 1 hour. Filtration, followed by removal of all volatiles *in vacuo*, yielded a red powder, which was subsequently extracted into toluene (10 mL) and left at −25°C for several days to produce deep red crystals. Yield: 2.04 g (66%). m.p. 190 °C (dec.). IR (Nujol, cm^{-1}): 1757m, 1654w, 1603m, 1559w, 1495w, 1459s, 1418s, 1379s, 1346m, 1324s, 1260s, 1234s, 1212m, 1120m, 1083w, 1031s, 910m, 874s, 821s, 793s, 729s, 696s, 664w. Elemental analysis Calculated (%) for $C_{51}H_{82}O_5Sm$ (MW: 925.55 $gmol^{-1}$): on fresh crystals Sm 16.99; Found (%) Sm 16.24. Microanalysis (after transport to London) Calculated (%) for $C_{32}H_{50}O_2Sm$ (MW 617.10 $gmol^{-1}$, loss of 3 thf and 1 PhMe): C 62.28; H 8.17. Found (%) C 60.78; H 8.39. ^{1}H NMR (400 MHz, C_6D_6, 25 °C, ppm): δ = 8.14 (s, 4H, $H_{3,5}(OAr^{Et})$), 7.11 (m, 5H, CH(toluene)), 3.17 (q, 4H, $CH_2(OAr^{Et})$), 2.50 (m, 2H, CH_2-thf), 2.12 (m, 3H, CH_3(Toluene)), 1.78 (t, 6H, $CH_3(OAr^{Et})$), 1.40 (s, 6H, $C(CH_3)_3(OAr^{Et})$), 0.86 (s, 30H, $C(CH_3)_3(OAr^{Et})$), -0.93 (m, 2H, CH_2-thf) with 2.5 thf lost.

[$(OAr^{Et})_2Sm(\mu$-$C_2N_4iPr_4)Sm(OAr^{Et})_2$]·2PhMe (6.4)

A solution of N,N′-di-isopropyl-carbodiimide (0.16 ml, 1.00 mmol) in toluene (10 mL) was added with stirring at room temperature to a dark red solution of $[Sm(OAr^{Et})_2(thf)_3]$·PhMe (0.926g, 1.00 mmol) in toluene. The colour gradually changed to light yellow, and the mixture was stirred continuously for 3 days. The resulting solution was filtered using a filtration cannula and concentrated in vacuo to approximately 10 mL and stored at -25 °C for 1 week, to yield light-yellow crystals. Yield: 0.43g (51%). m.p. 138-140 ℃ (dec.). Elemental analysis Calculated (%) for $C_{92}H_{144}N_4O_4Sm_2$ (MW: 1670.87 $gmol^{-1}$): on fresh crystals Sm 17.99; Found (%) Sm 17.26. Microanalysis (after transport to London) Calculated (%) for $C_{85}H_{136}N_4O_4Sm_2$ (MW 1578.77 $gmol^{-1}$, loss of 1 PhMe of crystallization) C 64.67, H 8.68, N 3.55 Found (%) C 65.00; H 8.86; N 3.74. IR (Nujol, cm^{-1}): 3064w, 2116s, 1758m, 1643m, 1604m, 1571m, 1495w, 1383m, 1350m, 1326w, 1311w, 1169w, 1140w, 1121s, 1081w, 1060w, 1009s, 910s, 891s, 874s, 832s, 795s, 781w, 764m, 729s, 694s, 639w, 535w. ^{1}H NMR (400 MHz, C_6D_6, 25 °C, ppm): δ = 8.05-8.48 (m, 8H, C_6H_2), 7.05 (m, 5H, ArH-toluene), 3.15–3.40 (m, 8H, CH_2), 2.58 (m, 4H, CH), 2.11 (m, 3H, CH_3-toluene), 0.3–2.04 (m, 36H, CH_3-Et, *i*Pr), -0.42–-0.79 (m, 72H, CH_3-*t*Bu) with one lattice PhMe lost.

[$Sm(OAr^{Et})_2$(CyNC(H)NCy)$(thf)_2$]·2thf (6.5)

A solution of N,N′-dicyclohexylcarbodiimide (DCC) (0.10 g, 0.48 mmol) in thf (10 mL) was added with stirring at room temperature to a dark red solution of $[Sm(OAr^{Et})_2(thf)_3]\cdot PhMe$ (0.30 g, 0.48 mmol) in thf. The colour gradually changed to light yellow, and the mixture was stirred continuously for 3 days. The resulting solution was filtered using a filtration cannula and concentrated in vacuo to approximately 10 mL and stored at -25 °C for 1 week, to yield light-yellow crystals. Yield: 0.16g (30%). m.p. 110 °C (dec.). Elemental analysis Calculated (%) for $C_{61}H_{105}N_2O_6Sm$ (MW: 1112.85 $gmol^{-1}$): on fresh crystals Sm 13.51; Found (%) Sm 13.60. Microanalysis (after transport to London) Calculated (%) for $C_{53}H_{89}N_2O_4Sm$ (MW 968.67 $gmol^{-1}$, loss of 2 thf of crystallization): C 65.72; H 9.26; N 2.89. Found (%) C 64.07; H 8.99; N 2.97. IR (Nujol, cm^{-1}): 2120s, 1753w, 1640s, 1604w, 1544s, 1459m, 1419m, 1384m, 1358w, 1325m, 1259m, 1234m, 1212w, 1158w, 1120m, 1072m, 1024w, 910w, 890w, 873m, 821s, 793s, 721w. ^{1}H NMR (400 MHz, C_6D_6, 25 °C, ppm): Satisfactory integrations could not be obtained (see Figure 6.7). δ = 8.15 (s, 4H, ArH), 7.98 (s, 1H, NC*H*N), 3.16-0.70 (m, CH_3-*t*Bu, CH_3-Et, CH_2-Et, CyNCNCy Hs overlapped by CH_2-thf resonance) with both lattice thf lost.

$[Yb^{III}\{CyNC(C{\equiv}CPh)NCy\}_3]\cdot 2thf$ (6.6)

A Schlenk flask was charged with $Hg(PhCC)_2$ (0.605 g, 1.5 mmol) and excess Yb metal filings (0.52 g, 3.0 mmol), followed by N,N′-dicyclohexylcarbodiimide (DCC) (0.619 g, 3.0 mmol) added inside a drybox. Anhydrous thf (15 mL) was then added *via* cannula, and the reaction mixture was stirred at room temperature for 3 days. After allowing the unreacted ytterbium metal and mercury suspension to settle, the supernatant was filtered using a filtration cannula. The resulting solution was concentrated in vacuo to approximately 10 mL and left to stand at room temperature to crystallize, yielding large yellow crystals after several days. Yield: 0.80g (64%). m.p. 195-200 °C. Elemental analysis for $C_{71}H_{97}N_6O_2Yb$ (MW: 1239.61 $gmol^{-1}$): Calculated (%) C 68.79; H 7.89; N 6.78; Yb 13.96; Found (%) C 68.58; H 7.95; N 6.85; Yb 13.72. IR (Nujol, cm^{-1}) : 2666w, 2209s, 1968w, 1947w, 1897w, 1877w, 1799w, 1750w, 1671m 1597m, 1573m, 1558w, 1311w, 1257s, 1245s, 1191s, 1171s, 1137s, 1073s, 1026m, 995s, 964w, 913s, 898s, 887s, 843s, 805m, 755s, 722w, 702m, 688s, 676w, 628s, 529w. ^{1}H NMR (400 MHz, C_6D_6, 25 °C, ppm): δ = 13.79 (s, 3H, ArH), 7.43-6.73 (m, ArH overlap with C_6D_6), 3.94-1.50 (m, 86H, 60 CH_2-CyNCNCy, 6 CH- CyNCNCy, 20 thf), -0.20 (s, 8H, CH_2-thf), -13.80 (s, 8H, CH_2-thf) .

$[Eu\{CyNC(C{\equiv}CPh)NCy\}_2(thf)_2]$ (6.7)

A Schlenk flask was charged with $Hg(PhCC)_2$ (0.403 g, 1.0 mmol) and excess Eu metal filings (0.303 g, 2.0 mmol), followed by N,N′-dicyclohexylcarbodiimide (DCC) (0.413 g, 2.0 mmol) added inside a drybox. Anhydrous thf (15 mL) was then added *via* cannula, and the reaction mixture was stirred at room temperature for 3 days. After allowing the unreacted europium metal and mercury suspension to settle, the supernatant was filtered using a filtration cannula. The resulting solution was concentrated in vacuo to approximately 10 mL and left to stand at room temperature to crystallize, yielding red crystals after several days. Yield: 0.51g (56%). m.p. 133-135 °C. Elemental analysis for $C_{50}H_{70}EuN_4O_2$ (MW: 911.08 $gmol^{-1}$): Calculated (%) C 65.91; H 7.74; N 6.15; Eu 16.68; Found (%) C 65.22; H 7.97; N 6.03 Eu 15.9. IR (Nujol, cm^{-1}) : 2122s, 1953m, 1883w, 1757w, 1686w, 1655w, 1596m, 1572w, 1560w, 1545m, 1379w, 1356w, 1319w, 1303w, 1256s, 1240w, 1165s, 1126m, 1110m, 1070s, 1043s, 991m, 915s, 886s, 843m, 796m, 756s, 721w, 691s, 670s, 615s, 592m, 526w.

$[Eu_2(Omes)_3(thf)_6][BPh_4]\cdot 1.5thf$ (6.8)

$[Et_3NH][BPh_4]$ (105 mg, 0.250 mmol) in thf was added to a stirred solution of $[Eu_3(Omes)_6(thf)_6]$ (353 mg, 0.250 mmol) in 15 ml of thf at room temperature and stirred overnight. The resulting filtered yellow solution was dried under vacuum. The solution was cooled to -25 °C for several day giving small yellow crystals. Yield: 0.115 g (59%). m.p. 108-110 °C (dec.). Elemental analysis Calculated (%) for $C_{81}H_{113}BEu_2O_{10.5}$ (MW: 1569.44 $gmol^{-1}$): on fresh crystals Eu 19.36; Found (%) Eu 19.13. Microanalysis (after transport to London) Calculated (%) for $C_{75}H_{101}BEu_2O_9$ (MW 1461.33 $gmol^{-1}$, loss of 1.5 thf of crystallization): C 61.64; H 6.97. Found (%) C 60.60; H 7.03. IR (Nujol, cm^{-1}): 2732w, 1608s, 1580s, 1377s, 1340w, 1305s, 1259s, 1185w, 1160m, 1150w, 1133w, 1064m, 1027s, 953m, 913w, 860s, 795s, 747s, 732s, 703s, 664m, 623w, 612s, 594m, 576w.

$[Yb(thf)_6][BPh_4]_2$ (6.9)

$[Et_3NH][BPh_4]$ (105 mg, 0.25 mmol) in thf was added to a stirred solution of $[Yb(OAr^{Et})_2(Et_2O)_2]$ (197 mg, 0.25 mmol) in 20 ml of thf at room temperature and stirred overnight. The resulting filtered yellow solution was dried under vacuum. The solution was cooled to -25 °C for several day giving small yellow crystals. Single crystals suitable for X-ray diffraction were obtained, and the compound was identified as $[Yb(thf)_6][BPh_4]_2$ based on unit cell: a = 11.95 Å, b = 13.34 Å, c = 21.10 Å, β = 94.66°, consistent with the reported unit cell: a = 11.9661(6) Å, b = 13.3457(7) Å, c = 21.0776(10) Å, β = 94.580(1)°.[59]

[Eu(thf)$_7$][BPh$_4$]$_2$·thf (6.10)

[Et$_3$NH][BPh$_4$] (105mg, 0.25 mmol) in thf was added to a stirred solution of [Eu(OAr^H)$_2$(thf)$_3$] (141 mg, 0.125 mmol) in 15 ml of thf at room temperature and stirred overnight. The resulting filtered yellow solution was dried under vacuum. The solution was cooled to -25 °C for several day giving small yellow crystals. Single crystals suitable for X-ray diffraction were obtained, and the compound was identified as [Eu(thf)$_7$][BPh$_4$]$_2$·thf based on unit cell: a = 18.2414(19) Å, b = 19.1418(19) Å, c = 20.220(2) Å, β = 94.512(5)°, in agreement with the reported unit cell: a = 18.2175(6) Å, b = 19.1237(6) Å, c = 20.2661(6) Å, β = 94.6320(10).[104]

6.5 X-ray Crystal Data

For details on X-ray crystallography, see Appendix One.

Crystal data and refinement details are shown in Table 6.8, 6.9 and 6.110.

Table 6.8: Crystal data and structural refinement for compounds **6.1**-**6.3**

Compound	**6.1**	**6.2**	**6.3**
Formula	$C_{46}H_{76}O_4Yb$	$C_{48}H_{82}EuO_6$	$C_{51}H_{82}O_5Sm$
M_r	866.10	907.09	925.51
Space group	$C2/c$	$P2_1/c$	$P2_1/c$
a (Å)	11.150(2)	9.7959(5)	15.8794(15)
b (Å)	16.100(3)	15.2391(8)	15.7810(16)
c (Å)	25.470(5)	32.0087(17)	19.568(2)
α (°)	90	90	90
β (°)	97.55(3)	93.269(3)	94.733(4)
γ (°)	90	90	90
V (Å^3)	4532.6(16)	4770.5(4)	4887.0(9)
Z	4	4	4
ρ_{calc}, gcm^{-3}	1.269	1.263	1.258
μ, mm^{-1}	2.101	1.358	1.244
N_τ	37762	154968	148048
N (R_{int})	4015(0.0292)	11918 (0.0689)	12141(0.0703)
$R_1(I > 2\sigma(I))$	0.0285	0.0341	0.0316
wR_2 (all data)	0.0810	0.0756	0.0800
GOF	1.069	1.074	1.084

Table 6.9: Crystal data and structural refinement for compounds **6.4-6.7**

Compound	**6.4**	**6.6**	**6.7**
Formula	$C_{92}H_{144}N_4O_4Sm_2$	$C_{71}H_{97}N_6O_2Yb$	$C_{50}H_{70}EuN_4O_2$
M_r	1670.80	1239.58	911.06
Space group	*P*-1	*P*-1	$P2_1/c$
a (Å)	12.8311(12)	14.3388(8)	13.9532(5)
b (Å)	15.6427(16)	15.1112(10)	10.4488(4)
c (Å)	22.177(2)	18.0388(10)	32.2541(10)
α (°)	91.453(5)	73.217(2)	90
β (°)	94.552(5)	73.249(2)	97.901(2)
γ (°)	94.353(5)	62.715(2)	90
V (Å^3)	4422.1(8)	3269.5(3)	4657.8(3)
Z	2	2	4
ρ_{calc}, gcm^{-3}	1.255	1.259	1.299
μ, mm^{-1}	1.364	1.478	1.388
N_τ	21090	267674	45817
N (R_{int})	21090	15022 (0.0490)	10798(0.1010)
$R_1(I > 2\sigma(I))$	0.1132	0.0221	0.0753
wR_2 (all	0.2694	0.0566	0.1761
GOF	1.088	1.059	1.085

Table 6.10: Crystal data and structural refinement for compounds **6.8**

Compound	**6.8**
Formula	$C_{81}H_{113}BEu_2O_{10.5}$
M_r	1569.44
Space group	*P*-1
a (Å)	15.8729(8)
b (Å)	16.5185(8)
c (Å)	18.8413(9)
α (°)	94.292(2)
β (°)	101.667(2)
γ (°)	118.457(2)
V (Å^3)	4168.6(4)
Z	2
ρ_{calc}, gcm^{-3}	1.250
μ, mm^{-1}	1.542
N_τ	43066
N (R_{int})	18965(0.0925)
$R_1(I > 2\sigma(I))$	0.0847
wR_2 (all data)	0.2586
GOF	1.018

6.6 References

1 W. H. Brown and T. Poon, Benzene and its derivatives in *Introduction to organic chemistry.*, Wiley, United States of America, 6th ed., pp. 266–312.

2 Zvi. Rappoport, *The chemistry of phenols*, John Wiley & Sons, Ltd, The Hebrew University, Jerusalem, 2003.

3 Z. Guo, R. Huo, Y. Q. Tan, V. Blair, G. B. Deacon and P. C. Junk, *Coord. Chem. Rev.*, 2020, **415**, 213232.

4 T. J. Boyle and L. A. M. Ottley, *Chem. Rev.*, 2008, **108**, 1896–1917.

5 D. M. Barnhart, D. L. Clark, J. C. Gordon, J. C. Huffman, R. L. Vincent, J. G. Watkin and B. D. Zwick, *Inorg. Chem.*, 1994, **33**, 3487–3497.

6 G. B. Deacon, N. Siegbert, P. MacKinnon and E. R. T. Tiekink, *Aust. J. Chem*, 1990, **43**, 1245–57.

7 G. B. Deacon, P. C. Junk and G. J. Moxey, *Chem. Asian J.*, 2009, **4**, 1309–1317.

8 G. B. Deacon, P. E. Fanwick, A. Gitlits, I. P. Rothwell, B. W. Skelton and A. H. White, *Eur. J. Inorg. Chem.*, 2001, 1505–1514.

9 G. B. Deacon, C. M. Forsyth, P. C. Junk, B. W. Skelton and A. H. White, *Chem. Eur. J.*, 1999, **5**, 1452–1459.

10 G. B. Deacon, P. C. Junk and G. J. Moxey, *Chem. Asian J.*, 2009, **4**, 1717–1728.

11 M. F. Lappert, A. Singh, R. G. Smith, H. A. Stecher and A. Sen, Hydrocarbon-Soluble Homoleptic Bulky Aryl Oxides of the Lanthanide Metals: [Ln(OArR)3)] in *Inorganic Syntheses*, ed. A. P. Ginsberg, Wiley-Interscience, New York, 1990, pp. 164–168.

12 P. B. Hitchcock, M. F. Lappert and A. Singh, *J. Chem. Soc. Chem. Commun.*, 1983, 1499–1501.

13 J. R. Van Den Hende, P. B. Hitchcock and M. F. Lappett, *J. Chem. Soc. Chem. Commun.,* 1994, 1413–1414.

14 J. R. van den Hende, P. B. Hitchcock, S. A. Holmes and M. F. Lappert, *J. Chem. Soc., Dalton Trans.*, 1995, 1435–1440.

15 G. B. Deacon, P.B. Hitchcook, S.A. Holmes, M.F. Lappert, P. MacKinnon and R. H. Newnham, *J. Chem. Soc. Chem. Commun.*, 1989, 935–937.

16 P. B. Hitchcock, M. F. Lappert and R. G. Smith, *Inorganica Chim. Acta*, 1987, **139**, 183.

17 L. Clark, G. B. Deacon, C. M. Forsyth, P. C. Junk, P. Mountford and J. P. Townley, *Dalton Trans.*, 2010, **39**, 6693–6704.

18 J. R. Van Den Hende, P. B. Hitchcock and M. F. Lappert, *J. Chem. Soc. Dalton Trans.*, 1995, 2251–2257.

19 H. A. Stecher, A. Sen and A. L. Rheingold, *Inorg. Chem.*, 1988, **27**, 1130–1132.

20 R. C. Mehrotra, A. Singh and U. M. Tripathi, *Chem. Rev.*, 1991, **91**, 1287–1303.

21 S. Hamidi, G. B. Deacon, P. C. Junk and P. Neumann, *Dalton Trans.*, 2012, **41**, 3541–3552.

22 Z. Hou, A. Fujita, Y. Zhang, T. Miyano, H. Yamazaki and Y. Wakatsuki, 1998, **120**, 754–766.

23 D. Bradley, R. C. Mehrotra, I. Rothwell and A. Singh, *Alkoxo and aryloxo derivatives of metals*, Elsevier, 2001.

24 W. J. Evans, M. A. Greci and J. W. Ziller, *Inorg. Chem.*, 2000, **39**, 3213–3220.

25 T. J. Boyle, S. D. Bunge, P. G. Clem, J. Richardson, J. T. Dawley, L. A. M. Ottley, M. A. Rodriguez, B. A. Tuttle, G. R. Avilucea and R. G. Tissot, *Inorg. Chem.*, 2005, **44**, 1588–1600.

26 F. Ortu, *Chem Rev*, 2022, **122**, 6040–6116.

27 S. J. Hsiang and P. G. Hayes, The Coordination Chemistry of Yttrium Complexes Supported by Multidentate Nitrogen Ancillary Ligands in *Comprehensive Coordination Chemistry III*, eds. E. C. Constable, G. Parkin, and L. Que Jr., Elsevier, Amsterdam, 2021, vol. 1–9, pp. 40–72.

28 T. J. Boyle and L. A. M. Ottley, *Chem Rev*, 2008, **108**, 1896–1917.

29 G. B. Deacon, J. E. Cosgriff, E. T. Lawrenz, C. M. Forsyth and D. L. Wilkinson, *Hermann-Brauer Synthetic Methods of Organometallic and Inorganic Chemistry*, Thieme: Stuttgart, 1997, vol. 6.

30 G. B. Deacon, C. M. Forsyth and S. Nickel, *J. Organomet. Chem.*, 2002, **647**, 50–60.

31 Z. Guo, V. Blair, G. B. Deacon and P. C. Junk, *Chem. Eur. J.*, 2018, **24**, 17464–17474.

32 R. Huo, Honours *thesis*, Monash University, 2020.

33 H. Taube and E. S. Gould, *J. Am. Chem. Soc*, 1961, **83**, 44.

34 F. F. Fan and E. S. Gould, *Inorg Chem*, 1974, **13**, 2639–2646.

35 P. K. Thamburaj and E. S. Gould, *Inorg. Chem.*, 1975, **14**, 15.

36 J. Doyle and A. G. Sykes, *J. Chem. Soc. (A)*, 1968, **17**, 2836–2839.

37 P. Girard, J. L. Namy and B. Kagan, 1980, **102**, 2693–2698.

38 M. Szostak and D. J. Procter, *Angew. Chem., Int. Ed.*, 2012, **51**, 9238–9256.

39 M. F. Lappert and B. Prokai, *Adv. Organomet. Chem.*, 1967, **5**, 225–319.

40 G. B. Deacon, C. M. Forsyth, P. C. Junk and J. Wang, *Inorg. Chem.*, 2007, **46**, 10022–10030.

41 L. Yang, Y. Qu, J. Wang, W. Xu, Y. Zhao and X. J. Yang, *Chem. Eur. J.*, 2023, **29**, e202301266.

42 A. Williams and I. T. Ibrahim, *Chem. Rev.*, 1981, **81**, 589–636.

43 Y. Wang, W. X. Zhang and Z. Xi, *Chem. Soc. Rev.*, 2020, **49**, 5810–5849.

44 Z. Li, R. J. Mayer, A. R. Ofial and H. Mayr, *J. Am. Chem. Soc.*, 2020, **142**, 8383–8402.

45 W. X. Zhang, L. Xu and Z. Xi, *Chem.Comm.,* 2015, **51**, 254–265.

46 F. Kurzer and K. Douraghi-Zadeh, *Chem. Rev.*, 1967, **67**, 107–152.

47 H. G. Khorana, *Chem Rev*, 1953, **53**, 145–166.

48 F. T. Edelmann, *Adv. Organomet. Chem.*, 2008, **57**, 183–352.

49 J. Zhang, R. Ruan, Z. Shao, R. Cai, L. Weng and X. Zhou, *Organometallics*, 2002, **21**, 1420–1424.

50 M. L. Cole, G. B. Deacon, C. M. Forsyth, P. C. Junk, D. P. Ceron and J. Wang, *Dalton Trans.*, 2010, **39**, 6732–6738.

51 G. Chandra, A. D. Jenkins, M. F. Lappert and R. C. Srivastava, *J. Chem. Soc. (A)*, 1970, 2550–2558.

52 C. Pi, Z. Zhang, Z. Pang, J. Zhang, J. Luo, Z. Chen, L. Weng and X. Zhou, *Organometallics*, 2007, **26**, 1934–1946.

53 J. Zhang, R. Cai, L. Weng and X. Zhou, *J. Organomet. Chem.*, 2003, **672**, 94–99.

54 A. A. Trifonov, D. M. Lyubov, E. A. Fedorova, G. G. Skvortsov, G. K. Fukin, Y. A. Kurskii, M. N. Bochkarev and G. A. Razuvaev, *Russ. Chem. Bull., Int. Ed.*, 2006, **55**, 435–441.

55 M. Deng, Y. Yao, Y. Zhang and Q. Shen, *Chem. Comm.,* 2004, 2742–2743.

56 M. Pasquali, C. Floriani, A. Chiesi-Villa and C. Guastini, *J. Am. Chem. Soc.*, 1979, **101**, 4740–4742.

57 W. J. Evans, J. W. Grate, I. Bloom, W. E. Hunter and J. L. Atwood, *J. Am. Chem. Soc*, 1985, **107**, 105–409.

58 W. J. Evans, R. A. Keyer and J. W. Ziuer, *J. Organomet. Chem.*, 1990, **394**, 87–97.

59 W. J. Evans, M. A. Johnston, M. A. Greci, T. S. Gummersheimer and J. W. Ziller, *Polyhedron*, 2003, **22**, 119–126.

60 H. T. Sheng, H. Zhou, H. D. Guo, H. M. Sun, Y. M. Yao, J. F. Wang, Y. Zhang and Q. Shen, *J. Organomet. Chem.*, 2007, **692**, 1118–1124.

61 G. B. Deacon and C. M. Forsyth, *Chem. Comm.,* 2002, 2522–2523.

62 W. J. Evans, C. A. Seibel and J. W. Ziller, 1998, **120**, 6745–6752.

63 W. J. Evans, J. M. Perotti, J. C. Brady and J. W. Ziller, *J. Am. Chem. Soc.*, 2003, **125**, 5204–5212.

64 G. B. Deacon and C. M. Forsyth, *Chem. Eur. J.*, 2004, **10**, 1798–1804.

65 P. M. Zeimentz, S. Arndt, B. R. Elvidge and J. Okuda, *Chem. Rev.*, 2006, **106**, 2404–2433.

66 G. B. Deacon, C. M. Forsyth and P. C. Junk, *Eur. J. Inorg. Chem.*, 2005, 817–821.

67 W. J. Evans, S. A. Kozimor and J. W. Ziller, *Chem. Comm.,* 2005, 4681–4683.

68 C. J. Schaverien, *Organometallics*, 1992, **11**, 3476–3478.

69 W. J. Evans, T. A. Ulibarri, L. R. Chamberlain, J. W. Zlller and D. Jr. Alvarez, 1990, **9**, 2124–2130.

70 P. N. Hazin and J. W. Bruno, *Organometallics*, 1990, **9**, 416–423.

71 W. J. Evans, J. M. Perotti and J. W. Ziller, *J. Am. Chem. Soc.*, 2005, **127**, 3894–3909.

72 W. J. Evans, T. M. Champagne and J. W. Ziller, *Organometallics*, 2007, **26**, 1204–1211.

73 W. J. Evans, J. M. Olofson and J. W. Ziller, *J. Am. Chem. Soc.*, 1990, **112**, 2308–2314.

74 H. T. Sheng, H. Zhou, H. D. Guo, H. M. Sun, Y. M. Yao, J. F. Wang, Y. Zhang and Q. Shen, *J. Organomet. Chem.*, 2007, **692**, 1118–1124.

75 G. B. Deacon, G. D. Fallon, C. M. Forsyth, S. C. Harris, P. C. Junk, B. W. Skelton and A. H. White, *Dalton Trans.*, 2006, 802–812.

76 G. B. Deacon, T. Feng, P. MacKinnon, R. H. Newnham, S. Nickel, B. W. Skelton and A. H. White, *Aust. J. Chem*, 1993, **46**, 387–399.

77 A. W. Addison, T. N. Rao, J. Reedijk, J. van Rijn, G. C. Verschoor, *J. Chem. Soc., Dalton Trans.,* 1984, 1349–1356.

78 J. R. van den Hende, P. B. Hitchcock, S. A. Holmes, M. F. Lappert, W.-P. Leung, T. C. W. Mak, S. Prashar, *J. Chem. Soc.,Dalton Trans.,* 1995, 1427-1433.

79 G.-Z. Qi, Q. Shen, Y.-H. Lin, *Acta Crystallogr., Sect. C,* 1994, **50**, 1456–1458.

80 G. B. Deacon, P. B. Hitchcock, S. A. Holmes, M. F. Lappert, P. MacKinnon, R. H. Newnham, *J. Chem. Soc., Chem. Comm.,* 1989, 935–937.

81 S. Beaini, G. B. Deacon, M. Hilder, P. C. Junk, D. R. Turner, *Eur. J. Inorg. Chem.,* 2006, 3434–3441.

82 M. Salehisaki, N. E. Rad, G. B. Deacon, J. Wang, Z. Guo and P. C. Junk, *Inorganica Chim. Acta.*, 2022, **539**, 120997.

83 G. J. Moxey, A. J. Blake, W. Lewis and D. L. Kays, *Eur. J. Inorg. Chem.*, 2015, 5892–5902.

84 R. P. Kelly, T. D. M. Bell, R. P. Cox, D. P. Daniels, G. B. Deacon, F. Jaroschik, P. C. Junk, X. F. Le Goff, G. Lemercier, A. Martinez, J. Wang and D. Werner, *Organometallics*, 2015, **34**, 5624–5636.

85 H. Sitzmann, T. Dezember, O. Schmitt, F. Weber, G. Wolmershäuser and M. Ruck, *Z. Anorg. Allg. Chem.*, 2000, **626**, 2241–2244.

86 L. H. J. Lajunen and G. R. Choppin, *Rev. Anal. Chem.*, 1989, **9**, 91–130.

87 D. P. Daniels, G. B. Deacon, D. Harakat, F. Jaroschik and P. C. Junk, *Dalton Trans.*, 2012, **41**, 267–277.

88 L. Hirneise, C. Maichle-Mössmer and R. Anwander, *Inorg. Chem.*, 2021, **60**, 18211–18224.

89 G. B. Deacon, A. J. Koplick, W. D. Raverty and D. G. Vince, *J. Organomet. Chem.*, 1979, **182**, 121–141.

90 M. L. Cole, G. B. Deacon, C. M. Forsyth, P. C. Junk, K. Konstas and J. Wang, *Chem. Eur. J.* 2007, **13**, 8092-8110.

91 G. B. Deacon, A. J. Koplick, T. D. Tuong, *Aust. J. Chem.,* 1982, **35**, 941-949.

92 L. J. Bellamy, *The Infrared Spectra of Complex Molecules Vol. 2 Advances in Infrared Group Frequencies*, Chapman & Hall, 1968.

93 J. D. Wilkins, *J. Organomet. Chem.*, 1974, **80**, 349–355.

94 Lewis, J., Miller, J. R., Richards, R. L., and Thompson, A., *J. Chem. Soc.,* 1965, 5850-5860.

95 F. H. Allen, O. Kennard, D. G. Watson, L. Brammer, A. G. Orpen and R. Taylor, *J. Chem. Soc. Perkin Trans. II*, 1987, S1–S15.

96 W. J. Evans, D. K. Drummond, L. R. Chamberlain, R. J. Doedens, S. G. Bott, H. Zhang and J. L. Atwood, *J. Am. Chem. Soc.*, 1988, **110**, 4983–4994.

97 X.-G. Zhou, Z.-E. Huang, R.-F. Cai, L.-X. Zhang, X.-F. Hou, X.-J. Feng and X.-Y. Huang, *J. Organomet. Chem.*, 1998, **563**, 101–112.

98 X. G. Zhou, Z. E. Huang, R. F. Cai, L. B. Zhang, L. X. Zhang and X. Y. Huang, *Organometallics*, 1999, **18**, 4128–4133.

99 R. Thomas, S. Lakshmi, S. K. Pati and G. U. Kulkarni, *J.Phys.Chem.B*, 2006, **110**, 24674–24677.

100 R. D. Shannon, *Acta Crystallogr. A*, 1976, **32**, 751–767.

101 P. K. Bakshi, A. Linden, B. R. Vincent, S. P. Roe, D. Adhikesavalu, T. S. Cameron and O. Knop, 1994, **72**, 1273–1293.

102 G. B. Deacon, C. M. Forsyth, P. C. Junk, B. W. Skelton and A. H. White, *Chem. Eur. J.*, 1999, **5**, 1452–1459.

103 W. Evans, W. G. McClelland, M. A. Greci and J. Ziller, *Eur. J. Solid State Inorg. Chem.*, 1996, **33**, 145–156.

104 M. Wiecko, Z. Guo, G. B. Deacon and P. C. Junk, *Molecules*, 2022, **27**, 7547.

105 B. G. Eglinton and W. Mccrae, *J. Chem. Soc.,* 1963, 2295–2299.

Chapter 7: Concluding Chapter

7.1 Overview and Concluding Remarks

This chapter will conclude the research study by summarizing the findings in relation to the research aims and the gaps identified in the Introduction Chapter, highlighting the value and contribution of the work. Additionally, it will address the limitations of the study and provide recommendations for future research.

In the Introduction, we discussed that organic systems, particularly compounds containing heteroatoms with high electron density, are considered to have a higher corrosion inhibiting performance due to their strong affinity for metallic surfaces. However, a significant knowledge gap was evident in the existing literature, particularly regarding the use of lanthanoid complexes of carboxylic acids containing hetero atoms as corrosion inhibitors. This thesis addresses this gap by selecting thiophene and furan derivatives, which have shown promising inhibition activities, supporting the theory. In Chapter 5, the goal was to create a library of complexes ranging from Li to Cs alkali metal salts of five different of organic carboxylic acid moieties, as the structural properties and corrosion inhibition potential of these complexes remain underexplored.

7.2 Summary of Findings

Chapter 2-4 discussed the synthesis of RE(III) carboxylate complexes [$RE(O_2CR)_3$] through simple metathesis reactions of RE salts with several carboxylate derivatives including 3-thiophenecarboxylate, 3-furoate and 2-methyl-3-furoate ligands. After successfully creating a library of lanthanoid carboxylate complexes, the next objective was to investigate the influence of chemical structure on inhibitory activity and to establish a structure-activity relationship. To achieve this, the metal complexes were characterised using various techniques: single-crystal X-ray crystallography, IR, elemental analysis, TGA measurements and powder XRD. In the final phase, the developed inhibitors were evaluated according to ASTM standards,[1] with weight loss experiments as the primary method for assessing the general corrosion inhibition behaviour. Additional studies using potentiodynamic polarization measurements provided more accurate corrosion rates.

Chapter 2 examined the inhibitory potential of sulfur-containing organic compounds as corrosion inhibitors, specifically testing thiophene derivatives for their anti-corrosion properties on mild steel in a NaCl medium. *The findings indicate that* $[Y_2(3tpc)_6(H_2O)_4]\cdot H_2O$ **(2.9)** and $[Gd_2(3tpc)_6(H_2O)_4]\cdot H_2O$ **(2.6)** were the most effective among the 11 compounds tested, acting predominantly as anodic inhibitors. Results show that all the compounds crystallized into one of the two structural groups, with the lanthanoid contraction reflected in the reduction of RE-O bond lengths and a decrease in coordination number.

Chapter 3 reflects on the limited use of furan derivatives in corrosion inhibition studies compared to thiophene derivatives. This chapter explored whether lanthanoid 3-furoate systems perform better or worse than their thiophene counterparts. The results, along with a comparison of Y complex data, suggests that incorporating a furoate moiety into a carboxylate is more effective than the thiophene group, but not as effective as a 3-(4'-methylbenzoyl) group.[2,3] Additionally, this chapter highlights that the stoichiometry used in the metathesis reaction influences the final complex formation. Lanthanoid contraction was evident, as shown by the reduction in the average RE-O bond distance across each series.

In chapter 4, the primary objective was to investigate the impact of structural variations in carboxylate frameworks on corrosion mitigation activity. The incorporation of a furoate functionality demonstrated its effect in adsorbing to corroding metal centres, thereby bringing the carboxylate and RE metals to the surface. However, the presence of a methyl group adjacent to the heteroatom had a detrimental effect; steric bulk around the heteroatom reduced the effectiveness of corrosion protection. Comparisons between the coordination environments of 2-methyl-3-furoate and 3-furoate complexes (from Chapter 3) indicate that the steric effect of the methyl group outweighs its electronic effect. This is evidenced by the significant simplification of carboxylate coordination in 2-methyl-3-furoate complexes, likely due to reduced access to one of the carboxylate oxygens caused by the bulk of the methyl group. Additionally, longer RE-O bond lengths in RE 2m3fur complexes compared to lanthanoid 3-furoates may be attributed to relieving strain around the metal center.

Chapter 5 compared the performances of alkali metal salts of carboxylate ions with their respective RE counterparts, commonly used as precursors in RE carboxylate-based inhibitors. The findings indicate that corrosion rates of alkali metal salt complexes, including well-known inhibitors like 4-hydroxycinnamates and 4-hydroxybenzoates, as well as new carboxylate complexes from Chapters 2, 3, and 4, are significantly higher than those of their

rare earth analogues, highlighting the value of rare earth carboxylates in corrosion inhibition. Another noteworthy observation is that even with the same ligand, different alkali metals formed unique structural motifs with varying coordination numbers and stereochemistry. Except for the dinuclear $[Li_2(2m3fur)_2(H_2O)_3]$ **(5.5)** complex, all other complexes crystallized as coordination polymers with diverse carboxylate-binding modes. Under conditions that typically yielded simple coordinated carboxylate groups, the ligation of hydrogen dicarboxylate ions $[HL_2]^-$ was observed in the $[Cs\{H(3tpc)_2\}]_n$ (**5.4)** and $[Rb\{H(4hocin)_2\}]_n{\cdot}nH_2O$ **(5.9)** complexes, featuring short H-bonds and short O…O distances associated with the acidic hydrogen, along with centrosymmetric O...H...O interactions between the carboxylate ions. No crystallographically suitable single crystals could be obtained for sodium derivatives.

In Chapter 6, there was a transition to studying more complex air sensitive chemistry, motivated by a desire to learn and explore a variety of new techniques during the PhD program. In this chapter skills to handle highly air and moisture sensitive lanthanoid compounds were developed for synthetic aspects of the project. This involved mastering vacuum-nitrogen line techniques and glove box techniques in an atmosphere of purified nitrogen, as well as the rigorous drying of solvents and specialized handling required for the characterisation of these air and moisture sensitive compounds.

In this chapter, the reactivity of carbodiimides with lanthanoid aryloxides was explored to investigate how steric and electronic factors affect product formation. The initial goal was to create new ligands *via* Ln–O insertion, but this reaction was not observed, likely due to the oxophilicity of lanthanoids. Among the various lanthanoid aryloxide complexes used for reactivity studies, only the divalent samarium bis(phenoxide) complex $[Sm(OAr^{Et})_2(thf)_3]{\cdot}thf$ **(6.3)** exhibited reductive reactivity with carbodiimides, rather than Ln–O insertion. One-electron reduction and coupling yielded the crowded bimetallic oxalamidinatosamarium(III) complex **(6.4)** and mononuclear formamidinatosamarium(III) complex **(6.5)**, depending on the size of the R group on the carbodiimide. Insertion reactions dominated when bis(phenylethynyl)lanthanoid(II) species, $Ln(CCPh)_2$ (Ln = Eu, Yb), reacted with N,N'-dicyclohexylcarbodiimide. $Eu(CCPh)_2$ formed a divalent *C*-phenylethynylamidinate **(6.7)**, while the ytterbium analogue yielded a trivalent product **(6.6)**, suggesting an additional oxidation and insertion step.

This chapter also briefly explored cationic lanthanoid(II) phenoxide complexes. Although isolating organolanthanoid(II) tetraphenylborates in donor solvents is challenging due to the tendency to form solvated dications, the first redox-active, cationic divalent europium phenoxide complex $[Eu_2(Omes)_3(thf)_6][BPh_4]\cdot 1.5thf$ **(6.8)** was successfully synthesized. In future studies, the synthesized novel cationic complex can be utilized for reactivity studies to determine its potential as a useful precursor for lanthanoid chemistry.

7.3 Recommendations for Future Research

Given that RE 3-furoate complexes, particularly $[Y(3fur)_3(H_2O)_2]_n$, have shown promising results and that cinnamate and its derivatives have already proven effective as corrosion inhibitors[4–6] future research could explore the use of (E)-(3-(n-furyl)acrylate). This compound combines the aromatic ring and oxygen atom of furoate with the C=C double bond characteristic of cinnamate, potentially offering enhanced corrosion inhibition properties.

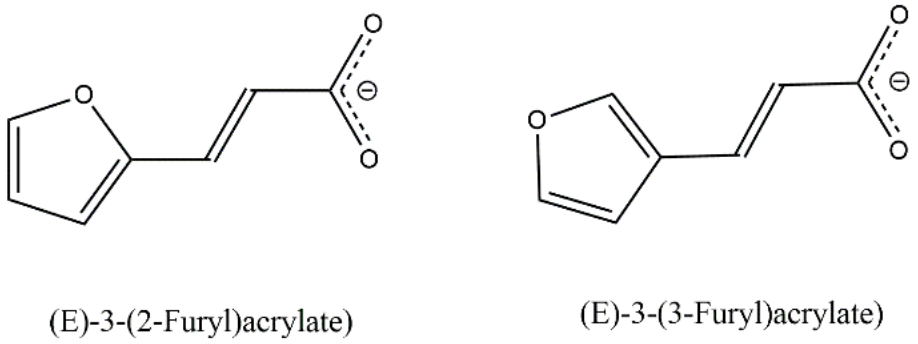


Figure 0.1: Structures of (E)-3-(nfuryl)acrylate (n=2,3)

To better understand the composition, structure, properties, and function of the protective film formed on steel surfaces by rare-earth metal (REM) corrosion inhibitors future studies could address the modeling of protective films by synthesizing Fe/Ln bimetallics with similar properties to the films.

Also, various advanced surface characterization techniques such as SEM, TEM, XPS, GDOES, XRPD, and ATR IR measurements and protective film chemistry could be utilized to better understand the implications of this study.

To overcome the crystallization limitations encountered in this study, future research could explore the addition of co-ligands such as 2,2'-bipyridine (bpy) to facilitate the formation of structurally characterized dimers. This approach would also enable a comparison of the structural and corrosion inhibition properties of aqua and bpy complexes. Similar comparisons

have been made in the literature with various phenylacetato rare earth complexes[7] and rare earth (III) 4-hydroxybenzoate (4hob) complexes.[8]

7.4 Contribution

The application of the best performing rare earth 3-furoates as practical corrosion inhibitors could involve dissolving the solid complexes in the water of cooling towers or radiators, or similar systems to create a very dilute solution. Additionally, these complexes could be suspended in paint for use as protective coating, though their effectiveness in this role has yet to be fully investigated.

After an extensive assessment of the anti-corrosion properties of the novel rare earth and alkali metal carboxylate salts prepared as corrosion inhibitors for mild steel surfaces, I believe I have contributed to our previous studies on other rare earth carboxylate complexes. This work not only enhances our understanding of the complexes obtained but also demonstrates their potential as effective corrosion inhibitors. The findings presented in these chapters contribute to our research group's long-term study and advance the field by establishing the structure-activity relationships involved in the corrosion mitigation process.

Chapter 6 explored the reactivity of highly reactive lanthanoid complexes with organic substrates under inert conditions, advancing our understanding of Ln(II) coordination chemistry, particularly regarding carbodiimide activation and the development of redox-active cationic species.

I believe that conducting research in both air-stable and air-sensitive chemistry has allowed me to gain a broad and comprehensive understanding of organometallic chemistry.

7.5 References

1 *American-Standard-Test-Methods in ASTM G31-72*, Philadelphia, USA, 2004.

2 A. E. Somers, B. R. W. Hinton, C. de Bruin-Dickason, G. B. Deacon, P. C. Junk and M. Forsyth, *Corros. Sci.*, 2018, **139**, 430–437.

3 V. P. Vithana, Z. Guo, G. B. Deacon, A. E. Somers and P. C. Junk, *New J. Chem.*, 2022, **46**, 19104–19111.

4 B. R. W. Hinton, *J. Alloys Compd.*, 1992, **180**, 15–25.

5 F. Blin, S. G. Leary, K. Wilson, G. B. Deacon, P. C. Junk and M. Forsyth, *J. Appl. Electrochem.*, 2004, **34**, 591–599.

6 G. B. Deacon, M. Forsyth, P. C. Junk, S. G. Leary and W. W. Lee, *Z. Anorg. Allg. Chem.*, 2009, **635**, 833–839.

7 E. Mottram, S. Hamilton, J. S. Moon, J. Wang, G. Bousrez, A. E. Somers, G. B. Deacon and P. C. Junk, *J. Coord.Chem.*, 2020, **73**, 2677–2697.

8 J. Moon, Z. Guo, O. A. Beaumont, S. Hamilton, G. Bousrez, E. Mottram, J. Wang, A. E. Somers, G. B. Deacon and P. C. Junk, *New J. Chem.*, 2023, **47**, 16843–16854.

Appendix One

Material and General Considerations

All commercially available solvents and chemicals were purchased from Sigma-Aldrich or BDH and used without further purification. Elemental analyses (C, H) were performed by either the Elemental Analysis Service Team, Science Centre, London Metropolitan University, England or the Chemical Analysis Facility, Department of Molecular Sciences, Macquarie University, NSW. Metal analysis was conducted by complexometric titration with 0.01 M EDTA using hexamethylenetetramine as a buffer and xylenol orange indicator. IR spectra were recorded on a Nicolet™ iS™ 5 FTIR Spectrometer in the range of 4000-500 cm^{-1}. Thermogravimetric (TGA) analyses were performed on a TA instrument SDT 650 using the standard 90 µl alumina metal pans in an N_2 atmosphere (50 $mlmin^{-1}$) from room temperature up to 750 ℃ (with a ramp of 10 ℃min^{-1}). X-ray powder diffraction patterns (PXRD) were measured at room temperature using a Bruker D2 PHASER diffractometer in the range of 2-60° with a 0.2° divergence slit and at 0.02° increments. The simulated powder patterns were generated from single-crystal X-ray diffraction data using the Mercury program provided by Cambridge Crystallographic Data Centre.[1] Melting points were determined in glass capillaries and were uncalibrated. LCMS data were collected on an Agilent 6100 Series Single Quad LC/MS coupled with an Agilent 1200 Series HPLC.

Corrosion Testing

Weight loss experiments were conducted according to the standard method ASTM G31-72[2] to assess the general corrosion and inhibition behaviour of synthesized compounds. Mild steel AS 1020 coupons were cut to approximately 20×20×1.5 mm and each of them was abraded progressively with sanding sheets of 80, 120, 240, 360, 800, 1200 and 2000 grits. Then the specimens were firstly rinsed with distilled water secondly with ethanol and dried under N_2 gas. A series of immersion tests were conducted immediately after polishing the coupons, up to 168h (7 days) in 0.01 M NaCl solutions with and without the respective concentration of the inhibitor compounds. Upon the completion of the test, the coupons were rinsed with distilled water. The corrosion product stuck to the substrate was firstly removed by sonicating in clean water followed by using finest sanding papers with minimum force to avoid the removal of sound material. Finally, the coupons were washed with ethanol and dried with N_2 gas.

The compounds showing the best performance in weight loss experiments were used to conduct Potentiodynamic Polarisation (PP) experiments, The tests were conducted on a Bio-Logic VMP3 multi-channel potentiostat in a three-electrode cell with an AS1020 steel rod as the working electrode surface, a titanium mesh counter electrode and a Ag/AgCl reference electrode, which was positioned very close to the working electrode surface. The steel rod was encased in epoxy, with a 10mm diameter exposed and polished to a 1200 grit finish. For each PP experiment 100mL of the test solution was used, with the solution quiescent and open to air. The Open Circuit Voltage (OCV) was monitored for 24 hours followed by the PP scan at a rate of 0.167mV/s over a scan range of 150mV below to 250mV above OCV. Corrosion current density (i_{corr}) and corrosion potential (E_{corr}) were extracted from the PP curves using Tafel extrapolation in EC Lab software V11.27. The curves were approximately linear over a range of 10-25 mV either side of E_{corr} and so the Tafel extrapolations were made over the data in this range. This range was chosen as it is in the activation region for this solution type. The point where the linear section of the anodic and cathodic sections of the PP curves intersected the value for E_{corr} was used to determine i_{corr}.

X-ray Crystallography

For the complexes **2.7, 2.10, 2.11** data were collected using a Rigaku SynergyS diffractometer. The SynergyS operated using microsource Mo-Kα radiation (λ = 0.71073 Å) at 123 K. The complexes **2.2, 2.3, 2.8, 5.2, 5.5** were measured on Oxford Diffraction Gemini Ultra dual source (Mo and Cu) CCD diffractometer collected at 123 K using either Mo X-ray source (λ = 0.71073 Å) or Cu source (λ = 1.54184 Å). Data processing was conducted using CrysAlisPro.55 software suite.[3] The compounds **2.1, 2.4, 2.5, 2.6, 2.9, 3.1-3.13, 4.1-4.6, 5.1, 5.3, 5.4, 5.6-5.14, 6.1** were collected on the MX1 beamline at the Australian Synchrotron. The compounds **6.2-6.10** were measured on a Bruker D8 Quest using Mo-Kα radiation (λ = 0.71073 Å) at 123 K.

Single crystals were mounted on glass fibres or loops using viscous hydrocarbon oil on the respective diffractometer. The data integration was processed with Blue-ice[4] and XDS[5] software programs. Structures were solved by SHELXT and refined by full-matrix least-squares methods against F2 using SHELX2018,[6] utilizing the Olex2 [7] graphical user interface. All hydrogen atoms were placed in calculated positions using the riding model. The graphical representations were generated using bitmap images GUI of Olex2.[7]

References

1 C. F. Macrae, I. Sovago, S. J. Cottrell, P. T. A. Galek, P. McCabe, E. Pidcock, M. Platings, G. P. Shields, J. S. Stevens, M. Towler and P. A. Wood, *J. Appl. Crystallogr.*, 2020, **53**, 226–235.

2 American-Standard-Test-Methods in ASTM G31-72, Philadelphia, USA, 2004.

3 CrysAlisPRO v.39. Agilent Technologies Ltd., Yarnton, Oxfordshire, England.

4 T. M. McPhillips, S. E. McPhillips, H. J. Chiu, A. E. Cohen, A. M. Deacon, P. J. Ellis, E. Garman, A. Gonzalez, N. K. Sauter, R. P. Phizackerley, S. M. Soltis and P. Kuhn, *J. Synchrotron Radiat.*, 2002, **9**, 401–406.

5 W. Kabsch, *J. Appl. Crystallogr.*, 1993, **26**, 795–800.

6 G. M. Sheldrick, *Acta Crystallogr., Sect. C: struct. Chem,* 2015, **71**, 3–8.

7 O. V. Dolomanov, L. J. Bourhis, R. J. Gildea, J. A. K. Howard and H. Puschmann, *J. Appl. Crystallogr.*, 2009, **42**, 339–341.

Appendix Two

Publications

1. **V. P. Vithana**, Z. Guo, G. B. Deacon, A. E. Somers and P. C. Junk, Synthesis, Structure, and Corrosion Inhibiting Properties of RE^{III} 3-Thiophenecarboxylate Complexes. *New J. Chem*. 2022, **46**, 19104–19111. (DOI: https://doi.org/10.1039/D2NJ03556A)

2. **V. P. Vithana**, Z. Guo, G. B. Deacon, A. E. Somers and P. C. Junk, RE(III) 3-Furoate Complexes: Synthesis, Structure, and Corrosion Inhibiting Properties. *Molecules* 2022, **27**, 8836. (DOI: https://doi.org/10.3390/molecules27248836)

3. **V. P. Vithana**, Z. Guo, G. B. Deacon, and P. C. Junk, Synthesis, structures, and corrosion inhibition of various alkali metal carboxylate complexes. *Molecules* 2023, **28**, 5515. (DOI: https://doi.org/10.3390/molecules28145515)

4. **V. P. Vithana**, Z. Guo, G. B. Deacon, and P. C. Junk, Rare Earth 2-Methyl-3-furoate Complexes: Effect of Steric Hindrance on Corrosion Inhibitor Properties. *Eur. J. Inorg. Chem.* 2024, e202300722. (DOI: https://doi.org/10.1002/ejic.202300722)

5. **V. P. Vithana**, Z. Guo, G. B. Deacon, and P. C. Junk, Contrasting reactions of carbodiimides with divalent lanthanoid species. *Chem. Eur. J.* 2025, e202500759. (https://doi.org/10.1002/chem.202500759)

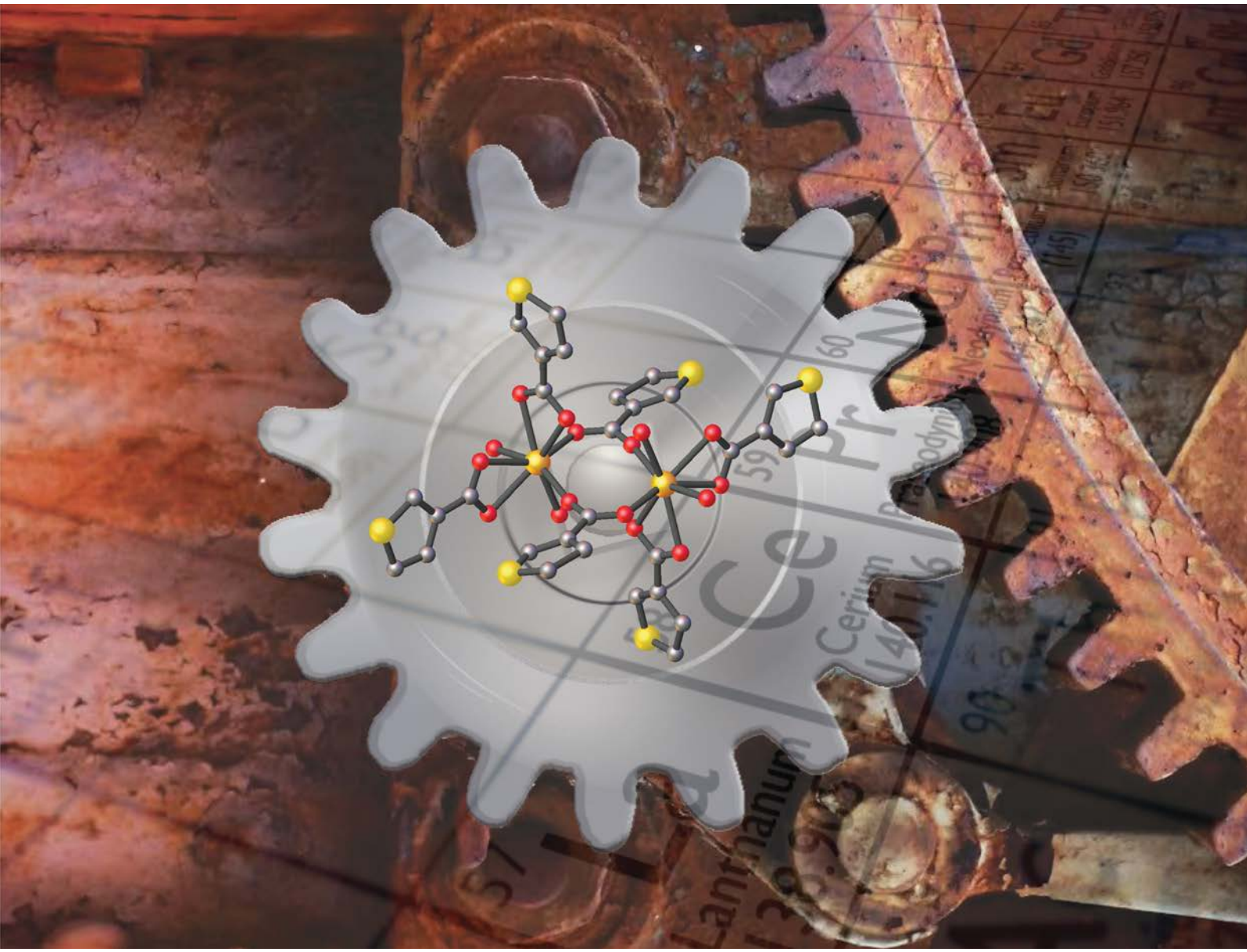
Volume 46
Number 40
28 October 2022
Pages 19075–19560

NJC

New Journal of Chemistry

A journal for new directions in chemistry

rsc.li/njc



ISSN 1144-0546

ROYAL SOCIETY OF CHEMISTRY

PAPER

Peter Junk *et al.*

Synthesis, structure, and corrosion inhibiting properties of RE^{III} 3-thiophenecarboxylate complexes

cnrs

NJC

ROYAL SOCIETY OF CHEMISTRY

PAPER

View Article Online
View Journal | View Issue

Published on 07 September 2022. Downloaded by JAMES COOK UNIVERSITY on 9/11/2024 11:53:50 PM.

Check for updates

Cite this: *New J. Chem.*, 2022, **46**, 19104

Synthesis, structure, and corrosion inhibiting properties of RE^{III} 3-thiophenecarboxylate complexes†

Vidushi P. Vithana,[a] Zhifang Guo,[a] Glen B. Deacon,[b] Anthony E. Somers[c] and Peter C. Junk*[a]

Received 19th July 2022,
Accepted 6th September 2022

DOI: 10.1039/d2nj03556a

rsc.li/njc

Two series of Rare Earth (RE) 3-thiophencarboxylate (3TPC) complexes have been synthesized by metathesis reactions between a suitable RE salt and Na(3TPC). Single crystal X-ray diffraction determined that light rare earth metals yield nonacoordinate 1D polymeric complexes $[Ln(3TPC)_3(H_2O)_3]_n$ (**Ln** = La (**1a**), Ce (**1b**), Pr (**1c**), Nd (**1d**), Sm (**1e**), Gd (**1f**)) while the heavier elements have a dimeric structure $[Ln_2(3TPC)_6(H_2O)_4]\cdot H_2O$ (**Ln** = Dy (**2a**), Ho (**2b**), Y (**2c**), Er (**2d**), Lu (**2e**)) with eight coordinated metal centers. Thermogravimetric analysis (TGA) and microanalysis data of all the compounds except for compound (**2e**) are consistent with the composition derived from single-crystal data. However, bulk compound $[Lu_2(3TPC)_6(H_2O)_4]\cdot H_2O$ (**2e**) lost both coordinated and lattice water during the drying process. Based on weight loss measurements, the corrosion inhibitory properties of the synthesized compounds on mild steel show that $[Y_2(3TPC)_6(H_2O)_4]\cdot H_2O$ (**2c**) has the greatest inhibition efficiency (68%). The potentiodynamic polarisation (PP) measurements are generally consistent with immersion test results. However, $[Gd(3TPC)_3(H_2O)_3]_n$ (**1f**) exhibited a similar optimum value with an inhibitor efficiency of 70% utilizing this technique. The PP curves show that these compounds act predominantly as anodic inhibitors.

1. Introduction

Corrosion is a widespread and extremely costly issue for engineering materials in diverse industries. To protect metals and alloys from corrosion, a range of approaches are used. Among them, one of the most promising and cost-efficient methods is using corrosion inhibitors.[1–3] Over a century, chromate compounds have been extensively used as corrosion inhibitors for a wide range of metals and alloys.[1,3–6] However, the high toxicity and carcinogenic properties associated with hexavalent chromium have led to a significant reduction in their use.[3,7] Rare earth (RE) salts have shown promise as alternatives to chromates, as they are effective with a relatively low cost and are environmentally friendly substances.[3,8,9]

Corrosion protection by organic corrosion inhibitors is related to the development of protective layers on metals.[10] Among organic systems, compounds containing hetero atoms are considered to have a higher inhibiting performance due to their strong affinity for metallic surfaces.[11–13] A group of CSIRO researchers developed a rapid screening test to investigate the inhibitive capacity of a series of structurally related compounds on aluminium alloys, and showed that *-para* and *-ortho* thiol substituted carboxylates could strongly inhibit corrosion on AA2024 and AA7075 alloys.[14] Further studies of the inhibitive effect of thiophene derivatives on carbon metal steel suggested that the inhibitive characteristics correlate with the dipole moment of the molecule and the number of adsorption centres present on the molecule. An increase in these features leads to stronger adsorption on the metal surface, hence greater inhibition efficiency.[15–18]

It has been shown that a combination of rare earth metals with organic corrosion inhibitors can form new complexes with improved inhibitory effects. These rare earth carboxylate complexes often suppress both cathodic and anodic reactions by combining the inhibitory properties of the individual components synergistically.[19] Over the past two decades, many rare earth carboxylates have been synthesized[20,21] and a number of them have been tested for corrosion inhibition.[10,19,22–26] Previous studies have found that cerium salicylate,[26] lanthanum 4-hydroxycinnamate[7] and yttrium 3-(4′-methylbenzoyl)propionates[27] are excellent inhibitors for mild steel in sodium chloride solutions.

In seeking improved rare earth carboxylate inhibitors, the focus of our current study is on developing new complexes with

[a] *College of Science & Engineering, James Cook University, Townsville, 4811, Qld, Australia. E-mail: peter.junk@jcu.edu.au*
[b] *School of Chemistry, Monash University, Clayton, 3800, Vic., Australia*
[c] *Institute for Frontier Materials, Deakin University, Burwood, 3125, Vic., Australia*

† Electronic supplementary information (ESI) available. CCDC 2183938–2183943 for **1a–1f** and 2183944–2183948 for **2a–2e**. For ESI and crystallographic data in CIF or other electronic format see DOI: https://doi.org/10.1039/d2nj03556a

 This journal is © The Royal Society of Chemistry and the Centre National de la Recherche Scientifique 2022

Published on 07 September 2022. Downloaded by JAMES COOK UNIVERSITY on 9/11/2024 11:53:50 PM.

known and putative organic carboxylic acid inhibitors. The excellent inhibitor properties of thiophene derivatives have led us to investigate the lanthanoid complexation by 3-thiophene carboxylate. Herein we now report the preparation and structural characterization of a range of rare-earth (RE) 3-thiophenecarboxylate (3TPC) complexes (Ln = La, Ce, Pr, Nd, Sm, Gd, Dy, Ho, Y, Er, Lu). The lanthanoid contraction results in the formation of two structural classes. Immersion tests and potentiodynamic polarisation were employed to determine the anti-corrosion properties of these compounds for mild steel, relative to a control.

2. Results and discussion

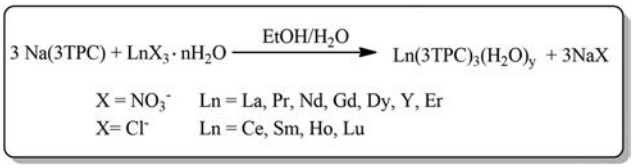
2.1 Synthesis and characterization

The complexes $[Ln(3TPC)_3(H_2O)_3]_n$ (**Ln** = La, Ce, Pr, Nd, Sm, Gd) and $[Ln_2(3TPC)_6(H_2O)_4]\cdot H_2O$ (**Ln** = Dy, Ho, Y, Er, Lu) were synthesized in moderate yields by metathesis reactions between sodium 3-thiophenecarboxylate and a suitable RE salt (mole ratio 1 : 3) as shown in Scheme 1.

In all cases, bulk products were separated as precipitates. Single crystals of the complexes suitable for X-ray crystallography were obtained by slow evaporation of the mother liquor. The compositions of the complexes were derived from X-ray crystallography together with elemental analysis and thermogravimetric analysis (TGA). The characterization of the bulk samples was carried out after drying to constant weight over silica gel. Only the Lu complex **2e** lost water from the single crystal composition under the drying conditions and both coordinated and lattice water was lost. Four complexes had low % C, a frequent problem with rare earth metal–organic compounds,[28–34] but additional % Ln analyses and TGA data leave little doubt as to the bulk composition.

The X-ray powder diffraction patterns of the bulk samples $[Ln(3TPC)_3(H_2O)_3]_n$ (**Ln** = La (**1a**), Ce (**1b**), Pr (**1c**), Nd (**1d**), Sm (**1e**), Gd (**1f**)) are identical to each other and agree with the simulated pattern of $[Pr(3TPC)_3(H_2O)_3]$ derived from the single-crystal data (Fig. S1, ESI†). Powder XRD analyses of $[Ln_2(3TPC)_6(H_2O)_4]\cdot H_2O$ (**Ln** = Dy (**2a**), Ho (**2b**), Y (**2c**), Er (**2d**), Lu (**2e**)) show similar powder diffractograms and they are almost identical to the generated powder diffractogram for $[Er_2(3TPC)_6(H_2O)_4]\cdot H_2O$ (Fig. S2, ESI†). In the case of **2e**, this similarity obtains despite dehydration.

The IR spectra within each isostructural series $[Ln(3TPC)_3(H_2O)_3]_n$ (**Ln** = La, Ce, Pr, Nd, Sm, Gd) (Fig. S3, ESI†) and $[Ln_2(3TPC)_6(H_2O)_4]\cdot H_2O$ (**Ln** = Dy, Ho, Y, Er, Lu) (Fig. S4, ESI†) are the same, apart from the absence of water absorption for **2e**.



Scheme 1 The synthesis of **Ln** 3-thiophenecarboxylate complexes.

Table 1 Selected infrared bands (cm^{-1}) of the RE 3-thiophenecarboxylate complexes

Complex	$\nu(OH)_{water}$	$\nu_{as}(CO_2)$	$\nu_s(CO_2)$	$\Delta\nu^a$	$\delta(CO_2)$
$[Pr(3TPC)_3(H_2O)_3]_n$	3381	1525, 1493	1395	98	685
$[Er_2(3TPC)_6(H_2O)_4]\cdot H_2O$	3326	1528, 1504	1394	110	699

[a] $\Delta\nu = \nu_{as}(CO_2) - \nu_s(CO_2)$.

Thus, important spectral data are listed for only one compound from each group (**Ln** = Pr (**1c**); **Ln** = Er (**2d**)) (Table 1). The data of the complexes in series **1** are only slightly different from that of series **2**. This observation suggests comparable binding modes in the compounds with each series. The broad bands at 3200–3550 cm^{-1} are characteristic of the coordinated and lattice water molecules. All the compounds exhibit the strong absorption bands characteristic of asymmetric and symmetric stretching vibrations of the carboxylate groups of the ligand 3TPC at 1530–1395 cm^{-1}. The relatively small splitting between the asymmetric and symmetric modes are consistent with the bridging and chelating carboxylates exhibited in the structures.[35]

The bulk samples of $[Ln(3TPC)_3(H_2O)_3]_n$ (**Ln** = La, Ce, Pr, Nd, Sm, Gd) and $[Ln_2(3TPC)_6(H_2O)_4]\cdot H_2O$ (**Ln** = Dy, Ho, Y, Er) (discussed above) gave TGA results (Fig. S5 and S6, ESI†) consistent with the single-crystal compositions, while the TGA data obtained from the bulk sample of $[Lu_2(3TPC)_6(H_2O)_4]\cdot H_2O$ (**2e**) showed significantly different behaviour as the compound had lost all the lattice and coordinated water from the structure derived from the single crystal composition prior to the measurement, and this is also evident from elemental analyses. Further defined loss is observed for all the compounds at *ca.* 400–500 °C, plausibly from the decomposition of the anhydrous complexes into $Ln_2(CO_3)_3$ and the diheteroaryl ketone. Such thermal behaviour of metal carboxylates is known.[36] This interpretation is supported by the infrared spectra (Fig. S7, ESI†) of the residues after thermolysis of $[Nd(3TPC)_3(H_2O)_3]_n$ and $[Er_2(3TPC)_6(H_2O)_4]\cdot H_2O$ to 500 °C as they corresponded closely to that reported for $[Dy_2(CO_3)_3].4H_2O$.[37] There is evidence of an intermediate formation in the TGA data of **1a–1d**, but not **1e,f**. The weight loss corresponds approximately to formation of $Ln_2(3TPC)_4(CO_3)$ (see Experimental). The instability of this intermediate for **1e,f** perhaps relates to greater stability of the final carbonate species relative to the intermediate as the ionic radius of Ln^{3+} decreases.

2.2 Structural description

Crystal structures of $[Ln(3TPC)_3(H_2O)_3]_n$ (**Ln** = La, Ce, Pr, Nd, Sm, Gd) and $[Ln_2(3TPC)_6(H_2O)_4]\cdot H_2O$ (**Ln** = Dy, Ho, Y, Er, Lu) were determined. The crystal and refinement data and bond lengths are given in supporting information in Tables S1–S5 (ESI†).

The complexes $[Ln(3TPC)_3(H_2O)_3]_n$ (Ln = La, Ce, Pr, Nd, Sm, Gd). The isostructural series of complexes $[Ln(3TPC)_3(H_2O)_3]_n$ (**Ln** = La(**1a**), Ce(**1b**), Pr(**1c**), Nd (**1d**), Sm(**1e**), Gd(**1f**)) form a 1D polymeric chain with nine coordinated rare-earth ions and crystallize in the monoclinic $P2_1/c$, with a tricapped trigonal prismatic geometry. The representative structure of $[Pr(3TPC)_3(H_2O)_3]_n$ is

Published on 07 September 2022. Downloaded by JAMES COOK UNIVERSITY on 9/11/2024 11:53:50 PM.

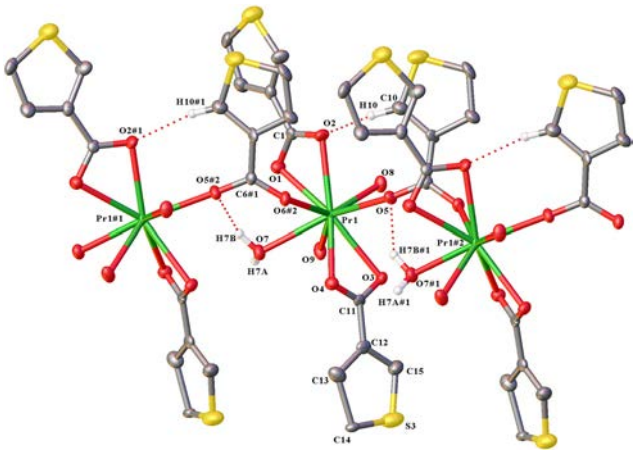


Fig. 1 Molecular diagram of $[Pr(3TPC)_3(H_2O)_3]_n$ (**1c**) (representative of La (**1a**), Ce (**1b**), Nd (**1d**), Sm (**1e**), Gd (**1f**)) The hydrogen atoms except for those forming hydrogen bonds have been omitted for clarity. Selected bond lengths (Å) and angles (°) (Data for **1a–1f** in supplementary information). **1c** Pr1–O1 2.570(5), Pr1–O2 2.531(5), Pr1–O3 2.577(5), Pr1–O4 2.523(5), Pr1–O5 2.468(5), Pr1–O6#1 2.489(5), Pr1–O7 2.538(5), Pr1–O8 2.485(5), Pr1–O9 2.495(5), Pr1#1–Pr1–Pr1#2 118.274(13), O8–Pr1–O9 71.056(16), O9–Pr1–O7 67.955(14)°, O7–Pr1–O8 135.002(16), C1···Pr1···C11 172.918(3), Symmetry Code: +*X*, 1/2 − *Y*, 1/2 + *Z*.

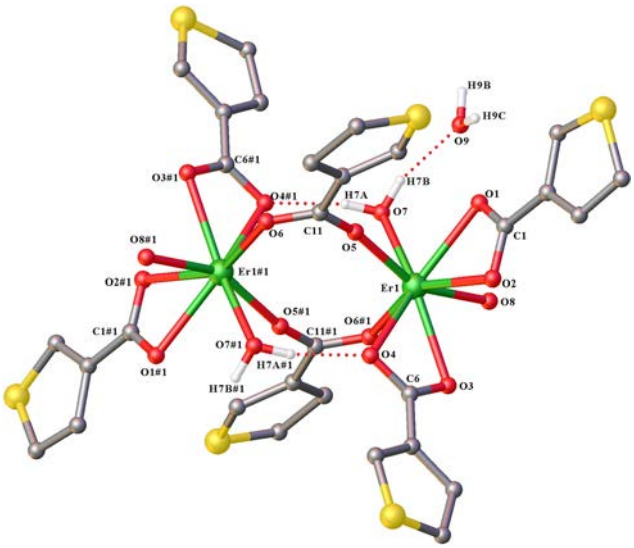


Fig. 2 Molecular diagram of $[Er_2(3TPC)_6(H_2O)_4]\cdot H_2O$ (**2d**) (representative of Dy(**2a**), Ho(**2b**), Y(**2c**), Lu(**2e**)) The hydrogen atoms except for those having hydrogen bonds have been omitted for clarity. Selected bond lengths (Å) (Data for **2a–2e** in supplementary information). **2d** Er1–O1 2.426(2), Er1–O2 2.398(2), Er1–O3 2.433(2), Er1–O4 2.394(2), Er1–O5 2.229(2), Er1–O6#1 2.283(2), Er1–O7 2.385(2), Er1–O8 2.330(2) O8–Er1–H7A 85.124(6), C1···Er1···C6 104.735(3), O5–Er1–O6#1 114.374(4). Symmetry Code: 2 − *X*,1 − *Y*, 1 − *Z*.

discussed here, and part of the polymeric structure is shown in Fig. 1. The coordination environment of the asymmetric unit comprises two different carboxylate ligand binding modes. There are four chelating oxygen atoms from two κ(O,O′) carboxylates (binding through O1,2 and O3,4), one bridging oxygen atom from each of two μ-1κ(O):2κ(O′)-carboxylate (binding through O5,6#2 and three ligated water oxygen atoms (O7, O8, O9). The structure forms a 1D polymeric chain through bridging carboxylate ligand O5#2–C6#1–O6#2 between the 9 coordinated Pr1 and Pr1#1 atoms. The distance between each adjacent Pr metal centre is 6.2763 Å, with Pr1#1–Pr1–Pr1#2 at an angle of 118.274(13)°. The average Pr–O bond length observed for complex **1c** is 2.526 Å, with the shortest bond Pr1–O5 (2.468 Å) and the longest bond Pr1–O3 (2.577 Å). The former involves a bridging oxygen rather than any of the terminal oxygens. The two chelating rings are quite symmetrical. The ligated water oxygen atoms have angles of 71.056(16)° (O8–Pr1–O9), 67.955(14)° (O9–Pr1–O7), and 135.002(16)° (O7–Pr1–O8) respectively. The two chelating carboxylate ligands have a *trans* disposition C1···Pr1···C11 172.918(3)°. There is hydrogen bonding from one of the bridging oxygen atoms O5 and one water oxygen atom O7#1 attached to the adjacent metal centre. Moreover, a rather unusual H bond forms between O2–H10–C10 resulting in an unusual 7-membered ring (Fig. 1 and Table S3, ESI†).

The effect of the ionic radii on the variation in the Ln–O bond length can be examined. (Table S2, ESI†) A decrease in the average Ln–O bond distance across the RE series from La to Gd [Ln = La 2.565 Å, Ce 2.548 Å, Pr 2.526 Å, Nd 2.510 Å, Sm 2.480 Å, Gd 2.462 Å] is consistent with lanthanoid contraction.[38]

The complexes $[Ln_2(3TPC)_6(H_2O)_4]\cdot H_2O$ (Ln = Dy, Ho, Y, Er, Lu). The molecular structure of $[Er_2(3TPC)_6(H_2O)_4]\cdot H_2O$ can be found in Fig. 2 and is a representative of the isomorphous series of dimeric complexes $[Ln_2(3TPC)_6(H_2O)_4]\cdot H_2O$ (**Ln** = Dy(**2a**), Ho(**2b**), Y(**2c**), Lu(**2e**)) that crystallizes in monoclinic $P2_1/c$ with eight coordinate lanthanoid ions. The stereochemistry of the Ln^{3+} ions can be described as slightly distorted square antiprismatic. The bond lengths of the isostructural series are given in Table S4 (ESI†). Only one half of the centrosymmetric dimer, containing Er1 is unique while Er1#1 is symmetry generated. The carboxylate ligands are coordinated through two different carboxylate binding modes. The complex **2d** contains four κ(O,O′) carboxylates binding through the oxygen atoms O1,2 and O3,4 at Er1 and O1#1,2#1 and O3#1,4#1 at Er1#1. The chelating carboxylate ligands show quite symmetric chelation. Two μ-1κ(O):2κ(O′)-carboxylate ligands bridge the two metal centres through O5,6 and O5#1,6#1. Finally, four coordinated water molecules are bound through O7,8 at Er1 and O7#1,8#1 at Er1#1. The Er–O bond length in complex **2d** ranges from 2.229 Å to 2.433 Å with an average of 2.36 Å. Similar to the nine coordinated $Ln(3TPC)_3(H_2O)_3]_n$, the shortest RE–O distance is observed for bridging oxygen. The coordinated water oxygen atoms form a O8–Er1–O7 angle of 85.12(7)° while the two chelating carboxylate ligands form a C1···Er1···C6 angle of 104.735(3)°. This contrasts the *trans* disposition in **1c**. The bridging oxygen atoms form an angle of 114.374(4)° between themselves through O5–Er1–O6#1. There is hydrogen bonding involving two of the κ(O,O′) carboxylate oxygen atoms O4, 4#1, two of the ligated water oxygen atoms O7#1,O7 and the lattice water oxygen atom O9 in the dimeric structure (Table S5, ESI†).

In accord with the lanthanoid contraction, a decrease in the average Ln–O bond lengths across the series from Dy to Lu

 This journal is © The Royal Society of Chemistry and the Centre National de la Recherche Scientifique 2022

Published on 07 September 2022. Downloaded by JAMES COOK UNIVERSITY on 9/11/2024 11:53:50 PM.

(Ln = Dy 2.390, Ho 2.374, Y 2.367, Er 2.360, Lu 2.328) is observed.[38]

2.3 Corrosion inhibition

2.3.1 Immersion tests. Table 2 provides a summary of the results obtained from weight loss measurements for steel coupons over seven days in 0.01M NaCl solutions in the presence of $RE(3TPC)_3$. At the end of the test period, visual inspections (Fig. S8, ESI†) of all the coupons indicated dullness and signs of pitting. However, when considering the general uniformity, the coupons placed in inhibitor solutions were significantly less affected compared to the control coupons. The weight loss of the coupons during the immersion test period is considered the primary measure of corrosion. Thus, the corrosion rates of the inhibitor solutions were calculated by using the equation described in eqn (1):

$$\text{Corrosion rate } (R) = \frac{KW}{ATD} \quad (1)$$

K = a constant; W = weight loss (g); A = coupon area (cm^2); T = time of exposure (168 h); D = density of the test metal.

Then using these data, the percentage corrosion inhibition (η) of each compound was calculated (eqn (2)):

$$\eta = \frac{R(\text{Control}) - R(\text{Inhibitor})}{R(\text{Control})} \times 100 \quad (2)$$

Consistent with visual inspections, weight loss measurements also indicated that $[La(3TPC)_3(H_2O)_3]_n$ (**1a**) has the lowest inhibition efficiency with an η = 36.5% and $[Y_2(3TPC)_6(H_2O)_4]\cdot H_2O$ (**2c**) resulted in the best performance with nearly 68% of effectiveness at the concentration used in the experiment (500 ppm). The inhibitive properties of the compounds correlate to some extent with the decreasing atomic radius of rare earth metals, but Gd and Y are positive outliers and Nd and Lu negative ones. The light rare earth (La–Nd) complexes were less effective than the heavier derivatives with Pr the best performer of the former group. In this context, it is interesting that the anti-corrosion performance of cerium diphenyl phosphate is enhanced by Pr.[39] The overall trend is dissimilar to behaviour of salicylate[26] and 4-hydroxycinnamate[7] complexes where Ce and La complexes respectively perform best. With heavier lanthanoids there is improved protection from Sm to Gd and then near similar behavior from Gd–Er with a decline to Lu. However, *Y* with a similar ionic radius to Er performs best, reminiscent of the superiority of the yttrium complex in the 3-(4′-methylbenzoyl)propanoate series.[27] This reinforces increasing evidence that the influence of the rare earth is ligand dependent. The low solubility of the complexes has deterred pursuing attempts at higher concentrations.

2.3.2 Potentiodynamic polarisation. The results of the potentiodynamic polarisation experiments are shown in Table 3. $[Gd(3TPC)_3(H_2O)_3]_n$ (**1f**) and $[Y_2(3TPC)_6(H_2O)_4]\cdot H_2O$ (**2c**) showed the lowest i_{corr}, at 0.953 and 0.981 μA cm^{-2} respectively. With the compounds present in the solution there is a shift in E_{corr} to more positive values as compared to the control, indicative of anodic inhibition dominating the reduction in i_{corr}. Representative PP scans in Fig. S9 (ESI†) show the marked reduction in the anodic arm when the compounds are present, with some reduction in the cathodic kinetics. Such a response is typical of these types of compounds.[5] However, the performance of the yttrium compound was somewhat inferior to that of yttrium 3-(4′-methylbenzoyl)propanoate.[40]

3. Conclusion

A series of RE 3-thiophenecarboxylate complexes have been successfully synthesized and characterized. All the compounds crystallized in one of the two structural groups based on single-crystal X-ray crystallography and on powder diffraction with similar IR spectra and TGA behaviour within each class. Type 1 structures, $[Ln(3TPC)_3(H_2O)_3]_n$ (**Ln** = La, Ce, Pr, Nd, Sm, Gd), are one dimensional polymers in which the coordination number of the Ln atom is nine. By contrast, Type 2 compounds form dimeric structures, $[Ln_2(3TPC)_6(H_2O)_4]\cdot H_2O$ (**Ln** = Dy, Ho, Y, Er, Lu), with a lanthanoid coordination number of eight. The

Table 2 Corrosion rates (μg m^{-2} s^{-1}, mm $year^{-1}$) and percentage inhibition (η) for mild steel coupons immersed in specific solutions for seven days

	Concentration		Solubilities[a]					
Solution	ppm	*M*	In H_2O	In NaCl (0.01 M)	Avg. weight loss (mg)	Corrosion rate (μg m^{-2} s^{-1})	Corrosion rate (mm $year^{-1}$)	Percentage inhibition (η)
Control-NaCl	580	0.01			16.5	30.5	0.1221	0
$[La(3TPC)_3(H_2O)_3]_n$	500	8.71×10^{-4}	900	580	10.4	19.36	0.0775	36.5
$[Ce(3TPC)_3(H_2O)_3]_n$	500	8.69×10^{-4}	900	590	9.95	18.8	0.0753	38.4
$[Pr(3TPC)_3(H_2O)_3]_n$	500	8.67×10^{-4}	900	590	8.99	16.28	0.0652	46.6
$[Nd(3TPC)_3(H_2O)_3]_n$	500	8.63×10^{-4}	950	590	9.75	18.91	0.0757	38.0
$[Sm(3TPC)_3(H_2O)_3]_n$	500	8.53×10^{-4}	850	550	7.55	14.87	0.0595	51.2
$[Gd(3TPC)_3(H_2O)_3]_n$	500	8.44×10^{-4}	790	520	6.0	11.87	0.0475	61.1
$[Dy_2(3TPC)_6(H_2O)_4]\cdot H_2O$	500	4.25×10^{-4}	920	520	6.77	12.62	0.0506	58.6
$[Ho_2(3TPC)_6(H_2O)_4]\cdot H_2O$	500	4.23×10^{-4}	870	530	6.0	12.01	0.0481	60.6
$[Y_2(3TPC)_6(H_2O)_4]\cdot H_2O$	500	4.85×10^{-4}	600	500	5.3	9.65	0.0386	68.4
$[Er_2(3TPC)_6(H_2O)_4]\cdot H_2O$	500	4.21×10^{-4}	700	540	6.25	11.58	0.0464	62.0
$[Lu_2(3TPC)_6]$	500	4.49×10^{-4}	900	550	7.3	14.13	0.0565	53.7

[a] Solubilities of the compounds in 0.01 M NaCl solution were lower than that in distilled water. Therefore, the immersion tests were done with the compounds at 500 ppm concentration.

Published on 07 September 2022. Downloaded by JAMES COOK UNIVERSITY on 9/11/2024 11:53:50 PM.

Table 3 Summary of corrosion parameters obtained from potentiodynamic polarisation tests in control and inhibited solutions after 24 h immersion

Solution	i_{corr} ($\mu A\ cm^{-2}$)	Std. dev.	E_{corr} (mV)	Std. dev.	Percentage inhibition
Control-NaCl	2.875	0.108	−638	4	—
$[Gd(3TPC)_3(H_2O)_3]_n$	0.953	0.135	−515	5	70
$[Y_2(3TPC)_6(H_2O)_4].\ H_2O$	0.981	0.121	−530	9	68
$[Er_2(3TPC)_6(H_2O)_4].\ H_2O$	1.414	0.263	−578	6	38

lanthanoid contraction is reflected in a reduction of Ln–O bond lengths as well as the decrease in coordination number.

Weight loss measurements indicate that $[Y_2(3TPC)_6(H_2O)_4]\cdot H_2O$ (**2c**) has the best corrosion inhibition performance for mild steel in aqueous NaCl solution, while $[La(3TPC)_3(H_2O)_3]_n$ (**1a**) is the least effective. Potentiodynamic polarisation confirmed the superior performance of $[Y_2(3TPC)_6(H_2O)_4]\cdot H_2O$ (**2c**) but also gave a similar result for $[Gd(3TPC)_3(H_2O)_3]_n$ (**1f**). The compounds act predominantly as anodic inhibitors. A comparison of Y complex data suggests introduction of a thiophene moiety into a carboxylate is not quite as effective as a 3-(4′-methylbenzoyl) group.[40]

4. Experimental section

4.1 General method and reagents

All commercially available solvents and chemicals were purchased from Sigma-Aldrich or BDH and used without further purification. Elemental analysis (C, H) was performed by either the Elemental Analysis Service Team, Science Centre, London Metropolitan University, England or the Chemical Analysis Facility, Department of Molecular Sciences, Macquarie University, NSW. Metal analysis was conducted by complexometric titration with 0.01 M EDTA using hexamethylenetetramine as a buffer and Xylenol Orange indicator. IR spectra were recorded on a Nicolet™ iS™ 5 FTIR Spectrometer in the range of 4000–500 cm^{-1}. Thermogravimetric analysis (TGA) was performed on TA instrument SDT 650 using the standard 90 μl alumina metal pans in an N_2 atmosphere (50 mL min^{-1}) from room temperature up to 750 °C (with a ramp of 10 °C min^{-1}). Powder diffraction patterns (PXRD) were measured at room temperature using a Bruker D2 PHASER diffractometer in the range of 2–60° with a 0.2° divergence slit and at 0.02° increments. The simulated powder patterns were generated from single-crystal X-ray diffraction data using the Mercury program provided by Cambridge Crystallographic Data Centre.[41] Melting points were determined in glass capillaries and are uncalibrated.

4.2 X-ray crystallography

Single crystals were mounted on glass fibres or loops using viscous hydrocarbon oil on the respective diffractometer. For the complexes **2a**, **2d**, **2e** data were collected using a Rigaku SynergyS diffractometer. The SynergyS operated using microsource Mo-Kα radiation (λ = 0.71073 Å) at 123 K. The complexes **1b**, **1c**, **2b** were measured on Oxford Diffraction Gemini Ultra dual source (Mo and Cu) CCD diffractometer collected at 123 K using either Mo X-ray source (λ = 0.71073 Å) or Cu source (λ = 1.54184 Å). Data processing was conducted using CrysAlisPro.55 software suite.[42] The data for the rest of the compounds (**1a**, **1d**, **1e**, **1f**, **2c**) were collected on the MX1 beamline at the Australian Synchrotron. The data integration was processed with Blue-ice[43] and XDS[44] software programs. Structures were solved by SHELXT and refined by full-matrix least-squares methods against F2 using SHELX2018,[45] utilizing the Olex2[46] graphical user interface. All hydrogen atoms were placed in calculated positions using the riding model. Crystal data and refinement details are shown in Table S1 (ESI†). CCDC 2183938–2183943 for **1a–1f** and 2183944–2183948 for **2a–2e**, contain the supplementary crystallographic data for this paper.†

4.3 Synthesis of 3-thiophenecarboxylate(3TPC)-RE aqua complexes

General Synthetic Method: 3-Thiophenecarboxylic acid was dissolved in 95% ethanol (15 mL) and treated with an equimolar amount of NaOH in distilled water (10 mL). The solution was stirred for 1 h and the pH was adjusted to 7–8. Three molar equivalents of the sodium 3-thiophenecarboxylate were slowly added to one equivalent of the lanthanoid salt in solution and stirred for 2 hours while maintaining the pH at 5. The resultant precipitate was collected and washed with distilled water followed by ethanol and air-dried for 2–3 days. The mother liquor was allowed to slowly evaporate at room temperature and XRD-suitable single crystals were separated from it.

$[La(3TPC)_3(H_2O)_3]_n$ (1a). $[La(3TPC)_3(H_2O)_3]_n$ White powder Yield: 86%, m.p. >300 °C. Elemental analysis for $C_{15}H_{15}LaO_9S_3$ (MW: 574.37 g mol^{-1}): Calculated (%) C 31.37; H 2.63; La 24.18. Found (%) C 31.56; H 2.50; La 23.39. IR (cm^{-1}): 3376 m, 3113 m, 1607 w, 1556 m, 1524 s, 1494 s, 1441 s, 1397 s, 1351 s, 1123 w, 1078 w, 935 w, 871 w, 835 m, 776 s, 755 s, 626 m, 685 m, 578 s, 520 s, 411 s; TGA weight loss (50–110 °C); 9.09% (Calc. for loss of 3 × H_2O = 9.40%); weight loss (340–460 °C); 15.4% (Calc. for formation of $La_2(CO_3)(O_2CR)_4$ = 16.9%); weight loss (340–540 °C); 38.0% (Calc. for formation of $La_2(CO_3)_3$ = 39.8%)

$[Ce(3TPC)_3(H_2O)_3]_n$ (1b). $[Ce(3TPC)_3(H_2O)_3]_n$ White powder Yield: 73%, m.p. >300 °C. Elemental analysis for $C_{15}H_{15}CeO_9S_3$ (MW: 575.58 g mol^{-1}): Calculated (%) C 31.30; H 2.63; Ce 24.34. Found (%) C 31.46; H 2.48; Ce 24.26. IR (cm^{-1}): 3380 m, 3113 m, 1608 w, 1554 m, 1522 s, 1492 s, 1440 s, 1396 s, 1348 s, 1123 w, 1077 w, 935 w, 871 w, 835 m, 776 s, 754 s, 626 m, 685 s, 578 s, 521 s, 408 s; TGA weight loss (50–110 °C); 9.02% (Calc. for loss of 3 × H_2O = 9.38%); weight loss (330–450 °C); 15.7% (Calc. for formation of $Ce_2(CO_3)(O_2CR)_4$ = 16.9%); weight loss (330–560 °C); 37.5% (Calc. for formation of $Ce_2(CO_3)_3$ = 39.9%)

$[Pr(3TPC)_3(H_2O)_3]_n$ (1c). $[Pr(3TPC)_3(H_2O)_3]_n$ Pale green powder Yield: 76%, m.p. >300 °C. Elemental analysis for $C_{15}H_{15}O_9PrS_3$ (MW: 576.38 g mol^{-1}): Calculated (%) C 31.26; H 2.62; Pr 24.45. Found (%) C 31.42; H 2.54; Pr 24.11. IR (cm^{-1}): 3381 m, 3112 m, 1609 w, 1556 m, 1525 s, 1493 s, 1441 s, 1395 s, 1351 s, 1123 w, 1078 w, 935 w, 871 w, 836 m, 777 s, 754 s, 685 s, 627 m, 579 s, 520 s, 411 s. TGA weight loss (50–110 °C); 9.43% (Calc. for loss of 3 × H_2O = 9.37%); weight loss (340–450 °C); 16.4% (Calc. for formation of $Pr_2(CO_3)(O_2CR)_4$ = 16.9%); weight loss (340–560 °C); 39.2% (Calc. for formation of $Pr_2(CO_3)_3$ = 40.1%)

 This journal is © The Royal Society of Chemistry and the Centre National de la Recherche Scientifique 2022

Published on 07 September 2022. Downloaded by JAMES COOK UNIVERSITY on 9/11/2024 11:53:50 PM.

$[Nd(3TPC)_3(H_2O)_3]_n$ (1d). $[Nd(3TPC)_3(H_2O)_3]_n$ Purple powder Yield: 76%, m.p. >300 °C. Elemental analysis for $C_{15}H_{15}NdO_9S_3$ (MW: 579.71 g mol^{-1}): Calculated (%) C 31.08; H 2.61; Nd 24.88. Found (%) C 31.28; H 2.49; Nd 24.62. IR (cm^{-1}): 3379 m, 3114 m, 1611 w, 1557 m, 1522 s, 1492 s, 1441 s, 1395 s, 1351 m, 1123 w, 1078 w, 871 w, 836 m, 777 s, 754 s, 626 m, 685 s, 579 s, 521 s, 408 s. TGA weight loss (50–110 °C); 9.74% (Calc. for loss of 3 × H_2O = 9.31%); weight loss (340–450 °C); 17.2% (Calc. for formation of $Nd_2(CO_3)(O_2CR)_4$ = 16.8%); weight loss (340–560 °C); 41.6% (Calc. for formation of $Nd_2(CO_3)_3$ = 40.4%)

$[Sm(3TPC)_3(H_2O)_3]_n$ (1e). $[Sm(3TPC)_3(H_2O)_3]_n$ White powder Yield: 54%, m.p. >300 °C. Elemental analysis for $C_{15}H_{15}O_9S_3Sm$ (MW: 585.83 g mol^{-1}): Calculated (%) C 30.75; H 2.58; Sm 25.67. Found (%) C 29.49; H 2.23; Sm 25.95. IR (cm^{-1}): 3373 m, 3116 m, 1612 w, 1559 m, 1522 s, 1491 s, 1438 s, 1395 s, 1351 s, 1123 w, 1078 w, 935 w, 872 w, 836 m, 754 s, 627 m, 684 s, 579 s, 519 s, 414 s. TGA weight loss (55–120 °C); 9.07% (Calc. for loss of 3 × H_2O = 9.17%); weight loss (370–540 °C); 37.0% (Calc. for formation of $Sm_2(CO_3)_3$ = 40.8%)

$[Gd(3TPC)_3(H_2O)_3]_n$ (1f). $[Gd(3TPC)_3(H_2O)_3]_n$ White powder Yield: 63%, m.p. >300 °C. Elemental analysis for $C_{15}H_{15}GdO_9S_3$ (MW: 592.72 g mol^{-1}): Calculated C 30.40; H 2.55; Gd 26.53. Found (%) C 29.22; H 2.16; Gd 26.96. IR (cm^{-1}): 3382 m, 3118 m, 1566 m, 1529 s, 1495 s, 1431 s, 1396 m, 1354 s, 1124 w, 1079 w, 873 m, 838 m, 784 m, 755 s, 685 s, 627 m, 580 m, 522 s, 414 s. TGA weight loss (55–115 °C); 9.00% (Calc. for loss of 3 × H_2O = 9.11%); weight loss (370–550 °C); 38.5% (Calc. for formation of $Gd_2(CO_3)_3$ = 41.7%)

$[Dy_2(3TPC)_6(H_2O)_4]\cdot H_2O$ (2a). $[Dy_2(3TPC)_6(H_2O)_4]\cdot H_2O$ White powder Yield: 69%, m.p. >300 °C. Elemental analysis for $C_{30}H_{28}Dy_2O_{17}S_6$ (MW: 1177.92 g mol^{-1}): Calculated (%) C 30.59; H 2.40; Dy 27.59. Found (%) C 29.37; H 2.12; Dy 27.19. IR (cm^{-1}): 3254 w, 3109 w, 1557 m, 1527 s, 1503 s, 1434 s, 1346 s, 1209 w, 1123 w, 1073 w, 940 w, 875 w, 837 s, 780 s, 755 s, 699 m, 628 m, 526 m, 423 s. TGA weight loss (40–95 °C); 7.76% (Calc. for loss of 5 × H_2O = 7.64%); weight loss (380–570 °C); 38.5% (Calc. for formation of $Dy_2(CO_3)_3$ = 42.9%)

$[Ho_2(3TPC)_6(H_2O)_4]\cdot H_2O$ (2b). $[Ho_2(3TPC)_6(H_2O)_4]\cdot H_2O$ Yellow powder Yield: 85%, m.p. >300 °C. Elemental analysis for $C_{30}H_{28}Ho_2O_{17}S_6$ (MW: 1182.78 g mol^{-1}): Calculated (%) C 30.46; H 2.39; Ho 27.89. Found (%) C 29.97; H 2.25; Ho 28.84. IR (cm^{-1}): 3292 w, 3111 w, 1566 m, 1528 s, 1503 s, 1428 s, 1348 s, 1123 w, 1073 w, 940 w, 875 w, 837 m, 781 m, 754 s, 699 m, 627 m, 526 m, 420 s. TGA weight loss (40–95 °C); 7.19% (Calc. for loss of 5 × H_2O = 7.61%); weight loss (395–570 °C); 36.1% (Calc. for formation of $Ho_2(CO_3)_3$ = 43.1%).

$[Y_2(3TPC)_6(H_2O)_4]\cdot H_2O$ (2c). $[Y_2(3TPC)_6(H_2O)_4]\cdot H_2O$ White powder Yield: 69%, m.p. >300 °C. Elemental analysis for $C_{30}H_{28}O_{17}S_6Y_2$ (MW: 1030.73 g mol^{-1}): Calculated (%) C 34.96; H 2.74; Y 17.25. Found (%) C 33.38; H 2.53; Y 17.55. IR (cm^{-1}): 3341 w, 3106 w, 1567 m, 1529 s, 1504 s, 1434 s, 1402 s, 1349 s, 1209 w, 1123 w, 1073 w, 940 w, 875 w, 838 m, 782 m, 754 s, 698 s, 627 m, 550 m, 525 m, 422 s. TGA weight loss (40–95 °C); 8.29% (Calc. for loss of 5 × H_2O = 8.73%); weight loss (400–570 °C); 38.4% (Calc. for formation of $Y_2(CO_3)_3$ = 34.7%).

$[Er_2(3TPC)_6(H_2O)_4]\cdot H_2O$ (2d). $[Er_2(3TPC)_6(H_2O)_4]\cdot H_2O$ Pink powder Yield: 72%, m.p. >300 °C. Elemental analysis for $C_{30}H_{28}Er_2O_{17}S_6$ (MW: 1187.44 g mol^{-1}): Calculated (%) C 30.34; H 2.38; Er 28.17. Found (%) C 30.32; H 2.36; Er 28.5. IR (cm^{-1}): 3326 w, 3106 w, 1568 m, 1528 s, 1504 s, 1435 s, 1394 s, 1348 s, 1123 w, 1073 w, 941 w, 875 w, 837 m, 782 m, 754 s, 699 m, 627 m, 525 m, 423 s. TGA weight loss (40–95 °C); 7.36% (Calc. for loss of 5 × H_2O = 7.58%); weight loss (380–600 °C); 43.7% (Calc. for formation of $Er_2(CO_3)_3$ = 43.3%)

$[Lu_2(3TPC)_6(H_2O)_4]\cdot H_2O$ (2e). $[Lu_2(3TPC)_6(H_2O)_4]\cdot H_2O$ White powder Yield: 84%, m.p. >300 °C. Elemental analysis calculated for $C_{30}H_{28}Lu_2O_{17}S_6$ (MW: 1202.86 g mol^{-1}) Calculated (%) C 30.16; H 1.69; Lu 29.29: $C_{30}H_{18}Lu_2O_{12}S_6$ (MW: 1112.78 g mol^{-1}, loss of 5 H_2O) Calculated (%) C 32.35; H 1.62; Lu 31.45. Found (%) C 32.04; H 1.56; Lu 32.07. IR (cm^{-1}): 3103 w, 1610 w, 1515 s, 1428 s, 1396 s, 1339 s, 1208 w, 1125 w, 1071 w, 941 w, 873 w, 834 m, 754 s, 699 m, 626 m, 529 w, 430 s. TGA weight loss (340–600 °C); 43.8% (Calc. for formation of $Lu_2(CO_3)_3$ = 44.1%)

4.4 Corrosion testing

Weight loss experiments were conducted according to the standard method ASTM G31-72[47] to assess the general corrosion and inhibition behaviour of synthesized compounds. Mild steel AS 1020 coupons were cut to approximately 20 × 20 × 1.5 mm and each of them was abraded progressively with sanding sheets of 80, 120, 240, 360, 800, 1200 and 2000 grits. Then the specimens were firstly rinsed with distilled water secondly with ethanol and dried under N_2 gas. A series of immersion tests were conducted immediately after polishing the coupons, up to 168 h (7 days) in 0.01 M NaCl solutions with and without 500 ppm of the inhibitor compounds. Upon the completion of the test, the coupons were rinsed with distilled water. The corrosion product stuck to the substrate was firstly removed by sonicating in clean water followed by using finest sanding papers with minimum force to avoid the removal of sound material. Finally, the coupons were washed with ethanol and dried with N_2 gas.

The same solutions were used for the compounds containing REs Y, Gd and Er to conduct Potentiodynamic Polarisation (PP) experiments, as these compounds showed the best performance in weight loss experiments. The tests were conducted on a Bio-Logic VMP3 multi-channel potentiostat in a three-electrode cell with an AS1020 steel rod as the working electrode surface, a titanium mesh counter electrode and a Ag/AgCl reference electrode, which was positioned very close to the working electrode surface. The steel rod was encased in epoxy, with a 10 mm diameter exposed and polished to a 1200 grit finish. For each PP experiment 100 mL of the test solution was used, with the solution quiescent and open to air. The Open Circuit Voltage (OCV) was monitored for 24 hours followed by the PP scan at a rate of 0.167 mV s^{-1} over a scan range of 150 mV below to 250 mV above OCV. Corrosion current density (i_{corr}) and corrosion potential (E_{corr}) were extracted from the PP curves using Tafel extrapolation in EC Lab software V11.27. The curves were approximately linear over a range of 10–25 mV either side of E_{corr} and so the Tafel extrapolations were made over the data in this range. This range was chosen as it is in the

Published on 07 September 2022. Downloaded by JAMES COOK UNIVERSITY on 9/11/2024 11:53:50 PM.

activation region for this solution type. The point where the linear section of the anodic and cathodic sections of the PP curves intersected the value for E_{corr} was used to determine i_{corr}.

Conflicts of interest

There are no conflicts of interest to declare. PCJ is an Associate Editor at New Journal of Chemistry.

Acknowledgements

P. C. J and G. B. D. gratefully acknowledge the ARC for funding (DP200100568). Parts of this research were undertaken on the MX1 beamline at the Australian Synchrotron, part of ANSTO.[48] The authors also acknowledge crystallographic assistance from Professor P. V. Bernhardt.

References

1 A. L. Chong, J. I. Mardel, D. R. MacFarlane, M. Forsyth and A. E. Somers, *ACS Sustainable Chem. Eng.*, 2016, **4**, 1746–1755.
2 M. Ghorbani, J. Soto Puelles, M. Forsyth, R. A. Catubig, L. Ackland, L. Machuca, H. Terryn and A. E. Somers, *J. Phys. Chem.*, 2020, **11**, 9886–9892.
3 J. Sinko, *Prog. Org. Coat.*, 2001, **42**, 267–282.
4 Y. Peng, A. E. Hughes, G. B. Deacon, P. C. Junk, B. R. W. Hinton, M. Forsyth, J. I. Mardel and A. E. Somers, *Corros. Sci.*, 2018, **145**, 199–211.
5 F. Blin, S. G. Leary, K. Wilson, G. B. Deacon, P. C. Junk and M. Forsyth, *J. Appl. Electrochem.*, 2004, **34**, 591–599.
6 M. Forsyth, T. Markley, D. Ho, G. B. Deacon, P. Junk, B. Hinton and A. Hughes, *Corrosion*, 2008, **64**, 191–197.
7 F. Blin, S. G. Leary, G. B. Deacon, P. C. Junk and M. Forsyth, *Corros. Sci.*, 2006, **48**, 404–419.
8 B. Hinton, Corrosion prevention and control, in *Handbook on the Physics and Chemistry of Rare Earths*, ed., K. A. Gschneidner, Jr. and L. Eyring, Elsevier Science B.V., 1995, vol. 21, pp. 29–92.
9 B. R. W. Hinton, *J. Alloys Compd.*, 1992, **180**, 15–25.
10 T. Markley, F. Blin, M. Forsyth and B. Hinton, Multifunctional rare earth organic corrosion inhibitors, in *Rare Earth-Based Corrosion Inhibitors*, ed., M. Forsyth and B. Hinton, Woodhead Publishing, Cambridge, 2014, ch. 4.
11 D. A. Winkler, M. Breedon, A. E. Hughes, F. R. Burden, A. S. Barnard, T. G. Harvey and I. Cole, *Green Chem.*, 2014, **16**, 3349–3357.
12 D. Daoud, T. Douadi, H. Hamani, S. Chafaa and M. Al-Noaimi, *Corros. Sci.*, 2015, **94**, 21–37.
13 C. Verma, E. E. Ebenso and M. A. Quraishi, Ionic Liquids as Green Corrosion Inhibitors for Industrial Metals and Alloys, in*Green Chemistry*, ed., Hosam El-Din M. Saleh and M. Koller, IntechOpen, London, 2018, ch. 6.
14 T. G. Harvey, S. G. Hardin, A. E. Hughes, T. H. Muster, P. A. White, T. A. Markley, P. A. Corrigan, J. Mardel, S. J. Garcia, J. M. C. Mol and A. M. Glenn, *Corros. Sci.*, 2011, **53**, 2184–2190.
15 A. Galal, N. F. Atta and M. H. S. Al-Hassan, *Mater. Chem. Phys.*, 2005, **89**, 38–48.
16 Z. Szklarska-Smialowska and M. Kaminski, *Corros. Sci.*, 1973, **13**, 10.
17 A. S. Fouda, *Monatsh. Chem.*, 1986, **117**, 159–165.
18 A. S. Fouda, A. A. Ibrahim and W. T. El-Behairy, *Der Pharma Chem.*, 2014, **6**, 144–157.
19 M. Forsyth, K. Wilson, T. Behrsing, C. Forsyth, G. B. Deacon and A. Phanasgoankar, *Corrosion*, 2002, **8**, 953–960.
20 A. E. Somers, Y. Peng, A. L. Chong, M. Forsyth, D. R. MacFarlane, G. B. Deacon, A. E. Hughes, B. R. W. Hinton, J. I. Mardel and P. C. Junk, *Corros. Eng., Sci. Technol.*, 2020, **55**, 311–321.
21 A. E. Somers, G. B. Deacon, B. R. W. Hinton, D. R. Macfarlane, P. C. Junk, M. Y. J. Tan and M. Forsyth, *J. Indian Inst. Sci.*, 2016, **96**, 285–292.
22 T. Behrsing, G. B. Deacon and P. C. Junk, The chemistry of rare earth metals, compounds, and corrosion inhibitors, in *Rare Earth-Based Corrosion Inhibitors*, ed., M. Forsyth and B. Hinton, Woodhead Publishing, Cambridge, 2014, ch. 1.
23 R. Janicki, A. Mondry and P. Starynowicz, *Coord. Chem. Rev.*, 2017, **340**, 98–133.
24 J. de Damborenea, A. Conde and M. A. Arenas, Corrosion Inhibition with Rare Earth Metal Compounds in Aqueous Solution, in *Rare Earth-Based Corrosion Inhibitors*, ed. M. Forsyth and B. Hinton, Woodhead Publishing, Cambridge, 2014, ch. 3.
25 A. E. Hughes, T. G. Harvey, N. Birbilis, A. Kumar and R. G. Buchheit, Coatings for corrosion prevention based on rare earths, in *Rare Earth-Based Corrosion Inhibitors*, ed. M. Forsyth and B. Hinton, Woodhead Publishing, Cambridge, 2014, ch. 7.
26 M. Forsyth, M. Seter, B. Hinton, G. Deacon and P. Junk, *Aust. J. Chem.*, 2011, **64**, 812–819.
27 Y. Peng, A. E. Hughes, G. B. Deacon, P. C. Junk, B. R. W. Hinton, M. Forsyth, J. I. Mardel and A. E. Somers, *Corros. Sci.*, 2018, **145**, 199–211.
28 M. Salehisaki, N. E. Rad, G. B. Deacon, J. Wang, Z. Guo and P. C. Junk, *Inorg. Chim. Acta*, 2022, **539**, 120997.
29 G. J. Moxey, A. J. Blake, W. Lewis and D. L. Kays, *Eur. J. Inorg. Chem.*, 2015, 5892–5902.
30 R. P. Kelly, T. D. M. Bell, R. P. Cox, D. P. Daniels, G. B. Deacon, F. Jaroschik, P. C. Junk, X. F. le Goff, G. Lemercier, A. Martinez, J. Wang and D. Werner, *Organometallics*, 2015, **34**, 5624–5636.
31 H. Sitzmann, T. Dezember, O. Schmitt, F. Weber, G. Wolmershäuser and M. Ruck, *Z. Anorg. Allg. Chem.*, 2000, **626**, 2241–2244.
32 L. H. J. Lajunen and G. R. Choppin, *Rev. Anal. Chem.*, 1989, **9**, 91–130.
33 D. P. Daniels, G. B. Deacon, D. Harakat, F. Jaroschik and P. C. Junk, *J. Chem. Soc., Dalton Trans.*, 2012, **41**, 267–277.
34 L. Hirneise, C. Maichle-Mössmer and R. Anwander, *Inorg. Chem.*, 2021, **60**, 18211–18224.
35 G. B. Deacon and R. J. Phillips, *Coord. Chem. Rev.*, 1980, **33**, 227–250.

 This journal is © The Royal Society of Chemistry and the Centre National de la Recherche Scientifique 2022

Published on 07 September 2022. Downloaded by JAMES COOK UNIVERSITY on 9/11/2024 11:53:50 PM.

36 (*a*) G. B. Deacon, S. J. Faulks and G. N. Pain, *Adv. Organomet. Chem.*, 1986, **25**, 237–276; (*b*) G. B. Deacon, *Organomet. Chem. Rev., Sect. A*, 1970, **5**, 355.
37 B. Vallina, J. D. Rodriguez-Blanco, A. P. Brown, J. A. Blanco and L. G. Benning, *J. Nanopart. Res.*, 2013, **15**, 1438.
38 R. D. Shannon, *Acta Crystallogr., Sect. A: Cryst. Phys., Diffr., Theor. Gen. Crystallogr.*, 1976, **32**, 751–767.
39 T. A. Markley, A. E. Hughes, T. C. Ang, G. B. Deacon, P. Junk and M. Forsyth, *Electrochem. Solid-State Lett.*, 2007, **10**, C72–C75.
40 A. E. Somers, B. R. W. Hinton, C. de Bruin-Dickason, G. B. Deacon, P. C. Junk and M. Forsyth, *Corr. Sci.*, 2018, **139**, 430–437.
41 C. F. Macrae, I. Sovago, S. J. Cottrell, P. T. A. Galek, P. McCabe, E. Pidcock, M. Platings, G. P. Shields, J. S. Stevens, M. Towler and P. A. Wood, *J. Appl. Crystallogr.*, 2020, **53**, 226–235.
42 *CrysAlisPRO v.39*. Agilent Technologies Ltd., Yarnton, Oxfordshire, England.
43 T. M. McPhillips, S. E. McPhillips, H. J. Chiu, A. E. Cohen, A. M. Deacon, P. J. Ellis, E. Garman, A. Gonzalez, N. K. Sauter, R. P. Phizackerley, S. M. Soltis and P. Kuhn, *J. Synchrotron Radiat.*, 2002, **9**, 401–406.
44 W. Kabsch, *J. Appl. Crystallogr.*, 1993, **26**, 795–800.
45 G. M. Sheldrick, *Acta Crystallogr., Sect. C: Struct. Chem.*, 2015, **71**, 3–8.
46 O. v Dolomanov, L. J. Bourhis, R. J. Gildea, J. A. K. Howard and H. Puschmann, *J. Appl. Crystallogr.*, 2009, **42**, 339–341.
47 American-Standard-Test-Methods in ASTM G31-72, Philadelphia, USA, 2004.
48 N. P. Cowieson, D. Aragao, M. Clift, D. J. Ericsson, C. Gee, S. J. Harrop, N. Mudie, S. Panjikar, J. R. Price, A. Riboldi-Tunnicliffe, R. Williamson and T. Caradoc-Davies, *J. Synchrotron Radiat.*, 2015, **22**, 187–190.

molecules

MDPI

Article

RE$^{(III)}$ 3-Furoate Complexes: Synthesis, Structure, and Corrosion Inhibiting Properties

Vidushi P. Vithana [1], Zhifang Guo [1], Glen B. Deacon [2], Anthony E. Somers [3] and Peter C. Junk [1,*]

[1] College of Science & Engineering, James Cook University, Townsville, QLD 4811, Australia
[2] School of Chemistry, Monash University, Clayton, VIC 3800, Australia
[3] Institute for Frontier Materials, Deakin University, Burwood, VIC 3125, Australia
* Correspondence: peter.junk@jcu.edu.au

Abstract: In this study, two types of Rare Earth (RE) 3-furoate complexes were synthesized by metathesis reactions between RE chlorides or nitrates and preformed sodium 3-furoate. Two different structural motifs were identified as Type **1RE** and Type **2RE**. The Type **1RE** monometallic complexes form 2D polymeric networks with the composition $[RE(3fur)_3(H_2O)_2]_n$ (**1RE** = 1La, 1Ce, 1Pr, 1Nd, 1Gd, 1Dy, 1Ho, 1Y; 3furH = 3-furoic acid) while Type **2RE** bimetallic complexes form 3D polymeric systems $[NaRE(3fur)_4]_n$ (**2RE** = 2Ho, 2Y, 2Er, 2Yb, 2Lu). The stoichiometric mole ratio used (RE: Na(3fur) = 1:3 or 1:4) in the metathesis reaction determines whether **1RE** or **2RE** (RE = Ho or Y) is formed, but **2RE** (RE = Er, Yb, Lu) were obtained regardless of the ratio. The corrosion inhibition behaviour of the compounds has been examined using immersion studies and electrochemical measurements on AS1020 mild steel surfaces by a 0.01 M NaCl medium. Immersion test results revealed that $[Y(3fur)_3(H_2O)_2]_n$ has the highest corrosion inhibition capability with 90% resistance after 168 h of immersion. Potentiodynamic polarisation (PP) measurements also indicate the dominant behaviour of the **1Y** compound, and the PP curves show that these rare earth carboxylate compounds act predominantly as anodic inhibitors.

Keywords: rare earth metal; metathesis; carboxylate complexes; 3-furoates; structures; corrosion inhibitors

check for updates

Citation: Vithana, V.P.; Guo, Z.; Deacon, G.B.; Somers, A.E.; Junk, P.C. RE$^{(III)}$ 3-Furoate Complexes: Synthesis, Structure, and Corrosion Inhibiting Properties. *Molecules* **2022**, *27*, 8836. https://doi.org/10.3390/molecules27248836

Academic Editor: Chris Douvris

Received: 28 November 2022
Accepted: 9 December 2022
Published: 13 December 2022

Publisher's Note: MDPI stays neutral with regard to jurisdictional claims in published maps and institutional affiliations.

Copyright: © 2022 by the authors. Licensee MDPI, Basel, Switzerland. This article is an open access article distributed under the terms and conditions of the Creative Commons Attribution (CC BY) license (https://creativecommons.org/licenses/by/4.0/).

1. Introduction

Mild steel is extensively used as an engineering material in diverse industries due to its relatively low cost, high machinability, and widespread availability [1]. However, these kinds of metals and alloys are vulnerable to corrosion degradation by chemical and/or electrochemical reactions [2,3]. A range of factors such as pressure, temperature, and aggressive acidic environmental conditions [3] can lead to premature failure in mild steel structures. Over 3% of the world's Gross Domestic Production equating to US $2.5 trillion is spent annually to replace and reduce the damage caused by corrosion [4,5]. A major part of this cost includes the maintenance and replacement of water recirculating pipelines, bridges, and water tanks associated with cooling systems [3,6]. Without a proper control method to mitigate corrosion, such assets would have a significantly limited lifetime [7]. The latest reports by NACE international's IMPACT researchers have revealed that the application of currently available corrosion control practices could save between US $375 and US $875 billion annually. Thus 15–35% of the global cost of corrosion could be saved [5]. To protect metals and alloys from corrosion, a range of approaches are used. Among them, one of the oldest and most cost-efficient protection methods is using corrosion inhibitors [8,9]. Corrosion inhibitors are widely incorporated in water treatment formulations, as pigments in paint coatings, pipeline streams, etc. [8,10]. Normally, these inhibitors make a protective barrier film on the metal surface to minimize corrosion attacks [11].

Among corrosion inhibitors, rare earth (RE) metal salts have been recognized as an effective and environmentally friendly nontoxic method to prevent corrosion [12–17]. The

use of rare earths as corrosion inhibitors has emerged as an alternative to replace hexavalent chromates, some of the most extensively used corrosion inhibitors, and their high toxicity and carcinogenic properties have led to a significant reduction in their use in nearly all cases [12,18].

Moreover, organic systems containing hetero atoms are considered to have an advanced inhibiting ability due to the strong interactions between N, O and S atoms and the metallic surfaces [19–22]. Although there are many studies of heterocyclic compounds as corrosion inhibitors for mild steel, only a limited amount of literature is reported on furan and its derivatives for such applications. Vaidyanathan and Hackerman investigated the structural effect of some furan derivatives on corrosion inhibition and the effect on the dissolution of iron. The inhibition efficiency of the tested compounds follows the order 2-furoic acid > furfurylamine > tetrahydrofurfurylamine. The inhibition ability of furoic acid was explained based on the electron-donating ability of the heterocyclic ring oxygen as well as the carboxylic oxygen [23]. Khaled tested three furan derivatives (methyl 2-furoate, ethyl 2-furoate, and amyl 2-furoate) on mild steel in 1M HCl to evaluate the anti-corrosive properties with respect to the changes in substituent and polarity of the compound. It was suggested that the protection of mild steel occurs through donating to or sharing electrons with the metal surface, forming a stable covalent coordination bond (chemisorption) [24].

The recent innovative approaches toward designing "Green" corrosion inhibitors have involved combining RE ions with an organic ligand to form new complexes with mixed inhibition functions [10,15,16]. RE-carboxylate complexes are readily formed due to the highly oxophilic nature of REs towards carboxylate ligands and they tend to adopt either dimeric or polymeric forms [25,26]. Over the years, several different coordination patterns have been observed with carboxylate ligands binding to metal atoms [25,27].

So far, several trivalent rare-earth carboxylates have been synthesized and evaluated for their corrosion inhibition properties on mild steel [7,10,15,16,28,29]. Some of the best-performing RE carboxylate complexes reported in recent years are cerium salicylate [10] lanthanum 4-hydroxycinnamate [30] and yttrium 3-(4′-methylbenzoyl)propionate [11]. The ligands feature an additional donor function, which may enable binding (bridging) to a steel surface. [10,15,16]. Our latest paper evaluated the inhibition properties of thiophene derivatives on mild steel by investigating the rare earth metal complexation by 3-thiophenecarboxylate complexes [31], where the S atom provides an opportunity for bridging to steel.

In this paper, we discuss the synthesis of RE 3-furoate complexes (3furH = 3-furoic acid, Chart 1) and the corrosion inhibitory properties for AS 1020 mild steel in 0.01 M NaCl corrosive media, to examine whether the oxygen donor atom might prove more efficacious than sulfur. The synthesized compounds were also characterized using several techniques including single crystal X-ray crystallography. Moreover, the corrosion inhibition properties of the synthesized compounds were determined by weight loss experiments combined with potentiodynamic polarization measurements.

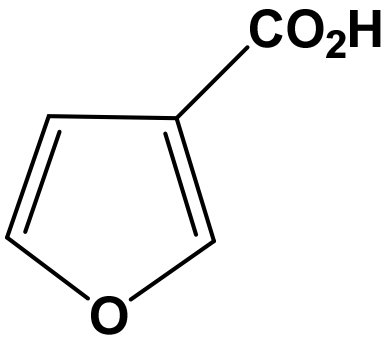
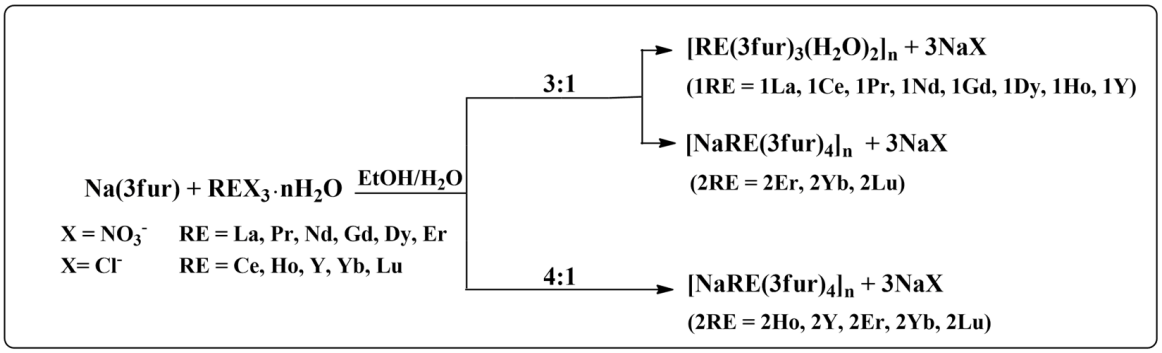


Chart 1. Structure of 3-furoic acid (3FurH).

2. Results

2.1. Synthesis and Characterization

When the syntheses were carried out with a ligand: RE stoichiometry of 3:1, eight homometallic complexes $[RE(3fur)_3(H_2O)_2]_n$ (**1RE** = 1La, 1Ce, 1Pr, 1Nd, 1Gd, 1Dy, 1Ho, 1Y), as well as Na-RE bimetallic complexes $[NaRE(3fur)_4]_n$ (**2RE** = 2Er, 2Yb, 2Lu), were obtained. Upon treating the ligand and RE salts in a 4:1 mole ratio, heterobimetallic complexes $[NaHo(3fur)_4]_n$ (**2Ho**) and $[NaY(3fur)_4]_n$ (**2Y**) were obtained in addition to the complexes **2RE** = 2Er, 2Yb and 2Lu, but La to Dy still gave $[RE(3fur)_3(H_2O)_2]_n$. Thus, the ratio used in the metathesis reaction appeared to affect the identity of the final complex for holmium and yttrium (Scheme 1).



Scheme 1. The synthesis of RE 3-furoate complexes. The ratios shown in the Scheme refer to the Na(3fur): REX_3 ratios of reactants.

In all cases, single crystals of the compounds were obtained by slow evaporation of the mother liquor. The bulk samples of complexes $[RE(3fur)_3(H_2O)_2]_n$ (**1RE** = 1La, 1Ce, 1Pr, 1Nd, 1Gd, 1Dy, 1Ho, 1Y) (Figure 1) and $[NaRE(3fur)_4]_n$ (**2RE** = 2Ho, 2Y, 2Er, 2Yb, 2Lu) (Figure 2) gave X-ray powder diffraction patterns that are identical to each other and are in agreement with the patterns generated from the single-crystal data.

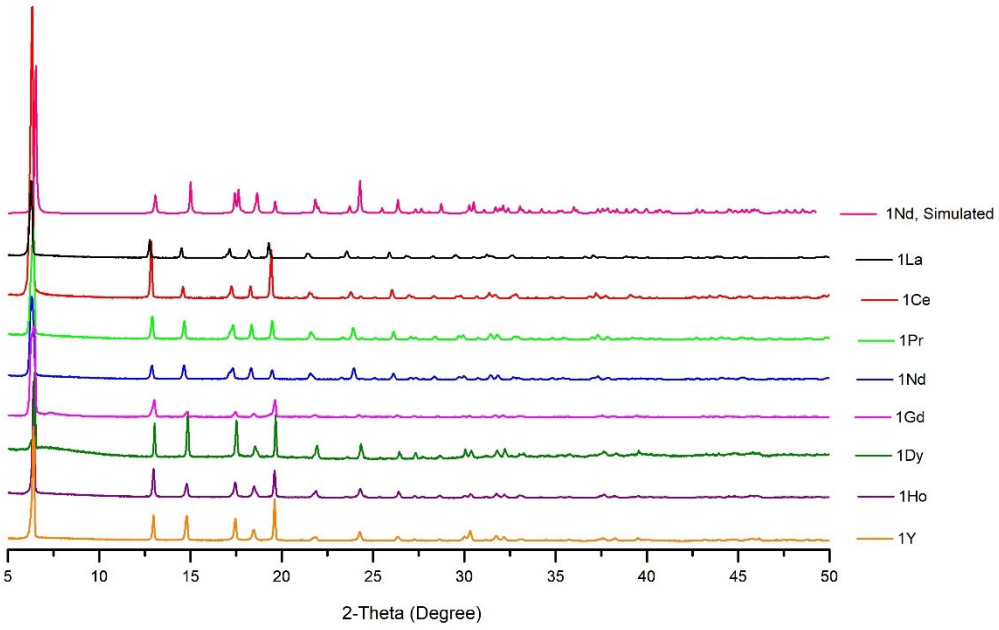


Figure 1. PXRD traces of the $[RE(3fur)_3(H_2O)_2]_n$ **1RE** series compared to the simulated pattern of $[Nd(3fur)_3(H_2O)_2]_n$ (**1Nd**).

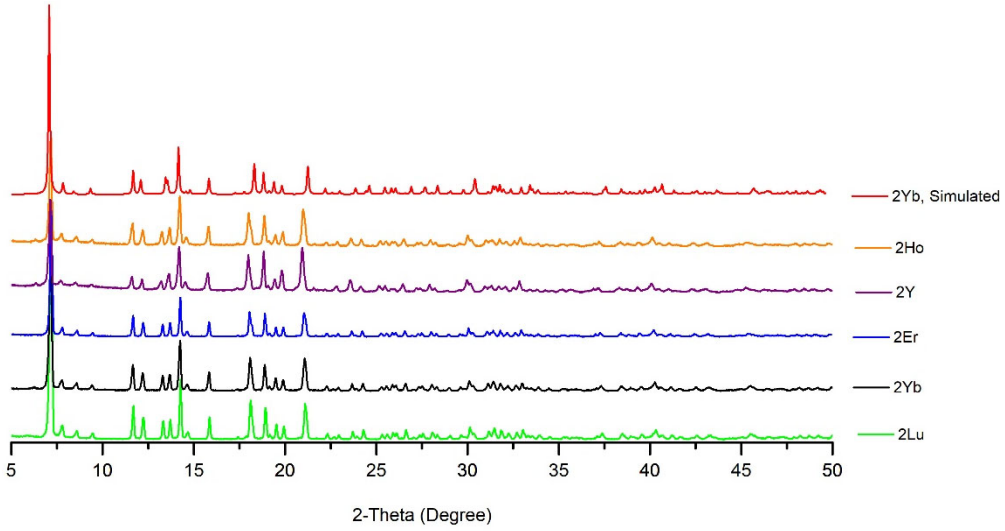


Figure 2. PXRD traces of the $[NaRE(3fur)_4]_n$ **2RE** series compared to the simulated pattern of $[NaYb(3fur)_4]_n$ (**2Yb**).

Satisfactory elemental analyses were obtained for all the compounds, with the exception of compound **2Yb**, with a low % C value. This is a frequent issue recognized for rare earth and alkaline earth complexes within previous literature [32–38]. However, X-ray crystallographic data together with additional % RE analyses and TGA data offer further evidence to confirm the final chemical compositions of the complexes.

The IR spectra of $[RE(3fur)_3(H_2O)_2]_n$ (**1RE** = 1La, 1Ce, 1Pr, 1Nd, 1Gd, 1Dy, 1Ho, 1Y) (Figure S1) and $[NaRE(3fur)_4]_n$ (**2RE** = 2Ho, 2Y, 2Er, 2Yb, 2Lu) (Figure S2) show strong similarities in major bands within each isostructural series. Thus, the significant IR bands for only one compound from each series (**1Nd** and **2Yb**) are listed in Table 1. For the **1RE** compounds broad O-H stretching bands in the range of 3200–3550 cm^{-1} are comparable and attributed to the presence of coordinated water molecules. IR spectra of all the RE complexes show strong asymmetric and symmetric carboxylate stretching bands at 1530–1350 cm^{-1}. Relatively small $\Delta\nu(CO_2^-)$ values are indicative of the presence of chelating and/or bridging carboxylate ligands [39].

Table 1. Selected infrared bands (cm^{-1}) of the RE^{III} 3-furoate complexes.

Compound	$\nu(OH)_{water}$	$\nu_{as}(CO_2^-)$	$\nu_s(CO_2^-)$	$\Delta\nu = (\nu_{as} - \nu_s)avg$	$\delta(CO_2)$
$[Nd(3fur)_3(H_2O)_2]_n$ (**1Nd**)	3431	1505	1365	140	598
$[NaYb(3fur)_4]_n$ (**2Yb**)	-	1502	1366	136	598

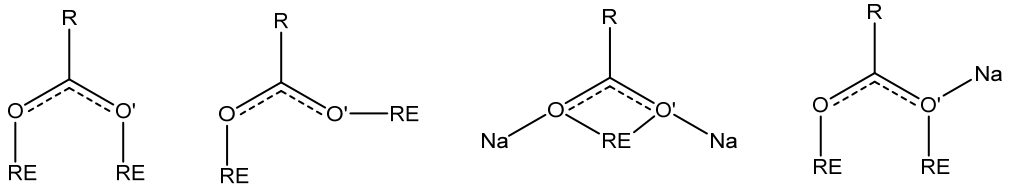
A TGA study was conducted to establish the thermal behaviour of the complexes as well as the intermediates and products formed during the thermolysis. TGA curves of the **1RE** bulk sample (Figure S3) showed a steep initial weight loss (*ca.* 75–130 °C), which corresponds to the loss of two molecules of water and the results are in agreement with the composition determined crystallographically as $[RE(3fur)_3(H_2O)_2]_n$. In line with the single-crystal compositions of the **2RE** compounds, their thermograms (Figure S4) do not indicate any weight loss owing to the loss of coordinated or lattice solvent molecules. Further weight loss is observed for all the compounds at ca. 370–500 °C. However, the TGA plot of **1La** exhibits significantly different behaviour as the product formation starts and finishes at lower temperatures than for the rest of the compounds in the isostructural series. The products plausibly resulted from the decomposition of the anhydrous complexes to the $RE_2(CO_3)_3$ in the **1RE** series and $Na_3RE(CO_3)_3$ in the **2RE** series. The IR spectra of the residues of compounds **1Ce** and **2Yb** after thermolysis to 500 °C support this interpretation [40,41] since they correspond well with the previously reported spectrum

of $[Dy_2(CO_3)_3].4H_2O$ (Figure S5) [42]. However, for the residues of $[RE(3fur)_3(H_2O)_2]_n$ compounds, there is not sufficient weight loss for $RE_2(CO_3)_3$ alone. Residual 3-furoate ligand could not be detected in the residue by IR spectra, so there must be an amorphous or IR silent coproduct such as $RE(OH)_3$, RE_2O_3, or REC_2. Metal carboxylates have a number of possible decomposition paths including the formation of carbonates and oxides [43,44].

Liquid chromatography-mass spectrometry (LCMS) studies have been used to investigate the composition of complexes **1Dy**, **2Ho** and **2Lu** in solution. In the mass spectrum of monometallic complex **1Dy** the molecular ion peak $[Dy(3fur)_2(H_2O)_2]^+$ can be detected at m/z 422.1 with the correct isotope patterns. Other than that, the related ion such as $[Dy(3fur)(OH)EtOH]^+$, can be also observed. The bimetallic complexes **2Ho** and **2Lu** were also examined by LCMS. In the positive mode of complex **2Ho**, $[Ho_2(3fur)_4(HCO_3)(H_2O)]^+$ and $[Na_2Ho(3fur)_3(3furH)(HCO_3)(H_2O)]^+$ were detected at m/z 853.5 and 735.2, respectively, with low intensity. Finally, compound **2Lu** in LCMS led to a highly intense peak as $[Na_2(CO_3)Lu(3fur)_4(H_2O)_2]^-$ in the negative mode at m/z 761. Interestingly, mass spectrometry results suggest that the bimetallic complexes remain considerably intact in solution. Furthermore, the observations of LCMS experiments have revealed that all the tested complexes retain some form of rare earth carboxylate fragments in solution.

2.2. X-ray Crystallography

There are three distinct carboxylate ligand binding modes, namely bridging μ-1κ(O):2κ(O′), chelating double bridging μ_3-1κ(O):2κ(O,O′):3κ(O′) and double bridging μ_3-1κ(O):2κ(O′):3κ(O′) observed in the structures (Figure 3).



(i)μ-1κ(O):2κ(O′) **1La-1Y** (ii) μ-1κ(O):2κ(O′) **1La-1Y** (iii) μ_3-1κ(O):2κ(O,O′):3κ(O′) **2Ho-2Lu** (iv) μ_3-1κ(O):2κ(O′):3κ(O′) **2Ho-2Lu**

Figure 3. Different coordination modes observed for carboxylate ligand (3-furoate) in rare earth complexes. (i): *syn-syn* (ii): *syn-anti*.

2.2.1. Monometallic 2D Polymeric Chains of $[RE(3fur)_3(H_2O)_2]_n$ Complexes (1RE = 1La, 1Ce, 1Pr, 1Nd, 1Gd, 1Dy, 1Ho, 1Y)

This isomorphous series of complexes crystallizes in the monoclinic *C*2/*c* space group and the compounds have 2D polymeric structures with eight-coordinate rare earth metal atoms with distorted square antiprismatic geometry. Crystal refinement data and bond lengths are provided in the Supplementary Material (Tables S1 and S2). A representative structure of $[Nd(3fur)_3(H_2O)_2]_n$ is shown in Figure 4. The coordination environment comprises of six bridging μ-1κ(O):2κ(O′) carboxylate ligands binding through O(1, 1#4, 2#1, 2#3, 5, 5#4) and two ligated aqua molecules O(4, 4#4). The backbone of the 1D polymeric chain is constructed through eight-membered rings (Nd1-O2#1-C1#1-O1#1-Nd1#1-O2-C1-O1) formed by *syn-syn* bridging bidentate carboxylates between adjacent Nd1 and Nd1#1 metal centres. The 1D polymeric chain of Nd atoms is nonlinear with Nd1#1-Nd1-Nd1#3 at an angle of 167.339(5)° and the distance between the adjacent Nd^{3+} metal centres in the chain is 5.1246(18) Å. The two ligated water oxygen atoms form a O4-Nd1-O4#4 *cisoid* angle of 127.16(6)°. Two of the bridging carboxylate oxygen atoms (O5 and O5#4) are involved in hydrogen bonding to water oxygen atoms (O4#3 and O4#1) attached to the adjacent metal centres. The 1D polymeric chain propagates into a 2D network by *syn-anti* bridging bidentate ligands (O5, 5#2) between Nd1 and Nd1#2 metal atoms. Experimentally found H bonds of the compound $[Nd(3fur)_3(H_2O)_2]_n$ are shown in Figure 4a and H bond lengths

are listed in Table S4. Lanthanoid contraction [45] is observed across the period from La to Y with a decrease in the average RE-O bond distance (Table S2) [RE = La 2.512 Å, Ce 2.487 Å, Pr 2.470 Å, Nd 2.454 Å, Gd 2.404 Å, Dy 2.379 Å, Ho 2.365 Å, Y 2.365 Å].

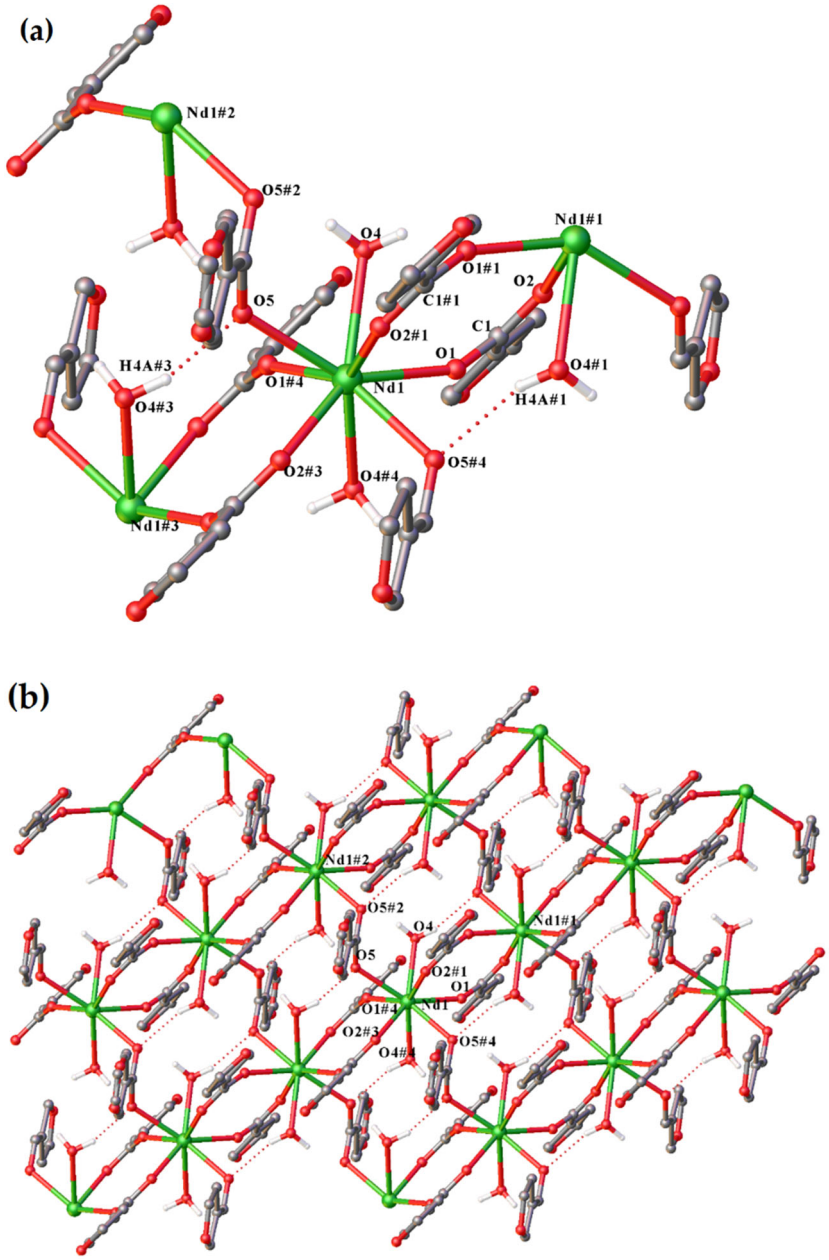


Figure 4. (**a**) The immediate coordination environment around Nd metal atoms in $[Nd(3fur)_3(H_2O)_2]_n$ (**1Nd**); (**b**) 2D polymeric chain of **1Nd** (representative of **1RE** = 1La, 1Ce, 1Pr, 1Gd, 1Dy, 1Ho, 1Y) Selected bond lengths (Å) and angles (°) (Data for all **1RE** in Supplementary information; Tables S2 and S3). **1Nd** Nd1-O1#4 2.3487(15), Nd1-O1 2.3487(15), Nd1-O2#1 2.3991(13), Nd1-O2#3 2.3991(13), Nd1-O5#4 2.4848(14), Nd1-O5 2.4848(14), Nd1-O4#4 2.5830(14), Nd1-O4 2.5830(14), Nd1 . . . Nd1#1 5.1246(18), Nd1#1-Nd1-Nd1#3 167.339(5), O4-Nd-O4#4 127.16(6), Symmetry Code: $^{\#1}$ 1/2-X,3/2-Y,-Z; $^{\#2}$ 1-X,+Y,3/2-Z; $^{\#3}$ 1/2+X,3/2-Y,1/2+Z:, $^{\#4}$ 1-X,+Y,1/2-Z.

2.2.2. Bimetallic 3D Polymeric Chains of $[NaRE(3fur)_4]_n$ Complexes (2RE = 2Ho, 2Y, 2Er, 2Yb, 2Lu)

Single crystals of X-ray crystallography quality were obtained for all five Ho, Y, Er, Yb and Lu analogues. The isostructural series of complexes forms a 3D polymeric network and crystallizes in the tetragonal *P*-4*n*2 space group. All RE^{3+} are eight coordinated with

two chelating ligands and four bridging ligands in distorted square antiprismatic geometry, Na1 is six-coordinate with six bridging ligands, and the donor atoms have an octahedral arrangement. Specific refinement parameters for individual structures are given in the Supplementary Material. A representative structure $[NaYb(3fur)_4]_n$ of the Type **2RE** can be found in Figure 5. The Yb1 and Yb2 atoms are bridged by the O1-Na1-O7 moiety present in the asymmetric unit of the crystal structure (Figure 5a). The Yb1 metal centre is bonded by chelating carboxylate oxygen atoms O1,2 and O1#1,2#1 of two μ_3-1κ(O):2κ(O,O′):3κ(O′) ligands. There are also four carboxylate ligands bridging through oxygen atoms O4, 4#1, 5#2, 5#3 of μ_3- 1κ(O):2κ(O′):3κ(O′) carboxylate groups. The ligand binding modes contained within the coordination sphere of the Yb2 metal atom are similar to those of the above-mentioned Yb1 metal atom, but Yb-O bond distances are different in each case (Table S5). Six coordinated Na1 is ligated through O1, 2#1, 7, 8#4 of four μ_3-1κ(O):2κ(O,O′):3κ(O′) coordinated modes and the other two sites are occupied by oxygen atoms O5#2 and O11#6 of two μ_3-1κ(O):2κ(O′):3κ(O′) carboxylate ligands. Yb1 and Na1, and Yb2 and Na1 are bridged by oxygen atoms O1, 2#1, O5#2 and O 7, 8#4, 11#6, respectively (Figure 5b).

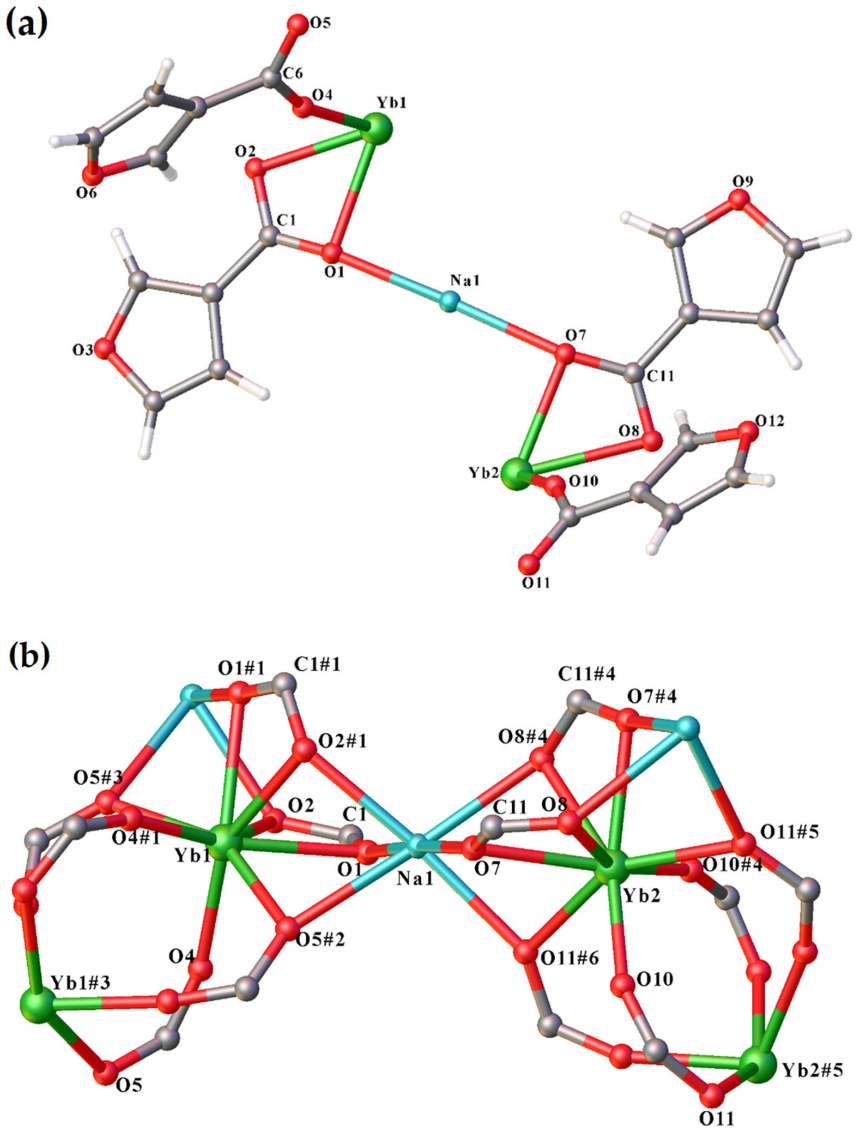


Figure 5. *Cont.*

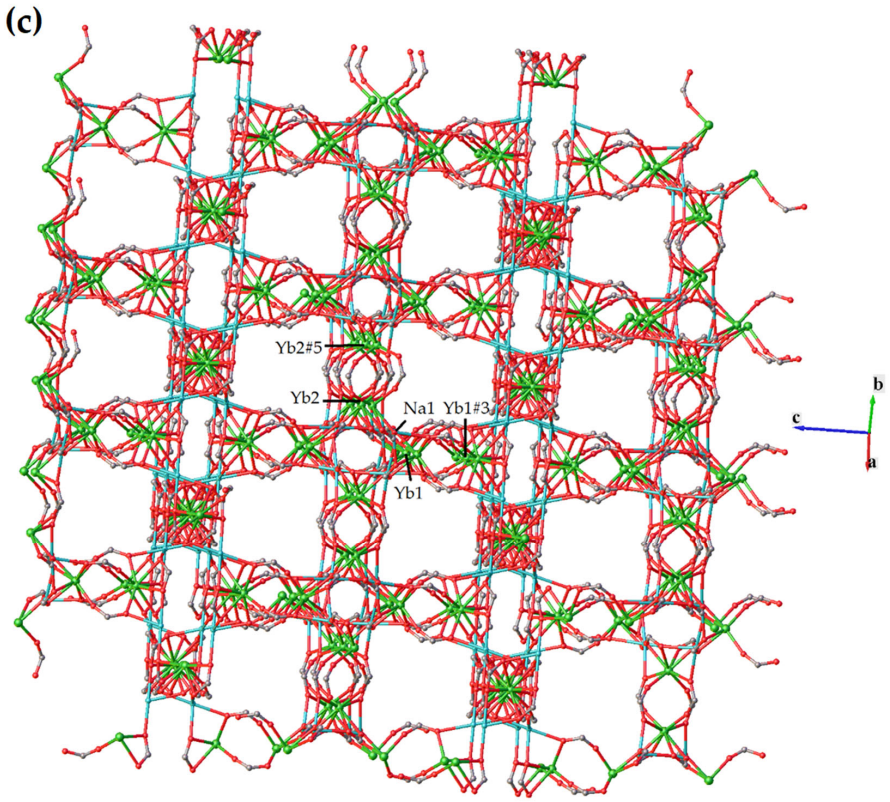


Figure 5. (**a**) Asymmetric unit of $[NaYb(3fur)_4]_n$ (**2Yb**) (representative of **2RE** = 2Ho, 2Y, 2Er, 2Lu) (**b**) The immediate coordination environment around Yb1, Yb2 and Na1 metals atoms in **2Yb** (furan rings are omitted for clarity); Selected bond lengths (Å) and angles (°) (Data for all **2RE** in Supplementary information; Tables S5 and S6). **2Yb** Yb1-O1 2.360(3), Yb1-O2 2.432(3), Yb1-O4 2.208(3), Yb1-O5#2 2.321(3), Yb2-O7 2.317(3), Yb2-O8 2.495(3), Yb2-O10 2.180(3), Yb2-O11#6 2.349(3), Na1-O1 2.317(3), Na1-O2#1 2.338(4), Na1-O5#2 2.428(4), Na1-O7 2.323(4), Na1-O8#4 2.369(4), Na1-O11#6 2.367(4), C1-Yb1-C1#1 85.81(19), C11-Yb2-C11#4 82.54(18), Yb1-Na1-Yb2 175.26(7); (**c**) The 3D framework of **2Yb**; Symmetry code: $^{\#1}$ 1-X,1-Y,+Z; $^{\#2}$ +Y,1-X,1-Z; $^{\#3}$ 1-Y,+X,1-Z; $^{\#4}$ 3/2-Y,3/2-X,3/2-Z; $^{\#5}$ -1/2+Y,1/2+X,3/2-Z; $^{\#6}$ 1-X,2-Y,+Z.

The RE-O and Na-O bond lengths are listed in Table S5. The average Yb1-O, Yb2-O and Na1-O bond lengths are 2.330 Å, 2.335 Å and 2.358 Å, correspondingly. The longest RE-O bond length observed in the structure is between Yb2-O8 and Yb2-O8#4 at 2.495(3) Å with Yb2-O10 and Yb2-O10#4 having the shortest RE-O bond distance of 2.180(3) Å. The longest Yb-O bonds are from the oxygen atoms O8 and O8#4 (both chelating and bridging), while the shortest bond lengths are from bridging oxygen atoms O10 and O10#4. The chelating μ_3-1κ(O):2κ(O,O′):3κ(O′) carboxylate ligands form *cisoid* angles of 85.81(19)° (C1-Yb1-C1#1) and 82.54(18)° (C11-Yb2-C11#4). The metal-metal distance between Yb1 . . . .Na1 and Yb2 . . . Na1 are 3.3826(18) and 3.3720(18), respectively, with Yb1-Na1-Yb2 at an angle of 175.26(7)°. The effect of lanthanoid contraction [45] is reflected across the series with the reduction of average RE-O bond distances in 1D chains (Table S5).

Yb1 and Yb1#3 metals are connected by four μ_3-1κ(O):2κ(O′):3κ(O′) ligands binding through O4-C6-O5, O5#2-C6#2-O4#2, O4#1-C6#1-O5#1 and O5#3-C6#3-O4#3 with all having same O-C-O bond angle of 123.6(4)°, and Yb1 . . . Yb1#3 distance of 4.0237(9) Å. In a similar manner, Yb2 is connected with Yb2#5 by four carboxylates with all of them having an O-C-O bond angle of 123.4(4)°. Yb2 atoms are linked through these bridging oxygens to form dimeric units with a Yb2 . . . Yb2 separation of 4.0006(4) Å and these dimers propagate to form 1D channels. However, the successive Yb2 chains are perpendicular to each other, thus constructing two types of chains. As mentioned above, symmetric bridging between adjacent $Yb1^{(III)}$ atoms leads to the formation of dimeric Yb1 channels

that crosslink the neighbouring Yb2 channels running along the perpendicular direction, into a two-dimensional grid. Finally, sodium metal atoms connect all dimers into a 3D coordination polymer, namely $[NaYb(3fur)_4]_n$. (Figure 5c).

2.3. Corrosion Inhibition

2.3.1. Immersion Tests

Immersion studies were conducted over seven days in 0.01 M NaCl control solution and in the presence of inhibition systems to access the longer-term performance of these inhibitors for mild steel. The testing was conducted for the compounds at 800 ppm as the solubility limit for $[Y(3fur)_3(H_2O)_2]_n$ in 0.01 M sodium chloride solution is close to 800 ppm. However, $[Ce(3fur)_3(H_2O)_2]_n$ and $[Pr(3fur)_3(H_2O)_2]_n$ compounds had maximum solubilities as high as 3000 ppm.

Table 2 presents a summary of the weight loss measurements after 168 h of immersion in specific inhibitor solutions. The corrosion rate (R) of each inhibitor compound was evaluated and then percentage corrosion inhibition (η) was calculated using Equation (1).

$$\eta = \frac{R(Control) - R\ (inhibitor)}{R(Control)} \times 100 \quad (1)$$

Table 2. Observed weight loss, corrosion rates (g/m^2h) and percentage inhibition (η) for mild steel coupons immersed in specific solutions at 800 ppm concentrations in 0.01 M NaCl for seven days.

Solution	Concentration		Solubility in 0.01 M NaCl (ppm)	Avg Weight Loss (mg)	Corrosion Rate (g/m^2h)	Inhibition, η (%)
	ppm	mM				
Control-NaCl	580	10	-	19.6	1406.1	-
$[La(3fur)_3(H_2O)_2]_n$ **1La**	800	1.57	2000	2.6	185.2	87
$[Ce(3fur)_3(H_2O)_2]_n$ **1Ce**	800	1.57	3000	3.7	298.6	79
$[Pr(3fur)_3(H_2O)_2]_n$ **1Pr**	800	1.57	3000	6.1	380.7	73
$[Nd(3fur)_3(H_2O)_2]_n$ **1Nd**	800	1.56	2500	5.1	365.9	74
$[Gd(3fur)_3(H_2O)_2]_n$ **1Gd**	800	1.57	1000	6.2	403.9	71
$[Dy(3fur)_3(H_2O)_2]_n$ **1Dy**	800	1.52	830	3.0	229.6	84
$[Ho(3fur)_3(H_2O)_2]_n$ **1Ho**	800	1.50	920	2.9	210.9	85
$[Y(3fur)_3(H_2O)_2]_n$ **1Y**	800	1.75	800	1.9	140.6	90
$[NaHo(3fur)_4]_n$ **2Ho**	800	1.27	1800	6.0	431.7	70
$[NaY(3fur)_4]_n$ **2Y**	800	1.44	1900	4.9	355.1	75
$[NaEr(3fur)_4]_n$ **2Er**	800	1.26	1800	5.1	365.9	74
$[NaYb(3fur)_4]_n$ **2Yb**	800	1.25	1700	2.4	168.7	88
$[NaLu(3fur)_4]_n$ **2Lu**	800	1.25	1500	7.7	480.6	66
[Na(3fur)]	800	5.97	>7000	16.51	993.6	29

The corrosion rates of the samples placed in the inhibitor solutions were found to be significantly lower than that of control coupons. As shown in Table 2, $[Y(3fur)_3(H_2O)_2]_n$ compound has the highest inhibitor efficiency of 90%. Furthermore, the visual inspection of the surface immersed in $[Y(3fur)_3(H_2O)_2]_n$ containing solutions also suggests a minimum corrosive attack on the steel surface with relatively less surface roughness (Figure S6). As a group, Type **1RE** $[RE(3fur)_3(H_2O)_2]_n$ complexes showed better inhibition performance than the Type **2RE** bimetallic $[NaRE(3fur)_4]_n$ species. This was evident from the better level of protection achieved by Type **1RE** monometallic Y^{III} and Ho^{III} inhibited solutions compared to the Type **2RE** Na-Y and Na-Ho bimetallic compounds. This may be a consequence of the presence of coordinated sodium in the compounds in the latter instance. The influence of sodium on inhibition efficiency can be seen by comparing the immersion test results of sodium 3-furoate (Na(3fur)) with the rare earth carboxylate complexes in Table 2. It has also been shown in previous literature that the corrosion rates of sodium carboxylates on

steel are generally higher than that of rare earth analogues [46]. However, the **2Yb** complex is a positive outlier since it gave the second-best performance with an η of 88%.

When considering lighter rare earths (La-Nd) the efficiency decreased from La-Nd. The level of protection by the heavy rare earths correlates with the decreasing atomic radius of the rare earth metals since the inhibitive effect increased from Gd-Y among the $[RE(3fur)_3(H_2O)_2]_n$ class. A similar trend was observed to some extent with $[NaRE(3fur)_4]_n$ complexes with improved protection from Ho to Yb, but Lu is a negative outlier. The low solubility of most of the complexes has hampered attempts at concentration studies. The performance was better than of the analogous rare earth 3-thiophenecarboxylates [31], suggesting that an oxygen substituent may be more beneficial than sulfur, but the 3fur complexes were tested at somewhat higher concentration owing to greater solubility.

2.3.2. Potentiodynamic Polarisation

The results of the potentiodynamic polarisation (PP) experiments are shown in Table 3. $[Y(3fur)_3(H_2O)_2]_n$ **1Y** showed the lowest i_{corr}, at 0.56 μA/cm^2, and **1Y** > **2Yb** > **1La** in effectiveness. After 24 h immersion, with the compounds present in the solution there is a shift in corrosion potential (E_{corr}) values towards more positive direction compared to the control solution, indicative of anodic inhibition dominating the reduction in i_{corr}.

Table 3. Summary of corrosion parameters obtained from potentiodynamic polarisation tests in control and inhibited solutions after 24 h immersion.

Solution	i_{corr} (μA/cm^2)	Std. Dev.	E_{corr} (mV)	Std. Dev.	Percentage Inhibition
Control-NaCl	2.88	0.11	−638	4	
$[La(3fur)_3(H_2O)_2]_n$ **1La**	1.09	0.09	−473	5	62
$[Y(3fur)_3(H_2O)_2]_n$ **1Y**	0.56	0.08	−445	4	80
$[NaYb(3fur)_4]_n$ **2Yb**	0.89	0.07	−468	29	69

Representative PP scans in Figure 6 show the marked reduction in the anodic branch with the addition of inhibitors, and some reduction in the cathodic kinetics. According to the previous literature [46], this is a typical behaviour of these types of compounds. However, the efficiency of the $[Y(3fur)_3(H_2O)_2]_n$ was somewhat inferior to that of yttrium 3-(4′-methylbenzoyl)propanoate [6], which though is limited by low solubility. For this reason, yttrium 3-furoate may potentially be more useful.

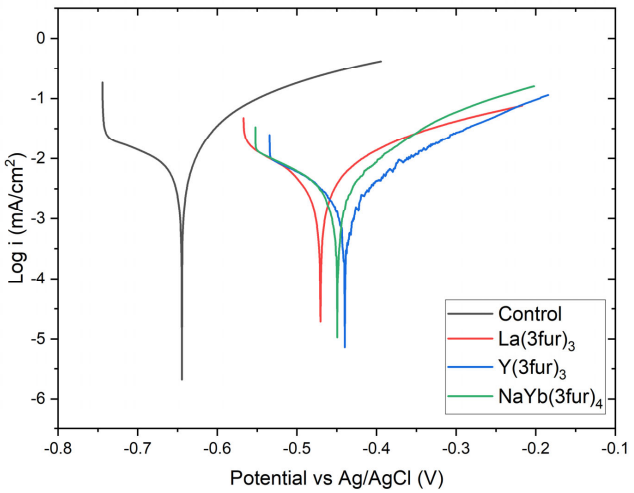


Figure 6. Representative potentiodynamic polarisation scans after 24 h for 0.01 M NaCl control, and solutions with 0.01 M NaCl and 800ppm of $[Y(3fur)_3(H_2O)_2]_n$ (**1Y**), $[La(3fur)_3(H_2O)_2]_n$ (**1La**) and $[NaYb(3fur)_4]_n$ (**2Yb**).

3. Materials and Methods

3.1. General Consideration

All reagents and solvents that were used are of standard commercial grade and used without further purification. IR spectra were collected using a Nicolet™ iS™ 5 FTIR Spectrometer in the range of 4000–500 cm^{-1}. Elemental analyses were performed by the Elemental Analysis Service Team, Science Centre, London Metropolitan University, England. Metal analysis was conducted by complexometric titration with 0.01 M EDTA using Xylenol Orange indicator and hexamethylenetetramine buffer. Thermogravimetric analysis (TGA) was conducted on a TA instrument SDT 650 using standard 90 µL alumina metal pans under an N_2 atmosphere (50 mL min^{-1}) from room temperature up to 750 °C (with a ramp of 10 °C min^{-1}). Melting points were determined in glass capillaries and are reported uncalibrated. Powder XRD measurements were obtained at room temperature using a Bruker D2 PHASER diffractometer in the range of 2–60° with a 0.2° divergence slit and at 0.02° increments. X-ray powder simulations were generated using the Mercury program provided by Cambridge Crystallographic Data Centre [47], from the obtained single-crystal X-ray diffraction data. LCMS was collected on an Agilent 6100 Series Single Quad LC/MS coupled with an Agilent 1200 Series HPLC.

3.2. X-ray Crystallography

Single crystals were mounted on loops using viscous hydrocarbon oil. Data were collected on the MX1 beamline at the Australian Synchrotron. The data integration was completed using Blue-ice [48] and XDS [49] software programs. Structures were solved by SHELXT and refined by full-umatrix least-squares methods against F2 using SHELX2018 [50], utilizing the Olex2 [51] graphical user interface. All hydrogen atoms were placed in calculated positions using the riding model. The graphical representations were generated using bitmap images GUI of Olex2 [51]. Crystal data and refinement details are given in Table S1.

3.3. Synthesis of $[RE(3fur)_3(H_2O)_2]_n$ and $[NaRE(3fur)_4]_n$ Complexes

General Synthetic Method: 3-furoic acid was dissolved in 95% ethanol (15 mL) and deprotonated with an equimolar amount of aqueous sodium hydroxide. The solution was stirred for 1 h and the pH was adjusted to 7–8. Treatment of the sodium 3-furoate with a hydrated rare earth chloride or nitrate (mole ratio 3:1) in water at pH 5 gave rare earth3-furoate complexes (**1RE** = 1La, 1Ce, 1Pr, 1Nd, 1Gd, 1Dy, 1Ho, 1Y and **2RE** = 2Er, 2Yb, 2Lu). Under similar reaction conditions, the metathesis reaction of the preformed ligand and the corresponding rare earth salt with 4:1 stoichiometry resulted in the Na-RE bimetallic 3-furoate complexes **2RE** = 2Ho, 2Y, 2Er, 2Yb and 2Lu, but not for La-Dy, which gave 1La-1Dy**.** The resultant precipitates were filtered off and air-dried for 2–3 days. Crystals were obtained upon slow evaporation of the mother liquor at room temperature.

1La: $[La(3fur)_3(H_2O)_2]_n$ white powder. Yield: 65%. m.p. 245 °C (dec). Elemental analysis for $C_{15}H_{13}LaO_{11}$ (MW: 508.16 $gmol^{-1}$): Calculated (%) C 35.45; H 2.58; La 27.33. Found (%) C 35.57; H 2.42; La 27.50. IR (cm^{-1}): 3421 w, 3132 w, 1575 s, 1507 s, 1437 s, 1364 s, 1235 m, 1219 m, 1209 m, 1151 m, 1068 m, 1003 m, 971 m, 875 s, 851 w, 784 s, 741 s, 731 m, 598 s, 550 s, 531 s, 435 s. TGA weight loss (76–131 °C); 7.0% (Calc. for loss of 2 × H_2O = 7.1%); weight loss (328–420 °C); 31.0% (Calc. for the formation of $La_2(CO_3)_3$ = 47.9%).

1Ce: $[Ce(3fur)_3(H_2O)_2]_n$ white powder. Yield: 76%. m.p.260 °C (dec). Elemental analysis for $C_{15}H_{13}CeO_{11}$ (MW: 509.37 $gmol^{-1}$): Calculated (%) C 35.37; H 2.57; Ce 27.51. Found (%) C 35.52; H 2.40; Ce 27.64. IR (cm^{-1}):3439 w, 3134 w, 1574 s, 1505 s, 1437 s, 1364 s, 1235 m, 1220 m, 1209 m, 1151 m, 1068 m, 1003 m, 972 m, 874 s, 851 w, 783 s, 741 s, 731 m, 598 s, 550 s, 531 s, 434 s. TGA weight loss (71–120 °C); 6.9% (Calc. for loss of 2 × H_2O = 7.1%); weight loss (364–475 °C); 31.9% (Calc. for the formation of $Ce_2(CO_3)_3$ = 47.8%).

1Pr: $[Pr(3fur)_3(H_2O)_2]_n$ pale green powder. Yield: 80%. m.p.240 °C (dec). Elemental analysis for $C_{15}H_{13}O_{11}Pr$ (MW: 510.16 $gmol^{-1}$): Calculated (%) C 35.31; H 2.57; Pr 27.62. Found (%) C 35.39; H 2.39; Pr 27.42. IR (cm^{-1}): 3442 w, 3133 w, 1573 s, 1525 w, 1504 s, 1434 s,

1364 s, 1234 m, 1220 m, 1209 m, 1150 m, 1069 m, 1003 m, 972 m, 875 s, 852 w, 786 s, 741 s, 730 m, 598 s, 552 s, 533 s, 438 s. TGA weight loss (70–154 °C); 6.9% (Calc. for loss of 2 × H_2O = 7.1%); weight loss (368–492 °C); 31.7% (Calc. for the formation of $Pr_2(CO_3)_3$ = 47.7%).

1Nd: $[Nd(3fur)_3(H_2O)_2]_n$ purple powder. Yield: 70%, m.p.260 °C (dec). Elemental analysis for $C_{15}H_{13}NdO_{11}$ (MW: 513.49 $gmol^{-1}$): Calculated (%) C 35.08; H 2.55; Nd 28.09. Found (%) C 35.35; H 2.33; Nd 27.94. IR (cm^{-1}): 3431 w, 3134 w, 1573 s, 1527 w, 1505 s, 1439 s, 1364 s, 1234 m, 1221 m, 1209 m, 1151 m, 1069 m, 1003 m, 973 m, 875 s, 852 w, 783 s, 741 s, 730 m, 598 s, 553 s, 534 s, 439 s. TGA weight loss (76–123 °C); 6.9% (Calc. for loss of 2 × H_2O = 7.0%); weight loss (365–495 °C); 32.4% (Calc. for the formation of $Nd_2(CO_3)_3$ = 47.4%).

1Gd: $[Gd(3fur)_3(H_2O)_2]_n$ white powder. Yield: 60%. m.p.260 °C (dec). Elemental analysis for $C_{15}H_{13}GdO_{11}$ (MW: 526.50 $gmol^{-1}$): Calculated C 34.22; H 2.49; Gd 29.87. Found (%) C 33.91; H 2.39; Gd 29.62. IR (cm^{-1}): 3440 w, 3134 w, 1574 s, 1537 w, 1505 s, 1443 s, 1365 s, 1234 m, 1222 m, 1209 m, 1151 m, 1068 m, 1002 m, 973 m, 875 s, 854 w, 784 s, 742 s, 730 m, 598 s, 556 s, 533 s, 438 s TGA weight loss (75–130°C); 6.9% (Calc. for loss of 2 × H_2O = 6.8 %); weight loss (374–490 °C); 30.2% (Calc. for the formation of $Gd_2(CO_3)_3$ = 46.2%).

1Dy: $[Dy(3fur)_3(H_2O)_2]_n$ white powder. Yield: 79%. m.p.260 °C (dec). Elemental analysis for $C_{15}H_{13}DyO_{11}$ (MW: 531.75 $gmol^{-1}$): Calculated (%) C 33.88; H 2.46; Dy 30.56. Found (%) C 33.52; H 2.34; Dy 30.70. IR (cm^{-1}): 3420 w, 3135 w, 1574 s, 1534 m, 1505 s, 1437 s, 1364 s, 1234 m, 1223 m, 1207 m, 1151 s, 1068 m, 1003 m, 974 m, 875 s, 855 w, 783 s, 742 s, 730 m, 598 s, 559 s, 534 s, 442 s. LCMS: (m/z): Calc. for $[Dy(3fur)(OH).EtOH]^+$ 338.0, $[Dy(3fur)_2(H_2O)_2]^+$ 422.0; found 337.1, 422.1. TGA weight loss (60–124 °C); 6.7% (Calc. for loss of 2 × H_2O = 6.8%); weight loss (390–482 °C); 30.1% (Calc. for the formation of $Dy_2(CO_3)_3$ = 45.7%).

1Ho: $[Ho(3fur)_3(H_2O)_2]_n$ yellow powder. Yield: 61%. m.p.260 °C (dec). Elemental analysis for $C_{15}H_{13}HoO_{11}$ (MW: 534.18 $gmol^{-1}$): Calculated (%) C 33.73; H 2.45; Ho 30.87. Found (%) C 33.75; H 2.35; Ho 30.84. IR (cm^{-1}): 3441 w, 3135 w, 1575 s, 1535 m, 1501 s, 1444 s, 1365 s, 1234 m, 1223 m, 1210 m, 1152 s, 1068 m, 1003 m, 973 m, 874 s, 855 m, 782 s, 742 s, 730 m, 598 s, 560 s, 533 s, 442 s. TGA weight loss 63–110 °C); 6.9% (Calc. for loss of 2 × H_2O = 6.7%); weight loss (380–491 °C); 31.5% (Calc. for the formation of $Ho_2(CO_3)_3$ = 45.5%).

1Y: $[Y(3fur)_3(H_2O)_2]_n$ white powder. Yield: 67%. m.p.230 °C (dec). Elemental analysis for $C_{15}H_{13}O_{11}Y$ (MW: 458.16 $gmol^{-1}$): Calculated (%) C 39.32; H 2.86; Y 19.40. Found (%) C 39.64; H 2.62; Y 19.80. IR (cm^{-1}): 3441 w, 3136 w, 1575 s, 1538 m, 1505 s, 1445 s, 1366 s, 1234 m, 1223 m, 1209 m, 1151 s, 1068 m, 1002 m, 974 m, 875 s, 855 m, 784 s, 742 s, 724 m, 598 s, 561 s, 531 s, 441 s. TGA weight loss (55–135 °C); 7.9% (Calc. for loss of 2 × H_2O = 7.9%); weight loss (372–498 °C); 35.1% (Calc. for the formation of $Y_2(CO_3)_3$ = 53.1%).

2Ho: $[HoNa(3fur)_4]_n$ yellow powder. Yield: 56%. m.p.200 °C (dec). Elemental analysis for $C_{20}H_{12}HoNaO_{12}$ (MW: 632.22 $gmol^{-1}$): Calculated (%) C 38.00; H 1.91; Ho 26.09. Found (%) C 37.52; H 1.90; Ho 26.11. IR (cm^{-1}): 3131 w, 2363 w, 1619 m, 1577 s, 1541 s, 1502 s, 1434 s, 1366 s, 1237 m, 1212 s, 1154 s, 1075 m, 1007 m, 971 m, 872 s, 840 w, 824 s, 815 s, 804 s, 776 s, 737 s, 598 s, 564 w, 539 w, 457 s. LCMS: (m/z): Calc. for $Na_2Ho(3fur)_3(3furH)(HCO_3)(H_2O)]^+$ 735.0, $[Ho_2(3fur)_4(HCO_3)(H_2O)]^+$ 853.0; found 735.2, 853.5. TGA weight loss (403–454 °C); 33.1% (Calc. for the formation of $Na_3Ho(CO_3)_3$ = 34.6%).

2Y: $[NaY(3fur)_4]_n$ white powder. Yield: 51%, m.p.240 °C (dec). Elemental analysis for $C_{20}H_{12}NaO_{12}Y$ (MW: 556.20 $gmol^{-1}$): Calculated (%) C 43.19; H 2.17; Y 15.98. Found (%) C 42.54; H 1.87; Y 15.81. IR (cm^{-1}): 3131 w, 2361 w, 1619 m, 1577 s, 1543 s, 1503 s, 1434 s, 1366 s, 1237 m, 1212 s, 1154 s, 1075 m, 1007m, 971 m, 872 s, 841 w, 824 s, 816 s, 804 s, 776 s, 737 s, 598 s, 563 w, 539 w, 461 s. TGA weight loss (410–457 °C); 37.1% (Calc. for the formation of $Na_3Y(CO_3)_3$ = 39.2%).

2Er: $[NaEr(3fur)_4]_n$ pink powder. Yield: 59%. m.p.240 °C (dec). Elemental analysis for $C_{20}H_{12}ErNaO_{12}$ (MW: 634.55 $gmol^{-1}$): Calculated (%) C 37.86; H 1.91; Er 26.36. Found (%) C 37.78; H 1.83; Er 26.54. IR (cm^{-1}): 3136 w, 2361 w, 1621 m, 1577 s, 1542 s, 1502 s, 1433 s, 1366 s, 1237 m, 1213 s, 1154 s, 1075 m, 1007 m, 971 m, 873 s, 840 w, 824 s, 816 s, 804 s, 776 s, 737 s, 598 s, 566 w, 539 w, 457 s; TGA weight loss (400–453 °C); 32.2% (Calc. for the formation of $Na_3Er(CO_3)_3$ = 34.4%).

2Yb: $[NaYb(3fur)_4]_n$ white powder. Yield: 60%. m.p.240 °C (dec). Elemental analysis for $C_{20}H_{12}YbNaO_{12}$ (MW: 640.33 $gmol^{-1}$): Calculated (%) C 37.51; H 1.89; Yb 27.02. Found (%) C 36.35; H 1.82; Yb 27.03. IR (cm^{-1}): 3132 w, 2360 w, 1624 m, 1578 s, 1545 s, 1502 s, 1434 s, 1366 s, 1237 m, 1213 s, 1154 s, 1075 m, 1007 m, 971 m, 873 s, 840 w, 825 s, 818 s, 804 s, 776 s, 738 s, 598 s, 567 w, 540 w, 457 s. TGA weight loss (400–452 °C); 31.3% (Calc. for the formation of $Na_3Yb(CO_3)_3$ = 34.1%).

2Lu: $[NaLu(3fur)_4]_n$ white powder. Yield: 51%. m.p.250 °C (dec). Elemental analysis calculated for $C_{20}H_{12}LuNaO_{12}$ (MW: 642.26 $gmol^{-1}$) Calculated (%) C 37.40; H 1.88; Lu 27.24. Found (%) C 36.75; H 1.82; Lu 27.31. IR (cm^{-1}): 3132 w, 2360 w, 1626 m, 1578 s, 1547 s, 1503 s, 1435 s, 1366 s, 1238 m, 1213 s, 1154 s, 1075 m, 1007 m, 971 m, 873 s, 840 w, 826 s, 818 s, 804 s, 776 s, 738 s, 598 s, 568 w, 540 w, 459 s. LCMS: (*m/z*): Calc. for $[Na_2(CO_3)Lu(3fur)_4(H_2O)_2]^-$ 761.0; found 761.0. TGA weight loss (397–450 °C); 32.2% (Calc. for the formation of $Na_3Lu(CO_3)_3$ = 33.9%).

3.4. Corrosion Testing

To evaluate the general corrosion and inhibition behaviour of synthesized compounds, corrosion immersion experiments were conducted according to the standard method ASTM G31-72 [52]. Mild steel alloy AS 1020 coupons used in the weight loss tests were cut to approximately 20 × 20 × 1.5 mm and abraded progressively with sanding sheets of 80, 120, 240, 360, 800, 1200 and 2000 grits. The specimens were rinsed with distilled water followed by ethanol and dried under flowing N_2 gas. The coupons were used immediately after polishing and washing to do a series of immersion tests, up to 168 h (7 days). The sample and the control coupons were suspended in beakers containing 0.01 M NaCl solutions with and without 800 ppm (1.25–1.75 mM) of the inhibitor compounds. In each setup, replicates were done by fully immersing the coupons at mid-depth with the use of Teflon strings. Upon the completion of the test, firstly, the corrosion product that clung to the substrate was removed by mild sonication in clean distilled water followed by using the finest sanding papers with minimum force to avoid the removal of sound material. Experiments were done in duplicate. Lastly, the coupons were washed with ethanol and dried with N_2 gas.

The compounds containing the REs Y, Yb and La were used to conduct Potentiodynamic Polarisation (PP) experiments, as they showed the best performance in weight loss experiments. The tests were performed using a Bio-Logic VMP3 multi-channel potentiostat with solutions containing the same concentrations as those used in the weight loss experiments. A three-electrode cell with a titanium mesh counter electrode, a Ag/AgCl reference electrode and an AS1020 mild steel rod as the working electrode surface was used. The working electrode consisted of a 10mm diameter steel rod steel rod in epoxy, polished to a 1200 grit finish. A test solution volume of 100mL was used, with the solution open to air. Open Circuit Voltage (OCV) was monitored for 24 h following which the PP scan was conducted over a scan range of 150 mV below to 250 mV above OCV at 0.167 mV/s. A Tafel extrapolation was used to determine the corrosion current densities (i_{corr}) and potentials (E_{corr}) from the PP curves using EC Lab software V11.27.

4. Conclusions

A series of novel rare earth 3-furoate complexes was synthesized and characterized. The 13 structures identified in this study could be separated into two groups based on their molecular composition as below.

- **Type 1**-Monometallic 2D polymeric network of $[RE(3fur)_3(H_2O)_2]_n$ (**1RE** = 1La, 1Ce, 1Pr, 1Nd, 1Gd, 1Dy, 1Ho, 1Y)
- **Type 2**-Bimetallic 3D polymeric network of $[NaRE(3fur)_4]_n$ (**2RE** = 2Ho, 2Y, 2Er, 2Yb, 2Lu)

The ability to obtain two different structural motifs from $HoCl_3$ and YCl_3 at 1:3 and 1:4 (rare earth: ligand) mole ratios indicates that the stoichiometry used in the metathesis reaction affects the final complex formation. The lanthanoid contraction was evident with a reduction of the average RE-O bond distance across each series.

The immersion studies showed that at 800 ppm inhibitor concentrations for mild steel in 0.01 M NaCl solutions, $[Y(3fur)_3(H_2O)_2]_n$ (**2Y**) was the best performing inhibitor with $[NaYb(3fur)_4]_n$ (**2Yb**) and $[La(3fur)_3(H_2O)_2]_n$ (**1La**) exhibiting comparable inhibition performance. Potentiodynamic polarisation confirmed the superior performance of $[Y(3fur)_3(H_2O)_2]_n$ (**1Y**). The compounds act predominantly as anodic inhibitors. A comparison of Y complex data suggests that the introduction of a furoate moiety into a carboxylate is more effective than the thiophene group but not as effective as a 3-(4′-methylbenzoyl) group [6,31]. Application of the rare earth 3-furoates as inhibitors would involve dissolution of the solid complexes in the water of cooling towers or radiators, etc., to give a very dilute solution. In protective coating, a suspension of the complexes in paint would be used, but the effectiveness in this role has still to be investigated.

Supplementary Materials: The following supporting information can be downloaded at: https://www.mdpi.com/article/10.3390/molecules27248836/s1, Figure S1: IR spectra of $[RE(3fur)_3(H_2O)_2]_n$ **1RE** series; Figure S2: IR spectra of $[NaRE(3fur)_4]_n$ **2RE** series; Figure S3: TGA plots of the $[RE(3fur)_3(H_2O)_2]_n$ **1RE** series; Figure S4: TGA plots of the $[NaRE(3fur)_4]_n$ **2RE** series; Figure S5: IR spectra of $Ce_2(CO_3)_3$ (Left) from thermal decomposition of **1Ce**, reported $Dy_2(CO_3)_3{\cdot}4H_2O$ (middle) and $Na_3Yb(CO_3)_3$ (right) from thermal decomposition of **2Yb**; Figure S6: Mild steel coupons immersed in control and the three best inhibited solutions for 168 h (Left—Trial 1; right—Trial 2.); Table S1: Crystal data and structural refinement for rare earth 3-furoate complexes; Table S2: Selected bond lengths and RE … RE distances (Å) for the isostructural $[RE(3fur)_3(H_2O)_2]_n$ **1RE** series; Table S3: Selected bond angles (°) for the isostructural $[RE(3fur)_3(H_2O)_2]_n$ **1RE** series; Table S4: Hydrogen bonds for $[RE(3fur)_3(H_2O)_2]_n$ (**1Nd**) [d/Å and </°]; Table S5: Selected bond lengths and Na … RE distances (Å) for the isostructural $[NaRE(3fur)_4]_n$ **2RE** series; Table S6: Selected bond angles (°) for the isostructural $[NaRE(3fur)_4]_n$ **2RE** series.

Author Contributions: Synthesis of the complexes, V.P.V.; characterization, V.P.V. and Z.G.; Electrochemical studies, A.E.S.; original draft preparation, V.P.V. and subsequent review and editing, Z.G., G.B.D. and P.C.J.; supervision, project administration and funding acquisition, G.B.D. and P.C.J. All authors have read and agreed to the published version of the manuscript.

Funding: This research was funded by the Australian Research Council (DP200100568).

Institutional Review Board Statement: Not applicable.

Informed Consent Statement: Not applicable.

Data Availability Statement: Crystal data can be obtained free of charge from The Cambridge Crystallographic Data Centre (CCDC 2218918-2218925 for complexes **1RE**, and 2218926-2218930 for complexes **2RE**).

Acknowledgments: P.C.J and G.B.D. gratefully acknowledge the ARC for funding (DP200100568). Parts of this research were undertaken on the MX1 beamline at the Australian Synchrotron, part of ANSTO [53].

Conflicts of Interest: The authors declare no conflict of interest.

References

1. Odio, O.B.; Chinwuko, C.E.; Chukwuneke, L.J.; Sinebe, E.J. Investigation of The Effect of Corrosion on Mild Steel in Five Different Environments. *Int. J. Sci. Technol. Res.* **2014**, *3*, 306–310.
2. Garcia, S.J.; Mol, J.M.C.; de Wit, J.H.W.; Muster, T.H.; Hughes, A.E.; Miller, T.; Markley, T.; Mardel, J.; Terryn, H. Advances in the Selection and Use of Rare-Earth-Based Inhibitors for Self-Healing Organic Coatings. In *Self-Healing Properties of New Surface Treatments*; Fedrizzi, L., Fürbeth, W., Montemor, F., Eds.; Maney Publishing: Leeds, UK, 2011; Volume 58, pp. 148–183.
3. Hossain, N.; Chowdhury, M.A.; Kchaou, M. An overview of green corrosion inhibitors for sustainable and environment friendly industrial development. *J. Adhes. Sci. Technol.* **2020**, *35*, 673–690. [CrossRef]
4. Mottram, E.; Hamilton, S.; Moon, J.S.; Wang, J.; Bousrez, G.; Somers, A.E.; Deacon, G.B.; Junk, P.C. Synthesis, structure, and corrosion inhibiting properties of phenylacetato-rare earth (III) complexes. *J. Coord. Chem.* **2020**, *73*, 2677–2697. [CrossRef]
5. Bowman, E.; Thompson, N.; Gl, D.; Moghissi, O.; Gould, M.; Payer, J. *International Measures of Prevention, Application, and Economics of Corrosion Technologies Study*; NACE International: Houston, TX, USA, 2016.

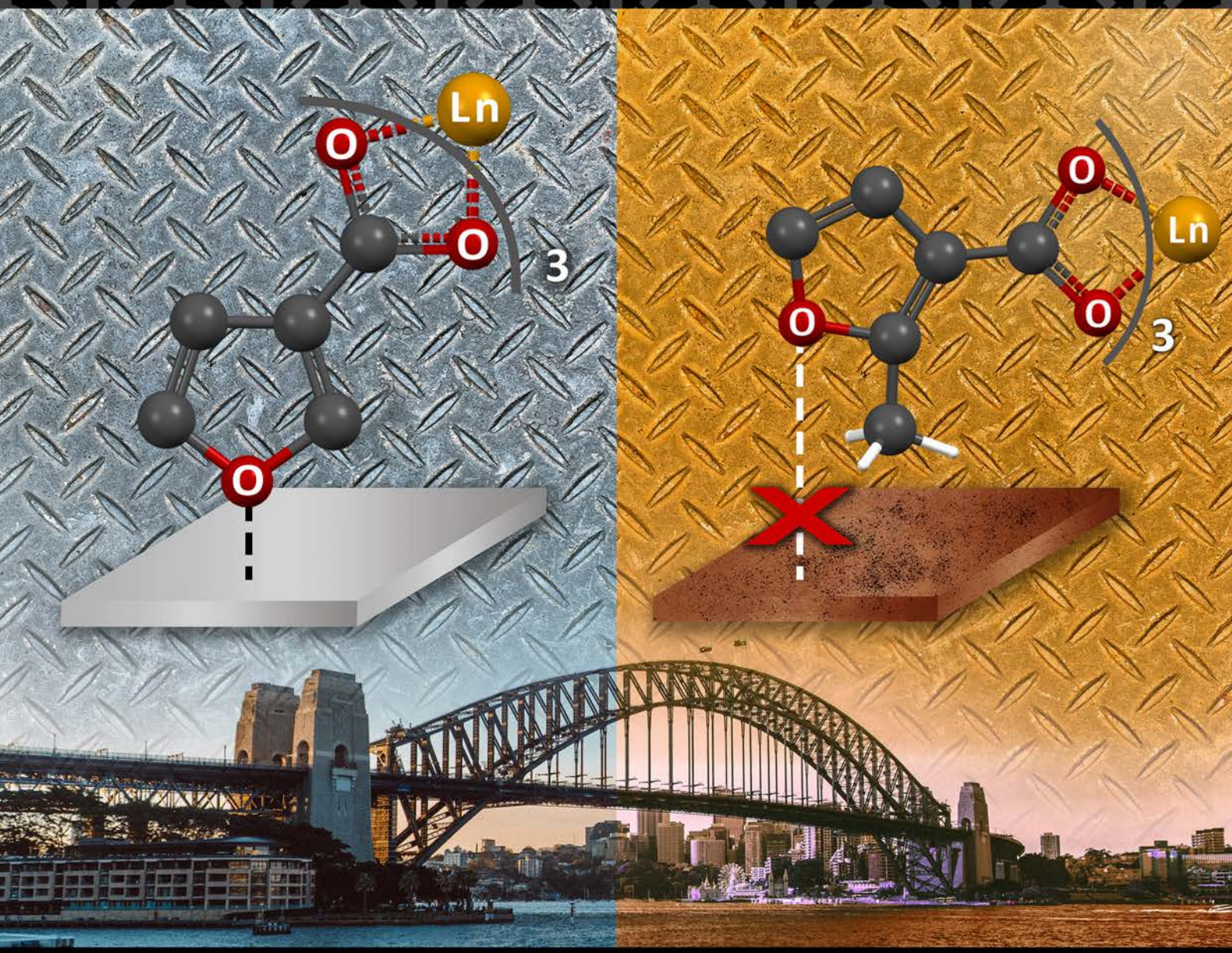
6. Somers, A.E.; Hinton, B.R.; de Bruin-Dickason, C.; Deacon, G.B.; Junk, P.C.; Forsyth, M. New, environmentally friendly, rare earth carboxylate corrosion inhibitors for mild steel. *Corros. Sci.* **2018**, *139*, 430–437. [CrossRef]
7. Forsyth, M.; Wilson, K.; Behrsing, T.; Forsyth, C.; Deacon, G.B.; Phanasgoankar, A. Effectiveness of Rare-Earth Metal Compounds as Corrosion Inhibitors for Steel. *Corrosion* **2002**, *58*, 953–960. [CrossRef]
8. Chong, A.L.; Mardel, J.I.; MacFarlane, D.R.; Forsyth, M.; Somers, A.E. Synergistic Corrosion Inhibition of Mild Steel in Aqueous Chloride Solutions by an Imidazolinium Carboxylate Salt. *ACS Sustain. Chem. Eng.* **2015**, *4*, 1746–1755. [CrossRef]
9. Ghorbani, M.; Soto Puelles, J.; Forsyth, M.; Catubig, R.A.; Ackland, L.; Machuca, L.; Terryn, H.; Somers, A.E. Corrosion Inhibition of Mild Steel by Cetrimonium Trans-4-Hydroxy Cinnamate: Entrapment and Delivery of the Anion Inhibitor through Speciation and Micellar Formation. *J. Phys. Chem. Lett.* **2020**, *11*, 9886–9892. [CrossRef]
10. Forsyth, M.; Seter, M.; Hinton, B.; Deacon, G.; Junk, P. New "Green" Corrosion Inhibitors Based on Rare Earth Compounds. *Aust. J. Chem.* **2011**, *64*, 812–819. [CrossRef]
11. Peng, Y.; Hughes, A.E.; Deacon, G.B.; Junk, P.C.; Hinton, B.R.; Forsyth, M.; Mardel, J.I.; Somers, A.E. A study of rare-earth 3-(4-methylbenzoyl)-propanoate compounds as corrosion inhibitors for AS1020 mild steel in NaCl solutions. *Corros. Sci.* **2018**, *145*, 199–211. [CrossRef]
12. Hinton, B. Corrosion Prevention and Control. In *Handbook on the Physics and Chemistry of Rare Earths*; Gschneidner, K.A., Eyring, L., Eds.; Elsevier: Amsterdam, The Netherlands, 1995; Volume 21, pp. 29–92.
13. Hinton, B.R.W. Corrosion Inhibition with Rare Earth Metal Salts. *J. Alloys Compd.* **1992**, *180*, 15–25. [CrossRef]
14. Mendez, J.A.C.; Vong, Y.M.; Bueno, J.D.J.P. Cerium and Other Rare Earth Salts as Corrosion Inhibitors—A Review. *Prot. Met. Phys. Chem. Surf.* **2022**, *58*, 801–810. [CrossRef]
15. Somers, A.E.; Deacon, G.B.; Hinton, B.R.W.; Macfarlane, D.R.; Junk, P.C.; Tan, M.Y.J.; Forsyth, M. Recent Developments in Environment-Friendly Corrosion Inhibitors for Mild Steel. *J. Indian Inst. Sci.* **2016**, *96*, 285–292.
16. Somers, A.E.; Peng, Y.; Chong, A.L.; Forsyth, M.; MacFarlane, D.R.; Deacon, G.B.; Hughes, A.E.; Hinton, B.R.W.; Mardel, J.I.; Junk, P.C. Advances in the Development of Rare Earth Metal and Carboxylate Compounds as Corrosion Inhibitors for Steel. *Corros. Eng. Sci. Technol.* **2020**, *55*, 311–321. [CrossRef]
17. Forsyth, M.; Hinton, B. *Rare Earth-Based Corrosion Inhibitors*, 1st ed.; Woodhead Publishing: Cambridge, UK, 2014.
18. Sinko, J. Challenges of chromate inhibitor pigments replacement in organic coatings. *Prog. Org. Coat.* **2001**, *42*, 267–282. [CrossRef]
19. Winkler, D.A.; Breedon, M.; Hughes, A.E.; Burden, F.R.; Barnard, A.S.; Harvey, T.G.; Cole, I. Towards Chromate-Free Corrosion Inhibitors: Structure-Property Models for Organic Alternatives. *Green Chem.* **2014**, *16*, 3349–3357. [CrossRef]
20. Daoud, D.; Douadi, T.; Hamani, H.; Chafaa, S.; Al-Noaimi, M. Corrosion Inhibition of Mild Steel by Two New S-Heterocyclic Compounds in 1 M HCl: Experimental and Computational Study. *Corros. Sci.* **2015**, *94*, 21–37. [CrossRef]
21. Verma, C.; Ebenso, E.E.; Quraishi, M.A. Ionic Liquids as Green Corrosion Inhibitors for Industrial Metals and Alloys. In *Green Chemistry*; Saleh, H.E.-D.M., Koller, M., Eds.; IntechOpen: London, UK, 2018.
22. Pham, T.H.; Lee, W.-H.; Son, G.-H.; Tran, T.T.; Kim, J.-G. Synthesis and Corrosion Inhibition Potential of Cerium/Tetraethylenepentamine Dithiocarbamate Complex on AA2024-T3 in 3.5% NaCl. *Materials* **2022**, *15*, 6631. [CrossRef]
23. Vaidyanathan, H.; Hackerman, N. Effect of furan derivatives on the anodic dissolution of Fe. *Corros. Sci.* **1971**, *11*, 737–750. [CrossRef]
24. Khaled, K.F. Understanding Corrosion Inhibition of Mild Steel in Acid Medium by Some Furan Derivatives: A Comprehensive Overview. *J. Electrochem. Soc.* **2010**, *157*, C116–C124. [CrossRef]
25. Ouchi, A.; Suzuki, Y.; Ohki, Y.; Koizumi, Y. Structure of Rare Earth Carboxylates in Dimeric and Polymeric Forms. *Coord. Chem. Rev.* **1988**, *92*, 29–43. [CrossRef]
26. Mehrotra, R.C.; Bohra, R. *Metal Carboxylates*; Academic Press: London, UK, 1983.
27. Janicki, R.; Mondry, A.; Starynowicz, P. Carboxylates of Rare Earth Elements. *Coord. Chem. Rev.* **2017**, *340*, 98–133. [CrossRef]
28. Behrsing, T.; Deacon, G.B.; Junk, P.C. The Chemistry of Rare Earth Metals, Compounds, and Corrosion Inhibitors. In *Rare Earth-Based Corrosion Inhibitors*; Forsyth, M., Hinton, B., Eds.; Woodhead Publishing: Cambridge, UK, 2014; pp. 1–37.
29. Markley, T.; Blin, F.; Forsyth, M.; Hinton, B. Multifunctional Rare Earth Organic Corrosion Inhibitors. In *Rare Earth-Based Corrosion Inhibitors*; Forsyth, M., Hinton, B., Eds.; Woodhead Publishing: Cambridge, UK, 2014; pp. 117–142.
30. Blin, F.; Leary, S.G.; Deacon, G.B.; Junk, P.C.; Forsyth, M. The Nature of the Surface Film on Steel Treated with Cerium and Lanthanum Cinnamate Based Corrosion Inhibitors. *Corros. Sci.* **2006**, *48*, 404–419. [CrossRef]
31. Vithana, V.P.; Guo, Z.; Deacon, G.B.; Somers, A.E.; Junk, P.C. Synthesis, Structure, and Corrosion Inhibiting Properties of RE^{III} 3-Thiophenecarboxylate Complexes. *N. J. Chem.* **2022**, *46*, 19104–19111. [CrossRef]
32. Lajunen, L.H.; Choppin, G.R. Analytical Chemistry of the Lanthanides Part 1. Atomic Absorption and Plasma Atomic Emission Spectroscopic Methods. *Rev. Anal. Chem.* **1989**, *9*, 91–130. [CrossRef]
33. Sitzmann, H.; Dezember, T.; Schmitt, O.; Weber, F.; Wolmershäuser, G.; Ruck, M. Metallocenes of Samarium, Europium, and Ytterbium with the Especially Bulky Cyclopentadienyl Ligands C5H(CHMe2)4, C5H2(CMe3)3, and C5(CHMe2)5. *Z. Anorg. Allg. Chem.* **2000**, *626*, 2241–2244. [CrossRef]
34. Daniels, D.P.; Deacon, G.B.; Harakat, D.; Jaroschik, F.; Junk, P.C. Synthesis and Characterisation of Alkaline Earth (Diphenylphosphano)Metallocene Complexes and Heterobimetallic Alkaline Metal/Platinum (II) Complexes $[Ae(Thf)_x(\eta^5\text{-}C_5H_4PPh_2)_2Pt(Me)_2]$ (Ae = Ca, Sr, Ba). *Dalton Trans.* **2012**, *41*, 267–277. [CrossRef] [PubMed]

35. Moxey, G.J.; Blake, A.J.; Lewis, W.; Kays, D.L. Alkaline Earth Complexes of a Sterically Demanding Guanidinate Ligand. *Eur. J. Inorg. Chem.* **2015**, *2015*, 5892–5902. [CrossRef]
36. Kelly, R.P.; Bell, T.D.M.; Cox, R.P.; Daniels, D.P.; Deacon, G.B.; Jaroschik, F.; Junk, P.C.; le Goff, X.F.; Lemercier, G.; Martinez, A.; et al. Divalent Tetra- and Penta-Phenylcyclopentadienyl Europium and Samarium Sandwich and Half-Sandwich Complexes: Synthesis, Characterization, and Remarkable Luminescence Properties. *Organometallics* **2015**, *34*, 5624–5636. [CrossRef]
37. Hirneise, L.; Maichle-Mössmer, C.; Anwander, R. Pentamethylcyclopentadienyl Complexes of Cerium (IV): Synthesis, Reactivity, and Electrochemistry. *Inorg. Chem.* **2021**, *60*, 18211–18224. [CrossRef]
38. Salehisaki, M.; Rad, N.E.; Deacon, G.B.; Wang, J.; Guo, Z.; Junk, P.C. Synthesis and Reactivity of Rare-Earth-N,N′-(Diphenyl) Formamidinate and Rare-Earth-N,N′-Bis(2,4-Dimethylphenyl) Formamidinate Complexes. *Inorg. Chim. Acta.* **2022**, *539*, 120997. [CrossRef]
39. Deacon, G.B.; Phillips, R.J. Relationships between the Carbon-Oxygen Stretching Frequencies of Carboxylato Complexes and the Type of Carboxylate Coordination. *Coord. Chem. Rev.* **1980**, *33*, 227–250. [CrossRef]
40. Chesman, A.S.R.; Turner, D.R.; Moubaraki, B.; Murray, K.S.; Deacon, G.B.; Batten, S.R. Lanthaballs: Chiral, Structurally Layered Polycarbonate Tridecanuclear Lanthanoid Clusters. *Chem. A Eur. J.* **2009**, *15*, 5203–5207. [CrossRef]
41. Chesman, A.S.R.; Turner, D.R.; Moubaraki, B.; Murray, K.S.; Deacon, G.B.; Batten, S.R. Tetradecanuclear Polycarbonatolanthanoid Clusters: Diverse Coordination Modes of Carbonate Providing Access to Novel Core Geometries. *Dalton Trans.* **2012**, *41*, 10903–10909. [CrossRef] [PubMed]
42. Vallina, B.; Rodriguez-Blanco, J.D.; Brown, A.P.; Blanco, J.A.; Benning, L.G. Amorphous Dysprosium Carbonate: Characterization, Stability, and Crystallization Pathways. *J. Nanopart. Res.* **2013**, *15*, 1438. [CrossRef]
43. Deacon, G.B. Syntheses of Organometallic Compounds by Thermal Decarboxylation. *Organomet. Chem. Rev. Sect. A* **1970**, *5*, 355.
44. Deacon, G.B.; Faulks, S.J.; Pain, G.N. The Synthesis of Organometallics by Decarboxylation Reactions. *Adv. Organomet. Chem.* **1986**, *25*, 237–276.
45. Shannon, R.D. Revised effective ionic radii and systematic studies of interatomic distances in halides and chalcogenides. *Acta Cryst.* **1976**, *A32*, 751–766. [CrossRef]
46. Blin, F.; Leary, S.G.; Wilson, K.; Deacon, G.; Junk, P.; Forsyth, M. Corrosion Mitigation of Mild Steel by New Rare Earth Cinnamate Compounds. *J. Appl. Electrochem.* **2004**, *34*, 591–599. [CrossRef]
47. MacRae, C.F.; Sovago, I.; Cottrell, S.J.; Galek, P.T.A.; McCabe, P.; Pidcock, E.; Platings, M.; Shields, G.P.; Stevens, J.S.; Towler, M.; et al. Mercury 4.0: From Visualization to Analysis, Design and Prediction. *J. Appl. Crystallogr.* **2020**, *53*, 226–235. [CrossRef]
48. McPhillips, T.M.; McPhillips, S.E.; Chiu, H.J.; Cohen, A.E.; Deacon, A.M.; Ellis, P.J.; Garman, E.; Gonzalez, A.; Sauter, N.K.; Phizackerley, R.P.; et al. Blu-Ice and the Distributed Control System: Software for Data Acquisition and Instrument Control at Macromolecular Crystallography Beamlines. *J. Synchrotron Radiat.* **2002**, *9*, 401–406. [CrossRef] [PubMed]
49. Kabsch, W. Automatic Processing of Rotation Diffraction Data from Crystals of Initially Unknown Symmetry and Cell Constants. *J. Appl. Crystallogr.* **1993**, *26*, 795–800. [CrossRef]
50. Sheldrick, G.M. Crystal structure refinement with *SHELXL*. *Acta Crystallogr. Sect. C Struct. Chem.* **2015**, *C71*, 3–8. [CrossRef] [PubMed]
51. Dolomanov, O.V.; Bourhis, L.J.; Gildea, R.J.; Howard, J.A.K.; Puschmann, H. OLEX2: A Complete Structure Solution, Refinement and Analysis Program. *J. Appl. Crystallogr.* **2009**, *42*, 339–341. [CrossRef]
52. American Society for Testing and Materials. *American-Standard-Test-Methods in ASTM G31-72*; American Society for Testing and Materials: Philadelphia, PA, USA, 2004.
53. Cowieson, N.P.; Aragao, D.; Clift, M.; Ericsson, D.; Gee, C.; Harrop, S.J.; Mudie, N.; Panjikar, S.; Price, J.; Riboldi-Tunnicliffe, A.; et al. MX1: A bending-magnet crystallography beamline serving both chemical and macromolecular crystallography communities at the Australian Synchrotron. *J. Synchrotron Radiat.* **2015**, *22*, 187–190. [CrossRef] [PubMed]

EurJIC
European Journal of Inorganic Chemistry

Chemistry Europe
European Chemical Societies Publishing

Front Cover:
P. C. Junk and co-workers
Rare Earth 2-Methyl-3-furoate Complexes: Effect of Steric Hindrance on Corrosion Inhibitor Properties



WILEY VCH
11/2024

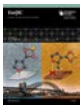
Check for updates

EurJIC
European Journal of Inorganic Chemistry

Research Article
doi.org/10.1002/ejic.202300722

Chemistry Europe
European Chemical Societies Publishing

www.eurjic.org



Rare Earth 2-Methyl-3-furoate Complexes: Effect of Steric Hindrance on Corrosion Inhibitor Properties

Vidushi P. Vithana,[a] Zhifang Guo,[a] Glen B. Deacon,[b] and Peter C. Junk*[a]

The preparation and characterization of six rare earth 2-methyl-3-furoate (2m3fur) complexes are detailed in this study. Analysis through single-crystal X-ray diffraction, as well as powder XRD, reveals that all six compounds belong to one of two structural groups: $\{[RE_2(2m3fur)_6(EtOH)]\cdot H_2O\}_n$ (RE = La, Ce, Pr) and $[RE_3(2m3fur)_9]_n$ (RE = Y, Er, Yb). These structural groups feature carboxylate coordinated linear polymers. The former complexes have two distinct metal centers, one ten coordinate and one nine, with lattice water participating in a hydrogen bond with coordinated ethanol. The latter structures, involving erbium, ytterbium, and yttrium, have three unique metal centers: two eight coordinate, and one seven-coordinated. In corrosion inhibition tests on mild steel in 0.01 M NaCl solution, the maximum efficiency was observed with $[Y_3(2m3fur)_9]_n$ at 59%, which is less effective than yttrium 3-furoate (90% efficiency). The results suggest that the steric effect of the methyl group adversely affects corrosion inhibition.

1. Introduction

Rare earth carboxylates constitute the largest class of rare earth-based coordination polymers,[1] showcasing diverse structural types and coordination modes.[2–5] These complexes are known for their high coordination numbers, achieved through the favourable large size and high charge of lanthanoid ions, the multiplicity of carboxylate binding modes, and the lack of directionality in lanthanoid-carboxylate binding.[2]

Over the past two decades, the combination of the properties of rare earth ions and aromatic carboxylates has given rise to the development of highly effective dual-function rare earth carboxylate corrosion inhibitors. These compounds have emerged as a promising and greener alternative to toxic chromates in the field of corrosion prevention.[1,6–10] Some of the best-performing compounds include cerium salicylate[8] lanthanum 4-hydroxycinnamate[11] and yttrium 3-(4′-methylbenzoyl)propionate[12] 3-furoate[13] and 4-hydroxybenzoate.[14] Emerging trends suggest that additional unsaturation, donor capacity, and the presence of donor hetero atoms play a significant role in achieving higher levels of inhibition.[8,9,12,13,15,16] Such observations support an inhibition model whereby a carboxylatolanthanoid species binds to a hydroxidoiron(III) group on a corroding surface through a donor group-hydroxide interaction.[8–10]

To examine this concept further, we have utilised our recent discovery of the high inhibitor activity of lanthanoid 3-furoate complexes.[13] Accordingly, we have introduced a 2-methyl group into the 3-furoate ion and examined the effect of its steric inhibition on carboxylate coordination and capacity for corrosion inhibition. Six lanthanoid complexes of 2-methyl-3-furoate have been prepared, their structures examined by X-ray crystallography, X-ray powder diffraction, and thermogravimetric analysis, and corrosion testing outcomes based on weight loss measurements determined. The structural change has a deleterious effect on inhibitor activity.

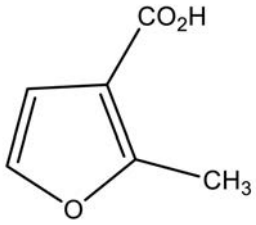


Chart 1. Structure of 2-methyl-3-furoic acid (2m3furH).

2. Results and Discussion

2.1. Synthesis and Characterization

The complexes $\{[RE_2(2m3fur)_6(EtOH)]\cdot H_2O\}_n$ (**1RE** = La, Ce, Pr) and $[RE_3(2m3fur)_9]_n$ (**2RE** = Y, Er, Yb) were prepared in moderate yields by using metathesis reactions between sodium 2-methyl-3-furoate and the corresponding RE salts (at a mole ratio of 3 : 1) as shown in Scheme 1.

The compositions of all these complexes were determined through a combination of X-ray crystallography, elemental analysis and TGA. Growing crystals for X-ray diffraction proved

[a] V. P. Vithana, Z. Guo, P. C. Junk
College of Science & Engineering, James Cook University, Townsville, 4811, Qld, Australia
E-mail: peter.junk@jcu.edu.au

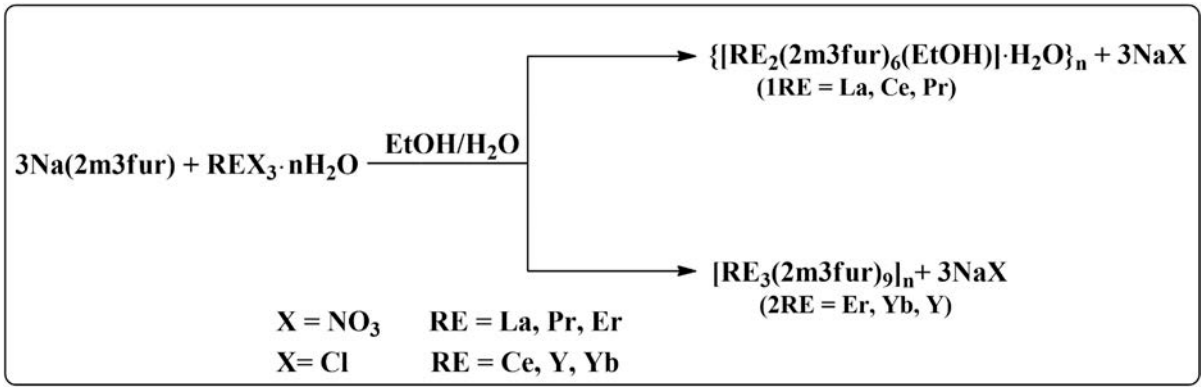
[b] G. B. Deacon
School of Chemistry, Monash University, Clayton, 3800, Vic., Australia

Supporting information for this article is available on the WWW under https://doi.org/10.1002/ejic.202300722

© 2024 The Authors. European Journal of Inorganic Chemistry published by Wiley-VCH GmbH. This is an open access article under the terms of the Creative Commons Attribution Non-Commercial NoDerivs License, which permits use and distribution in any medium, provided the original work is properly cited, the use is non-commercial and no modifications or adaptations are made.

© 2024 The Authors. European Journal of Inorganic Chemistry published by Wiley-VCH GmbH

Research Article
doi.org/10.1002/ejic.202300722



Scheme 1. The synthesis of RE 2-methyl-3-furoate complexes.

Table 1. Selected infrared bands (cm^{-1}) of the RE^{III} 2-methyl-3-furoate complexes.

Compound	$\nu(OH)_{water}$	$\nu_{as}(CO_2^-)$	$\nu_s(CO_2^-)$	$\Delta\nu = (\nu_{as}-\nu_s)avg$	$\delta(CO_2)$
$\{[Ce_2(2m3fur)_6(EtOH)]\cdot H_2O\}_n$ **(1b)**	3458	1518	1377,1360	149.5	684
$[Er_3(2m3fur)_9]_n$ **(2b)**	–	1531,1517	1381,1360	153.5	686

to be particularly challenging when using the 2-methyl-3-furoate ligand. However, in this study, we successfully obtained single crystals suitable for X-ray crystallography for **1c**, **2a**, **2b** and **2c**. In each instance, the bulk products were isolated as powders.

All attempts to obtain crystals of **1a** were unsuccessful. Nevertheless, X-ray powder diffractograms suggest it is isomorphous with **1c** (Figure S1). Data for **1b** were incomplete, resulting in the acquisition of only the unit cell. However, the unit cell parameters and the powder diffractogram of this complex indicate that it is isomorphous with **1c**.

TGA analyses of compound **1a** and **1b** yielded results consistent with the crystal composition of $\{[RE_2(2m3fur)_6(EtOH)]\cdot H_2O\}_n$, indicating the simultaneous loss of one water molecule and one ethanol molecule in a single step. The presence of a broad band in the range 3200–3550 cm^{-1} in the IR spectra of **1a** and **1b** is consistent with the presence of water and ethanol (O–H stretching) in the compounds. The elemental analysis data indicate that complexes **1a** and **1b** experienced ethanol loss from their single crystal compositions under the microanalysis drying conditions. As for compound **1c**, elemental analysis, TGA and IR indicate that, during the drying process, both coordinated ethanol and lattice water were removed from the crystals (Figure S2 and S3).

For compounds **2a**, **2b**, and **2c**, the powder XRD analyses closely resembled the patterns generated from the single-crystal data (see Figure S4). Consistent with the single-crystal compositions of compounds **2a** and **2b**, their thermograms and IR spectra do not exhibit any weight reduction attributable to the removal of coordinated or lattice solvent molecules (Figure S5 and Figure S6). Conversely, **2c** displayed hygroscopic properties, evident from the thermal analysis. Thus, TGA data for **2c** revealed additional water content, with the loss of four water molecules occurring in a single step below 150 °C (Figure S6). Nevertheless, the IR spectrum, recorded after drying to a constant weight, did not exhibit a broad band in the range 3200–3550 cm^{-1} (Figure S5), and the elemental analyses of **2a**–**2c** were consistent with anhydrous compounds.

The infrared spectra of all complexes exhibited distinctive peaks within the range of 1560–1360 cm^{-1} corresponding to carboxylate COO^- stretching bands. The IR spectra of the compounds exhibit strong similarities in major bands within each isostructural series. Therefore, we have listed the significant IR bands for only one compound from each series, specifically **1b** and **2b**, in Table 1.

2.2. Structural Description

There are only two distinct carboxylate ligand binding modes in the structures, namely bridging tridentate μ-1κ(O, O′):2κ(O′) and *syn-syn* bridging bidentate μ-1κ(O):2κ(O′) (Figure 1). In comparison, analogous 3fur complexes display four unique binding

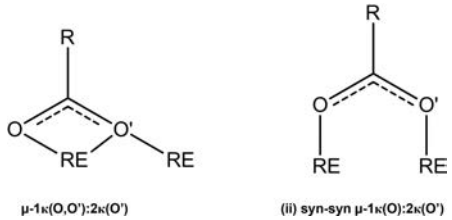


Figure 1. Coordination forms of 2-methyl-3-furoate ions in rare earth complexes. PLEASE ENSURE *syn-syn* are in italics in caption for (ii) and add (i) under the first compound

© 2024 The Authors. European Journal of Inorganic Chemistry published by Wiley-VCH GmbH

10990682c, 2024, 11, Downloaded from https://chemistry-europe.onlinelibrary.wiley.com/doi/10.1002/ejic.202300722 by Eddie Koiki Mabo Library, Wiley Online Library on [11/09/2024]. See the Terms and Conditions (https://onlinelibrary.wiley.com/terms-and-conditions) on Wiley Online Library for rules of use; OA articles are governed by the applicable Creative Commons License

Research Article
doi.org/10.1002/ejic.202300722

modes: *syn-syn* μ-1κ(O):2κ(O′), *syn-anti* μ-1κ(O):2κ(O′), μ_3-1κ(O):2κ(O,O′):3κ(O′) and μ_3-1κ(O):2κ(O′):3κ(O′).[13]

Due to poor quality of crystals of **2 b** (R_{int} 19.96 %), compound **2 b** is presented for connectivity purposes only. However, **2 b** is isomorphous with **2 a** and **2 c**.

2.2.1. 1D polymeric chains of {[RE$_2$(2m3fur)$_6$(EtOH)]·H$_2$O}$_n$ complexes (RE = La, Ce, Pr)

The molecular structure of {[Pr$_2$(2m3fur)$_6$(EtOH)]·H$_2$O}$_n$ **(1 c)** is depicted in Figure 2 and serves as a representative of the isomorphous series of 1D polymeric complexes, {[RE$_2$(2m3fur)$_6$(EtOH)]·H$_2$O}$_n$ (RE = La **(1 a)**, Ce **(1 b)** and Pr **(1 c)**). The structure of {[Pr$_2$(2m3fur)$_6$(EtOH)]·H$_2$O}$_n$ is binuclear, crystal-

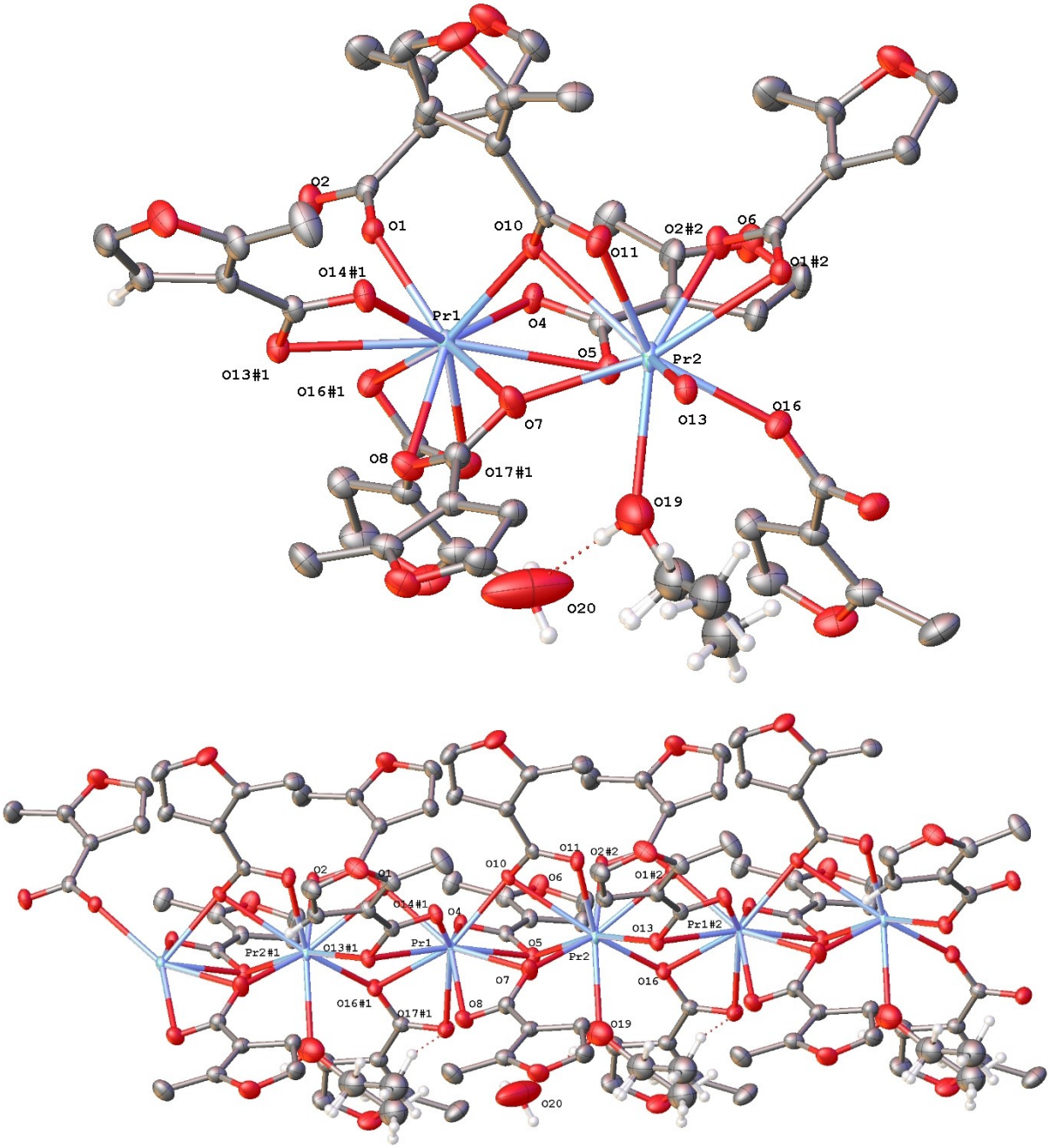


Figure 2. (a) The immediate coordination environment around Pr metal atoms in {[Pr$_2$(2m3fur)$_6$(EtOH)]·H$_2$O}$_n$ **(1 c)**; (**b**) 1D polymeric chain of **1 c** (representative of **1 a, 1 b**) Selected bond lengths (Å) and angles (°) (Complete data set for **1 c** is in the supplementary information; Table S2 and Table S3).**1 c** Pr1-O1 2.401(2), Pr1-O4 2.456(3), Pr1-O5 2.779(3), Pr1-O7 2.603(3), Pr1-O8 2.529(3), Pr1-O10 2.411(2), Pr1-O13#1 2.830(3), Pr1-O14#1 2.464(3), Pr1-O16#1 2.604(2), Pr1-O17#1 2.558(3), Pr2-O5 2.396(3), Pr2-O7 2.428(3), Pr2-O10 2.768(2), Pr2-O11 2.434(3), Pr2-O13 2.391(3), Pr2-O16 2.436(3), Pr2-O19 2.619(4), Pr2-O1#2 2.716(2), Pr2-O2#2 2.451(3), Pr1….Pr2 3.8477(8), Pr2…Pr1#2 3.8433(8), Pr2#1-Pr1-Pr2 177.360(9), Pr1-Pr2-Pr1#2 177.360(9), Pr1-O5-Pr2 95.78(8), Pr1-O7-Pr2 99.73(9), Pr1-O10-Pr2 95.70(3), Symmetry Code: $^{\#1}1+X,+Y,+Z$; $^{\#2}-1+X,+Y,+Z$.

© 2024 The Authors. European Journal of Inorganic Chemistry published by Wiley-VCH GmbH

10990682c, 2024, 11, Downloaded from https://chemistry-europe.onlinelibrary.wiley.com/doi/10.1002/ejic.202300722 by Eddie Koiki Mabo Library, Wiley Online Library on [11/09/2024]. See the Terms and Conditions (https://onlinelibrary.wiley.com/terms-and-conditions) on Wiley Online Library for rules of use; OA articles are governed by the applicable Creative Commons License

Research Article
doi.org/10.1002/ejic.202300722

10990682c, 2024, 11, Downloaded from https://chemistry-europe.onlinelibrary.wiley.com/doi/10.1002/ejic.202300722 by Eddie Koiki Mabo Library, Wiley Online Library on [11/09/2024]. See the Terms and Conditions (https://onlinelibrary.wiley.com/terms-and-conditions) on Wiley Online Library for rules of use; OA articles are governed by the applicable Creative Commons License

lizing in the monoclinic $P2_1/c$ space group, containing two distinct Pr^{+3} metal centers within the asymmetric unit. There only one carboxylate binding mode, resulting in a distorted bicapped square antiprism (SAP)-type deca coordination for Pr1 and a distorted tricapped triganol prism-type nine coordination for Pr2. Crystal refinement data and bond lengths of **1c** are provided in the supplementary material (Table S1 and S2).

The coordination sphere around the Pr1 metal center comprises eight chelating oxygen atoms from four μ-1κ(O,O′):2κ(O′) carboxylates (O4,5), (O7,8), (O13#1,14#1), (O16#1,17#1) and two bridging oxygen atoms from μ-1κ(O):2κ(O,O′) carboxylates (O1, O10). The Pr2 metal center is nine coordinate, featuring four chelating oxygen atoms from two μ-1κ(O,O′):2κ(O′) carboxylates (O10,11), (O1#2,2#2), four bridging oxygen atoms from μ-1κ(O):2κ(O,O′) carboxylates (O5, O7, O13, O16), and one oxygen atom (O19) from the ligated ethanol.

The two metal centres are connected by three ligands (through O5, O7, O10), forming a 1D polymeric chain and this chain propagates in an alternating sequence of Pr2#1…Pr1…Pr2…Pr1#2. The metal-metal distance between Pr1….Pr2 and Pr2…Pr1#2 are 3.8477(8) Å and 3.8433(8) Å respectively, with Pr2#1-Pr1-Pr2 and Pr1-Pr2-Pr1#2 angles of 177.360(9)°. The angles formed at the bridging oxygen atoms are 95.78(8)° (Pr1-O5-Pr2), 99.73(9)° (Pr1-O7-Pr2) and 95.70(3)° (Pr1-O10-Pr2).

Additionally, the lattice water oxygen atom (O20) forms a hydrogen bond with the oxygen atom (O19) of the ligated ethanol molecule within the asymmetric unit. The experimentally observed hydrogen bonding interactions are listed in Table S4.

At first sight, the higher coordination numbers (10, 9) in **1a–c** than in RE 3-furoate (3fur) complexes, $[RE(3fur)_3(H_2O)_2]_n$ (RE = La–Ho, Y), which are eight coordinate, is counter intuitive given the greater bulk of 2m3fur. However, the higher coordination numbers are associated with longer RE–O bonds relieving strain about the metal center (Table 2). The simpler carboxylate coordination in **1a–c** than in the 3fur analogues may be attributable to reduced access to one of the carboxylate oxygens owing the bulk of the Me group. Any electronic effect of the methyl group is outweighed by the steric effect as shown by the considerable simplification of the carboxylate coordination compared with that in lanthanoid 3-furoates.

2.2.2. 1D polymeric chains of $[RE_3(2m3fur)_9]_n$ complexes (RE = Y, Er, Yb)

The asymmetric unit of the isostructural series of complexes $[RE_3(2m3fur)_9]_n$ (RE = Y **(2a)**, Er **(2b)** and Yb **(2c)**) comprises three unique RE metal centers, forming a 1D polymeric chain. They crystallize in the $P2_1/c$ space group. Crystal data and specific refinement parameters are provided in the supplementary material. A representative structure, $[Yb_3(2m3fur)_9]_n$ is shown in Figure 3.

Yb1 and Yb3 are both octa-coordinate and Yb2 seven coordinate. The arrangement around the Yb1 metal center is distorted square antiprismatic, whereas a distorted dodecahedral arrangement can be seen around Yb3. Each Yb ion is coordinated by chelating oxygen atoms from two μ-1κ(O,O′):2κ(O′) carboxylates. Specifically, Yb1 is bound by (O15,16) and (O22#2,23#2), whereas Yb3 is coordinated by (O20,21) and (O11#1,12#1). In the case of Yb1, three additional coordination sites are occupied by carboxylate oxygen atoms (O4, O5, O14) originating from μ-1κ(O):2κ(O′) bridging ligands. Conversely, Yb3 possesses only two such bridging oxygen atoms (O3#1,25) surrounding it. The final coordination oxygen atom (O12) of Yb1 is derived from a μ-1κ(O):2κ(O,O′) bridge, while two of these bridging oxygen atoms (O18, 22) complete the coordination sphere around Yb3.

The stereochemistry of the seven coordinated Yb2 is pentagonal bipyramidal, and it is coordinated by two oxygen atoms (O17,18) from a μ-1κ(O,O′):2κ(O′) chelating carboxylate, two oxygen atoms (O16, O20) from μ-1κ(O):2κ(O,O′) bridging carboxylate ligands, and three bridging oxygen atoms (O7, O19, O24) from μ-1κ(O):2κ(O′) carboxylate groups.

The one-dimensional polymeric chain of **2c** exhibits a slight wave, with angles of 157.006(12)°, 160.657(10)°, and 148.256(15)° between Yb1-Yb2-Yb3, Yb2-Yb3-Yb1#1 and Yb#2-Yb1-Yb2, respectively.

Table S5 presents the list of Yb–O bond lengths observed in the crystal structure. The overall average Yb–O bond distance is 2.32 Å, with Yb3-O12#1 being the longest and Yb2-O7 the shortest. The average bond lengths around each Yb metal center are as follows: Yb1 (2.33 Å), Yb2 (2.29 Å), Yb3 (2.34 Å). There is an increase of approximately 0.04 Å in the average Yb–O bond length at Yb1 and Yb3 metal centers compared to the Yb2 metal center, a result which correlates with the increasing coordination number of Yb^{3+}.

The separation between each pair of Yb metal centers is as follows: Yb1…Yb2 (4.1275(9) Å), Yb2…Yb3 (3.8100(9) Å) and Yb3…Yb1#1 (3.7230(8) Å). Yb1…Yb2 is bridged by three oxygen atoms from one μ-1κ(O):2κ(O,O′) bridge and two μ-1κ(O):2κ(O′) bridges, while Yb2…Yb3 and Yb3…Yb1#1 are each bridged by oxygen atoms from two μ-1κ(O):2κ(O,O′) bridges and one μ-1κ(O):2κ(O′) bridge. The impact of the lanthanoid contraction[17] is evident in the decreased RE–O bond distances within the 1D chains of Y^{3+}, Er^{3+} and Yb^{3+} complexes (Table S5).

As two of the Y atoms of **2a** have the same coordination number as in $[Y(3fur)_3(H_2O)_2]_n$, it is possible to compare <Y–O> values (Table 3), and they suggest a slight lengthening in **2a**, consistent with a steric effect by the methyl group. Any electronic effect of the methyl group is outweighed by the steric effect as shown by the considerable simplification of the carboxylate coordination compared with that in lanthanoid 3-furoates, and by Y–O bond lengthening in **2a**.

Table 2. Average RE-O bond length comparison of Pr 3-furoate and Pr 2-methyl-3-furoate complexes

	RE1-O	RE2-O
$[Pr(3fur)_3(H_2O)_2]_n$ [13]	2.43	
$\{[Pr_2(2m3fur)_6(EtOH)]\cdot H_2O\}_n$	2.56	2.53

© 2024 The Authors. European Journal of Inorganic Chemistry published by Wiley-VCH GmbH

Research Article
doi.org/10.1002/ejic.202300722

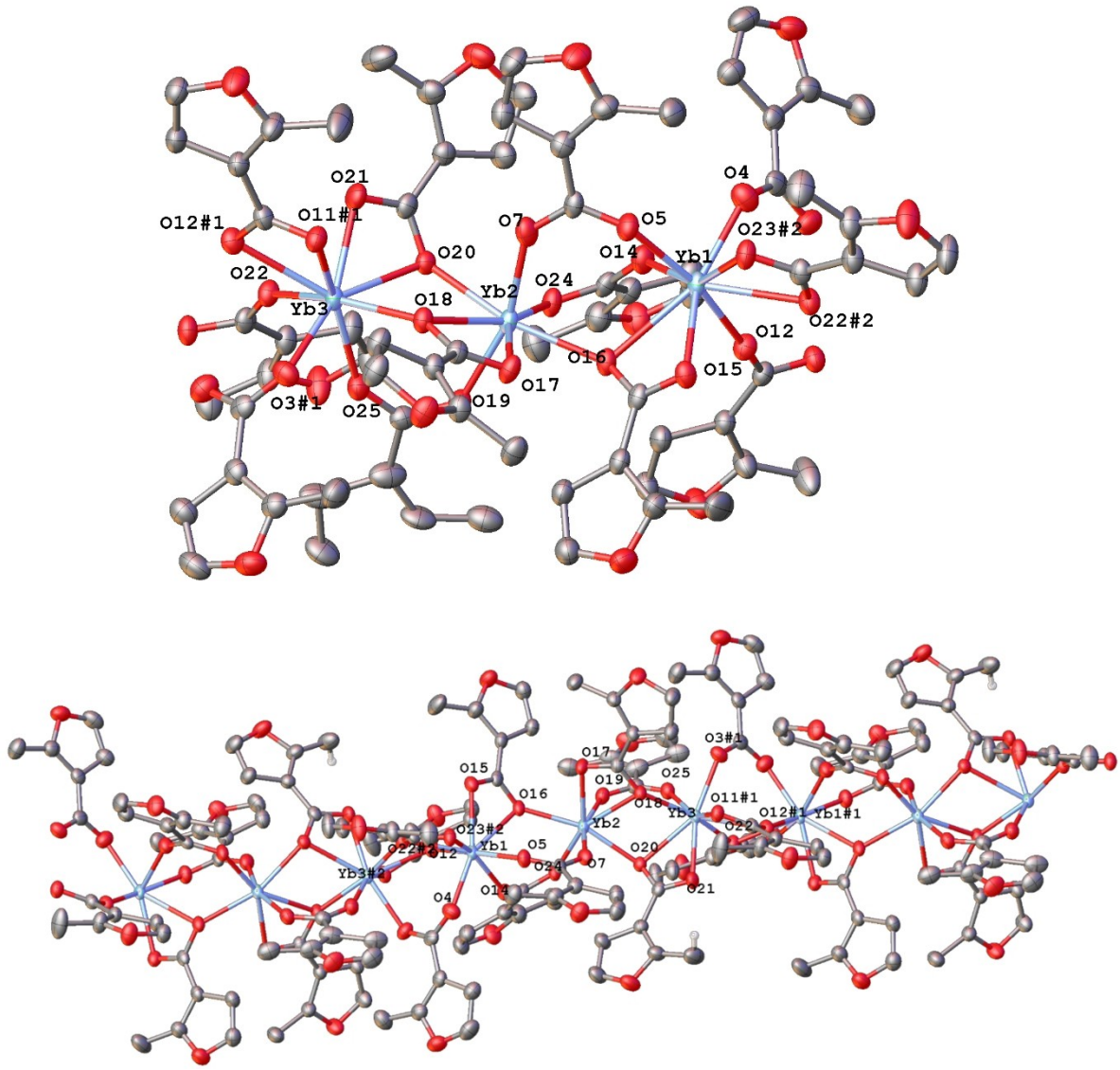


Figure 3. (a) The immediate coordination environment around Yb metal atoms in $RE_3(2m3fur)_9]_n$ (**2 b**); (**b**) 1D polymeric chain of **2 c** (representative of **2 a, 2 b**) Selected bond lengths (Å) and angles (°) (Data for all **2RE** are in the supplementary information; Table S5 and Table S6).**2 c** Yb1-O4 2.228(3), Yb1-O5 2.210(3), Yb1-O12 2.270(3), Yb1-O14 2.230(3), Yb1-O15 2.314(3), Yb1-O16 2.553(3), Yb1-O22#2 2.519(3), Yb1-O23#2 2.359(3), Yb2-O7 2.192(3), Yb2-O16 2.287(3), Yb2-O17 2.328(3), Yb2-O18 2.474(3), Yb2-O19 2.213(3), Yb2-O20 2.318(3), Yb2-O24 2.231(3), Yb3-O18 2.246(3), Yb3-O20 2.516(3) Yb3-O21 2.312(3), Yb3-O22 2.234(3), Yb3-O25 2.252(3), Yb3-O3#1 2.250(3) Yb3-O3#1 2.250(3), Yb3-O11#1 2.307(3), Yb3-O12#1 2.583(3), Yb1…Yb2 4.1275(9), Yb2…Yb3 3.8100(9), Yb3…Yb1#1 3.7230(8). Yb1-Yb2-Yb3 157.006(12), Yb2-Yb3-Yb1#1 160.657(10), Yb#2-Yb1-Yb2 148.256(15) Symmetry Code: [#1]1-X,1/2+Y,1/2-Z; [#2]1-X,–1/2+Y,1/2-Z.

Table 3. Average RE-O bond length comparison of Y 3-furoate and Y 2-methyl-3-furoate complexes.

	RE1-O	RE2-O	RE3-O
$[Y(3fur)_3(H_2O)_2]_n$[13]	2.32		
$[Y_3(2m3fur)_9]_n$	2.36	2.32	2.36

2.3. Corrosion Inhibition

2.3.1. Immersion Tests

Immersion studies were conducted over a seven-day period, both in a 0.01 M NaCl control solution and with the presence of inhibition systems at room temperature (25 °C), to evaluate the long-term performance of these inhibitors on mild steel.

Table 4 presents a summary of the weight loss measurements for mild steel coupons after 168 h of immersion in specific inhibitor solutions. The weight loss of the coupons during the immersion test period serves as a primary measure of corrosion. The testing was conducted for the compounds at 800 ppm, as the solubility limit for $[Er_3(2m3fur)_9]_n$ **2 b** in 0.01 M sodium chloride solution is 800 ppm.

The corrosion rate (R) for each inhibitor compound was evaluated using the following equation, Eqn (1).

© 2024 The Authors. European Journal of Inorganic Chemistry published by Wiley-VCH GmbH

10990682c, 2024, 11, Downloaded from https://chemistry-europe.onlinelibrary.wiley.com/doi/10.1002/ejic.202300722 by Eddie Koiki Mabo Library, Wiley Online Library on [11/09/2024]. See the Terms and Conditions (https://onlinelibrary.wiley.com/terms-and-conditions) on Wiley Online Library for rules of use; OA articles are governed by the applicable Creative Commons License

Research Article
doi.org/10.1002/ejic.202300722

10990682c, 2024, 11, Downloaded from https://chemistry-europe.onlinelibrary.wiley.com/doi/10.1002/ejic.202300722 by Eddie Koiki Mabo Library, Wiley Online Library on [11/09/2024]. See the Terms and Conditions (https://onlinelibrary.wiley.com/terms-and-conditions) on Wiley Online Library for rules of use; OA articles are governed by the applicable Creative Commons License

Table 4. Observed weight loss, corrosion rates (μg/m²s) and percentage inhibition (η) for mild steel coupons immersed in specific solutions at 800 ppm concentrations in 0.01 M NaCl for seven days.

Solution	Concentration		Solubility in 0.01 M NaCl (ppm)	Avg Weight Loss (mg)	Corrosion Rate (μg/m²s)	Inhibition, η (%)
	ppm	mM				
Control - NaCl	580	10	–	19.6	39.1	–
$\{[Ce_2(2m3fur)_6(EtOH)]\cdot H_2O\}_n$ **1 b**	800	0.731	1800	12.6	24.0	39
$\{[Pr_2(2m3fur)_6(EtOH)]\cdot H_2O\}_n$ **1 c**	800	0.730	1500	8.8	20.9	46
$[Y_3(2m3fur)_9]_n$ **2 a**	800	0.574	850	8.5	16.2	59
$[Er_3(2m3fur)_9]_n$ **2 b**	800	0.491	800	11.3	21.6	45
$[Yb_3(2m3fur)_9]_n$ **2 c**	800	0.486	830	9.7	18.5	53
$[Ce(3fur)_3(H_2O)_2]_n$ [13]	800	1.57	3000	3.7	8.3	79
$[Y(3fur)_3(H_2O)_2]_n$ [13]	800	1.75	800	1.9	3.9	90

$$\text{Corrosion rate } (R) = \frac{KW}{ATD} \quad (1)$$

Subsequently, the percentage corrosion inhibition (%) was calculated using Equation (2):

$$\eta = \frac{R(Control) - R\ (inhibitor)}{R(Control)} \times 100 \quad (2)$$

Consistent with visual inspections (Figure S7), weight loss measurements also indicated that $[Y_3(2m3fur)_9]_n$ **2 a** exhibited the highest inhibition efficiency at 59% among the tested compounds, while $\{[Ce_2(2m3fur)_6(EtOH)]\cdot H_2O\}_n$ **1 b** showed the lowest performance with an inhibition efficiency of approximately 39%.

The limited solubility of most of the complexes hindered attempts to conduct studies at higher concentration. The performance of the RE 2-methyl-3-furoate complexes was not as effective as the analogous rare earth 3-furoate complexes (see Table 4 for a comparison of Ce and Y complexes),[13] suggesting that the methyl substituent on the furoate ring may cause steric hindrance of inhibitor function. Because of the less effective inhibitor performance, electrochemical assessments of inhibition were not pursued.

3. Conclusions

Two series of RE 2-methyl-3-furoate complexes, $\{[RE_2(2m3fur)_6(EtOH)]\cdot H_2O\}_n$ **1RE** (RE = La, Ce, Pr) and $[RE_3(2m3fur)_9]_n$ **2RE** (RE = Y, Er, Yb) have been successfully synthesized. These compounds crystallized in one of the two distinct structural groups, as determined through single-crystal X-ray crystallography. The synthesis process yielded moderate isolated yields of crystalline materials, and these complexes were comprehensively characterized by various techniques, including IR spectroscopy, powder XRD, TGA, and microanalyses.

The light rare earth metals form one-dimensional polymeric structures, $\{[RE_2(2m3fur)_6(EtOH)]\cdot H_2O\}_n$ complexes (**RE** = La, Ce, Pr) with one ten and one nine coordinate RE atom. Conversely, the heavier rare earth metals have one-dimensional polymeric chains in the $[RE_3(2\ m3fur)_9]_n$ complexes (RE = Y, Er, Yb), with three unique RE metal centers, two eight coordinate and one seven coordinate.

In immersion studies conducted with mild steel in 0.01 M NaCl solutions at inhibitor concentrations of 800 ppm, $[Y_3(2m3fur)_9]_n$ **2 c** emerged as the most effective inhibitor among the compounds tested, demonstrating a 59% inhibition rate. Nevertheless, the most efficient inhibitor in this study proved to be less effective than the RE 3-thiophenecarboxylate[16] and 3-furoate[13] complexes studied previously. It is plausible that the steric effect of the methyl substituent impedes binding of the inhibitor to OH groups on the corroded steel surface, thereby reducing inhibitor protection.

Materials and Methods

General Considerations

All reagents and solvents used were of standard commercial grade and were employed without further purification. IR data were obtained in the region 4000–500 cm^{-1} by using a Nicolet™ iS™ 5 FTIR Spectrometer. Elemental analyses (C, H) were performed by the Microanalytical Laboratory at the Science Centre, London Metropolitan University, England. Metal analyses were conducted through complexometric titration with 0.01 M EDTA, Xylenol Orange indicator and hexamethylenetetramine buffer. Thermogravimetric analysis (TGA) was carried out using a TA instrument SDT 650 with standard 90 μl alumina metal pans under a N_2 atmosphere (at a flow rate of 50 ml min^{-1}), ranging from room temperature up to 750 °C (with a ramp of 10 °C min^{-1}) (Figure S2 and S6). Melting points were determined in glass capillaries and are reported without calibration. Powder XRD measurements were obtained at room temperature using a Bruker D2 PHASER diffractometer in the range of 5–50° with a 0.2° divergence slit and at 0.02° increments. X-ray powder simulations were generated using the Mercury program provided by the Cambridge Crystallographic Data Centre,[18] based on the obtained single-crystal X-ray diffraction data.

© 2024 The Authors. European Journal of Inorganic Chemistry published by Wiley-VCH GmbH

Research Article
doi.org/10.1002/ejic.202300722

10990682c, 2024, 11, Downloaded from https://chemistry-europe.onlinelibrary.wiley.com/doi/10.1002/ejic.202300722 by Eddie Koiki Mabo Library, Wiley Online Library on [11/09/2024]. See the Terms and Conditions (https://onlinelibrary.wiley.com/terms-and-conditions) on Wiley Online Library for rules of use; OA articles are governed by the applicable Creative Commons License

X-ray Crystallography

Single crystals of all samples were coated in viscous hydrocarbon oil and mounted on glass fibres or loops on the diffractometer. The data were collected on the MX1 beamline at the Australian Synchrotron, where the data integration was processed with Blue-ice[19] and XDS[20] software programs. Structures were solved by SHELXT and refined by full-matrix least-squares methods against F^2 using SHELX2018,[21] within the Olex2[22] interface. All hydrogen atoms were placed in calculated positions using the riding model. Crystal data and refinement details are shown in Table S1. CCDC 2308961 for **1 c** and 2308962–2308964 for compounds **2 a**-**2 c**, contain the supplementary crystallographic data for this paper. These data can be obtained free of charge from The Cambridge Crystallographic Data Centre.

Synthesis of 2-methyl-3-furoate (2m3fur) RE complexes

General Synthetic Method: 2-Methyl-3-furoic acid was dissolved in 95% ethanol (15 ml) and subjected to deprotonation by an equimolar quantity of aqueous sodium hydroxide. The solution mixture was stirred for one hour, after which the pH was adjusted to fall within the range 7–8. Subsequently, three molar equivalents of sodium 2-methyl-3-furoate were treated with one molar equivalent of the hydrated rare earth salt solution at a pH level of 5 to form rare earth 2-methyl-3-furoate complexes. The resulting solid precipitates were isolated by filtration and allowed to air-dry for 2–3 days. Finally, crystals were obtained through slow evaporation of the mother liquor at room temperature.

1 a: $\{[La_2(2m3fur)_6(EtOH)]\cdot H_2O\}_n$ white powder. Yield: 52%. m.p. 230 °C (dec). Elemental analysis calculated for $C_{38}H_{38}La_2O_{20}$ (MW: 1092.51 $gmol^{-1}$): Calculated (%) C 41.78; H 3.51; La 25.40: $C_{36}H_{32}La_2O_{19}$ (MW: 1046.44 $gmol^{-1}$, loss of 1 EtOH): Calculated (%) C 41.32; H 3.08; La 26.55; Found (%) C 41.39; H 2.62; La 26.65. IR (cm^{-1}): 3430w, 3123w, 2920w, 1682w, 1595 m, 1530s, 1519 s, 1445 m, 1414 s, 1376 s, 1359 s, 1232 m, 1213 s, 1134 m, 1101 s, 1033w, 946 m, 896 m, 875w, 817 s, 807 s, 731 s, 684 m, 634w, 599 m, 534 m, 462 s. TGA weight loss (30-200 °C); 4.9% (Calc. for loss of 1×H_2O and 1× EtOH = 5.8%).

1 b: $\{[Ce_2(2m3fur)_6(EtOH)]\cdot H_2O\}_n$ white powder. Yield: 52%. m.p.230 °C (dec). Elemental analysis for $C_{38}H_{38}Ce_2O_{20}$ (MW: 1094.93 $gmol^{-1}$): Calculated (%) C 41.68; H 3.50; Ce 25.60: $C_{36}H_{32}Ce_2O_{19}$ (MW: 1048.86 $gmol^{-1}$, loss of 1 EtOH): Calculated (%) C 41.22; H 3.08; Ce 26.72; Found (%) C 41.55; H 2.54; Ce 27.26. IR (cm^{-1}): 3458w, 3122w, 2922w, 1596 m, 1527 s, 1518 s, 1444 m, 1414 s, 1376 s, 1359 s, 1232 m, 1214 s, 1133 m, 1102 s, 1031w, 946 m, 895 m, 876w, 819 s, 807 s, 733 s, 684 m, 634w, 600 m, 534 m, 466 s, 457 s. TGA weight loss (30-175 °C); 4.8% (Calc. for loss of 1×H_2O and 1× EtOH = 5.8%); Monoclinic $P2_1/n$, unit Cell: $a = 7.6700(15)$, $b = 22.470(4)$, $c = 23.620(5)$, $\beta = 98.85(3)$, which is similar to **1 c.**

1 c: $\{[Pr_2(2m3fur)_6(EtOH)]\cdot H_2O\}_n$ pale green powder. Yield: 48%. m.p.230 °C (dec). Elemental analysis for $C_{38}H_{38}O_{20}Pr_2$ (MW: 1096.51 $gmol^{-1}$): Calculated (%) C 41.62; H 3.49; Pr 25.70: $C_{36}H_{30}O_{18}Pr_2$ (MW: 1032.43 $gmol^{-1}$, loss of 1 EtOH and 1 H_2O): Calculated (%) C 41.88; H 2.93; La 27.30.; Found (%) C 41.70; H 2.50; Pr 27.95; IR (cm^{-1}): 3122w, 2923w, 1596 m, 1548 s, 1534 m, 1515 s, 1412 s, 1375 s, 1358 s, 1235 m, 1214 s, 1133 m, 1102 s, 1030w, 946 m, 895 m, 876w, 836w, 821 s, 806 s, 737 s, 726 s, 685 m, 634w, 600 m, 535 m, 466 s, 458 s.

2 a: $[Y_3(2m3fur)_9]_n$ white powder. Yield: 73%. m.p.270 °C (dec). Elemental analysis for $C_{54}H_{45}O_{27}Y_3$ (MW: 1392.63 $gmol^{-1}$): Calculated (%) C 46.57; H 3.26; Y 19.20; Found (%) C 46.64; H 2.92; Y 19.60. IR (cm^{-1}): 3127w, 2922w, 1596 m, 1532 s, 1517 s, 1462 s, 1445 m, 1420s, 1381 m, 1360s, 1233 m, 1217 s, 1132 m, 1103 m, 1030w, 946 m, 895 m, 837 m, 802 s, 750 m, 728 s, 685 m, 600 m, 553w, 534w, 473 s.

2 b: $[Er_3(2m3fur)_9]_n$ pink powder. Yield: 70%. m.p.270 °C (dec). Elemental analysis for $C_{54}H_{45}O_{27}Er_3$ (MW: 1627.69 $gmol^{-1}$): Calculated C 39.85; H 2.79; Er 30.80; Found (%) C 39.80; H 2.58; Er 31.32. IR (cm^{-1}): 3127w, 1596 m, 1531 s, 1517 s, 1463 m, 1444 s, 1420s, 1381 m, 1360s, 1233 m, 1217 s, 1131 m, 1103 s, 1030w, 947 m, 895 m, 837 m, 802 s, 751w, 728 s, 688 m, 600 m, 553 m, 534w, 472 s.

2 c: $[Yb_3(2m3fur)_9]_n$ white powder. Yield: 55%. m.p.270 °C (dec). Elemental analysis for $C_{54}H_{45}O_{27}Yb_3$ (MW: 1645.04 $gmol^{-1}$): Calculated (%) C 39.43; H 2.76; Yb 31.60; Found (%) C 39.55; H 2.50; Yb 31.70. IR (cm^{-1}): 3129w, 2923w, 1599 m, 1538 m, 1513 s, 1460s, 1428 s, 1385 m, 1361 s, 1220s, 1130 m, 1107 m, 1030w, 945 m, 896 m, 840 m, 805 s, 729 s, 684 m, 634w, 600 m, 562 m, 536w, 469 s. TGA weight loss (90-175 °C); 4.4% (Calc. for loss of 4×H_2O (Assuming absorb water = 4.2%)).

Corrosion Testing

Weight loss experiments were carried out in accordance with the established ASTM G31-72 protocol[23] to evaluate the overall corrosion and inhibition characteristics of the synthesized compounds. For the weight loss tests, coupons made from AS 1020 mild steel alloy were prepared. These coupons were cut to dimensions of approximately 20×20×1.5 mm and subsequently subjected to gradual abrasion using sanding sheets with grit sizes ranging from 80 to 2000. Afterward, the samples were cleaned with distilled water and then ethanol, and they were dried using nitrogen gas. These coupons were immediately used for immersion tests, lasting up to 168 hours (7 days). Both the test samples and the control coupons were immersed in separate beakers filled with 0.01 M NaCl solutions, with and without the addition of 800 ppm of the inhibitor compounds. In each arrangement, replicates were carried out by completely immersing the coupons at a mid-depth level, using teflon strings.

After completing the test, the first step involved gently removing any corrosion product adhering to the substrate through mild sonication in clean distilled water. Subsequently, the finest sanding papers were used with minimal force to prevent the removal of the sound material. Finally, the coupons were rinsed with ethanol and dried using nitrogen (N_2) gas.

Acknowledgements

PCJ and GBD gratefully acknowledge the ARC for funding (DP200100568). Parts of this research were undertaken on the MX1 beamline at the Australian Synchrotron, part of ANSTO.[24] Open Access publishing facilitated by James Cook University, as part of the Wiley - James Cook University agreement via the Council of Australian University Librarians.

Conflict of Interests

The authors declare no conflict of interest.

© 2024 The Authors. European Journal of Inorganic Chemistry published by Wiley-VCH GmbH

Data Availability Statement

The data that support the findings of this study are available from the corresponding author upon reasonable request.

Keywords: rare earth metal · carboxylate complexes · metathesis · 2-methyl-3-furoates · corrosion inhibitors

[1] T. Behrsing, G. B. Deacon and P. C. Junk, in *Rare Earth-Based Corrosion Inhibitors*, (Eds. M. Forsyth B. Hinton), Woodhead Publishing, Cambridge, **2014**, pp. 1–37.
[2] N. C. Thomas, O. A. Beaumont, G. B. Deacon, C. Gaertner, C. M. Forsyth, A. E. Somers, P. C. Junk, *Aust J Chem* **2020**, *73*, 1250–1259.
[3] A. Ouchi, Y. Suzuki, Y. Ohki, Y. Koizumi, *Coord. Chem. Rev.* **1988**, *92*, 29–43.
[4] C.-H. Huang, *Rare earth coordination chemistry: fundamentals and applications*, John Wiley & Sons, **2010**, p. 592.
[5] R. Janicki, A. Mondry, P. Starynowicz, *Coord Chem Rev* **2017**, *340*, 98–133.
[6] B. Hinton, in *Handbook on the Physics and Chemistry of Rare Earths*, (Eds. K. A. Gschneidner, L. Eyring) Elsevier Science B. V., **1995**, vol. 21, pp. 29–92.
[7] J. Sinko, *Prog. Org. Coat.* **2001**, *42*, 267–282.
[8] M. Forsyth, M. Seter, B. Hinton, G. Deacon, P. Junk, *Aust. J. Chem.* **2011**, *64*, 812–819.
[9] A. E. Somers, G. B. Deacon, B. R. W. Hinton, D. R. Macfarlane, P. C. Junk, M. Y. J. Tan, M. Forsyth, *J. Indian Inst. Sci.* **2016**, *96*, 285–292.
[10] A. E. Somers, Y. Peng, A. L. Chong, M. Forsyth, D. R. MacFarlane, G. B. Deacon, A. E. Hughes, B. R. W. Hinton, J. I. Mardel, P. C. Junk, *Corros. Eng. , Sci. Technol.* **2020**, *55*, 311–321.
[11] F. Blin, S. G. Leary, G. B. Deacon, P. C. Junk, M. Forsyth, *Corros. Sci.* **2006**, *48*, 404–419.
[12] Y. Peng, A. E. Hughes, G. B. Deacon, P. C. Junk, B. R. W. Hinton, M. Forsyth, J. I. Mardel, A. E. Somers, *Corros. Sci.* **2018**, *145*, 199–211.
[13] V. P. Vithana, Z. Guo, G. B. Deacon, A. E. Somers, P. C. Junk, *Molecules* **2022**, *27*, 8836 (1-16).
[14] J. Moon, Z. Guo, O. A. Beaumont, S. Hamilton, G. Bousrez, E. Mottram, J. Wang, A. E. Somers, G. B. Deacon, P. C. Junk, *New J. Chem.* **2023**, *47*, 16843–16854.
[15] A. E. Somers, B. R. W. Hinton, C. de Bruin-Dickason, G. B. Deacon, P. C. Junk, M. Forsyth, *Corros. Sci.* **2018**, *139*, 430–437.
[16] V. P. Vithana, Z. Guo, G. B. Deacon, A. E. Somers, P. C. Junk, *New J. Chem.* **2022**, *46*, 19104–19111.
[17] R. D. Shannon, *Acta Crystallogr. A* **1976**, *32*, 751–767.
[18] C. F. MacRae, I. Sovago, S. J. Cottrell, P. T. A. Galek, P. McCabe, E. Pidcock, M. Platings, G. P. Shields, J. S. Stevens, M. Towler, P. A. Wood, *J. Appl. Crystallogr.* **2020**, *53*, 226–235.
[19] T. M. McPhillips, S. E. McPhillips, H. J. Chiu, A. E. Cohen, A. M. Deacon, P. J. Ellis, E. Garman, A. Gonzalez, N. K. Sauter, R. P. Phizackerley, S. M. Soltis, P. Kuhn, *J. Synchrotron Radiat.* **2002**, *9*, 401–406.
[20] W. Kabsch, *J. Appl. Crystallogr.* **1993**, *26*, 795–800.
[21] G. M. Sheldrick, *Acta Crystallographica Section C* **2015**, *71*, 3–8.
[22] O. V. Dolomanov, L. J. Bourhis, R. J. Gildea, J. A. K. Howard, H. Puschmann, *J. Appl. Crystallogr.* **2009**, *42*, 339–341.
[23] *American-Standard-Test-Methods in ASTM G31-72*, Philadelphia, USA, **2004**.
[24] N. P. Cowieson, D. Aragao, M. Clift, D. J. Ericsson, C. Gee, S. J. Harrop, N. Mudie, S. Panjikar, J. R. Price, A. Riboldi-Tunnicliffe, R. Williamson, T. Caradoc-Davies, *J. Synchrotron Radiat.* **2015**, *22*, 187–190.

Manuscript received: November 27, 2023
Revised manuscript received: January 2, 2024
Accepted manuscript online: January 5, 2024
Version of record online: January 15, 2024

© 2024 The Authors. European Journal of Inorganic Chemistry published by Wiley-VCH GmbH

10990682c, 2024, 11, Downloaded from https://chemistry-europe.onlinelibrary.wiley.com/doi/10.1002/ejic.202300722 by Eddie Koiki Mabo Library, Wiley Online Library on [11/09/2024]. See the Terms and Conditions (https://onlinelibrary.wiley.com/terms-and-conditions) on Wiley Online Library for rules of use; OA articles are governed by the applicable Creative Commons License

molecules

MDPI

Article

Syntheses, Structures, and Corrosion Inhibition of Various Alkali Metal Carboxylate Complexes

Vidushi P. Vithana [1], Zhifang Guo [1], Glen B. Deacon [2] and Peter C. Junk [1,*]

[1] College of Science & Engineering, James Cook University, Townsville, QLD 4811, Australia; vidushi.vithana@my.jcu.edu.au (V.P.V.); zhifang.guo@jcu.edu.au (Z.G.)
[2] School of Chemistry, Monash University, Clayton, VIC 3800, Australia; glen.deacon@monash.edu
* Correspondence: peter.junk@jcu.edu.au

Abstract: Complexes of the alkali metals Li-Cs with 3-thiophenecarboxylate (3tpc), 2-methyl-3-furoate (2m3fur), 3-furoate (3fur), 4-hydroxycinnamate (4hocin), and 4-hydroxybenzoate (4hob) ions were prepared via neutralisation reactions, and the structures of $[Li_2(3tpc)_2]_n$ (**1Li**); $[K_2(3tpc)_2]_n$ (**1K**); $[Rb(3tpc)(H_2O)]_n$ (**1Rb**); $[Cs\{H(3tpc)_2\}]_n$ (**1Cs**); $[Li_2(2m3fur)_2(H_2O)_3]$ (**2Li**); $[K_2(2m3fur)_2(H_2O)]_n$ (**2K**); $[Li(3fur)]_n$(**3Li**); $[K(4hocin](H_2O)_3]_n$ (**4K**); $[Rb\{H(4hocin)_2\}]_n.nH_2O$ (**4Rb**); $[Cs(4hocin)(H_2O)]_n$ (**4Cs**); $[Li(4hob)]_n$ (**5Li**); $[K(4hob)(H_2O)_3]_n$ (**5K**); $[Rb(4hob)(H_2O)]_n$ (**5Rb**); and $[Cs(4hob)(H_2O)]_n$ (**5Cs**) were determined via X-ray crystallography. Bulk products were also characterised via XPD, IR, and TGA measurements. No sodium derivatives could be obtained as crystallographically suitable single crystals. All were obtained as coordination polymers with a wide variety of carboxylate-binding modes, except for dinuclear **2Li**. Under conditions that normally gave coordinated carboxylate ions, the ligation of hydrogen dicarboxylate ions was observed in **1Cs** and **4Rb**, with short H-bonds and short O . . . O distances associated with the acidic hydrogen. The alkali-metal carboxylates showed corrosion inhibitor properties inferior to those of the corresponding rare-earth carboxylates.

Keywords: alkali metal; carboxylate complexes; 3-thiophenecarboxylate; 2-methyl-3-furoate; 3-furoate; 4-hydroxycinnamate; 4-hydroxybenzoate; structures; corrosion inhibitors

check for updates

Citation: Vithana, V.P.; Guo, Z.; Deacon, G.B.; Junk, P.C. Syntheses, Structures, and Corrosion Inhibition of Various Alkali Metal Carboxylate Complexes. *Molecules* **2023**, *28*, 5515. https://doi.org/10.3390/molecules28145515

Academic Editors: Andrea Bencini and Vito Lippolis

Received: 4 July 2023
Revised: 12 July 2023
Accepted: 13 July 2023
Published: 19 July 2023

Copyright: © 2023 by the authors. Licensee MDPI, Basel, Switzerland. This article is an open access article distributed under the terms and conditions of the Creative Commons Attribution (CC BY) license (https://creativecommons.org/licenses/by/4.0/).

1. Introduction

The addition of chemical corrosion inhibitors is a highly efficient approach in managing the multi-billion-dollar cost associated with corrosion in metallic structures, particularly in steel infrastructure [1]. Corrosion protection through the use of metal–organic corrosion inhibitors has emerged as a substitute for highly toxic and environmentally hazardous Cr(VI) compounds [2]. The use of metal–organic corrosion inhibitors is associated with the formation of protective layers on metals [2]. In recent years, rare-earth carboxylate derivatives have gained significant attention as effective corrosion inhibitors [3–7]. Our previous work demonstrated the usefulness of various rare-earth (RE) carboxylates as corrosion inhibitors [2,4,6–10]. Specifically, we found cerium salicylate [4], lanthanum 4-hydroxycinnamate [11], yttrium 3-(4′-methylbenzoyl)-propanoate [12], yttrium 3-furoate [13], and rare-earth 3-thiophenecarboxylates [14] and 4-hydroxybenzoates [15] to be promising. The numerous possible coordination modes of carboxylate ligands [16,17] have also made this area fruitful for coordination and structural chemistry.

Rare-earth carboxylates are normally prepared via metathesis reactions between sodium carboxylates, often prepared in situ, and rare-earth salts. Because it has been claimed that the use of alkali-metal salts of carboxylic acids prevent corrosion in water treatment facilities [10], the sodium salts are usually tested for comparison with the rare-earth carboxylates, and inevitably perform much worse [3,4,10,13,18]. Moreover, preliminary immersion studies performed by Wormwell and Mercer [19] demonstrated that lithium and potassium benzoates also exhibit inhibitory properties against mild-steel corrosion.

However, relatively high concentrations of alkali-metal carboxylates are needed to achieve a good inhibitory effect, where they often act as anodic inhibitors [11,20].

Mercer et al. examined a series of benzoate compounds as corrosion inhibitors and concluded that the introduction of various substituents (-CH_3, -NO_2, -NH_2, -OH, -CH=CH-) improves the inhibition performance of benzoates [10,21]. Whilst we have regularly compared the performances of sodium salts with those of their rare-earth counterparts, we have not examined Li, K, Rb, and Cs analogues. When we examined the CCDC structural database, there were no structures of the alkali-metal derivatives of the carboxylic acids (1)–(4) (Chart 1) used in our rare-earth inhibitors [22]. In the case of 4-hydroxybenzoic acid (4hobH, (5) Chart 1), only the structure of the sodium salt has been determined and from X-ray powder data [23], whilst the structures of potassium and rubidium hydrogen di-4-hydroxybenzoates [M[H(4hob)$_2$]] (M = K, Rb) [24,25], but not M(4hob) derivatives, are known. There is also a lack of vertical (Li-Cs) studies on structures of rare-earth carboxylates [26,27]. In view of this lack of detailed structural studies, we investigated the synt-heses, structures, and corrosion inhibitor properties of the alkali-metal complexes of these carboxylate ions.

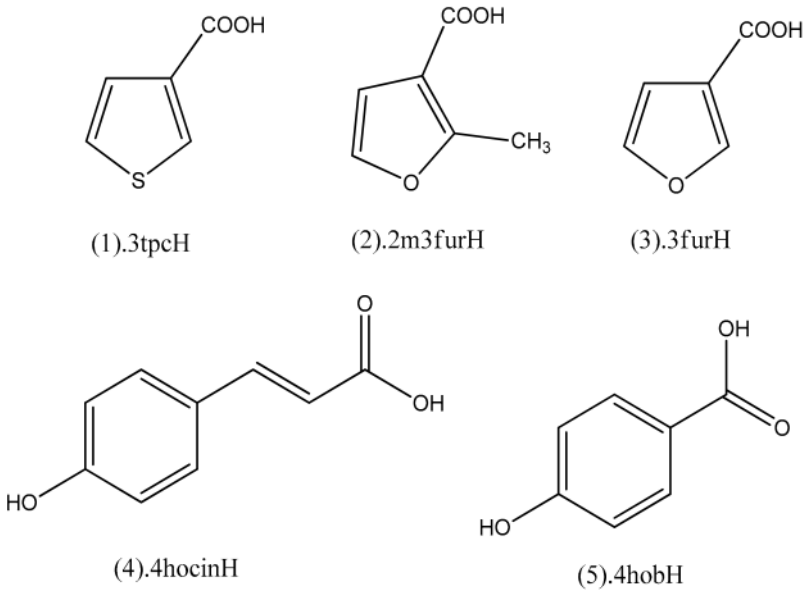


Chart 1. Structures of (**1**) 3-thiophenecarboxylic acid (3tpcH), (**2**) 2-methyl-3-furoic acid (2m3furH), (**3**) 3-furoic acid (3furH), (**4**) 4-hydroxycinnamic acid (4hocinH), and (**5**) 4-hydroxybenzoic acid (4hobH).

The alkali metals are highly prevalent in the Earth's crust, and two out of the eight most common elements found in the crust belong to the Group 1 elements. The importance of alkali metals in biology, and specifically Na^+ and K^+ ions, cannot be overstated [27]. Approximately one-third of all proteins rely on the presence of metal ions for their structural stability and proper functioning [26]. The extensive utilisation of alkali-metal compounds in diverse technical applications emphasises their immense importance in both chemistry and biology. These applications range from the utilisation of lithium compounds in batteries, organic synthesis, and pharmaceuticals, to the use of sodium in silicate-based glasses, and the use of potassium ions to enhance the scratch resistance of glass surfaces [27].

2. Results

2.1. Synthesis and Characterisation

By varying the preparative conditions, the syntheses of alkali-metal (Li–Cs) complexes of 3-thiophenecarboxylate (3tpc), 2-methyl-3-furoate (2m3fur), 3-furoate (3fur), 4-hydroxycinnamate (4hocin), and 4-hydroxybenzoate (4hob) were carried out via neutralisation reactions in an aqueous solution (Scheme 1). Only the complexes that were characterised by single-crystal XRD are reported in this paper. When complexed with

sodium, none of the five ligands formed crystalline products suitable for X-ray crystallography. The bulk samples of sodium complexes were characterised by powder XRD, IR, and TGA in the ESI^+, and the results suggest that they have dissimilar structural profiles compared to the other alkali-metal carboxylate complexes in the same group. Therefore, further characterisations were not carried out. In the case of **1Cs** and **4Rb**, acid salts [M{H(L)$_2$}] (M = Rb, Cs) were obtained, despite intentionally maintaining a 1:1 M:LH reaction stoichiometry (M = alkali metal; L = ligand) to prevent the incorporation of the carboxylic acid into the product (see Introduction for previous similar issues). Among the structures, **1Cs**, **2K**, and **5Li** exhibited slight hygroscopicity. This was evident from the thermal analysis of **1Cs** and **2K**, as well as the microanalysis of **5Li**, which showed values consistent with water absorption.

$$LH + KOH \xrightarrow{95\%\ EtOH} KL + H_2O \quad (1)$$

$$2LH + M_2CO_3 \xrightarrow{95\%\ EtOH} 2\ ML + CO_2 + H_2O \quad (M= Li, Rb, Cs) \quad (2)$$

Scheme 1. The synthesis of alkali-metal carboxylate complexes.

The compositions of the [M(3tpc)]$_n$ (M = Li, K, Rb, and Cs) complexes in the **1M** series were determined through X-ray crystallography, elemental analysis, and thermogravimetric analysis (TGA). The elemental analysis agreed with the single-crystal compositions for all four compounds. The TGA results of **1Li**, **1K**, and **1Rb** (Figure S1) were consistent with the compositions from the single-crystal data. However, the TGA of **1Cs** showed a loss of 0.5 water molecules in a single step below 150 °C. Nonetheless, the powder XRD analyses of all four compounds showed close similarities to the patterns generated from the single-crystal data (Figure S2).

In the [M(2m3fur)]$_n$ (M = Li, K) **2M** series, the TGA and elemental analysis of compound **2Li** aligns with the composition determined crystallographically as [Li$_2$(2m3fur)$_2$(H$_2$O)$_3$]. Although the elemental analysis of compound **2K** matches the composition of [K$_2$(2m3fur)$_2$(H$_2$O)]$_n$ of the crystal structure, the TGA of the bulk precipitate indicated the presence of water of crystallisation (Figure S4). The weight loss below 200 °C indicated the evolution of nearly two water molecules. This suggests that the compound may be hygroscopic after undergoing drying to a constant weight over silica gel. Nonetheless, the powder XRD analyses revealed similar d-spacings to those generated from the single-crystal data for both **2Li** and **2K** (Figure S5).

The elemental analysis of lithium-3-furoate (**3Li**) aligns with the calculated percentage composition for [Li(3fur)]$_n$ (**3Li**), and the thermogravimetric analysis (Figure S7) and IR analysis (Figure S9) of the sample confirm the absence of any water. Additionally, the powder diffractogram obtained from the bulk precipitate matches the calculated diffractogram based on the single-crystal data (Figure S8).

All three compounds in the M(4hocin) **4M** series (M = K, Rb, and Cs) have different compositions. The TGA of compound **4K** yielded results consistent with its crystal composition, revealing the loss of three water molecules in a single step below 100 °C (Figure S10), but the elemental analysis of it indicated a loss of 1.5 ligated water molecules due to the drying of the samples over silica gel. Nonetheless, the powder diffractogram of the bulk sample matches the one generated from the crystal data (Figure S11).

In the case of compound **4Rb**, the structure was determined as [Rb{H(4hocin)$_2$}]$_n$.nH_2O, but the analysis of the bulk product through microanalysis and TGA suggests that 0.75 4hocinH had been lost from the crystal composition. Unlike in **4K**, the experimental powder diffractogram of the bulk sample **4Rb** exhibited a noticeable difference when compared to the diffractogram generated from the crystal data attributed to the loss of

4hocinH. Upon drying the crystals of compound **4Rb** over silica gel, they seemed to lose their crystalline form and appeared more amorphous.

By comparison, the caesium analogue prepared under similar conditions was determined via crystallography to be $[Cs(4hocin)(H_2O)]_n$, which was consistent with the elemental analysis and TGA results. The powder XRD analysis of the bulk sample of **4Cs** closely resembles the powder diffractogram generated from the crystal data, but a few minor discrepancies can be observed (Figure S11).

The TGA thermal data of **5Li** (Figure S13) indicated that it is an anhydrous compound, which aligns with the X-ray composition of $[Li(4hob)]_n$. However, the elemental analysis of the complex indicated the presence of some water, suggesting it is slightly hygroscopic. The powder diffractogram closely resembles the generated powder diffractogram obtained from the crystal data (Figure S14), indicating that the structural integrity is maintained.

The TGA of **5K** revealed the loss of three water molecules in two steps, occurring below 75 °C and below 150 °C. However, the elemental analyses of the bulk sample yielded a molecular composition of $[K(4hob)(H_2O)]_n$, as opposed to the composition derived from the crystal data (namely, $[K(4hob)(H_2O)_3]_n$), indicating efflorescence. Additionally, the experimentally obtained powder diffractogram differs from the powder diffractogram generated based on its crystal data, consistent with the water loss (Figure S14).

The two complexes **5Rb** and **5Cs** have the general formulae $[M(4hob)(H_2O)]_n$ (M = Rb or Cs) from elemental analyses (C, H). The TGA results for **5Rb** are in support, but the bulk $[Cs(4hob)(H_2O)]_n$ (**5Cs**) lost a small fraction of coordinated water during drying prior to the TGA. The powder diffractograms of both compounds exhibited some similarities and displayed peaks that matched the generated diffractograms based on their crystal data.

The IR spectra of all the complexes displayed peaks corresponding to carboxylate COO^- stretching bands in the range of 1560–1360 cm^{-1} (Figure S15). These peaks included both asymmetric stretching bands (from 1509 to 1556 cm^{-1}) and symmetric stretching bands (1361–1399 cm^{-1}). Additionally, the presence of a broad band in the range of 3200–3550 cm^{-1} indicates the presence of water molecules and hydrogen-bonded alcohol O–H stretching (3400–3200 cm^{-1}) in the compounds. Having absorption bands in the region of 1617–1682 cm^{-1} in **1Cs** confirms the presence of an $[H(3tpc)_2]$ ligand with the C(O)OHO(O)C group (Figure S3). The IR spectra for all three compounds in the **4M** series have bands of moderate intensity in the range of 1633–1636 cm^{-1}, which corresponds to the stretching of the propenyl C=C double bond. The consistent υ(C=C) frequencies indicate that the propenyl group is not engaged in coordination [28]. The carbonyl absorption band of $[H(4hocin)_2]$ in the range of 1617–1682 cm^{-1} is not clear in the spectrum of compound **4Rb** (Figure S12). Table 1 presents a summary of the significant absorption bands observed in the IR spectra of all 14 compounds.

Table 1. Selected IR bands of alkali-metal 3tpc, 2m3fur, 3fur, 4hocin, and 4hob complexes.

Compounds	Significant Bands (cm^{-1})				
	ν(OH)	**n(C=C) Propenyl**	**$\nu_{as}(CO_2^-)$**	**$\nu_s(CO_2^-)$**	**Δν [a]**
$[Li_2(3tpc)_2]_n$ **1Li**	-	-	1566,1514	1414,1399	133.5
$[K_2(3tpc)_2]_n$ **1K**	-	-	1558,1516	1412,1401	130.5
$[Rb(3tpc)(H_2O)]_n$ **1Rb**	3348	-	1563,1512	1405	132.5
$[Cs\{H(3tpc)_2\}]_n$ **1Cs**	-	-	1560,1510	1398,1384	144
$[Li_2(2m3fur)_2(H_2O)_3]$ **2Li**	3301,3373	-	1544,1521	1428	104.5
$[K_2(2m3fur)_2(H_2O)]_n$ **2K**	3354	-	1532,1517	1418	106.5
$[Li(3fur)]_n$ **3Li**	-	-	1552	1428	124
$[K(4hocin)(H_2O)_3]_n$ **4K**	3114,3444	1636	1531,1511	1371	150

Table 1. *Cont.*

Compounds	Significant Bands (cm^{-1})				
	ν(OH)	**n(C=C) Propenyl**	**$\nu_{as}(CO_2^-)$**	**$\nu_s(CO_2^-)$**	**Δν [a]**
$[Rb\{H(4hocin)_2\}]_n.nH_2O$ **4Rb**	3241	1634	1537,1514	1381	144.5
$[Cs(4hocin)(H_2O)]_n$ **4Cs**	3200	1633	1537,1514	1378	147.5
$[Li(4hob)]_n$ **5Li**	3351	-	1556	1399	157
$[K(4hob)(H_2O)_3]_n$ **5K**	3437	-	1533	1361	172
$[Rb(4hob)(H_2O)]_n$ **5Rb**	3317	-	1529,1509	1381	138
$[Cs(4hob)(H_2O)]_n$ **5Cs**	3202	-	1529,1509	1376	143

[a] $\Delta\nu = \nu_{as}(CO_2)—\nu_s(CO_2)$.

2.2. X-ray Crystal Structures

The carboxylate-binding modes observed in the complexes are shown in Figure 1, and a summary of the features of the structures is given in Table 2. The increase in the average metal–oxygen bond distances, as well as the increase in the coordination number, can be observed as the ionic radius increases from Li to Cs [29] within each series. However, **4K** stands out as an outlier in this trend (Table 2). The ESI† provides detailed information regarding the bond distances and angles.

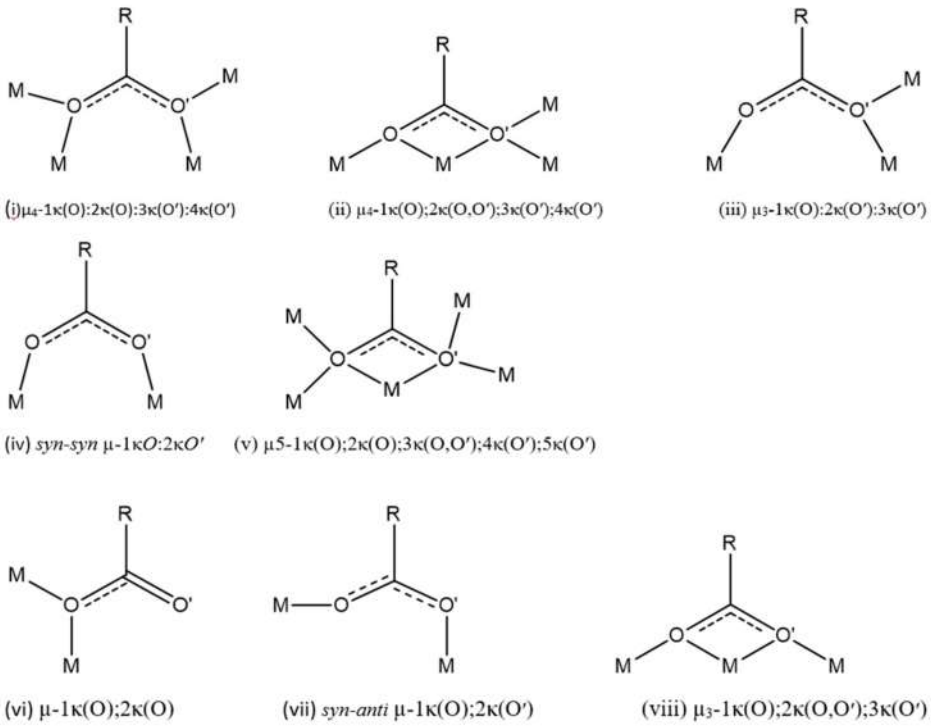


Figure 1. Different coordination modes observed for 3tpc, 2m3fur, 3fur, 4hocin, and 4hob ions.

2.2.1. M(3tpc) Complexes (1M = 1Li, 1K, 1Rb, 1Cs)

$[Li_2(3tpc)_2]_n$ (**1Li**) crystallises in the *Pna*2_1 space group as a two-dimensional network. There are two tetracoordinated metal atoms, each Li1 and Li2, with a tetrahedral geometry. Each lithium atom is coordinated by four μ_4-1κ(O):2κ(O):3κ(O′):4κ(O′) carboxylate oxygen atoms: Li1: O1, 3, 2#2, and 4#4, and Li2: O2, 3#3, 1#4, and 4#4. Li1 and Li2 are linked together in alternating six-member rings, forming a 1D chain produced by the bridging of five μ_4-1κ(O):2κ(O):3κ(O′):4κ(O′) carboxylate oxygen atoms (O1, O2, O4#4, O3, O4). The

Li1 … Li2 separation is 3.146(11) Å, and the Li1#4 … Li2 separation is 3.116(10) Å. The five oxygen atoms in the six-membered rings have distinct coordination angles: Li1–O1–C1 (139.3(4)°); Li2–O2–C1 (115.9(3)°); Li1–O4#4–Li2 (105.6(4)°); Li1-O3-C6 (138.7(4)°); and Li2#1-O4-C6 (115.6(3)°) (Figure 2).

Table 2. Crystallisation conditions, geometry, coordination number, carboxylate ligation, and average M-O bond distance for alkali-metal 3tpc, 2m3fur, 3fur, 4hocin, and 4hob complexes.

Compound	M Atom	Geometry	Coordination Number	Ligation	Avg M-O (Å)
1Li	Li1	Tetrahedral	4	4 × (i)	1.963
	Li2	Tetrahedral	4	4 × (i)	1.963
1K	K1	Irregular polyhedron	5	1 × (ii) [a]; 3 × (ii) [b]	2.791
	K2	Irregular polyhedron	5	1 × (ii) [a]; 3 × (ii) [b]	2.767
1Rb	Rb1	Distorted capped trigonal prismatic	7	3 × (iii); 4 × μ_4-H_2O	2.995
1Cs	Cs1	Cubic	8	8 × (i)	3.152
2Li	Li1	Tetrahedral	4	2 × (iv); 1 × H_2O; 2 × μ_2-H_2O	1.957
2K	K1	Distorted pseudo-pentagonal bipyramidal	8	1 × (ii) [a]; 3 × (v) [b]; 1 × (ii) [b]; 2 × μ_3-H_2O	2.841
	K2	Distorted pseudo-square pyramidal	6	1 × (v) [a]; 2 × (ii) [b]; 1 × (v) [b]; 1 × μ_3-H_2O	2.750
3Li	Li1	Tetrahedral	4	4 × (i)	1.978
4K	K1	Distorted tricapped trigonal prismatic	9	2 × (vi); 3 × μ_3-H_2O; 2 × μ_2-H_2O; 2 × μ_2-H_2O;	2.977
4Rb	Rb1	Irregular polyhedron	6	4 × (vii); 2 × phenolic O	2.932
4Cs	Cs1	Irregular polyhedron	8	1 × (viii) [a]; 2 × (viii) [b]; 2 × μ_2-H_2O; 2 × phenolic O	3.349
5Li	Li1	Tetrahedral	4	4 × (i)	1.953
5K	K1	Square antiprismatic	8	2 × (vi); 1 × H_2O; 3 × μ_3-H_2O; 2 × μ_2-H_2O	2.912
5Rb	Rb1	Square antiprismatic	8	4 × (i); 2 × μ_2-H_2O; 2 × phenolic O	3.049
5Cs	Cs1	Square antiprismatic	8	4 × (i); 2 × μ_2-H_2O; 2 × phenolic O	3.217

[a] Chelating; [b] unidentate.

The Li2#1-Li1-Li2-Li1#4 chain of the complex crosslinks with neighbouring chains through bridging 3tpc ligands, forming a 2D network. Li2 is connected to the Li1#3 metal atom of the neighbouring chain through oxygen atoms (O2 and O3#3), while Li1 is bound to Li2#2 through bridging oxygen atoms (O3 and O2#2). In both cases, there is a separation of 2.712(9) Å, forming four-membered rings that are perpendicular to each other (Figure 3). The longest metal–oxygen bond in the structure is between Li2 and O3#3, while the shortest bond is between Li1 and O3.

The complex $[K_2(3tpc)_2]_n$ (**1K**) crystallises in the orthorhombic $Pca2_1$ space group as a 2D polymer. The asymmetric unit is composed of two potassium atoms, K1 and K2, both of which are five-coordinated. The geometry around the five-coordinated K is distorted from any regular polyhedron due to the arrangements of three bridging ligands and one chelating ligand atom around the metal atoms. K1 and K2 are separated by a distance of 4.208(2) Å and are linked by two μ_4-1κ(O);2κ(O,O′);3κ(O′);4κ(O′) ligands (O1,2 and O3,4) (Figure 4).

The former pair are chelated to K1 and bridge to K2, K2#2, and K2#3, while the latter pair are chelated to K2 and bridge to K1, K1#1, and K1#5 through carboxylate oxygen bonds (Figure 5). The dinuclear units are connected into a 1D chain by the *chelating*, *bridging* ligands between K2 and K1#6 (through O1#6), as well as between K1 and K2#4 (through O4#4), separated by distances of 4.058 (2) Å and 4.108 (2) Å, respectively. The 1D polymeric chain extends into a 2D network via the coordination of the bridging ligand (through O3

and O2#1) to the metal atoms in neighbouring chains with an inter-chain distance (K1 ... K1#1 and K2 ... K2#1) of 3.9751 (1) Å. The longest metal–oxygen bond is 3.155(7) Å between K1 and O2, involving a chelating oxygen atom. The shortest metal–oxygen bond is 2.635(6) Å between K2 and O1#6, arising from a bridging oxygen atom.

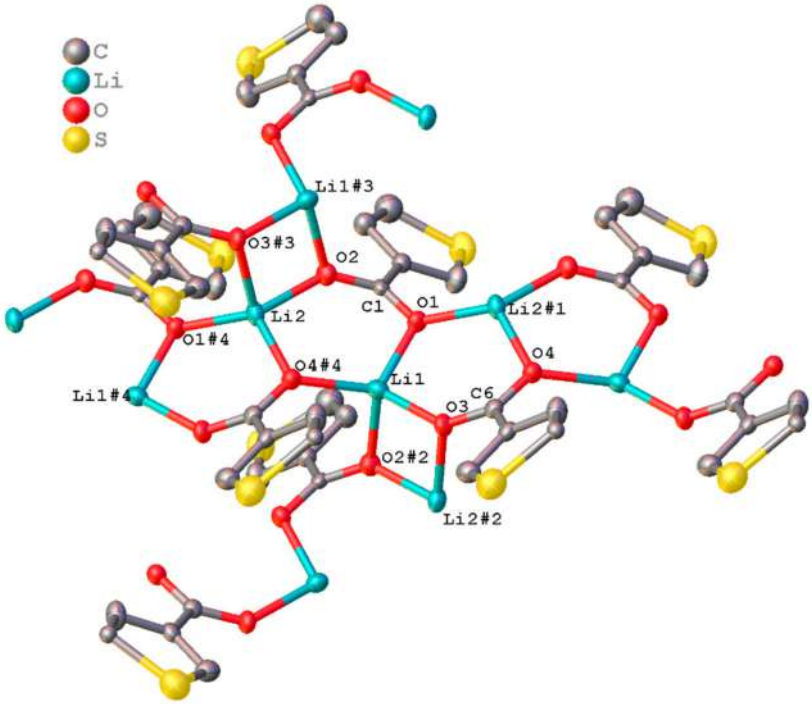


Figure 2. The asymmetric unit of $[Li_2(3tpc)_2]_n$ **1Li** expanded to show the Li coordination spheres. Symmetry code: $^{\#1}$ + X,1 + Y, + Z; $^{\#2}$ 1/2 + X,1/2-Y, + Z; $^{\#3}$ -1/2 + X,1/2-Y, + Z; $^{\#4}$ + X,-1 + Y, + Z.

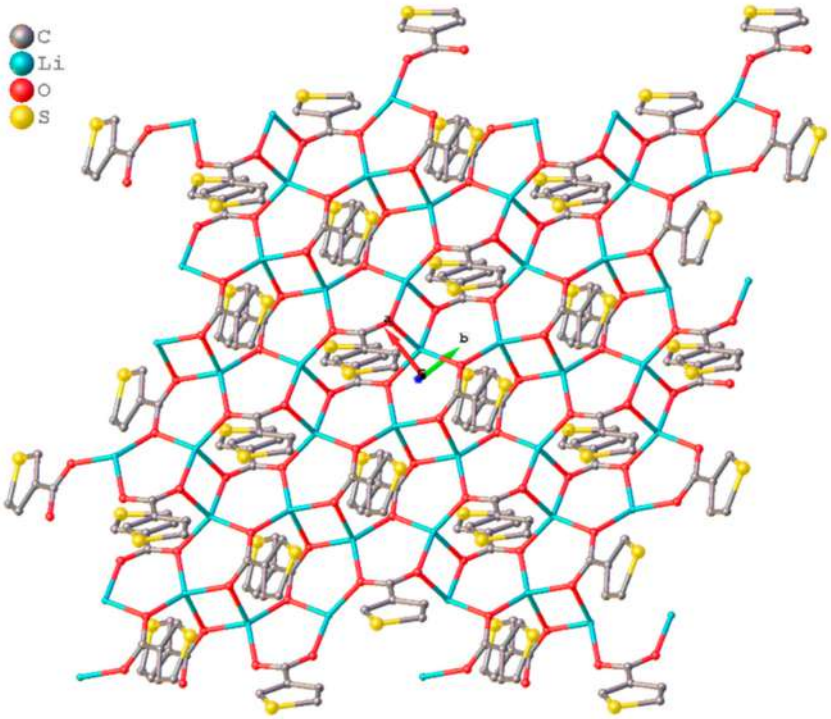


Figure 3. Projection along the c-axis showing the crystal packing of **1Li** into a **2D** network.

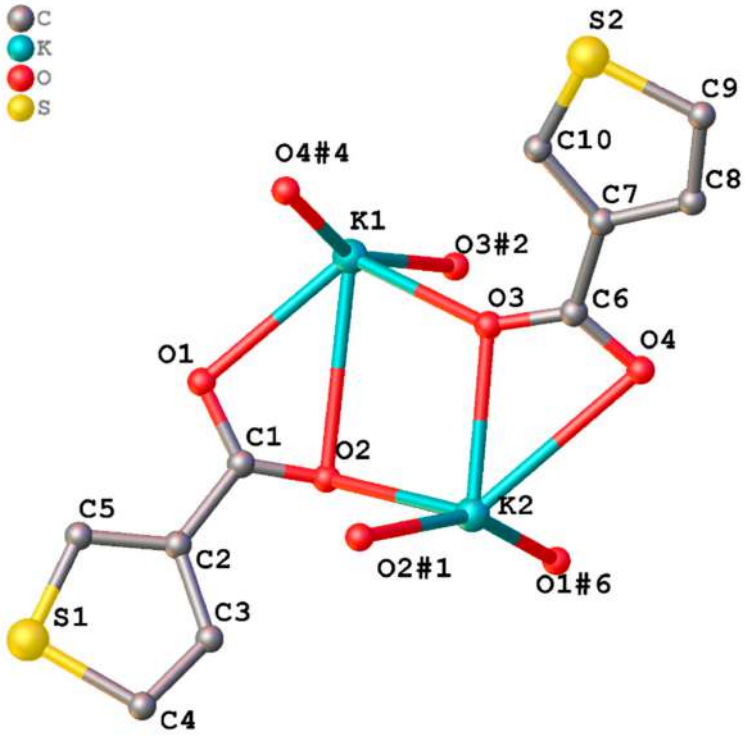


Figure 4. The asymmetric unit of $[K_2(3tpc)_2]_n$ **1K** expanded to show the K coordination. Symmetry code: #1 + X,-1 + Y, + Z; #2 + X,1 + Y, + Z; #4 1/2 + X,-Y, + Z; #6 -1/2 + X,1-Y, + Z.

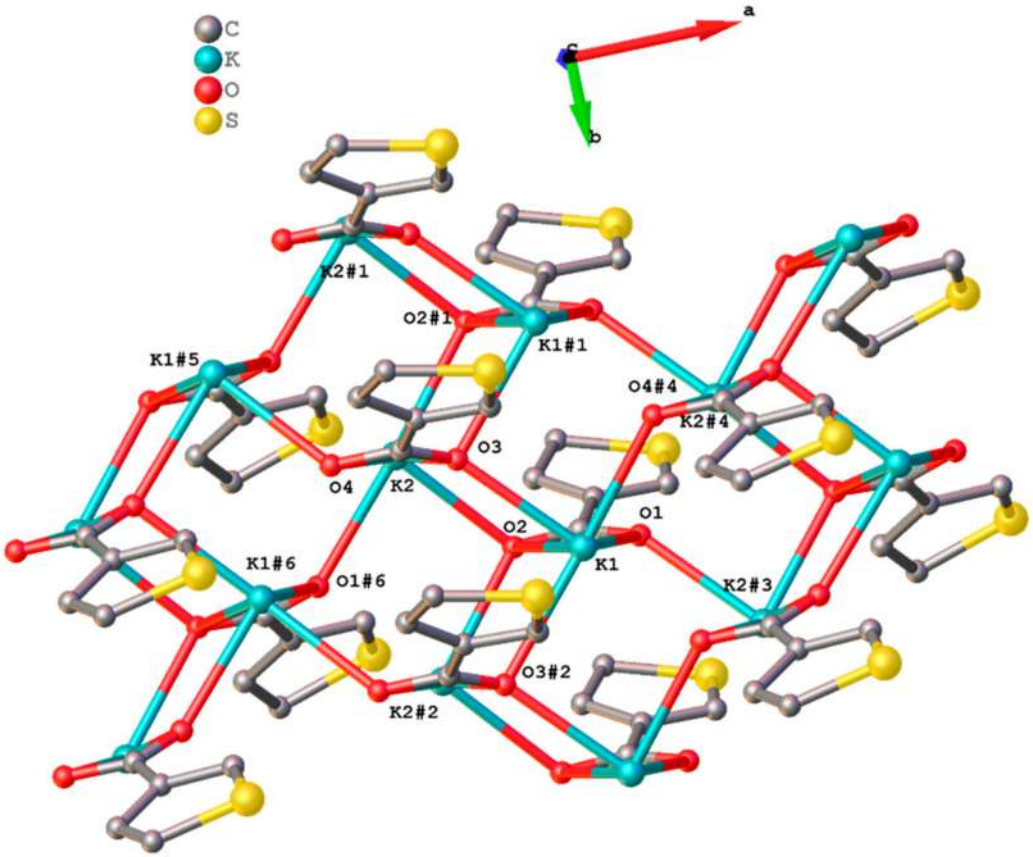


Figure 5. A c-axis projection of the crystal packing of **1K**. Symmetry code: #1 + X,-1 + Y, + Z; #2 + X,1 + Y, + Z; #3 1/2 + X,1-Y, + Z; #4 1/2 + X,-Y, + Z; #5 -1/2 + X,-Y, + Z; #6 -1/2 + X,1-Y, + Z.

The complex $[Rb(3tpc)(H_2O)]_n$ (**1Rb**) consists of mononuclear units and crystallises in the monoclinic $P2_1/c$ space group (Figure 6). The seven-coordinate rubidium metal centres have a distorted capped trigonal prismatic geometry. Three of the seven coordinating oxygen atoms are provided by carboxylate ligands, while the remaining four oxygen atoms are from water. In the structure, only one carboxylate binding mode is observed, with three μ_3-1κ(O):2κ(O′):3κ(O′) carboxylates coordinating through the oxygen atoms O1, O1#2, and O2#6. The four oxygen atoms in the ligated water molecules are O3, O3#4, O3#7, and O3#8, with each water oxygen bound to four rubidium atoms. Specifically, O3 binds to Rb1, Rb1#1, Rb1#2, and Rb1#7. μ_4-aqua ligands are rare but known [30–33]. Compound **1Rb** forms a one-dimensional (1D) polymer via bridged Rb1#7 . . . Rb1 . . . Rb1#1 chains. The separation between the Rb metal centres is Rb1 . . . Rb1#1 (5.1213(12) Å) and Rb1#7 . . . Rb1 (4.8220(13) Å), respectively, with Rb1#7 . . . Rb1 . . . Rb1#1 at an angle of 51.910(19)°.

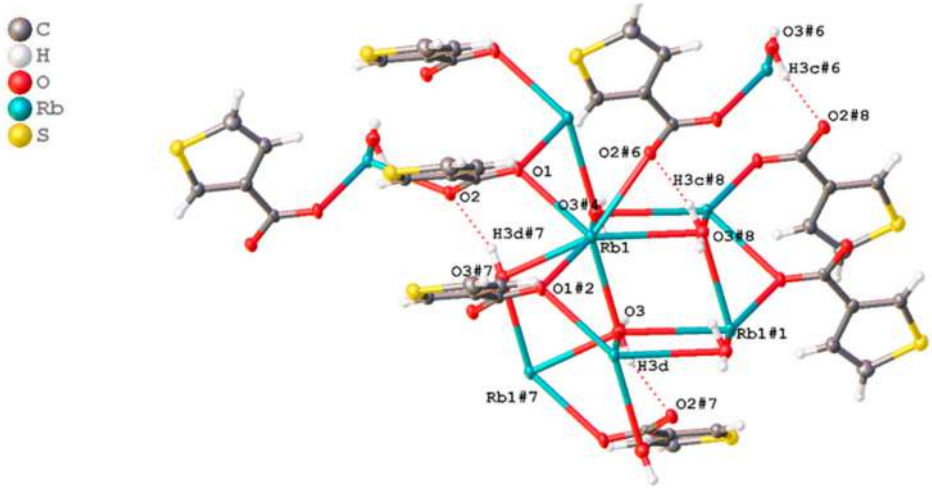


Figure 6. The immediate coordination environment around Rb metal atom in $[Rb(3tpc)(H_2O)]_n$ **1Rb**. Symmetry code: #1 1-X,1/2 + Y,3/2-Z; #2 + X,1 + Y, + Z; #4 + X,-1 + Y, + Z; #6 + X,1/2-Y,1/2 + Z; #7 1-X,2-Y,1-Z; #8 1-X,-1/2 + Y,3/2-Z.

The longest Rb–O bond is from a water oxygen, Rb1–O3#8 (3.278(3) Å), and the shortest bond is for a bridging carboxylate Rb1–O1 (2.828(2) Å). The coordinated water oxygens O3 and O3#4 appear to connect the wave-like 1D polymers into a two-dimensional (2D) chain (Figure 7). All four water oxygen atoms found in the Rb coordination environment are involved in hydrogen bonding to carboxylate-O (Figure 6, Table S12), forming an extensive network of hydrogen bonding and further linking the 2D network together.

The polymeric complex $[Cs\{H(3tpc)_2\}]_n$ (**1Cs**) crystallises in the space group *C*2/*c*. Although the reaction stoichiometry was intentionally maintained at 1:1 Cs:3tpcH to avoid the incorporation of excess unreacted proligands in the structure, only partial deprotonation of the carboxylic acid group occurred. As a result, a hydrogen atom is symmetrically shared between two carboxylate groups, making a $(HL_2)^-$ ligand. The Cs atom is eight-coordinate with cubic geometry. In the asymmetric unit, the ligand bridges Cs1 and Cs1#2 via O1, and the only binding mode observed for the structure is μ_4-1κ(O):2κ(O):3κ(O′):4κ(O′). Even though the crystal structure of **1Cs** does not indicate the presence of either coordinated or lattice water molecules, the TGA of the bulk sample revealed the presence of 0.5 water molecules.

The observed partial deprotonation results in both the Cs^+ cation and O–H hydrogen atom being located on crystallographic inversion centres. In the asymmetric unit, both entities carry an effective charge of 0.5+, effectively counterbalancing the negative charge of the $3tpc^-$ anion. The oxygen atoms of the carboxylate groups from the two 3tpc ions are involved in forming symmetrical bonds with the hydrogen atom located on the inversion centre (Figure 8). This results in O–H bond lengths of 1.232(4) Å, which are longer than those

of a typical O–H covalent bond (0.97 Å) [34], but shorter compared to the lengths observed in O..H hydrogen-bond interactions. The symmetrical hydrogen bond that is observed is commonly accompanied by a significantly short O...O distance (2.460 Å here). The coordinated O from the $3tpc^{-}$ anion bridges the 1D polymers, forming a two-dimensional (2D) chain (Figure 9).

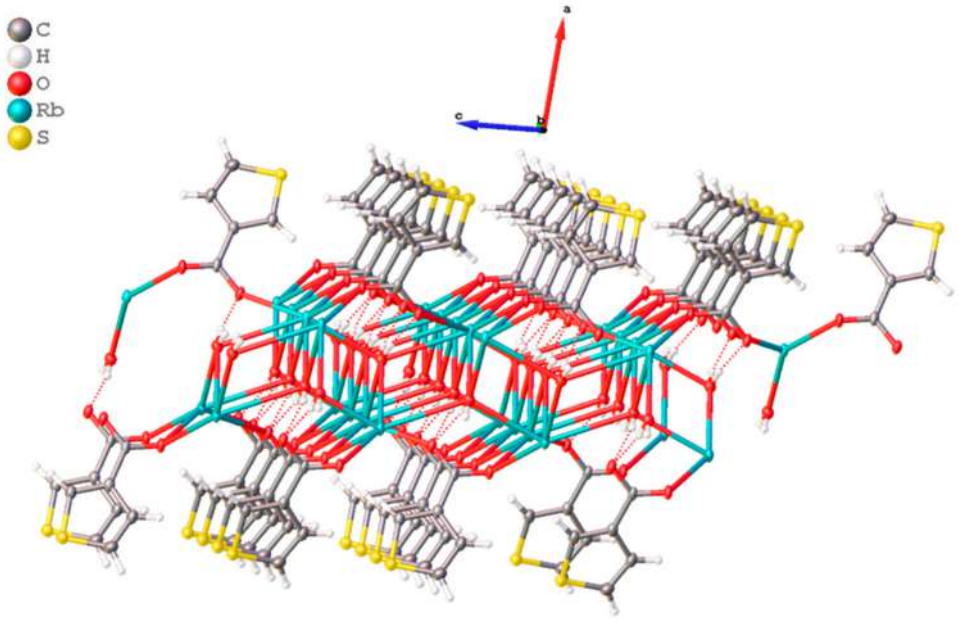


Figure 7. Projection along the b-axis of **1Rb** showing the 2D network.

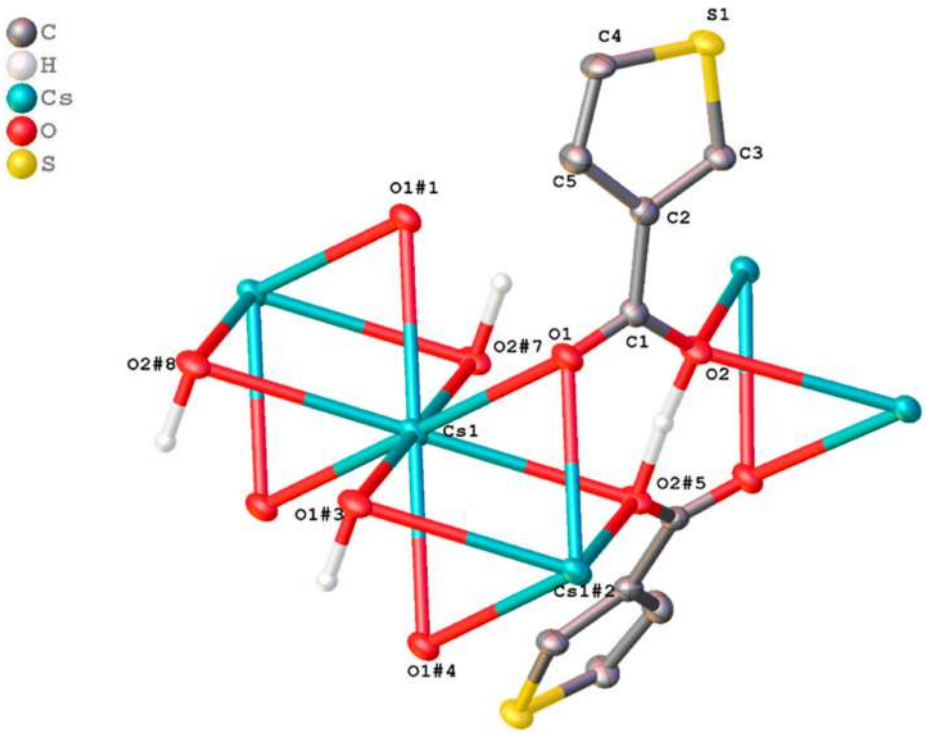


Figure 8. The asymmetric unit of $[Cs\{H(3tpc)_2\}]_n$ **1Cs** expanded to illustrate the Cs coordination, highlighting the presence of a centrosymmetric hydrogen atom located between the two carboxylate groups. Symmetry code: $^{\#1}$ + X,1 + Y, + Z; $^{\#2}$ + X,-1 + Y, + Z; $^{\#3}$ 1-X,2-Y,1-Z; $^{\#4}$ 1-X,1-Y,1-Z; $^{\#5}$ 1-X, + Y,1/2-Z; $^{\#7}$ 1-X,1 + Y,1/2-Z; $^{\#8}$ + X,2-Y,1/2 + Z.

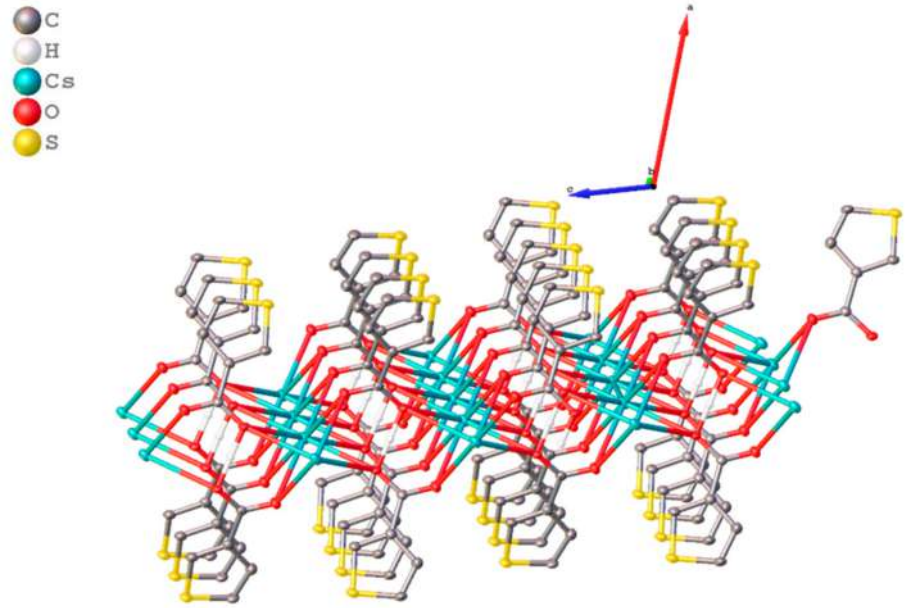


Figure 9. The crystal packing of **1Cs** is shown in a b-axis projection. The hydrogen atoms, except for those forming symmetrical hydrogen bonds, have been omitted for clarity.

Despite multiple attempts to refine the hydrogen atom as disordered, appearing on either side of the inversion centre, it consistently reverted back to the inversion centre. Determining the precise location of a hydrogen atom solely based on X-ray diffraction data presents a challenge. Nonetheless, by examining the distance between oxygen atoms and analysing the hydrogen atom behaviour during refinement, we have confidence in its location. Therefore, we can conclude that only the partial deprotonation of 3tpcH occurs in **1Cs**.

2.2.2. M(2m3fur) Complexes (2M = 2Li, 2K)

The dinuclear unit of $[Li_2(2m3fur)_2(H_2O)_3]$ (**2Li**) consists of two tetracoordinated lithium metal centres, and it crystallises in the orthorhombic *Pbcn* space group. The stereochemistry around each metal is tetrahedral (Figure 10).

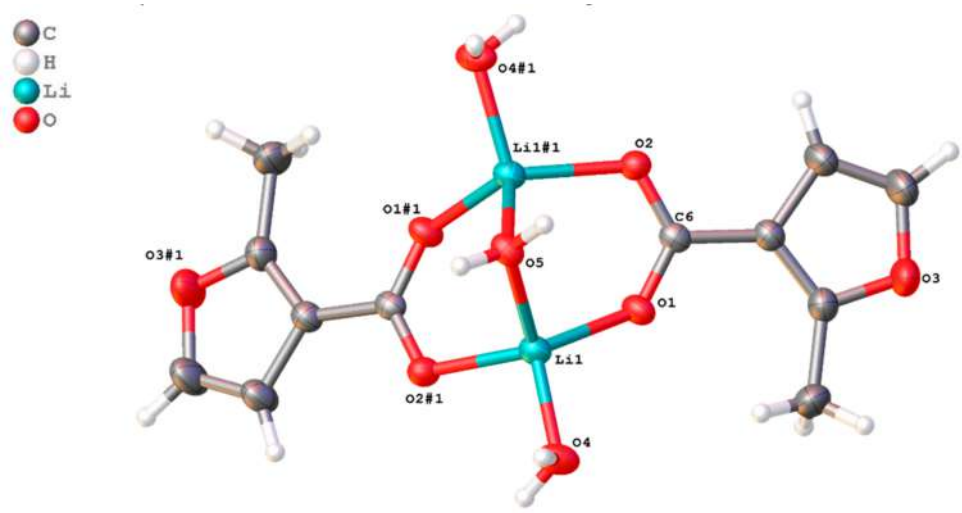


Figure 10. Molecular diagram of the dinuclear $[Li_2(2m3fur)_2(H_2O)_3]$ (**2Li**). Symmetry code: $^{\#1}$ 1-X, + Y,1/2-Z.

The complex **2Li** contains two *syn–syn* μ-1κ*O*:2κ*O*′ carboxylate ligands (O(1,2) and symmetry-related O(1#1,2#1) and three-coordinated (O4, O4#1,O5) water molecules. The

Li1 . . . Li1#1 separation measured is 2.758(8) Å. The shortest Li-O bond is formed by the ligated water molecule O4 and its symmetry equivalent O4#1 (1.893(3) Å), while the longest bond is Li1-O5 (2.034(3) Å) of the bridging water molecule. The bridging oxygen atoms of the carboxylate ligands form an angle of 123.49(14)° at O1-Li1-O2#1 (and the symmetry-equivalent O1#1-Li1-O2). The O5 oxygen atom from a coordinated water molecule bridges the two metal atoms of the dinuclear complex, forming a Li1-O5-Li1#1 angle of 85.41(15)°. The angle between the bound water molecules and the metal is *cisoid* for O4-Li-O5 and its symmetry equivalent, O4#1-Li1#1-O5 (116.51(13)°).

The two-dimensional polymer $[K_2(2m3fur)_2(H_2O)]_n$ (**2K**) crystallises in the monoclinic $P2_1/c$ space group. Despite the crystal structure being a monohydrate, thermal analysis of the bulk precipitate indicated the presence of an extra water molecule. The asymmetric unit of the compound contains two distinct potassium metal centres. K1 is eight-coordinated; but it can be considered as pseudo-seven-coordinated if the carboxylate takes one coordinated site, resulting in a distorted pseudo-pentagonal bipyramidal stereochemistry. Thus, O4 and a chelating carboxylate are in axial positions, with an O4-K1-C7#5 angle of 168.53 (4)°, while O1, O1#5, O2#4, O7#2, and O7#6 are in equatorial positions. The six-coordinated K2 can be regarded as distorted pseudo-square pyramidal if the carboxylate is considered to occupy one coordination position. In this case, four basal oxygen atoms (O2#3, 4#1, 5, 7) form a square plane, while the carboxylate is in the axial position.

The carboxylate ligand binds in two unique modes: μ_5-1κ(O);2κ(O);3κ(O,O′);4κ(O′); 5κ(O′) and μ_4-1κ(O);2κ(O);3κ(O,O′);4κ(O′). Eight-coordinated K1 is ligated by two chelating oxygen atoms (O4#5,5#5) of a μ_4-1κ(O);2κ(O);3κ(O,O′);4κ(O′) linked carboxylate, bridging oxygen atoms (O1, O1#5, O2#4) of three μ_5-1κ(O);2κ(O);3κ(O,O′);4κ(O′);5κ(O′) ligands, one bridging oxygen atom (O4) of a μ_4-1κ(O);2κ(O);3κ(O,O′);4κ(O′) oxylatecarb, and two ligated water oxygen atoms (O7#2,7#6). K2 is surrounded by a μ_5-1κ(O);2κ(O);3κ(O,O′); 4κ(O′);5κ(O′) chelate (O1#1,2#1), two bridging oxygen atoms from a μ_4-1κ(O);2κ(O); 3κ(O,O′);4κ(O′) (O5,O4#1) ligand, one bridging oxygen atom from μ_5-1κ(O);2κ(O);3κ(O,O′); 4κ(O′);5κ(O′) (O2#3) bridges, and one ligated water oxygen atom (O7), resulting in a six-coordinate metal atom (Figure 11).

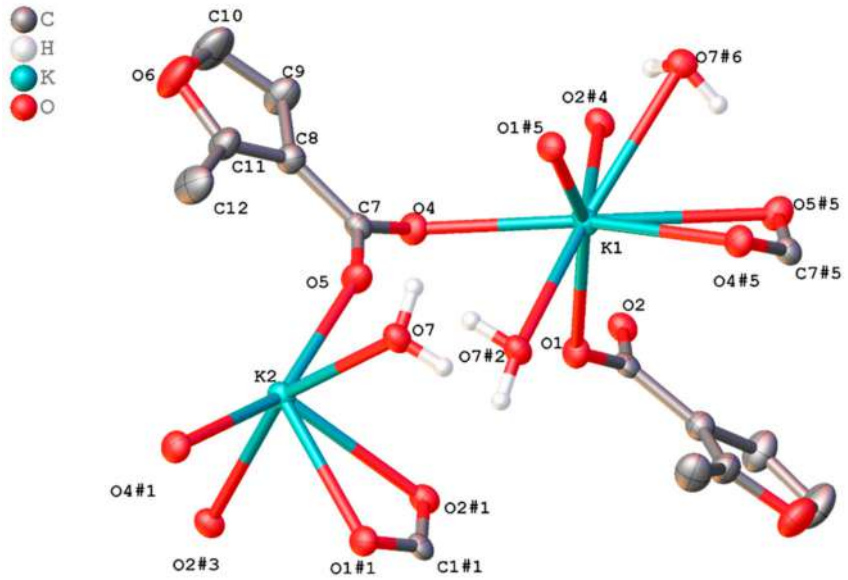


Figure 11. The expanded asymmetric unit of $[K_2(2m3fur)_2(H_2O)]_n$ **2K** extended to show the K1 and K2 coordination sphere. Symmetry code: #1 + X,3/2-Y,-1/2 + Z; #2 1-X,1-Y,1-Z; #3 1-X,1/2 + Y,3/2-Z; #4 1-X,1-Y,2-Z; #5 1-X,-1/2 + Y,3/2-Z; #6 + X,1/2-Y,1/2 + Z. #7 1-X,1 + Y,1/2-Z; #8 + X,2-Y,1/2 + Z.

The repeating asymmetric units in the one-dimensional polymeric chain are oriented in opposite directions with a slight wave. The propagation of the complex into a 1D polymer

occurs through bridged K2 . . . K1 . . . K2#7 . . . K1#7 . . . K2#8 chains, and four-membered rings of K1–O4–K2#7–O2#4 are formed between the adjacent asymmetric units in the 1D polymeric chain. Adjacent metal centres in **2K** have K2 . . . K1 separations of 6.1085(12) Å and K1 . . . K2#7 of 3.6743(8) Å. The average K–O bond lengths observed in **2K** are as follows: K1 with a bond length of 2.841 Å, and K2 with a bond length of 2.750 Å. The longer bond length observed for K1 can be attributed to its higher coordination number. The K–O bond distances vary within the structure, ranging from the shortest bond involving bridging K2-O5 (2.6548(12) Å) to the longest bond involving chelating K1-O5#5 (3.0462(13) Å). The latter bond length is consistent with K1 being the eight-coordinated metal centre in **2K**.

The adjacent polymeric chains are oriented in opposite directions, and they further extend to form a 2D network through the bridging of the water oxygen atoms, as well as the carboxylate oxygen, from within the chain to the neighbouring chain (Figure 12).

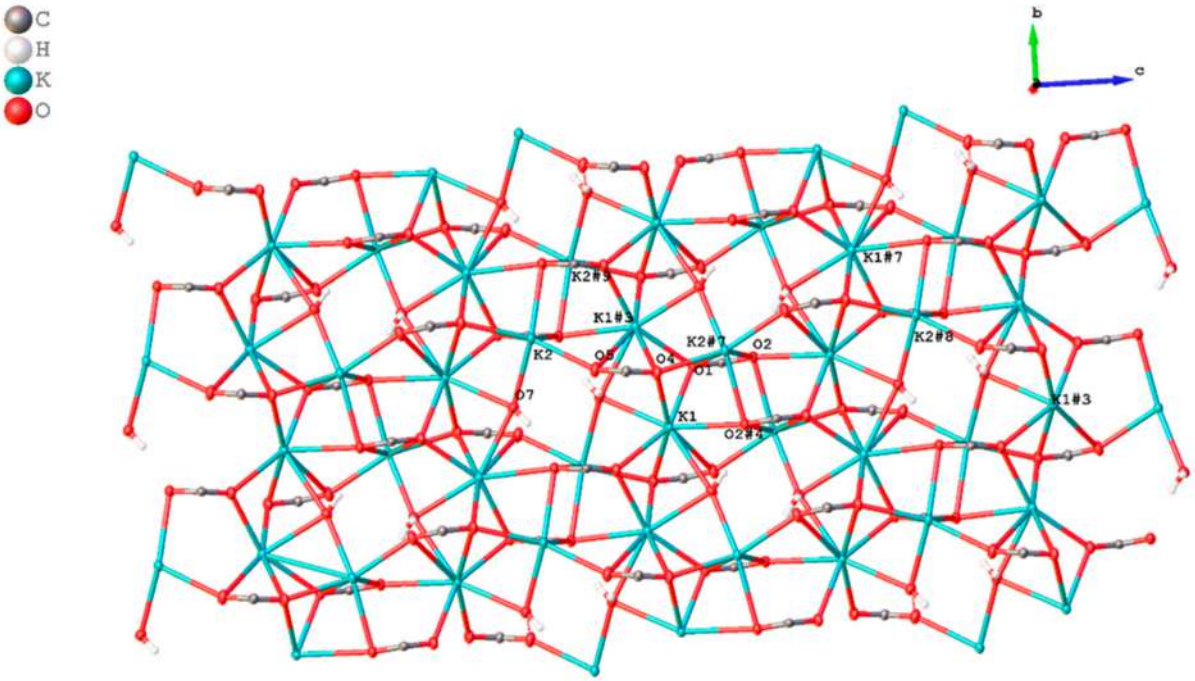


Figure 12. An a-axis projection of the crystal packing of **2K** (2-methyl-3-furan rings have been omitted for clarity). Symmetry code: [#3] 1-X,1/2 + Y,3/2-Z; [#4] 1-X,1-Y,2-Z; [#7] 1-X,1 + Y,1/2-Z; [#8] + X,2-Y,1/2 + Z; [#9] 1-X,2-Y,1-Z.

2.2.2.1. 2D Polymeric Chain of the $[Li(3fur)]_n$ (3Li) Complex

The complex $[Li(3fur)]_n$ (**3Li**) forms a 2D polymeric sheet with tetracoordinated lithium ions and crystallises in the monoclinic $P2_1/c$ space group with a tetrahedral stereochemistry. Four μ_4 -1κ(O);2κ(O);3κ(O′);4κ(O′) oxygen atoms (O1, O1#3, O2#4, O2#5) complete the coordination sphere around the metal centre (Figure 13).

The Li–O bond lengths range from 1.935(3) Å (Li1-O1) to 2.025(3) Å (Li1-O1#3), with an average bond length of 1.978 Å. The two unique, alternating six-membered rings formed by the five-bridging oxygen atoms O1, O2, O2#4, O1#4, and O2#5 form the backbone of the 1D polymeric chain, where Li1#1 . . . Li1 . . . Li1#4 forms an angle of 114.93 (16)° with Li1-Li#1 and Li1-Li1#4 separations of 3.155(3) Å. The successive 1D chains are oriented in opposite directions, thereby constructing two types of chains. The carboxylate oxygen atoms O1, O1#3 of the carboxylate μ_4-1κ(O);2κ(O);3κ(O′);4κ(O′) ligand bridge lithium metals of neighbouring chains, leading to the formation of a two-dimensional (2D) network with a Li1-Li#3 distance of 2.758(5) Å (Figure 14).

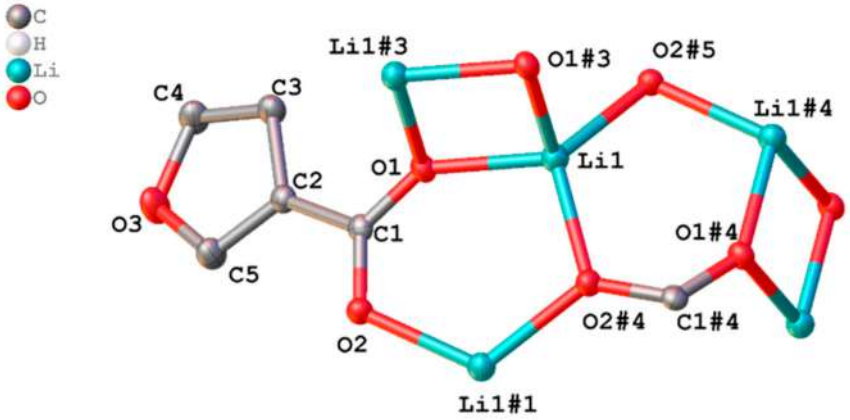


Figure 13. The asymmetric unit of $[Li(3fur)]_n$ (**3Li**) expanded to show the Li coordination sphere. Symmetry code: #1 1-X,1/2 + Y,3/2-Z; #3 1-X,-Y,1-Z; #4 1-X,-1/2 + Y,3/2-Z; #5 + X,-1 + Y, + Z.

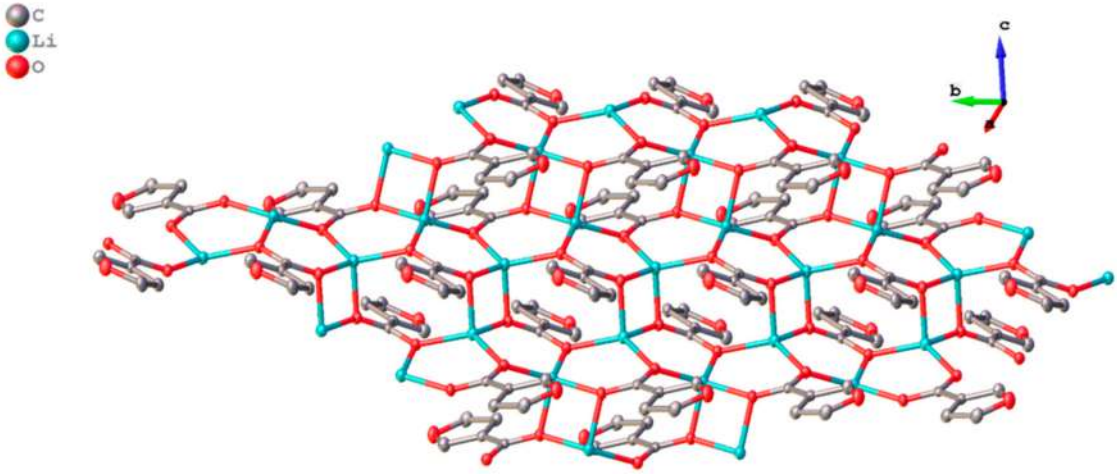


Figure 14. Crystal packing of **3Li** into a **2D** network (aromatic H atoms- are omitted for clarity).

2.2.3. M(4hocin) Complexes (4M = 4K, 4Rb, 4Cs)

The 2D polymeric complex $[K(4hocin)(H_2O)_3]_n$ (**4K**) crystallises in the space group $P2_1/c$ with a distorted tricapped trigonal prismatic geometry. The nine-coordinate potassium atoms are each attached to two μ-1κ(O);2κ(O) carboxylates and seven oxygen atoms from aqua ligands. The water oxygen atom O4 is bound to three potassium atoms (K1, K1#2, K1#3), while O5 and O6 are each bound to two potassium atoms: K1 and K1#3 and K1 and K1#1, respectively. The chain propagation exhibits a twist, with an angle of 126.48(2)° between K1#1, K1 and K1#2, and the distance between K1 and K1#1 is 3.9478 (7) Å. Four ligated aqua molecules link neighbouring polymeric chains that run in opposite directions, forming a 2D network through O4, O4#3, O5, and O5#3 (Figure 15). μ_3-H_2O coordination is known. For recent examples, see [35–37].

The longest metal–oxygen bond occurs between K1 and O5 (3.3762(14) Å), while the shortest bond is between K1 and O6 (2.7326(15) Å), both originating from ligated water molecules. The ligated water molecules form an extensive network of hydrogen bonding (Figure 16 and Table S12), along with the carboxylate oxygen atoms of the ligands, which further interconnect the adjacent 1D chains into a 2D intermolecular framework.

The three-dimensional polymeric complex $[Rb\{H(4hocin)_2\}]_n.nH_2O$ (**4Rb**) crystallises in the space group *C*2/*c*. Similar to compound **1Cs**, **4Rb** exhibits only partial deprotonation of the ligand despite utilising equal amounts of metal salt and ligand. The hydrogen atom exhibits centrosymmetric sharing between the carboxylate groups, making a $[HL_2]^-$ ligand, which is reinforced by the positioning of both the Rb^+ cation and the O...H...O hydrogen

atom on crystallographic inversion centres. A noticeably short O . . . O distance (2.469(2) Å) and the behaviour of the hydrogen atom observed during refinement further support this centrosymmetric arrangement and confirm the location of this hydrogen atom.

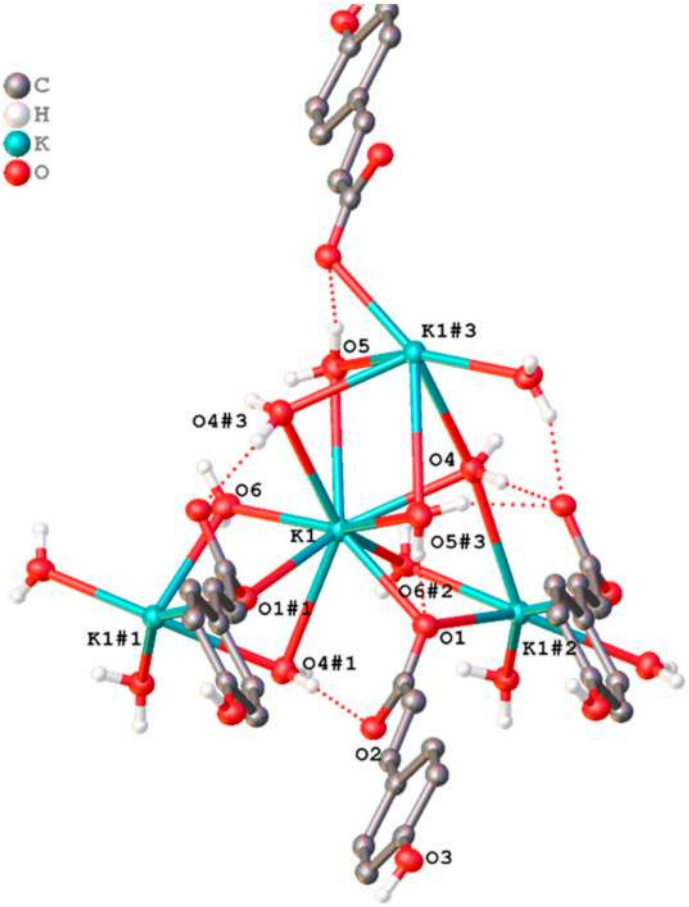


Figure 15. The immediate coordination environment of potassium in $[K(4hocin)(H_2O)_3]_n$ (**4K**) (hydrogen atoms, except for those forming H-bonds, are omitted for clarity). Symmetry code: $^{\#1}$ + X,3/2-Y,1/2 + Z; $^{\#2}$ + X,3/2-Y,-1/2 + Z; $^{\#3}$ -X,2-Y,-Z.

The asymmetric unit of **4Rb** consists of a single type of Rb atom and is expanded to depict the complete Rb coordination sphere in Figure 17. The arrangement of the six-coordinated Rb metal centre is distorted from any regular polyhedron. Contrary to **1Cs**, in the asymmetric unit of **4Rb**, the ligand is connected to Rb1 by the carboxylate oxygen atom (O1), which also binds to an H atom on the inversion centre. Within the structure, the water molecule functions as a focus for crystallisation through hydrogen bonding, and it does not form coordination bonds with the rubidium centre. The coordination sphere of **4Rb** consists of four bridging μ-1κ(O):2κ(O′) carboxylate-O atoms (O1, 1#5, 2#3, 2#4) and two phenolic-O atoms (O3#1 and O3#2) of the ligand.

The Rb-O bond lengths vary from a shorter distance of 2.8868(12) Å for Rb1-O1 and the symmetry-equivalent Rb1-O1#5, involving the bridging μ-1κ(O):2κ(O′) oxygen atoms (O1 and O1#5), to a longer distance of 2.9685(13) Å between Rb1-O2#3 and Rb1-O2#4, involving the bridging μ-1κ(O):2κ(O′) oxygen atoms (O2#3 and O2#4). The metal atoms within the 1D chains are linked together by phenolic-hydroxy groups of the 4-hydroxybenzoate ligands. The adjacent chains in the 2D network are further connected by the bridging carboxylate oxygen atoms. The hydrogen bonding involving the phenolic-hydroxy groups and the carboxylate oxygen atoms of the ligand with the lattice water of crystallisation holds the neighbouring chains of polymers together, forming an extended three-dimensional packing arrangement of the polymeric chains (Figure 18 and Table S12).

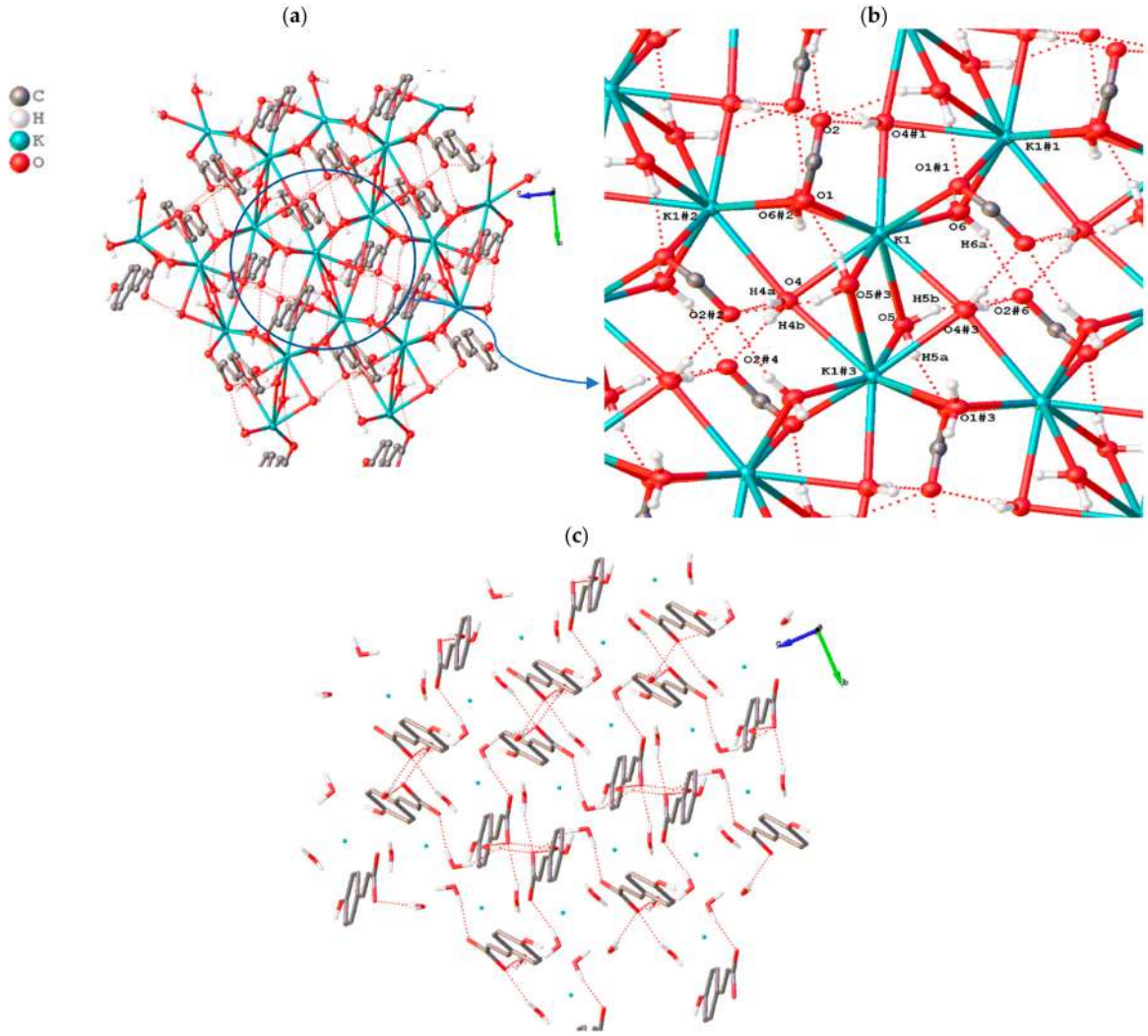


Figure 16. (**a**) A projection along the a-axis of **4K**. (**b**) H-bonded interaction in $[K(4hocin)(H_2O)_3]_n$. (**c**) The hydrogen-bonded network formed by the 4hocin and water molecules. (K–O coordination bonds are omitted for clarity). Symmetry code: #1 + X,3/2-Y,-1/2 + Z; #2 1-X,1-Y,1-Z; #3 1-X,1/2 + Y,3/2-Z; #4 1-X,1-Y,2-Z; #6 + X,1/2-Y,1/2 + Z.

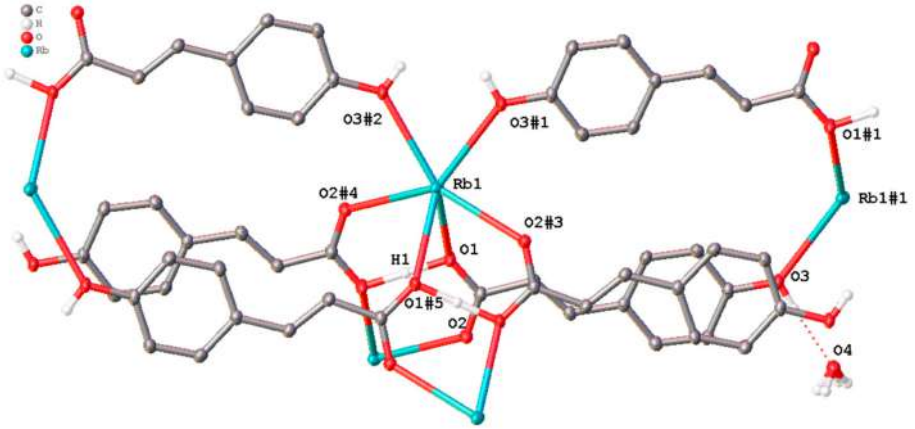


Figure 17. The expanded asymmetric unit of **4Rb** reveals the coordination of Rb atoms. (H atoms of the ligand, except for the phenolic hydroxyl group, are omitted for clarity; H of $H(4hocin)_2$—is H1.) Symmetry Code: #1 3/2-X,3/2-Y,1-Z; #2 -1/2 + X,3/2-Y,-1/2 + Z; #3 + X,1-Y,1/2 + Z; #4 1-X,1-Y,-Z; #5 1-X, + Y,1/2-Z.

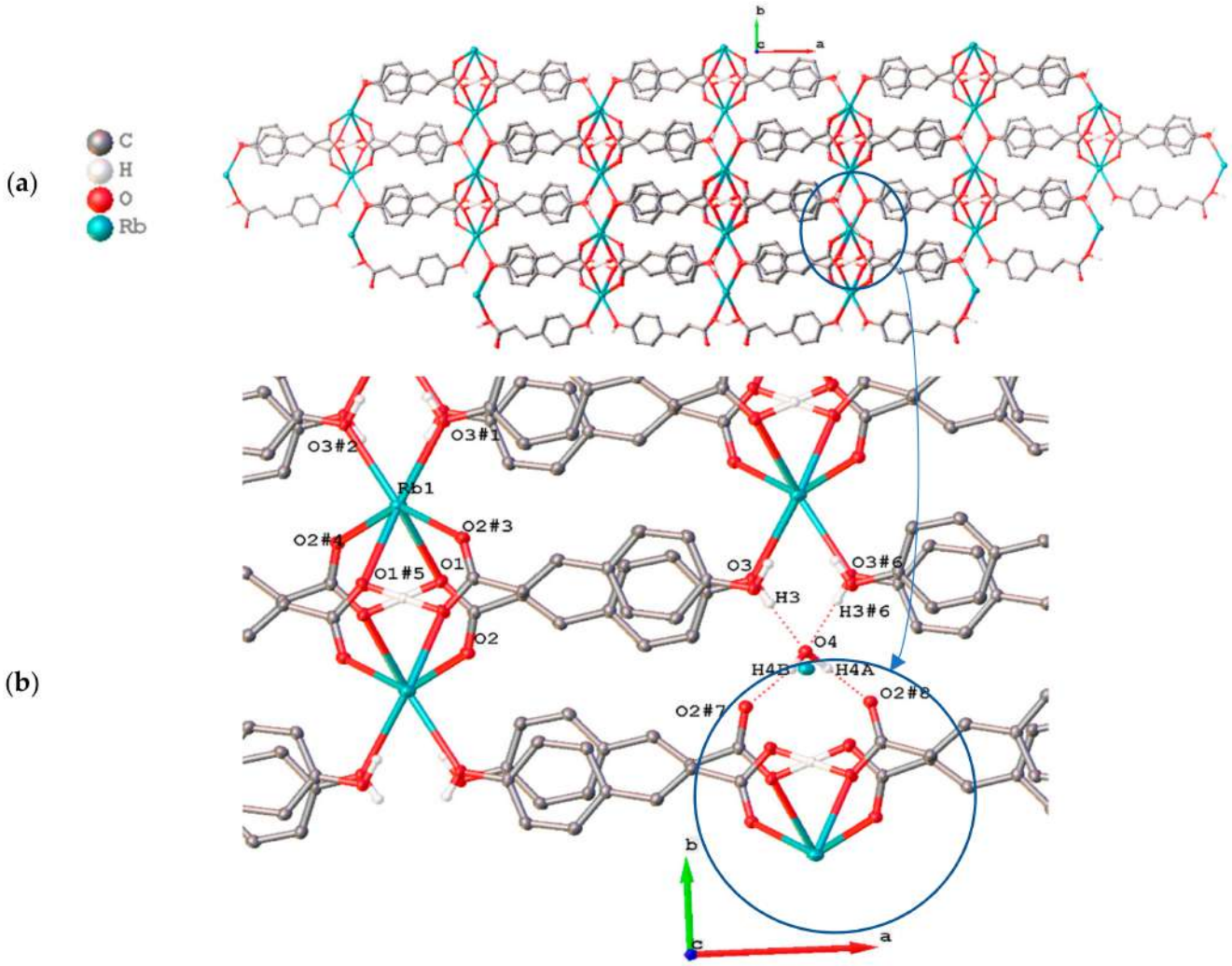


Figure 18. (**a**) A c-axis projection of the crystal packing of **4Rb**. (**b**) An alternative view of the crystal packing by omitting the Rb-O coordination to show the hydrogen bonds forming an extended 3D packing arrangement. $^{\#1}$ + X,3/2-Y,-1/2 + Z; $^{\#2}$ 1-X,1-Y,1-Z; $^{\#3}$ 1-X,1/2 + Y,3/2-Z; $^{\#4}$ 1-X,1-Y,2-Z; $^{\#5}$ 1-X,-1/2 + Y,3/2-Z; $^{\#6}$ + X,1/2-Y,1/2 + Z. $^{\#7}$ 1-X,1 + Y,1/2-Z; $^{\#8}$ + X,2-Y,1/2 + Z.

The X-ray crystal structure of $[Cs(4hocin)(H_2O)]_n$ (**4Cs**) reveals **a** monoclinic crystal system with a $P2_1$ space group. The eight-coordinate caesium atoms have two bridging oxygen atoms (O1, O2#2) and two chelating oxygen atoms (O1#1,2#1) from three μ_3-1κ(O);2κ(O,O′);3κ(O′) ligands, two water molecules (O4, O4#3), and two phenolic oxygen atoms of the ligand (O3#4, O3#5). Four oxygen atoms are close to the plane with the Cs centre, while the other four oxygen atoms sit on one side of the plane. This arrangement creates an irregular eight-coordinate polyhedron (Figure 19).

The Cs-O bond lengths for the bridging carboxylates are consistently shorter than their chelating counterparts (Table S8). The angle between the bridging water oxygen atoms O4 and O4#3, which originates from the adjacent caesium atom, has an O4-Cs1-O4#3 angle of 138.84(10)°. The carboxylate-O1,2, as well as the phenolic oxygen atom O3#5, link the metal centres into a 1D chain with a Cs1 . . . Cs1#6 distance of 4.3870(9) Å and a Cs1#1...Cs1 . . . Cs1#6 angle of 180°. A phenolic oxygen atom, O3, bridges an adjacent metal centre in neighbouring chains, forming a 2D-layer network in the ac-plane (Figure 20a). A projection along the a-axis (Figure 20b) illustrates the interconnection of these 2D networks via a bridging polydentate ligand (via O1, 2), a coordinated aqua molecule (O4), as well as hydrogen-bonding interactions (Table S12) into an overall 3D structure.

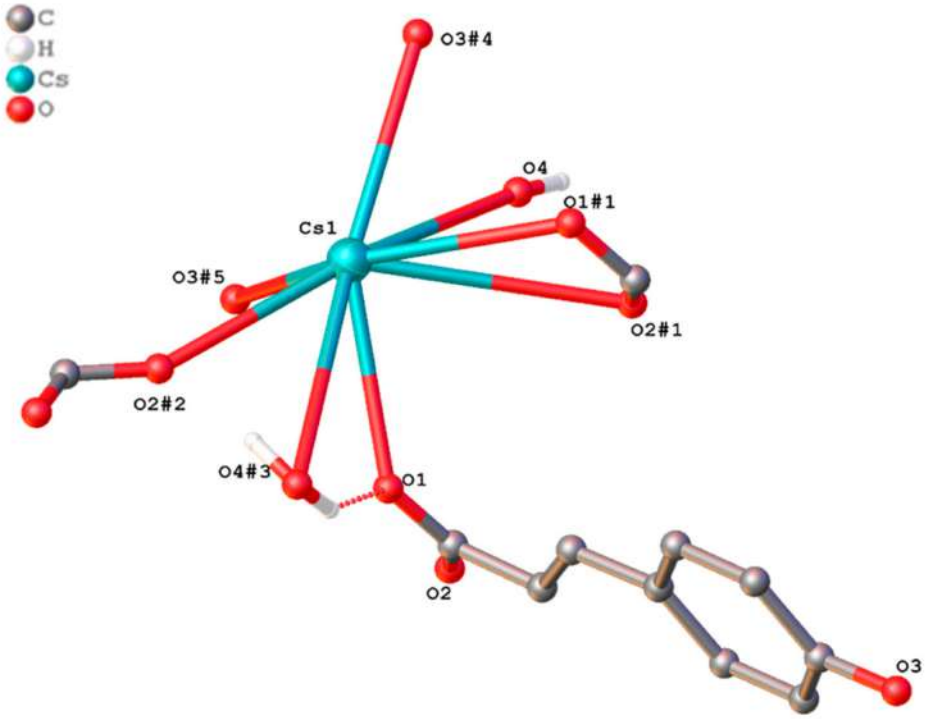


Figure 19. The asymmetric unit of $[Cs(4hocin)(H_2O)]_n$ (**4Cs**) expanded to show the complete Cs coordination sphere. Symmetry code: #1 1 + X, + Y, + Z; #2 -X,1/2 + Y,2-Z; #3 1-X,1/2 + Y,2-Z; #4 + X, + Y,-1 + Z; #5 -1 + X, + Y,-1 + Z.

2.2.4. M(4hob) Complexes (5M = 5Li, 5K, 5Rb, 5Cs)

The complex $[Li(4hob)]_n$ (**5Li**) crystallises in the monoclinic $P2_1/c$ space group and exhibits similar ligand-binding modes and coordination environments to the **3Li** structure (Table 2). Analogous to the **3Li** structure, the structure of **5Li** also forms a 1D polymeric chain through the two alternate six-membered rings involving the bridging oxygen atoms O1, O2, O2#4, O1#4, and O2#5 (Figure 21).

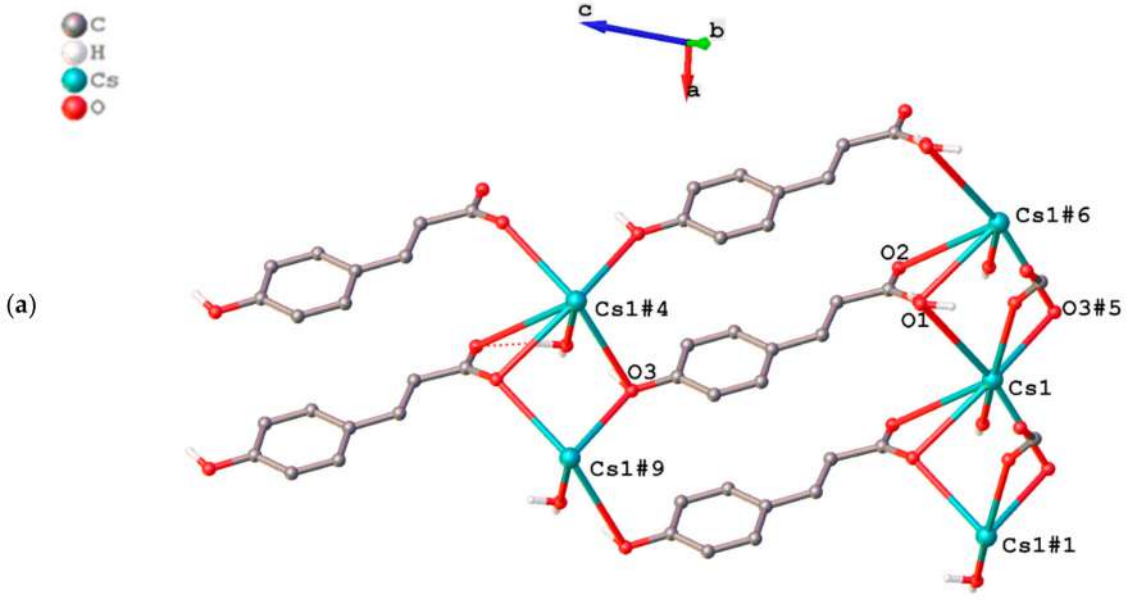


Figure 20. *Cont.*

(**b**)

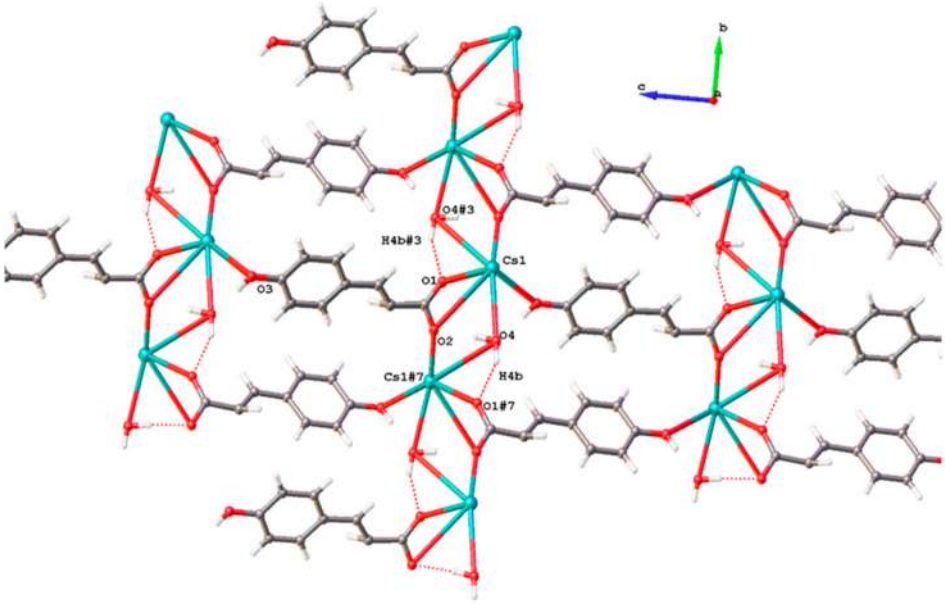


Figure 20. (**a**) A projection along the ac-plane shows the formation of a 2D-layer network of **4Cs** (H atoms, except for those forming H-bonds, are omitted for clarity). (**b**) A projection along the a-axis showing interaction that links the 2D networks together. Symmetry code: #1 + X,3/2-Y,-1/2 + Z; #3 1-X,1/2 + Y,3/2-Z; #4 1-X,1-Y,2-Z; #5 1-X,-1/2 + Y,3/2-Z; #6 + X,1/2-Y,1/2 + Z; #7 1-X,1 + Y,1/2-Z; #9 1+X,+ Y,1+Z.

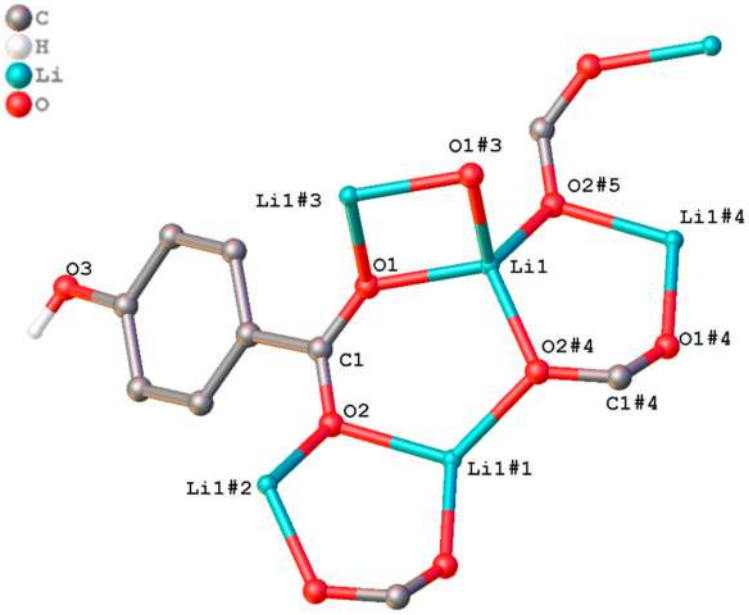


Figure 21. The asymmetric unit of $[Li(4hob)]_n$ (**5Li**) expanded to show the Li coordination sphere. Symmetry code: #1 1-X,1/2 + Y,1/2-Z; #2 +X,1 + Y, + Z; #3 1-X,-Y,1-Z; #4 1-X,-1/2 + Y,1/2-Z; #5 + X,-1 + Y, + Z.

In comparison, the compound **5Li** forms an angle of 109.6(4)° between Li1#1 ... Li1 ... Li1#4, with Li1 ... Li1#1 and Li1 ... Li1#4 separations of 3.086(8) Å. The shortest and longest Li-O bonds are attributed to Li1-O1 (1.921(7) Å) and Li-O1#3 (1.969(8) Å), respectively. A 2D layer is formed in a similar manner to the **3Li** compound through the bridging oxygen atoms (O1, O1#3) of the μ_4-1κ(O);2κ(O);3κ(O′);4κ(O′) ligand, linking Li ... Li1#3 at a distance of 2.700(14) Å (Figure 22). Although the crystallographic determination

indicated the compound as anhydrous, the elemental analysis data of the complex revealed the presence of a quarter of a water molecule.

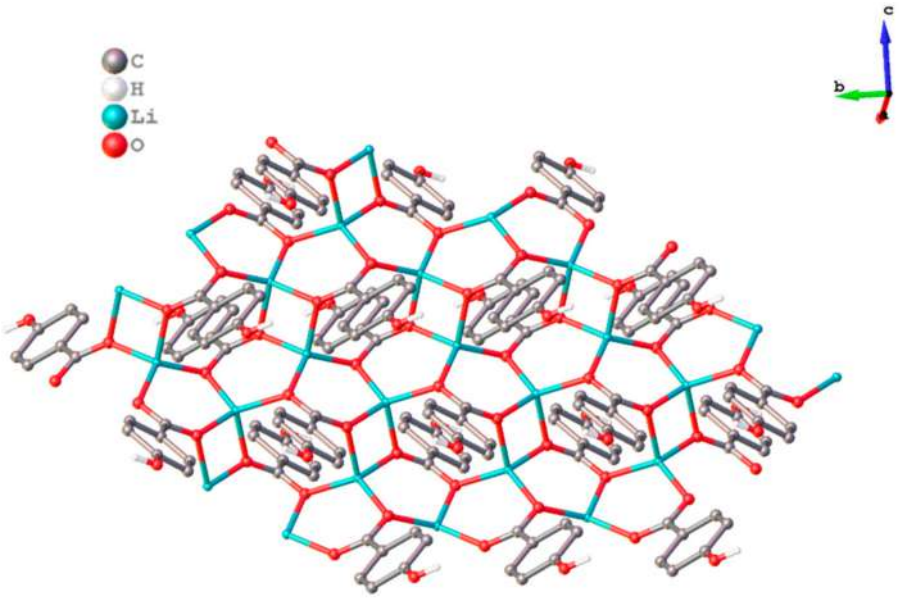


Figure 22. Extended diagram of **5Li** (aromatic C-H bonds are omitted for clarity).

The $[K(4hob)(H_2O)_3]_n$ (**5K**) complex forms a 2D polymeric sheet with eight-coordinate potassium ions and crystallises in the monoclinic $P2_1/c$ space group with a square antiprismatic array. A partial representation of the polymeric structure is shown in Figure 23. In the asymmetric unit, there is one μ_2-1κ(O):2κ(O) carboxylate bond (binding through O2), along with three ligated water molecules (O4, O5, and O6). The metal atom achieves a total coordination of eight by interacting with another μ_2-1κ(O):2κ(O) oxygen atom (O2#1) and three additional ligated water oxygen atoms (O4#2, O5#3, O5#4) from adjacent metal atoms. The structure forms a nonlinear 1D polymeric chain through bridging oxygen O2, connecting K1 and K1#2 and O2#1 between the K1 and K1#1 atoms (both at 3.9243(7) Å), with K1#1 . . . K1 . . . K1#2 at an angle of 128.53(2)°.

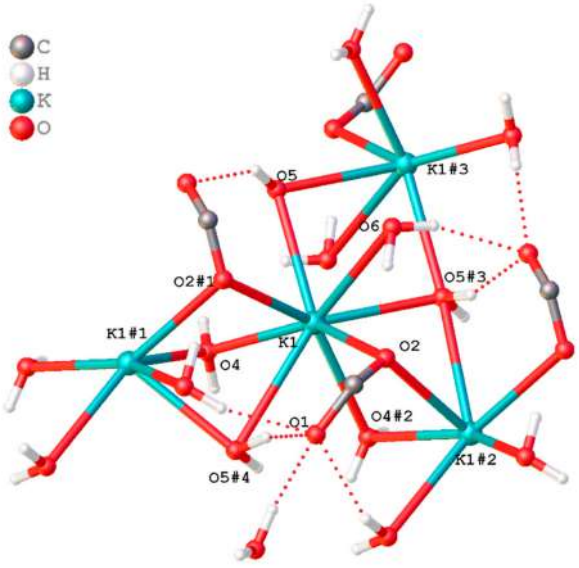


Figure 23. The asymmetric unit of $[K(4hob)(H_2O)_3]_n$ (**5K**) expanded to show the K coordination. Symmetry code: #1 + X,3/2-Y,-1/2 + Z; #2 + X,3/2-Y,1/2 + Z; #3 2-X,2-Y,1-Z; #4 2-X,-1/2 + Y,1/2-Z.

The average K-O bond length observed in complex **5K** is 2.9123 Å, with the shortest bond being K1-O4 (2.734(13) Å), and the longest bond being K1-O5#4 (3.172(5) Å). Both the longest and shortest bonds involve aqua ligands rather than any of the bridging carboxylate oxygens. The adjacent polymeric chains connect to form a 2D network through the bridging of the water oxygen atoms (O5, O5#3). There is a significant presence of hydrogen bonding in the system, involving the carboxylate oxygen atoms and the OH groups of all six-coordinated water molecules. Figure 24 illustrates the hydrogen-bonding pattern observed, while Table S12 provides the corresponding hydrogen-bond lengths. These hydrogen bonds play a crucial role in holding the neighbouring chains of polymers tightly together, further connecting the extended two-dimensional packing. It is noteworthy that none of the phenolic-hydroxy groups participate in these hydrogen-bonding interactions.

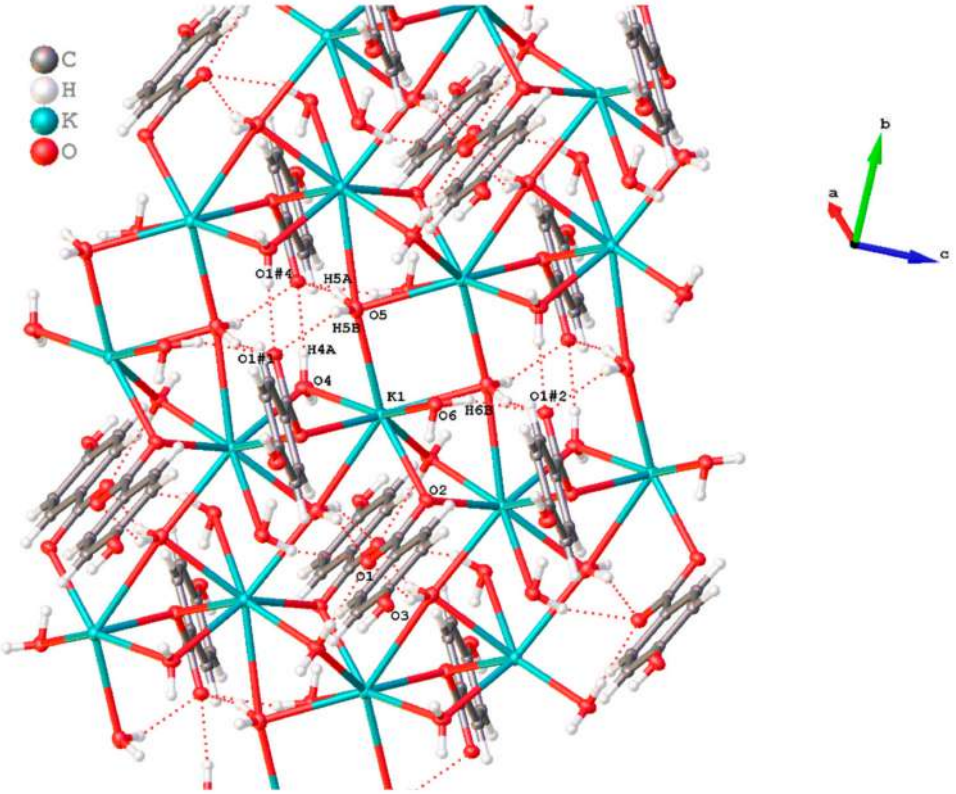


Figure 24. The packing diagram of the 1D polymeric chains of **5K** linked by O . . . H...O hydrogen bonds into a 2D network. (The 1D polymeric chain is propagating along the *c*-axis). Symmetry code: #1 + X,3/2-Y,-1/2 + Z; #2 + X,3/2-Y,1/2 + Z; #4 2-X,-1/2 + Y,1/2-Z.

$[Rb(4hob)(H_2O)]_n$ (**5Rb**) crystallises in the monoclinic $P2_1/c$ space group with a square antiprismatic donor atom arrangement around Rb. Figure 25 illustrates the structure of the extended asymmetric unit of **5Rb**.

Within the polymeric structure, there are eight-coordinate rubidium atoms bonded by four bridging carboxylate oxygen atoms (O1, O1#1, O2#4, O2#5). Additionally, two phenolic oxygen atoms (O(3#2, 3#3)) from the μ_4-1κ(O);2κ(O);3κ(O′);4κ(O′) 4hob ligand and two coordinated water oxygen atoms (O4 and O4#6) contribute to the coordination. The metal centre achieves a total coordination of eight by incorporating another ligated water oxygen atom (O4#6) bridging from the adjacent metal centre. The binding of the phenolic oxygen atom to the metal centre is also observed in the **4Cs** structure. Each 4-hydroxybenzoate ligand in the chain forms bonds with four Rb atoms, following the same coordination pattern. For **5Rb**, the average Rb-O bond distance is 3.0486 Å. Among the Rb-O bonds, the bridging Rb1-O1 bond is the shortest (2.844(14) Å). In contrast, one of the

ligated water molecules exhibits the longest Rb-O bond distance of 3.570 (16) Å (Rb1-O4#6). The two ligated water oxygen atoms form an O4-Rb1-O4#6 angle of 82.89(4)°.

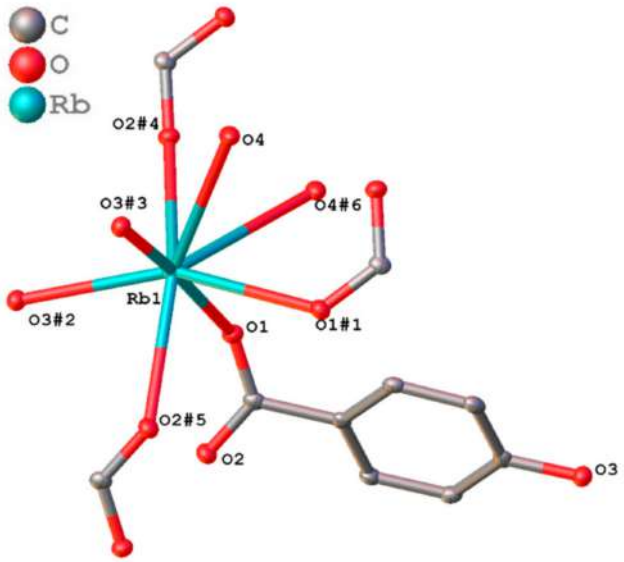


Figure 25. The asymmetric unit of $[Rb(4hob)(H_2O)]_n$ (**5Rb**) showing the total coordination sphere (hydrogen atoms are omitted for clarity). Symmetry code: $^{\#1}$ + X,1/2-Y,-1/2 + Z; $^{\#2}$ -1 + X, + Y, + Z; $^{\#3}$ -1 + X,1/2-Y,-1/2 + Z; $^{\#4}$ -X,-1/2 + Y,3/2-Z; $^{\#5}$ -X,1-Y,1-Z; $^{\#6}$ -X,-Y,1-Z.

The metal atoms in the 1D chain (Rb1#1 . . . Rb1 . . . Rb1#7) are linked together through carboxylate-O1 and the phenolic oxygen atom O3#2 with a Rb1 . . . Rb1#1 distance of 4.0584(8) Å at an angle of 162.109(5)°. A phenolic oxygen atom, O3, bridges to a Rb metal in a neighbouring chain, forming a 2D network in the ac-plane (Figure 26a). When projected along the a-axis (Figure 26b), it becomes apparent how these 2D networks are linked together by alternative four-membered rings (through coordinated aqua molecules (O4 and O4#4)) and eight-membered rings (through two bridging ligands), resulting in an overall 3D structure.

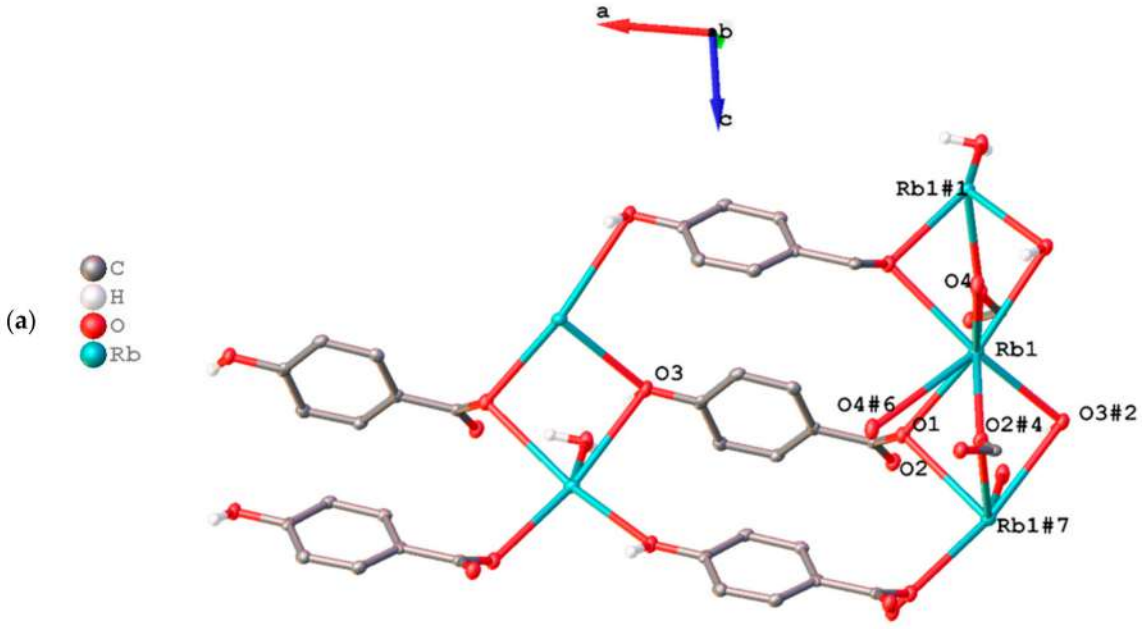


Figure 26. *Cont.*

(**b**)

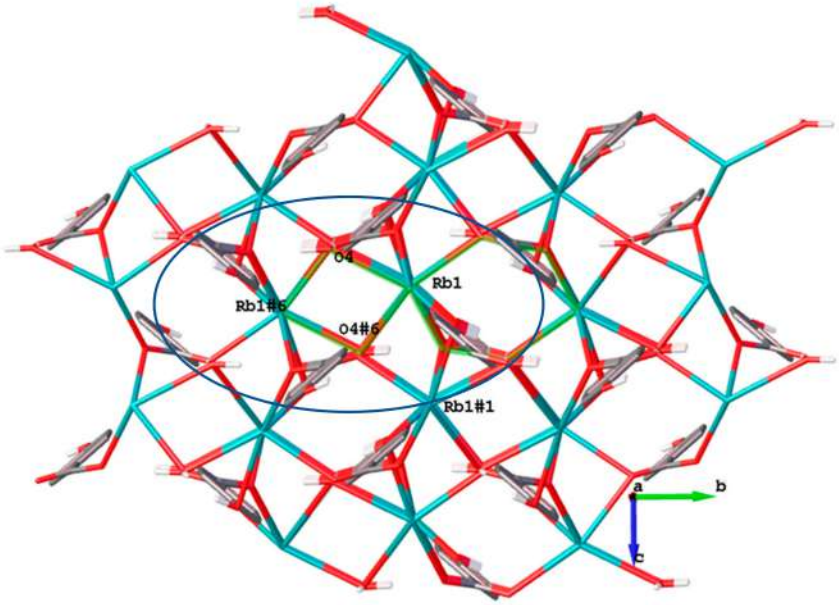


Figure 26. (**a**) A projection along the ac-plane showing the formation of a 2D-layer network of **5Rb**. (**b**) A projection along the a-axis of **5b** showing alternative four- and eight-membered rings (circled) that link the 2D networks together. Symmetry code: $^{\#1}$ + X,3/2-Y,-1/2 + Z; $^{\#2}$ 1-X,1-Y,1-Z; $^{\#4}$ 1-X,1-Y,2-Z; $^{\#6}$ + X,1/2-Y,1/2 + Z; $^{\#7}$ 1-X,1 + Y,1/2-Z.

$[Cs(4hob)(H_2O)]_n$ (**5Cs**) crystallises in the monoclinic $P2_1/c$ space group and exhibits square antiprismatic eight-coordination. Although the crystal structures of **5Rb** and **5Cs** have different unit cells due to the inequivalent b-angles and a slight variation in the c-axis, the ligand-binding modes within the asymmetric units remain the same. Furthermore, the eight-coordinated metal atoms in both cases have similar coordination environments (Table 2). The 1D polymeric chain of Cs atoms is nonlinear, with Cs1#1-Cs1-Cs1#7 at an angle of 168.391(8)°. The separation of the metal atoms in the 1D chains is longer in **5Cs** (4.3322(9) Å) compared to the 4.0584 (8) Å in **5Rb**. In contrast to **5Rb**, the average Cs-O bond distance in **5Cs** is slightly longer (3.2165 Å). The disparity in the metal–metal distance and the average metal–oxygen bond distances between **5Rb** and **5Cs** aligns with the increase in the ionic radii of eight-coordinate monovalent caesium compared to rubidium [29]. Similar to **5Rb**, the bridging Cs1-O1 bond in **5Cs** is the shortest (3.012(3) Å), while the coordinated water oxygen O4#6 exhibits the longest Cs-O bond distance of 3.761(3) Å (Cs1-O4#6). The two ligated water oxygen atoms form an O4-Cs1-O4#6 angle of 81.89(4)°.

Additionally, the interactions that join the 1D networks and contribute to the overall 3D structure are similar in both **5Rb** and **5Cs**. However, the **5Cs** structure exhibits a network of H-bonding (Table S12) that holds the 3D network together (Figure 27).

2.3. Corrosion Inhibition

Immersion Tests

The immersion tests were conducted as an initial screening, lasting for seven days in a 0.01M NaCl control solution. After the completion of the test, digital photographs were taken of the sample coupons (Figure S16). Because the primary objective of the current study was to observe and compare the effectiveness of alkali-metal complexes of various carboxylate derivatives with rare-earth-metal carboxylate corrosion inhibitors, detailed immersion analysis was not pursued for any of the compounds.

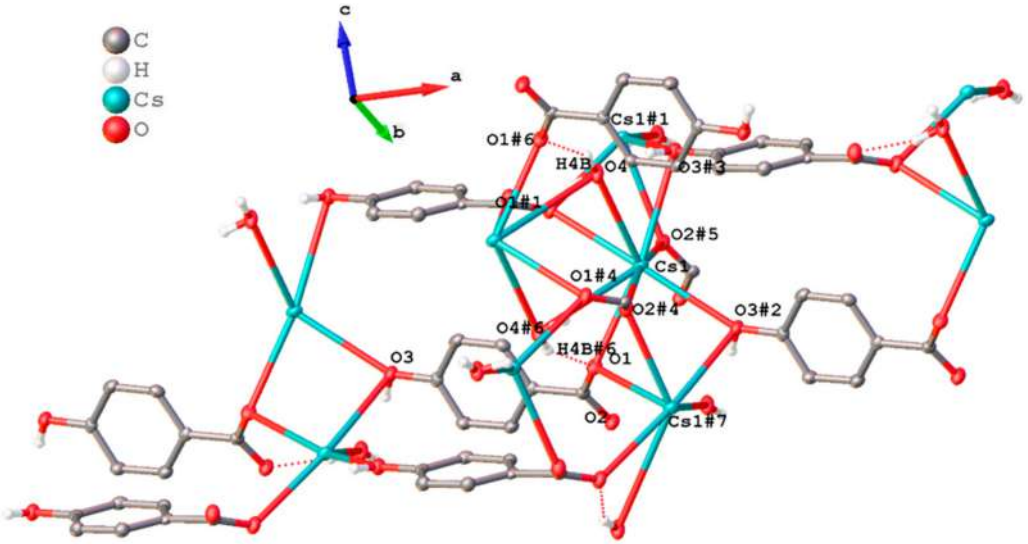


Figure 27. Molecular diagram of $[Cs(4hob)(H_2O)]_n$ **5Cs** indicating the immediate coordination environment around Cs1. Hydrogen atoms, except for those involved in forming H-bonds, are omitted for clarity. (The 1D polymeric chain propagates along the *c*-axis, while a 2D framework forms in the ac-plane. The 2D polymeric chains are linked by alternative four- and eight-membered rings, resulting in the formation of a 3D network along the *b*-axis). Symmetry code: $^{\#1}$ + X,1/2-Y,1/2 + Z; $^{\#2}$ 1 + X, + Y, + Z; $^{\#3}$ 1 + X,1/2-Y,1/2 + Z; $^{\#4}$ 2-X,-1/2 + Y,1/2-Z; $^{\#5}$ 2-X,1-Y,1-Z,; $^{\#6}$ 2-X,-Y,1-Z; $^{\#7}$ + X,1/2-Y,-1/2 + Z.

Table 3 provides a summary of the weight-loss measurements obtained after 168 h of immersing the samples in specific inhibitor solutions. Upon examination of the results, it was found that the mild-steel coupons immersed in 800 ppm $[K(4Hocin)(H_2O)_3]_n$ (**4K**) exhibited the highest corrosion inhibition rates, reaching 80%. $[K_2(2m3fur)_2(H_2O)]_n$ (**2K**) displayed the lowest inhibition efficiency, with only 9% corrosion inhibition. The remaining tested compounds demonstrated inhibition efficiencies ranging from 25% to 31%.

Table 3. Observed weight loss, corrosion rates ($\mu gm^{-2}s^{-1}$), and percentage inhibition (η) for mild steel. Coupons immersed in specific solutions at 800 ppm concentrations in 0.01 M NaCl for seven days.

Solution	Concentration		Corrosion Rate ($\mu gm^{-2}s^{-1}$)	% Inhibition (η)
	ppm	mM		
Control—NaCl	580	10	39.1	-
$[Li_2(3tpc)_2]_n$ (**1Li**)	800	2.98	27.1	31
$[K_2(3tpc)_2]_n$ (**1K**)	800	2.41	28.8	26
$[Rb(3tpc)(H_2O)]_n$ (**1Rb**)	800	3.47	27.4	30
$[K_2(2m3fur)_2(H_2O)]_n$ (**2K**)	800	2.31	35.7	9
$[Li(3fur)]_n$ (**3Li**)	800	6.78	29.2	25
$[K(4hocin)(H_2O)_3]_n$ (**4K**)	800	3.12	7.5	80
$[K(4hob)(H_2O)_3]_n$ (**5K**)	800	3.47	29.7	24

Previous studies involving 4-hydroxycinnamate as the ligand have indicated that the corrosion rates calculated from the weight-loss data were generally higher for sodium salts compared to their rare earth metal-substituted analogues [18]. In our most recent studies with RE 3-thiophenecarboxylate [14] and 3-furoate [13], we demonstrated the inhibition properties of the rare-earth-metal complexes. By comparing both sets of results

(Tables 3 and 4), it is evident that the corrosion rates of alkali-metal carboxylates on steel are generally much higher than those of rare-earth analogues, indicating the value of rare-earth carboxylates in inhibition.

Table 4. Anticorrosion data for some corresponding rare-earth carboxylates.

Ligand	Solutions	Concentration		Corrosion Rate ($\mu gm^{-2}s^{-1}$)	% Inhibition (η)	Ref
		ppm	mM			
1-3tpc	$[La(3tpc)_3(H_2O)_3]_n$	500	0.871	19.4	36	[14]
1-3tpc	$[Ce(3tpc)_3(H_2O)_3]_n$	500	0.869	18.8	38	[14]
1-3tpc	$[Y_2(3tpc)_6(H_2O)_4]. H_2O$	500	0.485	9.65	68	[14]
3-3fur	$[La(3fur)_3(H_2O)_2]_n$	800	1.57	5.14	87	[13]
3-3fur	$[Ce(3fur)_3(H_2O)_2]_n$	800	1.57	8.3	79	[13]
3-3fur	$[Y(3fur)_3(H_2O)_2]_n$	800	1.75	3.9	90	[13]
4-4ohcin	$La(4hocin)_3$	500	0.7	3.2	91	[18]
4-4ohcin	$Ce(4hocin)_3$	200	0.28	5.7	84	[18]

3. Materials and Methods

3.1. General Consideration

The experiments were carried out utilising commercially available chemicals and reagents of standard quality, which were used without undergoing any additional purification steps. The elemental Analysis Service Team at the Science Centre, London Metropolitan University, England, performed the elemental analyses. Melting points were determined using glass capillaries, and the values were reported without calibration. To obtain infrared (IR) spectra, a Nicolet™ iS™ 5 FTIR Spectrometer (ThermoFisher Scientific, Waltham, MA, USA) was employed in ATR mode, covering the range of 4000–500 cm^{-1}. Powder diffraction patterns were conducted at room temperature using a Bruker D2 PHASER diffractometer (Bruker corporation, Billerica, MA, USA). The measurements were conducted within the range of 2–60, using a 0.2° divergence slit and with increments of 0.02°. To generate X-ray powder simulations, the Mercury program provided by the Cambridge Crystallographic Data Centre [38] was employed. These simulations utilised the single-crystal X-ray diffraction data. Thermogravimetric analysis (TGA) was performed on a TA instrument SDT 650 (TA Instruments, New Castle, DE, USA), using standard 90 µL alumina metal pans. The analysis was conducted at a heating rate of 10 °C/min under a nitrogen atmosphere with a flow rate of 50 mL/min.

3.2. X-ray Crystallography

The mounting of single crystals was performed on loops using viscous hydrocarbon oil on the respective diffractometers. For the complexes, **2Li** and **1K** data were collected using the Oxford Diffraction Gemini Ultra dual-source (Mo and Cu) CCD diffractometer collected at 123 K using a Cu source (λ = 1.54184 Å). Data processing was conducted using the CrysAlisPro.55 software suite [39]. Data collection for the rest of the compounds took place at the MX1 beamline located at the Australian Synchrotron. The integration of the data was carried out using Blue-ice [40] and XDS [41] software programs. The structures were solved using SHELXT, and they were refined using full-matrix least-squares methods against F2 with SHELX2018 [42]. The refinement was performed using the Olex2 [43] graphical user interface (GUI). The graphical representations were created using the bitmap image GUI of Olex2 [43]. All hydrogen atoms were placed in calculated positions using the riding model. Detailed information regarding the crystal data and refinement can be found in Table S1.

3.3. Synthesis of Alkali-Metal Carboxylate Complexes

General Synthetic Method: Each ligand acid (LH; L = 3tpc, 2m3fur, 3fur, 4hocin, and 4hob) was dissolved in 15 mL of 95% ethanol and neutralised with an equimolar amount of aqueous potassium hydroxide, as shown in Scheme 1 (1), to produce KL compounds. Sodium complexes were also synthesised using the same procedure, employing NaOH instead. For the syntheses of lithium, rubidium, and caesium carboxylate complexes, ligand acid solutions in ethanol (LH) were neutralised with a half-molar amount of aqueous Li_2CO_3, Rb_2CO_3, and Cs_2CO_3, respectively (Scheme 1, (2)). The resulting solutions were stirred at room temperature for 2 h, transferred to separate vials, and left to stand for several days at room temperature, resulting in precipitates. These precipitates were dried over silica gel. Crystals were obtained by the subsequent recrystallisation of the bulk products of **1Li**, **1K**, **1Rb**, **2Li**, **2K** from 95% ethanol and **1Cs**, **3Li**, **4M** (M = K, Rb, Cs) and **5M** (M = Li, K, Rb, Cs) from water/ethanol (95/5 %v/v).

1Li: $[Li_2(3tpc)_2]_n$ white-colour powder. Yield: 50.1%. m.p. >300 °C. Elemental analysis calculated for $C_{10}H_6Li_2O_4S_2$ (MW: 268.15 $gmol^{-1}$): calculated (%) C: 44.79; H: 2.26; found (%) C: 44.08; H: 2.20. IR (cm^{-1}): 3123w, 3105w, 3083w, 1566s, 1514s, 1414s, 1399s, 1352s, 1206m, 119m, 1071m, 935w, 913w, 896w, 869m, 827m, 756s, 694s, 626m, 585m, 540m, 430s.

1K: $[K_2(3tpc)_2]_n$ white-colour powder. Yield: 49.5%. m.p. >300 °C. Elemental analysis calculated for $C_{10}H_6K_2O_4S_2$ (MW: 332.47 $gmol^{-1}$): calculated (%) C: 36.12; H: 1.82; found (%) C: 36.26; H: 1.77. IR (cm^{-1}): 3115w, 3083w, 2358w, 2340w, 1738w, 1614w, 1558s, 1516s, 1412s, 1401s, 1348s, 1204m, 1121m, 1109m, 1067m, 916w, 870m, 849w, 830m, 779m, 753s, 683s, 624m, 574w, 514m, 457w, 442w.

1Rb: $[Rb(3tpc)(H_2O)]_n$ white-colour powder. Yield: 90.0%. m.p. >300 °C. Elemental analysis calculated for $C_5H_5O_3RbS$ (MW: 230.62 $gmol^{-1}$): calculated (%) C: 26.04; H: 2.19; found (%) C: 26.54; H: 1.98. IR (cm^{-1}): 3348w, 3100w, 3083w, 1723w, 1563s, 1512s, 1405s, 1341s, 1210m, 1199m, 1125m, 1108m, 1065m, 866m, 827m, 760s, 692s, 624m, 553m, 511m, 458w. TGA weight loss (26–110 °C); 7.4% (calc. for loss of 1 × H_2O = 7.8%).

1Cs: $[Cs\{H(3tpc)_2\}]_n$ white-colour powder. Yield: 20%. m.p. >300 °C. Elemental analysis calculated for $C_{10}H_7CsO_4S_2$ (MW: 388.20 $gmol^{-1}$): calculated (%) C: 30.94; H: 1.82; found (%) C: 30.80; H: 1.73. IR (cm^{-1}): 3097w, 1682w, 1636w, 1617w, 1560s, 1510s, 1398s, 1384s, 1342s, 1280w, 1261w, 1197w, 1152w, 1106m, 1063w, 1015w, 994w, 973w, 945w, 926w, 864m, 826m, 765s, 757s, 696s, 670w, 624m, 591w, 557w, 537w, 508m, 439w. TGA weight loss (40–220 °C); 2.5% (calc. for loss of 0.5 × H_2O (assuming absorbed water = 2.3%)).

2Li: $[Li_2(2m3fur)_2(H_2O)_3]$ white-colour powder. Yield: 51%. m.p. 250 °C (dec.). Elemental analysis calculated for $C_{12}H_{16}Li_2O_9$ (MW: 318.13 $gmol^{-1}$): calculated (%) C: 45.30; H: 5.07; found (%) C: 44.56; H: 4.68. IR (cm^{-1}): 3373m, 3301m, 3128w, 2926w, 1675w, 1598s, 1544m, 1521s, 1458m, 1428s, 1383s, 1361m, 1349m, 1289w, 1248w, 1231w, 1219m, 1138m, 1104s, 1052w, 1035w, 944m, 895m, 852w, 815s, 761w, 729s, 685m, 618s, 599s, 588s, 530s, 500s, 462s. TGA weight loss (50–120 °C); 17.68% (calc. for loss of 3 × H_2O = 16.97%).

2K: $[K_2(2m3fur)_2(H_2O)]_n$ white-colour powder. Yield: 50%. m.p. 280 °C (dec.). Elemental analysis calculated for $C_{12}H_{12}K_2O_7$ (MW: 346.42 $gmol^{-1}$): calculated (%) C: 41.61; H: 3.49; found (%) C: 41.53; H: 3.29. IR (cm^{-1}): 3373m, 3301m, 3128w, 2926w, 1675w, 1598s, 1544s, 1521s, 1458m, 1428s, 1383s, 1361s, 1349s, 1289w, 1231w, 1219s, 1138m, 1104s, 1052w, 1035w, 944m, 895m, 815s, 761w, 729s, 685m, 618s, 599s, 588s, 530s, 500s, 462s. TGA weight loss (35–180 °C); 9.4% (calc. for loss of 2 × H_2O (assuming absorbed water = 9.9%)).

3Li: $[Li(3fur)]_n$ white-colour powder. Yield: 80%. m.p. 280 °C (dec.). Elemental analysis calculated for $C_5H_3LiO_3$ (MW: 118.01 $gmol^{-1}$): calculated (%) C: 50.88; H: 2.56; found (%) C: 50.78; H: 2.50. IR (cm^{-1}): 3154w, 3132w, 2298w, 1563s, 1552s, 1505s, 1428s, 1368m, 1251w, 1213m, 1149m, 1069m, 1004m, 970mw, 873m, 780s, 752s, 606m, 595m, 553m, 468s.

4K: $[K(4hocin)(H_2O)_3]_n$ white-colour powder. Yield: 69%. m.p. 200 °C (dec.). Elemental analysis calculated for $C_9H_{13}KO_6$ (MW: 256.29 $gmol^{-1}$): calculated (%) C: 42.18; H: 5.11; $C_9H_{10}KO_{4.5}$ (MW: 229.27 $gmol^{-1}$, loss of 1.5 H_2O): calculated (%) C: 47.15; H: 4.40; found (%) C: 46.51; H: 4.27. IR (cm^{-1}): 3444m, 3023w, 2815w, 1636m, 1607w, 1590m, 1531w, 1511s,

1454w, 1371s, 1289m, 1270m, 1237s, 1167m, 1102m, 1013w, 973s, 936w, 874w, 829s, 802m, 697m, 641w, 516s, 465s, 452s, 460m. TGA weight loss (25–90 °C); 20.3% (calc. for loss of 3 × H_2O = 21.1%).

4Rb: [Rb{H(4hocin)$_2$}]$_n$.nH_2O white-colour powder. Yield: 59%. m.p. 200 °C (dec.). Elemental analysis calculated for $C_{18}H_{17}O_7Rb$ (MW: 430.79 gmol^{-1}): calculated (%) C: 50.19; H: 3.98; $C_{11.25}H_{11}O_{4.75}Rb$ (MW: 307.67 gmol^{-1}, loss of 0.75 4hocin): calculated (%) C: 43.92; H: 3.60; found (%) C: 44.19; H: 3.67. IR (cm^{-1}): 3287w, 2624m, 1634m, 1608w, 1591m, 1537w, 1514s, 1454s, 1381s, 1288w, 1243s, 1198w, 1171m, 1103m, 1010w, 979s, 939m, 900m, 864m, 828s, 804s, 748w, 710m, 628w, 551s, 525s, 515s, 458m. TGA weight loss (50–115 °C); 6.0% (calc. for loss of 1 × H_2O from {[Rb(4hocin)(4hocinH)$_{0.25}$] (H_2O)}$_n$ = 5.9%).

4Cs: [Cs(4hocin)(H_2O)]$_n$ white-colour powder. Yield: 86%. m.p. 200 °C (dec.). Elemental analysis calculated for $C_9H_9CsO_4$ (MW: 314.07 gmol^{-1}): calculated (%) C: 34.53; H: 2.58; found (%) C: 34.41; H: 2.90. IR (cm^{-1}): 3212m, 2999m, 2808m, 2687m, 1887w, 1633m, 1607m, 1588m, 1535w, 1514s, 1453s, 1379s, 1287w, 1243s, 1167m, 1099m, 1010w, 978s, 938w, 878m, 861w, 827s, 802m, 748w, 710m, 661w, 641w, 549s, 511s, 459m. TGA weight loss (50–120 °C); 5.4% (calc. for loss of 1 × H_2O = 5.7%).

5Li: [Li(4hob)]$_n$ white-colour powder. Yield: 72%. m.p. 270 °C (dec.). Elemental analysis calculated for $C_7H_5LiO_3$ (MW: 144.05 gmol^{-1}): calculated (%) C: 58.37; H: 3.50; $C_7H_{5.5}LiO_{3.25}$(MW: 148.56 gmol^{-1}, absorbed 0.25 H_2O): calculated (%) C: 56.59; H: 3.73; found (%) C: 56.37; H: 3.36. IR (cm^{-1}): 3357m, 1602s, 1556, 1399s, 1360m, 1238s, 1168s, 1143m, 1100s, 1011m, 978w, 858m, 841w, 805m, 787s, 701m, 638w, 619s, 548m, 518m, 503w, 450s, 425s.

5K: [K(4hob)(H_2O)$_3$]$_n$ white-colour powder. Yield: 83%. m.p. 260 °C (dec.). Elemental analysis calculated for $C_7H_{11}KO_6$ (MW: 230.26 gmol^{-1}): calculated (%) C: 36.51; H: 4.81; $C_7H_7KO_4$ (MW: 194.23 gmol^{-1},loss of 2 H_2O): calculated (%) C: 43.29; H: 3.63; found (%) C: 43.84; H: 3.38. IR (cm^{-1}): 3437s, 3175s, 2689w, 1635w, 1599s, 1533s, 1501m, 1438w, 1361s, 1297w, 1268m, 1248s, 1163s, 1138m, 1100s, 1008w, 953w, 854s, 787s, 776s, 695s, 614s, 530m, 470s, 432s. TGA weight loss (27–150 °C); 21.2% (calc. for loss of 3 × H_2O = 23.4%).

5Rb: [Rb(4hob)(H_2O)]$_n$ white-colour powder. Yield: 56%. m.p. 270 °C (dec.). Elemental analysis calculated for $C_7H_7O_4Rb$ (MW: 240.60 gmol^{-1}): calculated (%) C: 34.94; H: 2.93; found (%) C: 34.92; H: 2.77. IR (cm^{-1}): 3300w, 3018m, 2890m, 2798m, 2694m, 1914w, 1694w, 1597s, 1530s, 1510s, 1462m, 1380s, 1252s, 1165s, 1142m, 1100s,1011w, 967w, 849s, 834s, 816w 784s, 704s, 614s, 549s, 496s. TGA weight loss (100–140 °C); 7.5% (calc. for loss of 1 × H_2O = 7.5%).

5Cs: [Cs(4hob)(H_2O)]$_n$ white-colour powder. Yield: 91%. m.p. 270 °C (dec.). Elemental analysis calculated for $C_7H_7CsO_4$ (MW: 288.04 gmol^{-1}): calculated (%) C: 29.19; H: 2.45; found (%) C: 29.39; H: 2.41. IR (cm^{-1}): 3194m, 3036w, 2809w, 2675w, 2522w, 2114w, 1660s, 1607s, 1591s, 1512w, 1440m, 1377m, 1355m, 1316w, 1267m, 1227s, 1162s, 1099s, 925m, 849s, 768s, 697s, 666m, 638m, 612s, 546m, 522w, 498s. TGA weight loss (75–130 °C); 5.3% (calc. for loss of 1 × H_2O = 6.2%)

3.4. Corrosion Testing

In order to assess the general corrosion and inhibition characteristics of the synthesised compounds, corrosion immersion experiments were conducted following the standard method ASTM G31-72 [44]. To conduct weight-loss tests, mild-steel alloy AS 1020 coupons were prepared by cutting them into approximately 20 × 20 × 1.5 mm dimensions and progressively abrading them using sanding sheets of grits ranging from 80 to 2000. The specimens were subsequently rinsed with distilled water, followed by ethanol, and dried under flowing N_2 gas. These coupons were immediately used for a series of immersion tests lasting up to 168 h (7 days). Both the sample and the control coupons were placed in separate beakers containing 0.01 M NaCl solutions, with and without the presence of 800 ppm of the inhibitor compounds. In each setup, coupons were fully immersed at mid-depth using Teflon strings. After completing the tests, the corrosion product adhering to the substrate was initially removed by subjecting it to mild sonication in clean, distilled

water. Subsequently, the finest sanding papers were used with minimum force to prevent the removal of intact material. The experiments were carried out in duplicate to ensure reliability. Finally, the coupons were washed with ethanol and dried using N_2 gas. The corrosion rates (Rs) of the inhibitor solutions were determined by applying Equation (3), outlined below:

$$\text{Corrosion rate (R)} = \frac{KW}{ATD} \quad (3)$$

where K is the A constant; W is the weight loss (g); A is the coupon area (cm^2); T is the time of exposure (168 h); D is the density of the test metal.

The percentage corrosion inhibition (η) was determined using Equation (4):

$$\eta = \frac{R(Control) - R\ (inhibitor)}{R(Control)} \times 100 \quad (4)$$

4. Conclusions

Fourteen new complexes of the alkali metals with 3-thiophenecarboxylate (3tpc), 2-methyl-3-furoate (2m3fur), 3-furoate (3fur), 4-hydroxycinnamate (4hocin), and 4-hydroxybenzoate (4hob) were synthesised. The preparations gave moderate yields of crystalline materials, and the complexes were characterised via IR spectroscopy, powder XRD, TGA, and micro-analyses. Furthermore, X-ray crystallographic examination of the single crystals of all the compounds revealed unique structures for each of them. In the series of compounds, only the $[Li_2(2m3fur)_2(H_2O)_3]$ **2Li** complex crystallised as a coordination dinuclear complex with four-coordinate lithium atoms. In contrast, all other complexes were found to be polymeric, with varying coordination numbers and stereochemistry. Compounds **1Cs** and **4Rb** incorporate $[HL_2]^-$ ligands rather than simple carboxylate groups and exhibit centrosymmetric O...H...O interactions between the carboxylate ions.

To investigate the potential application of the complexes as corrosion inhibitors, weight-loss measurements were conducted, but the compounds were less effective than their rare-earth counterparts.

Supplementary Materials: The following supporting information can be downloaded at https://www.mdpi.com/article/10.3390/molecules28145515/s1, Figure S1: TGA plots of $[M(3tpc)]_n$ **1M** series (M = Na, Li, K, Rb, Cs); Figure S2: PXRD traces of $[M(3tpc)]_n$ (M = Na, Li, K, Rb, Cs) **1M** series at room temperature compared to their simulated patterns; Figure S3: IR spectra of $[M(3tpc)]_n$ **1M** series (M = Na, Li, K, Rb, Cs); Figure S4: TGA plots of $[M(2m3fur)]_n$ **2M** series (M = Na, Li, K); Figure S5: PXRD traces of $[M(2m3fur)]_n$ **2M** series (M = Na, Li, K) at room temperature compared to their simulated patterns; Figure S6: IR spectra of $[M(2m3fur)]_n$ **2M** series (M = Na, Li, K); Figure S7: TGA plots of [Na3fur] and $[Li(3fur)]_n$ (**3Li**); Figure S8: PXRD traces of [Na3fur] and $[Li(3fur)]_n$ (**3Li**) at room temperature compared to their simulated patterns; Figure S9: IR spectra of [Na3fur] and $[Li(3fur)]_n$ (**3Li**); Figure S10: TGA plots of $[M(4hocin)]_n$ **4M** series (M = Na, K, Rb, Cs); Figure S11: PXRD traces of $[M(4hocin)]_n$ **4M** series (M = Na, K, Rb, Cs) at room temperature compared to their simulated patterns; Figure S12: IR spectra of [M(4hocin)]n **4M** series (M = Na, K, Rb, Cs); Figure S13: TGA plots of $[M(4hob)]_n$ **5M** series (M = Na, Li, K, Rb, Cs); Figure S14: PXRD traces of $[M(4hob)]_n$ **5M** series (M = Na, Li, K, Rb, Cs) series at room temperature compared to their simulated patterns; Figure S15: IR spectra of [M(4hob)]n **5M** series (M = Na, Li, K, Rb, Cs); Figure S16: Mild-steel coupons immersed in control and the inhibited solutions for 168 h (left—Trial 1; right—Trial 2.); Table S1: Crystal data and structural refinement for the alkali-metal carboxylate complexes; Table S2: Selected bond lengths and M ... M distances (Å) for $[M(3tpc)]_n$ **1M** series (M = Li, K, Rb, Cs); Table S3: Selected bond angles (°) for $[M(3tpc)]_n$ **1M** series (M = Li, K, Rb); Table S4: Selected bond lengths and M ... M distances (Å) for $[M(2m3fur)]_n$ **2M** series (M = Li, K); Table S5: Selected bond angles (°) for $[M(2m3fur)]_n$ **2M** series (M = Li, K); Table S6: Selected bond lengths and M ... M distances (Å) for $[Li(3fur)]_n$ (**3Li**); Table S7: Selected bond angles (°) for $[Li(3fur)]_n$ (**3Li**); Table S8: Selected bond lengths and M ... M distances (Å) for $[M(4hocin)]_n$ **4M** series (M = K, Rb, Cs); Table S9: Selected bond angles (°) for $[M(4hocin)]_n$ **4M** series (M = K, Rb, Cs); Table S10: Selected bond lengths and M ... M distances (Å) for $[M(4hob)]_n$ **5M** series (M = Li, K, Rb, Cs); Table S11: Selected bond angles (°)

for $[M(4hob)]_n$ **5M** series (M = Li, K, Rb, Cs); Table S12: Hydrogen-bonding parameters [d/Å and </°] for the compounds **1Rb**, **4K**, **4Rb**, **4Cs**, **5K**, **5Cs**.

Author Contributions: Syntheses of the complexes, V.P.V.; characterisation, V.P.V. and Z.G.; immersion studies, V.P.V.; original draft preparation, V.P.V. and subsequent review and editing, Z.G., G.B.D. and P.C.J.; supervision, project administration, and funding acquisition, G.B.D. and P.C.J. All authors have read and agreed to the published version of the manuscript.

Funding: This research was funded by the Australian Research Council (DP200100568).

Institutional Review Board Statement: Not applicable.

Informed Consent Statement: Not applicable.

Data Availability Statement: Crystal data can be obtained free of charge from The Cambridge Crystallographic Data Centre (CCDC 2268145-2268148 for complexes **1M**, 2268149-2268150 for complexes **2M**, 2268151 for complex 3**M**, 2268152-2268154 for complexes **4M**, and 2268155-2268158 for complexes **5M**).

Acknowledgments: P.C.J and G.B.D. gratefully acknowledge the ARC for the funding (DP200100568). Parts of this research were undertaken on the MX1 beamline at the Australian Synchrotron, part of ANSTO [45]. The authors also acknowledge the crystallographic assistance from Professor P. V. Bernhardt, University of Queensland.

Conflicts of Interest: The authors declare no conflict of interest.

References

1. Revie, R.W.; Uhlig, H.H. *Corrosion and Corrosion Control: An Introduction to Corrosion Science and Engineeering*, 4th ed.; John Wiley & Sons: Hoboken, NJ, USA, 2008.
2. Markley, T.; Blin, F.; Forsyth, M.; Hinton, B. Multifunctional Rare Earth Organic Corrosion Inhibitors. In *Rare Earth-Based Corrosion Inhibitors*; Forsyth, M., Hinton, B., Eds.; Woodhead Publishing: Cambridge, UK, 2014; pp. 117–142. ISBN 9780857093585.
3. Somers, A.E.; Hinton, B.R.W.; de Bruin-Dickason, C.; Deacon, G.B.; Junk, P.C.; Forsyth, M. New, Environmentally Friendly, Rare Earth Carboxylate Corrosion Inhibitors for Mild Steel. *Corros. Sci.* **2018**, *139*, 430–437. [CrossRef]
4. Forsyth, M.; Seter, M.; Hinton, B.; Deacon, G.; Junk, P. New "Green" Corrosion Inhibitors Based on Rare Earth Compounds. *Aust. J. Chem.* **2011**, *64*, 812–819. [CrossRef]
5. Seter, M.; Girard, G.M.A.; Lee, W.W.; Deacon, G.; Junk, P.; Hinton, B.; Forsyth, M. The Influence of Organic Structure and Rare Earth Metal Cation on the Corrosion Efficiency Observed on AS1020 Steel Compared with La(4OHCin)3. *AIMS Mater. Sci.* **2015**, *2*, 1–15. [CrossRef]
6. Somers, A.E.; Peng, Y.; Chong, A.L.; Forsyth, M.; MacFarlane, D.R.; Deacon, G.B.; Hughes, A.E.; Hinton, B.R.W.; Mardel, J.I.; Junk, P.C. Advances in the Development of Rare Earth Metal and Carboxylate Compounds as Corrosion Inhibitors for Steel. *Corros. Eng. Sci. Technol.* **2020**, *55*, 311–321. [CrossRef]
7. Somers, A.E.; Deacon, G.B.; Hinton, B.R.W.; Macfarlane, D.R.; Junk, P.C.; Tan, M.Y.J.; Forsyth, M. Recent Developments in Environment-Friendly Corrosion Inhibitors for Mild Steel. *J. Indian Inst. Sci.* **2016**, *96*, 285–292.
8. Behrsing, T.; Deacon, G.B.; Junk, P.C. The Chemistry of Rare Earth Metals, Compounds, and Corrosion Inhibitors. In *Rare Earth-Based Corrosion Inhibitors*; Forsyth, M., Hinton, B., Eds.; Woodhead Publishing: Cambridge, UK, 2014; pp. 1–37.
9. De Damborenea, J.; Conde, A.; Arenas, M.A. Corrosion Inhibition with Rare Earth Metal Compounds in Aqueous Solutions. In *Rare Earth-Based Corrosion Inhibitors*; Woodhead Publishing: Cambridge, UK, 2014; pp. 84–116. [CrossRef]
10. Forsyth, M.; Wilson, K.; Behrsing, T.; Forsyth, C.; Deacon, G.B.; Phanasgoankar, A. Effectiveness of Rare-Earth Metal Compounds as Corrosion Inhibitors for Steel. *Corrosion* **2002**, *58*, 953–960. [CrossRef]
11. Blin, F.; Leary, S.G.; Deacon, G.B.; Junk, P.C.; Forsyth, M. The Nature of the Surface Film on Steel Treated with Cerium and Lanthanum Cinnamate Based Corrosion Inhibitors. *Corros. Sci.* **2006**, *48*, 404–419. [CrossRef]
12. Peng, Y.; Hughes, A.E.; Deacon, G.B.; Junk, P.C.; Hinton, B.R.W.; Forsyth, M.; Mardel, J.I.; Somers, A.E. A Study of Rare-Earth 3-(4-Methylbenzoyl)-Propanoate Compounds as Corrosion Inhibitors for AS1020 Mild Steel in NaCl Solutions. *Corros. Sci.* **2018**, *145*, 199–211. [CrossRef]
13. Vithana, V.P.; Guo, Z.; Deacon, G.B.; Somers, A.E.; Junk, P.C. RE(III) 3-Furoate Complexes: Synthesis, Structure, and Corrosion Inhibiting Properties. *Molecules* **2022**, *27*, 8836. [CrossRef]
14. Vithana, V.P.; Guo, Z.; Deacon, G.B.; Somers, A.E.; Junk, P.C. Synthesis, Structure, and Corrosion Inhibiting Properties of RE^{III} 3-Thiophenecarboxylate Complexes. *New J. Chem.* **2022**, *46*, 19104–19111. [CrossRef]
15. Moon, J.S.; Guo, Z.; Beaumont, O.A.; Hamilton, S.; Bousrez, G.; Mottram, E.; Wang, J.; Somers, A.E.; Deacon, G.B.; Junk, P.C. 4-Hydroxybenzoato-Rare Earth(III) Complexes—Syntheses, Structures, Coordination Diversity and Corrosion Inhibition Behaviour. *New J. Chem.* 2023, *submitted*.

16. Ouchi, A.; Suzuki, Y.; Ohki, Y.; Koizumi, Y. Structure of Rare Earth Carboxylates in Dimeric and Polymeric Forms. *Coord. Chem. Rev.* **1988**, *92*, 29–43. [CrossRef]
17. Janicki, R.; Mondry, A.; Starynowicz, P. Carboxylates of Rare Earth Elements. *Coord. Chem. Rev.* **2017**, *340*, 98–133. [CrossRef]
18. Blin, F.; Leary, S.G.; Wilson, K.; Deacon, G.B.; Junk, P.C.; Forsyth, M. Corrosion Mitigation of Mild Steel by New Rare Earth Cinnamate Compounds. *J. Appl. Electrochem.* **2004**, *34*, 591–599. [CrossRef]
19. Wormwell, F.; Mercer, A.D. Sodium Benzoate and Other Metal Benzoates as Corrosion-Inhibitors in Water and in Aqueous Solutions. *J. Appl. Chem.* **1952**, *2*, 150–160. [CrossRef]
20. Forsyth, M.; Forsyth, C.M.; Wilson, K.; Behrsing, T.; Deacon, G.B. ATR Characterisation of Synergistic Corrosion Inhibition of Mild Steel Surfaces by Cerium Salicylate. *Corros. Sci.* **2002**, *44*, 2651–2656. [CrossRef]
21. Mercer, A.D. The Properties of Carboxylates as Corrosion Inhibitors for Steel and Other Metals in Neutral Aqueous Solutions. In *Proceedings of the 5th European Symposium on Corrosion Inhibitors*; University of Ferrara: Ferrara, Italy, 1980; pp. 563–581.
22. *ConQuest 2.0.4.* Version 5.41; ConQuest: Cambridge, UK, 2023.
23. Dinnebier, R.E.; Dreele, R.; Stephens, P.W.; Jelonek, S.; Sieler, J. Structure of Sodium Para-Hydroxybenzoate, NaO 2 C±C 6 H 4 OH by Powder Diffraction: Application of a Phenomenological Model of Anisotropic Peak Width. *J. Appl. Cryst.* **1999**, *32*, 761–769. [CrossRef]
24. Skinner, J.M.; Speakman, J.C. The Crystal Structures of the Acid Salts of Some Monobasic Acids. Part II. Potassium Hydrogen Di-p-Hydroxybenzoate Hydrate. *J. Chem. Soc.* **1951**, 185–191. [CrossRef]
25. Manojlovi, L. A Reinvestigation of the Crystal Structure of Potassium Hydrogen Di-p-Hydroxybenzoate Hydrate. *Acta Cryst.* **1968**, *24*, 326. [CrossRef]
26. Hanusa, T.P. Group 1s and 2s Metals. In *Comprehensive Coordination Chemistry II*; McCleverty, J.A., Meyer, T.B., Eds.; Elsevier: Oxford, UK, 2004; Volume 3, pp. 1–92.
27. Koby, R.F.; Hanusa, T.P. Lithium, Sodium, Potassium, Rubidium, and Cesium. *Compr. Coord. Chem. III* **2021**, *1–9*, 2–48. [CrossRef]
28. Pavia, D.L.; Lampman, G.M.; Kriz, G.S. *Introduction to Spectroscopy*; Thompson Learning, Inc.: Novato, CA, USA, 2001.
29. Shannon, R.D. Revised Effective Ionic Radii and Systematic Studies of Interatomic Distances in Halides and Chalcogenides. *Acta Crystallogr. A* **1976**, *32*, 751–767. [CrossRef]
30. Dai, F.R.; Qiao, Y.; Wang, Z. Designing Structurally Tunable and Functionally Versatile Synthetic Supercontainers. *Inorg. Chem. Front.* **2016**, *3*, 243–249. [CrossRef]
31. Mustapha, A.; Reglinski, J.; Kennedy, A.R. Metal Complexes as Potential Ligands: The Deprotonation of Aminephenolate Metal Complexes. *Inorg. Chem. Commun.* **2010**, *13*, 464–467. [CrossRef]
32. Deacon, G.B.; Forsyth, C.M.; Harika, E.; Junk, P.C.; Ziller, J.W.; Evans, W.J. Hydrocarbon-Soluble, Polymetallic, Lanthanoid Aryloxides Constructed Utilising Ligands with Distal But Groups. *J. Mater. Chem.* **2004**, *14*, 3144–3149. [CrossRef]
33. Dai, F.R.; Wang, Z. Modular Assembly of Metal-Organic Supercontainers Incorporating Sulfonylcalixarenes. *J. Am. Chem. Soc.* **2012**, *134*, 8002–8005. [CrossRef]
34. Demaison, J.; Herman, M.; Lievin, J. The Equilibrium OH Bond Length. *Int. Rev. Phys. Chem.* **2007**, *26*, 391–420. [CrossRef]
35. Wu, J.; Liu, J.Q. Assembly of 3D Metal-Organic Framework Based on Heterobimetallic Cu-K Unit and Oxalate Linkage. *Synth. React. Inorg. Met.-Org. Nano-Met. Chem.* **2010**, *40*, 237–240. [CrossRef]
36. Yuan, F.; Zhou, Y.; Li, L.; Qian, H. Synthesis and Crystal Structure of a Trinuclear Aminobis(Phenolate) Ytterbium Hydroxide Complex. *Synth. React. Inorg. Met.-Org. Nano-Met. Chem.* **2016**, *46*, 913–916. [CrossRef]
37. Mehring, M.; Nolde, C.; Schürmann, M. Octameric Sodium Trimethylsilanolate Hemihydrate Hemi-THF Solvate, $[NaOSiMe_3 \cdot 1/2H_2O \cdot 1/2THF]_8$. *Appl. Organomet. Chem.* **2004**, *18*, 487–488. [CrossRef]
38. MacRae, C.F.; Sovago, I.; Cottrell, S.J.; Galek, P.T.A.; McCabe, P.; Pidcock, E.; Platings, M.; Shields, G.P.; Stevens, J.S.; Towler, M.; et al. Mercury 4.0: From Visualization to Analysis, Design and Prediction. *J. Appl. Crystallogr.* **2020**, *53*, 226–235. [CrossRef]
39. Agilent Technologies. *CrysAlisPRO v.39*; Agilent Technologies Ltd.: Yarnton, UK, 2013.
40. McPhillips, T.M.; McPhillips, S.E.; Chiu, H.J.; Cohen, A.E.; Deacon, A.M.; Ellis, P.J.; Garman, E.; Gonzalez, A.; Sauter, N.K.; Phizackerley, R.P.; et al. Blu-Ice and the Distributed Control System: Software for Data Acquisition and Instrument Control at Macromolecular Crystallography Beamlines. *J. Synchrotron Radiat.* **2002**, *9*, 401–406. [CrossRef] [PubMed]
41. Kabsch, W. Automatic Processing of Rotation Diffraction Data from Crystals of Initially Unknown Symmetry and Cell Constants. *J. Appl. Crystallogr.* **1993**, *26*, 795–800. [CrossRef]
42. Sheldrick, G.M. Crystal Structure Refinement with SHELXL. *Acta Crystallogr. C Struct. Chem.* **2015**, *71*, 3–8. [CrossRef]
43. Dolomanov, O.V.; Bourhis, L.J.; Gildea, R.J.; Howard, J.A.K.; Puschmann, H. OLEX2: A Complete Structure Solution, Refinement and Analysis Program. *J. Appl. Crystallogr.* **2009**, *42*, 339–341. [CrossRef]

44. *ASTM G31-72;* Standard Practice for Laboratory Immersion Corrosion Testing of Metals. ASTM: West Conshohocken, PA, USA, 2004.
45. Cowieson, N.P.; Aragao, D.; Clift, M.; Ericsson, D.J.; Gee, C.; Harrop, S.J.; Mudie, N.; Panjikar, S.; Price, J.R.; Riboldi-Tunnicliffe, A.; et al. MX1: A Bending-Magnet Crystallography Beamline Serving Both Chemical and Macromolecular Crystallography Communities at the Australian Synchrotron. *J. Synchrotron Radiat.* **2015**, *22*, 187–190. [CrossRef] [PubMed]

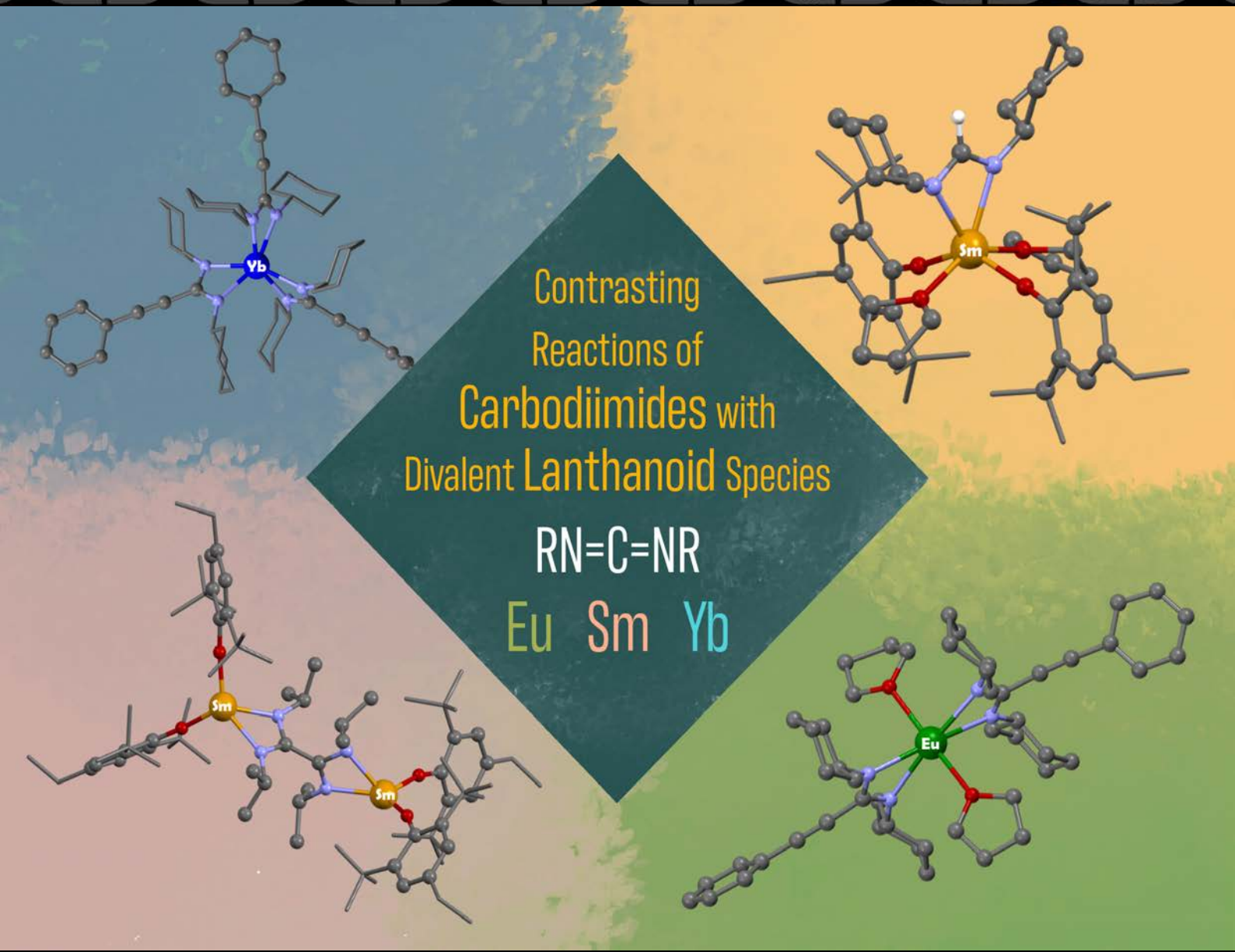
Disclaimer/Publisher's Note: The statements, opinions and data contained in all publications are solely those of the individual author(s) and contributor(s) and not of MDPI and/or the editor(s). MDPI and/or the editor(s) disclaim responsibility for any injury to people or property resulting from any ideas, methods, instructions or products referred to in the content.

Chemistry A European Journal

Chemistry Europe
European Chemical Societies Publishing

Celebrating 30 Years

Cover Feature:
P. C. Junk and co-workers
Contrasting Reactions of Carbodiimides with Divalent Lanthanoid Species



WILEY VCH

28/2025

Check for updates

Chemistry–A European Journal

Research Article
doi.org/10.1002/chem.202500759

Chemistry Europe
European Chemical Societies Publishing

www.chemeurj.org

Contrasting Reactions of Carbodiimides with Divalent Lanthanoid Species

Vidushi P. Vithana,[a] Zhifang Guo,[a] Glen B. Deacon,[b] and Peter C. Junk*[a]

Reactions of lanthanoid species with carbodiimides (RN = C = NR′) show considerable variety. Thus, treatment of the divalent 2,6-di-*tert*-butyl-4-ethylphenolatosamarium complex, $[Sm(OAr^{Et})_2(thf)_3]$·PhMe with *N*,*N*′-diisopropylcarbodiimide (*i*PrNCN*i*Pr) resulted in the formation of the oxalamidinatosamarium(III) complex $[(OArEt)_2Sm(\mu\text{-}C_2N_4iPr_4)Sm(OAr^{Et})_2]$·2PhMe (1). In contrast, the use of the bulkier *N*,*N*′-dicyclohexylcarbodiimide (CyNCNCy) led to the formation of a formamidinatosamarium(III) complex $[Sm(OAr^{Et})_2(CyNC(H)NCy)(thf)_2]$·2thf **(2)**. Reactions between rare earth metals (RE = Yb, Eu) with one molar equivalent of bis(phenylethynyl)mercury ($Hg(PhCC)_2$) and two molar equivalents of *N*,*N*′-dicyclohexylcarbodiimide (CyNCNCy) in tetrahydrofuran (thf) at room temperature yielded lanthanoid *C*-phenylethynylamidinate complexes, trivalent $[Yb^{III}\{CyNC(C{\equiv}CPh)NCy\}_3]$·2thf **(3)** and divalent $[Eu\{CyNC(C{\equiv}CPh)NCy\}_2(thf)_2]$ **(4)**. $[Sm(OAr^{Et})_2(thf)_3]$.PhMe was obtained from $SmI_2(thf)_2$ and the in situ generated potassium aryl oxide and is a five-coordinate monomer with a stereochemistry between trigonal bipyramidal and square pyramidal.

1. Introduction

Carbodiimides (RN═C═NR′) are important substrates in metal-based reactivity studies, leading to the formation of diverse range of coordination compounds with modified organic fragments.[1–6] These compounds serve as excellent building blocks for the synthesis of a wide range of complex organic compounds and are considered as one of the most important classes of nitrogen reagents due to their diverse chemical properties,[3,5–10] and are isoelectronic with CO_2.

Carbodiimide insertion into metal–carbon sigma bonds forms amidinato complexes and they have been utilized in lanthanoid metal coordination chemistry, offering a route to lanthanoid amidinates.[11–13] Guanidinates, introduced in 1970, also form through carbodiimide insertion, specifically into Ln—N bonds of lanthanoid amides, yielding low-valent lanthanoid species.[14–17] Reductive coupling of carbodiimides with low-valent metal complexes has provided an exciting and straightforward reaction method, leading to novel metallocycles. Organosamarium(II) complexes, in particular, are strong reducing agents that react with various unsaturated substrates, producing bimetallic complexes by reductive coupling reactions.[2,11,18–21]

In this study, contrasting reactions of unsaturated carbodiimide substrates (RN═C═NR′) with Ln^{II} aryloxides have been explored, offering a promising route to novel amidinatolanthanoid complexes. In addition, the reactivity of a carbodiimide with organolanthanoid alkynyl complexes generated by redox transmetallation, has been explored to examine insertion into Ln—C sigma bonds.

2. Results and Discussion

2.1. Synthesis

*2.1.1. Reactions of carbodiimides with samarium(II) Bis(2,6-di-*tert*-butyl-4-ethylphenolate)*

The reaction of $[Sm(OAr^{Et})_2(thf)_3]$·PhMe (preparation in Scheme 1) with an equivalent amount of *N*,*N*′-diisopropylcarbodiimide (*i*PrC═N═C*i*Pr) (DIC) in thf at room temperature resulted in the formation of the oxalamidinatosamarium(III) complex $[(OAr^{Et})_2Sm(\mu\text{-}C_2N_4iPr_4)Sm(OAr^{Et})_2]$·2PhMe (1). Substituting the diisopropylcarbodiimide with the bulkier *N*,*N*′-dicyclohexylcarbodiimide (CyC═N═CCy) (DCC) gave the formamidinatosamarium(III) complex $[Sm(OAr^{Et})_2(CyNC(H)NCy)]$·2thf (2) (Scheme 1). Furthermore, no evidence was found of competitive insertion of the carbodiimide into the Sm—O bond, probably owing to the oxophilicity of lanthanoids. The differing outcomes can be rationalized by 1 electron transfer to the carbodiimide forming a radical anion (species A in Scheme 1), which, for the less bulky carbodiimide, dimerizes to form the oxalamidinate ligand. The bulkier radical undergoes hydrogen abstraction from the solvent or reagents before dimerization can occur. H-abstraction from thf in

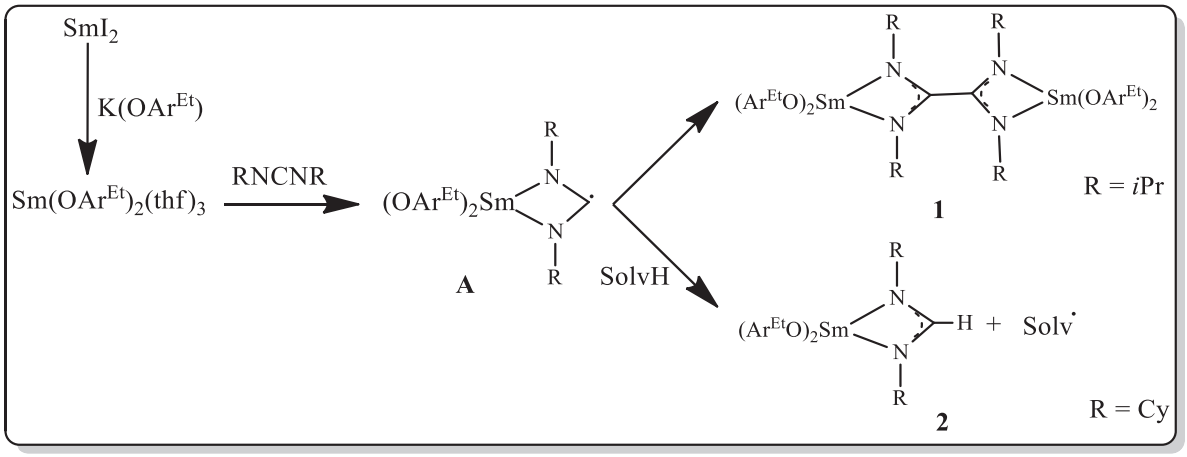
[a] *V. P. Vithana, Z. Guo, P. C. Junk*
College of Science & Engineering, James Cook University, Townsville, Queensland 4811, Australia
E-mail: peter.junk@jcu.edu.au

[b] *G. B. Deacon*
School of Chemistry, Monash University, Clayton, Victoria 3800, Australia

Supporting information for this article is available on the WWW under https://doi.org/10.1002/chem.202500759

© 2025 The Author(s). Chemistry – A European Journal published by Wiley-VCH GmbH. This is an open access article under the terms of the Creative Commons Attribution-NonCommercial-NoDerivs License, which permits use and distribution in any medium, provided the original work is properly cited, the use is non-commercial and no modifications or adaptations are made.

© 2025 The Author(s). Chemistry – A European Journal published by Wiley-VCH GmbH



Scheme 1. Proposed reaction pathways leading to the formation of oxalamidinate (1) and formamidinate (2) complexes via reduction of carbodiimides by $[Sm(OAr^{Et})_2(thf)_3]\cdot PhMe$.

lanthanoid chemistry has precedent.[22,23] This outcome is simpler than when H-abstraction occurs from the methine moiety of the diisopropyl group, which leads to coupling through the methine carbons.[2]

Fresh samples of compounds **1** and **2** gave satisfactory %Sm values, whilst microanalyses after transport to the UK showed loss of 1 toluene of crystallization and two thf of crystallization from the crystal composition of **1** and **2**, respectively. The solvent loss was also detected by ^{1}H NMR spectroscopy (see Section 6). **2** also gave a low %C, a common issue with rare-earth metal-organic compounds.[24–30] The ^{1}H NMR spectrum of **1** is shifted from the normal diamagnetic region due to the paramagnetic Sm^{III} ion. The spectrum of **1** is complex, with the *t*-butyl resonances appearing as three sharp singlets at −0.79, −0.64, and −0.42 ppm, integrating overall to 72 hydrogens. The isopropyl CH_3 protons, along with the CH_3 resonances from the ethyl substituent on the OAr^{Et} group, are spread over a wide chemical shift range of 0.30–2.04 ppm. Only one lattice toluene molecule is observed in the proton NMR spectrum (Figure S1). In the 1H NMR spectrum of complex **2**, signal broadening occurs due to the paramagnetic Sm^{III} ion, complicating assignment and integration, especially in the upfield region. A pronounced downfield shift is observed for the formamidinate backbone NC*H*N, which appears as a singlet at δ = 7.98 ppm. The singlet at δ = 8.15 ppm is assigned to the aromatic CH protons of the phenyl ring. Coordinated thf CH_2 signals are expected in the broad upfield region, but no lattice thf was detected in the proton NMR spectrum (Figure S2).

2.1.2. The one pot reactions of Ln metals with $Hg(PhCC)_2$ and N,N′-dicyclohexylcarbodiimide (CyNCNCy)

The reaction between an excess of rare earth metal, one molar equivalent of bis(phenylethynyl)mercury, and two molar equivalents of *N*,*N*′-dicyclohexylcarbodiimide (CyNCNCy) in tetrahydrofuran (thf) at room temperature gave amidinate complexes resulting from insertion of carbodiimide molecules into the Ln—C sigma bonds of Ln-CCPh species. The observed reactions are formulated in Scheme 2.

The reaction with Yb proceeds with the formation of yellow crystals of the homoleptic tris(amidinato) complex $[Yb^{III}\{CyNC(C{\equiv}CPh)NCy\}_3]\cdot 2thf$ (**3**). As the redox transmetallation between Yb metal and $Hg(CCPh)_2$ yields a divalent polymer $[Yb(CCPh)_2]_n$,[31] the oxidation state outcome is unexpected, and a divalent complex analogous to **4** was anticipated. The formation of **3** is explicable if the expected $[Yb(CyNC(C{\equiv}CPh)NCy)_2]$ is strongly reducing as it can then be oxidized by $Hg(CCPh)_2$ to give a trivalent alkynyl $[Yb(CyNC(C{\equiv}CPh)NCy)_2CCPh]$ into which a further carbodiimide can be inserted to give **3** (see Equations 1 and 2).

$$2\left[Yb\{CyNC(C{\equiv}CPh)NCy\}_2\right] + Hg(CCPH)_2 \longrightarrow 2\left[Yb\{CyNC(C{\equiv}CPh)NCy\}_2(CCPH)\right] + Hg \quad (1)$$

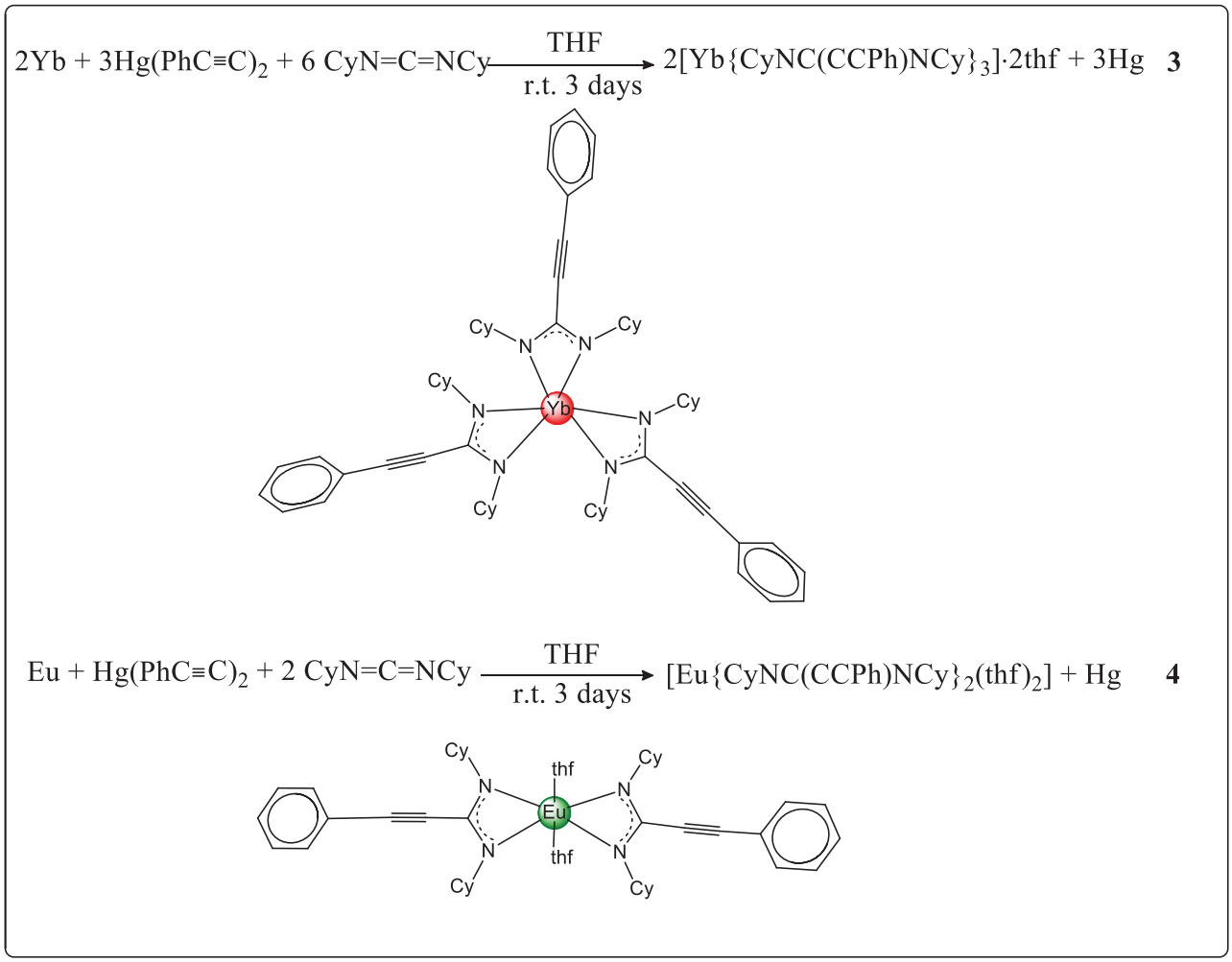
$$\left[Yb\{CyNC(C{\equiv}CPh)NCy\}_2(CCPH)\right] + CyN{=}C{=}NCy \longrightarrow \left[Yb\{CyNC(C{\equiv}CPh)NCy\}_3\right] \quad (2)$$

There is precedent for reaction (1) in that the divalent Sm complex $[Sm(DippForm)_2(thf)_2]$, (DippFormH = *N*,*N*′-bis(2,6-diisopropylphenyl)formamidine), reacts with bis(phenylethynyl)mercury to give $[Sm(DippForm)_2CCPh(thf)]$ with deposition of mercury metal.[23]

Elemental analyses of complexes **3** and **4** were consistent with the single crystal compositions. The ^{1}H NMR spectrum of **3** exhibited broadening and shifting of signals due to the paramagnetism of Yb^{III}, making assignment and integration challenging, particularly in the upfield region. The cyclohexyl protons appeared alongside an additional 2.5 equivalents of thf from the solution, spanning a range of 3.94–1.50 ppm. The crystals were highly moisture sensitive and had to be quickly removed from the solution to ensure stability for NMR analysis. As a result, they retained 20 hydrogen atoms from residual free thf. The aromatic CH protons of the phenyl group were observed as two distinct resonances, one at 13.79 ppm, while the rest appeared over a range of 7.43–6.73 ppm, along with protons from C_6D_6 solvent. A meaningful NMR spectrum could not be obtained for **4** because of paramagnetism. The most noteworthy features of the

© 2025 The Author(s). Chemistry – A European Journal published by Wiley-VCH GmbH

15213765, 2025, 28, Downloaded from https://chemistry-europe.onlinelibrary.wiley.com/doi/10.1002/chem.202500759 by James Cook University, Wiley Online Library on [21/05/2025]. See the Terms and Conditions (https://onlinelibrary.wiley.com/terms-and-conditions) on Wiley Online Library for rules of use; OA articles are governed by the applicable Creative Commons License



Scheme 2. Synthesis of **3** and **4**.

IR spectra of **3** and **4** are bands attributable to C≡C stretching at 2210–2120 cm^{-1}.[32] Bands observed around 1500–1650 cm^{-1} are assigned to delocalized C—N stretching vibrations.[33] The IR spectrum of **4** also displayed two distinct bands at 1043 and 886 cm^{-1}, corresponding to coordinated thf.[34]

Several attempts were made to extend the study of Yb and Eu with *N,N′*-diisopropylcarbodiimide to establish a direct comparison with the Sm system. Unfortunately, none of these reactions produced crystals suitable for x-ray crystallography after trying many methods and solvents, so further studies were not conducted. Likewise, the reaction of Sm metal with $Hg(CCPh)_2$ and either carbodiimide did not have a satisfactory outcome.

3. Molecular Structures

3.1. The complex $[(OAr^{Et})_2Sm(\mu\text{-}C_2N_4iPr_4)Sm(OAr^{Et})_2]\cdot 2PhMe$ (1)

Complex **1** crystallizes in the triclinic space group *P*-1, and the molecular structure adopts a diamidinate configuration. Each Sm atom is bound to opposing sides of the tetraisopropyloxalamidinate ($(iPr)_2N_2C\text{-}CN_2(iPr)_2^{2-}$) ligand, which functions as a bridging tetradentate ligand by chelating both Sm atoms

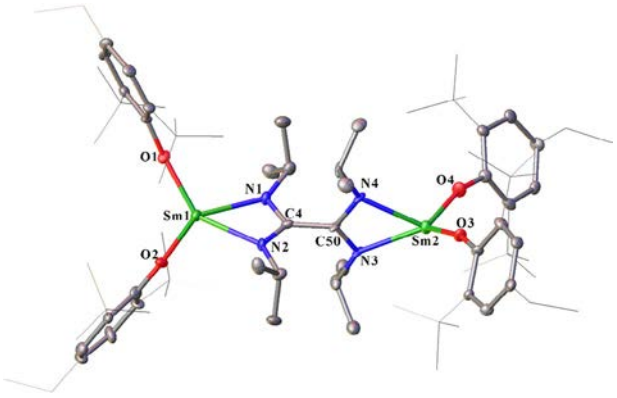


Figure 1. Molecular diagram of complex **1**. Hydrogen atoms and the two lattice toluene molecules are omitted for clarity. *Tert*-butyl and ethyl groups are drawn as wireframe for clarity. Selected bond lengths (Å): C4–C50 1.488(17), N1–C4 1.370(15), N2–C4 1.337(16), N4–C50 1.378(15), N3–C50 1.288(15), Sm1–N1 2.364(11), Sm1–N2 2.416(10), Sm2–N4 2.36(1), Sm2–N3 2.382(10), Sm1–O1 2.090(8), Sm1–O2 2.063(9), Sm2–O3 2.140(9), Sm2–O4 2.115(9).

(Sm1 and Sm2) through four nitrogen atoms (N1, N2, N3, N4) (Figure 1). Two OAr^{Et} ligands coordinate to each metal, giving the Sm atoms a coordination number of four (binding through

© 2025 The Author(s). Chemistry – A European Journal published by Wiley-VCH GmbH

15213765, 2025, 28, Downloaded from https://chemistry-europe.onlinelibrary.wiley.com/doi/10.1002/chem.202500759 by James Cook University, Wiley Online Library on [21/05/2025]. See the Terms and Conditions (https://onlinelibrary.wiley.com/terms-and-conditions) on Wiley Online Library for rules of use; OA articles are governed by the applicable Creative Commons License

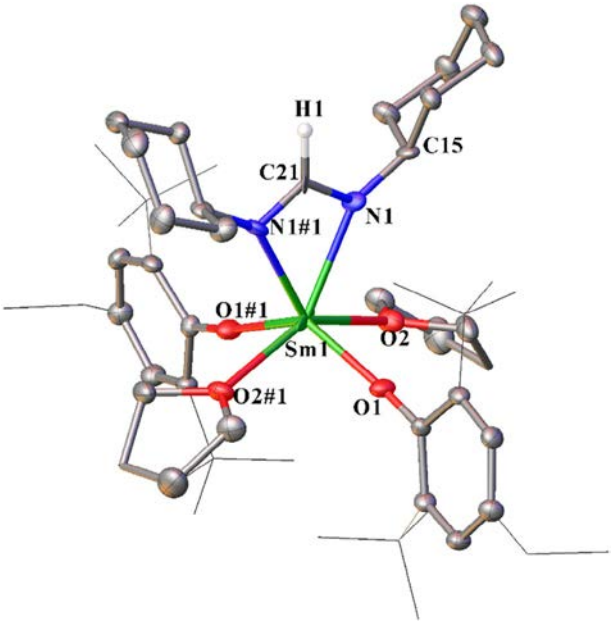


Figure 2. Molecular diagram of complex **2**. Hydrogen atoms (except for the hydrogen in the formamidinate fragment), as well as two lattice thf molecules are omitted for clarity. *Tert*-butyl and ethyl groups were drawn as wireframe for clarity.

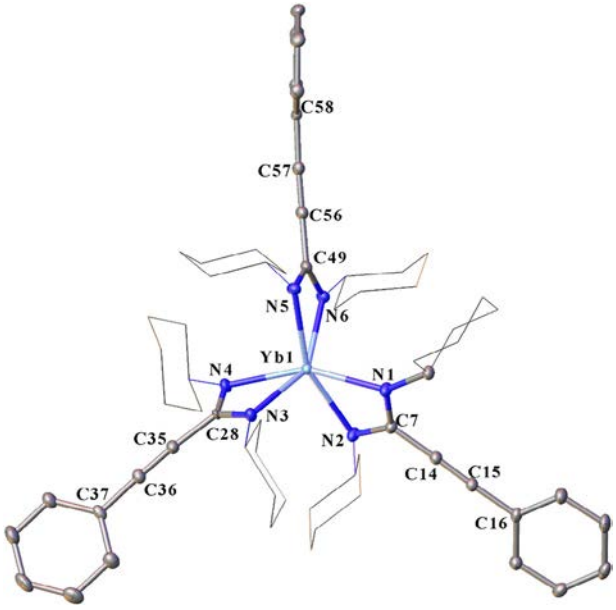


Figure 3. Molecular diagram of complex **3**. Hydrogen atoms along with two lattice thf molecules are omitted for clarity. Cyclohexyl rings were drawn as wireframe for clarity. Selected bond lengths (Å): Yb1–N1 2.3179(15), Yb1–N2 2.3366(15), Yb1–N3 2.3358(16), Yb1–N4 2.3236(15), Yb1–N5 2.3183(15), Yb1–N6 2.3224(15), N1–C7 1.334(2), N2–C7 1.328(2), N6–C49 1.332(2), N5–C49 1.332(2), N3–C28 1.317(2), N4–C28 1.350(2), C14–C15 1.193(3), C35–C36 1.196(3), C56–C57 1.194(3).

O1,O2 at Sm1 and O3,O4 at Sm2). Each metal atom adopts a pseudo–trigonal–planar geometry if the oxalamidinate ligands are considered point donors (through C4 and C50). The phenolate groups are positioned above and below the plane formed by the Sm, two nitrogen atoms, and one of the central carbon atoms of the oxalamidinate ligand, oriented to minimize interactions with the isopropyl groups.

The two planes formed by the atoms Sm1, N1, N2, C4 and Sm2, N3, N4, C50 are nearly perpendicular, with dihedral angle of 91.0(5)° between them while the trigonal planes are also approximately orthogonal (dihedral angle 85.3(3)°). This staggered arrangement minimizes interactions between the neighboring isopropyl groups. The central C—C bond length is characteristic of a single bond, while the C—N bond lengths in the C_2N_4 unit fall between typical single and double bond lengths, indicating electronically delocalized CN_2 units within the diamidinate moiety.

3.2. The complex [Sm(OAr^{Et})$_2$(CyNC(H)NCy)(thf)$_2$]·2thf (2)

The complex [Sm(OAr^{Et})$_2$CyNC(H)NCy)(thf)$_2$]·2thf crystallizes in the monoclinic $P2_1/c$ space group, containing half of the molecule in the asymmetric unit. Because of the quality of the structure, it is discussed only for connectivity. The samarium atom is six-coordinate, bonded to two OAr^{Et} ligands (through O1 and O1#1), two thf molecules (through O2 and O2#1), and two nitrogen atoms (through N1 and N1#1) from the chelating formamidinate fragment (Figure 2). The geometry around the samarium center is near pseudo square pyramidal, considering the $\kappa(N,N')$ formamidinate ligand as a single-point donor from the central carbon atom of the 1,3-diazaallyl unit. Despite the limitation of the crystallographic data, they still establish proof of concept of the synthetic utility of the reaction giving **2** (Scheme 1).

3.3. The complex [Yb^{III}{CyNC(C≡CPh)NCy}$_3$]·2thf (3)

The six coordinated complex **3** crystallizes in the triclinic *P-1* space group, adopting a pseudo-trigonal planar geometry if the phenylethynyl-substituted amidinate ligands are considered to be point donors located at the central carbon atoms. The complex has six nitrogen atoms from three $\kappa(N,N')$ amidinate CyNC(C≡CPh)NCy ligands, binding through N1,2, N3,4 and N5,6, which are arranged in a three-vane propeller configuration. The C≡CPh groups, bound to the carbon atom of the CyNCNCy backbone are linear, with the Ph group positioned furthest from the metal (Figure 3).

The C—N bond lengths in the amidinate groups are nearly equivalent and significantly shorter than typical C—N single bonds,[35] suggesting that the π electrons of the C═N double bonds are delocalized across the N—C—N unit. The Yb—N distances of Cy-substituted nitrogen atoms fall between the typical Yb—N single bond lengths and donor N:→ Yb bond lengths, which range from 2.19–2.69 Å.[16,36–38] In particular, they are similar to but marginally shorter than those (2.328(4)–2.354(5)Å)[23] of six coordinate [Yb(EtForm)$_3$].2thf (EtForm = *N,N'*-bis(2,6-diethylphenyl)formamidinate), suggesting comparable steric demands between the present amidinate ligand and the bulky fomamidinate EtForm. The C≡C bond lengths are close to those (1.204(2) and 1.206(2) Å) of diphenylacetylene.[39]

© 2025 The Author(s). Chemistry – A European Journal published by Wiley-VCH GmbH

15213765, 2025, 28, Downloaded from https://chemistry-europe.onlinelibrary.wiley.com/doi/10.1002/chem.202500759 by James Cook University, Wiley Online Library on [21/05/2025]. See the Terms and Conditions (https://onlinelibrary.wiley.com/terms-and-conditions) on Wiley Online Library for rules of use; OA articles are governed by the applicable Creative Commons License

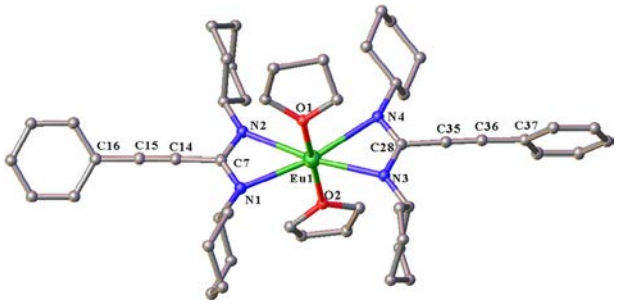


Figure 4. Molecular diagram of complex **4**. Hydrogen atoms are omitted for clarity. Selected bond lengths (Å): Eu1–O1 2.535(5), Eu1–O2 2.538(5), Eu1–N1 2.546(5), Eu1–N2 2.611(6), Eu1–N3 2.520(6), Eu1–N4 2.616(5), N1–C7 1.312(9), N2–C7 1.328(8), N3–C28 1.331(8), N4–C28 1.315(8), C14–C15 1.188(8), C35–C36 1.189(8).

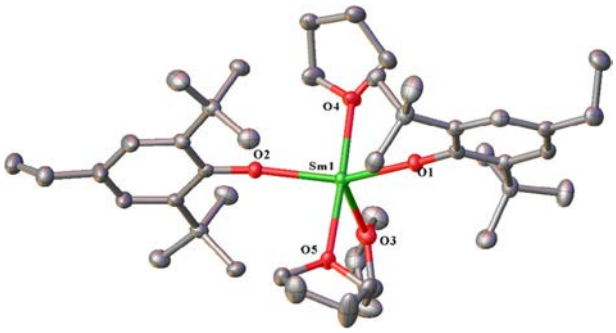


Figure 5. Molecular diagrams of $[Sm(OAr^{Et})_2(thf)_3]$·PhMe. Hydrogen atoms and lattice solvents are omitted for clarity. Selected bond lengths (Å): Sm1–O1 2.3202(15), Sm1–O2 2.3351(15), Sm1–O3 2.5434(18), Sm1–O4 2.5618(16), Sm1–O5 2.5833(16).

3.4. The complex $[Eu\{CyNC(C{\equiv}CPh)NCy\}_2(thf)_2]$ (4)

Complex **4** crystallizes in the monoclinic system, space group $P2_1/c$. The molecular structure is depicted in Figure 4. In the monomeric complex, the Eu atom is six-coordinate, with four N atoms from chelating amidinates fragments (binding through N1,2 and N3,4) coordinating in a κ-*N,N′*-fashion and two *trans*-thf donor molecules (O1 and O2; O1-Eu-O2 174.7(2)°). The coordination geometry is pseudo–square planar, when regarding the κ-*N,N′*-amidinate CyNC(C≡CPh)NCy ligands occupying a single coordination site at the central carbon atoms (C7 and C28) of the NCN fragments. The europium—nitrogen bond lengths in complex **4** are longer than those in complex **3** by 0.25 Å, which is less than the 0.30 Å expected from the ionic radius difference between six coordinate Eu^{2+} and six coordinate Yb^{3+}.[40] This implies greater crowding in **3** than expected for the reduction in size. As for **3,** the C≡C bond lengths are near those of diphenylacetylene.[39]

3.5. The structure of $[Sm(OAr^{Et})_2(thf)_3]$·PhMe

The structure of the reactant aryl oxide, prepared by metathesis from $SmI_2(thf)_2$, was also determined. It crystallizes in the monoclinic space group $P2_1/c$ as a monomeric five coordinate (low coordination number) complex, analogous to several $[Ln(OAr^{Me})_2(thf)_3]$ (Ln = Sm, Eu, Yb; OAr^{Me} = 2,6-di-*tert*-butyl-4-methylphenolate) complexes,[41–44] and isomorphous with $[Sm(OAr^{OMe})_2(thf)_3]$.thf (OAr^{OMe} = 2,6-di-*tert*-butyl-4-methoxyphenolate),[45] despite the different 4-substitutent (though similar chain length) and solvent of crystallization (Figure 5). The Reedijk parameter[46] is 0.54 indicating a stereochemistry essentially midway between square pyramidal and trigonal bipyramidal, but just favoring the latter. The Sm—O bond lengths are comparable with those of the isomorph.[45]

4. Conclusions

The divalent samarium bis(phenoxide) complex $[Sm(OAr^{Et})_2(thf)_3]$·PhMe exhibits differing reductive reactivity with carbodiimides, depending on steric factors, and not insertion into the Sm—O bonds. With the less bulky *N,N′*-bis(diisopropylcarbodiimide), one electron reduction and coupling yields a bimetallic oxalamidinatosamarium(III) complex **1**, whereas the bulkier *N,N′*-dicyclohexylcarbodiimide gives the mononuclear formamidinatosamarium(III) complex 2. On the other hand, insertion reactions dominate on reaction of bis(phenylethynyl)lanthanoid(II) species, $Ln(CCPh)_2$ (Ln = Eu, Yb), generated in situ from Ln metal and $Hg(CCPh)_2$, with *N,N′*-dicyclohexylcarbodiimide. Whilst $Eu(CCPh)_2$, gives a divalent C-phenylethynylamidinate, $[Eu\{CyNC(C{\equiv}CPh)NCy\}_2(thf)_2]$ **(4)**, the ytterbium analogue yields trivalent $[Yb^{III}\{CyNC(C{\equiv}CPh)NCy\}_3]\cdot 2thf$ **(3)**. Since the redox transmetallation between Yb metal and $Hg(CCPh)_2$ is known to yield divalent $Yb(CCPh)_2$, an additional oxidation and insertion step must be involved in the current reaction. Thus, carbodiimide reactions with divalent lanthanoid species provide a wide variety of outcomes.

5. Experimental Section

5.1. General

The compounds prepared in this work are extremely sensitive to air and moisture, and all manipulations were performed under a nitrogen atmosphere using vacuum–nitrogen line techniques, and a glove box with purified nitrogen, ensuring rigorous exclusion of air and water. Lanthanoid metals were obtained from Molycorp or Eutectix. Large chunks were filed in the drybox before use. Solvents (thf, C_6D_6, toluene) were pre-dried by distillation over sodium or sodium benzophenone ketyl and stored under a nitrogen atmosphere over 4 Å molecular sieves.

The following reagents were commercially available and used without further purification: 2,6-di-*tert*-butyl-4-ethylphenol ($HOAr^{Et}$), 1,2-diiodoethane, *N,N″*-dicyclohexylcarbodiimide (DCC) and *N,N″*-diisopropylcarbodiimide (DIC). Bis(phenylethynyl)mercury[47] and $SmI_2(thf)_2$[48] were prepared using literature methods. Infrared spectra (4000–400 cm^{-1}) were obtained as Nujol mulls between NaCl plates with a Nicolet iS FTIR spectrometer. ^1H spectra were recorded on a Bruker 400 MHz instrument, with chemical shifts referenced against residual solvent peaks. Microanalyses were conducted by the Elemental Analysis Service, London Metropolitan University, with all samples sealed in tubes under nitrogen before transport. Metal

© 2025 The Author(s). Chemistry – A European Journal published by Wiley-VCH GmbH

15213765, 2025, 28, Downloaded from https://chemistry-europe.onlinelibrary.wiley.com/doi/10.1002/chem.202500759 by James Cook University, Wiley Online Library on [21/05/2025]. See the Terms and Conditions (https://onlinelibrary.wiley.com/terms-and-conditions) on Wiley Online Library for rules of use; OA articles are governed by the applicable Creative Commons License

analyses were performed by using EDTA titrations with xylenol orange as the indicator, following acid digestion and buffering with hexamethylenetatramine. Melting points were determined in sealed glass capillaries under nitrogen and are uncalibrated.

CCDC 2426980 for compound **1**, 2426981–2426982 for compounds **3** and **4**, 2426983 for compound $[Sm(OAr^{Et})_2(thf)_3]\cdot PhMe$, contain the supplementary crystallographic data for this paper. These data can be obtained free of charge from The Cambridge Crystallographic Data Centre via www.ccdc.cam.ac.uk/data_request/cif.

5.2. Syntheses

5.2.1. $[(OAr^{Et})_2Sm(\mu\text{-}C_2N_4iPr_4)Sm(OAr^{Et})_2]\cdot 2PhMe$ (1)

A solution of *N,N′*-di-isopropyl-carbodiimide (0.16 mL, 1.00 mmol) in toluene (10 mL) was added with stirring at room temperature to a dark red solution of $[Sm(OAr^{Et})_2(thf)_3]\cdot PhMe$ (0.926 g, 1.00 mmol) in toluene. The color gradually changed to light yellow, and the mixture was stirred continuously for 3 days. The resulting solution was filtered using a filtration cannula and concentrated in vacuo to approximately 10 mL and stored at −25°C for 1 week, to yield light-yellow crystals. Yield: 0.43 g (51%). m.p. 138–140 °C (dec.). Elemental analysis calculated (%) for $C_{92}H_{144}N_4O_4Sm_2$ (MW: 1670.87 $gmol^{-1}$): on fresh crystals Sm 17.99; found (%) Sm 17.26. Microanalysis (after transport to London) calculated (%) for $C_{85}H_{136}N_4O_4Sm_2$ (MW 1578.77 $gmol^{-1}$, loss of 1 PhMe of crystallization) C 64.67, H 8.68, N 3.55 Found (%) C 65.00; H 8.86; N 3.74. IR (Nujol, cm^{-1}): 3064w, 2116s, 1758 m, 1643 m, 1604 m, 1571 m, 1495w, 1383 m, 1350 m, 1326w, 1311w, 1169w, 1140w, 1121s, 1081w, 1060w, 1009s, 910s, 891s, 874s, 832s, 795s, 781w, 764 m, 729s, 694s, 639w, 535w. ^1H NMR (400 MHz, C_6D_6, 25°C, ppm): δ = 8.05–8.48 (m, 8H, C_6H_2), 7.05 (m, 5H, ArH-toluene), 3.15–3.40 (m, 8H, CH_2), 2.58 (m, 4H, CH), 2.11 (m, 3H, CH_3-toluene), 0.3–2.04 (m, 36H, CH_3-Et, *i*Pr), −0.42–0.79 (m, 72H, CH_3-*t*Bu) with one lattice PhMe lost.

5.2.2. $[Sm(OAr^{Et})_2(CyNC(H)NCy)(thf)_2]\cdot 2thf$ (2)

A solution of *N,N′*-dicyclohexylcarbodiimide (DCC) (0.10 g, 0.48 mmol) in thf (10 mL) was added with stirring at room temperature to a dark red solution of $[Sm(OAr^{Et})_2(thf)_3]\cdot PhMe$ (0.30 g, 0.48 mmol) in thf. The color gradually changed to light yellow, and the mixture was stirred continuously for 3 days. The resulting solution was filtered using a filtration cannula and concentrated in vacuo to approximately 10 mL and stored at −25°C for 1 week, to yield light-yellow crystals. Yield: 0.16 g (30%). m.p. 110°C (dec.). Elemental analysis calculated (%) for $C_{61}H_{105}N_2O_6Sm$ (MW: 1112.85 $gmol^{-1}$): on fresh crystals Sm 13.51; found (%) Sm 13.60. Microanalysis (after transport to London) calculated (%) for $C_{53}H_{89}N_2O_4Sm$ (MW 968.67 $gmol^{-1}$, loss of 2 thf of crystallization): C 65.72; H 9.26; N 2.89. Found (%) C 64.07; H 8.99; N 2.97. IR (Nujol, cm^{-1}): 2120s, 1753w, 1640s, 1604w, 1544s, 1459 m, 1419 m, 1384 m, 1358w, 1325 m, 1259 m, 1234 m, 1212w, 1158w, 1120 m, 1072 m, 1024w, 910w, 890w, 873 m, 821s, 793s, 721w. ^1H NMR (400 MHz, C_6D_6, 25°C, ppm): Satisfactory integrations could not be obtained (see Figure S2). δ = 8.15 (s, 4H, ArH), 7.98 (s, 1H, NC*H*N), 3.16–0.70 (m, CH_3-*t*Bu, CH_3-Et, CH_2-Et, CyNCNCy Hs overlapped by CH_2-thf resonance) with both lattice thf lost.

5.2.3. General procedure for 3 and 4

A Schlenk flask was charged with $Hg(PhCC)_2$ (0.605 g, 1.5 mmol) and excess Yb metal filings (0.52 g, 3.0 mmol) **(3)**/Eu metal filings (0.455 g, 3.0 mmol) **(4)**, followed by *N,N′*-dicyclohexylcarbodiimide (DCC) (0.619 g, 3.0 mmol) added inside a drybox. Anhydrous thf (15 mL) was then added and stirred at room temperature for 3 days. After allowing the unreacted lanthanoid metal and mercury suspension to settle, the supernatants were filtered using a filtration cannula. The resulting solutions were concentrated in vacuo to approximately 10 mL and left to stand at room temperature to crystallize.

5.2.4. $[Yb\{CyNC(C{\equiv}CPh)NCy\}_3]\cdot 2thf$ (3)

Yellow crystals (0.80 g, 64%); m.p. 195°C–200°C. Elemental analysis for $C_{71}H_{97}N_6O_2Yb$ (MW: 1239.61 $gmol^{-1}$): Calculated (%) C 68.79; H 7.89; N 6.78; Yb 13.96; Found (%) C 68.58; H 7.95; N 6.85; Yb 13.72. IR (Nujol, cm^{-1}): 2666w, 2209s, 1968w, 1947w, 1897w, 1877w, 1799w, 1750w, 1671 m 1597 m, 1573 m, 1558w, 1311w, 1257s, 1245s, 1191s, 1171s, 1137s, 1073s, 1026 m, 995s, 964w, 913s, 898s, 887s, 843s, 805 m, 755s, 722w, 702 m, 688s, 676w, 628s, 529w. ^1H NMR (400 MHz, C_6D_6, 25°C, ppm): δ = 13.79 (s, 3H, ArH), 7.43–6.73 (m, ArH overlap with C_6D_6), 3.94–1.50 (m, 86H, 60 CH_2-CyNCNCy, 6 CH- CyNCNCy, 20 thf), −0.20 (s, 8H, CH_2-thf), -13.80 (s, 8H, CH_2-thf).

5.2.5. $[Eu\{CyNC(C{\equiv}CPh)NCy\}_2(thf)_2]$ (4)

Red crystals (0.51 g, 56%); m.p. 133°C–135°C. Elemental analysis for $C_{50}H_{70}EuN_4O_2$ (MW: 911.08 $gmol^{-1}$): calculated (%) C 65.91; H 7.74; N 6.15; Eu 16.68; found (%) C 65.22; H 7.97; N 6.03 Eu 15.90. IR (Nujol, cm^{-1}): 2122s, 1953 m, 1883w, 1757w, 1686w, 1655w, 1596 m, 1572w, 1560w, 1545 m, 1379w, 1356w, 1319w, 1303w, 1256s, 1240w, 1165s, 1126 m, 1110 m, 1070s, 1043s, 991 m, 915s, 886s, 843 m, 796 m, 756s, 721w, 691s, 670s, 615s, 592 m, 526w.

5.2.6. $[Sm(OAr^{Et})_2(thf)_3]\cdot PhMe$

Under a N_2 atmosphere, tetrahydrofuran (30 mL) was distilled onto 2,6-di-*tert*-butyl-4-ethylphenol ($HOAr^{Et}$) (2.3438 g, 10.0 mmol) and excess potassium (0.44 g, 11.0 mmol). After 4 h, this solution was directly filtered and added dropwise to a deep blue solution of $[Sm(I)_2(thf)_2]$ (2.74 g, 5.0 mmol), in tetrahydrofuran (20 mL). The resulting deep red solution was stirred overnight. The solution was then evaporated to dryness, dissolved in toluene (30 mL) and stirred for 1 h. Filtration, followed by removal of all volatiles in vacuo, yielded a red powder, which was subsequently extracted into toluene (10 mL) and left at −25°C for several days to produce deep red crystals. Yield: 2.04 g (66%). m.p. 190°C (dec.). Elemental analysis calculated (%) for $C_{51}H_{82}O_5Sm$ (MW: 925.55 $gmol^{-1}$): on fresh crystals Sm 16.99; found (%) Sm 16.24. Microanalysis (after transport to London) calculated (%) for $C_{32}H_{50}O_2Sm$ (MW 617.10 $gmol^{-1}$, loss of 3 thf and 1 PhMe): C 62.28; H 8.17. Found (%) C 60.78; H 8.39. IR (Nujol, cm^{-1}): 1757 m, 1603 m, 1559w, 1544w, 1495w, 1459s, 1418s, 1379s, 1346 m, 1324s, 1260s, 1234s, 1212 m, 1120 m, 1083w, 1031s, 910 m, 874s, 821s, 793s, 729s, 696s, 664w. ^1H NMR (400 MHz, C_6D_6, 25°C, ppm): δ = 8.14 (s, 4H, $H_{3,5}(OAr^{Et})$), 7.11 (m, 5H, CH(toluene)), 3.17(q, 4H, $CH_2(OAr^{Et})$), 2.50 (m, 2H, CH_2-thf), 2.12 (m, 3H, CH_3(Toluene)), 1.78 (t, 6H, $CH_3(OAr^{Et})$), 1.40 (s, 6H, $C(CH_3)_3(OAr^{Et})$), 0.86 (s, 30H, $C(CH_3)_3(OAr^{Et})$), −0.93 (m, 2H, CH_2-thf) with 2.5 thf lost.

Acknowledgments

GBD and PCJ gratefully acknowledge the ARC for funding (DP230100112).

© 2025 The Author(s). Chemistry – A European Journal published by Wiley-VCH GmbH

15213765, 2025, 28, Downloaded from https://chemistry-europe.onlinelibrary.wiley.com/doi/10.1002/chem.202500759 by James Cook University, Wiley Online Library on [21/05/2025]. See the Terms and Conditions (https://onlinelibrary.wiley.com/terms-and-conditions) on Wiley Online Library for rules of use; OA articles are governed by the applicable Creative Commons License

Open access publishing facilitated by James Cook University, as part of the Wiley - James Cook University agreement via the Council of Australian University Librarians.

Conflicts of Interest

The authors declare no conflict of interest.

Data Availability Statement

The data that support the findings of this study are available from the corresponding author upon reasonable request.

Keywords: aryloxide · carbodiimide · insertion · lanthanoids · redox transmetallation · reductive coupling

[1] M. F. Lappert, B. Prokai, *Advances in Organometallic Chemistry*, Vol. 5, 1st ed., Academic Press, New York, **1967**.
[2] G. B. Deacon, C. M. Forsyth, P. C. Junk, J. Wang, *Inorg. Chem.* **2007**, *46*, 10022.
[3] L. Yang, Y. Qu, J. Wang, W. Xu, Y. Zhao, X. J. Yang, *Chem.-Eur. J.* **2023**, *29*, e202301266.
[4] J. Louie, *Curr. Org. Chem.* **2005**, *9*, 605.
[5] Y. Wang, W. X. Zhang, Z. Xi, *Chem. Soc. Rev.* **2020**, *49*, 5810.
[6] Z. Li, R. J. Mayer, A. R. Ofial, H. Mayr, *J. Am. Chem. Soc.* **2020**, *142*, 8383.
[7] L. Xu, W. X. Zhang, Z. Xi, *Organometallics* **2015**, *34*, 1787.
[8] C. Alonso-Moreno, F. Carrillo-Hermosilla, A. Garcés, A. Otero, I. López-Solera, A. M. Rodríguez, A. Antiñolo, *Organometallics* **2010**, *29*, 2789.
[9] F. Zeng, H. Alper, *Org. Lett.* **2010**, *12*, 1188.
[10] R. T. Yu, T. Rovis, *J. Am. Chem. Soc.* **2008**, *130*, 3262.
[11] M. L. Cole, G. B. Deacon, C. M. Forsyth, P. C. Junk, D. P. Ceron, J. Wang, *Dalton Trans.* **2010**, *39*, 6732.
[12] J. Zhang, R. Ruan, Z. Shao, R. Cai, L. Weng, X. Zhou, *Organometallics.* **2002**, *21*, 1420.
[13] F. T. Edelmann, *Adv. Organomet. Chem.* **2008**, *57*, 183.
[14] G. Chandra, A. D. Jenkins, M. F. Lappert, R. C. Srivastava, *J. Chem. Soc. A* **1970**, 2550.
[15] C. Pi, Z. Zhang, Z. Pang, J. Zhang, J. Luo, Z. Chen, L. Weng, X. Zhou, *Organometallics* **2007**, *26*, 1934.
[16] J. Zhang, R. Cai, L. Weng, X. Zhou, *J. Organomet. Chem.* **2003**, *672*, 94.
[17] A. A. Trifonov, D. M. Lyubov, E. A. Fedorova, G. G. Skvortsov, G. K. Fukin, Y. A. Kurskii, M. N. Bochkarev, G. A. Razuvaev, *Russ. Chem. Bull.* **2006**, *55*, 435.
[18] W. J. Evans, J. W. Grate, I. Bloom, W. E. Hunter, J. L. Atwood, *J. Am. Chem. Soc.* **1985**, *107*, 105.
[19] W. J. Evans, R. A. Keyer, J. W. Ziuer, *J. Organomet. Chem.* **1990**, *394*, 87.
[20] Z. Hou, A. Fujita, Y. Zhang, T. Miyano, H. Yamazaki, Y. Wakatsuki, **1998**, *120*, 754.
[21] M. Deng, Y. Yao, Y. Zhang, Q. Shen, *ChemComm* **2004**, 2742.
[22] G. B. Deacon, A. J. Koplick, W. D. Raverty, D. G. Vince, *J. Organomet. Chem.* **1979**, *182*, 121.
[23] M. L. Cole, G. B. Deacon, C. M. Forsyth, P. C. Junk, K. Konstas, J. Wang, *Chem.-Eur. J.* **2007**, *13*, 8092.
[24] M. Salehisaki, N. E. Rad, G. B. Deacon, J. Wang, Z. Guo, P. C. Junk, *Inorg. Chim. Acta* **2022**, *539*, 120997.
[25] G. J. Moxey, A. J. Blake, W. Lewis, D. L. Kays, *Eur. J. Inorg. Chem.* **2015**, 5892.
[26] R. P. Kelly, T. D. M. Bell, R. P. Cox, D. P. Daniels, G. B. Deacon, F. Jaroschik, P. C. Junk, X. F. Le Goff, G. Lemercier, A. Martinez, J. Wang, D. Werner, *Organometallics* **2015**, *34*, 5624.
[27] H. Sitzmann, T. Dezember, O. Schmitt, F. Weber, G. Wolmershäuser, M. Ruck, *Z. Anorg. Allg. Chem.* **2000**, *626*, 2241.
[28] L. H. J. Lajunen, G. R. Choppin, *Rev. Anal. Chem.* **1989**, *9*, 91.
[29] D. P. Daniels, G. B. Deacon, D. Harakat, F. Jaroschik, P. C. Junk, *Dalton Trans.* **2012**, *41*, 267.
[30] L. Hirneise, C. Maichle-Mössmer, R. Anwander, *Inorg. Chem.* **2021**, *60*, 18211.
[31] G. B. Deacon, A. J. Koplick, T. D. Tuong, *Aust. J. Chem.* **1982**, *35*, 941.
[32] L. J. Bellamy, *The Infrared Spectra of Complex Molecules*, *Advances in Infrared Group Frequencies*, Vol. 2, Chapman & Hall, London, **1968**.
[33] J. D. Wilkins, *J. Organomet. Chem.* **1974**, *80*, 349.
[34] Lewis, J., Miller, J. R., Richards, R. L., Thompson, A., *J. Chem. Soc.* **1965**, 5850.
[35] F. H. Allen, O. Kennard, D. G. Watson, L. Brammer, A. G. Orpen, R. Taylor, *J. Chem. Soc., Perkin Trans. 2* **1987**, S1.
[36] W. J. Evans, D. K. Drummond, L. R. Chamberlain, R. J. Doedens, S. G. Bott, H. Zhang, J. L. Atwood, *J. Am. Chem. Soc.* **1988**, *110*, 4983.
[37] X.-G. Zhou, Z.-E. Huang, R.-F. Cai, L.-X. Zhang, X.-F. Hou, X.-J. Feng, X.-Y. Huang, *J. Organomet. Chem.* **1998**, *563*, 101.
[38] X. G. Zhou, Z. E. Huang, R. F. Cai, L. B. Zhang, L. X. Zhang, X. Y. Huang, *Organometallics* **1999**, *18*, 4128.
[39] R. Thomas, S. Lakshmi, S. K. Pati, G. U. Kulkarni, *J. Phys. Chem. B* **2006**, *110*, 24674.
[40] R. D. Shannon, *Acta Crystallogr., Sect. A* **1976**, *32*, 751.
[41] J. R. van den Hende, P. B. Hitchcock, S. A. Holmes, M. F. Lappert, W.-P. Leung, T. C. W. Mak, S. Prashar, *Dalton Trans.* **1995**, 1427.
[42] G.-Z. Qi, Q. Shen, Y.-H. Lin, *Acta Crystallogr., Sect. C* **1994**, *50*, 1456.
[43] G. B. Deacon, P. B. Hitchcock, S. A. Holmes, M. F. Lappert, P. MacKinnon, R. H. Newnham, *J. Chem. Soc., Chem. Commun.* **1989**, 935.
[44] S. Beaini, G. B. Deacon, M. Hilder, P. C. Junk, D. R. Turner, *Eur. J. Inorg. Chem.* **2006**, *2006*, 3434.
[45] G. B. Deacon, G. D. Fallon, C. M. Forsyth, S. C. Harris, P. C. Junk, B. W. Skelton, A. H. White, *Dalton Trans.* **2006**, 802.
[46] A. W. Addison, T. N. Rao, J. Reedijk, J. van Rijn, G. C. Verschoor, *Dalton Trans.* **1984**, 1349.
[47] B. G. Eglinton, W. Mccrae, *J. Chem. Soc.* **1963**, 2295.
[48] P. Girard, J. L. Namy, B. Kagan, *J. Am. Chem. Soc.* **1980**, *102*, 2693.

Manuscript received: February 26, 2025
Revised manuscript received: March 19, 2025
Version of record online: April 9, 2025

© 2025 The Author(s). Chemistry – A European Journal published by Wiley-VCH GmbH

15213765, 2025, 28, Downloaded from https://chemistry-europe.onlinelibrary.wiley.com/doi/10.1002/chem.202500759 by James Cook University, Wiley Online Library on [21/05/2025]. See the Terms and Conditions (https://onlinelibrary.wiley.com/terms-and-conditions) on Wiley Online Library for rules of use; OA articles are governed by the applicable Creative Commons License